The Anatomy of Electro–Weak Symmetry Breaking

Tome II: The Higgs bosons in the Minimal Supersymmetric Model

ABDELHAK DJOUADI
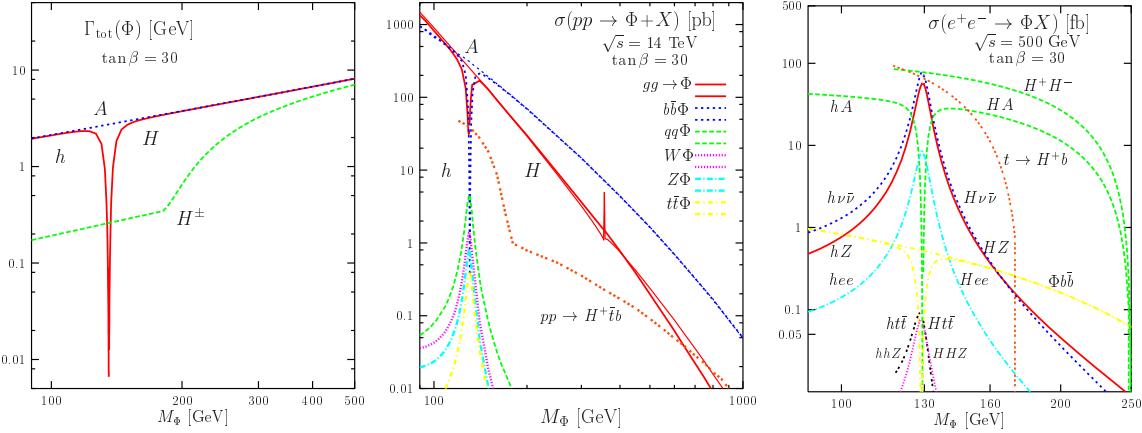
Laboratoire de Physique Théorique d'Orsay, UMR8627–CNRS,
Université Paris–Sud, Bât. 210, F–91405 Orsay Cedex, France.

Laboratoire de Physique Mathématique et Théorique, UMR5825–CNRS,
Université de Montpellier II, F–34095 Montpellier Cedex 5, France.

E–mail : Abdelhak.Djouadi@cern.ch

Abstract

The second part of this review is devoted to the Higgs sector of the Minimal Supersymmetric Standard Model. The properties of the neutral and charged Higgs bosons of the extended Higgs sector are summarized and their decay modes and production mechanisms at hadron colliders and at future lepton colliders are discussed.

The total decay widths of the neutral and charged MSSM Higgs bosons and their production cross sections at the LHC and at a 500 GeV e^+e^- collider in the main channels.

Contents

Préambule

Virtues of low energy Supersymmetry

Despite its enormous success in describing almost all known experimental data available today [1,2], the Standard Model (SM) of the strong and electroweak interactions of elementary particles [3,4], which incorporates the Higgs mechanism for the generation of the weak gauge boson and fermion masses [5], is widely believed to be an effective theory valid only at the presently accessible energies. Besides the fact it does not say anything about the fourth fundamental force of Nature, the gravitational force, does not explain the pattern of fermion masses, and in its simplest version does even not incorporate masses for the neutrinos, it has at least three severe problems which call for New Physics:

– The model is based on $SU(3)_C \times SU(2)_L \times U(1)_Y$ gauge symmetry, the direct product of three simple groups with different coupling constants and, in this sense, does not provide a true unification of the electroweak and strong interactions. Therefore, one expects the existence of a more fundamental Grand Unified Theory (GUT), which describes the three forces within a single gauge group, such as $SU(5)$ or $SO(10)$, with just one coupling constant [6–8]. However, given the high–precision measurements at LEP and elsewhere [1, 2] and the particle content of the SM, the renormalization group evolution of the gauge coupling constants is such that they fail to meet at a common point, the GUT scale [9]. This is the [gauge coupling] unification problem.

– It is known for some time [10, 11] that there is present a large contribution of non–baryonic, non–luminous matter to the critical density of the Universe, and several arguments point toward the fact that this matter should be non–relativistic. More recently, the WMAP satellite measurements in combination with other cosmological data, have shown that this cold Dark Matter (DM) makes up $\approx 25\%$ of the present energy of the Universe [12]. A particle that is absolutely stable, fairly massive, electrically neutral and having only very weak interactions is thus required [11]. The SM does not include any candidate particle to account for such a Dark Matter component.

– In the SM, when calculating the radiative corrections to the Higgs boson mass squared, one encounters divergences quadratic in the cut–off scale Λ beyond which the theory ceases to be valid and New Physics should appear [13]. If we choose the cut–off Λ to be the GUT scale, the mass of the Higgs particle which is expected, for consistency reasons, to lie in the range of the electroweak symmetry breaking scale, $v \sim 250$ GeV, will prefer to be close to the very high scale unless an unnatural fine adjustment of parameters is performed. This is what is called the naturalness or fine–tuning problem [14]. A related issue, called the hierarchy problem, is why $\Lambda \gg v$, a question that has no satisfactory answer in the SM.

Supersymmetry (SUSY), which predicts the existence of a partner to every known par-

ticle which differs in spin by $\frac{1}{2}$, is widely considered as the most attractive extension of the Standard Model. Firstly, Supersymmetry has many theoretical virtues [15–18]: it is the first non–trivial extension of the Poincaré group in quantum field theory, incorporates gravity if the Supersymmetry is made local and appears naturally in Superstrings theories. These features may help to reach the goal of elementary particle physics: the final theory of all known interactions, including gravity. However, the most compelling arguments for Supersymmetry are phenomenological ones. When they are realized at low energies [19, 20], softly–broken SUSY theories can simultaneously solve all the three problems of the SM mentioned above:

– The new SUSY particle spectrum contributes to the renormalization group evolution of the three gauge coupling constants and alters their slopes so that they meet [modulo a small discrepancy that can be accounted for by threshold contributions] at an energy scale slightly above 10^{16} GeV [9, 21]. It happens that this value of M_{GUT} is large enough to prevent a too fast decay of the proton, as is generally the case with the particle content of the SM when only the unification of the two electroweak couplings is required [22].

– In minimal supersymmetric extensions of the SM [19, 20], one can introduce a discrete symmetry, called R–parity [23], to enforce in a simple way lepton and baryon number conservation. A major consequence of this symmetry is that the lightest supersymmetric particle is absolutely stable. In most cases, this particle happens to be the lightest of the four neutralinos, which is massive, electrically neutral and weakly interacting. In large areas of the SUSY parameter space, the lightest neutralino can have the right cosmological relic density to account for the cold Dark Matter in the universe [24, 25].

– The main reason for introducing low energy supersymmetric theories in particle physics was, in fact, their ability to solve the naturalness and hierarchy problems [26]. Indeed, the new symmetry prevents the Higgs boson mass from acquiring very large radiative corrections: the quadratic divergent loop contributions of the SM particles to the Higgs mass squared are exactly canceled by the corresponding loop contributions of their supersymmetric partners [in fact, if SUSY were an exact symmetry, there would be no radiative corrections to the Higgs boson mass at all]. This cancellation stabilizes the huge hierarchy between the GUT and electroweak scale and no extreme fine-tuning is required.

However, SUSY is not an exact symmetry as the new predicted particles have not been experimentally observed, and thus have much larger masses than their SM partners in general [this is, in fact, needed for the three problems discussed above to be solved]. This SUSY breaking has several drawbacks as will be discussed later, but it has at least, one important virtue if it "soft" [27], that is, realized in a way which does not reintroduce the quadratic divergences to the Higgs mass squared. Indeed, soft SUSY–breaking allows one to understand the origin of the hierarchy between the GUT and electroweak scales and the origin of the breaking of the electroweak symmetry itself in terms of radiative gauge symmetry breaking

[28]. In the SM, the mass squared term of the scalar Higgs doublet field is assumed negative, leading to the "Mexican hat" shape of the scalar potential. The neutral component of the scalar field develops a non–zero vacuum expectation value that leads to the spontaneous breaking of the electroweak symmetry which generates the weak gauge boson and fermion masses. In softly broken Grand Unified SUSY theories, the form of this scalar potential is derived: the mass squared term of the scalar field is positive at the high scale and turns negative at the electroweak scale as a consequence of the logarithmic renormalization group evolution in which particles with strong Yukawa couplings [such as the top quark and its SUSY partners] contribute. The logarithmic evolution explains the huge difference between the GUT scale and the electroweak scale. Thus, electroweak symmetry breaking is more natural and elegant in SUSY–GUTs than in the SM.

The MSSM and its Higgs sector

The most economical low–energy globally supersymmetric extension of the SM is the Minimal Supersymmetric Standard Model (MSSM) [19, 20, 29–33]. In this model, one assumes the minimal gauge group [i.e., the SM $SU(3)_C \times SU(2)_L \times U(1)_Y$ symmetry], the minimal particle content [i.e., three generations of fermions without right–handed neutrinos and their spin–zero partners as well as two Higgs doublet superfields to break the electroweak symmetry], and R–parity conservation, which makes the lightest neutralino absolutely stable. In order to explicitly break SUSY, a collection of soft terms is added to the Lagrangian [27,34]: mass terms for the gauginos, mass terms for the scalar fermions, mass and bilinear terms for the Higgs bosons and trilinear couplings between sfermions and Higgs bosons.

In the general case, if one allows for intergenerational mixing and complex phases, the soft SUSY–breaking terms will introduce a huge number of unknown parameters, $\mathcal{O}(100)$ [35], in addition to the 19 parameters of the SM. However, in the absence of phases and intergenerational mixing and if the universality of first and second generation sfermions is assumed [to cope, in a simple way, with the severe experimental constraints], this number reduces to $\mathcal{O}(20)$ free parameters [36]. Furthermore, if the soft SUSY–breaking parameters obey a set of boundary conditions at high energy scales [34], all potential phenomenological problems of the general MSSM can be solved with the bonus that, only a handful of new free parameters are present. These general and constrained MSSMs will be discussed in §1.

The MSSM requires the existence of two isodoublets of complex scalar fields of opposite hypercharge to cancel chiral anomalies and to give masses separately to isospin up–type and down–type fermions [19, 20, 26]. Three of the original eight degrees of freedom of the scalar fields are absorbed by the $W^\pm$ and Z bosons to build their longitudinal polarizations and to acquire masses. The remaining degrees of freedom will correspond to five scalar Higgs bosons. Two CP–even neutral Higgs bosons h and H, a pseudoscalar A boson and a pair of charged

scalar particles $H^\pm$ are, thus, introduced by this extension of the Higgs sector. Besides the four masses, two additional parameters define the properties of these particles at tree–level: a mixing angle α in the neutral CP–even sector and the ratio of the two vacuum expectation values $\tan\beta$, which from GUT restrictions is assumed in the range $1 \lesssim \tan\beta \lesssim m_t/m_b$ with the lower and upper ranges favored by Yukawa coupling unification.

Supersymmetry leads to several relations among these parameters and only two of them, taken in general to be M_A and $\tan\beta$, are in fact independent. These relations impose a strong hierarchical structure on the mass spectrum, $M_h < M_Z, M_A < M_H$ and $M_W < M_{H^\pm}$, which is, however, broken by radiative corrections [37]. The leading part of these radiative corrections grows as the fourth power of m_t and logarithmically with the common top squark masses M_S which sets the SUSY–breaking scale. The mixing or trilinear coupling in the stop sector A_t plays an important role in this context. These corrections are very large and, for instance, the upper bound on the mass of the lighter Higgs boson h is shifted from the tree–level value M_Z to $M_h \sim 140$ GeV for large values of the parameter $\tan\beta$ and for values $A_t \sim \sqrt{6}M_S$ with $M_S \sim \mathcal{O}(1$ TeV$)$. The masses of the heavier neutral and charged Higgs particles are expected to be in the range of the electroweak symmetry breaking scale.

The phenomenology of the MSSM Higgs sector is much richer than the one of the SM with its single doublet scalar field and hence unique Higgs boson. The study of the properties of the MSSM scalar Higgs bosons and of those of the supersymmetric particles is one of the most active fields of elementary particle physics. The search for these new particles, and if they are discovered, the determination of their fundamental properties, is one of the major goals of high–energy colliders. In this context, the probing of the Higgs sector has a double importance since, at the same time, it provides the clue of the electroweak symmetry breaking mechanism and it sheds light on the SUSY–breaking mechanism. Moreover, while SUSY particles are allowed to be relatively heavy unless one invokes fine–tuning arguments to be discussed later, the existence of a light Higgs boson is a strict prediction of the MSSM and this particle should manifest itself at the next round of high–energy experiments. Since these experiments are starting rather soon, we are in a situation where either Supersymmetry with its Higgs sector is discovered or, in the absence of a light Higgs boson, the whole SUSY edifice, at least in the way it is presently viewed, collapses.

Probing the MSSM Higgs sector: a brief survey of recent developments

SUSY theories have been introduced in the mid–seventies, mostly for aesthetic reasons. In the early eighties, the most important phenomenological virtues of low energy SUSY realizations such as the MSSM, that is, the fact that they provide possible solutions to the hierarchy, gauge unification and Dark Matter problems, were acknowledged. A huge effort has been since then devoted to the investigation of the pattern of the soft SUSY–breaking

Lagrangian and to the determination of the properties of the predicted new particles.

For what concerns the MSSM Higgs sector, after the pioneering investigations of the late seventies and early eighties, the two Higgs doublet structure of the model that obeys the SUSY constraints has been put into almost the shape that is known nowadays in a series of seminal papers written by Gunion and Haber [38–40] and shortly thereafter in the late eighties in *The Higgs Hunter's Guide* [41]. In this book, the profile of the MSSM Higgs sector was extensively reviewed and the properties of the five Higgs particles described in detail. As in the case of the SM Higgs boson, the constraints from the experimental data available at that time and the prospects for discovering the Higgs particles at the upcoming high–energy experiments, the LEP, the SLC, the late SSC and the LHC, as well as at possible higher energy e^+e^- colliders, were analyzed and summarized. The review also guided theoretical and phenomenological studies of the MSSM Higgs sector as well as experimental searches performed over the last fifteen years.

Since then, similarly to the SM Higgs case, a number of major developments took place. On the experimental front, the LEP experiment was completed without having discovered any fundamental scalar particle [42]. Nevertheless, the searches that have been performed in the clean environment of e^+e^- collisions allowed to set severe limits on the masses of the lighter h and A particles, $M_h \sim M_A \gtrsim M_Z$. Another important outcome of LEP is that the high–precision measurements [2] favor weakly interacting theories which incorporate light scalar Higgs particles and in which the other predicted new particles decouple from low energy physics, as is the case of the MSSM. Moreover, the top quark, which because it is so heavy, plays an extremely important role in the MSSM Higgs sector, was discovered at the Tevatron [43] and its mass measured [44]. In fact, if the top quark were not that heavy, the entire MSSM would have been ruled out from LEP2 searches as the lighter Higgs boson mass is predicted to be less than M_Z at tree–level, that is, without the radiative corrections that are largely due to the heavy top quark and its scalar partners.

Major developments occurred as well in the planning and design of high–energy colliders. The SSC was canceled, the energy and luminosity of the LHC were fixed to their known current values and the Tevatron was upgraded, its energy and luminosity raised to values allowing for the search of the MSSM Higgs particle beyond the reach of LEP. Furthermore, the path toward future high–energy electron–positron colliders, which are powerful instruments to search for the Higgs bosons and to study their properties, started to be more concrete [in particular since the recent recommendations of the panel for an International Linear Collider, ILC]. In addition, the option of searching for the Higgs bosons in the $\gamma\gamma$ option of future linear e^+e^- colliders as well as at future $\mu^+\mu^-$ colliders became possible.

However, it is on the phenomenological side that the most important developments took place. Soon after Ref. [41] was published, it was realized that the radiative corrections in

the MSSM Higgs sector play an extremely important role and alter in a significant way the properties of the Higgs particles. In the subsequent years and, still until recently, an impressive theoretical effort was devoted to the calculation of these radiative corrections. A vast literature also appeared on the precise determination of the decay and production properties of the MSSM Higgs particles, including radiative corrections as well. Furthermore, a large number of phenomenological and experimental analyses have been performed to assess to what extent the MSSM Higgs particles can be discovered and their properties studied at the upcoming machines, the Tevatron, the LHC, future linear colliders and other colliders. These studies cover many different issues as the MSSM Higgs sector is rather rich and has a very close connection to the SUSY particle sector.

Objectives and limitations of the review

In this second part of the review devoted to the study of the electroweak symmetry breaking mechanism, we will discuss in an extensive way the Higgs sector of the MSSM with a special focus on the developments which occurred in the last fifteen years. As already discussed in the introduction to the first part of the review [45], we believe that after the completion of LEP and in preparation of the challenges ahead, with the launch of the LHC about to take place [and the accumulation of enough data at the Tevatron], it would be useful to collect and summarize the large theoretical and experimental work carried out on the subject.

In the present report, we will be concerned exclusively with the MSSM and its constrained versions. More precisely, besides the minimal gauge structure and R–parity conservation, we assume the minimal particle content with only two Higgs doublets to break the electroweak symmetry. Extensions of the Higgs sector with additional singlets, doublets or higher representations for the Higgs fields will be discussed in a forthcoming report [46]. Furthermore, we assume a minimal set of soft SUSY–breaking parameters when considering the unconstrained MSSM with the mass and coupling matrices being diagonal and real. The effects of CP–violating phases and intergenerational mixing will be thus also postponed to Ref. [46]. Finally, we assume [although this will have little impact on our study] that all SUSY and Higgs particles have masses not too far from the scale of electroweak symmetry, and thus we ignore models such as split–Supersymmetry [which, anyhow gives up one of the main motivations for low energy SUSY models: the resolution of the hierarchy problem].

Even in this restricted framework, the number of existing studies is extremely large and many important issues need to be addressed. As was already stated in Ref. [45], it is impossible to cover all aspects of the subject, and in many instances we had to make some difficult choices and privilege some aspects over others. Some of these choices are of course personal, although we tried to be guided by the needs of future experiments. We apologize in advance if some topics have been overlooked or not given enough consideration.

Complementary material on the foundations of SUSY and the MSSM, which will be discussed here only briefly, can be found in standard textbooks and general reviews [17, 18, 29–33] and on the various calculations, theoretical studies and phenomenological analyses in many excellent reviews to be quoted in due time. For more detailed accounts on the detection of the MSSM Higgs particles at the various colliders, we will refer to specialized reviews and to the proceedings of the various workshops which were devoted to the subject.

Synopsis of the review

The report is organized as follows. We start the first chapter with a brief discussion of the hierarchy problem, which is our main motivation for low energy Supersymmetric theories, and sketch the basic features of SUSY and the unconstrained and constrained MSSMs; the SUSY particle spectrum and the constraints on the SUSY parameters will be briefly described. We will then discuss in detail the MSSM Higgs sector and derive the Higgs masses and couplings, including the important radiative corrections. A brief summary of the various regimes of the MSSM Higgs sector will be given. In a last section, we will discuss the theoretical and experimental constraints on the Higgs boson masses and couplings, in particular, the direct Higgs searches at LEP and the Tevatron and the indirect searches for the virtual effects of the Higgs bosons in high–precision observables.

The second chapter is devoted to several phenomenological aspects of the MSSM Higgs sector. In the first section, the various decays of the neutral CP–even Higgs bosons, which follow closely those of the SM Higgs particle, and the decays of the CP–odd and charged Higgs bosons are presented and the new features, compared the SM case, highlighted. The total decay widths and the branching ratios are summarized in the various regimes of the MSSM, including all important ingredients such as the higher order decays and the radiative corrections. We then summarize, in this context, the main effects of relatively light SUSY particles either directly, when they appear as final states in the decay processes, or indirectly, when they alter the standard decay modes through loop contributions. A third section focuses on the decays of the heavy top quark into charged Higgs bosons and the various decays of SUSY particles into the neutral and charged Higgs bosons. In a last section, we will briefly discuss the important role played by the MSSM Higgs sector in the determination of the cosmological relic density and detection rates of the SUSY DM candidate, the neutralino.

The production of the MSSM Higgs particles at hadron colliders is discussed in the third chapter. The most important production mechanisms of the neutral CP–even Higgs bosons follow qualitatively but not quantitatively those of the SM Higgs boson, while important differences arise in the case of the CP–odd Higgs boson and, obviously, new production mechanisms occur in the charged Higgs boson case. All the mechanisms, including higher orders channels which might provide valuable information, are discussed and their main

features summarized. We pay special attention to the new features and to the radiative corrections which have not been discussed in the SM case. The detection of the Higgs particles and the experimental determination of some important parameters at the Tevatron and the LHC are discussed in the various production and decay channels and in all possible MSSM regimes. A final section is devoted to the effects of light SUSY particles on the production cross sections and on the detection strategies.

In the last chapter, we address the issue of producing and studying the MSSM Higgs particles at lepton colliders, mainly concentrating on e^+e^- machines in the energy range 350–1000 GeV as planed for the ILC. We study the main production channels, which allow for the discovery of the MSSM Higgs particles, as well as several "subleading" processes which are very important for the determination of their fundamental properties, such as associated production with heavy fermions and Higgs pair production. The effects of radiative corrections and those of light SUSY particles are highlighted and the detection and precision tests which can be performed in the clean environment of these colliders presented. We then briefly summarize the additional information which can be obtained on the MSSM Higgs sector in s–channel neutral Higgs production at $\gamma\gamma$ and $\mu^+\mu^-$ colliders, concentrating on the physics aspects that cannot be probed in a satisfactory way in the e^+e^- option. In a last section, we discuss the tests and consistency checks of the MSSM Higgs sector that can be achieved via the high–precision measurements to be performed at the lepton colliders in the various options and their complementarity with those performed at the LHC and in astroparticle experiments.

In many cases, we heavily rely on the detailed material which has been presented for the SM Higgs boson in the first tome of this review. We consequently concentrate on the new features which appear in SUSY extensions and, in general, simply refer to the relevant sections of Ref. [45] for all the aspects which have been discussed for the SM Higgs boson and which can be readily adapted to the MSSM Higgs sector. We try to be as complete and comprehensive as possible, but with the limitations mentioned previously. We will update the analyses on the total Higgs decay widths, branching ratios and production cross sections at the Tevatron, the LHC and future e^+e^- colliders at various center of mass energies and present summary plots in which all the information that is currently available is included.

1 The Higgs sector of the MSSM

1.1 Supersymmetry and the MSSM

1.1.1 The hierarchy problem

As is well known[1], when calculating the radiative corrections to the SM Higgs boson mass, one encounters divergences which are quadratic in the cut–off scale Λ at which the theory stops to be valid and New Physics should appear. To summarize the problem, let us consider the one–loop contributions to the Higgs mass, Fig. 1.1a, of a fermion f with a repetition number N_f and a Yukawa coupling $\lambda_f = \sqrt{2}m_f/v$. Assuming for simplicity that the fermion is very heavy so that one can neglect the external Higgs momentum squared, one obtains [13]

$$\Delta M_H^2 \;\;=\;\; N_f\frac{\lambda_f^2}{8\pi^2}\Big[-\Lambda^2 + 6m_f^2\log\frac{\Lambda}{m_f} - 2m_f^2\Big] + \mathcal{O}(1/\Lambda^2) \tag{1.1}$$

which shows the quadratically divergent behavior, $\Delta M_H^2 \propto \Lambda^2$. If we chose the cut–off scale Λ to be the GUT scale, $M_{\rm GUT} \sim 10^{16}$ GeV, or the Planck scale, $M_P \sim 10^{18}$ GeV, the Higgs boson mass which is supposed to lie in the range of the electroweak symmetry breaking scale, $v \sim 250$ GeV, will prefer to be close to the very high scale and thus, huge. For the SM Higgs boson to stay relatively light, at least $M_H \lesssim 1$ TeV for unitarity and perturbativity reasons, we need to add a counterterm to the mass squared and adjust it with a precision of $\mathcal{O}(10^{-30})$, which seems highly unnatural. This is what is called the naturalness or fine–tuning problem [14]. A related question, called the hierarchy problem, is why $\Lambda \gg M_Z$.

The problem can be seen as being due to the lack of a symmetry which protects M_H against very high scales. In the case of fermions, chiral symmetry is a protection against large radiative corrections to their masses [and the breaking of chiral symmetry generates radiative corrections which are only logarithmically divergent], while local gauge symmetry protects the photons from acquiring a mass term. In the case of the Higgs boson, there is no such a symmetry. [Note that the divergence is independent of the Higgs mass and does not disappear if $M_H=0$; this can be understood since the choice of a massless Higgs boson does not increase the symmetry of the SM].
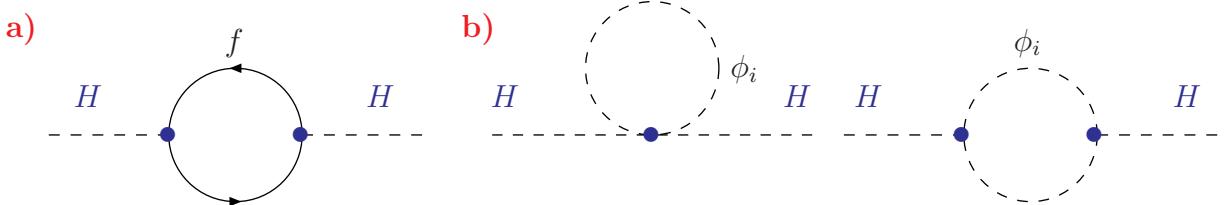
Figure 1.1: *Diagrams for the contributions of fermions and scalars to the Higgs boson mass.*

---

[1]Some aspects of this issue have been discussed in section 1.4.3 of the first part of this review: §I.1.4.3.

Let us now assume the existence of a number N_S of scalar particles with masses m_S and with trilinear and quadrilinear couplings to the Higgs boson given, respectively, by $v\lambda_S$ and λ_S. They contribute to the Higgs boson self–energy via the two diagrams of Fig. 1.1b, which lead to a contribution to the Higgs boson mass squared

$$\Delta M_H^2 = \frac{\lambda_S N_S}{16\pi^2}\Big[-\Lambda^2 + 2m_S^2\log\Big(\frac{\Lambda}{m_S}\Big)\Big] - \frac{\lambda_S^2 N_S}{16\pi^2}v^2\Big[-1 + 2\log\Big(\frac{\Lambda}{m_S}\Big)\Big] + \mathcal{O}\Big(\frac{1}{\Lambda^2}\Big) \quad (1.2)$$

Here again, the quadratic divergences are present. However, if we make the assumption that the Higgs couplings of the scalar particles are related to the Higgs–fermion couplings in such a way that $\lambda_f^2 = 2m_f^2/v^2 = -\lambda_S$, and that the multiplicative factor for scalars is twice the one for fermions, $N_S = 2N_f$, we then obtain, once we add the two scalar and the fermionic contributions to the Higgs boson mass squared

$$\Delta M_H^2 = \frac{\lambda_f^2 N_f}{4\pi^2}\Big[(m_f^2 - m_S^2)\log\Big(\frac{\Lambda}{m_S}\Big) + 3m_f^2\log\Big(\frac{m_S}{m_f}\Big)\Big] + \mathcal{O}\Big(\frac{1}{\Lambda^2}\Big) \quad (1.3)$$

As can be seen, the quadratic divergences have disappeared in the sum [26]. The logarithmic divergence is still present, but even for values $\Lambda \sim M_P$ of the cut–off, the contribution is rather small. This logarithmic divergence disappears also if, in addition, we assume that the fermion and the two scalars have the same mass $m_S = m_f$. In fact, in this case, the total correction to the Higgs boson mass squared vanishes altogether.

The conclusion of this exercise is that, if there are scalar particles with a symmetry which relates their couplings to the couplings of the standard fermions, there is no quadratic divergence to the Higgs boson mass: the hierarchy and naturalness problems are technically solved. If, in addition, there is an exact "supersymmetry", which enforces that the scalar particle masses are equal to the fermion mass, there are no divergences at all since, then, even the logarithmic divergences disappear. The Higgs boson mass is thus protected by this "supersymmetry". One can generalize the argument to include the contributions of the other particles of the SM in the radiative corrections to M_H: by introducing fermionic partners to the W/Z and Higgs bosons, and by adjusting their couplings to the Higgs boson, all the quadratically divergent corrections to the Higgs boson mass are canceled.

If this symmetry is badly broken and the masses of the scalar particles are much larger than the fermion and Higgs masses, the hierarchy and naturalness problems would be reintroduced again in the theory, since the radiative corrections to the Higgs mass, $\propto (m_f^2 - m_S^2)\log(\Lambda/m_S)$, become large again and M_H will have the tendency to exceed the unitarity and perturbativity limit of $\mathcal{O}(1\ \mathrm{TeV})$. Therefore, to keep the Higgs mass in the range of the electroweak symmetry breaking scale, $M_H = \mathcal{O}(100\ \mathrm{GeV})$, we need the mass difference between the SM and the new particles to be rather small. For the radiative corrections to be of the same order as the tree–level Higgs boson mass, the new particles should not be much heavier than the TeV scale, $m_{S,F} = \mathcal{O}(1\ \mathrm{TeV})$.

1.1.2 Basics of Supersymmetry

Supersymmetry (SUSY) is a symmetry relating particles of integer spin, i.e. spin–0 and spin–1 bosons, and particles of spin $\frac{1}{2}$, i.e. fermions [we ignore, for the moment, the graviton and its partner]. In this subsection, we recall very briefly the basic features of Supersymmetry; for a more detailed discussion, see Refs. [17, 18] for instance.

The SUSY generators $\mathcal{Q}$ transform fermions into bosons and vice–versa

$$\mathcal{Q}|\text{Fermion}\rangle >= |\text{Boson}\rangle \ , \quad \mathcal{Q}|\text{Boson}\rangle = |\text{Fermion}\rangle \tag{1.4}$$

When the symmetry is exact, the bosonic fields, i.e. the scalar and gauge fields of spin 0 and spin 1, respectively, and the fermionic fields of spin $\frac{1}{2}$ have the same masses and quantum numbers, except for the spin. The particles are combined into superfields and the simplest case is the chiral or scalar superfield which contains a complex scalar field S with two degrees of freedom and a Weyl fermionic field with two components ζ. Another possibility is the vector superfield containing [in the Wess–Zumino gauge] a massless gauge field A_μ^a, with a being the gauge index, and a Weyl fermionic field with two components λ_a.

All fields involved have the canonical kinetic energies given by the Lagrangian

$$\mathcal{L}_{\text{kin}} = \sum_i \left\{ (D_\mu S_i^*)(D^\mu S_i) + i\overline{\psi}_i D_\mu \gamma^\mu \psi_i \right\} + \sum_a \left\{ -\frac{1}{4} F_{\mu\nu}^a F^{\mu\nu a} + \frac{i}{2}\overline{\lambda}_a \sigma^\mu D_\mu \lambda_a \right\} \tag{1.5}$$

with D_μ the usual gauge covariant derivative, $F_{\mu\nu}$ the field strengths, $\sigma_{1,2,3}, -\sigma_0$ the 2×2 Pauli and unit matrices. Note that the fields ψ and λ have, respectively, four and two components. The interactions among the fields are specified by SUSY and gauge invariance

$$\mathcal{L}_{\text{int. scal-fer.-gauginos}} = -\sqrt{2} \sum_{i,a} g_a \left[S_i^* T^a \overline{\psi}_{iL} \lambda_a + \text{h.c.} \right] \tag{1.6}$$

$$\mathcal{L}_{\text{int. quartic scal.}} = -\frac{1}{2} \sum_a \left(\sum_i g_a S_i^* T^a S_i \right)^2 \tag{1.7}$$

with T^a and g_a being the generators and coupling constants of the corresponding groups. At this stage, all interactions are given in terms of the gauge coupling constants. Thus, when SUSY is exact, everything is completely specified and there is no new adjustable parameter.

The only freedom that one has is the choice of the superpotential W which gives the form of the scalar potential and the Yukawa interactions between fermion and scalar fields. However, the superpotential should be invariant under SUSY and gauge transformations and it should obey the following three conditions:

$i)$ it must be a function of the superfields z_i only and not their conjugate z_i^*;

$ii)$ it should be an analytic function and therefore, it has no derivative interaction;

iii) it should have only terms of dimension 2 and 3 to keep the theory renormalizable.

In terms of the superpotential W, the interaction Lagrangian may be written as

$$\mathcal{L}_W = -\sum_i \left|\frac{\partial W}{\partial z_i}\right|^2 - \frac{1}{2}\sum_{ij}\left[\overline{\psi}_{iL}\frac{\partial^2 W}{\partial z_i \partial z_j}\psi_j + \text{h.c.}\right] \tag{1.8}$$

where, to obtain the interactions explicitly, one has to take the derivative of W with respect to the fields z_i, and then evaluate in terms of the scalar fields S_i.

The supersymmetric part of the tree–level scalar potential V_{tree} is the sum of the so–called F– and D–terms, where the F–terms [47] come from the superpotential through derivatives with respect to all scalar fields S_i

$$V_F = \sum_i |W^i|^2 \ \ \text{with } W^i = \partial W/\partial S_i \tag{1.9}$$

and the D–terms [48] corresponding to the $U(1)_Y, SU(2)_L$ and $SU(3)_C$ introduced earlier

$$V_D = \frac{1}{2}\sum_{a=1}^{3}\left(\sum_i g_a S_i^* T^a S_i\right)^2 \tag{1.10}$$

Nevertheless, SUSY cannot be an exact symmetry since there are no fundamental scalar particles having the same mass as the known fermions [in fact, no fundamental scalar has been observed at all]. Therefore, SUSY must be broken. However, we need the SUSY–breaking to occur in a way such that the supersymmetric particles are not too heavy as to reintroduce the hierarchy problem and, as discussed in the preamble, to solve the two other problems that we have within the Standard Model, namely: the slope of the evolution of the three gauge couplings has to be modified early enough by the sparticle contributions to achieve unification, and the Dark Matter problem calls for the existence of a new stable, neutral and weakly interacting particle that is not too heavy in order to have the required cosmological relic density.

In the breaking of Supersymmetry, we obviously need to preserve the gauge invariance and the renormalizability of the theory and, also, the fact that there are still no quadratic divergences in the Higgs boson mass squared. Since up to now there is no completely satisfactory dynamical way to break SUSY [although many options have been discussed in the literature], a possibility is to introduce by hand terms that break SUSY explicitly and parametrize our ignorance of the fundamental SUSY–breaking mechanism. This gives a low energy effective SUSY theory, the most economic version being the Minimal Supersymmetric Standard Model (MSSM) [19] and [20,26] that we will discuss in the next subsections and the subsequent ones. The detailed discussion of the Higgs sector of the MSSM will be postponed to §1.2 and the subsequent sections.

16

1.1.3 The Minimal Supersymmetric Standard Model

The unconstrained MSSM is defined by the following four basic assumptions [18, 29–32]:

(a) **Minimal gauge group:** The MSSM is based on the group $SU(3)_C \times SU(2)_L \times U(1)_Y$, i.e. the SM gauge symmetry. SUSY implies then that the spin–1 gauge bosons and their spin–$\frac{1}{2}$ partners, the gauginos [the bino $\tilde{B}$, the three winos $\tilde{W}_{1-3}$ and the eight gluinos $\tilde{G}_{1-8}$ corresponding to the gauge bosons of U(1), SU(2) and SU(3), respectively], are in vector supermultiplets; Table 1.1.

Superfields	$SU(3)_C$	$SU(2)_L$	$U(1)_Y$	Particle content
$\hat{G}_a$	8	1	0	$G_a^\mu,\ \tilde{G}_a$
$\hat{W}_a$	1	3	0	$W_a^\mu,\ \tilde{W}_a$
$\hat{B}$	1	1	0	$B^\mu,\ \tilde{B}$

Table 1.1: The superpartners of the gauge bosons in the MSSM and their quantum numbers.

(b) **Minimal particle content:** There are only three generations of spin–$\frac{1}{2}$ quarks and leptons [no right–handed neutrino] as in the SM. The left– and right–handed fields belong to chiral superfields together with their spin–0 SUSY partners, the squarks and sleptons: $\hat{Q}, \hat{U}_R, \hat{D}_R, \hat{L}, \hat{E}_R$. In addition, two chiral superfields $\hat{H}_1, \hat{H}_2$ with respective hypercharges -1 and $+1$ are needed for the cancellation of chiral anomalies [19, 20, 26]. Their scalar components, H_1 and H_2, give separately masses to the isospin $-\frac{1}{2}$ and $+\frac{1}{2}$ fermions in a SUSY invariant way [recall that the SUSY potential should not involve conjugate fields and we cannot generate with the same doublet the masses of both types of fermions]. The various fields are summarized in Table 1.2. As will be discussed later, the two doublet fields lead to five Higgs particles: two CP–even h, H bosons, a pseudoscalar A boson and two charged $H^\pm$ bosons. Their spin–$\frac{1}{2}$ superpartners, the higgsinos, will mix with the winos and the bino, to give the "ino" mass eigenstates: the two charginos $\chi_{1,2}^\pm$ and the four neutralinos $\chi_{1,2,3,4}^0$.

Superfield	$SU(3)_C$	$SU(2)_L$	$U(1)_Y$	Particle content
$\hat{Q}$	3	2	$\frac{1}{3}$	$(u_L, d_L),\ (\tilde{u}_L, \tilde{d}_L)$
$\hat{U}^c$	$\overline{3}$	1	$-\frac{4}{3}$	$\overline{u}_R,\ \tilde{u}_R^*$
$\hat{D}^c$	$\overline{3}$	1	$\frac{2}{3}$	$\overline{d}_R,\ \tilde{d}_R^*$
$\hat{L}$	1	2	-1	$(\nu_L, e_L),\ (\tilde{\nu}_L, \tilde{e}_L)$
$\hat{E}^c$	1	1	2	$\overline{e}_R,\ \tilde{e}_R^*$
$\hat{H}_1$	1	2	-1	$H_1,\ \tilde{H}_1$
$\hat{H}_2$	1	2	1	$H_2,\ \tilde{H}_2$

Table 1.2: The superpartners of the fermions and Higgs bosons in the MSSM.

(c) Minimal Yukawa interactions and R–parity conservation: To enforce lepton and baryon number conservation in a simple way, a discrete and multiplicative symmetry called R–parity is imposed [23]. It is defined by

$$R_p = (-1)^{2s+3B+L} \tag{1.11}$$

where L and B are the lepton and baryon numbers and s is the spin quantum number. The R–parity quantum numbers are then $R_p = +1$ for the ordinary particles [fermions, gauge bosons and Higgs bosons], and $R_p = -1$ for their supersymmetric partners. In practice, the conservation of R–parity has the important consequences that the SUSY particles are always produced in pairs, in their decay products there is always an odd number of SUSY particles, and the lightest SUSY particle (LSP) is absolutely stable.

[The three conditions listed above are sufficient to completely determine a globally supersymmetric Lagrangian. The kinetic part of the Lagrangian is obtained by generalizing the notion of covariant derivative to the SUSY case. The most general superpotential, compatible with gauge invariance, renormalizability and R–parity conservation is written as

$$W = \sum_{i,j=gen} -Y_{ij}^u \, \hat{u}_{Ri} \hat{H}_2 \cdot \hat{Q}_j + Y_{ij}^d \, \hat{d}_{Ri} \hat{H}_1 \cdot \hat{Q}_j + Y_{ij}^\ell \, \hat{\ell}_{Ri} \hat{H}_1 \cdot \hat{L}_j + \mu \hat{H}_2 \cdot \hat{H}_1 \tag{1.12}$$

The product between $SU(2)_L$ doublets reads $H \cdot Q \equiv \epsilon_{ab} H^a Q^b$ where a, b are $SU(2)_L$ indices and $\epsilon_{12} = 1 = -\epsilon_{21}$, and $Y_{ij}^{u,d,\ell}$ denote the Yukawa couplings among generations. The first three terms in the previous expression are nothing else but a superspace generalization of the Yukawa interaction in the SM, while the last term is a globally supersymmetric Higgs mass term. From the superpotential above, one can then write explicitly the F terms of the tree level potential V_{tree}.]

(d) Minimal set of soft SUSY–breaking terms: Finally, to break Supersymmetry while preventing the reappearance of the quadratic divergences, the so–called soft SUSY–breaking, one adds to the Lagrangian a set of terms which explicitly break SUSY [27, 34].

- Mass terms for the gluinos, winos and binos:

$$-\mathcal{L}_{\text{gaugino}} = \frac{1}{2} \left[M_1 \tilde{B}\tilde{B} + M_2 \sum_{a=1}^{3} \tilde{W}^a \tilde{W}_a + M_3 \sum_{a=1}^{8} \tilde{G}^a \tilde{G}_a + \text{h.c.} \right] \tag{1.13}$$

- Mass terms for the scalar fermions:

$$-\mathcal{L}_{\text{sfermions}} = \sum_{i=gen} m_{\tilde{Q}_i}^2 \, \tilde{Q}_i^\dagger \tilde{Q}_i + m_{\tilde{L}_i}^2 \, \tilde{L}_i^\dagger \tilde{L}_i + m_{\tilde{u}_i}^2 |\tilde{u}_{R_i}|^2 + m_{\tilde{d}_i}^2 |\tilde{d}_{R_i}|^2 + m_{\tilde{\ell}_i}^2 |\tilde{\ell}_{R_i}|^2 \tag{1.14}$$

18

- Mass and bilinear terms for the Higgs bosons:

$$-\mathcal{L}_{\text{Higgs}} = m_{H_2}^2 H_2^\dagger H_2 + m_{H_1}^2 H_1^\dagger H_1 + B\mu(H_2 \cdot H_1 + \text{h.c.}) \qquad (1.15)$$

- Trilinear couplings between sfermions and Higgs bosons

$$-\mathcal{L}_{\text{tril.}} = \sum_{i,j=gen} \left[A_{ij}^u Y_{ij}^u \tilde{u}_{R_i}^* H_2 \cdot \tilde{Q}_j + A_{ij}^d Y_{ij}^d \tilde{d}_{R_i}^* H_1 \cdot \tilde{Q}_j + A_{ij}^l Y_{ij}^\ell \tilde{\ell}_{R_i}^* H_1 \cdot \tilde{L}_j \; + \; \text{h.c.} \right] (1.16)$$

The soft SUSY–breaking scalar potential is the sum of the three last terms:

$$V_{\text{soft}} = -\mathcal{L}_{\text{sfermions}} - \mathcal{L}_{\text{Higgs}} - \mathcal{L}_{\text{tril.}} \qquad (1.17)$$

Up to now, no constraint is applied to this Lagrangian, although for generic values of the parameters, it might lead to severe phenomenological problems [49], such as flavor changing neutral currents (FCNC), an unacceptable amount of additional CP–violation, color and charge breaking minima (CCB), *etc...* The MSSM defined by the four hypotheses (a)–(d) above, is generally called the unconstrained MSSM.

1.1.4 The unconstrained and constrained MSSMs

In the unconstrained MSSM, and in the general case where one allows for intergenerational mixing and complex phases, the soft SUSY–breaking terms will introduce a huge number (105) of unknown parameters, in addition to the 19 parameters of the SM [35]. This large number of parameters makes any phenomenological analysis in the MSSM very complicated. In addition, many "generic" sets of these parameters are excluded by the severe phenomenological constraints discussed above. A phenomenologically more viable MSSM can be defined, for instance, by making the following assumptions: (i) All the soft SUSY–breaking parameters are real and therefore there is no new source of CP–violation generated, in addition to the one from the CKM matrix; (ii) the matrices for the sfermion masses and for the trilinear couplings are all diagonal, implying the absence of FCNCs at the tree–level; (iii) the soft SUSY–breaking masses and trilinear couplings of the first and second sfermion generations are the same at low energy to cope with the severe constraints from K^0–$\bar{K}^0$ mixing, *etc.*

Making these three assumptions will lead to only 22 input parameters:

$\tan\beta$: the ratio of the vevs of the two–Higgs doublet fields;

$m_{H_1}^2, m_{H_2}^2$: the Higgs mass parameters squared;

M_1, M_2, M_3: the bino, wino and gluino mass parameters;

$m_{\tilde{q}}, m_{\tilde{u}_R}, m_{\tilde{d}_R}, m_{\tilde{l}}, m_{\tilde{e}_R}$: the first/second generation sfermion mass parameters;

A_u, A_d, A_e: the first/second generation trilinear couplings;

$m_{\tilde{Q}}, m_{\tilde{t}_R}, m_{\tilde{b}_R}, m_{\tilde{L}}, m_{\tilde{\tau}_R}$: the third generation sfermion mass parameters;

A_t, A_b, A_τ: the third generation trilinear couplings.

Two remarks can be made at this stage: (i) The Higgs–higgsino (supersymmetric) mass parameter $|\mu|$ (up to a sign) and the soft SUSY–breaking bilinear Higgs term B are determined, given the above parameters, through the electroweak symmetry breaking conditions [20,28,50,51] as will be discussed later. Alternatively, one can trade the values of $m_{H_1}^2$ and $m_{H_2}^2$ with the "more physical" pseudoscalar Higgs boson mass M_A and parameter μ. (ii) Since the trilinear sfermion couplings will be always multiplied by the fermion masses, they are in general important only in the case of the third generation; there are, however, a few exceptions such as the electric and magnetic dipole moments for instance.

Such a model, with this relatively moderate number of parameters has much more predictability and is much easier to investigate phenomenologically, compared to the unconstrained MSSM, given the fact that in general only a small subset appears when one looks at a given sector of the model. One can refer to this 22 free input parameters model as the "phenomenological" MSSM or pMSSM [36].

Almost all problems of the general or unconstrained MSSM are solved at once if the soft SUSY–breaking parameters obey a set of universal boundary conditions at the GUT scale. If one takes these parameters to be real, this solves all potential problems with CP violation as well. The underlying assumption is that SUSY–breaking occurs in a hidden sector which communicates with the visible sector only through gravitational–strength interactions, as specified by Supergravity. Universal soft breaking terms then emerge if these Supergravity interactions are "flavor–blind" [like ordinary gravitational interactions]. This is assumed to be the case in the constrained MSSM or minimal Supergravity (mSUGRA) model [34,52].

Besides the unification of the gauge coupling constants $g_{1,2,3}$ which is verified given the experimental results from LEP1 [9] and which can be viewed as fixing the Grand Unification scale, $M_U \sim 2 \cdot 10^{16}$ GeV, the unification conditions in mSUGRA, are as follows [34].

– Unification of the gaugino [bino, wino and gluino] masses:

$$M_1(M_U) = M_2(M_U) = M_3(M_U) \equiv m_{1/2} \tag{1.18}$$

– Universal scalar [i.e. sfermion and Higgs boson] masses [i is the generation index]:

$$
\begin{aligned}
m_{\tilde{Q}_i}(M_U) &= m_{\tilde{u}_{Ri}}(M_U) = m_{\tilde{d}_{Ri}}(M_U) = m_{\tilde{L}_i}(M_U) = m_{\tilde{\ell}_{Ri}}(M_U) \\
&= m_{H_1}(M_U) = m_{H_2}(M_U) \equiv m_0
\end{aligned}
\tag{1.19}
$$

– Universal trilinear couplings:

$$A_{ij}^u(M_U) = A_{ij}^d(M_U) = A_{ij}^\ell(M_U) \equiv A_0 \, \delta_{ij} \tag{1.20}$$

Besides the three parameters $m_{1/2}, m_0$ and A_0, the supersymmetric sector is described at the GUT scale by the bilinear coupling B and the supersymmetric Higgs(ino) mass parameter

μ. However, one has to require that EWSB takes place at some low energy scale. This results in two necessary minimization conditions of the two–Higgs doublet scalar potential which fix the values μ^2 and $B\mu$ with the sign of μ not determined. Therefore, in this model, one is left with only four continuous free parameters, and an unknown sign

$$\tan\beta \ , \ m_{1/2} \ , \ m_0 \ , \ A_0 \ , \ \ \mathrm{sign}(\mu) \tag{1.21}$$

All soft SUSY–breaking parameters at the weak scale are then obtained via RGEs [20,53,54].

There also other constrained MSSM scenarios and we briefly mention two of them, the anomaly and gauge mediated SUSY–breaking models.

In anomaly mediated SUSY–breaking (AMSB) models [55, 56], SUSY–breaking occurs also in a hidden sector, but it is transmitted to the visible sector by the super–Weyl anomaly. The gaugino masses, the scalar masses and the trilinear couplings are then simply related to the scale dependence of the gauge and matter kinetic functions. This leads to soft SUSY–breaking scalar masses for the first two generation sfermions that are almost diagonal [when the small Yukawa couplings are neglected] which solves the SUSY flavor problem which affects general SUGRA models for instance. In these models, the soft SUSY–breaking parameters are given in terms of the gravitino mass $m_{3/2}$, the β functions for the gauge and Yukawa couplings g_a and Y_i, and the anomalous dimensions γ_i of the chiral superfields. One then has, in principle, only three input parameters $m_{3/2}, \tan\beta$ and $\mathrm{sign}(\mu)$ [μ^2 and B are obtained as usual by requiring correct EWSB]. However, this picture is spoiled by the fact that the anomaly mediated contribution to the slepton scalar masses squared is negative. This problem can be cured by adding a positive non–anomaly mediated contribution to the soft masses, an m_0^2 term at M_{GUT}, as in mSUGRA models.

In gauge mediated SUSY–breaking (GMSB) models [57–59], SUSY–breaking is transmitted to the MSSM fields via the SM gauge interactions. In the original scenario, the model consists of three distinct sectors: a secluded sector where SUSY is broken, a "messenger" sector containing a singlet field and messenger fields with $\mathrm{SU(3)_C} \times \mathrm{SU(2)_L} \times \mathrm{U(1)_Y}$ quantum numbers, and a sector containing the fields of the MSSM. Another possibility, the so–called "direct gauge mediation" has only two sectors: one which is responsible for the SUSY–breaking and contains the messenger fields, and another sector consisting of the MSSM fields. In both cases, the soft SUSY–breaking masses for the gauginos and squared masses for the sfermions arise, respectively, from one–loop and two–loop diagrams involving the exchange of the messenger fields, while the trilinear Higgs–sfermion–sfermion couplings can be taken to be negligibly small at the messenger scale since they are [and not their square as for the sfermion masses] generated by two–loop gauge interactions. This allows an automatic and natural suppression of FCNC and CP–violation. In this model, the LSP is the gravitino which can have a mass below 1 eV.

1.1.5 The supersymmetric particle spectrum

Let us now discuss the general features of the chargino/neutralino and sfermion sectors of the MSSM. The Higgs sector will be discussed in much more detail later.

The chargino/neutralino/gluino sector

The general chargino mass matrix, in terms of the wino mass parameter M_2, the higgsino mass parameter μ and the ratio of vevs $\tan\beta$, is given by [30, 38]

$$\mathcal{M}_C = \begin{bmatrix} M_2 & \sqrt{2}M_W s_\beta \\ \sqrt{2}M_W c_\beta & \mu \end{bmatrix} \tag{1.22}$$

where we use $s_\beta \equiv \sin\beta$, $c_\beta \equiv \cos\beta$ *etc.* It is diagonalized by two real matrices U and V,

$$U\mathcal{M}_C V^{-1} \quad \to \quad U = \mathcal{O}_- \text{ and } V = \begin{cases} \mathcal{O}_+ & \text{if } \det\mathcal{M}_C > 0 \\ \sigma_3 \mathcal{O}_+ & \text{if } \det\mathcal{M}_C < 0 \end{cases} \tag{1.23}$$

where σ_3 is the Pauli matrix to make the chargino masses positive and $\mathcal{O}_\pm$ are rotation matrices with angles $\theta_\pm$ given by

$$\tan 2\theta_- = \frac{2\sqrt{2}M_W(M_2 c_\beta + \mu s_\beta)}{M_2^2 - \mu^2 - 2M_W^2 c_\beta} \quad , \quad \tan 2\theta_+ = \frac{2\sqrt{2}M_W(M_2 s_\beta + \mu c_\beta)}{M_2^2 - \mu^2 + 2M_W^2 c_\beta} \tag{1.24}$$

This leads to the two chargino masses

$$m_{\chi_{1,2}^\pm}^2 = \frac{1}{2} \left\{ M_2^2 + \mu^2 + 2M_W^2 \mp \left[(M_2^2 - \mu^2)^2 + 4M_W^2(M_W^2 c_{2\beta}^2 + M_2^2 + \mu^2 + 2M_2\mu s_{2\beta}) \right]^{\frac{1}{2}} \right\} \tag{1.25}$$

In the limit $|\mu| \gg M_2, M_W$, the masses of the two charginos reduce to

$$m_{\chi_1^\pm} \simeq M_2 - M_W^2 \mu^{-2} (M_2 + \mu s_{2\beta}) \quad , \quad m_{\chi_2^\pm} \simeq |\mu| + M_W^2 \mu^{-2} \epsilon_\mu (M_2 s_{2\beta} + \mu) \tag{1.26}$$

where ϵ_μ is for the sign of μ. For $|\mu| \to \infty$, the lightest chargino corresponds to a pure wino with a mass $m_{\chi_1^\pm} \simeq M_2$, while the heavier chargino corresponds to a pure higgsino with a mass $m_{\chi_2^\pm} = |\mu|$. In the opposite limit, $M_2 \gg |\mu|, M_Z$, the roles of $\chi_1^\pm$ and $\chi_2^\pm$ are reversed.

In the case of the neutralinos, the four–dimensional mass matrix depends on the same two mass parameters μ and M_2, as well as on $\tan\beta$ and M_1 [if the latter is not related to M_2 as in constrained models]. In the $(-i\tilde{B}, -i\tilde{W}_3, \tilde{H}_1^0, \tilde{H}_2^0)$ basis, it has the form [30, 38]

$$\mathcal{M}_N = \begin{bmatrix} M_1 & 0 & -M_Z s_W c_\beta & M_Z s_W s_\beta \\ 0 & M_2 & M_Z c_W c_\beta & -M_Z c_W s_\beta \\ -M_Z s_W c_\beta & M_Z c_W c_\beta & 0 & -\mu \\ M_Z s_W s_\beta & -M_Z c_W s_\beta & -\mu & 0 \end{bmatrix} \tag{1.27}$$

It can be diagonalized analytically [60] by a single real matrix Z. The expressions of the matrix elements Z_{ij} with $i, j = 1, .., 4$ as well as the resulting masses $m_{\chi_i^0}$ are rather involved. In the limit of large $|\mu|$ values, $|\mu| \gg M_{1,2} \gg M_Z$, they however simplify to [61]

$$
\begin{aligned}
m_{\chi_1^0} &\simeq M_1 - \frac{M_Z^2}{\mu^2} \left(M_1 + \mu s_{2\beta} \right) s_W^2 \\
m_{\chi_2^0} &\simeq M_2 - \frac{M_Z^2}{\mu^2} \left(M_2 + \mu s_{2\beta} \right) c_W^2 \\
m_{\chi_{3/4}^0} &\simeq |\mu| + \frac{1}{2} \frac{M_Z^2}{\mu^2} \epsilon_\mu (1 \mp s_{2\beta}) \left(\mu \pm M_2 s_W^2 \mp M_1 c_W^2 \right)
\end{aligned}
\tag{1.28}
$$

where $\epsilon_\mu = \mu/|\mu|$ is the sign of μ. Again, for $|\mu| \to \infty$, two neutralinos are pure gaugino states with masses $m_{\chi_1^0} \simeq M_1$ and $m_{\chi_2^0} = M_2$, while the two other neutralinos are pure higgsinos with masses $m_{\chi_3^0} \simeq m_{\chi_4^0} \simeq |\mu|$. In the opposite limit, the roles are again reversed and one has instead, $m_{\chi_1^0} \simeq m_{\chi_2^0} \simeq |\mu|, m_{\chi_3^0} \simeq M_1$ and $m_{\chi_4^0} \simeq M_2$.

Finally, the gluino mass is identified with M_3 at the tree–level

$$
m_{\tilde{g}} = M_3
\tag{1.29}
$$

In constrained models with boundary conditions at the high energy scale M_U, the evolution of the gaugino masses are given by the RGEs [53]

$$
\frac{\mathrm{d}M_i}{\mathrm{d}\log(M_U/Q^2)} = -\frac{g_i^2 M_i}{16\pi^2} b_i \ , \ \ b_1 = \frac{33}{5} \ , \ \ b_2 = 1 \ , b_3 = -3
\tag{1.30}
$$

where in the coefficients b_i we have assumed that all the MSSM particle spectrum contributes to the evolution from Q to the high scale M_U. These equations are in fact related to those of the $SU(3)_C \times SU(2)_L \times U(1)_Y$ gauge coupling constants $\alpha_i = g_i^2/(4\pi)$, where with the input gauge coupling constants at the scale of the Z boson mass, $\alpha_1(M_Z) \simeq 0.016, \alpha_2(M_Z) \simeq 0.033$ and $\alpha_3(M_Z) \simeq 0.118$, one has $M_U \sim 1.9 \times 10^{16}$ GeV for the GUT scale and $\alpha_U \simeq 0.041$ for the common coupling constant at this scale. Choosing a common value $m_{1/2}$ at the scale M_U, one then obtains for the gaugino mass parameters at the weak scale

$$
M_3 : M_2 : M_1 \sim \alpha_3 : \alpha_2 : \alpha_1 \sim 6 : 2 : 1
\tag{1.31}
$$

Note that in the electroweak sector, we have taken into account the GUT normalization factor $\frac{5}{3}$ in α_1. In fact, for a common gaugino mass at the scale M_U, the bino and wino masses are related by the well known formula, $M_1 = \frac{5}{3} \tan^2 \theta_W M_2 \simeq \frac{1}{2} M_2$, at low scales.

The sfermion sector

The sfermion system is described, in addition to $\tan\beta$ and μ, by three parameters for each sfermion species: the left– and right–handed soft SUSY–breaking scalar masses $m_{\tilde{f}_L}$ and

$m_{\tilde{f}_R}$ and the trilinear couplings A_f. In the case of the third generation scalar fermions [throughout this review, we will assume that the masses of the first and second generation fermions are zero, as far as the SUSY sector is concerned] the mixing between left– and right–handed sfermions, which is proportional to the mass of the partner fermion, must be included [62]. The sfermion mass matrices read

$$\mathcal{M}_{\tilde{f}}^2 = \begin{pmatrix} m_f^2 + m_{LL}^2 & m_f\, X_f \\ m_f\, X_f & m_f^2 + m_{RR}^2 \end{pmatrix} \tag{1.32}$$

with the various entries given by

$$\begin{aligned} m_{LL}^2 &= m_{\tilde{f}_L}^2 + (I_f^{3L} - Q_f s_W^2)\, M_Z^2\, c_{2\beta} \\ m_{RR}^2 &= m_{\tilde{f}_R}^2 + Q_f s_W^2\, M_Z^2\, c_{2\beta} \\ X_f &= A_f - \mu(\tan\beta)^{-2I_f^{3L}} \end{aligned} \tag{1.33}$$

They are diagonalized by 2×2 rotation matrices of angle θ_f, which turn the current eigenstates $\tilde{f}_L$ and $\tilde{f}_R$ into the mass eigenstates $\tilde{f}_1$ and $\tilde{f}_2$

$$R^{\tilde{f}} = \begin{pmatrix} c_{\theta_f} & s_{\theta_f} \\ -s_{\theta_f} & c_{\theta_f} \end{pmatrix} \quad , \quad c_{\theta_f} \equiv \cos\theta_{\tilde{f}} \ \text{ and } \ s_{\theta_f} \equiv \sin\theta_{\tilde{f}} \tag{1.34}$$

The mixing angle and sfermion masses are then given by

$$s_{2\theta_f} = \frac{2m_f X_f}{m_{\tilde{f}_1}^2 - m_{\tilde{f}_2}^2} \quad , \quad c_{2\theta_f} = \frac{m_{LL}^2 - m_{RR}^2}{m_{\tilde{f}_1}^2 - m_{\tilde{f}_2}^2} \tag{1.35}$$

$$m_{\tilde{f}_{1,2}}^2 = m_f^2 + \frac{1}{2}\left[m_{LL}^2 + m_{RR}^2 \mp \sqrt{(m_{LL}^2 - m_{RR}^2)^2 + 4m_f^2 X_f^2} \right] \tag{1.36}$$

The mixing is very strong in the stop sector for large values of the parameter $X_t = A_t - \mu\cot\beta$ and generates a mass splitting between the two mass eigenstates which makes the state $\tilde{t}_1$ much lighter than the other squarks and possibly even lighter than the top quark itself. For large values of $\tan\beta$ and $|\mu|$, the mixing in the sbottom and stau sectors can also be very strong, $X_{b,\tau} = A_{b,\tau} - \mu\tan\beta$, leading to lighter $\tilde{b}_1$ and $\tilde{\tau}_1$ states.

Note that in the case of degenerate sfermion soft SUSY–breaking masses, $m_{LL} \sim m_{RR}$, that we will often consider in this review, in most of the MSSM parameter space the sfermion mixing angle is either close to zero [no mixing] or to $-\frac{\pi}{4}$ [maximal mixing] for respectively, small and large values of the off–diagonal entry $m_f X_f$ of the sfermion mass matrix. One then has $s_{2\theta_f} \sim 0$ and $|s_{2\theta_f}| \sim 1$ for the no mixing and maximal mixing cases, respectively.

In constrained models such as mSUGRA for instance, assuming universal scalar masses m_0 and gaugino masses $m_{1/2}$ at the GUT scale, one obtains relatively simple expressions for the left– and right–handed soft masses when performing the RGE evolution to the weak

scale at one–loop if the Yukawa couplings are neglected. This approximation is rather good for the two first generations and one has [53]

$$m_{\tilde{f}_{L,R}}^2 = m_0^2 + \sum_{i=1}^{3} F_i(f) m_{1/2}^2 \ , \quad F_i = \frac{c_i(f)}{b_i} \left[1 - \left(1 - \frac{\alpha_U}{4\pi} b_i \log\frac{Q^2}{M_U^2} \right)^{-2} \right] \qquad (1.37)$$

with $\alpha_U = g_i^2(M_U)/4\pi$, the coefficients b_i have been given before and the coefficients $c(\tilde{f}) = (c_1, c_2, c_3)(\tilde{f})$ depend on the isospin, hypercharge and color of the sfermions

$$c(\tilde{L}) = \begin{pmatrix} \frac{3}{10} \\ \frac{3}{2} \\ 0 \end{pmatrix}, \ c(\tilde{l}_R) = \begin{pmatrix} \frac{6}{5} \\ 0 \\ 0 \end{pmatrix}, \ c(\tilde{Q}) = \begin{pmatrix} \frac{1}{30} \\ \frac{3}{2} \\ \frac{8}{3} \end{pmatrix}, \ c(\tilde{u}_R) = \begin{pmatrix} \frac{8}{15} \\ 0 \\ \frac{8}{3} \end{pmatrix}, \ c(\tilde{d}_R) = \begin{pmatrix} \frac{2}{15} \\ 0 \\ \frac{8}{3} \end{pmatrix} (1.38)$$

With the input gauge coupling constants at M_Z as measured at LEP1 and their derived value $\alpha_U \simeq 0.041$ at the GUT scale M_U, one obtains approximately for the left– and right–handed sfermions mass parameters [31]

$$m_{\tilde{q}_i}^2 \sim m_0^2 + 6m_{1/2}^2 \ , \quad m_{\tilde{\ell}_L}^2 \sim m_0^2 + 0.52m_{1/2}^2 \ , \quad m_{\tilde{e}_R}^2 \sim m_0^2 + 0.15m_{1/2}^2 \qquad (1.39)$$

For third generation squarks, neglecting the Yukawa couplings in the RGEs is a poor approximation since they can be very large, in particular in the top squark case. Including these couplings, an approximate solution of the RGEs in the small $\tan\beta$ regime, is given by

$$m_{\tilde{t}_L}^2 = m_{\tilde{b}_L}^2 \sim m_0^2 + 6m_{1/2}^2 - \frac{1}{3}X_t \ , \quad m_{\tilde{t}_R}^2 = m_{\tilde{b}_L}^2 \sim m_0^2 + 6m_{1/2}^2 - \frac{2}{3}X_t \qquad (1.40)$$

with $X_t \sim 1.3m_0^2 + 3m_{1/2}^2$ [31]. This shows that, in contrast to the first two generations, one has generically a sizable splitting between $m_{\tilde{t}_L}^2$ and $m_{\tilde{t}_R}^2$ at the electroweak scale, due to the running of the large top Yukawa coupling. This justifies the choice of different soft SUSY–breaking scalar masses and trilinear couplings for the third generation and the first/second generation sfermions [as well as for slepton and squark masses, see eq. (1.39)].

1.1.6 The fermion masses in the MSSM

Since the fermion masses play an important role in Higgs physics, and in the MSSM also in the SUSY sector where they provide one of the main inputs in the RGEs and in sfermion mixing, it is important to include the radiative corrections to these parameters [63–70]. For instance, to absorb the bulk of the higher–order corrections, the fermion masses to be used in the sfermion matrices eq. (1.32) should be the running masses [63,64] at the SUSY scale. [Note that also the soft SUSY–breaking scalar masses and trilinear couplings should be running parameters [70] evaluated at the SUSY or electroweak symmetry breaking scale.]

For quarks, the first important corrections to be included are those due to standard QCD and the running from the scale m_Q to the high scale Q. The relations between the pole quark masses and the running masses defined at the scale of the pole masses, $\overline{m}_Q(m_Q)$, have been discussed in the $\overline{\text{MS}}$ scheme in §I.1.1.4 of part 1. However, in the MSSM [and particularly in constrained models such as mSUGRA for instance] one usually uses the modified Dimensional Reduction $\overline{\text{DR}}$ scheme [71] which, contrary to the $\overline{\text{MS}}$ scheme, preserves Supersymmetry [by suitable counterterms, one can however switch from a scheme to another; see Ref. [72]]. The relation between the $\overline{\text{DR}}$ and $\overline{\text{MS}}$ running quark masses at a given scale μ reads [73]

$$\overline{m}_Q^{\overline{\text{DR}}}(\mu) = \overline{m}_Q^{\overline{\text{MS}}}(\mu) \left[1 - \frac{1}{3}\frac{\alpha_s(\mu^2)}{\pi} - k_Q \frac{\alpha_s^2(\mu^2)}{\pi^2} + \cdots \right] \tag{1.41}$$

where the strong coupling constant α_s is also evaluated at the scale μ, but defined in the $\overline{\text{MS}}$ scheme instead; the coefficient of the second order term in α_s is $k_b \sim \frac{1}{2}$ and $k_t \sim 1$ for bottom and top quarks, and additional but small electroweak contributions are present[2].

In addition, one has to include the SUSY–QCD corrections which, at first order, consist of squark/gluino loops. In fact, electroweak SUSY radiative corrections are also important in this context and in particular, large contributions can be generated by loops involving chargino/neutralino and stop/sbottom states, the involved couplings being potentially strong. In the case of b quarks, the dominant sbottom/gluino and stop/chargino one–loop corrections can be written as [69]

$$
\begin{aligned}
\frac{\Delta m_b}{m_b} &= -\frac{\alpha_s}{3\pi}\left[-s_{2\theta_b}\frac{m_{\tilde{g}}}{m_b}\Big(B_0(m_b, m_{\tilde{g}}, m_{\tilde{b}_1}) - B_0(m_b, m_{\tilde{g}}, m_{\tilde{b}_2}) \Big) \right] + B_1(m_b, m_{\tilde{g}}, m_{\tilde{b}_1}) \\
&+ B_1(m_b, m_{\tilde{g}}, m_{\tilde{b}_2}) - \frac{\alpha}{8\pi s_W^2}\frac{m_t \mu}{M_W^2 \sin 2\beta}\, s_{2\theta_t}\, [B_0(m_b, \mu, m_{\tilde{t}_1}) - B_0(m_b, \mu, m_{\tilde{t}_2})] \\
&- \frac{\alpha}{4\pi s_W^2}\left[\frac{M_2 \mu \tan\beta}{\mu^2 - M_2^2}\Big(c_{\theta_t}^2 B_0(m_b, M_2, m_{\tilde{t}_1}) + s_{\theta_t}^2 B_0(m_b, M_2, m_{\tilde{t}_2}) \Big) + (\mu \leftrightarrow M_2) \right]
\end{aligned} \tag{1.42}
$$

where the finite parts of the Passarino–Veltman two–point functions [74] are given by

$$
\begin{aligned}
B_0(q^2, m_1, m_2) &= -\log\left(\frac{q^2}{\mu^2}\right) - 2 \\
&\quad -\log(1 - x_+) - x_+\log(1 - x_+^{-1}) - \log(1 - x_-) - x_-\log(1 - x_-^{-1}) \\
B_1(q^2, m_1, m_2) &= \frac{1}{2q^2}\left[m_2^2\left(1 - \log\frac{m_2^2}{\mu^2}\right) - m_1^2\left(1 - \log\frac{m_1^2}{\mu^2}\right) \right. \\
&\quad \left. + (q^2 - m_2^2 + m_1^2) B_0(q^2, m_1, m_2) \right]
\end{aligned} \tag{1.43}
$$

---

[2]Since the difference between the quark masses in the two schemes is not very large, $\Delta m_Q/m_Q \sim 1\%$, to be compared with an experimental error of the order of 2% for $m_b(m_b)$ for instance, it is common practice to neglect this difference, at least in unconstrained SUSY models where one does not evolve the parameters up to the GUT scale.

with μ^2 denoting the renormalization scale and

$$x_\pm = \frac{1}{2q^2}\left(q^2 - m_2^2 + m_1^2 \pm \sqrt{(q^2 - m_2^2 + m_1^2)^2 - 4q^2(m_1^2 - i\epsilon)}\right) \tag{1.44}$$

In the limit where the b–quark mass is neglected and only the large correction terms are incorporated, one can use the approximate expression [67, 68]

$$\frac{\Delta m_b}{m_b} \equiv \Delta_b \simeq \left[\frac{2\alpha_s}{3\pi}\mu m_{\tilde{g}}\, I(m_{\tilde{g}}^2, m_{\tilde{b}_1}^2, m_{\tilde{b}_2}^2) + \frac{\lambda_t^2}{16\pi^2}A_t\mu\, I(\mu^2, m_{\tilde{t}_1}^2, m_{\tilde{t}_2}^2)\right]\tan\beta \tag{1.45}$$

with $\lambda_t = \sqrt{2}m_t/(v\sin\beta)$ [and $\lambda_b = \sqrt{2}m_b/(v\cos\beta)$] and the function I is given by

$$I(x, y, z) = \frac{xy\log(x/y) + yx\log(y/z) + zx\log(z/x)}{(x - y)(y - z)(z - x)} \tag{1.46}$$

and is of order $1/\max(x, y, z)$. This correction is thus very important in the case of large values of $\tan\beta$ and μ, and can increase or decrease [depending of the sign of μ] the b–quark mass by more than a factor of two. To take into account these large corrections, a "resummation" procedure is required [68] and the $\overline{\text{DR}}$ running b–quark mass evaluated at the scale $Q = M_Z$ can be defined in the following way

$$\widehat{m}_b \equiv \bar{m}_b(M_Z)_{\text{MSSM}}^{\overline{\text{DR}}} = \frac{\bar{m}_b^{\overline{\text{DR}}}(M_Z)}{1 - \Delta_b} \tag{1.47}$$

It has been shown in Ref. [68] that defining the running MSSM bottom mass as in eq. (1.47) guarantees that the large threshold corrections of $\mathcal{O}(\alpha_s\tan\beta)^n$ are included in $\widehat{m}_b$ to all orders in the perturbative expansion.

In the case of the top quark mass, the QCD corrections are the same as for the b–quark mass discussed above, but the additional electroweak corrections due to stop/neutralino and sbottom/chargino loops are different and enhanced by $A_t\mu$ or μ^2 terms [69]

$$\frac{\Delta m_t}{m_t} \equiv \Delta_t \simeq -\frac{2\alpha_s}{3\pi}m_{\tilde{g}}A_t\, I(m_{\tilde{g}}^2, m_{\tilde{t}_1}^2, m_{\tilde{t}_2}^2) - \frac{\lambda_b^2}{16\pi^2}\mu^2 I(\mu^2, m_{\tilde{b}_1}^2, m_{\tilde{b}_2}^2) \tag{1.48}$$

For the τ lepton mass, the only relevant corrections are the electroweak corrections stemming from chargino–sneutrino and neutralino–stau loops but they are very small [67, 69]

$$\frac{\Delta m_\tau}{m_\tau} \equiv \Delta_\tau \simeq \frac{\alpha}{4\pi}\left[\frac{M_1\mu}{c_W^2}I(M_1^2, m_{\tilde{\tau}_1}^2, m_{\tilde{\tau}_2}^2) - \frac{M_2\mu}{s_W^2}I(M_2^2, m_{\tilde{\nu}_\tau}^2, \mu^2)\right]\tan\beta \tag{1.49}$$

These SUSY particle threshold corrections will alter the relations between the masses of the fermions and their Yukawa couplings in a significant way. This will be discussed in some detail at a later stage.

1.1.7 Constraints on the MSSM parameters and sparticle masses

As discussed in the beginning of this subsection, the SUSY particle masses and, thus, the soft SUSY–breaking parameters at the weak scale, should not be too large in order to keep the radiative corrections to the Higgs masses under control. In other words, one has to require low values for the weak–scale parameters to avoid the need for excessive fine–tuning [75] in the electroweak symmetry breaking conditions to be discussed later. One thus imposes a bound on the SUSY scale that we define as the geometrical average of the two stop masses

$$M_S = \sqrt{m_{\tilde{t}_1} m_{\tilde{t}_2}} < 2 \text{ TeV} \tag{1.50}$$

However, it is important to bear in mind that, in the absence of a compelling criterion to define the maximal acceptable amount of fine–tuning, the choice of the upper bound on M_S is somewhat subjective. Note also that in some cases the SUSY scale will be taken as the arithmetic average of the stop masses, $M_S = \frac{1}{2}(m_{\tilde{t}_1} + m_{\tilde{t}_2})$; in the case of equal stop masses, the two definitions coincide. If in addition the mixing parameter X_t is not large, one can approximately write $M_S \simeq \frac{1}{2}(m_{\tilde{t}_L} + m_{\tilde{t}_R})$.

As we will see later, the trilinear couplings of the third generation sfermions and in particular the stop trilinear coupling A_t, will play a particularly important role in the MSSM Higgs sector. This parameter can be constrained in at least two ways, besides the trivial requirement that it should not make the off–diagonal term of the sfermion mass matrices too large to generate too low, or even tachyonic, masses for the sfermions:

(i) A_t should not be too large to avoid the occurrence of charge and color breaking (CCB) minima in the Higgs potential [76]. For the unconstrained MSSM, a rather stringent CCB constraint on this parameter, to be valid at the electroweak scale, reads [77]

$$A_t^2 \lesssim 3(m_{\tilde{t}_L}^2 + m_{\tilde{t}_R}^2 + \mu^2 + m_{H_2}^2) \tag{1.51}$$

(ii) Large values of A_t lead to a large splitting of the top squark masses and the breaking of the custodial SU(2) symmetry, generating potentially large contributions to the ρ parameter [78, 79] that are proportional to differences of squark masses squared. Neglecting the mixing in the sbottom sector for simplicity, the contribution of the $(\tilde{t}, \tilde{b})$ doublet to $\Delta\rho$ reads [80,81]

$$\Delta\rho(\tilde{t}, \tilde{b}) = \frac{3G_\mu}{8\pi^2\sqrt{2}} \left[c_{\theta_t}^2 f(m_{\tilde{t}_1}^2, m_{\tilde{b}_1}^2) + s_{\theta_t}^2 f(m_{\tilde{t}_2}^2, m_{\tilde{b}_1}^2) - c_{\theta_t}^2 s_{\theta_t}^2 f(m_{\tilde{t}_1}^2, m_{\tilde{t}_2}^2) \right] \tag{1.52}$$

where $f(x,y) = x + y - 2xy/(x-y)\log(x/y)$ with $f(x,x) = 1$ and $f(x,0) = x$ [the two–loop QCD corrections to this relation [82] induce a 30% increase of the contribution]. Note that if the requirement $\Delta\rho(\tilde{t}, \tilde{b}) \lesssim \mathcal{O}(10^{-3})$ is made to cope with the high–precision electroweak data [2], the constraint for $\Delta\rho$ supersedes sometimes the CCB constraint eq. (1.51).

Finally, there are lower bounds on the masses of the various sparticles from the negative searches for SUSY performed in the last decade at LEP and at the Tevatron. A brief summary of these experimental bounds is as follows [1, 83]

$$\text{LEP2 searches} \quad : \quad \begin{aligned} & m_{\chi_1^\pm} \geq 104 \text{ GeV} \\ & m_{\tilde{f}} \gtrsim 100 \text{ GeV for } \tilde{f} = \tilde{\ell}, \tilde{\nu}, \tilde{t}_1, (\tilde{b}_1) \end{aligned}$$

$$\text{Tevatron searches} \quad : \quad \begin{aligned} & m_{\tilde{g}} \gtrsim 300 \text{ GeV} \\ & m_{\tilde{q}} \gtrsim 300 \text{ GeV for } \tilde{q} = \tilde{u}, \tilde{d}, \tilde{s}, \tilde{c}, (\tilde{b}) \end{aligned} \qquad (1.53)$$

Although rather robust, these bounds might not hold in some regions of the MSSM parameter space. For instance, the lower bound on the lightest chargino mass $m_{\chi_1^\pm}$ is $\mathcal{O}(10 \text{ GeV})$ lower than the one quoted above when the lightest chargino is higgsino like and thus degenerate in mass with the LSP neutralino; in this case, the missing energy due to the escaping neutralino is rather small, leading to larger backgrounds. When the mass difference is so small that the chargino is long–lived, one can perform searches for almost stable charged particles [another possibility is to look for ISR photons] but the obtained mass bound is smaller than in eq. (1.53). For the same reason, the experimental bound on the lightest τ slepton is also lower than 100 GeV when $\tilde{\tau}_1$ is almost degenerate in mass with the LSP. In turn, the LEP2 bound on the mass of the lightest sbottom $\tilde{b}_1$ which is valid for any mixing pattern is superseded by the Tevatron bound when mixing effects do not make the sbottom behave very differently from first/second generation squarks. Also, the bounds from Tevatron searches shown above assume mass–degenerate squarks and gluinos [they are ~ 100 GeV lower for $m_{\tilde{g}} \neq m_{\tilde{q}}$ values] while the bound on the $\tilde{t}_1$ mass can be larger than the one obtained at LEP in some areas of the parameter space. For a more detailed discussion, see Refs. [1, 83].

From the lightest chargino mass limit at LEP2 [and in the gaugino region, when $|\mu| \gg M_2$, also from the limit on the gluino mass at the Tevatron], one can infer a bound on the mass of the lightest neutralino which is stable and therefore invisible in collider searches. For gaugino– or higgsino–like lightest neutralinos, one approximately obtains

$$\begin{aligned} \text{gaugino} \quad & : \quad m_{\chi_1^0} \simeq M_1 \simeq \frac{5}{3} \tan^2 \theta_W M_2 \simeq \frac{1}{2} M_2 \simeq \frac{1}{2} m_{\chi_1^\pm} \gtrsim 50 \text{ GeV} \\ \text{higgsino} \quad & : \quad m_{\chi_1^0} \simeq |\mu| \simeq m_{\chi_1^\pm} \gtrsim 90 \text{ GeV} \end{aligned} \qquad (1.54)$$

[Additional information is also provided by the search for the associated production of the LSP with the next–to–lightest neutralino]. An absolute lower bound of $m_{\chi_1^0} \gtrsim 50$ GeV can be obtained in constrained models [83]. However, if the assumption of a universal gaugino mass at the GUT scale, $M_1 = \frac{5}{3} \tan^2 \theta_W M_2$, is relaxed there is no lower bound on the mass of the LSP neutralino if it has a large bino component, except possibly from the one required to make it an acceptable candidate for the Dark Matter in the universe.

1.2 The Higgs sector of the MSSM

1.2.1 The Higgs potential of the MSSM

In the MSSM, we need two doublets of complex scalar fields of opposite hypercharge

$$H_1 = \begin{pmatrix} H_1^0 \\ H_1^- \end{pmatrix} \text{ with } Y_{H_1} = -1 \quad , \quad H_2 = \begin{pmatrix} H_2^+ \\ H_2^0 \end{pmatrix} \text{ with } Y_{H_2} = +1 \tag{1.55}$$

to break the electroweak symmetry. There are at least two reasons for this requirement[3].

In the SM, there are in principle chiral or Adler–Bardeen–Jackiw anomalies [85] which originate from triangular fermionic loops involving axial–vector current couplings and which spoil the renormalizability of the theory. However, these anomalies disappear because the sum of the hypercharges or charges of all the 15 chiral fermions of one generation in the SM is zero, $\text{Tr}(Y_f) = \text{Tr}(Q_f) = 0$. In the SUSY case, if we use only one doublet of Higgs fields as in the SM, we will have one additional charged spin $\frac{1}{2}$ particle, the higgsino corresponding to the SUSY partner of the charged component of the scalar field, which will spoil this cancellation. With two doublets of Higgs fields with opposite hypercharge, the cancellation of chiral anomalies still takes place [86].

In addition, in the SM, one generates the masses of the fermions of a given isospin by using the same scalar field Φ that also generates the W and Z boson masses, the isodoublet $\tilde{\Phi} = i\tau_2\Phi^*$ with opposite hypercharge generating the masses of the opposite isospin–type fermions. However, in a SUSY theory and as discussed in §1.1.2, the Superpotential should involve only the superfields and not their conjugate fields. Therefore, we must introduce a second doublet with the same hypercharge as the conjugate $\tilde{\Phi}$ field to generate the masses of both isospin–type fermions [19, 20, 26].

In the MSSM, the terms contributing to the scalar Higgs potential V_H come from three different sources [18, 38]:

i) The D terms containing the quartic Higgs interactions, eq. (1.10). For the two Higgs fields H_1 and H_2 with $Y = -1$ and $+1$, these terms are given by

$$\text{U(1)}_Y \quad : \quad V_D^1 = \frac{1}{2}\left[\frac{g_1}{2}(|H_2|^2 - |H_1|^2)\right]^2$$

$$\text{SU(2)}_L \quad : \quad V_D^2 = \frac{1}{2}\left[\frac{g_2}{2}(H_1^{i*}\tau_{ij}^a H_1^j + H_2^{i*}\tau_{ij}^a H_2^j)\right]^2 \tag{1.56}$$

with $\tau^a = 2T^a$. Using the SU(2) identity $\tau_{ij}^a\tau_{kl}^a = 2\delta_{il}\delta_{jk} - \delta_{ij}\delta_{kl}$, one obtains the potential

$$V_D = \frac{g_2^2}{8}\left[4|H_1^\dagger\cdot H_2|^2 - 2|H_1|^2|H_2|^2 + (|H_1|^2)^2 + (|H_2|^2)^2\right] + \frac{g_1^2}{8}(|H_2|^2 - |H_1|^2)^2 \tag{1.57}$$

---

[3]A higher number of Higgs doublets would also spoil the unification of the gauge coupling constants if no additional matter particles are added; see for instance Ref. [84].

ii) The F term of the Superpotential eq. (1.12) which, as discussed, can be written as $V_F = \sum_i |\partial W(\phi_j)/\partial \phi_i|^2$. From the term $W \sim \mu \hat{H}_1 \cdot \hat{H}_2$, one obtains the component

$$V_F = \mu^2 (|H_1|^2 + |H_2|^2) \tag{1.58}$$

iii) Finally, there is a piece originating from the soft SUSY–breaking scalar Higgs mass terms and the bilinear term

$$V_{\text{soft}} = m_{H_1}^2 H_1^\dagger H_1 + m_{H_2}^2 H_2^\dagger H_2 + B\mu(H_2 \cdot H_1 + \text{h.c.}) \tag{1.59}$$

The full scalar potential involving the Higgs fields is then the sum of the three terms [38]

$$\begin{aligned} V_H & = (|\mu|^2 + m_{H_1}^2)|H_1|^2 + (|\mu|^2 + m_{H_2}^2)|H_2|^2 - \mu B \epsilon_{ij}(H_1^i H_2^j + \text{h.c.}) \\ & \quad + \frac{g_2^2 + g_1^2}{8}(|H_1|^2 - |H_2|^2)^2 + \frac{1}{2}g_2^2|H_1^\dagger H_2|^2 \end{aligned} \tag{1.60}$$

Expanding the Higgs fields in terms of their charged and neutral components and defining the mass squared terms

$$\overline{m}_1^2 = |\mu|^2 + m_{H_1}^2, \quad \overline{m}_2^2 = |\mu|^2 + m_{H_2}^2, \quad \overline{m}_3^2 = B\mu \tag{1.61}$$

one obtains, using the decomposition into neutral and charged components eq. (1.55)

$$\begin{aligned} V_H & = \overline{m}_1^2(|H_1^0|^2 + |H_1^-|^2) + \overline{m}_2^2(|H_2^0|^2 + |H_2^+|^2) - \overline{m}_3^2(H_1^- H_2^+ - H_1^0 H_2^0 + \text{h.c.}) \\ & \quad + \frac{g_2^2 + g_1^2}{8}(|H_1^0|^2 + |H_1^-|^2 - |H_2^0|^2 - |H_2^+|^2)^2 + \frac{g_2^2}{2}|H_1^{-*}H_1^0 + H_2^{0*}H_2^+|^2 \end{aligned} \tag{1.62}$$

One can then require that the minimum of the potential V_H breaks the $\text{SU}(2)_\text{L} \times \text{U}_\text{Y}$ group while preserving the electromagnetic symmetry $\text{U}(1)_\text{Q}$. At the minimum of the potential $V_H^{\min}$ one can always choose the vacuum expectation value of the field H_1^- to be zero, $\langle H_1^- \rangle = 0$, because of SU(2) symmetry. At $\partial V/\partial H_1^- = 0$, one obtains then automatically $\langle H_2^+ \rangle = 0$. There is therefore no breaking in the charged directions and the QED symmetry is preserved. Some interesting and important remarks can be made at this stage [18, 38]:

• The quartic Higgs couplings are fixed in terms of the $\text{SU}(2) \times \text{U}(1)$ gauge couplings. Contrary to a general two–Higgs doublet model where the scalar potential V_H has 6 free parameters and a phase, in the MSSM we have only three free parameters: $\overline{m}_1^2, \overline{m}_2^2$ and $\overline{m}_3^2$.

• The two combinations $m_{H_1, H_2}^2 + |\mu|^2$ are real and, thus, only $B\mu$ can be complex. However, any phase in $B\mu$ can be absorbed into the phases of the fields H_1 and H_2. Thus, the scalar potential of the MSSM is CP conserving at the tree–level.

• To have electroweak symmetry breaking, one needs a combination of the H_1^0 and H_2^0 fields to have a negative squared mass term. This occurs if

$$\overline{m}_3^2 > \overline{m}_2^2 \overline{m}_2^2 \tag{1.63}$$

31

if not, $\langle H_1^0 \rangle = \langle H_2^0 \rangle$ will a stable minimum of the potential and there is no EWSB.

- In the direction $|H_1^0| = |H_2^0|$, there is no quartic term. V_H is bounded from below for large values of the field H_i only if the following condition is satisfied:

$$\overline{m}_1^2 + \overline{m}_2^2 > 2|\overline{m}_3^2| \tag{1.64}$$

- To have explicit electroweak symmetry breaking and, thus, a negative squared term in the Lagrangian, the potential at the minimum should have a saddle point and therefore

$$\mathrm{Det}\left(\frac{\partial^2 V_H}{\partial H_i^0 \partial H_j^0}\right) < 0 \Rightarrow \overline{m}_1^2\, \overline{m}_2^2 < \overline{m}_3^4 \tag{1.65}$$

- The two above conditions on the masses $\bar{m}_i$ are not satisfied if $\overline{m}_1^2 = \overline{m}_2^2$ and, thus, we must have non–vanishing soft SUSY–breaking scalar masses m_{H_1} and m_{H_2}

$$\overline{m}_1^2 \neq \overline{m}_2^2 \Rightarrow m_{H_1}^2 \neq m_{H_2}^2 \tag{1.66}$$

Therefore, to break the electroweak symmetry, we need also to break SUSY. This provides a close connection between gauge symmetry breaking and SUSY–breaking. In constrained models such as mSUGRA, the soft SUSY–breaking scalar Higgs masses are equal at high–energy, $m_{H_1} = m_{H_1}$ [and their squares positive], but the running to lower energies via the contributions of top/bottom quarks and their SUSY partners in the RGEs makes that this degeneracy is lifted at the weak scale, thus satisfying eq. (1.66). In the running one obtains $m_{H_2}^2 < 0$ or $m_{H_2}^2 \ll m_{H_1}^2$ which thus triggers EWSB: this is the radiative breaking of the symmetry [28]. Thus, electroweak symmetry breaking is more natural and elegant in the MSSM than in the SM since, in the latter case, we needed to make the ad hoc choice $\mu^2 < 0$ while in the MSSM this comes simply from radiative corrections.

1.2.2 The masses of the MSSM Higgs bosons

Let us now determine the Higgs spectrum in the MSSM, following Refs. [18, 38, 41]. The neutral components of the two Higgs fields develop vacuum expectations values

$$\langle H_1^0 \rangle = \frac{v_1}{\sqrt{2}} \ , \ \ \langle H_2^0 \rangle = \frac{v_2}{\sqrt{2}} \tag{1.67}$$

Minimizing the scalar potential at the electroweak minimum, $\partial V_H/\partial H_1^0 = \partial V_H/\partial H_2^0 = 0$, using the relation

$$(v_1^2 + v_2^2)^2 = v^2 = \frac{4M_Z^2}{g_2^2 + g_1^2} = (246 \ \mathrm{GeV})^2 \tag{1.68}$$

and defining the important parameter

$$\tan\beta = \frac{v_2}{v_1} = \frac{(v\sin\beta)}{(v\cos\beta)} \tag{1.69}$$

one obtains two minimization conditions that can be written in the following way

$$B\mu = \frac{(m_{H_1}^2 - m_{H_2}^2)\tan 2\beta + M_Z^2 \sin 2\beta}{2}$$

$$\mu^2 = \frac{m_{H_2}^2 \sin^2 \beta - m_{H_1}^2 \cos^2 \beta}{\cos 2\beta} - \frac{M_Z^2}{2} \tag{1.70}$$

These relations show explicitly what we have already mentioned: if m_{H_1} and m_{H_2} are known [if, for instance, they are given by the RGEs at the weak scale once they are fixed to a given value at the GUT scale], together with the knowledge of $\tan \beta$, the values of B and μ^2 are fixed while the sign of μ stays undetermined. These relations are very important since the requirement of radiative symmetry breaking leads to additional constraints and lowers the number of free parameters.

To obtain the Higgs physical fields and their masses, one has to develop the two doublet complex scalar fields H_1 and H_2 around the vacuum, into real and imaginary parts

$$H_1 = (H_1^0, H_1^-) = \frac{1}{\sqrt{2}} \left(v_1 + H_1^0 + iP_1^0 \ , \ H_1^- \right)$$

$$H_2 = (H_2^+, H_2^0) = \frac{1}{\sqrt{2}} \left(H_2^+ \ , \ v_2 + H_2^0 + iP_2^0 \right) \tag{1.71}$$

where the real parts correspond to the CP–even Higgs bosons and the imaginary parts corresponds to the CP–odd Higgs and the Goldstone bosons, and then diagonalize the mass matrices evaluated at the vacuum

$$\mathcal{M}_{ij}^2 = \frac{1}{2} \left. \frac{\partial^2 V_H}{\partial H_i \partial H_j} \right|_{\langle H_1^0 \rangle = v_1/\sqrt{2}, \langle H_2^0 \rangle = v_2/\sqrt{2}, \langle H_{1,2}^\pm \rangle = 0} \tag{1.72}$$

To obtain the Higgs boson masses and their mixing angles, some useful relations are

$$\mathrm{Tr}(\mathcal{M}^2) = M_1^2 + M_2^2 \ , \quad \mathrm{Det}(\mathcal{M}^2) = M_1^2 M_2^2 \tag{1.73}$$

$$\sin 2\theta = \frac{2\mathcal{M}_{12}}{\sqrt{(\mathcal{M}_{11} - \mathcal{M}_{22})^2 + 4\mathcal{M}_{12}^2}} \ , \quad \cos 2\theta = \frac{\mathcal{M}_{11} - \mathcal{M}_{22}}{\sqrt{(\mathcal{M}_{11} - \mathcal{M}_{22})^2 + 4\mathcal{M}_{12}^2}} \tag{1.74}$$

where M_1 and M_2 are the physical masses and θ the mixing angle.

In the case of the CP–even Higgs bosons, one obtains the following mass matrix

$$\mathcal{M}_R^2 = \begin{bmatrix} -\bar{m}_3^2 \tan \beta + M_Z^2 \cos^2 \beta & \bar{m}_3^2 - M_Z^2 \sin \beta \cos \beta \\ \bar{m}_3^2 - M_Z^2 \sin \beta \cos \beta & -\bar{m}_3^2 \cot \beta + M_Z^2 \sin^2 \beta \end{bmatrix} \tag{1.75}$$

while for the neutral Goldstone and CP–odd Higgs bosons, one has the mass matrix

$$\mathcal{M}_I^2 = \begin{bmatrix} -\bar{m}_3^2 \tan \beta & \bar{m}_3^2 \\ \bar{m}_3^2 & -\bar{m}_3^2 \cot \beta \end{bmatrix} \tag{1.76}$$

33

In this case, since $\text{Det}(\mathcal{M}_I^2) = 0$, one eigenvalue is zero and corresponds to the Goldstone boson mass, while the other corresponds to the pseudoscalar Higgs mass and is given by

$$M_A^2 = -\bar{m}_3^2(\tan\beta + \cot\beta) = -\frac{2\bar{m}_3^2}{\sin 2\beta} \tag{1.77}$$

The mixing angle θ which gives the physical fields is in fact simply the angle β

$$\begin{pmatrix} G^0 \\ A \end{pmatrix} = \begin{pmatrix} \cos\beta & \sin\beta \\ -\sin\beta & \cos\beta \end{pmatrix} \begin{pmatrix} P_1^0 \\ P_2^0 \end{pmatrix} \tag{1.78}$$

In the case of the charged Higgs boson, one can make exactly the same exercise as for the pseudoscalar A boson and obtain the charged fields

$$\begin{pmatrix} G^\pm \\ H^\pm \end{pmatrix} = \begin{pmatrix} \cos\beta & \sin\beta \\ -\sin\beta & \cos\beta \end{pmatrix} \begin{pmatrix} H_1^\pm \\ H_2^\pm \end{pmatrix} \tag{1.79}$$

with a massless charged Goldstone and a charged Higgs boson with a mass

$$M_{H^\pm}^2 = M_A^2 + M_W^2 \tag{1.80}$$

Coming back to the CP–even Higgs case, and injecting the expression of M_A^2 into $\mathcal{M}_R^2$, one obtains for the CP–even Higgs boson masses after calculating the trace and the determinant of the matrix and solving the resulting quadratic equation

$$M_{h,H}^2 = \frac{1}{2}\left[M_A^2 + M_Z^2 \mp \sqrt{(M_A^2 + M_Z^2)^2 - 4M_A^2 M_Z^2 \cos^2 2\beta} \right] \tag{1.81}$$

The physical CP–even Higgs bosons are obtained from the rotation of angle α

$$\begin{pmatrix} H \\ h \end{pmatrix} = \begin{pmatrix} \cos\alpha & \sin\alpha \\ -\sin\alpha & \cos\alpha \end{pmatrix} \begin{pmatrix} H_1^0 \\ H_2^0 \end{pmatrix} \tag{1.82}$$

where the mixing angle α is given by

$$\cos 2\alpha = -\cos 2\beta \frac{M_A^2 - M_Z^2}{M_H^2 - M_h^2} \ , \quad \sin 2\alpha = -\sin 2\beta \frac{M_H^2 + M_h^2}{M_H^2 - M_h^2} \tag{1.83}$$

or, in a more compact way

$$\alpha = \frac{1}{2}\arctan\left(\tan 2\beta \frac{M_A^2 + M_Z^2}{M_A^2 - M_Z^2}\right) \ , \quad -\frac{\pi}{2} \leq \alpha \leq 0 \tag{1.84}$$

Thus, the supersymmetric structure of the theory has imposed very strong constraints on the Higgs spectrum. Out of the six parameters which describe the MSSM Higgs sector, $M_h, M_H, M_A, M_{H^\pm}, \beta$ and α, only two parameters, which can be taken as $\tan\beta$ and M_A, are free parameters at the tree–level. In addition, a strong hierarchy is imposed on the mass spectrum and besides the relations $M_H > \max(M_A, M_Z)$ and $M_{H^\pm} > M_W$, we have the very important constraint on the lightest h boson mass at the tree–level

$$M_h \leq \min(M_A, M_Z) \cdot |\cos 2\beta| \leq M_Z \tag{1.85}$$

34

1.2.3   The couplings of the MSSM Higgs bosons

The Higgs couplings to gauge bosons

The Higgs boson couplings to the gauge bosons [38] are obtained from the kinetic terms of the fields H_1 and H_2 in the Lagrangian

$$\mathcal{L}_{\text{kin.}} = (D^\mu H_1)^\dagger (D_\mu H_1) + (D^\mu H_2)^\dagger (D_\mu H_2) \tag{1.86}$$

Expanding the covariant derivative D_μ and performing the usual transformations on the gauge and scalar fields to obtain the physical fields, one can identify the trilinear couplings $V_\mu V_\nu H_i$ among one Higgs and two gauge bosons and $V_\mu H_i H_j$ among one gauge boson and two Higgs bosons, as well as the couplings between two gauge and two Higgs bosons $V_\mu V_\nu H_i H_j$. The Feynman diagrams of these three sets of couplings are given in Fig. 1.2, and the Feynman rules for all possible couplings are given below; to simplify the expressions, we have used the abbreviated couplings $g_W = g_2$ and $g_Z = g_2/c_W$.
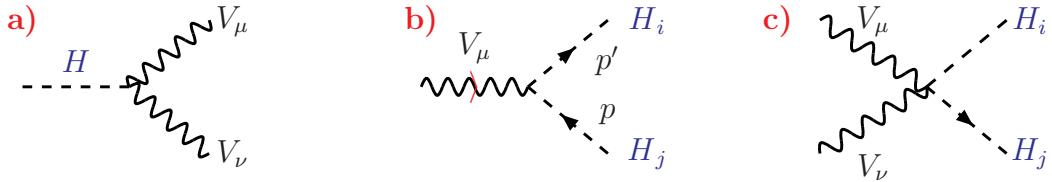

Figure 1.2: Feynman diagrams for the couplings between one Higgs and two gauge bosons (a), two Higgs and one gauge boson (b) and two Higgs and two gauge bosons (c). The direction of the momenta of the gauge and Higgs bosons are indicated when important.

$$Z_\mu Z_\nu h \; : \; ig_Z M_Z \sin(\beta - \alpha) g_{\mu\nu} \quad , \quad Z_\mu Z_\nu H \; : \; ig_Z M_Z \cos(\beta - \alpha) g_{\mu\nu}$$

$$W_\mu^+ W_\nu^+ h \; : \; ig_W M_W \sin(\beta - \alpha) g_{\mu\nu} \quad , \quad W_\mu^+ W_\nu^- H \; : \; ig_W M_W \cos(\beta - \alpha) g_{\mu\nu} \tag{1.87}$$

$$Z_\mu h A : +\frac{g_Z}{2} \cos(\beta - \alpha)(p + p')_\mu \quad , \quad Z_\mu H A : -\frac{g_Z}{2} \sin(\beta - \alpha)(p + p')_\mu$$

$$Z_\mu H^+ H^- : -\frac{g_Z}{2} \cos 2\theta_W (p + p')_\mu \quad , \quad \gamma_\mu H^+ H^- : -ie(p + p')_\mu$$

$$W_\mu^\pm H^\pm h : \mp i\frac{g_W}{2} \cos(\beta - \alpha)(p + p')_\mu \quad , \quad W_\mu^\pm H^\pm H : \pm i\frac{g_2}{2} \sin(\beta - \alpha)(p + p')_\mu$$

$$W_\mu^\pm H^\pm A : \frac{g_W}{2}(p + p')_\mu \quad , \quad W_\mu^\pm G^\pm G^0 : \frac{g_W}{2}(p + p')_\mu \tag{1.88}$$

$$W_\mu^+ W_\nu^- H_i H_j \; : \; \frac{ig_W^2}{2} g_{\mu\nu} c_i \delta_{ij} \; , \quad c_i = 1 \text{ for } H_i = h, H, A \; H^\pm$$

$$Z_\mu Z_\nu H_i H_i \; : \; \frac{ig_Z^2}{2} g_{\mu\nu} c_i \delta_{ij} \; , \quad c_i = 1 \, (\cos^2 2\theta_W) \text{ for } H_i = h, H, A \; (H^\pm)$$

$$\gamma_\mu \gamma_\nu H_i H_i \; : \; 2ie^2 \, g_{\mu\nu} c_i \delta_{ij} \; , \quad c_i = 0 \, (1) \text{ for } h, H, A \; (H^\pm)$$

$$\gamma_\mu Z_\nu H_i H_i \; : \; ieg_Z \, g_{\mu\nu} c_i \delta_{ij} \; , \quad c_i = 0 \, (\cos^2 2\theta_W) \text{ for } H_i = h, H, A \; (H^\pm)$$

$$Z_\mu W_\nu^\pm H^\pm H_i \; : \; \frac{ig_Z^2 \sin 2\theta_W}{2} c_i g_{\mu\nu} \; , \quad c_i = -\cos(\beta - \alpha), +\sin(\beta - \alpha), \pm 1 \text{ for } H_i = h, H, A$$

$$\gamma_\mu W_\nu^\pm H^\pm H_i \; : \; -\frac{ig_W e}{2} c_i g_{\mu\nu} \; , \quad c_i = -\cos(\beta - \alpha), +\sin(\beta - \alpha), \pm 1 \text{ for } H_i = h, H, A$$

A few remarks are to be made here:

– In the case of the couplings between one Higgs boson and two gauge bosons, since the photon is massless, there are no Higgs–$\gamma\gamma$ and Higgs–$Z\gamma$ couplings. CP–invariance also forbids WWA, ZZA and $WZH^{\pm}$ couplings [a summary of allowed Higgs couplings in a general two–Higgs doublet model and in the MSSM, will be given later]. The couplings of the neutral CP–even Higgs bosons h and H to VV states with $V = W, Z$ are proportional to either $\sin(\beta - \alpha)$ or $\cos(\beta - \alpha)$; in terms of the Higgs boson masses the latter factor is given by

$$\cos^2(\beta - \alpha) = \frac{M_h^2(M_Z^2 - M_h^2)}{M_A^2(M_H^2 - M_h^2)} \tag{1.89}$$

The couplings G_{hVV} and G_{HVV} are thus complementary and the sum of their squares is just the square of the SM Higgs boson coupling $g_{H_{\mathrm{SM}}VV}$

$$G_{hVV}^2 + G_{HVV}^2 = g_{H_{\mathrm{SM}}VV}^2 \tag{1.90}$$

This complementarity will have very important consequences as will be seen later.

– For the couplings between two Higgs bosons and one gauge boson, CP–invariance implies that the two Higgs bosons must have opposite parity and, thus, there are no Zhh, ZHh, ZHH and ZAA couplings. Only the ZhA and ZHA couplings are allowed in the neutral case while, in the charged case, the three couplings among $W^{\pm}H^{\pm}$ and h, H, A states are present [see §1.2.5]. The couplings to Goldstone bosons have not been displayed, but they can be obtained from those involving the pseudoscalar and charged Higgs bosons by replacing A and $H^{\pm}$ by G^0 and $G^{\pm}$, respectively. When the CP–even h, H bosons are involved, one has to replace in addition $\sin(\beta - \alpha)$ by $-\cos(\beta - \alpha)$ and $\cos(\beta - \alpha)$ by $\sin(\beta - \alpha)$. The couplings of the CP–even h and H bosons to ZA and $W^{\pm}H^{\pm}$ states are also complementary and one can write

$$
\begin{aligned}
G_{hAZ}^2 + G_{HAZ}^2 &= (4M_Z^2)^{-1} g_{H_{\mathrm{SM}}ZZ}^2 \\
G_{hH^{\pm}W^{\pm}}^2 + G_{HH^{\pm}W^{\pm}}^2 &= G_{AH^{\pm}W^{\pm}}^2 = (4M_W^2)^{-1} g_{H_{\mathrm{SM}}WW}^2
\end{aligned}
\tag{1.91}
$$

[This complementarity is required to avoid unitarity violation in scattering processes involving Higgs bosons such as $AZ \to AZ$ and $AZ \to W^+W^-$ [87,88].]

– For the couplings between two Higgs bosons and two gauge bosons, we have also not listed those involving Goldstone bosons. They can be obtained from those of the pseudoscalar and charged Higgs bosons by making the same replacements as above, that is A and $H^{\pm}$ by G^0 and $G^{\pm}$ and when the CP–even h, H bosons are involved, the coupling factors $\sin(\beta - \alpha)$ and $\cos(\beta - \alpha)$ accordingly. In addition, for the $\gamma W^{\pm}AH^{\pm}$ and $ZW^{\pm}AH^{\pm}$ couplings and those where $AH^{\pm}$ are replaced by $G^0G^{\pm}$, the directions of the $W^{\pm}$ and $H^{\pm}(G^{\pm})$ momenta are important. In the rules which have been displayed, the momentum of the $W^{\pm}(H^{\pm})$ boson is entering (leaving) the vertex.

Yukawa couplings to fermions

As seen previously, SUSY imposes that the doublet H_1 generates the masses and couplings of isospin $-\frac{1}{2}$ fermions and H_2 those of isospin $+\frac{1}{2}$ fermions. This automatically forbids Higgs boson mediated flavor changing neutral currents as proved in a theorem due to Glashow and Weinberg [89]. The Higgs boson couplings to fermions originate from the superpotential W which leads to the Yukawa Lagrangian [39]

$$\mathcal{L}_{\text{Yuk}} = -\frac{1}{2} \sum_{ij} \left[\overline{\psi}_{iL} \frac{\partial^2 W}{\partial z_i \partial z_j} \psi_j + \text{h.c.} \right] \tag{1.92}$$

to be evaluated in terms of the scalar fields H_1 and H_2. Discarding the bilinear terms in the superpotential, assuming diagonal Y matrices and using the left– and right–handed projection operators $P_{L/R} = \frac{1}{2}(1 \mp \gamma_5)$ with $(\bar{\psi}_1 P_L \psi_2)^\dagger = (\bar{\psi}_2 P_R \psi_1)$, the Yukawa Lagrangian with the notation of the first fermion family is then

$$\mathcal{L}_{\text{Yuk}} = -\lambda_u [\bar{u} P_L u H_2^0 - \bar{u} P_L d H_2^+] - \lambda_d [\bar{d} P_L d H_1^0 - \bar{d} P_L u H_1^-] + \text{h.c.} \tag{1.93}$$

The fermion masses are generated when the neutral components of the Higgs fields acquire their vacuum expectation values and they are related to the Yukawa couplings by

$$\lambda_u = \frac{\sqrt{2} m_u}{v_2} = \frac{\sqrt{2} m_u}{v \sin \beta} \quad , \quad \lambda_d = \frac{\sqrt{2} m_d}{v_1} = \frac{\sqrt{2} m_d}{v \cos \beta} \tag{1.94}$$

Expressing the fields H_1 and H_2 in terms of the physical fields, one obtains the Yukawa Lagrangian in terms of the fermion masses [90, 91]

$$\begin{aligned}
\mathcal{L}_{\text{Yuk}} = & -\frac{g_2 m_u}{2 M_W \sin \beta} \left[\bar{u} u (H \sin \alpha + h \cos \alpha) - i \bar{u} \gamma_5 u \, A \cos \beta \right] \\
& -\frac{g_2 m_d}{2 M_W \cos \beta} \left[\bar{d} d (H \cos \alpha - h \sin \alpha) - i \bar{d} \gamma_5 d \, A \sin \beta \right] \\
& +\frac{g_2}{2\sqrt{2} M_W} V_{ud} \left\{ H^+ \bar{u} [m_d \tan \beta (1 + \gamma_5) + m_u \cot \beta (1 - \gamma_5)] d + \text{h.c.} \right\}
\end{aligned} \tag{1.95}$$

with V_{ud} the CKM matrix element which is present in the case of quarks. The additional interactions involving the neutral and charged Goldstone bosons G^0 and $G^\pm$ can be obtained from the previous equation by replacing A and $H^\pm$ by G^0 and $G^\pm$ and setting $\cot \beta = 1$ and $\tan \beta = -1$. The MSSM Higgs boson couplings to fermions are given by

$$G_{huu} = i \frac{m_u}{v} \frac{\cos \alpha}{\sin \beta} \, , \quad G_{Huu} = i \frac{m_u}{v} \frac{\sin \alpha}{\sin \beta} \, , \quad G_{Auu} = \frac{m_u}{v} \cot \beta \, \gamma_5$$

$$G_{hdd} = -i \frac{m_d}{v} \frac{\sin \alpha}{\cos \beta} \, , \quad G_{Hdd} = i \frac{m_d}{v} \frac{\cos \alpha}{\cos \beta} \, , \quad G_{Add} = \frac{m_d}{v} \tan \beta \, \gamma_5$$

$$G_{H^+ \bar{u} d} = -\frac{i}{\sqrt{2} v} V_{ud}^* [m_d \tan \beta (1 + \gamma_5) + m_u \cot \beta (1 - \gamma_5)]$$

$$G_{H^- u \bar{d}} = -\frac{i}{\sqrt{2} v} V_{ud} [m_d \tan \beta (1 - \gamma_5) + m_u \cot \beta (1 + \gamma_5)] \tag{1.96}$$

One can notice that the couplings of the $H^\pm$ bosons have the same $\tan\beta$ dependence as those of the pseudoscalar A boson and that for values $\tan\beta > 1$, the A and $H^\pm$ couplings to isospin down–type fermions are enhanced, while the couplings to up–type fermions are suppressed. Thus, for large values of $\tan\beta$, the couplings of these Higgs bosons to b quarks, $\propto m_b \tan\beta$, become very strong while those to the top quark, $\propto m_t/\tan\beta$, become rather weak. This is, in fact, also the case of the couplings of one of the CP–even Higgs boson h or H to fermions; with a normalization factor $(i)g_2 m_f/2M_W = im_f/v$, they can alternatively be written as

$$
\begin{aligned}
g_{hbb} &= -\frac{\sin\alpha}{\cos\beta} = \sin(\beta-\alpha) - \tan\beta\cos(\beta-\alpha) \\
g_{htt} &= \frac{\cos\alpha}{\sin\beta} = \sin(\beta-\alpha) + \cot\beta\cos(\beta-\alpha) \\
g_{Hbb} &= \frac{\cos\alpha}{\cos\beta} = \cos(\beta-\alpha) + \tan\beta\sin(\beta-\alpha) \\
g_{Htt} &= \frac{\sin\alpha}{\sin\beta} = \cos(\beta-\alpha) - \cot\beta\sin(\beta-\alpha)
\end{aligned}
\tag{1.97}
$$

and one can see that the bb (tt) coupling of either the h or H boson are enhanced (suppressed) by a factor $\tan\beta$, depending on the magnitude of $\cos(\beta-\alpha)$ or $\sin(\beta-\alpha)$. Ignoring the missing $i\gamma_5$ factor, the reduced pseudoscalar–fermion couplings are simply

$$
g_{Abb} = \tan\beta , \quad g_{Att} = \cot\beta
\tag{1.98}
$$

The trilinear and quartic scalar couplings

The trilinear and quadrilinear couplings between three or four Higgs fields can be obtained from the scalar potential V_H by performing the following derivatives

$$
\begin{aligned}
\lambda_{ijk} &= \frac{\partial^3 V_H}{\partial H_i \partial H_j \partial H_k}\Big|_{\langle H_1^0\rangle = v_1/\sqrt{2},\,\langle H_2^0\rangle = v_2/\sqrt{2},\,\langle H_{1,2}^\pm\rangle = 0} \\
\lambda_{ijkl} &= \frac{\partial^4 V_H}{\partial H_i \partial H_j \partial H_k \partial H_l}\Big|_{\langle H_1^0\rangle = v_1/\sqrt{2},\,\langle H_2^0\rangle = v_2/\sqrt{2},\,\langle H_{1,2}^\pm\rangle = 0}
\end{aligned}
\tag{1.99}
$$

with the H_i fields expressed in terms of the fields $h, H, A, H^\pm$ and $G^0, G^\pm$ with the rotations through angles β and α discussed in the previous section. The various trilinear couplings among neutral Higgs bosons, in units of $\lambda_0 = -iM_Z^2/v$, are given by [41]

$$
\begin{aligned}
\lambda_{hhh} &= 3\cos 2\alpha \sin(\beta+\alpha) \\
\lambda_{Hhh} &= 2\sin 2\alpha \sin(\beta+\alpha) - \cos 2\alpha \cos(\beta+\alpha) \\
\lambda_{HHH} &= 3\cos 2\alpha \cos(\beta+\alpha) \\
\lambda_{HHh} &= -2\sin 2\alpha \cos(\beta+\alpha) - \cos 2\alpha \sin(\beta+\alpha) \\
\lambda_{HAA} &= -\cos 2\beta \cos(\beta+\alpha) \\
\lambda_{hAA} &= \cos 2\beta \sin(\beta+\alpha)
\end{aligned}
\tag{1.100}
$$

38

while the trilinear couplings involving the $H^\pm$ bosons, $\lambda_{HH^+H^-}$ and $\lambda_{hH^+H^-}$, are related to those involving the pseudoscalar Higgs boson with contributions proportional to the couplings of the h and H particles to gauge bosons

$$\begin{aligned}
\lambda_{HH^+H^-} &= -\cos 2\beta \cos(\beta+\alpha) + 2c_W^2 \cos(\beta-\alpha) = \lambda_{HAA} + 2c_W^2 g_{HVV} \\
\lambda_{hH^+H^-} &= \cos 2\beta \sin(\beta+\alpha) + 2c_W^2 \sin(\beta-\alpha) = \lambda_{hAA} + 2c_W^2 g_{hVV}
\end{aligned} \tag{1.101}$$

The couplings of h and H to two Goldstone bosons $G^0 G^0$ and $G^+ G^-$ are the same as the ones to AA and $H^+ H^-$ states except that the sign is reversed and the contribution proportional to c_W^2 is set to zero in the latter case. The hAG^0 and HAG^0 couplings are obtained from the hAA and HAA couplings by replacing $\cos 2\beta$ by $\sin 2\beta$, $\lambda_{AG^\pm H^\pm} = \pm i c_W^2$ and the two remaining trilinear couplings are given by $\lambda_{HG^+H^-} = -\sin 2\beta \cos(\beta+\alpha) + c_W^2 \sin(\beta-\alpha)$ and $\lambda_{hG^+H^-} = \sin 2\beta \sin(\beta+\alpha) - c_W^2 \cos(\beta-\alpha)$.

Finally, the quartic couplings among the MSSM Higgs bosons are more numerous and can be found in Ref. [41]. Some important ones, in units of $\lambda_0/v = -iM_Z^2/v^2$, are the couplings between four h or H bosons

$$\lambda_{hhhh} = \lambda_{HHHH} = 3\cos^2 2\alpha \tag{1.102}$$

1.2.4 The Higgs couplings to the SUSY particles

Couplings to sfermions

The MSSM Higgs boson couplings to scalar fermions come from three different sources: the F terms due to the superpotential W, the D terms due to the [supersymmetrized and gauge–covariantized] kinetic part of the sfermions in $\mathcal{L}$, and the Lagrangian $\mathcal{L}_{\text{tril.}}$ which softly breaks Supersymmetry [we recall that instead, the leading part of the scalar masses come directly from the soft SUSY–breaking potential $\mathcal{L}_{\text{soft}}$]. Normalized to g_2/M_W and using the notation of the third generation, the Higgs couplings to two squarks, $g_{\tilde{q}_i \tilde{q}_j' \Phi}$, read[4]

$$g_{\tilde{q}_i \tilde{q}_j' \Phi} = \sum_{k,l=1}^{2} (R^q)_{ik}^{\text{T}} C_{\Phi\tilde{q}\tilde{q}'}^{kl} \left(R^{q'}\right)_{lj} \tag{1.103}$$

with the matrices $C_{\Phi\tilde{q}\tilde{q}'}$ summarizing the couplings of the Higgs bosons to the squark current eigenstates; for the h, H, A and $H^\pm$ particles, they are given by

$$C_{h\tilde{q}\tilde{q}} = \begin{pmatrix} -\left(I_q^{3L} - Q_q s_W^2\right) M_Z^2 \sin(\beta+\alpha) + m_q^2 s_1^q & \frac{1}{2}m_q(A_q s_1^q + \mu s_2^q) \\ \frac{1}{2}m_q(A_q s_1^q + \mu s_2^q) & -Q_q s_W^2 M_Z^2 \sin(\beta+\alpha) + m_q^2 s_1^q \end{pmatrix} \tag{1.104}$$

---

[4]Note that there are also couplings of the Goldstone bosons G^0 and $G^\pm$ to sfermion pairs, as well as quartic couplings between two Higgs or Goldstone bosons to two sfermions; these couplings will not be needed in our discussion and they can be found in Ref. [38, 41] for instance. The couplings to leptons can be derived from those listed below by setting $m_d = m_\ell$ and $m_u = 0$.

$$C_{H\tilde{q}\tilde{q}} = \begin{pmatrix} (I_q^{3L} - Q_q s_W^2) M_Z^2 \cos(\beta + \alpha) + m_q^2 r_1^q & \frac{1}{2} m_q (A_q r_1^q + \mu r_2^q) \\ \frac{1}{2} m_q (A_q r_1^q + \mu r_2^q) & Q_q s_W^2 M_Z^2 \cos(\beta + \alpha) + m_q^2 r_1^q \end{pmatrix} \quad (1.105)$$

$$C_{A\tilde{q}\tilde{q}} = \begin{pmatrix} 0 & -\frac{1}{2} m_q \left[\mu + A_q (\tan\beta)^{-2I_3^q} \right] \\ \frac{1}{2} m_q \left[\mu + A_q (\tan\beta)^{-2I_3^q} \right] & 0 \end{pmatrix} \quad (1.106)$$

$$C_{H^\pm \tilde{t}\tilde{b}} = \frac{1}{\sqrt{2}} \begin{pmatrix} m_b^2 \tan\beta + m_t^2 \cot\beta - M_W^2 \sin 2\beta & m_b (A_b \tan\beta + \mu) \\ m_t (A_t \cot\beta + \mu) & m_t m_b (\tan\beta + \cot\beta) \end{pmatrix} \quad (1.107)$$

with the coefficients $r_{1,2}^q$ and $s_{1,2}^q$

$$s_1^u = -r_2^u = \frac{\cos\alpha}{\sin\beta} , \quad s_2^u = r_1^u = \frac{\sin\alpha}{\sin\beta} , \quad s_1^d = r_2^d = -\frac{\sin\alpha}{\cos\beta} , \quad s_2^d = -r_1^d = \frac{\cos\alpha}{\cos\beta} \quad (1.108)$$

These couplings are thus potentially large since they involve terms $\propto m_t^2$ and $m_t A_t$ in the stop case and, in the case of sbottoms, there are terms $\propto m_b \tan\beta$ that can be strongly enhanced for large values of $\tan\beta$. For instance, in the case $\alpha = \beta - \frac{\pi}{2}$ [which, as we will see later, corresponds to the decoupling limit $M_A \gg M_Z$], the $h\tilde{t}\tilde{t}$ couplings, simply read

$$g_{h\tilde{t}_1\tilde{t}_1} = \cos 2\beta M_Z^2 \left[\frac{1}{2} \cos^2\theta_t - \frac{2}{3} s_W^2 \cos 2\theta_t \right] + m_t^2 + \frac{1}{2} \sin 2\theta_t m_t X_t$$

$$g_{h\tilde{t}_2\tilde{t}_2} = \cos 2\beta M_Z^2 \left[\frac{1}{2} \sin^2\theta_t - \frac{2}{3} s_W^2 \cos 2\theta_t \right] + m_t^2 - \frac{1}{2} \sin 2\theta_t m_t X_t$$

$$g_{h\tilde{t}_1\tilde{t}_2} = \cos 2\beta \sin 2\theta_t M_Z^2 \left[\frac{2}{3} s_W^2 - \frac{1}{4} \right] + \frac{1}{2} \cos 2\theta_t m_t X_t \quad (1.109)$$

and involve components which are proportional to $X_t = A_t - \mu \cot\beta$. For large values of the parameter X_t, which incidentally make the $\tilde{t}$ mixing angle almost maximal, $|\sin 2\theta_t| \simeq 1$ and lead to lighter $\tilde{t}_1$ states, the last components can strongly enhance the $g_{h\tilde{t}_1\tilde{t}_1}$ coupling and make it larger than the top quark coupling of the h boson, $g_{htt} \propto m_t/M_Z$.

Couplings to charginos and neutralinos

The Higgs boson couplings to neutralinos and charginos come also from several sources such as the superpotential [in particular from the bilinear term] and are affected also by the gaugino masses in $\mathcal{L}_{\text{soft}}$. They are made more complicated by the higgsino–gaugino mixing, the diagonalization of the chargino/neutralino mass matrices, and the Majorana nature of the neutralinos. The Feynman rules for these couplings are given in Ref. [41]. Here, we simply display them in a convenient form [92] which will be used later.

Denoting the Higgs bosons by H_k with $k = 1, 2, 3, 4$, corresponding to H, h, A and $H^\pm$, respectively, and normalizing to the electric charge e, the Higgs couplings to chargino and neutralino pairs can be written as

$$g_{\chi_i^0 \chi_j^+ H^+}^{L,R} = g_{ij4}^{L,R} \quad \text{with} \quad \begin{aligned} g_{ij4}^L &= \frac{\cos\beta}{s_W} \left[Z_{j4} V_{i1} + \frac{1}{\sqrt{2}} (Z_{j2} + \tan\theta_W Z_{j1}) V_{i2} \right] \\ g_{ij4}^R &= \frac{\sin\beta}{s_W} \left[Z_{j3} U_{i1} - \frac{1}{\sqrt{2}} (Z_{j2} + \tan\theta_W Z_{j1}) U_{i2} \right] \end{aligned} \quad (1.110)$$

$$g^{L,R}_{\chi^-_i \chi^+_j H^0_k} = g^{L,R}_{ijk} \quad \text{with} \quad \begin{aligned} g^L_{ijk} &= \tfrac{1}{\sqrt{2}s_W} \left[e_k V_{j1} U_{i2} - d_k V_{j2} U_{i1} \right] \\ g^R_{ijk} &= \tfrac{1}{\sqrt{2}s_W} \left[e_k V_{i1} U_{j2} - d_k V_{i2} U_{j1} \right] \epsilon_k \end{aligned} \tag{1.111}$$

$$g^{L,R}_{\chi^0_i \chi^0_j H^0_k} = g^{L,R}_{ijk} \quad \text{with} \quad \begin{aligned} g^L_{ijk} &= \tfrac{1}{2s_W} \left(Z_{j2} - \tan\theta_W Z_{j1} \right) \left(e_k Z_{i3} + d_k Z_{i4} \right) \ + \ i \leftrightarrow j \\ g^R_{ijk} &= \tfrac{1}{2s_W} \left(Z_{j2} - \tan\theta_W Z_{j1} \right) \left(e_k Z_{i3} + d_k Z_{i4} \right) \epsilon_k \ + \ i \leftrightarrow j \end{aligned} \tag{1.112}$$

where Z and U/V are the 4×4 and 2×2 matrices which diagonalize the neutralino and chargino matrices and $\epsilon_{1,2} = -\epsilon_3 = 1$; the coefficients e_k and d_k read

$$e_1 = +\cos\alpha \ , \ \ e_2 = -\sin\alpha \ , \ \ e_3 = -\sin\beta$$
$$d_1 = -\sin\alpha \ , \ \ d_2 = -\cos\alpha \ , \ \ d_3 = +\cos\beta \tag{1.113}$$

Note that the Higgs couplings to the χ^0_1 LSP, for which Z_{11}, Z_{12} are the gaugino components and Z_{13}, Z_{14} the higgsino components, vanish if the LSP is a pure gaugino or a pure higgsino. This statement can be generalized to all neutralino and chargino states and the Higgs bosons couple only to higgsino–gaugino mixtures or states[5]. The couplings of the neutral Higgs bosons to neutralinos can also accidentally vanish for certain values of $\tan\beta$ and α [and thus, M_A] which enter in the coefficients d_k and e_k.

Couplings to gravitinos

Finally, in gauge mediated SUSY–breaking (GMSB) models [58], where the gravitinos are very light, we will need the couplings between the Higgs bosons, the neutralinos and charginos, and the gravitinos. These couplings can be also written in an effective and convenient form which will be used later

$$\begin{aligned} |g_{\tilde{G}\chi^0_i H^0_k}|^2 &= |e_k Z_{i3} + d_k Z_{i4}|^2 \ , \qquad\qquad k = 1,2,3 \\ |g_{\tilde{G}\chi^\pm_i H^\mp_k}|^2 &= |V_{i2}|^2 \cos^2\beta + |U_{i2}|^2 \sin^2\beta \end{aligned} \tag{1.114}$$

The coefficients e_k and d_k have been given above, eq. (1.113). The structure of eq. (1.114) is due to the fact that gravitinos only couple to members of the same supermultiplet in the current basis, and each term is the product of the higgsino component of the ino and the component of the corresponding Higgs current eigenstate in the relevant Higgs mass eigenstate. Thus, the $H_k \tilde{G} \chi$ couplings are large only if the charginos and neutralinos have large higgsino components.

---

[5]In the case of pure gaugino and higgsino states, the couplings of the Higgs bosons to neutralinos (and charginos) can be generated through radiative corrections where the most important contributions come from the third generation fermions and sfermions which, as seen previously, can have strong couplings. The induced couplings remain, however, rather small; see the discussion in Ref. [93].

1.2.5 MSSM versus 2HDMs

As a result of the SUSY constraints, the pattern of the Higgs boson masses and couplings in the MSSM is rather special. To highlight the unique features of the MSSM Higgs sector, it is common practice to compare it with a general two–Higgs doublet model (2HDM). A brief summary of the main differences is sketched below; see e.g. Refs. [41, 94, 95] for more details.

In a 2HDM, the most general Higgs potential compatible with gauge invariance, the correct breaking of the $SU(2)_L \times U(1)_Y$ symmetry and CP conservation is given by [96]

$$
\begin{aligned}
V &= \lambda_1(|\phi_1|^2 - v_1^2)^2 + \lambda_2(|\phi_2|^2 - v_2^2)^2 + \lambda_3[(|\phi_1|^2 - v_1^2) + (|\phi_2|^2 - v_2^2)]^2 \\
&\quad + \lambda_4[|\phi_1|^2|\phi_2|^2 - |\phi_1^\dagger\phi_2|^2] + \lambda_5[\mathrm{Re}(\phi_1^\dagger\phi_2) - v_1v_2]^2 + \lambda_6[\mathrm{Im}(\phi_1^\dagger\phi_2)]^2
\end{aligned}
\tag{1.115}
$$

with ϕ_1, ϕ_2 the two Higgs–doublet fields and $\langle\phi_1\rangle = v_1, \langle\phi_2\rangle = v_2$ their vevs [note the change of normalization]. We have also assumed that the discrete symmetry $\phi_1 \to -\phi_1$ is only broken softly; an additional term, $\lambda_7[\mathrm{Re}(\phi_1^\dagger\phi_2) - v_1v_2]\mathrm{Im}(\phi_1^\dagger\phi_2)$, can be eliminated by redefining the phases of the scalar fields [38]. Parameterizing the Higgs doublets by

$$
\phi_1 = \begin{pmatrix} \phi_1^+ \\ v_1 + \eta_1 + i\chi_1 \end{pmatrix}, \quad \phi_2 = \begin{pmatrix} \phi_2^+ \\ v_2 + \eta_2 + i\chi_2 \end{pmatrix}
\tag{1.116}
$$

one obtains for the mass terms in the CP–even Higgs sector

$$
(\eta_1, \eta_2) \begin{pmatrix} 4(\lambda_1 + \lambda_3)v_1^2 + \lambda_5 v_2^2 & (4\lambda_3 + \lambda_5)v_1 v_2 \\ (4\lambda_3 + \lambda_5)v_1 v_2 & 4(\lambda_2 + \lambda_3)v_2^2 + \lambda_5 v_1^2 \end{pmatrix} \begin{pmatrix} \eta_1 \\ \eta_2 \end{pmatrix}
\tag{1.117}
$$

while in the CP–odd and charged Higgs sectors, one has

$$
\lambda_6(\chi_1, \chi_2) \begin{pmatrix} v_2^2 & -v_1 v_2 \\ -v_1 v_2 & v_1^2 \end{pmatrix} \begin{pmatrix} \chi_1 \\ \chi_2 \end{pmatrix}, \quad \lambda_4(\phi_1^-, \phi_2^-) \begin{pmatrix} v_2^2 & -v_1 v_2 \\ -v_1 v_2 & v_1^2 \end{pmatrix} \begin{pmatrix} \phi_1^+ \\ \phi_2^+ \end{pmatrix}
\tag{1.118}
$$

Diagonalizing the mass matrices and using eq. (1.73) one obtains the physical masses of the Higgs bosons, which in the case of the pseudoscalar and charged Higgs bosons, read

$$
M_A^2 = \lambda_6 v^2 \quad \text{and} \quad M_{H^\pm}^2 = \lambda_4 v^2
\tag{1.119}
$$

where here, $v^2 \equiv v_1^2 + v_2^2 = (174 \text{ GeV})^2$; the mixing angle α in the CP–even Higgs sector is obtained from the mass matrix using the relation given in eq. (1.74). Inverting these relations, one obtains the λ's in terms of the Higgs masses, and the angles α and β [41]

$$
\begin{aligned}
\lambda_1 &= \frac{1}{4\cos^2\beta v^2}(\cos^2\alpha M_H^2 + \sin^2\alpha M_h^2) - \frac{\sin 2\alpha}{\sin 2\beta}\frac{M_H^2 - M_h^2}{4v^2} + \frac{\lambda_5}{4}\left(1 - \frac{\sin^2\beta}{\cos^2\beta}\right), \\
\lambda_2 &= \frac{1}{4\sin^2\beta v^2}(\sin^2\alpha M_H^2 + \cos^2\alpha M_h^2) - \frac{\sin 2\alpha}{\sin 2\beta}\frac{M_H^2 - M_h^2}{4v^2} + \frac{\lambda_5}{4}\left(1 - \frac{\cos^2\beta}{\sin^2\beta}\right), \\
\lambda_3 &= \frac{\sin 2\alpha}{\sin 2\beta}\frac{M_H^2 - M_h^2}{4v^2} - \frac{\lambda_5}{4}, \quad \lambda_4 = \frac{M_{H^\pm}^2}{v^2}, \quad \lambda_6 = \frac{M_A^2}{v^2}
\end{aligned}
\tag{1.120}
$$

In a general 2HDM, the four masses M_h, M_H, M_A and $M_{H^\pm}$ as well as the mixing angles α and β are free parameters. In addition, as one can see from the previous equations, the parameter λ_5 cannot be fixed by the masses and the mixing angles, unless one imposes a strict $\phi_1 \to -\phi_1$ symmetry resulting in $\lambda_5 = 0$. This is a mere reflection of the fact that the model had originally seven inputs, $\tan\beta$ being also a free parameter. In contrast, SUSY imposes strong constraints on the parameter space of the MSSM Higgs sector in such a way that only two parameters are free. Taking $\tan\beta$ and λ_1 as the basics inputs, one has

$$\lambda_2 = \lambda_1 \ , \ \ \lambda_3 = \frac{1}{8}(g_1^2 + g_2^2) - \lambda_1 \ , \ \ \lambda_4 = -\frac{1}{2}g_1^2 + 2\lambda_1 \ ,$$

$$\lambda_5 = \lambda_6 = 2\lambda_1 - \frac{1}{2}(g_1^2 + g_2^2) \equiv \frac{M_A^2}{v^2} \tag{1.121}$$

Nevertheless, even in the 2HDM, the Higgs couplings to gauge bosons are the same as in the MSSM, that is, they are suppressed by the same factors $\cos(\beta - \alpha)$ and $\sin(\beta - \alpha)$; however, here, the parameter α is free.

In fact, in an arbitrary Higgs sector, the Higgs couplings to gauge bosons follow their spin–parity quantum number assignments [41]. In the absence of fermions, the CP–even H_i bosons [that is the linear combinations of $\mathrm{Re}(\phi_i)$] are $J^{\mathrm{PC}} = 0^{++}$ states, while the CP–odd A_i particles [the linear combinations of $\mathrm{Im}(\phi_i)$] have $J^{\mathrm{PC}} = 0^{+-}$, and both P and C symmetries are conserved[6]. The charged Higgs boson is a $J^{\mathrm{C}} = 0^+$ state, while the Z and W bosons are mixtures of, respectively, $1^{--}/1^{++}$ and $1^-/1^+$ states. From these J^{PC} assignments, one can infer the general properties of the Higgs couplings to gauge bosons, including their existence or their absence at the tree–level and the possibility of inducing them by loops [39, 97]. A summary of possible tree–level and loop induced couplings among two Higgs bosons and one gauge boson as well as one Higgs boson and two gauge bosons is given in Table 1.3 [97]. CP is assumed to be conserved in the Higgs sector [also in the fermionic couplings] and only Higgs doublets and singlets are considered [the H^+W^-Z coupling can be present at the tree–level in higher extensions of the Higgs sector; see Refs. [98, 99] for instance].

The interaction of the Higgs bosons with fermions are model–dependent and there are two options which are generally discussed. In Type II models [90, 91], the field ϕ_1 generates the masses of isospin down–type fermions and ϕ_2 the masses of up–type quarks and the couplings are just like in the MSSM [with again α being free]. In turn, in Type I models [91, 100], the field ϕ_2 couples to both up– and down–type fermions. The couplings of the neutral Higgs bosons to gauge bosons and fermions are given in Table 1.4 in the two models; the couplings of the charged Higgs boson to fermions follow that of the CP–odd Higgs particle.

---

[6] This is no longer the case when fermions are involved and, in this case, only CP–symmetry is approximately conserved. However, since in the Higgs–fermion Yukawa coupling the $f\bar{f}$ system has zero total angular momentum and thus has $C = +$ charge conjugation, the H_i and A_i states behave as scalar and pseudoscalar particles, respectively.

HHV couplings			HVV couplings		
Coupling	Tree–level?	Loop?	Coupling	Tree–level?	Loop?
H_iH_iZ, A_iA_iZ	NO: Bose statistics		H_iZZ, H_iWW	YES	–
$H_iH_i\gamma, A_iA_i\gamma$	NO (Bose statistics)		$H_i\gamma\gamma, H_i\gamma Z$	NO ($Q=0$)	1–loop
$H_iH_j\gamma, A_iA_j\gamma$	NO ($Q=0$)	3–loop	H_igg	NO (col=0)	1–loop
H_iH_jZ, A_iA_jZ	NO (CPc)	3–loop	A_iZZ, A_iWW	NO (Cc)	1–loop
$H_iA_j\gamma^*$	NO ($Q=0$)	1–loop	$A_i\gamma\gamma, A_i\gamma Z$	NO (Cc,$Q=0$)	1–loop
H_iA_jZ	YES	–	A_igg	NO (Cc, col=0)	1–loop
$H^+H^-Z(\gamma)$	YES	–	H^+W^-Z	NO for doublets	1–loop
$H^+W^-H_i(A_i)$	YES	–	$H^+W^-\gamma$	NO (U(1)$_Q$–c)	1–loop

Table 1.3: The tree–level and loop induced Higgs couplings to one gauge boson and two gauge bosons in a general model with Higgs doublets where CP symmetry is assumed to be conserved in the Higgs and fermionic (except in the CKM matrix) sectors; Cc, CPc, $Q=0$, col $=0$ mean, respectively C, CP, charge and color conservation.

Φ	$g_{\Phi\bar{u}u}$		$g_{\Phi\bar{d}d}$		$g_{\Phi VV}$
	Type I	Type II	Type I	Type II	Type I/II
h	$\cos\alpha/\sin\beta$	$\cos\alpha/\sin\beta$	$\cos\alpha/\sin\beta$	$-\sin\alpha/\cos\beta$	$\sin(\beta-\alpha)$
H	$\sin\alpha/\sin\beta$	$\sin\alpha/\sin\beta$	$\sin\alpha/\sin\beta$	$\cos\alpha/\cos\beta$	$\cos(\beta-\alpha)$
A	$\cot\beta$	$\cot\beta$	$\cot\beta$	$\tan\beta$	0

Table 1.4: The neutral Higgs couplings to fermions and gauge bosons in 2HDMs of Type I and II compared to the SM Higgs couplings. The $H^\pm$ couplings to fermions follow that of A.

Finally, the coupling among Higgs bosons are completely different in the two scenarios. Using the same normalization as in the case of the λ couplings in the MSSM, the CP–even Higgs boson couplings to $H^\pm$ bosons are, for instance, given by [95]

$$\lambda_{hH^+H^-} = \frac{M_h^2 - \lambda_5 v^2}{M_W^2}\cos(\beta+\alpha) + \frac{2M_{H^\pm}^2 - M_h^2}{2M_W^2}\sin 2\beta\sin(\beta-\alpha)$$

$$\lambda_{HH^+H^-} = \frac{M_H^2 - \lambda_5 v^2}{M_W^2}\sin(\beta+\alpha) + \frac{2M_{H^\pm}^2 - M_H^2}{2M_W^2}\sin 2\beta\cos(\beta-\alpha) \quad (1.122)$$

and may diverge in the limit of very heavy $H^\pm$ bosons contrary to the MSSM case, if the decoupling limit is not properly taken; see e.g. Ref. [101].

1.3 Radiative corrections in the MSSM Higgs sector

1.3.1 The radiative corrections and the upper bound on M_h

The upper bound on the lighter Higgs boson mass

As discussed at the end of §1.2.2, Supersymmetry imposes strong constraints on the MSSM Higgs mass spectrum. In particular, eq. (1.85) shows that the lighter CP–even Higgs boson should have a mass below M_Z. This upper bound is saturated, $M_h \simeq M_Z$, when the mass of the pseudoscalar Higgs boson A is larger than M_Z and $|\cos 2\beta| \simeq 1$, implying $\beta \simeq \frac{\pi}{2}$ and thus large values of the parameter $\tan\beta$. In addition, for a heavy pseudoscalar Higgs boson, the mixing angle α in the CP–even Higgs sector will approach the value $\alpha \simeq \frac{\pi}{2} - \beta$. This has the important consequence that the h boson couplings to fermions and gauge bosons are SM–like, $g_{huu} \simeq g_{hdd} \simeq g_{hVV} \simeq 1$. [This is in fact the decoupling limit [101–103] which will be discussed later in more detail.]

Since the h boson is light and has almost SM–like couplings when M_A is large, it should have been observed at LEP2, if it were not for the radiative corrections which push its mass upward from the tree–level upper bound M_Z, to a value beyond the reach of LEP2 [42]. Indeed, these radiative corrections can be very large since rather strong couplings, such as the Higgs couplings to the top quarks and to their spin–zero SUSY partners, are involved in the Higgs sector; for recent reviews, see Refs. [104–106]. Thus, at least the radiative corrections due to top and stop quark loops should be incorporated in the MSSM Higgs sector.

In the limits $M_A \gg M_Z$ and $\tan\beta \gg 1$ that one has to consider for the upper bound on M_h, these corrections are in fact rather simple to evaluate, in particular if one assumes in addition that the two stop squarks have the same mass, $m_{\tilde{t}_1} = m_{\tilde{t}_2} = m_{\tilde{t}} \equiv M_S$, and do not mix with each other, $X_t = A_t - \mu \cot\beta \ll M_S$. In this case, the Higgs boson couplings to these particles are particularly simple. An additional simplification is provided by the assumption that the Higgs boson is much lighter than the top quark and squarks, $M_h \ll m_t, m_{\tilde{t}}$, so that the external momentum of its self–energy can be neglected.

Figure 1.3: Tadpole contributions to the Higgs boson masses at one–loop.

In addition to the two–point functions including top and stop loops that we have already seen in §1.1.1, when we presented the contributions of a fermion and two scalars to the Higgs

boson mass, one has also counterterm tadpole contributions depicted in Fig. 1.3. With the Higgs couplings written above, this additional contribution is given by

$$\Delta M_h^2|_{\text{tad}} \quad = \quad -\frac{3\lambda_t^2}{4\pi^2}\left[m_{\tilde{t}}^2\log\left(\frac{\Lambda}{m_{\tilde{t}}}\right) - m_t^2\log\left(\frac{\Lambda}{m_{\tilde{t}}}\right)\right] \tag{1.123}$$

and if one adds the contribution of eq. (1.3), one obtains the total radiative correction to the upper bound on M_h. Using the relation $v = (\sqrt{2}G_\mu)^{-1/2}$, this correction reads [37]

$$\Delta M_h^2 \quad = \quad \frac{3G_\mu}{\sqrt{2}\pi^2}m_t^4\log\frac{M_S^2}{m_t^2} \tag{1.124}$$

As can be seen, the correction grows quartically with top quark mass, $\Delta M_h^2 \propto m_t^4$, and logarithmically with the stop masses, $\Delta M_h^2 \propto \log(m_{\tilde{t}}^2/m_t^2)$. It is therefore very large and increases the h boson mass by several tens of GeV, shifting its maximal value from M_Z to $M_h^{\max} \sim 140$ GeV. This explains why the h boson has not been seen at LEP2: the upper bound on M_h in the MSSM, when the one–loop radiative corrections are included, is such that the h boson can be kinematically not accessible at LEP2 energies.

Status of the radiative corrections in the Higgs sector

The fact that the inclusion of the one–loop $\mathcal{O}(\lambda_t^2)$ corrections[7], which rise as m_t^4 and $\log M_S$, may push the lighter Higgs mass well above the tree–level bound, was first realized in Ref. [37]. In the subsequent years, an impressive theoretical effort has been devoted to the precise determination of the Higgs boson masses in the MSSM. A first step was to provide the full one–loop computation including the contributions of all SUSY particles, the sfermion contributions with the bottom–sbottom loops being quite important, the chargino–neutralino corrections and the contribution of the gauge bosons and MSSM Higgs bosons; these calculations have been performed in Refs. [69, 108, 109]. A second step was the addition of the dominant two–loop corrections which involve the strongest couplings of the theory, the QCD coupling constant and the Yukawa couplings of the heavy third generation fermions[8]: the leading logarithmic effects at two loops have been included via appropriate RGEs [110–112], and the genuine two–loop corrections of $\mathcal{O}(\alpha_s\lambda_t^2)$ [113–117] and $\mathcal{O}(\alpha_s\lambda_b^2)$ [118,119] have been evaluated in the limit of zero external momentum. The two–loop Yukawa corrections of $\mathcal{O}(\lambda_t^4)$ [113,116,120] and $\mathcal{O}(\lambda_t^2\lambda_b^2)$ [107] have been also evaluated in the limit of zero external momentum and to complete the calculation of the two–loop corrections controlled by third–generation fermion couplings, the expectedly small corrections that are proportional to the τ–lepton Yukawa coupling have been determined recently in Ref. [121].

---

[7]Here and in the following, by $\mathcal{O}(\lambda_t^2)$ we mean $\mathcal{O}(\lambda_t^2m_t^2)$, that is, there are four powers of m_t; similarly, by $\mathcal{O}(\lambda_t^2\alpha_s)$ we mean $\mathcal{O}(\lambda_t^2m_t^2\alpha_s)$. See, for instance, Ref. [107] for a discussion.

[8]As seen previously, although the masses of the bottom quark and the τ lepton are relatively tiny compared to the top quark mass, the b and τ Yukawa couplings can be strongly enhanced for large values of $\tan\beta$.

The tadpole corrections needed to minimize the effective scalar potential V_H and to obtain the pseudoscalar Higgs boson mass which, together with $\tan\beta$, is generally used as an input parameter for the Higgs sector, have also been calculated at the one–loop [50, 69] and two–loop [107, 121, 122] levels for the strong coupling and the top, bottom quark and τ–lepton Yukawa couplings. Finally, the full two–loop corrections to the MSSM effective potential have been calculated in Ref. [123], together with a first study of the two–loop corrections to M_h controlled by the weak gauge couplings [124] and the momentum–dependent corrections [125].

The calculation of the radiative corrections to the Higgs boson masses and couplings requires the choice of a renormalization scheme. For example, one might choose to express the corrections in terms of "on–shell" parameters, such as pole particle masses and suitably defined mixing angles; this is the scheme adopted in Refs. [109, 114] for instance, where the corrections have been calculated in the Feynman diagrammatic approach. However, in constrained models where the parameters at the weak scale are derived from unified ones at the GUT scale through RG evolution, they come naturally as unphysical "running" quantities expressed in the $\overline{\text{DR}}$ scheme, which is usually adopted since it preserves Supersymmetry. A more direct strategy would be then to perform the computation of the Higgs boson masses directly in this scheme. The results must be equivalent to those of the on–shell calculation up to terms that are formally of higher order in the perturbative expansion. The numerical differences can be taken as an estimate of the size of the corrections that are still uncomputed, which can be viewed, together with the choice of the renormalization scale at which the corrections are evaluated, as part of the theoretical uncertainty in the calculation.

The theoretical work on the radiative corrections in the MSSM Higgs sector in the on–shell scheme or Feynman diagrammatic approach, as well as a comparison with the results in the RG approach including the ones in the $\overline{\text{DR}}$ scheme, has been recently reviewed in Ref. [105] to which we refer for details. Also recently, the implementation of a purely two–loop $\overline{\text{DR}}$ calculation of the neutral MSSM Higgs boson masses and the angle α into the latest versions of three public codes for the RG evolution of the MSSM parameters and the calculation of the superparticle and Higgs boson mass spectrum, i.e. `SuSpect` [126], `SOFTSUSY` [127] and `SPHENO` [128], has been performed [121]; most parts of our discussion in this section will be based on this work.

The numerical results that we will display here are obtained by using either the program `SuSpect` which implements the full $\overline{\text{DR}}$ calculation or the Fortran code `HDECAY` [129] in which one of the routines `FeynHiggsFast1.2` [130] or `SUBH` [131] for the calculation of the radiative corrections will be adopted. The former calculates the corrections in the Feynman diagrammatic approach while the latter uses an RGE improved effective potential approximation. Before presenting these numerical results for the Higgs masses and couplings, let us first

display some analytical formulae for the dominant components of the radiative corrections in the Higgs sector of the phenomenological MSSM, to get some insight in the main effects.

Approximations for the radiative corrections

In the phenomenological MSSM defined in §1.1.4, since there are 22 free parameters in the model, the phenomenological analyses should be rather complicated to carry out. However, only a small subset of parameters plays a significant role in the Higgs sector. Indeed, at the tree level, the Higgs sector of the pMSSM can be described by two input parameters in addition to the SM ones. As already mentioned, these parameters are in general taken to be the mass of the CP–odd Higgs boson M_A and $\tan\beta$. The mass matrix for the CP–even Higgs bosons is given at the tree–level by eq. (1.75) with M_A given by eq. (1.77). This mass matrix receives radiative corrections at higher orders and it can be written as

$$\mathcal{M}^2 = \begin{bmatrix} \mathcal{M}_{11}^2 + \Delta\mathcal{M}_{11}^2 & \mathcal{M}_{12}^2 + \Delta\mathcal{M}_{12}^2 \\ \mathcal{M}_{12}^2 + \Delta\mathcal{M}_{12}^2 & \mathcal{M}_{22}^2 + \Delta\mathcal{M}_{22}^2 \end{bmatrix} \tag{1.125}$$

The leading one–loop radiative corrections $\Delta\mathcal{M}_{ij}^2$ to the mass matrix are controlled by the top Yukawa coupling λ_t which, as already seen, appears with the fourth power. One can obtain a very simple analytical expression if only this contribution is taken into account [112]

$$\begin{aligned} \Delta\mathcal{M}_{11}^2 &\sim \Delta\mathcal{M}_{12}^2 \sim 0 \,, \\ \Delta\mathcal{M}_{22}^2 &\sim \epsilon = \frac{3\,\bar{m}_t^4}{2\pi^2 v^2 \sin^2\beta}\left[\log\frac{M_S^2}{\bar{m}_t^2} + \frac{X_t^2}{2\,M_S^2}\left(1 - \frac{X_t^2}{6\,M_S^2}\right)\right] \end{aligned} \tag{1.126}$$

where M_S is the arithmetic average of the stop masses $M_S = \frac{1}{2}(m_{\tilde{t}_1} + m_{\tilde{t}_2})$, X_t is the stop mixing parameter given in eq. (1.33), and $\bar{m}_t$ is the running $\overline{\text{MS}}$ top quark mass to account for the leading two–loop QCD and electroweak corrections in a RG improvement.

The corrections controlled by the bottom Yukawa coupling λ_b are in general strongly suppressed by powers of the b–quark mass m_b. However, this suppression can be compensated by a large value of the product $\mu\tan\beta$, providing a non–negligible correction to $\mathcal{M}^2$. Some of the soft SUSY–breaking parameters, in particular μ, A_t and A_b, can also have an impact on the loop corrections. Including these subleading contributions at one–loop, plus the leading logarithmic contributions at two–loops, the radiative corrections to the CP–even mass matrix elements can still be written in a compact form [104, 111, 112, 132]

$$\begin{aligned} \Delta\mathcal{M}_{11}^2 &= -\frac{v^2 \sin^2\beta}{32\pi^2}\bar{\mu}^2\left[x_t^2\lambda_t^4(1 + c_{11}\ell_S) + a_b^2\lambda_b^4(1 + c_{12}\ell_S)\right] \\ \Delta\mathcal{M}_{12}^2 &= -\frac{v^2 \sin^2\beta}{32\pi^2}\bar{\mu}\left[x_t\lambda_t^4(6 - x_t a_t)(1 + c_{31}\ell_S) - \bar{\mu}^2 a_b\lambda_b^4(1 + c_{32}\ell_S)\right] \\ \Delta\mathcal{M}_{22}^2 &= \frac{v^2 \sin^2\beta}{32\pi^2}\left[6\lambda_t^4\ell_S(2 + c_{21}\ell_S) + x_t a_t\lambda_t^4(12 - x_t a_t)(1 + c_{21}\ell_S) - \bar{\mu}^4\lambda_b^4(1 + c_{22}\ell_S)\right] \end{aligned} \tag{1.127}$$

where the abbreviations $\ell_S = \log(M_S^2/m_t^2)$, $\bar{\mu} = \mu/M_S$, $a_{t,b} = A_{t,b}/M_S$ and $x_t = X_t/M_S$ have been used. The factors c_{ij} take into account the leading two–loop corrections due to the top and bottom Yukawa couplings and to the strong coupling constant g_3; they read

$$c_{ij} = \frac{1}{32\pi^2}(t_{ij}\lambda_t^2 + b_{ij}\lambda_b^2 - 32g_3^2) \qquad (1.128)$$

with the various coefficients given by

$$
\begin{aligned}
(t_{11}, t_{12}, t_{21}, t_{22}, t_{31}, t_{32}) &= (12, -4, 6, -10, 9, 7) \\
(b_{11}, b_{12}, b_{21}, b_{22}, b_{31}, b_{32}) &= (-4, 12, 2, 6, 18, -1, 15)
\end{aligned} \qquad (1.129)
$$

The expressions eq. (1.127) provide a good approximation of the bulk of the radiative corrections. However, one needs to include the full set of corrections mentioned previously to have precise predictions for the Higgs boson masses and couplings to which we turn now.

1.3.2 The radiatively corrected Higgs masses

The radiately corrected CP–even Higgs boson masses are obtained by diagonalizing the mass matrix eq. (1.125). In the approximation where only the leading correction controlled by the top Yukawa coupling, eq. (1.126), are implemented, the masses are simply given by [37]

$$M_{h,H}^2 = \frac{1}{2}(M_A^2 + M_Z^2 + \epsilon)\left[1 \mp \sqrt{1 - 4\frac{M_Z^2 M_A^2 \cos^2 2\beta + \epsilon(M_A^2 \sin^2 \beta + M_Z^2 \cos^2 \beta)}{(M_A^2 + M_Z^2 + \epsilon)^2}}\right] (1.130)$$

In this approximation, the charged Higgs mass does not receive radiative corrections, the leading contributions being of $\mathcal{O}(\alpha m_t^2)$ in this case [69,110,133]. A very simple expression for the corrected charged Higgs boson mass, which gives a result that is rather accurate is [134]

$$M_{H^\pm} = \sqrt{M_A^2 + M_W^2 - \epsilon_+} \quad \text{with} \quad \epsilon_+ = \frac{3G_\mu M_W^2}{4\sqrt{2}\pi^2}\left[\frac{\overline{m}_t^2}{\sin^2\beta} + \frac{\overline{m}_b^2}{\cos^2\beta}\right]\log\left(\frac{M_S^2}{m_t^2}\right) \quad (1.131)$$

As seen earlier, for large values of the pseudoscalar Higgs boson mass, $M_A \gg M_Z$, the lighter Higgs boson mass reaches its maximum for a given $\tan\beta$ value. In the ϵ approximation, this value reads

$$M_h \stackrel{M_A \gg M_Z}{\longrightarrow} \sqrt{M_Z^2 \cos^2 2\beta + \epsilon \sin^2\beta}\left[1 + \frac{\epsilon M_Z^2 \cos^2\beta}{2M_A^2(M_Z^2 + \epsilon \sin^2\beta)} - \frac{M_Z^2 \sin^2\beta + \epsilon \cos^2\beta}{2M_A^2}\right](1.132)$$

In this limit, the heavier CP–even and charged Higgs bosons, with squared masses given by

$$M_H \stackrel{M_A \gg M_Z}{\longrightarrow} M_A\left[1 + \frac{M_Z^2 \sin^2 2\beta + \epsilon \cos^2\beta}{2M_A^2}\right] \ , \ M_{H^\pm} \stackrel{M_A \gg M_Z}{\longrightarrow} M_A\left[1 + \frac{M_W^2}{2M_A^2}\right] \qquad (1.133)$$

become almost degenerate in mass $M_H \simeq M_{H^\pm} \simeq M_A$. This is an aspect of the decoupling limit [103] which will be discussed in more detail later.

Although transparent and useful for a qualitative understanding, the ϵ approach is not a very good approximation in many cases. A more accurate determination of the CP–even Higgs boson masses is obtained by including the RGE improved corrections of eq. (1.127). However, the additional non–logarithmic contributions can generate shifts of a few GeV in the Higgs boson masses and should therefore also be included. Before turning to this point, let us first briefly describe the situation in which these corrections can be large and maximize the lighter Higgs boson mass. At tree–level, we have already seen that the maximal h boson mass is obtained when M_A and $\tan\beta$ take large values. At the one–loop level, the radiative corrections are enhanced when the logarithm in the first term of eq. (1.126) is large, i.e. for large M_S values, corresponding to heavy stops. In addition, the corrections are largest and maximize the lightest h boson mass in the so–called "maximal mixing" scenario, where the trilinear stop coupling in the $\overline{\rm DR}$ scheme is such that

$$\text{maximal mixing scenario} \; : \quad X_t = A_t - \mu \cot\beta \sim \sqrt{6}\, M_S \qquad (1.134)$$
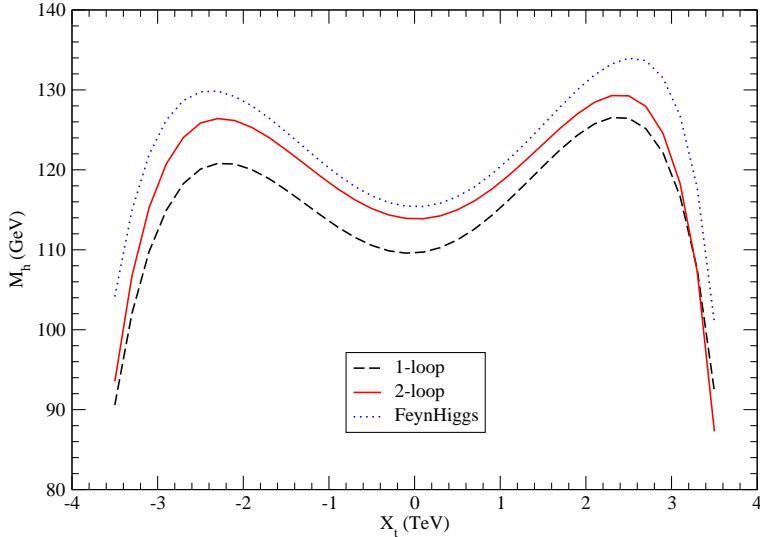
while the radiative corrections are much smaller for small values of X_t, close to the

$$\text{no mixing scenario} : \quad X_t = 0 \qquad (1.135)$$

An intermediate scenario, sometimes called the "typical–mixing scenario", is when X_t is of the same order as the SUSY scale, $X_t \simeq M_S$ [135]. The impact of stop mixing is exemplified in Fig. 1.4, where the lighter Higgs boson mass is displayed as a function of the parameter X_t, for $m_t = 178$ GeV [44], $m_b = 4.88$ GeV [136], $M_S = M_A = 1$ TeV and $\tan\beta = 10$; the one– and two–loop corrections, as calculated in the $\overline{\rm DR}$ scheme by the program SuSpect, are shown. As one can see, the h boson mass M_h has a local minimum for zero stop mixing, and it increases with $|X_t|$ until it reaches a local maximum at the points $X_t = \pm\sqrt{6}\, M_S \sim 2.45$ TeV [the maximum being higher for positive values of X_t], where it starts to decrease again.

Note that if the radiative corrections were implemented in the on–shell scheme, the maximal mixing scenario would have occurred for $X_t^{\rm OS} \sim 2M_S^{\rm OS}$, where $X_t^{\rm OS}$ and $M_S^{\rm OS}$ are the unphysical parameters obtained by rotating the diagonal matrix of the on–shell stop masses by the on–shell mixing angle; see e.g. Ref. [137] for a discussion. In Fig. 1.4, the dotted curve is obtained with the program FeynHiggs which uses the on–shell scheme, but since M_h is plotted as a function of the $\overline{\rm DR}$ parameter X_t, the maximum value of M_h is roughly at the same place. Comparing the solid and dotted lines, it can be seen that the results obtained in the $\overline{\rm DR}$ and on–shell schemes are different [up to 3–4 GeV higher in the OS calculation]. The difference can be used as an estimate of the higher–order corrections.

Let us now discuss the individual effects of the various components of the corrections, starting with the case of the top/stop loops. In Fig. 1.5, the mass of the lighter h boson is displayed as a function of M_A in the no–mixing (left) and maximal mixing (right) scenarios

Figure 1.4: The lighter MSSM Higgs boson mass as a function of X_t in the $\overline{\text{DR}}$ scheme for $\tan\beta = 10$ and $M_S = M_A = 1$ TeV with $m_t = 178$ GeV. The full and dashed lines correspond, respectively, to the two–loop and one–loop corrected masses as calculated with the program SuSpect, *while the dotted line corresponds to the two–loop M_h value obtained in the Feynman diagrammatic approach with* FeynHiggs; *from Ref. [121].*

for $\tan\beta = 2, 20$ and $M_S = 1$ TeV; the on–shell scheme has been adopted. While the one–loop contributions increase M_h by approximately 30 to 50 GeV depending on the mixing in the stop sector, the inclusion of the QCD and leading logarithmic top Yukawa coupling corrections decrease the correction by ~ 10–15 GeV. The full $\mathcal{O}(\alpha_t^2)$ contributions increase again the correction by a few GeV [in the $\overline{\text{DR}}$ scheme, the two loop corrections are much smaller; see Fig. 1.4 for instance]. The impact of the additional corrections due to the bottom–quark Yukawa coupling at both the one–loop and two-loop levels, where in the latter case only the $\mathcal{O}(\alpha_s\alpha_b)$ are included, is displayed in Fig. 1.6 for a large values of the mixing parameter $X_b = A_b - \mu\tan\beta \approx -\mu\tan\beta$. For the chosen values, $\tan\beta = 45$ and $\mu = -1$ TeV, they induce an additional negative shift of a few GeV. Smaller shifts can also be generated by the $\mathcal{O}(\alpha_t\alpha_b)$ and $\mathcal{O}(\alpha_b^2)$ contributions which are not displayed. The corrections due to the τ–Yukawa coupling, which complete the set of corrections due to strong interactions and third generation Yukawa couplings, are negligibly small.

In Fig. 1.6, the impact of the radiative corrections is also shown for the heavier CP–even Higgs mass. For small M_A values, $M_A \lesssim 100$–140 GeV, the trend is very similar to what has been discussed for the h boson. However for large M_A values, when the decoupling limit is reached, all the corrections become very small and H and A stay almost degenerate in mass even after including radiative corrections. This is also the case of the lighter Higgs boson for small M_A values, in this case the roles of the H and h bosons are interchanged.

51
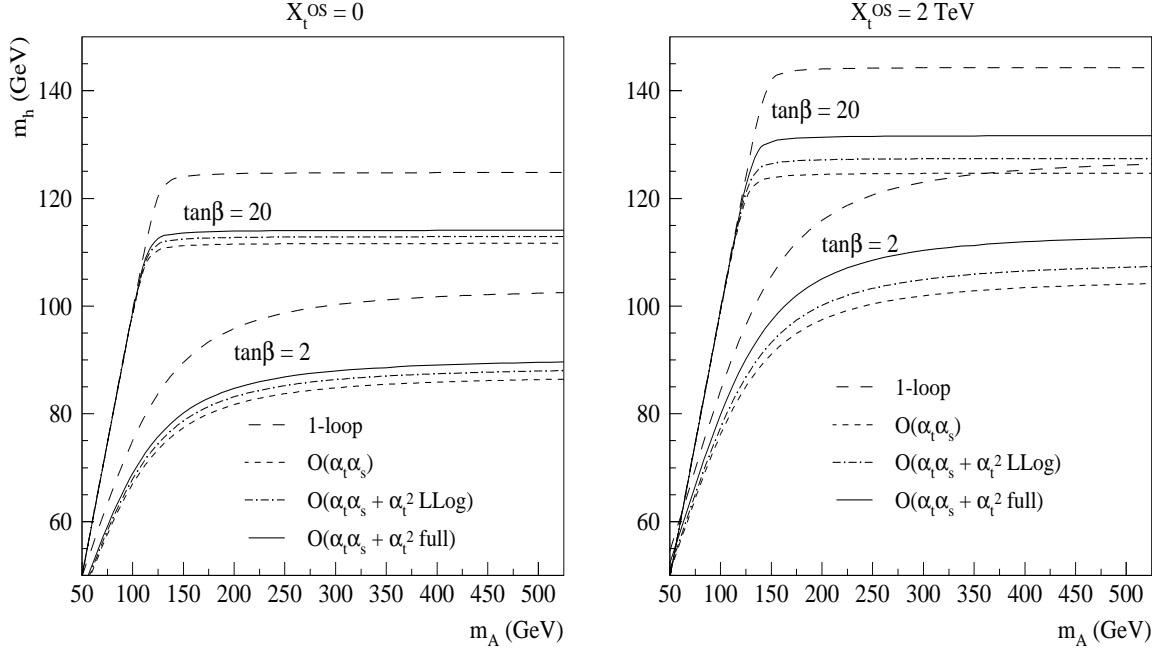
Figure 1.5: The radiatively corrected mass M_h of the lighter CP–even Higgs boson as a function of M_A for two values $\tan\beta = 2$ and 20 in various approximations for the no mixing (left) and maximal mixing (right) scenarios with $M_S = 1$ TeV. Only the top/stop loops have been included at the two–loop level and $m_t = 175$ GeV; from Ref. [120].
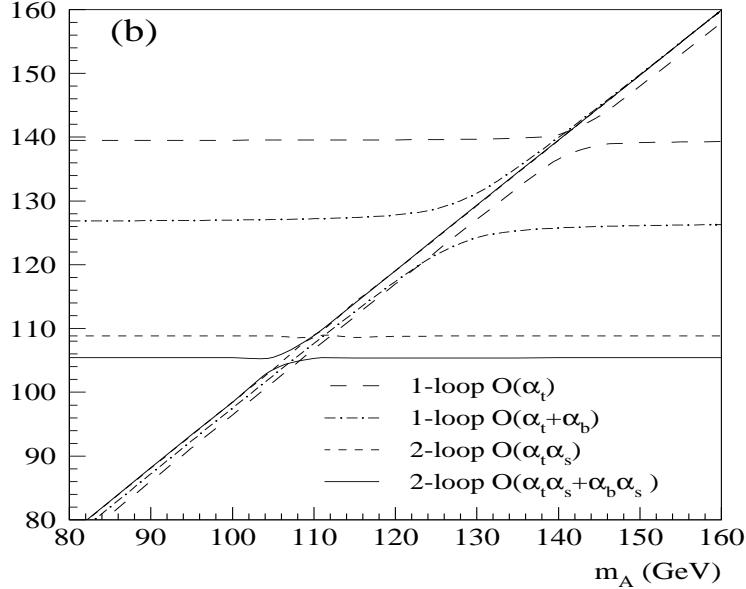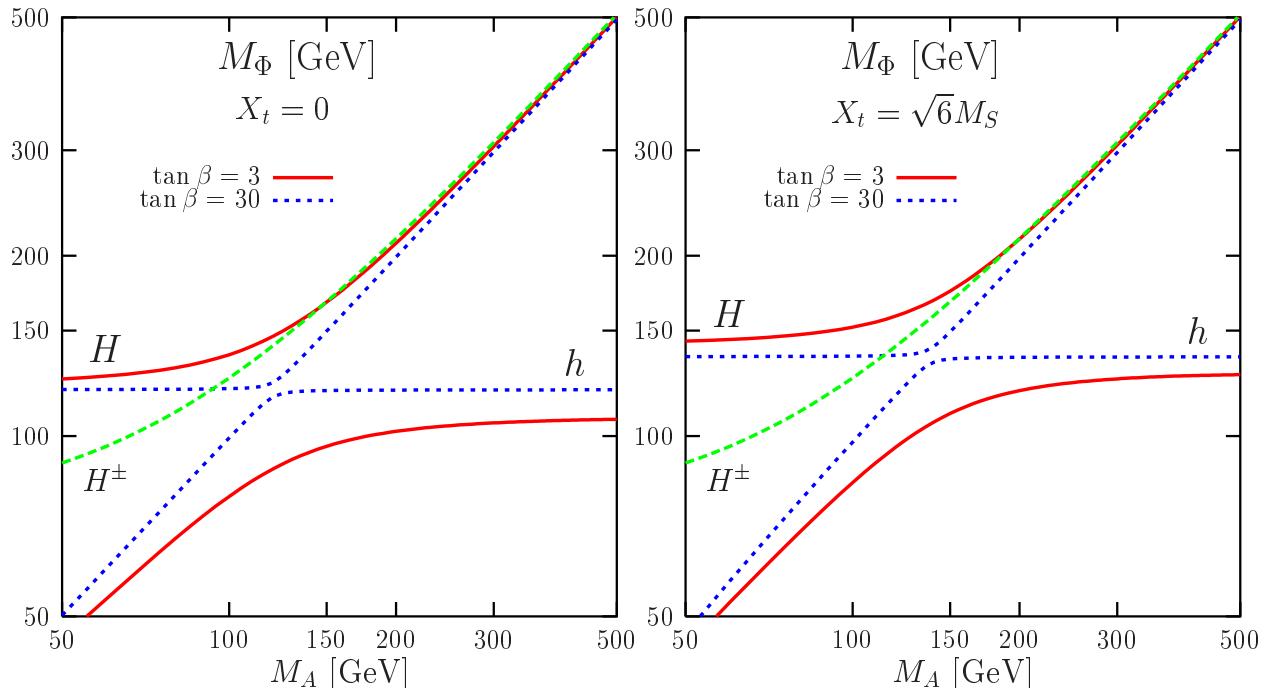

Figure 1.6: The impact of the bottom/sbottom loop contributions to the radiatively corrected masses of the CP–even Higgs bosons M_h and M_H as a function of M_A for the scenario where $\tan\beta = 45$ with $A_t \approx -\mu \approx M_S \approx 1$ TeV and $A_b = 0$; $m_t = 175$ GeV. From Ref. [118].

The radiatively corrected masses of the neutral CP–even and the charged Higgs bosons are displayed in Fig. 1.7 as a function of M_A for the two values $\tan\beta = 3$ and 30. The full set of radiative corrections has been included and the "no–mixing" scenario with $X_t = 0$ (left) and "maximal mixing" scenario with $X_t = \sqrt{6}M_S$ (right) have been assumed. The SUSY scale has been set to $M_S = 2$ TeV and the other SUSY parameters except for A_t to 1 TeV; the SM input parameters are fixed to $m_t = 178$ GeV, $m_b = 4.88$ GeV and $\alpha_s(M_Z) = 0.1172$. The program HDECAY [129] which incorporates the routine FeynHiggsFast1.2 [130] for the calculation of the radiative corrections in the MSSM Higgs sector, has been used.

Figure 1.7: *The masses of the MSSM Higgs bosons as a function of M_A for two values $\tan\beta = 3$ and 30, in the no mixing (left) and maximal mixing (right) scenarios with $M_S = 2$ TeV and all the other SUSY parameters set to 1 TeV. The full set of radiative corrections is included with $m_t = 178$ GeV, $m_b = 4.88$ GeV and $\alpha_s(M_Z) = 0.1172$.*

As can be seen, a maximal value for the lighter Higgs mass, $M_h \sim 135$ GeV, is obtained for large M_A values in the maximal mixing scenario with $\tan\beta = 30$ [the mass value is almost constant if $\tan\beta$ is increased]. For no stop mixing, or when $\tan\beta$ is small, $\tan\beta \lesssim 3$, the upper bound on the h boson mass is smaller by more than 10 GeV in each case and the combined choice $\tan\beta = 3$ and $X_t = 0$, leads to a maximal value $M_h^{\max} \sim 110$ GeV. Also for large M_A values, the A, H and $H^\pm$ bosons [the mass of the latter being almost independent of the stop mixing and on the value of $\tan\beta$] become degenerate in mass. In the opposite case, i.e. for a light pseudoscalar Higgs boson, $M_A \lesssim M_h^{\max}$, it is M_h which is very close to M_A, and the mass difference is particularly small for large $\tan\beta$ values.

1.3.3 The radiatively corrected Higgs couplings

We turn now to the couplings of the Higgs bosons, which determine to a large extent their production cross sections and their decay widths. The couplings to fermions and gauge bosons strongly depend on the value of $\tan\beta$ but also on the value of the mixing angle α in the CP–even Higgs sector. Normalized to the SM Higgs couplings as indicated in the caption, they are summarized in Table 1.5 for convenience.

Φ	$g_{\Phi\bar{u}u}$	$g_{\Phi\bar{d}d}$	$g_{\Phi VV}$	$g_{\Phi AZ}$	$g_{\Phi H^\pm W^\mp}$
$H_{\rm SM}$	1	1	1	0	0
h	$\cos\alpha/\sin\beta$	$-\sin\alpha/\cos\beta$	$\sin(\beta-\alpha)$	$\cos(\beta-\alpha)$	$\mp\cos(\beta-\alpha)$
H	$\sin\alpha/\sin\beta$	$\cos\alpha/\cos\beta$	$\cos(\beta-\alpha)$	$-\sin(\beta-\alpha)$	$\pm\sin(\beta-\alpha)$
A	$\cot\beta$	$\tan\beta$	0	0	1

Table 1.5: *Neutral Higgs boson couplings to fermions and gauge bosons in the MSSM normalized to the SM Higgs boson couplings $g_{H_{\rm SM}ff} = [\sqrt{2}G_\mu]^{1/2}m_f, g_{H_{\rm SM}VV} = 2[\sqrt{2}G_\mu]^{1/2}M_V^2$ and the couplings of two Higgs bosons with one gauge boson, normalized to $g_W = [\sqrt{2}G_\mu]^{1/2}M_W$ for $g_{\Phi H^\pm W^\mp}$ and $g_Z = [\sqrt{2}G_\mu]^{1/2}M_Z$ for $g_{\Phi AZ}$.*

These couplings are renormalized by the same radiative corrections which affect the neutral Higgs boson masses. For instance, in the ϵ approximation which has been discussed earlier, the corrected angle $\bar{\alpha}$ will be given by
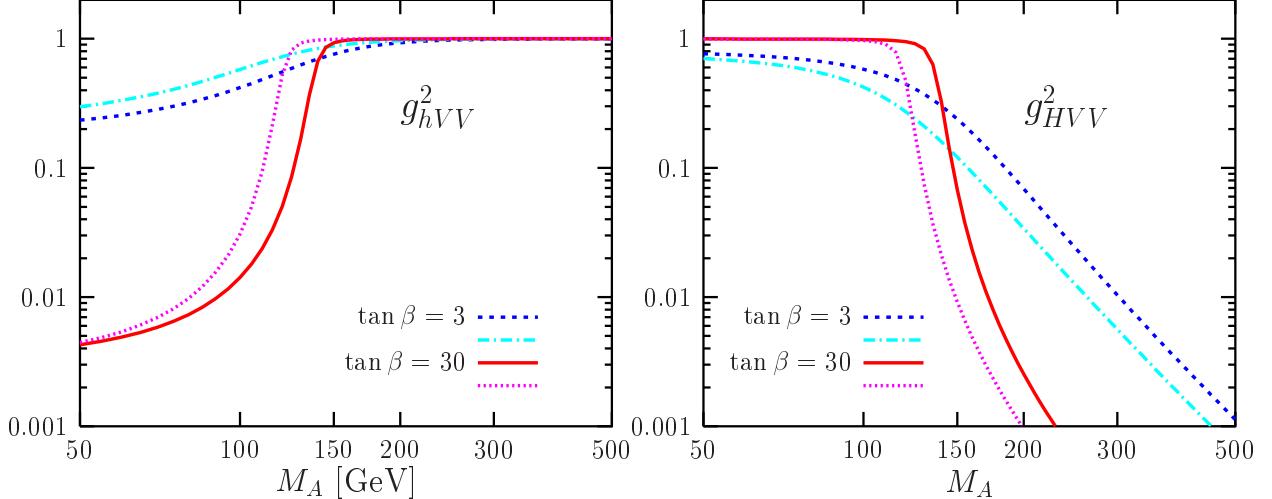
$$\tan 2\bar{\alpha} = \tan 2\beta \, \frac{M_A^2 + M_Z^2}{M_A^2 - M_Z^2 + \epsilon/\cos 2\beta} \, , \qquad -\frac{\pi}{2} \leq \alpha \leq 0 \qquad (1.136)$$

The radiatively corrected reduced couplings of the neutral CP–even Higgs particles to gauge bosons are then simply given by

$$g_{hVV} = \sin(\beta - \bar{\alpha}) \ , \ \ g_{HVV} = \cos(\beta - \bar{\alpha}) \qquad (1.137)$$

where the renormalization of α has been performed in the same approximation as for the renormalized Higgs boson masses. The squares of the two renormalized Higgs couplings to gauge bosons are displayed in Fig. 1.8 as a function of M_A for the two values $\tan\beta = 3, 30$ in the no mixing and maximal mixing scenarios. The SUSY and SM parameters are chosen as in Fig. 1.7. One notices the very strong variation with M_A and the different pattern for values above and below the critical value $M_A \simeq M_h^{\rm max}$. For small M_A values the couplings of the lighter h boson to gauge bosons are suppressed, with the suppression/enhancement being stronger with large values of $\tan\beta$. For values $M_A \gtrsim M_h^{\rm max}$, the normalized h boson couplings tend to unity and reach the values of the SM Higgs couplings, $g_{hVV} = 1$ for $M_A \gg M_h^{\rm max}$; these values are reached more quickly when $\tan\beta$ is large. The situation in

the case of the heavier CP–even H boson is just opposite: its couplings are close to unity for $M_A \lesssim M_h^{\max}$ [which in fact is very close to the minimal value of M_H, $M_H^{\min} \simeq M_h^{\max}$, in particular at large $\tan\beta$], while above this limit, the H couplings to gauge bosons are strongly suppressed. Note that the mixing X_t in the stop sector does not alter this pattern, its main effect being simply to shift the value of $M_h^{\max}$.


Figure 1.8: The normalized couplings squared of the CP–even MSSM neutral Higgs bosons to gauge bosons as a function of M_A for two values $\tan\beta = 3$ and 30, in the no mixing (light lines) and maximal mixing (thick lines) scenarios. The full set of radiative corrections is included with the same inputs as in Fig. 1.7.

In the case of the Higgs–fermion couplings, there are additional one–loop vertex corrections which modify the tree–level Lagrangian that incorporates them [67–70]. In terms of the two Higgs doublets H_1 and H_2 which generate the couplings of up–type and down–type fermions, the effective Lagrangian can be written at one–loop as [104]

$$
\begin{aligned}
-\mathcal{L}_{\text{Yuk}} &= \epsilon_{ij}\left[(\lambda_b + \delta\lambda_b)\bar{b}_R H_1^i Q_L^j + (\lambda_t + \delta\lambda_t)\bar{t}_R Q_L^i H_2^j + (\lambda_\tau + \delta\lambda_\tau)\bar{\tau}_R H_1^i L^j\right] \\
&+ \Delta\lambda_b \bar{b}_R Q_L^i H_2^{i*} + \Delta\lambda_\tau \bar{\tau}_R L^i H_2^{i*} + \Delta\lambda_t \bar{t}_R Q_L^i H_1^{i*} + \text{h.c.}
\end{aligned} \tag{1.138}
$$

Thus, at this order, in addition to the expected corrections $\delta\lambda_{t,b}$ which alter the tree–level Lagrangian, a small contribution $\Delta\lambda_t$ ($\Delta\lambda_b$) to the top (bottom) quark will be generated by the doublet H_1 (H_2). The top and bottom quark Yukawa couplings [the discussion for the τ couplings follows that of the b–quark couplings], defining $\lambda_b \Delta_b = \delta\lambda_b + \Delta\lambda_b \tan\beta$ and $\lambda_t \Delta_t = \delta\lambda_t + \Delta\lambda_t \cot\beta$, are then given by [67–70]

$$
\lambda_b = \frac{\sqrt{2}m_b}{v\cos\beta}\frac{1}{1+\Delta_b} \;, \quad \lambda_t = \frac{\sqrt{2}m_t}{v\sin\beta}\frac{1}{1+\Delta_t} \tag{1.139}
$$

The leading parts of the total corrections $\Delta_{t,b}$ are in fact those which affect the b and t quark masses in the MSSM, already discussed in §1.1.6 and given in eqs. (1.45) and (1.48). The

b quark corrections are enhanced by $\tan\beta$ factors while those affecting the top quark are sizable for large A_t or μ values. Rather than attributing these corrections to the running quark masses, one can map them into the Yukawa couplings and the masses will be simply those obtained from a standard RG running in the SM (MSSM) at a scale below (above) the SUSY scale. In the case of the neutral Higgs boson couplings to bottom quarks, one may then write [70, 104]

$$
\begin{aligned}
g_{hbb} &\simeq -\frac{\sin\bar\alpha}{\cos\beta}\Big[1 - \frac{\Delta_b}{1+\Delta_b}(1 + \cot\bar\alpha\cot\beta)\Big] \\
g_{Hbb} &\simeq +\frac{\cos\bar\alpha}{\cos\beta}\Big[1 - \frac{\Delta_b}{1+\Delta_b}(1 - \tan\bar\alpha\cot\beta)\Big] \\
g_{Abb} &\simeq \tan\beta\Big[1 - \frac{\Delta_b}{1+\Delta_b}\frac{1}{\sin^2\beta}\Big]
\end{aligned}
\tag{1.140}
$$
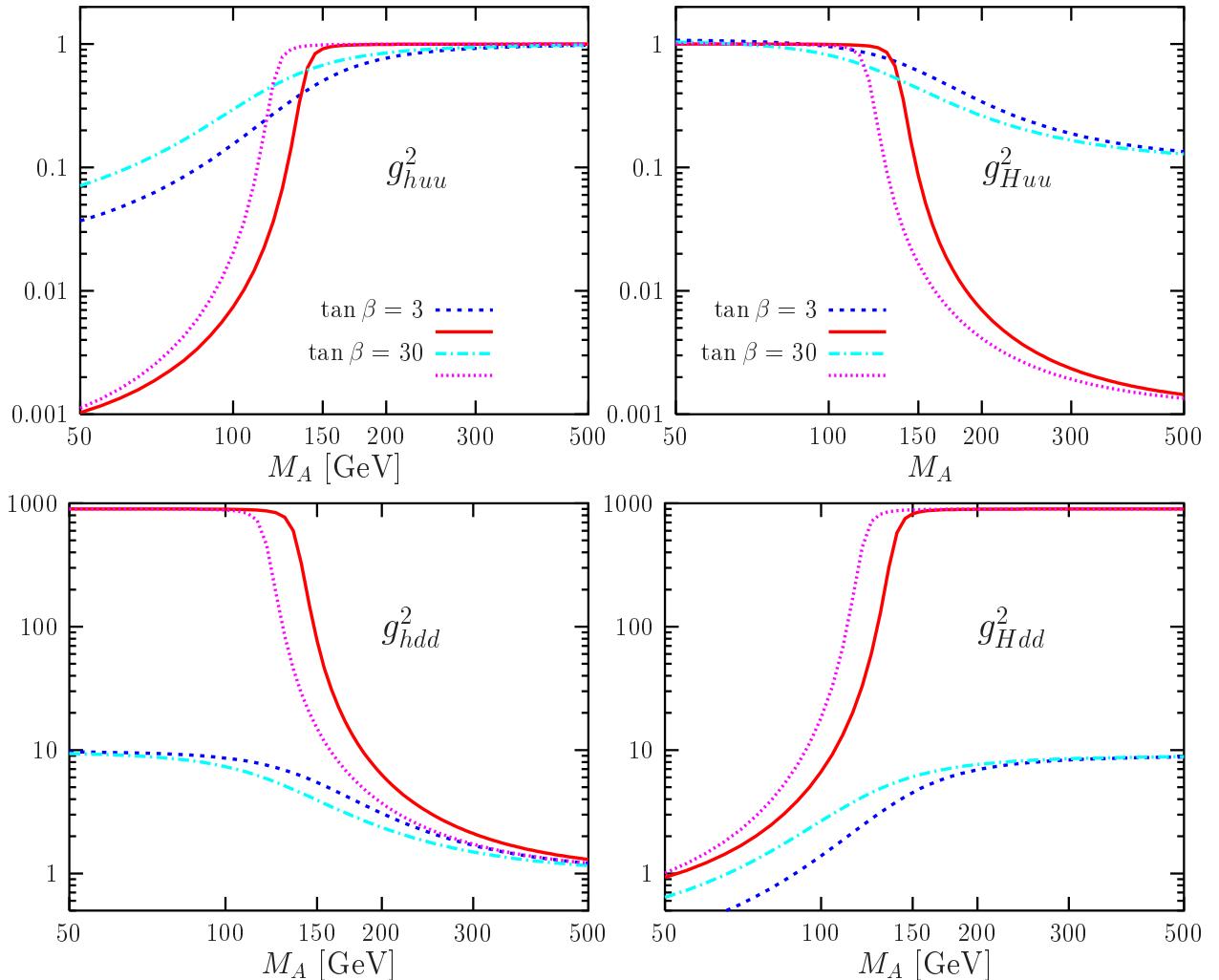
Figure 1.9: *The normalized couplings squared of the CP–even MSSM neutral Higgs bosons to fermions as a function of M_A for $\tan\beta = 3$ and 30, in the no mixing (light lines) and maximal mixing (thick lines) scenarios, using the same inputs as in Fig. 1.7.*

The couplings squared of the neutral CP–even Higgs bosons to isospin up– and down–type fermions are displayed in Fig. 1.9 as a function of M_A for the same set of parameters as in Fig. 1.7. As in the case of the VV couplings, there is again a very strong variation with M_A and different behaviors for values above and below the critical mass $M_A \simeq M_h^{\mathrm{max}}$. For $M_A \lesssim M_h^{\mathrm{max}}$ the lighter h boson couplings to up–type fermions are suppressed, while the couplings to down–type fermions are enhanced, with the suppression/enhancement being stronger at high $\tan\beta$. For $M_A \gtrsim M_h^{\mathrm{max}}$, the normalized h couplings tend to unity and reach the values of the SM Higgs couplings, $g_{hff} = 1$, for $M_A \gg M_h^{\mathrm{max}}$; the limit being reached more quickly when $\tan\beta$ is large. As in the HVV case, the situation of the H boson couplings to fermions is just opposite: they are close to unity for $M_A \lesssim M_h^{\mathrm{max}}$, while for $M_A \gtrsim M_h^{\mathrm{max}}$, the H couplings to up–type (down–type) fermions are strongly suppressed (enhanced). For $M_H \gg M_h^{\mathrm{max}}$, the H boson couplings become approximately equal to those of the A boson which couples to down–type and up–type fermions proportionally to, respectively, $\tan\beta$ and $\cot\beta$. In fact, in this limit, also the H coupling to gauge bosons approach zero, i.e. as in the case of A boson.

Finally, the trilinear Higgs couplings are renormalized not only indirectly by the renormalization of the angle α, but also directly by additional contributions to the vertices [138–143]. In the ϵ approximation, which here gives only the magnitude of the correction, i.e. about ten percent in general, the additional shifts in the neutral Higgs self–couplings $\Delta\lambda = \lambda^{1-\mathrm{loop}}(\bar\alpha) - \lambda^{\mathrm{Born}}(\alpha \to \bar\alpha)$ are given [as mentioned previously $\lambda_{hH^+H^-}$ and $\lambda_{HH^+H^-}$ follow the couplings of respectively, the h and H bosons into AA and VV states] [138]

$$\Delta\lambda_{hhh} = 3\frac{\epsilon}{M_Z^2}\frac{\cos\alpha}{\sin\beta}\cos^2\alpha \,, \ \ \Delta\lambda_{hHH} = 3\frac{\epsilon}{M_Z^2}\frac{\cos\alpha}{\sin\beta}\sin^2\alpha \,, \ \ \Delta\lambda_{hAA} = \frac{\epsilon}{M_Z^2}\frac{\cos\alpha}{\sin\beta}\cos^2\beta \ (1.141)$$

$$\Delta\lambda_{Hhh} = 3\frac{\epsilon}{M_Z^2}\frac{\sin\alpha}{\sin\beta}\cos^2\alpha \,, \ \ \Delta\lambda_{HHH} = 3\frac{\epsilon}{M_Z^2}\frac{\sin\alpha}{\sin\beta}\sin^2\alpha \,, \ \ \Delta\lambda_{HAA} = \frac{\epsilon}{M_Z^2}\frac{\sin\alpha}{\sin\beta}\cos^2\beta$$

The trilinear couplings among the neutral Higgs bosons are shown in Fig. 1.10 for the same set–up as previously, while those involving charged Higgs boson pairs are shown in Fig. 1.11. In the case of the λ_{hhh} coupling, it is strongly suppressed for $M_A \lesssim M_h^{\mathrm{max}}$, in particular at large $\tan\beta$, $\lambda_{hhh} \sim 0$, and rises quickly above this mass value to reach $\lambda_{hhh} \sim 3M_h^2/M_Z^2$ which is the SM value. This value is of course larger in the case of maximal stop mixing and large $\tan\beta$. For λ_{Hhh}, it is positive and slightly below unity for $M_A \lesssim M_h^{\mathrm{max}}$ and steeply decreases around this value. For large M_A values, it reaches a plateau which depends on $\tan\beta$, $\lambda_{Hhh} \to \frac{3}{2}\sin 4\beta$, when radiative corrections are ignored. In fact, at large $\tan\beta$ values, all couplings of the H boson to neutral and charged Higgs pairs vanish in the limit $M_A \gg M_Z$, while those of of the lighter h boson are correspondingly very small for $M_A \ll M_Z$. A strong variation of the couplings is to be noticed at the critical mass $M_A \sim M_h^{\mathrm{max}}$; far below and above this value the couplings reach asymptotic regimes.
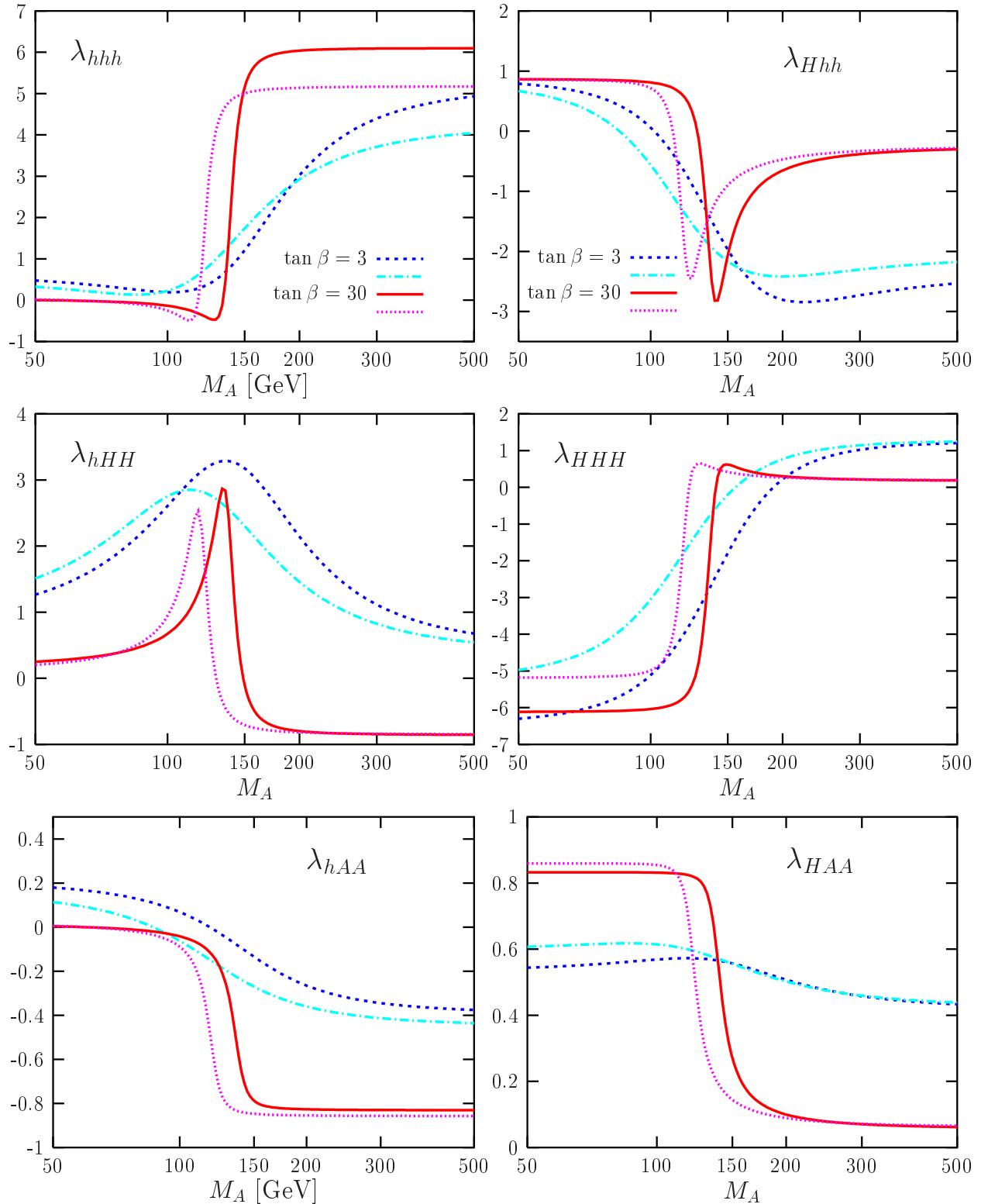
Figure 1.10: *The trilinear self–couplings among the neutral MSSM Higgs bosons [normalized to $-iM_Z^2/v$] as a function of M_A for $\tan\beta = 3$ and 30, in the no mixing (light lines) and maximal mixing (thick lines) scenarios, with the same inputs as in Fig. 1.7.*
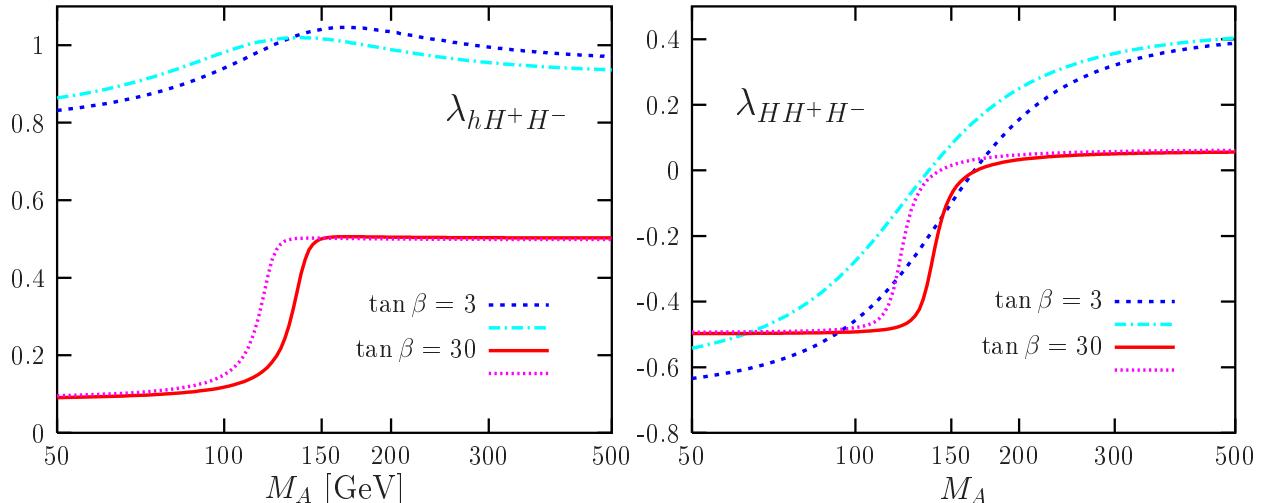
Figure 1.11: *The same as in Fig. 1.10 but for the couplings involving charged Higgs bosons.*

1.3.4 The decoupling regime of the MSSM Higgs sector

As mentioned several times before, when the pseudoscalar Higgs mass becomes large compared to M_Z, $M_A \gg M_Z$, the lighter CP–even Higgs boson h approaches its maximal mass value, given by $M_h^2 = \sqrt{\cos^2 2\beta M_Z^2 + \epsilon}$ when the dominant radiative corrections are included, reaching the value $M_h \simeq \sqrt{M_Z^2 + \epsilon}$ when $\tan\beta$ is large. The mass of the heavier CP–even Higgs boson, $M_H = \sqrt{M_A^2 + \sin^2 2\beta M_Z^2}$, and the one of the charged Higgs boson, $M_{H^\pm} = \sqrt{M_A^2 + c_W^2 M_Z^2}$, become very close to M_A. This is one aspect of the decoupling regime in the MSSM, where there is only one light Higgs boson in the theory and all the other Higgs particles are very heavy and degenerate in mass, $M_H \simeq M_{H^\pm} \simeq M_A$ [103].

The other very important aspect of the decoupling regime is related to the Higgs couplings to SM particles. As seen previously, CP–invariance prohibits tree–level couplings of the pseudoscalar and charged Higgs bosons to two gauge bosons. The couplings of the CP–even h and H bosons to WW and ZZ states are suppressed by mixing angle factors but are complementary, the sum of their squares being the square of the $H_{\rm SM}VV$ coupling. For large M_A values, one can expand these couplings in powers of M_Z/M_A to obtain at tree–level

$$g_{HVV} = \cos(\beta - \alpha) \overset{M_A \gg M_Z}{\longrightarrow} \frac{M_Z^2}{2M_A^2}\sin 4\beta \overset{\tan\beta \gg 1}{\longrightarrow} -\frac{2M_Z^2}{M_A^2 \tan\beta} \to 0$$

$$g_{hVV} = \sin(\beta - \alpha) \overset{M_A \gg M_Z}{\longrightarrow} 1 - \frac{M_Z^4}{8M_A^4}\sin^2 4\beta \overset{\tan\beta \gg 1}{\longrightarrow} 1 - \frac{2M_Z^4}{M_A^4 \tan^2\beta} \to 1 \quad (1.142)$$

where we have also displayed the limits for large values of $\tan\beta$ using the relation $\sin 4\beta = 4\tan\beta(1-\tan^2\beta)(1+\tan^2\beta)^{-2} \overset{\tan\beta \gg 1}{\longrightarrow} -4\cot\beta$. One sees that for $M_A \gg M_Z$, g_{HVV} vanishes while g_{hVV} reaches unity, i.e. the SM value. This occurs more quickly if $\tan\beta$ is large, since the first term of the expansion involves this parameter in the denominator.

59

This statement can be generalized to the couplings of two Higgs bosons and one gauge boson and to the quartic couplings between two Higgs and two gauge bosons, which are proportional to either $\cos(\beta - \alpha)$ or $\sin(\beta - \alpha)$ [there are also several angle independent couplings, such as the $\gamma H^+ H^-$, $ZH^+ H^-$ and $W^\pm H^\mp A$ couplings and those involving two identical gauge and Higgs bosons as well as the $H^\pm A$ states]. In particular, all couplings involving at least one gauge boson and exactly one non–minimal Higgs particle $A, H, H^\pm$ vanish for $M_A \gg M_Z$, while all the couplings involving no other Higgs boson than the lighter h boson reduce to their SM values. [The last statement, for instance, can be checked explicitly in the case of the trilinear λ_{hhh} couplings.]

Turning to the Higgs couplings to fermions, and expressing the couplings of the CP–even h and H bosons to isospin $\frac{1}{2}$ and $-\frac{1}{2}$ fermions as in eq. (1.97) in terms of $\cos(\beta - \alpha)$ with the latter given by eq. (1.142) in the decoupling limit, one has for $M_A \gg M_Z$ [61]

$$g_{huu} \quad \overset{M_A \gg M_Z}{\longrightarrow} \quad 1 + \frac{M_Z^2}{2M_A^2}\frac{\sin 4\beta}{\tan\beta} \quad \overset{\tan\beta \gg 1}{\longrightarrow} \quad 1 - \frac{2M_Z^2}{M_A^2 \tan^2\beta} \to 1 \qquad (1.143)$$

$$g_{hdd} \quad \overset{M_A \gg M_Z}{\longrightarrow} \quad 1 - \frac{M_Z^2}{2M_A^2}\sin 4\beta \tan\beta \quad \overset{\tan\beta \gg 1}{\longrightarrow} \quad 1 + \frac{2M_Z^2}{M_A^2} \to 1$$

$$g_{Huu} \quad \overset{M_A \gg M_Z}{\longrightarrow} \quad -\cot\beta + \frac{M_Z^2}{2M_A^2}\sin 4\beta \quad \overset{\tan\beta \gg 1}{\longrightarrow} \quad -\cot\beta\left(1 + \frac{2M_Z^2}{M_A^2}\right) \to -\cot\beta$$

$$g_{Hdd} \quad \overset{M_A \gg M_Z}{\longrightarrow} \quad \tan\beta + \frac{M_Z^2}{2M_A^2}\sin 4\beta \quad \overset{\tan\beta \gg 1}{\longrightarrow} \quad \tan\beta\left(1 - \frac{2M_Z^2}{M_A^2 \tan^2\beta}\right) \to \tan\beta$$

Thus, the couplings of the h boson approach those of the SM Higgs boson, $g_{huu} = g_{hdd} = 1$, while the couplings of the H boson reduce, up to a sign, to those of the pseudoscalar Higgs boson, $g_{Huu} \simeq g_{Auu} = \cot\beta$ and $g_{Hdd} \simeq g_{Add} = \tan\beta$. Again, as a result of the presence of the $\tan\beta$ factors in the denominators of the expansion terms, eq. (1.143), these limits are reached more quickly at large values of $\tan\beta$, except for g_{hdd} and g_{Huu}.

These results are not significantly altered by the inclusion of the radiative corrections in general [except for two exceptional situations which will be discussed later]. A quantitative change, though, is the value of M_A at which the decoupling occurs. For instance, at large $\tan\beta$, the decoupling limit is already reached for $M_A \gtrsim M_Z$ at tree–level, but the inclusion of the radiative corrections shifts this value to $M_A \gtrsim M_h^{\max}$. In addition, even in the presence of the threshold corrections $\Delta_{t,b}$ in the Yukawa couplings, one still recovers the SM coupling for the h boson, $g_{hbb} = 1$, once they are implemented as in eq. (1.140).

In the case of the trilinear Higgs couplings, it is instructive to keep the radiative corrections since without these contributions, most of them would vanish. Using the abbreviations, $x_0 = M_h^2/M_Z^2, x_1 = \sqrt{(x_0 - \epsilon_Z \sin^2\beta)(1 - x_0 + \epsilon_Z \sin^2\beta)}$ with $\epsilon_Z = \epsilon/M_Z^2$, one obtains for the self–couplings among the neutral Higgs bosons in the ϵ approach [144]

$$\lambda_{hhh} \overset{M_A \gg M_Z}{\longrightarrow} 3x_0 \,, \quad \lambda_{hHH} \overset{M_A \gg M_Z}{\longrightarrow} 2 - 3(x_0 - \epsilon_Z) \,, \quad \lambda_{hAA} \overset{M_A \gg M_Z}{\longrightarrow} -(x_0 - \epsilon_Z) \,, \qquad (1.144)$$

$$\lambda_{Hhh} \overset{M_A \gg M_Z}{\longrightarrow} -3x_1 - 3\epsilon_Z \sin\beta\cos\beta \,, \ \lambda_{HHH} \sim \frac{1}{3}\lambda_{HAA} \overset{M_A \gg M_Z}{\longrightarrow} 3x_1 - 3\epsilon_Z \cot\beta\cos^2\beta$$

At high–$\tan\beta$, one has $x_0 - \epsilon_Z = 1$ leading to $x_1 = 0$, so that the expressions simplify to

$$\lambda_{hhh} \simeq 3M_h^2/M_Z^2 \,, \ \lambda_{hHH} \simeq \lambda_{hAA} = -1 \,, \ \lambda_{Hhh} \simeq \lambda_{HHH} \simeq \lambda_{HAA} \simeq 0 \qquad (1.145)$$

in qualitative agreement with the behavior shown in Fig. 1.10 for $\tan\beta = 30$.

To summarize: for large values of M_A, in practice for $M_A \gtrsim 300$ GeV for low $\tan\beta$ and $M_A \gtrsim M_h^{\max}$ for $\tan\beta \gtrsim 10$, the h boson reaches its maximal mass value and its couplings to fermions and gauge bosons as well as its trilinear self–coupling become SM–like. The heavier H boson has approximately the same mass as the A boson and its interactions are similar, i.e. its couplings to gauge bosons almost vanish and the couplings to isospin $(\frac{1}{2}) -\frac{1}{2}$ fermions are (inversely) proportional to $\tan\beta$. The charged Higgs boson is also degenerate in mass with the A boson and its couplings to single h bosons are suppressed. Thus, in the decoupling limit, the heavier Higgs bosons decouple and the MSSM Higgs sector reduces effectively to the SM Higgs sector, but with a light Higgs boson with a mass $M_h \lesssim 140$ GeV.

1.3.5 The other regimes of the MSSM Higgs sector

There are also other regimes of the MSSM which have interesting phenomenological consequences and that we briefly summarize below.

The anti–decoupling regime

If the pseudoscalar Higgs boson is very light[9], $M_A \ll M_Z$, the situation is exactly opposite to the one in the decoupling regime. Indeed, in this case, the lighter CP–even Higgs boson mass is given by $M_h \simeq M_A|\cos 2\beta|$ while the heavier CP–even Higgs mass is given by $M_H \simeq M_Z(1 + M_A^2 \sin^2 2\beta/M_Z^2)$. At large values of $\tan\beta$, the h boson is degenerate in mass with the pseudoscalar Higgs boson A, $M_h \simeq M_A$, while the H boson is degenerate in mass with the Z boson, $M_H \simeq M_Z$ [145]. This is similar to the decoupling regime, except that the roles of the h and H bosons are reversed, and since there is an upper bound on M_h, all Higgs particles are light. We will call this scenario, the anti–decoupling regime.

In contrast to the decoupling regime, for $M_A \ll M_Z$, it is $\cos(\beta - \alpha)$ which is large and $\sin(\beta - \alpha)$ which is small, in particular at high values of $\tan\beta$ where one has

$$\cos^2(\beta - \alpha) \overset{M_A \ll M_Z}{\longrightarrow} \cos^2 2\beta \left(1 - \frac{M_A^2}{M_Z^2}\sin^2 2\beta\right) \overset{\tan\beta \gg 1}{\longrightarrow} 1 \qquad (1.146)$$

---

[9]The values $M_A \lesssim M_Z$ are excluded experimentally in the MSSM as will be discussed in the next section. However, when including the radiative corrections, the above limit becomes $M_A \ll \sqrt{M_Z^2 + \epsilon}$ and is valid, in particular at high $\tan\beta$ values, for $M_A \lesssim \sqrt{M_Z^2 + \epsilon}$ as we will see shortly.

From eq. (1.97) one then sees that it is the h boson which has couplings that behave as those of the pseudoscalar Higgs boson A, while the H boson couplings are SM–like

$$g_{huu} \overset{M_A \ll M_Z}{\longrightarrow} \cot\beta \quad , \quad g_{hdd} \overset{M_A \ll M_Z}{\longrightarrow} -\tan\beta$$
$$g_{Huu} \overset{M_A \ll M_Z}{\longrightarrow} 1 \quad , \quad g_{Hdd} \overset{M_A \ll M_Z}{\longrightarrow} 1 \tag{1.147}$$

Again, the radiative corrections do not qualitatively change this pattern and the only effect is to to shift the value at which this situation occurs, *i.e.* from $M_A \sim M_Z$ to $M_A \sim M_h^{\max} \sim \sqrt{M_Z^2 + \epsilon}$. Thus, in the low M_A regime and for large $\tan\beta$ values, the H boson has a mass $M_H \sim M_h^{\max} \simeq \sqrt{M_Z^2 + \epsilon}$ and its couplings to gauge bosons and fermions are SM–like, while the lighter h boson is degenerate in mass with the pseudoscalar Higgs boson, $M_h \simeq M_A$ and has approximately the same couplings, that is, very suppressed couplings to gauge bosons and isospin up–type fermions and enhanced couplings to isospin down–type fermions. This can explicitly be seen in Figs. 1.8 and 1.9 where the masses and the couplings, including the full set of radiative corrections, are plotted against M_A.

The intense–coupling regime

An interesting situation would be the one where the mass of the pseudoscalar A boson is close to M_Z at tree–level, or when radiative corrections in the Higgs sector are taken into account, close to the maximal value allowed for the lighter Higgs boson mass M_h. In this case, the three neutral Higgs bosons h, H and A [and even the charged Higgs particles] will have comparable masses, $M_h \sim M_H \sim M_A \sim M_h^{\max}$. The mass degeneracy is more effective when $\tan\beta$ is large. This scenario, called the intense–coupling regime, has been discussed in detail in Refs. [134, 146].

In fact, this regime can be defined as the one where the two CP–even Higgs bosons h and H are almost degenerate in mass, $M_h \simeq M_H$. Including the radiative corrections in the ϵ approach for illustration and solving eq. (1.130) for $M_H^2 - M_h^2 = 0$, which is a second order polynomial equation in the variable M_A^2

$$M_A^4 + 2M_A^2[M_Z^2(1 - 2\cos^2 2\beta) + \epsilon \cos 2\beta] + M_Z^4 + \epsilon^2 - 2M_Z^2\epsilon \cos 2\beta = 0 \tag{1.148}$$

one obtains a discriminant $\Delta' = -\sin^2 2\beta(2M_Z^2 \cos 2\beta - \epsilon)^2 \leq 0$. The only way for the solution to be real is therefore to have either $\sin 2\beta = 0$ or $\epsilon = 2M_Z^2 \cos 2\beta$. The last possibility gives $M_A^2 = -M_Z^2$ which has to be rejected, while the former possibility gives $M_A^2 = M_Z^2 + \epsilon$ with $\beta = \frac{\pi}{2}$. In fact, this solution or critical mass corresponds to the maximal value allowed for M_h and the minimal value that M_H can take

$$M_C = M_h^{\max} = M_H^{\min} = \sqrt{M_Z^2 + \epsilon} \tag{1.149}$$

In addition, in the large $\tan\beta$ regime, eq. (1.130) for the h and H masses simplifies to $M_{h,H}^2 = \frac{1}{2}(M_A^2 + M_Z^2 + \epsilon \mp |M_A^2 - M_Z^2 - \epsilon|)$, which means that

$$M_A \gtrsim M_C \quad \Rightarrow \quad M_H \simeq M_A \quad \text{and} \quad M_h \simeq M_C$$
$$M_A \lesssim M_C \quad \Rightarrow \quad M_h \simeq M_A \quad \text{and} \quad M_H \simeq M_C \qquad (1.150)$$

and therefore the A boson is always degenerate in mass with one of the CP–even Higgs bosons, that we will call Φ_A, while the other CP–even Higgs particle, called Φ_H, is very close in mass with M_C. In addition, the CP–even Φ_A boson will have almost the same couplings as A, while the Φ_H particle will have almost the couplings of the SM Higgs boson. If $M_A \gtrsim M_C$ we are in fact in the decoupling limit, while for $M_A \lesssim M_C$ we are in the anti–decoupling regime, the two situations which have been discussed previously.

If the masses of the neutral Higgs bosons are approximately equal, $M_h \simeq M_H \simeq M_A \simeq M_C$, we are in the transition regime where both the Φ_A and Φ_H bosons have still enhanced couplings to down–type fermions and suppressed couplings to gauge bosons and up–type fermions. This can be seen from eq. (1.97) where one sets $\cos^2(\beta - \alpha) \sim \sin^2(\beta - \alpha) \sim \frac{1}{2}$ and obtains for large $\tan\beta$ values

$$|g_{hVV}| \simeq |g_{huu}| \simeq |g_{HVV}| \simeq |g_{Huu}| \simeq \frac{1}{\sqrt{2}} \quad , \quad |g_{hdd}| \simeq |g_{Hdd}| \simeq \tan\beta \qquad (1.151)$$

This leads to interesting phenomenological implications which will be discussed later.

The intermediate–coupling regime

For low values of $\tan\beta$, $\tan\beta \lesssim 3$–5, and a not too heavy pseudoscalar Higgs boson, $M_A \lesssim 300$–500 GeV, we are not yet in the decoupling regime and both $\cos^2(\beta - \alpha)$ and $\sin^2(\beta - \alpha)$ are sizable, implying that both CP–even Higgs bosons have significant couplings to gauge bosons. The couplings between one gauge boson and two Higgs bosons, which are suppressed by the same mixing angle factors, are also significant. In addition, the couplings of the neutral Higgs bosons to down–type (up–type) fermions are not strongly enhanced (suppressed) since $\tan\beta$ is not too large.

In this case, interesting phenomenological features occur. Although, the H, A and $H^\pm$ bosons are relatively heavy, they do not completely decouple from gauge bosons and up–type fermions. Many interesting decay modes, such as the decays $A \to hZ$ and $H^\pm \to W^\pm h$, as well as the decay $H \to hh$ and possibly $H/A \to t\bar{t}$, occur at visible rates, since at the same time the phase space is favorable and the couplings among the particles are not suppressed [and the decays into $b\bar{b}$ pairs which are overwhelming at large $\tan\beta$ are not too strongly enhanced]. These decays will be discussed in detail in the next section.

The vanishing–coupling regime

Finally, for relatively large values of $\tan\beta$ and intermediate to large values of M_A, as well as for specific values of the other MSSM parameters which enter the radiative corrections, there is a possibility of the suppression of the couplings of one of the CP–even Higgs bosons to fermions or gauge bosons, as a result of the cancellation between tree–level terms and the radiative corrections [132, 147–150]. Indeed, reconsidering the expansion of the h boson couplings to down type fermions g_{hdd} in the large M_A and $\tan\beta$ limits, eq. (1.143), and including the radiative corrections in the parametrization of eq. (1.127), one obtains

$$g_{hdd} = -\frac{\sin\alpha}{\cos\beta} \sim 1 + 2\frac{M_Z^2}{M_A^2} - \frac{\Delta\mathcal{M}_{12}^2}{M_Z^2}\frac{M_Z^2}{M_A^2}\tan\beta \qquad (1.152)$$

If $\tan\beta$ is large, the radiative corrections are strongly enhanced and can become of the same order as the tree–level contribution. The cancellation of the two occurs at approximately $\Delta\mathcal{M}_{12}^2 \sim (M_A^2 + 2M_Z^2)\cot\beta$ and in this case, g_{hdd} vanishes. The exact point for which this phenomenon occurs depends on all the SUSY parameters which enter the radiative corrections [132], as well as on the approximation which is used to implement them [for instance, this cancellation does obviously not occur in the ϵ approach since in this case, $\Delta\mathcal{M}_{12}^2 \sim 0$, eq. (1.126)]. However, there is in general a sizable portion of the parameter space where the $h b\bar{b}$ and $h\tau^+\tau^-$ coupling are strongly suppressed. In addition, in the case of the hbb couplings, additional strong suppression might occur [150] as a result of large vertex corrections due to gluino exchange. These situations lead to peculiar phenomenological consequences, in particular for the decays of the h boson as will be discussed later.

Note that the other couplings of the Higgs bosons can be obtained by setting $\bar{\alpha} = 0$. This leads to $g_{huu} \sim \sin^{-1}\beta$ and $g_{hVV} \sim \sin\beta$ but since $\tan\beta$ is large, $\sin\beta \sim 1$ and the couplings are very close to unity as in the decoupling limit. This is also the case of the couplings of the H boson, $g_{Huu} \sim 0$ and $g_{Hdd}^{-1} \sim g_{HVV} \sim \cos\beta \sim 0$, which are as in the decoupling regime.

There is also another exceptional situation in which some Higgs boson coupling accidentally vanishes. In the parameterization of the radiative corrections of eq. (1.127), $\cos(\beta - \alpha)$ which governs the coupling of the heavier CP–even H boson to gauge bosons [and also the decoupling limit, the pattern of which is thus affected] is given by [104]

$$\cos(\beta - \alpha) \sim \left(1 + \frac{\Delta\mathcal{M}_{11}^2 - \Delta\mathcal{M}_{22}^2}{2M_Z^2\cos 2\beta} - \frac{\Delta\mathcal{M}_{12}^2}{2M_Z^2\sin 2\beta}\right)\left[\frac{M_Z^2\sin 4\beta}{2M_A^2} + \mathcal{O}\left(\frac{M_Z^4}{M_A^4}\right)\right] \quad (1.153)$$
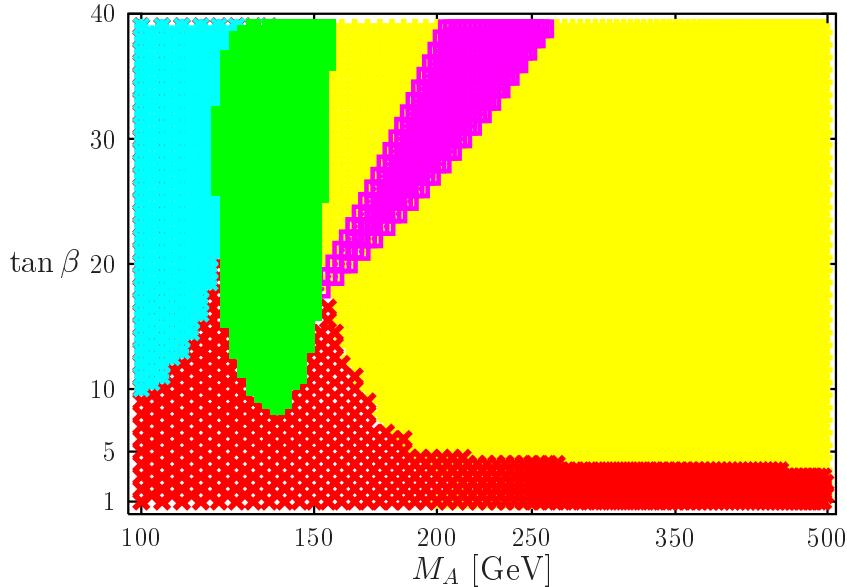
which goes to zero for $M_A \gg M_Z$. However, there is another possibility for $\cos(\beta - \alpha)$ to vanish, namely, that the first factor of eq. (1.153) is zero. At large $\tan\beta$ values, this happens independently of the value of M_A for $\tan\beta = (2M_Z^2 - \Delta\mathcal{M}_{11}^2 + \Delta\mathcal{M}_{22}^2)/\Delta\mathcal{M}_{12}^2$. The occurrence of this phenomenon, called the M_A independent decoupling in Ref. [104], depends also on the various SUSY parameters which enter the $\Delta\mathcal{M}_{ij}^2$ corrections.

Summary of the various regimes

To illustrate and summarize the previous discussions, let us take as an example, the following quantitative requirements for the various regimes of the MSSM Higgs sector

$$
\begin{aligned}
\text{decoupling regime} \quad &: \quad \cos^2(\beta - \alpha) \leq 0.05 \\
\text{anti} - \text{decoupling regime} \quad &: \quad \cos^2(\beta - \alpha) \geq 0.9 \\
\text{intense} - \text{coupling regime} \quad &: \quad g_{hbb}^2 \text{ and } g_{Hbb}^2 \geq 30 \\
\text{vanishing} - \text{coupling regime} \quad &: \quad g_{hbb}^2 \leq 0.1 \\
\text{intermediate} - \text{coupling regime} \quad &: \quad M_A \gtrsim 2M_Z \ : \ g_{Htt}^2/g_{Hbb}^2 \geq 10^{-2} \\
&\qquad M_A \lesssim 2M_Z \ : \ \text{complementary region} \quad (1.154)
\end{aligned}
$$

In the M_A–$\tan\beta$ plane, these constraints result in the areas displayed in Fig. 1.12; in the way they are defined, some of these regions overlap. The radiative corrections in the Higgs sector are implemented in the scenario described in the Appendix, except for the vanishing–coupling regime where we have set $M_3 = M_2 = 2M_1 = \frac{1}{5}\mu = \frac{1}{2}M_S = \frac{1}{3}X_t = \frac{1}{3}X_b = 0.5$ TeV, in such a way that indeed it occurs. Note that the intermediate–coupling regime is defined here by requiring a strong enough $H t\bar{t}$ coupling only for $M_A \gtrsim 2M_Z$; below this mass range, we have simply included the complementary area not covered by the other regimes.

Figure 1.12: Illustration for the various regimes of the MSSM Higgs sector as defined in the text in the $\tan\beta$–M_A plane. The radiative corrections are implemented in the usual scenario except for the vanishing–coupling regime where the parameters are as described in the text. The leftmost area is for the anti–decoupling, the one next to it for the intense–coupling, the area on the right is for the vanishing–coupling and the lower area is for the intermediate–coupling regimes; the rest of the plane is occupied by the decoupling regime.

1.4 Constraints on the MSSM Higgs sector

1.4.1 Theoretical bounds on $\tan\beta$ and the Higgs masses

Theoretical bounds on $\tan\beta$

In the MSSM, $\tan\beta$ is in principle a free parameter which can take arbitrary small or large values. However, from the requirement that the Higgs boson couplings to fermions should remain perturbative, one can attempt to impose constraints on this parameter. Recalling that the couplings of the pseudoscalar and charged Higgs bosons, as well as the coupling of the h (H) boson for small (large) values of M_A, to isospin up–type and down–type fermions are proportional to, respectively, $\cot\beta$ and $\tan\beta$, and the value of the top and bottom quark masses $m_t \simeq 178$ GeV and $\overline{m}_b(m_b) \simeq 4.25$ GeV, the condition that the Yukawa couplings of the third generation heavy quarks are smaller than, say $\sqrt{4\pi}$, leads to $0.3 \lesssim \tan\beta \lesssim 150$. Nevertheless, this is only a guess since first, the quark masses are smaller at high scales such as M_A or M_S and second, perturbativity might hold even if the couplings are larger than $2\sqrt{\pi}$ since the expansion parameter is in general $\lambda_f^2/(16\pi^2)$ rather than $\lambda_f^2/(4\pi)$.

However, in constrained MSSM models, perturbation theory indeed breaks down well before the limits on $\tan\beta$ given above are reached. In fact, in the minimal SUGRA model and more generally, in models with universal boundary conditions at the GUT scale, one obtains the much stronger condition [151]

$$1 \lesssim \tan\beta \lesssim m_t/m_b \tag{1.155}$$

which, when applied at the SUSY scale $M_S \sim 1$ TeV, leads to $1 \lesssim \tan\beta \lesssim 60$. The bound follows from the minimization of the scalar Higgs potential which leads to the two relations of eq. (1.70) which can be conveniently written as

$$\tan\beta = \frac{v_2}{v_1} = \frac{\overline{m}_1^2 + \frac{1}{2}M_Z^2}{\overline{m}_2^2 + \frac{1}{2}M_Z^2} \tag{1.156}$$

The RGEs for the difference of the squares of the soft SUSY–breaking Higgs boson mass terms, retaining only the dominant top–quark Yukawa coupling, can be also rewritten as

$$\frac{\mathrm{d}}{\mathrm{d}\log Q}(\overline{m}_1^2 - \overline{m}_2^2) = -\frac{3}{8\pi^2}\lambda_t^2 F_t \ , \quad F_t = m_{\tilde{t}_L}^2 + m_{\tilde{t}_R}^2 + m_{H_2}^2 + A_t^2 \tag{1.157}$$

with the boundary conditions at the GUT scale being $\overline{m}_1^2(M_U) = \overline{m}_2^2(M_U)$. If one now assumes that $\tan\beta < 1$, the observation that $m_t \gg m_b$ implies that $\lambda_t \propto m_t/v_2 \gg \lambda_b \propto m_b/v_1$, which incidentally makes that eq. (1.157) is a rather good approximation. Solving the previous equation at the SUSY scale M_S, and since $F_t > 0$, one obtains $\overline{m}_1 > \overline{m}_2$. However, from eq. (1.156), one should obtain $\tan\beta > 1$ in this case, which is in contradiction with the starting assumption $\tan\beta < 1$. Thus, $\tan\beta$ should be larger than unity. Similarly, including

in eq. (1.157) the contribution of the bottom quark Yukawa coupling, one arrives at the conclusion that $\tan\beta < m_t/m_b$ at the SUSY scale [151].

Note that from the requirement of Yukawa coupling unification at the GUT scale, as predicted for instance in minimal SU(5) for the b and τ couplings, one can put strong constraints on $\tan\beta$ [152]. For the value $m_t \sim 175$ GeV and $\bar{m}_b(m_b) \sim 4.25$ GeV, the parameter is restricted to two narrow ranges, $\tan\beta \sim 1.5$ and $\tan\beta \sim m_t/m_b \sim 50$–60 [153].

Bounds on M_h

As discussed previously, the mass of the lighter MSSM Higgs boson M_h is bounded from above by M_Z at tree–level, but loop corrections increase this bound by several tens of GeV. To obtain the maximal value of M_h, one needs to choose the parameters which are relevant for the Higgs sector in such a way that the one–loop radiative corrections, e.g. ϵ in eq. (1.126), are maximized. In particular, one can obtain a very good approximation of the maximal M_h value when requiring: i) large values of the parameter $\tan\beta$, $\tan\beta \gtrsim 30$; ii) a decoupling regime with a heavy pseudoscalar Higgs boson, $M_A \sim \mathcal{O}(\text{TeV})$; iii) heavy stops, i.e. large M_S values[10]; iv) a stop trilinear coupling such that X_t is close to $+\sqrt{6}\,M_S$.

For instance, in the scenario of maximal mixing with a SUSY scale $M_S = 2$ TeV and $M_2 \simeq 2M_1 = -\mu = \frac{1}{4}M_3 = \frac{1}{5}M_S$ [that we more or less used in our previous discussion, and which is rather close to the benchmark point [135] used for LEP2 Higgs analyses that we will discuss later], one obtains for $\tan\beta \sim 60$ and $M_A = 1$ TeV, $M_h^{\text{max}} \simeq 138$ GeV when the central value of the top quark mass, $m_t = 178$ GeV, is used. However, this bound is not yet fully optimized. In order to find the absolute maximal M_h value, one has still to vary in a reasonable range the SUSY parameters entering the radiative corrections and maximize the chargino/neutralino/gluino and non leading fermion/sfermion contributions. A full scan of the MSSM parameter space has been performed in Ref. [121] [see also [154]] , with the requirement that the set of SUSY parameters should fulfill all the known theoretical and experimental constraints, leading to the upper bound on the lighter Higgs boson mass

$$M_h^{\text{max}} \simeq 144 \text{ GeV for } m_t = 178 \text{ GeV} \tag{1.158}$$

To obtain an even more conservative bound on M_h, one still has to include the theoretical as well as experimental uncertainties. In Ref. [121], the uncertainties due to the renormalization scheme dependence, the variation with the renormalization scale and the error from the approximation of using zero–momentum transfer in the two–loop radiative corrections to the Higgs masses, have been estimated to lead to a total error of $\Delta M_h \sim 3$–4 GeV on the Higgs mass. Adding this theoretical uncertainty and using the 1σ experimental upper bound

---

[10]Note, however, that heavier stops correspond to more fine–tuning of the parameters in order to achieve the correct minimum of the Higgs potential and we choose $M_S = 2$ TeV as a maximal value.
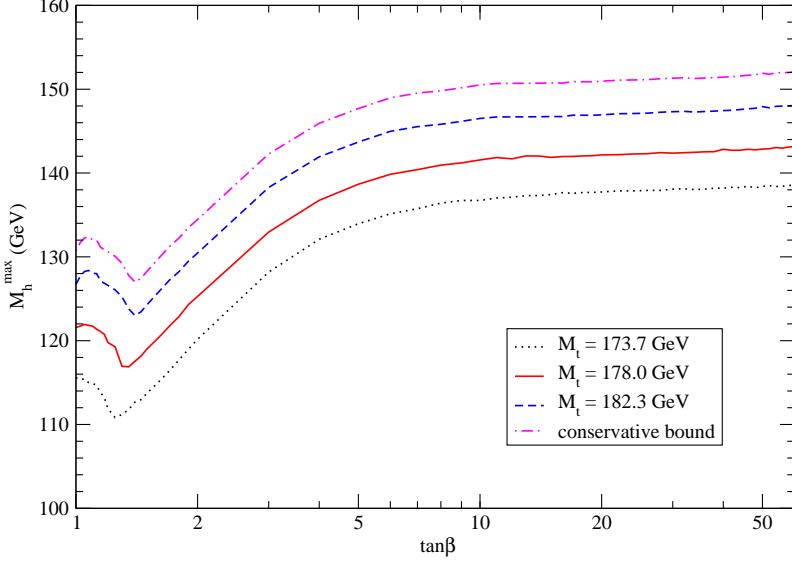
Figure 1.13: The upper bound on M_h in the pMSSM as a function of $\tan\beta$ as obtained from a full scan of the parameter space for the top quark mass values $m_t = 173.7, 178.0$ and 182.3 GeV. The thick dotted line on the top is for the conservative case, eq. (1.159).

on the top quark mass, one obtain the *maximum maximorum M_h* value

$$M_h^{\max} \sim 150 \text{ GeV for } m_t \simeq 182 \text{ GeV} \tag{1.159}$$

In Fig. 1.13, we display the variation of the upper bound on the lighter Higgs boson mass M_h in the pMSSM as a function of $\tan\beta$, that has resulted from the full scan of Ref. [121]. The full, dashed and dotted lines show the values of $M_h^{\max}$ for the top mass values $m_t = 173.7, 178.0$ and 182.3 GeV, respectively, while the thick dotted line on the top is for the conservative case where $m_t = 182.3$ GeV is used and a 4 GeV theoretical error is added linearly.

In constrained models, such as mSUGRA, GMSB and AMSB, the various parameters which enter the radiative corrections are not all independent, due to the relations between SUSY–breaking parameters that are set at the high–energy scale. In addition, the radiative electroweak symmetry breaking constraint must be fulfilled for each set of input parameters [in the pMSSM, this is automatic since M_A and μ are used as inputs]. Thus, in contrast with what occurs in the pMSSM, it is not possible to freely tune all relevant weak–scale parameters in order to get the maximal value of M_h eq. (1.159). The obtained bounds on M_h from a full scan of the parameter space of the previous models are stricter [121, 155–157].

Finally, note that there is in principle no constraint on the heavier H, A and $H^\pm$ bosons, which can be very heavy. In particular, contrary to the SM [158], there is no upper bound from perturbative unitarity since, at large masses, the heavier CP–even H boson will decouple from the W/Z bosons, $g_{HVV} \sim \cos(\beta - \alpha) \to 0$, and the pseudoscalar A and charged $H^\pm$

particles do not couple to gauge boson pairs; the CP–odd and charged Higgs boson couplings to respectively, hZ and hW, are also proportional to this factor and vanish in the decoupling limit. In addition, in contrast to the SM where the self–couplings are proportional to $M_{H_{\rm SM}}^2$, the trilinear and quartic Higgs couplings in the MSSM are all proportional to the gauge couplings and never become large; in fact, they all tend to either zero or ± 1 when expressed in units of M_Z^2/v, as seen in §1.3.3. Nevertheless, since these particles are the remnants of the electroweak symmetry breaking which occurs at the Fermi scale, they are expected to have masses not too far from this scale, i.e. $M_{H,A,H^\pm} \lesssim \mathcal{O}(1 \text{ TeV})$.

1.4.2 Constraints from direct Higgs searches

The neutral Higgs bosons

The search for the Higgs bosons was the main motivation for extending the LEP2 energy up to $\sqrt{s} \simeq 209$ GeV [159]. At these energies, there are two main processes for the production of the neutral Higgs bosons of the MSSM: the Higgs–strahlung process [158,160–162] already discussed in the SM Higgs case [see §I.4.2], and the associated production of CP–even and CP–odd Higgs bosons [163,164]; Fig. 1.14. In the case of the lighter h particle, denoting the SM Higgs cross section by $\sigma_{\rm SM}$, the production cross sections are given by

$$
\begin{aligned}
\sigma(e^+e^- \to hZ) &= g_{hZZ}^2\, \sigma_{\rm SM}(e^+e^- \to hZ) \\
\sigma(e^+e^- \to hA) &= g_{hAZ}^2\, \sigma_{\rm SM}(e^+e^- \to hZ) \times \frac{\lambda_{Ah}^3}{\lambda_{Zh}(\lambda_{Zh}^2 + 12M_Z^2/s)}
\end{aligned}
\tag{1.160}
$$

where $\lambda_{ij} = (1 - M_i^2/s - M_i^2/s)^2 - 4M_i^2M_j^2/s^2$ is the two–body phase space function; the additional factor for the last process accounts for the fact that two spin–zero particles are produced and the cross section should be proportional to λ_{ij}^3 as discussed in §I.4.2.2.
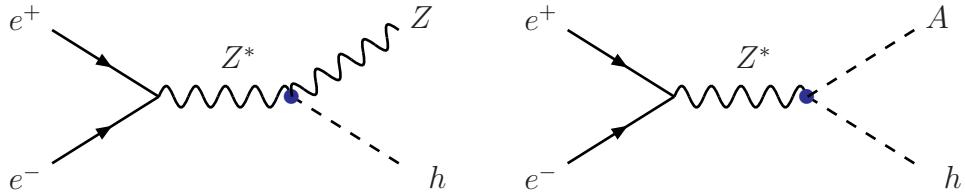
Figure 1.14: Diagrams for MSSM neutral Higgs production at LEP2 energies.

Since $g_{AhZ}^2 = \cos^2(\beta - \alpha)$ while $g_{hZZ}^2 = \sin^2(\beta - \alpha)$, the processes $e^+e^- \to hZ$ and $e^+e^- \to hA$ are complementary[11]. In the decoupling limit, $M_A \gg M_Z$, $\sigma(e^+e^- \to hA)$ vanishes since $g_{hAZ}^2 \sim 0$ while $\sigma(e^+e^- \to hZ)$ approaches the SM limit since $g_{hZZ}^2 \sim 1$. In

---

[11]As will be discussed in the next section, this remark can be extended to the heavier CP–even Higgs boson and the complementarity is doubled in this case: there is one between the processes $e^+e^- \to HZ$ and $e^+e^- \to HA$ as for the h boson, but there is also a complementarity between the production of the h and H bosons. The radiative corrections to these processes will also be discussed in §4.1.

turn, for low M_A values, $\sigma(e^+e^- \to hZ)$ is small but the cross section $\sigma(e^+e^- \to hA)$ becomes maximal. In fact, the sum of the cross sections of the two processes is approximately equal to that the production of a SM Higgs boson with a mass equal to M_h, almost independently of the value of M_A, except near the phase–space boundary. This is exemplified in Fig. 1.15, where the production cross sections are shown at a c.m. energy $\sqrt{s} = 209$ GeV as a function of M_h for the two values $\tan\beta = 3$ and 30 in the no mixing and maximal mixing scenarios [the other parameters are as in Fig. 1.7]. The H boson is too heavy to be produced in the process $e^+e^- \to HZ$, but for small M_A values the process $e^+e^- \to HA$ is possible.

The decays of the MSSM Higgs bosons will be discussed in the next section; we simply note at this stage that for large values of M_A the h boson will have SM–like decays, while for small M_A and $\tan\beta \gtrsim 5$ both h and A will mainly decay into $b\bar{b}$ and $\tau^+\tau^-$ final states with branching fractions of, respectively, $\sim 90\%$ and $\sim 10\%$.
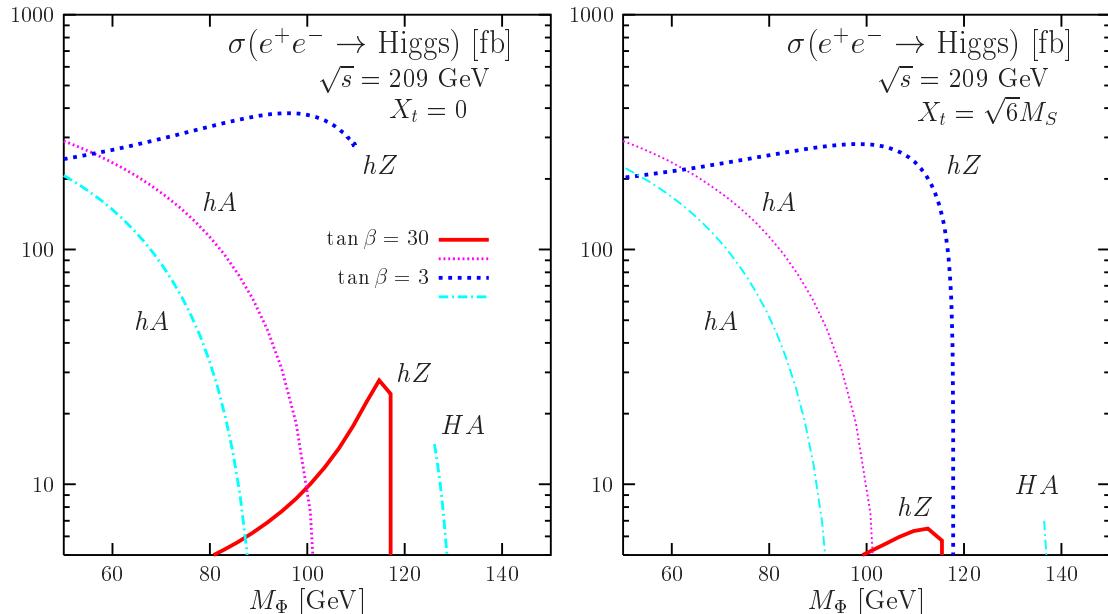
Figure 1.15: The production cross sections for the neutral MSSM Higgs bosons at LEP2 as a function of $M_{h,H}$ for $\tan\beta = 3$ and 30 in the no mixing (left) and maximal mixing (right) scenarios. The c.m. energy is fixed to $\sqrt{s} = 209$ GeV.

In the SM, a lower bound $M_{H_{\mathrm{SM}}} > 114.4$ GeV has been set at the 95% confidence level, by investigating the Higgs–strahlung process, $e^+e^- \to ZH_{\mathrm{SM}}$ [165]. In the MSSM, this bound is valid for the lighter CP–even Higgs particle h if its coupling to the Z boson is SM–like, i.e. if $g^2_{ZZh} \simeq 1$ [when we are almost in the decoupling regime] or in the less likely case of the heavier H particle if $g^2_{ZZH} \equiv \cos^2(\beta - \alpha) \simeq 1$ [i.e. in the anti–decoupling regime with a rather light M_A]. Almost the same bound can be obtained independently of the Higgs boson decay products, by looking at the recoil mass against the Z boson.

The complementary search of the neutral Higgs bosons in the associated production processes $e^+e^- \to hA$ and HA, allowed the LEP collaborations to set the following combined 95% CL limits on the h and A boson masses [166]

$$M_h > 91.0 \text{ GeV} \quad \text{and} \quad M_A > 91.9 \text{ GeV} \qquad (1.161)$$

These bounds[12] are obtained in the limit where the coupling of the Z boson to hA pairs is maximal, $g_{ZhA}^2 \equiv \cos^2(\beta - \alpha) \simeq 1$, i.e. in the anti–decoupling regime and for large values of $\tan\beta$. It is lower than the one from Higgs–strahlung, due to the less distinctive signal, $4b$, $2b + 2\tau$ or 4τ final states, and the λ^3 suppression for spin–zero particle pair production[13].

Deriving a precise bound on M_h for arbitrary values of M_A and $\tan\beta$ [i.e. not only in the decoupling and anti–decoupling limits] and hence, for all possible values of the angle α, is more complicated since one has to combine results from two different production channels. Nevertheless, exclusion plots for $\sin^2(\beta - \alpha)$ versus M_h from the Higgs–strahlung process [and which can be used to constrain the mass of the H boson if $\sin^2(\beta - \alpha)$ is replaced by $\cos^2(\beta - \alpha)$] and $\cos^2(\beta - \alpha)$ versus $M_A + M_h$ [with $M_h \sim M_A$] from the pair production processes, have been given by the LEP collaborations [165, 167] and are shown in Fig. 1.16.

These plots can be turned into exclusion regions in the MSSM parameter space. This is shown for the $\tan\beta$–M_h (left) and $\tan\beta$–M_A planes in Fig. 1.17 where the maximal mixing scenario is chosen with $M_S = 1$ TeV [rather than $M_S = 2$ TeV used in our discussion] and $m_t = 179.3$ GeV, which is close to the experimental value $m_t = 178$ GeV; $\tan\beta$ is also allowed to be less than unity. As can be seen, with these specific assumptions, a significant portion of the parameter space is excluded for the maximal mixing scenario; values $0.9 \lesssim \tan\beta \lesssim 1.5$ are ruled out at the 95% CL. The exclusion regions are of course much larger in the no–mixing scenario since $M_h^{\max}$ is smaller by approximately 20 GeV and not far the value that is experimentally excluded at LEP2 in the decoupling limit, $M_h \gtrsim 114.4$ GeV. As shown in the lower left panel, only a small portion of the M_h–$\tan\beta$ remains allowed in this case, resulting into a 95% CL exclusion of the range $0.4 \lesssim \tan\beta \lesssim 5.6$.

These constraints on $\tan\beta$ can be relaxed first by taking a larger value of the top quark mass and second, by maximizing further the radiative corrections [for instance by increasing

---

[12]These mass bounds depend slightly on the chosen scenario and, in particular, on the mixing in the stop sector. A recent analysis [167], performed with $m_t = 179.3$ GeV [which is closer to the current experimental value than the one, $m_t = 175$ GeV, used in the analysis [166] which led to the limits shown above] gives the lower bounds: $M_h > 92.9\,(93.3)$ GeV and $M_A > 93.4\,(93.3)$ GeV for the maximal (no) mixing scenario. In addition, Monte–Carlo simulations in the absence of a signal give expectations for the limits which are ~ 2 GeV higher than the previous mass values. Note also that besides the known ~ 1.5 excess of events at a mass of ~ 115 GeV compared to SM backgrounds, there is also a $\sim 2\sigma$ excess pointing toward a Higgs boson with a mass of ~ 100 GeV. Although the total significance is still small, this feature has triggered discussions about the fact that both h and H bosons might have been already observed at LEP2 [168].

[13]Note that the Yukawa processes $e^+e^- \to b\bar{b}/+h, A$ or $e^+e^- \to \tau\tau/+h, A$ [169] which can have significant rates at large $\tan\beta$ have been also searched for [170].
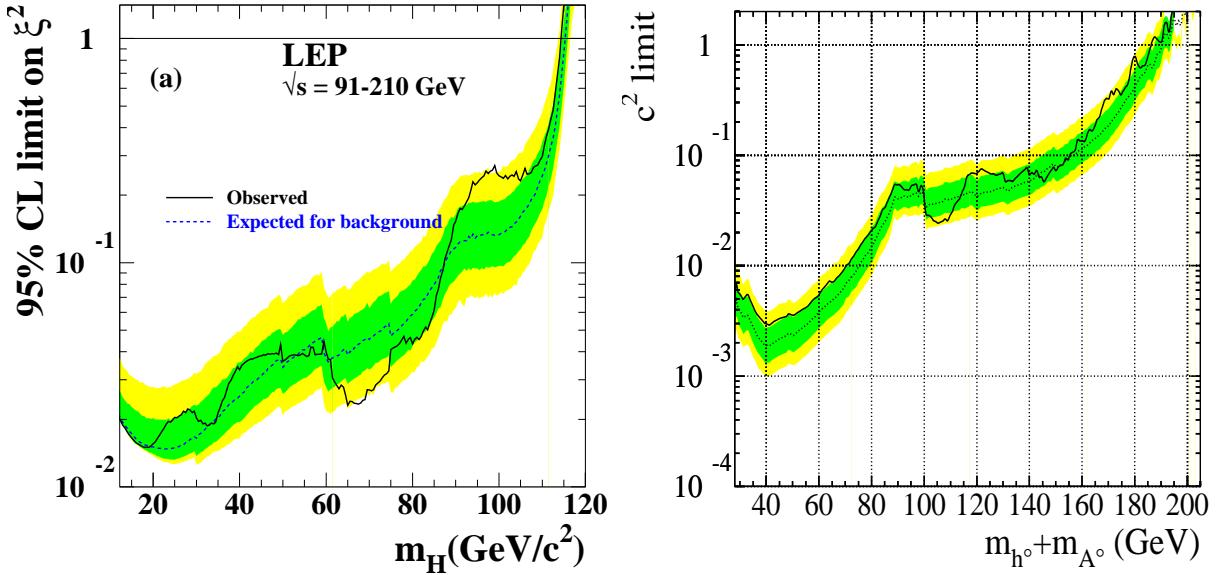
Figure 1.16: The 95% bounds on the factors $\sin^2(\beta - \alpha)$ (left) and $\cos^2(\beta - \alpha)$ (right) from searches at LEP2 in the Higgs–strahlung and associated hA production channels. The Higgs bosons are assumed to decay into $b\bar{b}$ and $\tau^+\tau^-$ as predicted in the MSSM. The lines represent the observed limit and the one expected for the background, while the dark (light) bands are for the 68% (95%) probability bands; from Ref. [167].

the SUSY scale to 2 TeV]; the constraints are even more relaxed when the expected theoretical error on the value of M_h is added. In fact, to obtain the absolute lower limit on the parameter $\tan\beta$, one needs to perform the same analysis as for the determination of the maximal M_h value discussed in the previous subsection. Fig. 1.13, which displays the variation of the upper bound on M_h in the pMSSM as a function of $\tan\beta$, and which has been obtained from a full scan of the MSSM parameter space, shows in fact these constraints. As can be seen from this figure, for the default value $m_t = 178$ GeV, the LEP2 bound of 114.4 GeV on M_h is always satisfied and therefore, no absolute bound on $\tan\beta$ [provided that it is larger than unity] can be derived in the pMSSM.

This is of course also the case for the larger top mass value $m_t = 182.3$ GeV and, *a fortiori*, for the conservative case in which a theoretical error is taken into account, where all values $1 \leq \tan\beta \leq 60$ are allowed by the LEP2 constraint. Only in the case of a lighter top quark, $M_t = 173.7$ GeV, the range $\tan\beta \lesssim 1.6$ is excluded by the requirement $M_h \geq 114.4$ GeV. However, if a theoretical error of 4 GeV on M_h is included [meaning, in practice, that the LEP2 Higgs mass bound translates to the bound $M_h \geq 110.4$ GeV on the prediction obtained without including the theoretical error], again, no bound on the parameter $\tan\beta$ can be obtained from the LEP2 constraint. [In constrained models, values $\tan\beta \lesssim 2$ might be excluded, since there is less freedom for the tuning of the parameters [121, 155–157].]

Note that searches for the neutral Higgs bosons have also been performed at the Tevatron
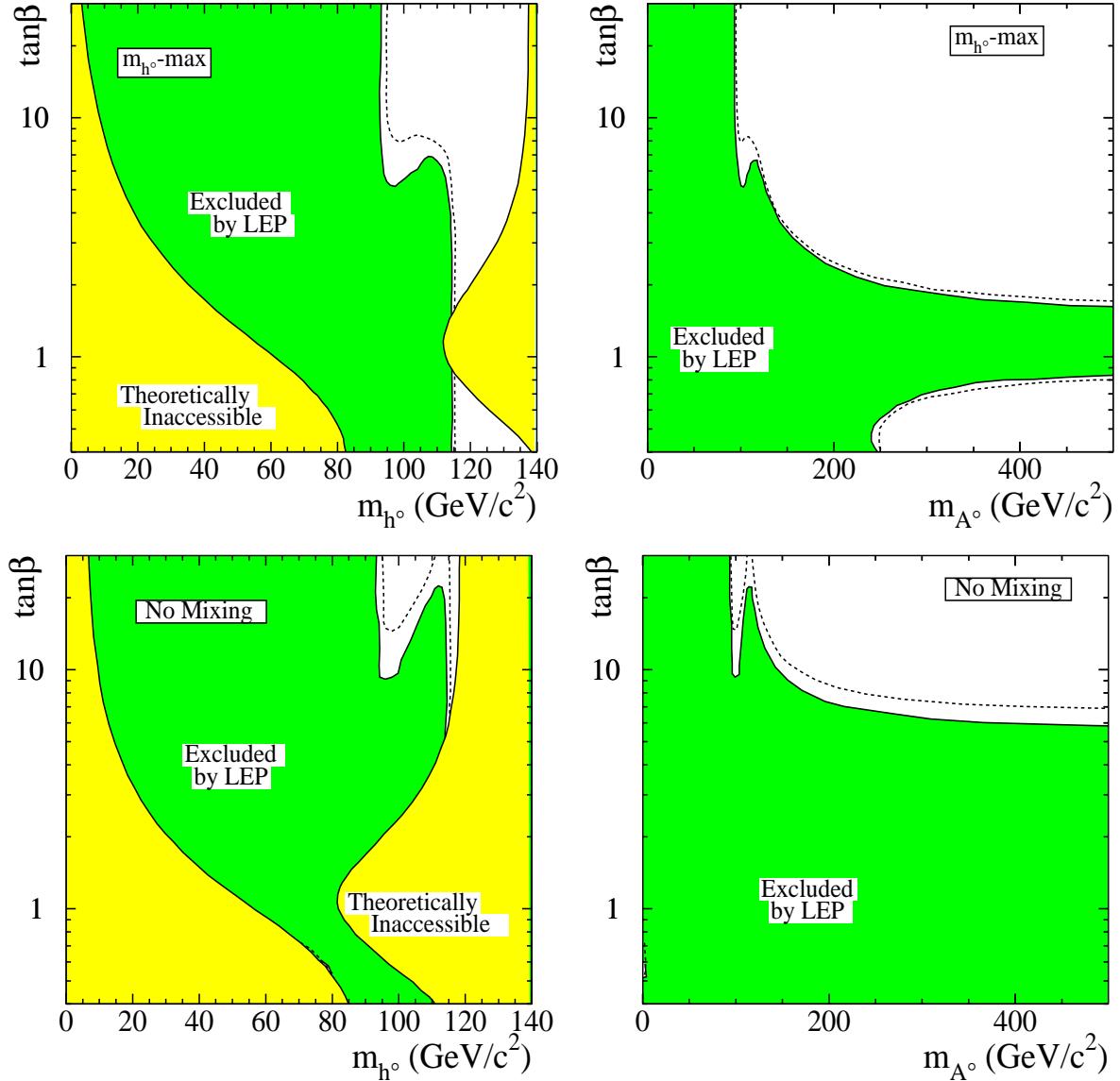
Figure 1.17: 95% CL contours in the $\tan\beta$–M_h *(left) and* $\tan\beta$–M_A *(right) planes excluded by the negative searches of MSSM neutral Higgs bosons at LEP2, from Ref. [167]. They are displayed in the maximal mixing (top figures) and no–mixing (lower figures) scenarios with* $M_S = 1$ *TeV and* $m_t = 179.3$ *GeV. The dashed lines indicate the boundaries that are excluded on the basis of Monte–Carlo simulations in the absence of a signal.*

[171, 172] but the obtained bounds are not yet competitive with those discussed above.

The charged Higgs boson

In e^+e^- collisions, the production of a pair of charged Higgs bosons [163, 173] proceeds through virtual photon and Z boson exchange; Fig. 1.18a. The cross section depends only

on the charged Higgs boson mass and on no other unknown parameter; it is given by

$$\sigma(e^+e^- \to H^+H^-) = \frac{\pi\alpha^2(s)}{3s}\left[1 + \frac{2a_e v_e v_H}{1 - M_Z^2/s} + \frac{(a_e^2 + v_e^2)v_H^2}{(1 - M_Z^2/s)^2}\right]\beta_{H^\pm}^3 \qquad (1.162)$$

with the standard Z charges $v_e = (-1 + 4s_W^2)/4c_W s_W$, $a_e = -1/4c_W s_W$ and $v_H = (-1 + 2s_W^2)/2c_W s_W$, and $\beta_{H^\pm} = (1 - 4M_{H^\pm}^2/s)^{1/2}$ being the velocity of the $H^\pm$ bosons. The QED coupling constant should be evaluated at the scale s, giving $\alpha \sim 1/128$. The cross section at a c.m. energy $\sqrt{s} = 209$ GeV is shown in the right–hand side of Fig. 1.19 as a function of $M_{H^\pm}$. It is rather large except near the kinematical threshold where it drops steeply as a consequence of the β^3 suppression factor for spin–zero particle production near threshold.
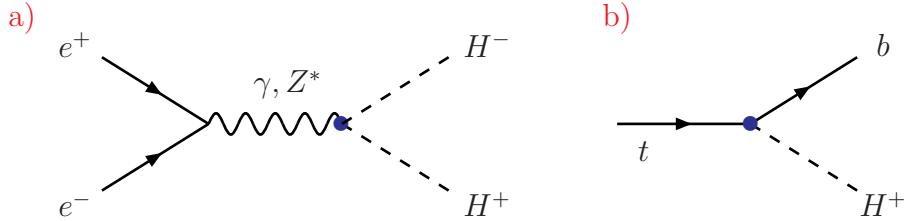
Figure 1.18: Diagrams for charged Higgs production at LEP2 and the Tevatron.

For $M_{H^\pm} \lesssim 130$ GeV, the $H^\pm$ bosons will decay mainly into $\tau\nu$ and cs final states as will be seen later. The former decay is dominant at large values of $\tan\beta$ since the couplings to τ–leptons are strongly enhanced. Searches for the charged Higgs boson in these two decay modes have been performed at LEP2 [174, 175]. An absolute bound of $M_{H^\pm} > 79.3$ GeV has been set by the ALEPH collaboration, independently of the relative magnitude of the $\tau\nu$ and cs branching ratios. If BR($H^\pm \to \tau\nu$) is close to unity, as is the case for $\tan\beta \gg 1$, the bound extends to $M_{H^\pm} > 87.8$ GeV, while for very low values of $\tan\beta$ when the decay $H^+ \to c\bar{s}$ is dominant, the bound becomes $M_{H^\pm} > 80.4$ GeV; see the right–hand side of Fig. 1.19. Slightly lower bounds have been obtained by the other LEP collaborations.

Note that in the MSSM, the charged Higgs boson mass is constrained to be $M_{H^\pm} = \sqrt{M_W^2 + M_A^2}$ [which can be relaxed by radiative corrections but only very slightly]. In view of the absolute lower bound on the mass of the pseudoscalar Higgs boson, $M_A \gtrsim 92$ GeV, this implies that $M_{H^\pm} \gtrsim 122$ GeV. Therefore, the previous bounds derived from LEP2 searches do not provide any additional constraint in the MSSM.

The charged Higgs particles have also been searched at the Tevatron [176, 177] in the decays of the heavy top quark; Fig. 1.18b. Indeed, if $M_{H^\pm} \lesssim m_t - m_b \sim 170$ GeV, the decay $t \to bH^+$ can occur [178, 179]. Compared to the dominant standard top–quark decay mode $t \to bW^+$, the branching ratio is given at leading order[14] by

$$\frac{\Gamma(t \to bH^+)}{\Gamma(t \to bW^+)} = \frac{(\bar{m}_t^2 + \bar{m}_b^2 - M_{H^\pm}^2)(\bar{m}_t^2\cot^2\beta + \bar{m}_b^2\tan^2\beta) + 4\bar{m}_t^2\bar{m}_b^2}{M_W^2(m_t^2 + m_b^2 - 2M_W^2) + (m_t^2 - m_b^2)^2}\frac{\lambda_{H^\pm,b;t}^{1/2}}{\lambda_{W,b;t}^{1/2}} \qquad (1.163)$$

---

[14]This process, including the radiative corrections, will be discussed in more detail in the next section.
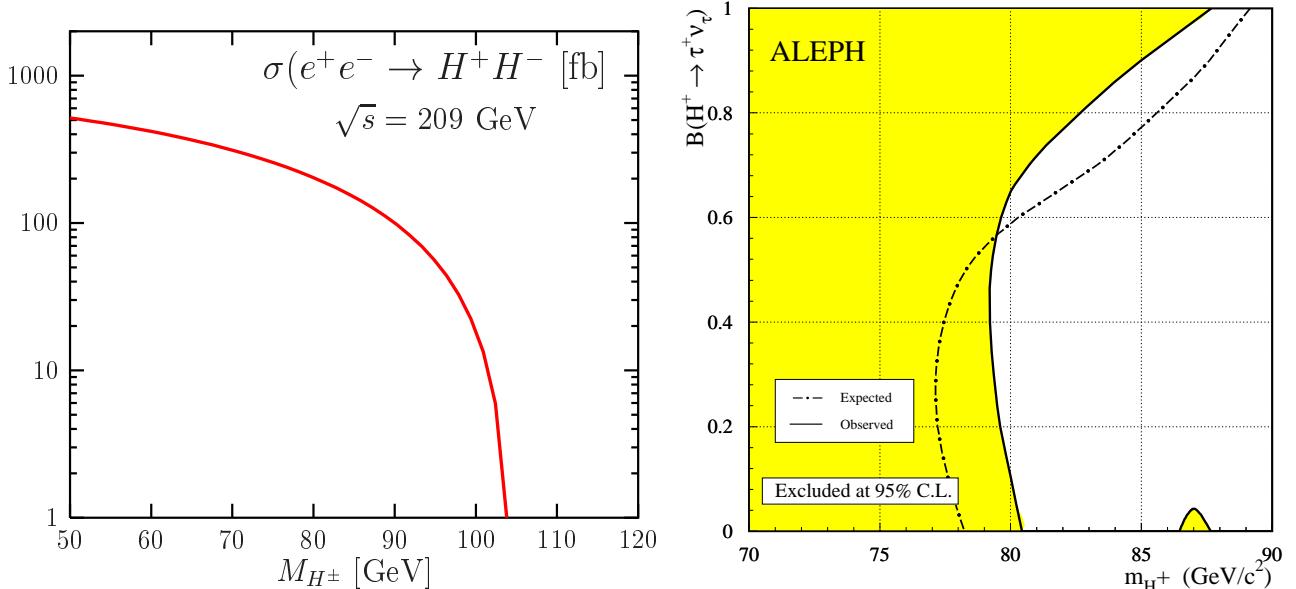
Figure 1.19: The cross section for the production of charged Higgs boson pairs at LEP2 at a c.m. energy of $\sqrt{s} = 209$ GeV (left) and the constraint on $M_{H^\pm}$ as a function of $BR(H^\pm \to \tau\nu)$ from the negative searches of the ALEPH collaboration at LEP2 [175] (right).

The branching ratio $BR(t \to bH^+)$ is shown in the left–hand side of Fig. 1.20 as a function of $\tan\beta$ for three values $M_{H^\pm} = 120, 140$ and 160 GeV. As can be seen, the branching ratio is large only for rather small, $\tan\beta \lesssim 3$, and large, $\tan\beta \gtrsim 30$, values when the $H^\pm tb$ coupling is strongly enhanced.

These decays have been searched for at the Tevatron by the CDF and DØ collaborations in two ways: (i) directly by looking for $H^+ \to \tau\nu$ decays using τ identification via its hadronic decays; this search is thus sensitive only in the large $\tan\beta$ region [177], and (ii) indirectly by looking for a suppression of the SM decay mode [176] . The second method turned out to be more powerful and the limits in the $\tan\beta$–$M_{H^\pm}$ plane obtained by the CDF and DØ collaborations are shown in the right–hand side of Fig. 1.20. As can be seen, it is only for $M_{H^\pm} \lesssim 140$ GeV and only for $\tan\beta$ values below unity and above 60 [i.e. outside the theoretically favored $\tan\beta$ range in the MSSM] that the constraints are obtained.

1.4.3 Indirect constraints from precision measurements

Indirect constraints on the parameters of the MSSM Higgs sector, in particular on M_A and $\tan\beta$, come from the high–precision data. Among these are the measurements of the ρ parameter, the decay $Z \to b\bar{b}$, the muon anomalous magnetic moment $(g_\mu - 2)$ and some measurements in the B system, such as the radiative decay $b \to s\gamma$. In discussing these individual constraints, we will not consider the contributions of the SUSY particles that we will assume to be rather heavy [the global fit including these contributions will be commented
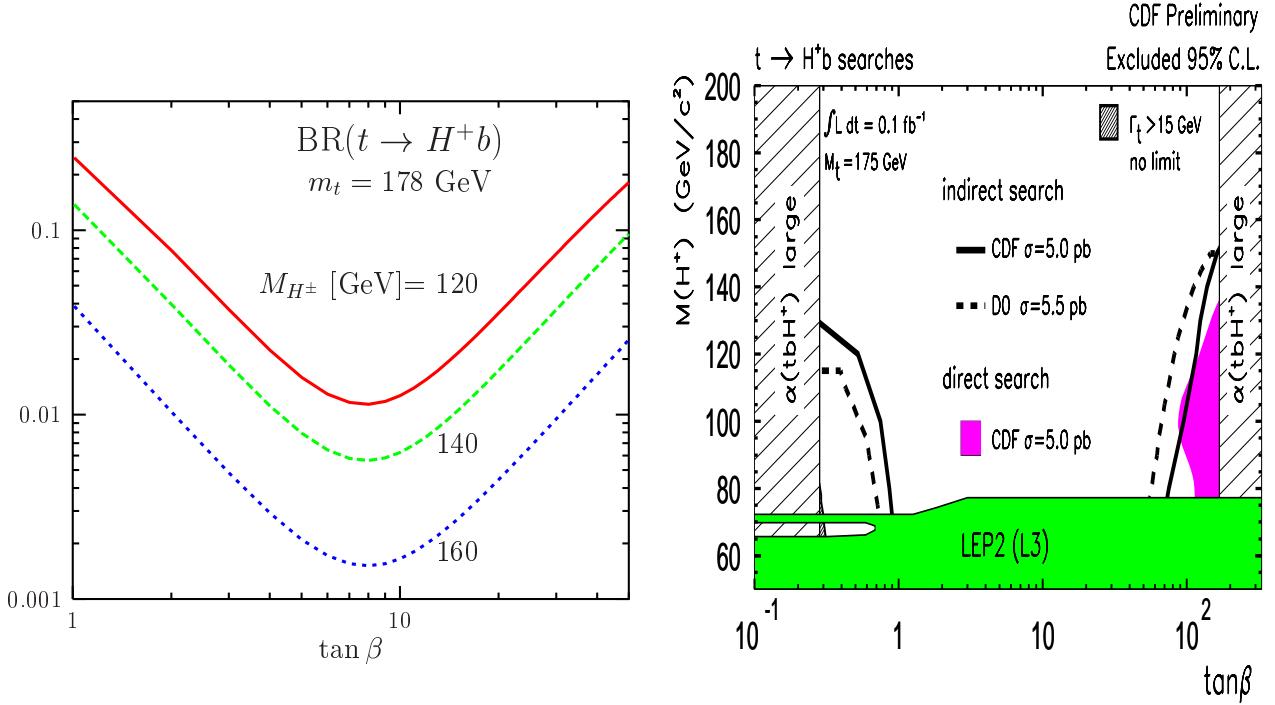
Figure 1.20: The branching ratio for the decay $t \to bH^+$ as a function of $\tan\beta$ for several values of $M_{H^\pm}$ and for $m_t = 178$ GeV (left) and the $\tan\beta$–$M_{H^\pm}$ parameter space excluded by the CDF and D0 collaborations from the non–observation of these decays [180] (right).

upon at the end]. It will be instructive to consider not only the decoupling limit, but also the anti–decoupling regime where $M_h \sim M_A$ for $\tan\beta \gg 1$.

The ρ parameter

As discussed in §I.1.2, precision measurements constrain the New Physics contributions to the electroweak observables to be rather small. In particular, the shift in the ρ parameter is required to be $\Delta\rho^{\mathrm{NP}} \lesssim 10^{-3}$ at the 1σ level [1,2]. The contribution of the MSSM Higgs bosons to the ρ parameter can be written as [81]

$$
\begin{aligned}
\Delta\rho^{\mathrm{Higgs}} &= -\frac{G_\mu M_W^2}{8\sqrt{2}\pi^2}\Big\{ 3\sin^2(\beta-\alpha) f_1\Big(\frac{M_h^2}{M_Z^2}\Big) + 3\cos^2(\beta-\alpha) f_1\Big(\frac{M_H^2}{M_Z^2}\Big) \\
&+ \sin^2(\beta-\alpha)\Big[f_2\Big(\frac{M_{H^\pm}^2}{M_W^2},\frac{M_H^2}{M_W^2}\Big) - f_2\Big(\frac{M_A^2}{M_W^2},\frac{M_H^2}{M_W^2}\Big)\Big] + f_2\Big(\frac{M_{H^\pm}^2}{M_W^2},\frac{M_A^2}{M_W^2}\Big) \\
&+ \cos^2(\beta-\alpha)\Big[f_2\Big(\frac{M_{H^\pm}^2}{M_W^2},\frac{M_h^2}{M_W^2}\Big) - f_2\Big(\frac{M_A^2}{M_W^2},\frac{M_h^2}{M_W^2}\Big)\Big]\Big\}
\end{aligned}
\tag{1.164}
$$

with the two functions f_1 and f_2 given by [81]

$$
f_1(x) = x\left[\frac{\log c_W^2 - \log x}{c_W^2 - x} + \frac{\log x}{c_W^2(1-x)}\right] \quad, \quad f_2(x_1,x_2) = \frac{x_1 x_2}{x_1 - x_2}\log\frac{x_2}{x_1} + \frac{1}{2}(x_1 + x_2) \tag{1.165}
$$

The contributions through the function f_1 are those where the CP–even Higgs bosons are exchanged together with W/Z bosons in the loops, while the contributions through the function f_2 account for those where two Higgs MSSM bosons are exchanged. In the latter case, one notices that $f_2(x,x) = 0$ so that only loops which involve particles which have a large mass splitting will contribute significantly.

In the decoupling limit, all the A, H and $H^\pm$ bosons are heavy and degenerate in mass, $M_H \sim M_{H^\pm} \sim M_A$, while the mass of the lighter Higgs boson reaches its maximal value, $M_h \sim M_h^{\max} \sim M_C$. In addition, one has $\cos^2(\beta - \alpha) \to 0$ and $\sin^2(\beta - \alpha) \to 1$. In this case, one obtains for the MSSM Higgs boson contributions to $\Delta\rho$

$$\Delta\rho_{\mathrm{SM}}^{\mathrm{Higgs}} = -3G_\mu M_W^2/(8\sqrt{2}\pi^2) f_1(M_C^2/M_Z^2) \tag{1.166}$$

which is simply the contribution of the SM Higgs boson with a mass $M_{H_{\mathrm{SM}}} = M_C$ that is very close to the Higgs mass, $M_{H_{\mathrm{SM}}} = \mathcal{O}(100 \text{ GeV})$, favored by the global fits to the electroweak precision data [2].

In the opposite limit, $M_A \sim M_Z$, the most important contribution is the one involving the H boson which has SM–like couplings and a mass $M_H \simeq M_C$. The additional contribution,

$$\Delta\rho_{\mathrm{non-SM}}^{\mathrm{Higgs}} = -G_\mu M_W^2/(4\sqrt{2}\pi^2) f_2(M_{H^\pm}^2/M_W^2, M_A^2/M_W^2) \tag{1.167}$$

is always extremely small since, in this case, the mass difference between the $H^\pm$ and A bosons is not large enough. For $M_A \sim 90$ GeV and $\tan\beta = 50$, one obtains $\Delta_{\mathrm{non-SM}}^{\mathrm{Higgs}} \sim -0.5 \cdot 10^{-4}$.

The Zbb vertex

An observable where the MSSM Higgs sector can in principle have sizable effects is the Z boson decay into $b\bar{b}$ final states. The neutral Higgs particles h, H, A as well as the charged $H^\pm$ bosons can be exchanged in the $Zb\bar{b}$ vertex [181, 182], and can alter the values of the partial decay width $\Gamma(Z \to b\bar{b})$ [or equivalently the ratio $R_b = \Gamma(Z \to b\bar{b})/\Gamma(Z \to \text{hadrons})$] and the forward–backward asymmetry A_{FB}^b. In the decoupling limit, the H, A and $H^\pm$ bosons are too heavy and only the h boson will contribute to the vertex and, as as discussed in §I.1.3 for the SM case, this contribution is rather small as a result of the tiny $hb\bar{b}$ Yukawa coupling. However, in the opposite (anti–decoupling) limit $M_A \sim M_Z$ and for large values of $\tan\beta$, for which the Higgs boson couplings to b quarks are strongly enhanced, the contributions could in principle be much larger.

The analytical expressions of the MSSM neutral (N) and charged (C) Higgs boson contributions to the left– and right–handed Z couplings to bottom quarks, $g_{L/R}^f = I_f^{3L,3R} - e_f s_W^2$

$$\delta g_{R/L}^b = \delta g_{R/L}^b|_N + \delta g_{R/L}^b|_C \tag{1.168}$$

77

are rather involved. These expressions simplify in the limit where the Higgs masses are much larger than the momentum transfer $Q = M_Z$. This is certainly a good approximation in the case of the H, A and $H^\pm$ bosons on the way to the decoupling limit, but it can also be extended to the case of the h and A bosons for masses close to the maximal value $M_h^{\max} = 130$–140 GeV. Setting $Q^2 \sim 0$, one obtains for the contributions of the MSSM Higgs sector to the $Zb\bar{b}$ couplings at large $\tan\beta$ values [182]

$$
\begin{aligned}
\delta g_{L/R}^b|_N &= \mp \Big(\frac{g_2 m_b \tan\beta}{8\pi\sqrt{2}M_W} \Big)^2 \Big[\sin^2\alpha f_1 \Big(\frac{M_h^2}{M_A^2} \Big) + \cos^2\alpha f_1 \Big(\frac{M_H^2}{M_A^2} \Big) \Big] \\
\delta g_R^b|_C &= + \Big(\frac{g_2 m_b \tan\beta}{8\pi\sqrt{2}M_W} \Big)^2 f_2 \Big(\frac{m_t^2}{M_{H^\pm}^2} \Big) \ , \quad \delta g_L^b|_C = 0
\end{aligned}
\tag{1.169}
$$

where the two functions f_1 and f_2 are given by

$$
f_1(x) = 1 + \frac{1}{2}\frac{1+x}{1-x}\log x \ , \quad f_2(x) = \frac{x}{1-x}\Big(1 + \frac{1}{1-x}\log x \Big)
\tag{1.170}
$$

[For small $\tan\beta$ values, only a not too heavy charged Higgs boson could have sizable effects in the vertex and its contribution can be obtained by simply replacing in the expression of δg_R^b above $m_b \tan\beta$ by $m_t \cot\beta$.]

In view of the experimental values $R_b = 0.21653 \pm 0.00069$ and $A_{FB}^b = 0.099 \pm 0.002$, the virtual effects of the MSSM Higgs bosons should be, in relative size, of the order of 0.3% in R_b and 2% in A_{FB}^b to be detectable. This is far from being the case: even for $\tan\beta \sim 50$ and $M_A \sim 90$ GeV [where the full analytical expressions, that is for $Q^2 = M_Z^2$, have been used], the contributions are respectively, $\Delta R_b/R_b \sim -10^{-4}$ and $\Delta A_{FB}^b/A_{FB}^b \sim 2.5 \cdot 10^{-3}$. The discrepancy between the SM and experimental values of A_{FB}^b can thus not be attributed to the MSSM Higgs sector[15].

g–2 of the muon

The precise measurement of the anomalous magnetic moment of the muon performed in the recent years at BNL [184]

$$
a_\mu \equiv g_\mu - 2 = 11659202(20) \cdot 10^{-10}
\tag{1.171}
$$

is roughly in accord with the SM prediction [185] and provides very stringent tests of models of New Physics. In the MSSM, the Higgs sector will contribute to a_μ through loops involving the exchange of the neutral Higgs bosons h, H and A with muons and the exchange of charged

---

[15]Note that this discrepancy cannot be explained also by the chargino–stop loop contributions to the $Zb\bar{b}$ vertex in the MSSM. These contributions can be much larger than the ones due to the Higgs sector for small enough sparticle masses [183] but, once the experimental limits on the $\chi_1^\pm$ and $\tilde{t}_1$ masses eq. (1.54) are imposed, they are too small. A large SUSY contribution to A_{FB}^b would have affected anyway R_b in an unacceptable way.

Higgs bosons $H^\pm$ with neutrinos. The contributions are sizable only for large values of $\tan\beta$ for which the $\Phi\mu^+\mu^-$ and $H^+\mu\nu_\mu$ couplings are enhanced; for an analysis, see Ref. [186].

Taking into account only the leading, $\propto \tan^2\beta$, contributions [i.e. neglecting the contribution of the SM–like CP–even Higgs boson Φ_H] and working in the limit $M_A \sim M_h \sim M_Z$ and large values of $\tan\beta$, one obtains for the MSSM Higgs sector contribution to a_μ

$$a_\mu^{\text{Higgs}} \simeq \frac{G_\mu m_\mu^2}{24\pi^2\sqrt{2}}\tan^2\beta\left[4\frac{m_\mu^2}{M_A^2} - \frac{m_\mu^2}{M_{H^\pm}^2}\right] \tag{1.172}$$

This generates a contribution $\Delta a_\mu^{\text{Higgs}} \sim 5 \cdot 10^{-12}$ for $\tan\beta \sim 50$ and $M_A \sim 90$ GeV, i.e. far too small to lead to any new constraint on the Higgs sector.

The decay $b \to s\gamma$

In the radiative and flavor changing $b \to s\gamma$ transition, in addition to the main SM contribution built–up by W boson and top quark loops, the virtual exchange of charged Higgs bosons and top quarks can significantly contribute in the MSSM, together with SUSY particle loops [187]. Since SM and MSSM Higgs contributions appear at the same order of perturbation theory, the measurement of the inclusive branching ratio of the $B \to X_s\gamma$ decay is a very powerful tool for constraining the charged Higgs boson mass [188, 189].

The recent measurement by the Belle collaboration of the branching ratio with a cut–off $E_\gamma > 1.8$ GeV on the photon energy as measured in the B–meson rest frame [189]

$$\text{BR}(b \to s\gamma)|_{\text{exp}} = (3.38 \pm 0.30 \pm 0.29) \cdot 10^{-4} \tag{1.173}$$

is in a good agreement with a recent renormalization group improved calculation of the branching fraction in the SM $\text{BR}(b \to s\gamma)|_{\text{SM}} = (3.44 \pm 0.53 \pm 0.35) \cdot 10^{-4}$ [190], where the first and second errors are an estimate of, respectively, the theoretical and parametric uncertainties. The difference between the two values, $\text{BR}_{\text{exp}} - \text{BR}_{\text{SM}} \lesssim 1.4 \cdot 10^{-4}$ at 95% CL, can be used to constrain the size of non–standard contributions. If only the one due to an MSSM $H^\pm$ boson is taken into account, one arrives when including the dominant QCD radiative corrections to the decay rate, at the constraint $M_{H^\pm} \gtrsim 200$ GeV [190].

However, it is well known that in the MSSM, additional contributions can be very important. In particular, the chargino–stop loop contributions are sizable and can have both signs; they can thus interfere destructively with the $H^\pm$ loop contribution and the previous bound on $M_{H^\pm}$ can be evaded. This cancellation phenomenon actually occurs in many observables in the B–system as well as in K–physics and, in general, one cannot consider only the Higgs sector of the MSSM but also the SUSY sector. For an account of the various constraints on the MSSM from heavy flavor physics[16], see Ref. [192].

[16]Note that near future searches, in particular at the Tevatron Run II, will start to be sensitive to the decay $B_s \to \mu^+\mu^-$ which has a rate that is enhanced $\propto \tan^6\beta$ at large $\tan\beta$ values [191].

The sparticle contributions and a summary of the constraints

Finally, let us make a brief comment on the contributions of the SUSY particles to the high precision data and summarize this discussion. A global fit to all electroweak data has been performed within the full MSSM in Ref. [193]. The results are shown in Fig. 1.21 where the predictions in the SM and in the MSSM for both the unconstrained and constrained [the mSUGRA model denoted by CMSSM] cases with $\tan\beta = 35$ are compared with the experimental data. As can be seen, there is no significant deviation in addition to those in the SM. In fact, the MSSM predictions for M_W and $g_\mu - 2$ are in better agreement with the data than in the SM; slight improvements also occur for the total width Γ_Z and for the decay $b \to s\gamma$. In turn, for A_{FB}^b, the MSSM does not improve on the $\sim 3\sigma$ deviation of the measurement. For $m_t = 175$ GeV, the global fit in the MSSM has a lower χ^2 value than in the SM and the overall fit probability is slightly better in the MSSM than in the SM.
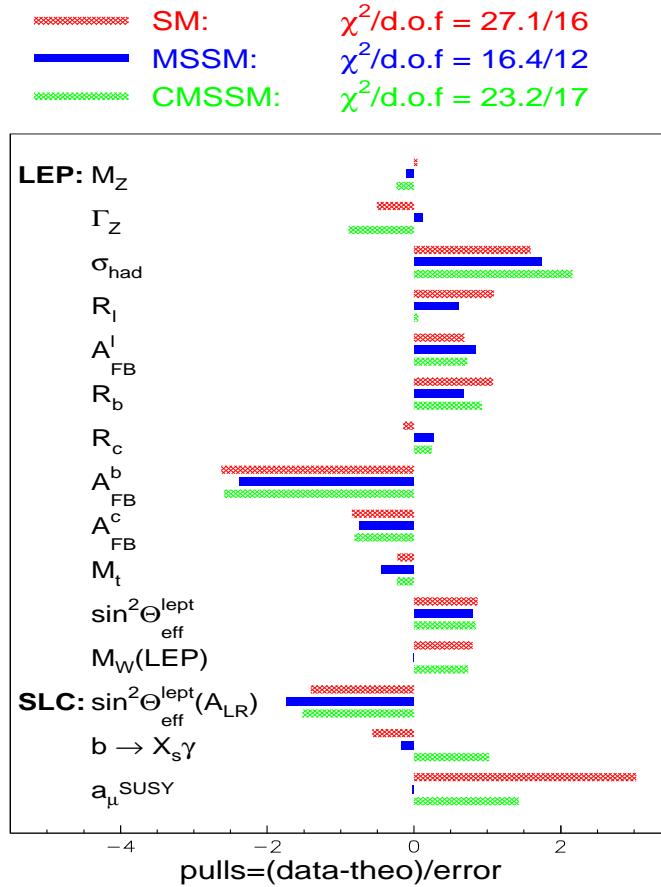
Figure 1.21: *The predictions in the SM, the MSSM and the mSUGRA scenario (CMSSM) are compared with the high precision data. Deviations between theory and experiment are indicated in units of one standard deviation of the experimental results; from Ref. [193].*

2 Higgs decays and other phenomenological aspects

Contrary to the SM case, where they are fully determined once the Higgs boson mass is fixed, the decay rates [and the production cross sections] of the MSSM Higgs bosons depend to a large extent on their couplings to fermions and gauge bosons as well as their self–couplings. The most important couplings in this context have been summarized in Table 1.5, when normalized to those of the SM Higgs boson, and the masses of the fermions and gauge bosons which enter these mechanisms have been collected in the Appendix.

The most important decay modes of the neutral MSSM Higgs bosons are in general simply those of the SM Higgs particle which have been discussed in detail in the first part of this review; §I.2. As already seen, in the decoupling limit, the MSSM Higgs sector effectively reduces to the SM Higgs sector and all the features discussed for a light SM Higgs boson, with a mass in the range $\sim$ 100–150 GeV, will hold for the lighter CP–even Higgs particle. However, for the other Higgs bosons and even for the h boson outside the decoupling regime, there can be major differences compared to the SM case. For instance, the presence of additional Higgs particles will induce new decay modes, which especially occur in the intermediate–coupling regime. Another major difference occurs for large $\tan\beta$ values when the Higgs boson couplings to down–type fermions are strongly enhanced; the bottom quark and the τ lepton will then play a much more important role than in the SM Higgs sector. Most of the analytical material needed to describe these channels has been given in part I, since we have also discussed sometimes the case of a CP–odd Higgs boson that we have confronted with the SM Higgs case. In this section, we thus present only the additional material specific to the MSSM, but in some cases and when important, the discussions held earlier will be summarized for completeness. The situation is of course different in the case of the charged Higgs particle, which is the most distinctive signature of the extension of the Higgs sector. The decay modes, although formally similar to those of the neutral Higgs particles, are in general slightly more complicated since for the two–body modes for instance, they involve two different particles in the final state. New analytical material will therefore be needed for these processes and will be given whenever appropriate.

Another major difference between the SM and MSSM cases is the presence of the additional SUSY particle spectrum. Of course, one can decouple this spectrum from the Higgs sector by assuming that all SUSY particles are very heavy, and this is what we will do in a first step. However, in view of the lower bounds on the various SUSY particles from the negative searches performed at LEP2 and the Tevatron, eq. (1.53), at least the lighter charginos and neutralinos, and possibly sleptons and third generation squarks, can be light enough to affect the decays of the MSSM Higgs bosons. We will thus summarize the main effects of such relatively light particles either directly, when they appear as final states in the decay processes, or indirectly, when they alter the standard decays through loop contributions.

If the SUSY particles are heavy, but still within the kinematical reach of future colliders, one could have a new source for MSSM Higgs bosons: the production from the decays of these particles. The branching rates for decays of heavier charginos and neutralinos into lighter ones and Higgs bosons can be substantial, and decays of heavier third generation squarks into lighter ones plus Higgs bosons can also be important in some cases. In addition, the charged Higgs particle, if light enough, can be produced in decays of the heavy top quark, the latter being produced either directly in $pp/p\bar{p}$ or e^+e^- collisions, or from the cascade decays of strongly interacting SUSY particles. We find it more convenient not to postpone the discussion of these decays to the next two chapters where MSSM Higgs production will be discussed, since these decay processes do not depend on the considered collider.

In the following, we first summarize the main qualitative differences between the SM and MSSM Higgs boson decay processes, paying a special attention to the case of the charged Higgs boson and to the effect of the extended Higgs sector and the SUSY particle spectrum. We give some numerical illustrations of the magnitude of the rates in the different regimes discussed earlier[17] as well as in the SUSY regime. We then analyze MSSM Higgs production from SUSY particle decays. In the last section, we briefly address a subject that is more related to cosmology than to collider physics: the important role played by the MSSM Higgs sector in the determination of the relic density and detection rates of the SUSY particle candidate for the Dark Matter in the universe, the LSP neutralino.

For the radiative corrections to the specific processes, we briefly discuss the QCD ones and summarize the main effects of the electroweak corrections when important, without going into too many details [most of the material which is needed was already given in part I of this review]. The important corrections specific to the MSSM Higgs sector have been presented in the previous chapter. In the numerical analyses where a choice for the various SUSY parameters is needed, we adopt in most cases the benchmark scenario given in the Appendix, where the mixing in the stop sector is maximal with $M_S = 2$ TeV and which is close to the one already used in the analysis of the Higgs masses and couplings, Figs. 1.7–1.11. The basic inputs will be M_A, to be varied from its experimental lower bound to the decoupling limit of 1 TeV, and $\tan\beta$ which will be in general fixed to a low and large value, $\tan\beta = 3$ and 30. However, in some specific cases, for instance when we discuss the effects of SUSY particles, we will adopt different scenarios which will be then indicated, and in which we will try to comply with the bounds on the SUSY particle and MSSM Higgs boson masses discussed, respectively, in §1.1.7 and §1.4. Finally, most of the numerical illustrations given in this section will be made with the code HDECAY [129]; in particular and unless otherwise stated, the updated figures presented in this chapter will be based on this program.

---

[17]In some cases, we will discuss processes that are now obsolete, such as the $H \rightarrow AA$ two–body decays, or regions of the parameter space, such as $M_A < M_Z$, which are ruled out by the LEP2 searches. However, since these situations might occur in extensions of the MSSM, they will be worth mentioning.

2.1 MSSM Higgs decays into SM and Higgs particles

2.1.1 Higgs decays into fermions

Neutral Higgs decays

The partial decay width of a neutral Higgs boson $\Phi = h, H, A$ into fermion pairs is given in the Born approximation, Fig. 2.1a, by [38, 194]

$$\Gamma(\Phi \to f\bar{f}) \;=\; N_c \frac{G_\mu m_f^2}{4\sqrt{2}\pi} g_{\Phi ff}^2 M_\Phi \beta_f^p \tag{2.1}$$

where $\beta_f = (1 - 4m_f^2/M_\Phi^2)^{1/2}$ and $p = 3\,(1)$ for the CP–even (odd) Higgs boson; the Higgs couplings $g_{\Phi ff}$ normalized to the SM Higgs couplings are listed in Table 1.5.

a) h, H, A — f — $\bar{f}$ **b)** H/A — t, $\bar{t}$, W^-, $\bar{b}$
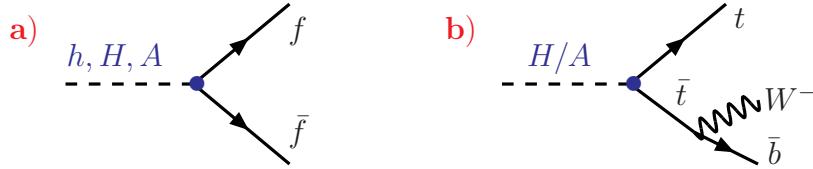
Figure 2.1: Feynman diagrams for 2 and 3–body decays of neutral Higgs bosons into fermions.

For final state quarks, one has to include the important QCD corrections [195–198] and for the light quarks, the running masses defined at the scale of the Higgs masses [which have been discussed in §I.1.1.4] have to be adopted to absorb the bulk of these corrections. If the $\overline{\text{DR}}$ scheme is to be used, the running quark masses have to be expressed in terms of the usual $\overline{\text{MS}}$ masses as in eq. (1.41). For bottom and charm quarks and for $M_\Phi \sim 100$–1000 GeV [the running between the two scales is mild], this results in a decrease of the partial decay widths by roughly a factor of two and four, respectively, as in the SM Higgs case.

The additional direct QCD corrections to the light quark Higgs decays are given by

$$\Gamma(\Phi \to q\bar{q}) \;=\; \frac{3G_\mu}{4\sqrt{2}\pi} g_{\Phi qq}^2 M_\Phi \overline{m}_q^2(M_\Phi^2) \left[1 + \Delta_{qq} + \Delta_\Phi^2\right] \tag{2.2}$$

where, as usual, the strong coupling constant $\bar{\alpha}_s \equiv \alpha_s(M_\Phi^2)$ as well as the running masses $\overline{m}_q(M_\Phi^2)$, are defined at the scale M_Φ. In the chiral limit $M_\Phi \gg m_q$, the coefficient Δ_{qq} is the same for CP–odd and CP–even particles and has been discussed in §I.2.1,

$$\Delta_{qq} = 5.67\bar{\alpha}_s/\pi + (35.94 - 1.36N_f)\bar{\alpha}_s^2/\pi^2 \cdots \tag{2.3}$$

The additional corrections Δ_Φ^2 of $\mathcal{O}(\alpha_s^2)$ involve logarithms of the light quark and top quark masses and thus break chiral symmetry. In the case of the CP–even $\mathcal{H} = h, H$ and CP–odd A bosons, they read at $\mathcal{O}(\alpha_s^2)$ [65, 66]

$$\Delta_\mathcal{H}^2 \;=\; \frac{\bar{\alpha}_s^2}{\pi^2} \left(1.57 - \frac{2}{3}\log\frac{M_\mathcal{H}^2}{m_t^2} + \frac{1}{9}\log^2\frac{\overline{m}_q^2}{M_\mathcal{H}^2}\right)$$

$$\Delta_A^2 \;=\; \frac{\bar{\alpha}_s^2}{\pi^2} \left(3.83 - \log\frac{M_A^2}{m_t^2} + \frac{1}{6}\log^2\frac{\overline{m}_q^2}{M_A^2}\right) \tag{2.4}$$

There are also radiative corrections that are due to SUSY particles. Those affecting the third generation fermion masses, which can be very important in particular in the case of the bottom quark at high values of $\tan\beta$, can be directly implemented in the Yukawa couplings together with the radiative corrections from the MSSM Higgs sector, as discussed in §1.3. The additional electroweak and QCD radiative corrections to the partial decay widths $\Gamma(\Phi \to f\bar{f})$, which originate from the direct contribution of SUSY particle loops to the decay vertices, have been calculated in Refs. [109, 150, 199–201] and reviewed very recently in Ref. [105]; they are rather small and they will be neglected in our analysis. The only exception will be the gluino effects that we will discuss in the next section.

For the decays of the heavier neutral $\Phi = H$ and A bosons into top quark pairs, the one loop standard QCD corrections may be written as

$$\Gamma(\Phi \to t\bar{t}) = \frac{3G_\mu}{4\sqrt{2}\pi}\, g_{\Phi tt}^2\, M_\Phi\, m_t^2\, \beta_t^p \left[1 + \frac{4}{3}\frac{\alpha_s}{\pi}\Delta_\Phi^t(\beta_t)\right] \tag{2.5}$$

where the correction factors $\Delta_\Phi^t(\beta_t)$, which are different in the CP–even and CP–odd cases [196, 197] as $m_t \neq 0$, are given by

$$
\begin{aligned}
\Delta_{\mathcal{H}}^t(\beta) &= \frac{1}{\beta}A(\beta) + \frac{1}{16\beta^3}(3 + 34\beta^2 - 13\beta^4)\log\frac{1+\beta}{1-\beta} + \frac{3}{8\beta^2}(7\beta^2 - 1) \\
\Delta_A^t(\beta) &= \frac{1}{\beta}A(\beta) + \frac{1}{16\beta}(19 + 2\beta^2 + 3\beta^4)\log\frac{1+\beta}{1-\beta} + \frac{3}{8}(7 - \beta^2)
\end{aligned} \tag{2.6}
$$

where, using the abbreviation $x_\beta = (1 - \beta)/(1 + \beta)$, the function $A(\beta)$ is given by

$$A(\beta) = (1 + \beta^2)\left[4\mathrm{Li}_2(x_\beta) + 2\mathrm{Li}_2\left(-x_\beta\right) + 3\log x_\beta \log\frac{2}{1+\beta} + 2\log x_\beta \log\beta\right] - 3\beta\log\frac{4\beta^{4/3}}{1-\beta^2} \tag{2.7}$$

The two–loop QCD corrections have been evaluated in Ref. [202] in both the CP–even and CP–odd cases, but the electroweak corrections have not been studied in detail. Additional SUSY contributions are also present, but the dominant ones are those which affect the quark mass discussed earlier and which, again, can be mapped into the Yukawa couplings.

Finally, for masses slightly below the $t\bar{t}$ threshold, the heavier CP–even and the CP–odd Higgs bosons can decay into one on–shell and one off–shell top quarks, $H/A \to tt^* \to tbW$ [203–205]. Although there are additional contributions compared to the SM case, the amplitude is dominated by the contribution of Fig. 2.1b where the virtual top quark is nearly on–shell. In this case, the Dalitz density for both $\Phi = H, A$ decays can be written as

$$\frac{\mathrm{d}\Gamma}{\mathrm{d}x_1\mathrm{d}x_2}(\Phi \to t\bar{t}^* \to t\bar{b}W^-) = \frac{3G_\mu^2}{32\pi^3}\, g_{\Phi tt}^2\, M_\Phi^3\, m_t^2\, \frac{\Gamma_\Phi^t}{y_1^2 + \gamma_t\kappa_t} \tag{2.8}$$
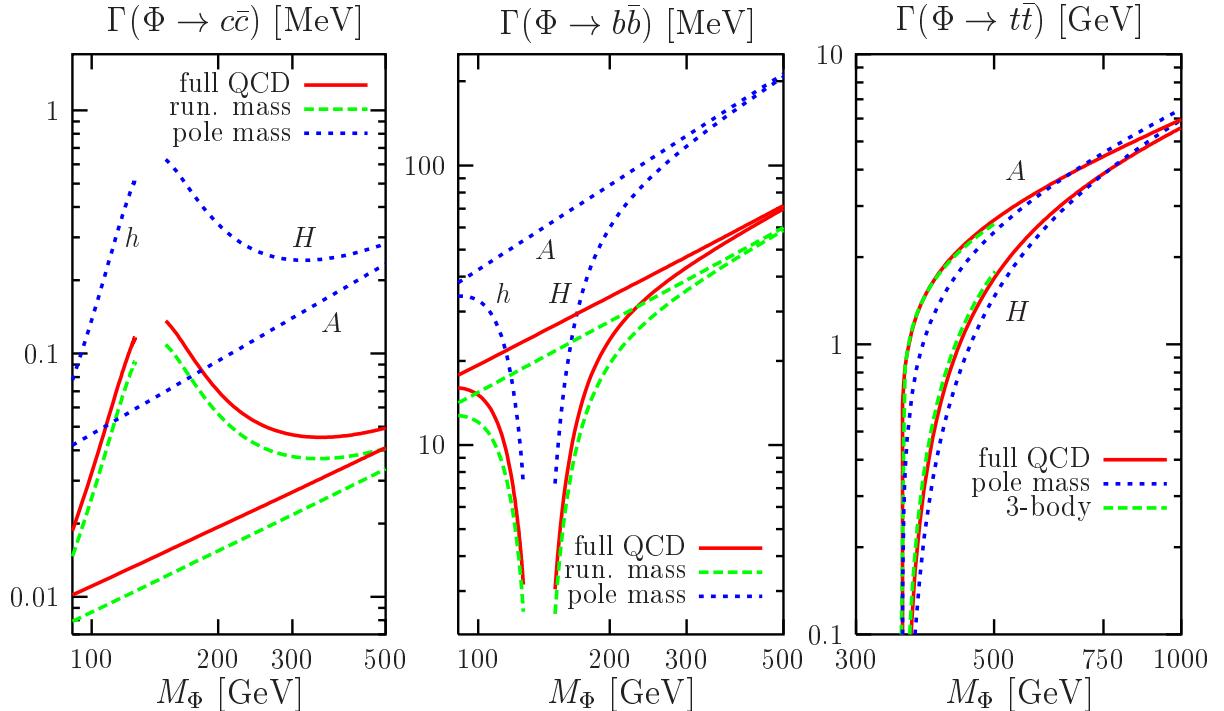
with the reduced energies $x_{1,2} = 2E_{t,b}/M_\Phi$, the scaling variables $y_{1,2} = 1 - x_{1,2}$, $\kappa_i = M_i^2/M_\Phi^2$ and the reduced decay width of the virtual top quark $\gamma_t = \Gamma_t^2/M_\Phi^2$. The squared amplitudes,

which are again different for H/A decays, read in the scalar and pseudoscalar Higgs cases [203]

$$
\begin{aligned}
\Gamma_A^t &= y_1^2(1 - y_1 - y_2 + \kappa_W - \kappa_t) + 2\kappa_W(y_1y_2 - \kappa_W) - \kappa_t(y_1y_2 - 2y_1 - \kappa_W - \kappa_t) \\
\Gamma_{\mathcal{H}}^t &= y_1^2(1 - y_1 - y_2 + \kappa_W - 5\kappa_t) + 2\kappa_W(y_1y_2 - \kappa_W - 2\kappa_t y_1 + 4\kappa_t\kappa_W) \\
&\quad - \kappa_t y_1 y_2 + \kappa_t(1 - 4\kappa_t)(2y_1 + \kappa_W + \kappa_t)
\end{aligned}
\tag{2.9}
$$

For both the H and A bosons, the below–threshold branching ratios are significant only for relatively small $\tan\beta$ values and very close to the $t\bar{t}$ threshold.

The preceding discussion on the neutral MSSM Higgs decays into c, b and t quarks is summarized in Fig. 2.2 where the partial decay widths for the three decays are shown as a function of the Higgs masses. The value of $\tan\beta$ is fixed to $\tan\beta = 3$ for all decays. The partial widths are shown in the Born approximation with the pole quark masses, in the approximation where the running quark masses at the scale of the Higgs masses are used instead, and in the case where the full set of standard QCD corrections has been taken into account [in all cases, and in particular for b quarks where they can be important, the SUSY–QCD corrections are ignored at this stage]. For H/A decays into $t\bar{t}$ final states, the effect of allowing one of the top quarks to be off–shell is also displayed.

Figure 2.2: *The partial widths of the neutral MSSM Higgs bosons into $c\bar{c}, b\bar{b}$ and $t\bar{t}$ as a function of their masses for $\tan\beta = 3$ in the various approximations described in the text. The pole quark masses have been chosen to be $m_c = 1.64$ GeV, $m_b = 4.88$ GeV and $m_t = 178$ GeV and the QCD coupling constant is normalized to $\alpha_s(M_Z) = 0.1172$.*

Charged Higgs decays

The charged Higgs bosons decay into charged lepton and neutrino pairs, Fig. 2.3a, with a partial width [178]

$$\Gamma(H^+ \to \ell^+ \nu_\ell) = \frac{G_\mu M_{H^\pm}}{4\sqrt{2}\pi} m_\ell^2 \tan^2\beta \left(1 - \frac{m_\ell^2}{M_{H^\pm}^2}\right)^3 \tag{2.10}$$
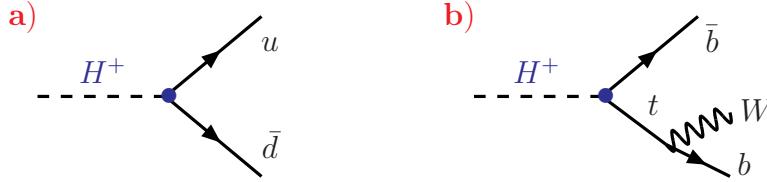
Figure 2.3: Two–and three–body decays of the charged Higgs boson into fermions.

In the case of charged Higgs particle decays into quarks, $H^+ \to u\bar{d}$ with the notation of the first generation quarks, retaining the masses of both the up–type and down–type quarks and including the full one–loop standard QCD corrections [197, 206], one obtains for the partial width [197]

$$
\begin{aligned}
\Gamma(H^+ \to u\bar{d}) &= \frac{3G_\mu M_{H^\pm}}{4\sqrt{2}\pi} |V_{ud}|^2 \lambda^{1/2} \left\{ (1 - \mu_u - \mu_d) \left[m_u^2 \cot^2\beta \left(1 + \frac{4}{3}\frac{\alpha_s}{\pi}\Delta_{ud}^+ \right) \right. \right. \\
&\left. \left. + m_d^2 \tan^2\beta \left(1 + \frac{4}{3}\frac{\alpha_s}{\pi}\Delta_{du}^+ \right) \right] - 4 m_u m_d \sqrt{\mu_u \mu_d} \left(1 + \frac{4}{3}\frac{\alpha_s}{\pi}\Delta_{ud}^- \right) \right\}
\end{aligned} \tag{2.11}
$$

where $\mu_i = m_i^2/M_{H^\pm}^2$ and $\lambda = (1 - \mu_u - \mu_d)^2 - 4\mu_u\mu_d$; the quark masses $m_{u,d}$ are the pole masses at this stage and V_{ud} is the CKM matrix element.

The QCD factors $\Delta_{ij}^\pm \ (i,j = u,d)$ are given by

$$
\begin{aligned}
\Delta_{ij}^+ &= \frac{9}{4} + \frac{3 - 2\mu_i + 2\mu_j}{4} \log\frac{\mu_i}{\mu_j} + \frac{(\frac{3}{2} - \mu_i - \mu_j)\lambda + 5\mu_i\mu_j}{2\lambda^{1/2}(1 - \mu_i - \mu_j)}\log x_i x_j + B_{ij} \\
\Delta_{ij}^- &= 3 + \frac{\mu_j - \mu_i}{2}\log\frac{\mu_i}{\mu_j} + \frac{\lambda + 2(1 - \mu_i - \mu_j)}{2\lambda^{1/2}}\log x_i x_j + B_{ij}
\end{aligned} \tag{2.12}
$$

with the scaling variables $x_i = 2\mu_i/[1 - \mu_i - \mu_j + \lambda^{1/2}]$ and the generic function

$$
\begin{aligned}
B_{ij} &= \frac{1 - \mu_i - \mu_j}{\lambda^{1/2}} [4\mathrm{Li}_2(x_i x_j) - 2\mathrm{Li}_2(-x_i) - 2\mathrm{Li}_2(-x_j) + 2\log x_i x_j \log(1 - x_i x_j) \\
&\quad - \log x_i \log(1 + x_i) - \log x_j \log(1 + x_j)] - 4\left[\log(1 - x_i x_j) + \frac{x_i x_j}{1 - x_i x_j}\log x_i x_j \right] \\
&\quad + \left[\frac{\lambda^{1/2} + \mu_i - \mu_j}{\lambda^{1/2}} \left(\log(1 + x_i) - \frac{x_i}{1 + x_i}\log x_i \right) + \mu_i \leftrightarrow \mu_j \right]
\end{aligned}
$$
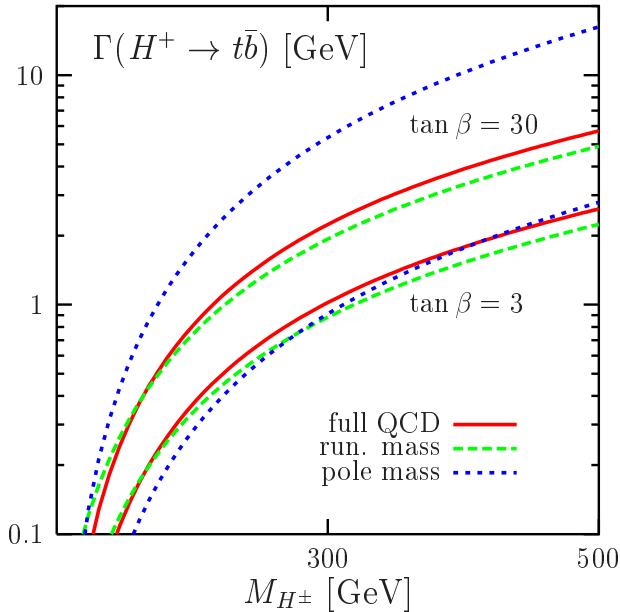
where the Spence function defined by $\mathrm{Li}_2(x) = -\int_0^x dy\, y^{-1}\log(1 - y)$ has been used.

For light quark final states, the decay width of the charged Higgs boson reduces to

$$\Gamma(\,H^+ \to u\bar{d}\,) = \frac{3G_\mu M_{H^\pm}}{4\sqrt{2}\pi}\,|V_{ud}|^2\,\left[\overline{m}_u^2(M_{H^\pm}^2)\cot^2\beta + \overline{m}_d^2(M_{H^\pm}^2)\tan^2\beta\right](1+\Delta_{qq}) \quad (2.13)$$

where the QCD correction factor Δ_{qq} is the same as for neutral Higgs bosons, eq. (2.3), and where large the logarithmic terms have been absorbed in the running $\overline{\text{MS}}$ masses $\overline{m}_{u,d}(M_{H^\pm}^2)$. For $M_{H^\pm} \sim 100$ GeV, the QCD corrections reduce the $c\bar{b}$ and $c\bar{s}$ decay widths by about a factor 2 to 4. Note that the dominant SUSY–QCD and EW corrections [207, 208] can also be absorbed in the Yukawa couplings; the remaining ones will be discussed later.

Again, the situation is summarized in Fig. 2.4 where we display the partial width $\Gamma(H^+ \to t\bar{b})$ in the various approximations discussed above for the values $\tan\beta = 3\,(30)$ where the component of the $H^\pm$ coupling involving the bottom (top) quark mass is dominant. While the use of the running top and bottom quark masses is a reasonable approximation, which approaches the full result at the 20% level, using simply the pole b–quark mass, in particular at high values of $\tan\beta$, leads to an overestimate of the width by a large factor.

Figure 2.4: *The partial widths of the charged Higgs boson into tb final states as a function of its mass for the values $\tan\beta = 3$ and $\tan\beta = 30$ in the various approximations discussed in the text. The pole quark masses have been chosen to be $m_b = 4.88$ GeV and $m_t = 178$ GeV and the QCD coupling constant is normalized to $\alpha_s(M_Z) = 0.1172$.*

Finally, for the decay $H^+ \to t\bar{b}$, the below threshold effects have to be taken into account for $M_{H^\pm} < m_t + m_b$ and the decay will then lead to $H^+ \to b\bar{b}W^+$ final states, Fig. 2.3b, if $M_{H^\pm} > M_W + 2m_b$ [203, 204, 209]. If the b–quark mass is neglected in the matrix element

squared and in the phase–space, one obtains a rather simple analytical expression for the partial width [203]

$$\Gamma(H^+ \to W b \bar{b}) \;=\; \frac{3 G_\mu^2 m_t^4}{64 \pi^3 \tan^2\beta} M_{H^\pm} \left\{ \frac{\kappa_W^2}{\kappa_t^3} (4\kappa_W \kappa_t + 3\kappa_t - 4\kappa_W) \log \frac{\kappa_W(\kappa_t - 1)}{\kappa_t - \kappa_W} \right.$$
$$+ (3\kappa_t^2 - 4\kappa_t - 3\kappa_W^2 + 1) \log \frac{\kappa_t - 1}{\kappa_t - \kappa_W} - \frac{5}{2} \qquad (2.14)$$
$$\left. + \frac{1 - \kappa_W}{\kappa_t^2}(3\kappa_t^3 - \kappa_t\kappa_W - 2\kappa_t\kappa_W^2 + 4\kappa_W^2) + \kappa_W \left(4 - \frac{3}{2}\kappa_W\right) \right\}$$

where the scaling variables $\kappa_W = M_W^2/M_{H^\pm}^2$ and $\kappa_t = m_t^2/M_{H^\pm}^2$ have been used. This expression is valid for small values of $\tan\beta$, where the off–shell branching ratio can reach the percent level for charged Higgs masses not too far from the tb threshold.

2.1.2 Decays into Higgs and massive vector bosons

Decays into W and Z bosons

The CP–even Higgs bosons $\mathcal{H} = h, H$ can decay into weak gauge bosons $\mathcal{H} \to VV$ with $V = W$ or Z, Fig. 2.5. The partial widths with on–shell or off–shell gauge bosons are exactly as in the SM [158, 194, 210, 211] except that they are damped by the scaled Higgs couplings

$$\Gamma(\mathcal{H} \to V^{(*)} V^{(*)}) \;=\; g_{\mathcal{H}VV}^2 \Gamma_{\rm SM}(\mathcal{H} \to V^{(*)}V^{(*)}) \qquad (2.15)$$

where the partial decay widths in the SM Higgs case in the two–, three– and four–body approximations, have been given in §I.2.2.
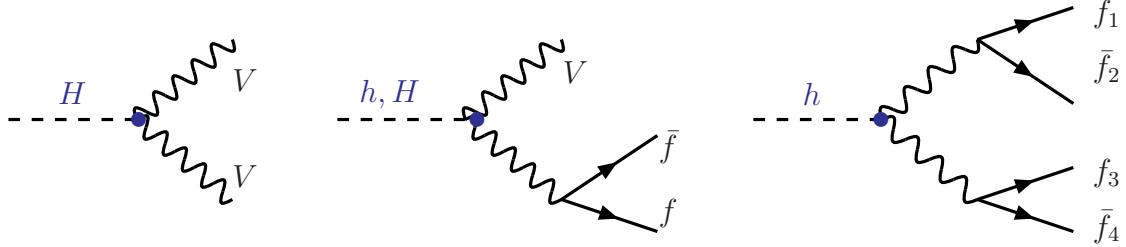
Figure 2.5: Feynman diagrams for the decays of the CP–even neutral MSSM Higgs bosons into real and/or virtual gauge bosons.

In fact, for the lighter h boson, only the three– or four–body decays are allowed since $M_h^{\rm max} < 2M_W$. In the case of the H boson, since $M_H \gtrsim 130$ GeV, it is sufficient to consider only the three– and two–body modes. However, when the latter takes place, the branching ratios are in general small since for $M_H \gtrsim 2M_Z$ the coupling squared $g_{HVV}^2 = \cos^2(\beta - \alpha) \sim M_Z^4/M_H^4$ is suppressed, in particular for large $\tan\beta$ values when in addition the decay $H \to b\bar{b}$ is enhanced and controls the total width.

Note that in the MSSM, the CP–even Higgs particles never acquire large total widths: the h boson is too light for the M_h^3 increase of the width to be effective, and the decays of the H boson into weak bosons are suppressed by the factor g_{HVV}^2 at large masses. In addition, the radiative corrections due to the Higgs self–couplings [which, in the SM, lead to the breakdown of perturbation theory for Higgs masses in the TeV range] are small in the MSSM as a consequence of their relation to the gauge couplings. These corrections and more generally the electroweak radiative corrections which are not included in the renormalization of the Higgs masses and the mixing angle α, will be neglected here.

The various distributions in these decays are as those of the SM Higgs boson [212] and only the overall normalizations are different. The CP–even Higgs boson does not decay into massive gauge bosons as a result of CP–invariance which forbids a tree–level AVV coupling [the charged Higgs boson also does not decay into WZ bosons for the same reason]. Very small couplings can however be induced through loop corrections and the partial decay widths and various energy or angular distributions will be as those discussed in §I.2.2.4, when the pseudoscalar Higgs case has been confronted to the SM Higgs case.

Decays into Higgs bosons

In small domains of the parameter space, in particular in the intermediate–coupling regime where both M_H and $\tan\beta$ are not too large, the heavy neutral Higgs boson H can also decay into two lighter CP–even or CP–odd Higgs bosons, Fig. 2.6a, with partial widths [213]

$$\Gamma(H \to \varphi\varphi) = \frac{G_\mu}{16\sqrt{2}\pi} \frac{M_Z^4}{M_H} \left(1 - 4\frac{M_\varphi^2}{M_H^2}\right)^{1/2} \lambda_{H\varphi\varphi}^2 \qquad (2.16)$$

with $\varphi = h$ or A and where the normalized trilinear Higgs couplings λ_{Hhh} and λ_{HAA} have been given in eq. (1.100) and the dominant radiative corrections, implemented in the ϵ approach, in eq. (1.141). The additional direct corrections to these decays, which are in general modest, have been derived in Ref. [139]. Note that, in the case of final state A bosons, the possibility for this decay is ruled out by the constraint $M_A \gtrsim 90$ GeV from LEP2 searches.
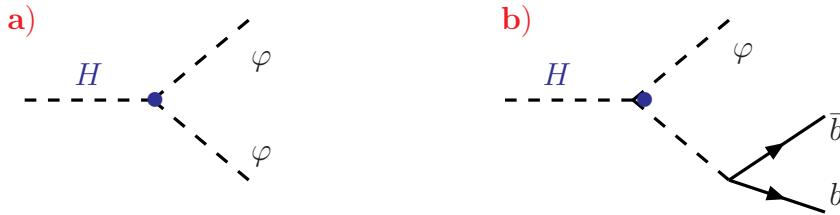
Figure 2.6: Feynman diagrams for the two–body and three–body decays of the heavier CP–even neutral MSSM Higgs boson into two lighter Higgs bosons.

For $M_\varphi \lesssim M_H \lesssim 2M_\varphi$ and for large values of $\tan\beta$, there is a possibility that the H boson decays into an on–shell and an off–shell lighter Higgs bosons, with the latter decaying

into $b\bar{b}$ pairs, $H \to \varphi b\bar{b}$; Fig. 2.6b [203]. The partial width for this three–body decay, using the reduced variable $\kappa_\varphi = M_\varphi^2/M_H^2$, is given by

$$
\Gamma(H \to \varphi\varphi^*) = \frac{3G_\mu^2 M_Z^4}{16\pi^3 M_H} \lambda_{H\varphi\varphi}^2\, g_{\varphi bb}^2\, m_b^2 \left[(\kappa_\varphi - 1)\left(2 - \frac{1}{2}\log\kappa_\varphi\right) \right.
$$
$$
\left. + \frac{1 - 5\kappa_\varphi}{\sqrt{4\kappa_\varphi - 1}}\left(\arctan\frac{2\kappa_\varphi - 1}{\sqrt{4\kappa_\varphi - 1}} - \arctan\frac{1}{\sqrt{4\kappa_\varphi - 1}}\right) \right] \qquad (2.17)
$$

There are also decays of the heavier Higgs bosons $H, A, H^\pm$ into lighter Higgs bosons and weak gauge bosons, $\Phi \to \varphi V$ [214]. At the two–body level, Fig. 2.7a, the partial width for the generic decay is given by

$$
\Gamma(\Phi \to \varphi V) = \frac{G_\mu M_V^2}{8\sqrt{2}\pi}\, g_{\Phi\varphi V}^2\, \lambda^{1/2}(M_V^2, M_\varphi^2; M_\Phi^2)\, \lambda(M_\Phi^2, M_\varphi^2; M_V^2) \qquad (2.18)
$$

with $\lambda(x, y; z) = (1 - x/z - y/z)^2 - 4xy/z^2$ being the usual two–body phase space function.
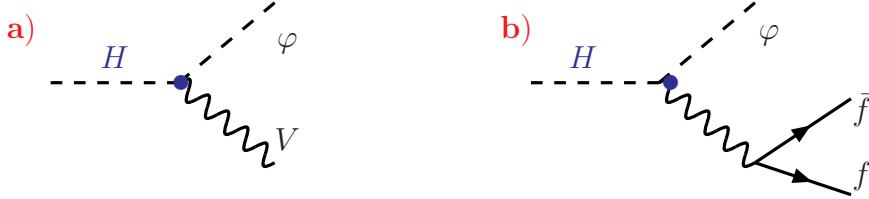
Figure 2.7: *Feynman diagrams for the two–body and three–body decays of heavier MSSM Higgs bosons into a lighter Higgs and a massive gauge boson.*

In practice, and because of the SUSY constraints on the mass spectrum, only the decays

$$
A \to hZ \quad \text{and} \quad H^\pm \to W^\pm h \qquad (2.19)
$$

are allowed at this two–body level. In fact, in these two cases, even the three–body final state decays $\Phi \to \varphi V^*$ with $V^* \to f\bar{f}$, Fig. 2.7b, can be rather important slightly below the $M_\varphi + M_V$ threshold [203–205, 209]. The partial decay widths read in this case [203]

$$
\Gamma(\Phi \to \varphi V^*) = \frac{9G_\mu^2 M_V^4}{8\pi^3}\, \delta_V'\, M_\Phi\, g_{\Phi\varphi V}^2\, G(M_\varphi^2/M_\Phi^2, M_V^2/M_\Phi^2) \qquad (2.20)
$$

where the coefficients δ_V' for $V = W, Z$ are the same as those appearing in $\mathcal{H} \to VV^*$ decays, $\delta_W' = 1$ and $\delta_Z' = \frac{7}{12} - \frac{10}{9}\sin^2\theta_W + \frac{40}{9}\sin^4\theta_W$. In terms of $\lambda_{ij} = -1 + 2\kappa_i + 2\kappa_j - (\kappa_i - \kappa_j)^2$ with $\kappa_i = M_i^2/M_\Phi^2$, the function G is given by

$$
G(\kappa_i, \kappa_j) = \frac{1}{4}\left\{ 2(-1 + \kappa_j - \kappa_i)\sqrt{\lambda_{ij}}\left[\frac{\pi}{2} + \arctan\left(\frac{\kappa_j(1 - \kappa_j + \kappa_i) - \lambda_{ij}}{(1 - \kappa_i)\sqrt{\lambda_{ij}}}\right)\right] \right.
$$
$$
\left. + (\lambda_{ij} - 2\kappa_i)\log\kappa_i + \frac{1}{3}(1 - \kappa_i)\left[5(1 + \kappa_i) - 4\kappa_j - \frac{2}{\kappa_j}\lambda_{ij}\right] \right\} \qquad (2.21)
$$

The virtuality of the final state gauge boson allows to kinematically open this type of decay channels in some other cases where they were forbidden at the two–body level

$$H \to AZ^* \to A(H)f\bar{f} \ , \ H \to H^\pm W^{\pm *} \to H^\pm f\bar{f}' \ , \ H^\pm \to AW^{\pm *} \to Af\bar{f}'$$
$$A \to HZ^* \to Hf\bar{f} \ , \ A \to H^\pm W^{\pm *} \to H^\pm f\bar{f}' \ , \ H^\pm \to HW^{\pm *} \to Hf\bar{f}' \qquad (2.22)$$

At low $\tan\beta$ values, the branching ratio for some of these decays, in particular $H^\pm \to AW^*$, can be sizable enough to be observable.

Finally, let us note that the direct radiative corrections to the $H^\pm \to AW$ decays have been calculated in Ref. [215]. They are in general small, not exceeding the 10% level, except when the tree–level partial widths are strongly suppressed; however, the total tree–level plus one–loop contribution in this case, is extremely small and the channels are not competitive. The same features should in principle apply in the case of $H^\pm \to hW$ and $A \to hZ$ decays.

2.1.3 Loop induced Higgs decays

The $\gamma\gamma$ and γZ couplings of the neutral Higgs bosons in the MSSM are mediated by charged heavy particle loops built up by W bosons, standard fermions f and charged Higgs bosons $H^\pm$ in the case of the CP–even $\Phi = h, H$ bosons and only standard fermions in the case of the pseudoscalar Higgs boson; Fig. 2.8. If SUSY particles are light, additional contributions will be provided by chargino $\chi_i^\pm$ and sfermion $\tilde{f}$ loops in the case of the CP–even Higgs particles and chargino loops in the case of the pseudoscalar Higgs boson.
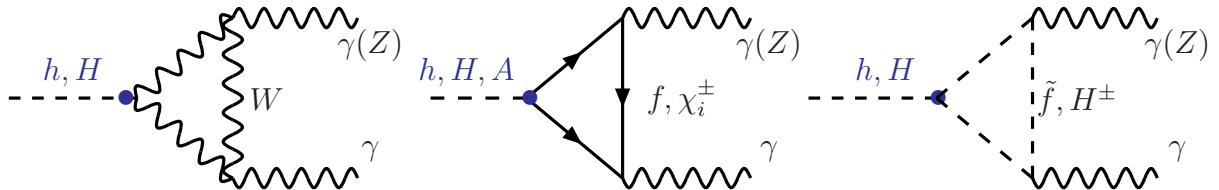
Figure 2.8: Decays of the h, H, A bosons into two photons or a photon and a Z boson.

In the case of the gluonic decays, only heavy quark loops contribute, with additional contributions due to light squarks in the case of the CP–even Higgs bosons h and H; Fig. 2.9.
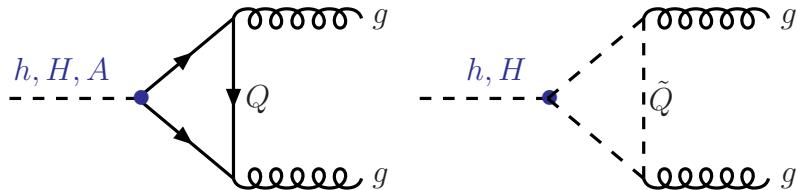
Figure 2.9: Loop induced decays of the neutral MSSM Higgs bosons into two gluons.

In this subsection, we will discuss only the contributions of the SM and $H^\pm$ particles, postponing those of the SUSY particles, which are assumed to be heavy, to the next section.

Decays into two photons

The partial decay widths of scalar $\mathcal{H} = h, H$ [160, 216–219] and pseudoscalar [217, 219] Higgs bosons into two photons are given by

$$\Gamma(\mathcal{H} \to \gamma\gamma) = \frac{G_\mu \alpha^2 M_\mathcal{H}^3}{128\sqrt{2}\pi^3} \Big| \sum_f N_c Q_f^2 g_{\mathcal{H}ff} A_{1/2}^\mathcal{H}(\tau_f) + g_{\mathcal{H}VV} A_1^\mathcal{H}(\tau_W)$$

$$+ \frac{M_W^2 \lambda_{\mathcal{H}H^+H^-}}{2c_W^2 M_{H^\pm}^2} A_0^\mathcal{H}(\tau_{H^\pm}) + \mathcal{A}_{\mathrm{SUSY}}^\mathcal{H} \Big|^2 \tag{2.23}$$

$$\Gamma(A \to \gamma\gamma) = \frac{G_\mu \alpha^2 M_A^3}{128\sqrt{2}\pi^3} \Big| \sum_f N_c Q_f^2 g_{Aff} A_{1/2}^A(\tau_f) + \mathcal{A}_{\mathrm{SUSY}}^A \Big|^2 \tag{2.24}$$

The reduced couplings $g_{\Phi ff}$ and $g_{\Phi VV}$ of the Higgs bosons to fermions and W bosons are given in Tab. 1.5, while the trilinear $\lambda_{\Phi H^+H^-}$ couplings to charged Higgs bosons are given in eq. (1.101). The amplitudes A_i at lowest order for the spin–1, spin–$\frac{1}{2}$ and spin–0 particle contributions are given by [41]

$$\begin{aligned}
A_{1/2}^\mathcal{H}(\tau) &= 2[\tau + (\tau - 1)f(\tau)]\,\tau^{-2} \\
A_1^\mathcal{H}(\tau) &= -[2\tau^2 + 3\tau + 3(2\tau - 1)f(\tau)]\,\tau^{-2} \\
A_0^\mathcal{H}(\tau) &= -[\tau - f(\tau)]\,\tau^{-2}
\end{aligned} \tag{2.25}$$

in the case of the CP–even Higgs bosons $\mathcal{H} = h, H$, while in the case of the CP–odd A particle, one has for the amplitude of spin–$\frac{1}{2}$ fermions,

$$A_{1/2}^A(\tau) = 2\tau^{-1} f(\tau) \tag{2.26}$$

where the scaling variables are defined as $\tau_i = M_\Phi^2/4M_i^2$ with M_i denoting the loop mass, and the universal scaling function $f(\tau)$ can be found in §I.2.3.

The real and imaginary parts of these form factors are shown in Fig. 2.10 as a function of the variable τ for the CP–even (top) and CP–odd (bottom) Higgs bosons. The amplitudes $A_1^\mathcal{H}$ for the W bosons and $A_{1/2}^\mathcal{H}$ for fermions have been discussed in the case of the SM Higgs boson. For light CP–even Higgs bosons, when the couplings suppression is not effective, the former is largely dominating compared to the latter, $A_1^\mathcal{H}(\tau) \to -7$ compared to $A_{1/2}^\mathcal{H} \to \frac{4}{3}$ for $\tau \to 0$. The amplitude for scalar particles is even smaller than the fermionic amplitude, $A_0^\mathcal{H}(\tau) = \frac{1}{3}$ in the limit of very heavy particles and has a maximum at $\mathrm{Re}(A_0^\mathcal{H}) \sim 1.5$ and $\mathrm{Im}(A_0^\mathcal{H}) \sim 1$ for $\tau \sim 1$. If, in addition, one recalls that the charged Higgs boson has couplings to the h, H particles that are not proportional to the $H^\pm$ mass, its contribution to the two–photon Higgs couplings is damped by the loop factor $M_W^2/M_{H^\pm}^2$ and becomes very small for high masses. Thus, contrary to the case of SM fermions and gauge bosons, heavy charged Higgs bosons decouple completely from the two–photon coupling.

In the case of the pseudoscalar Higgs boson, the form factor for spin–$\frac{1}{2}$ particles approaches the value 2 in the heavy fermion limit, while for very light fermions it has the same value as in the CP–even Higgs boson case [for the leading terms in the quark mass expansion] as a result of chiral symmetry

$$M_A^2 \gg 4m_f^2 \qquad A_{1/2}^A(\tau) = A_{1/2}^{\mathcal{H}}(\tau) \to -[\log(4\tau) - i\pi]^2/(2\tau)$$
$$M_A^2 \ll 4m_f^2 \qquad A_{1/2}^A(\tau) \to 2 \tag{2.27}$$

Near the fermion threshold, $\beta_f = \sqrt{1 - \tau_f^{-1}} \sim 0$ or $\tau_f \to 1$, the amplitude approaches the constant value $A_{1/2}^A(\tau) \to \frac{1}{2}\pi^2 + 2i\pi\beta_f$.
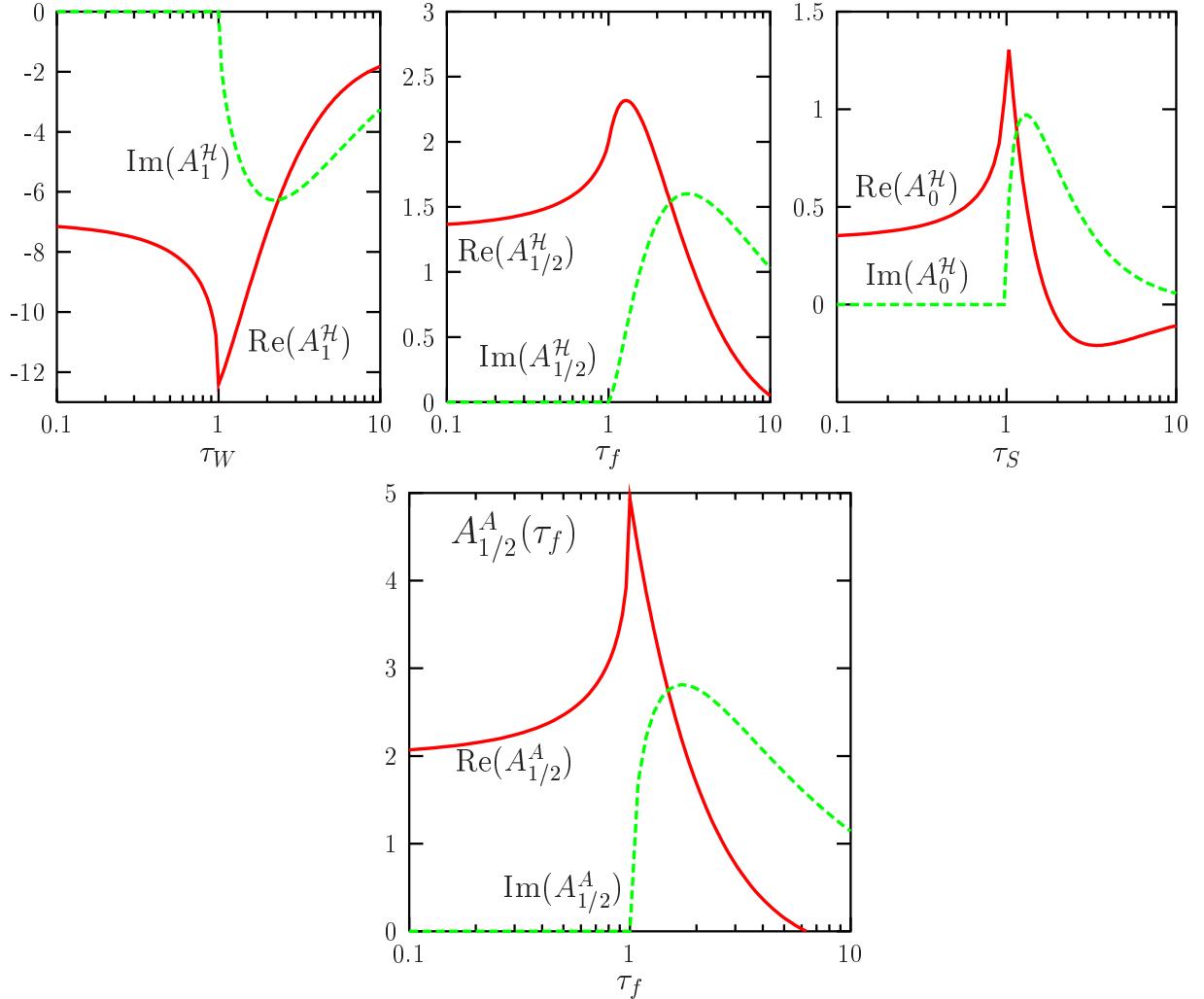
Figure 2.10: *The form factors for spin* $1, \frac{1}{2}, 0$ *particle contributions to the two–photon couplings of a CP–even Higgs boson (top) and the form factor for the contribution of a spin–$\frac{1}{2}$ particle to the two–photon coupling of a CP–odd Higgs boson, as a function of* $\tau_i = M_\Phi^2/4M_i^2$ *with* M_i *the mass of the loop particle.*

The partial decay widths are in general much smaller than in the SM, except in the case of the lighter Higgs boson in the decoupling limit or the heavier CP–even Higgs boson in the anti–decoupling regime. This is mainly due to the fact that since the Higgs couplings to gauge bosons are either suppressed or absent, the by far dominant contribution of the W loop is much smaller. The top quark contribution is in general also very small because of the suppressed $g_{\Phi tt}$ couplings for $\tan\beta > 1$ and, in fact, the dominant contribution comes from the bottom quark loop when $\tan\beta$ is very large and results in strongly enhanced $g_{\Phi bb}$ couplings. Furthermore, in view of the present MSSM bounds on $M_{H^\pm}$, the contribution of the charged Higgs particle is very small as it is damped by the factor $M_W^2/M_{H^\pm}^2$, in addition to the smallness of the form–factor $A_0^\mathcal{H}(\tau_{H^\pm})$. This is shown in Fig. 2.11 where the two–photon partial widths are shown as a function of the Higgs masses for the values $\tan\beta = 3$ and 30; the partial width in the SM Higgs boson case is also displayed for comparison.
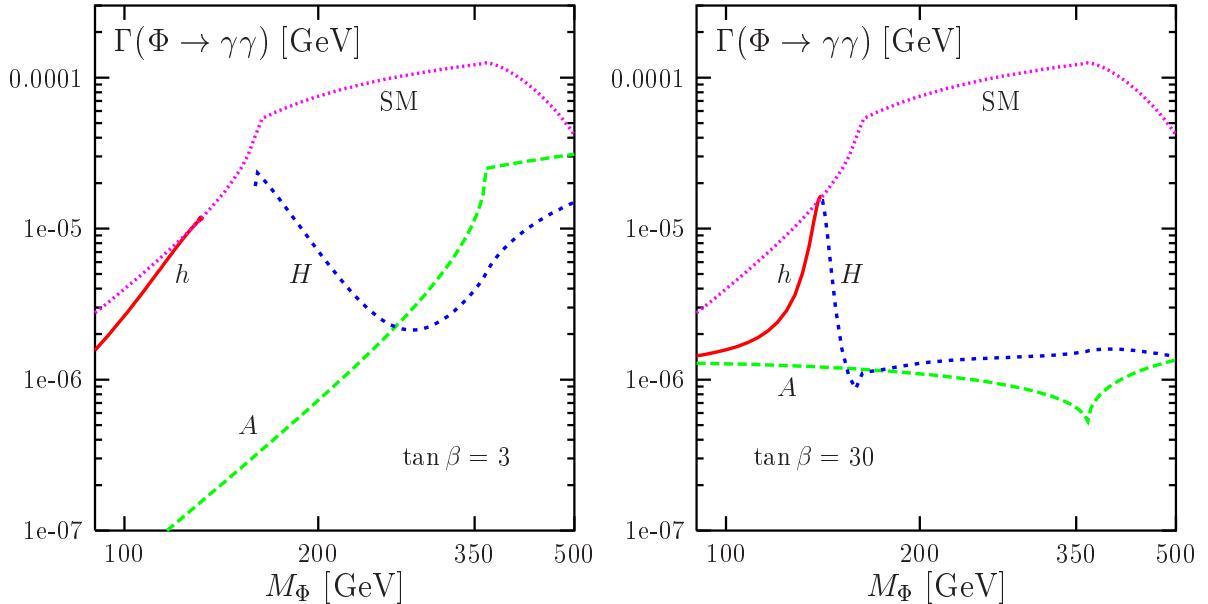
Figure 2.11: The partial decay widths of the MSSM neutral Higgs bosons into two photons as a function of their masses for $\tan\beta = 3$ (left) and $\tan\beta = 30$ (right). For comparison, the width in the SM Higgs case is also displayed.

The QCD corrections to the decays of a CP–even Higgs boson into two photons [220–222], assuming that the squarks are too heavy to contribute in the loops, follow that of the SM Higgs boson that we have discussed in §I.2.3.1 to which we refer for details. For the QCD corrections to the $A \to \gamma\gamma$ decay, and in the case where only the contribution of quark loops are taken into account, the two–loop Feynman diagrams are the same as for the SM Higgs boson. The calculation has been performed in the general massive case in Refs. [221, 222] and the discussion goes along the same lines as in the SM Higgs case. There are however, a few subtleties because of the CP–odd character of the Higgs particle.

To regularize the pseudoscalar amplitude involving the γ_5 coupling, one can adopt the 't Hooft–Veltman prescription [223] which reproduces the axial–vector anomaly at LO automatically [85]. However, there is a subtle problem: the multiplicative renormalization factor of the pseudoscalar ($Q\bar{Q}$) current is given by $Z_{AQQ} = 1 - Z_2 Z_m$ where Z_2, Z_m are the wave–function and mass renormalization factors, respectively. To ensure the chiral–symmetry relation $\Gamma_5(p', p) \rightarrow \gamma_5 \Gamma(p', p)$ in the limit $m_Q \rightarrow 0$ for the fermionic matrix element of the pseudoscalar and scalar currents, the renormalization factor of the pseudoscalar current has to be chosen as $Z_{AQQ} = Z_{HQQ} + 8\alpha_s/(3\pi)$ [224], the additional term being due to spurious anomalous contributions that must be subtracted by hand.

Another significant difference between the CP–even and CP–odd cases is for masses near the quark threshold, $M_{H/A} \simeq 2m_Q$. As discussed earlier in the SM case [§I.2.3.1], since $Q\bar{Q}$ pairs cannot form 0^{++} states at the threshold, $\mathrm{Im}(C_H)$ vanishes there, while $\mathrm{Re}(C_H)$ develops a maximum. In contrast, since $Q\bar{Q}$ pairs do form 0^{+-} states, the imaginary part $\mathrm{Im}(C_A)$ develops a step that is built up by the Coulombic gluon exchange [familiar from the singularity of the QCD correction to $q\bar{q}$ production in $e^+ e^-$ annihilation] and $\mathrm{Re}(C_A)$ is singular at the threshold. The singularity is regularized by including the top quark width [225].

To sum up, while in the light quark limit the QCD correction factor for the amplitude

$$A^\Phi_{1/2}(\tau_Q) = A^\Phi_{1/2}(\tau_Q)|_{\mathrm{LO}} \left[1 + C_\Phi \frac{\alpha_s}{\pi}\right] \tag{2.28}$$

is exactly the same as in the scalar case as anticipated from chiral symmetry [the subleading terms are not the same],

$$m_Q(\mu_Q^2) \rightarrow 0: \quad C_{\mathcal{H},A} \rightarrow -\frac{1}{18} \log^2(-4\tau - i\epsilon) - \frac{2}{3} \log(-4\tau - i\epsilon) + 2 \log \frac{\mu_Q^2}{m_Q^2} \tag{2.29}$$

it vanishes exactly in the opposite heavy quark limit [221] contrary to the scalar case

$$m_Q \rightarrow \infty: \quad C_{\mathcal{H}} \rightarrow -1, \quad C_A \rightarrow 0 \tag{2.30}$$

In fact, similarly to the relation between the $H\gamma\gamma$ coupling and the anomaly of the trace of the energy–momentum tensor [see §I.2.4], there is a relation between the coupling of a pseudoscalar Higgs boson to photons and the anomaly of the axial–vector current [85]

$$\partial_\mu j^5_\mu = 2m_Q \overline{Q} i\gamma_5 Q + N_c Q_Q^2 \frac{\alpha}{4\pi} F_{\mu\nu} \widetilde{F}_{\mu\nu} \tag{2.31}$$

where $\widetilde{F}_{\mu\nu} = \epsilon_{\mu\nu\alpha\beta} F_{\alpha\beta}$ is the dual field strength tensor. Since, the matrix element $\langle \gamma\gamma | \partial_\mu j^\mu_5 | 0 \rangle$ of the divergence of the axial–vector current vanishes for zero photon energy, the matrix element $\langle \gamma\gamma | m_Q \bar{Q} i\gamma_5 Q | 0 \rangle$ of the Higgs source can be linked directly to the anomalous term in

eq. (2.31). It is well–known that the anomaly is not renormalized by strong interactions [85] and as a result, the effective $A\gamma\gamma$ Lagrangian

$$\mathcal{L}_{\text{eff}}(A\gamma\gamma) = N_c Q_Q^2 \frac{\alpha}{8\pi} \left(\sqrt{2} G_F\right)^{1/2} F_{\mu\nu} \widetilde{F}_{\mu\nu} A \tag{2.32}$$

is valid to all orders of perturbation theory in α_s in the limit $M_A^2 \ll 4m_Q^2$. This has been explicitly verified at $\mathcal{O}(\alpha_s)$ as discussed previously.

The correction factors C_Φ in the CP–even and CP–odd cases are compared to each other in the top panel of Fig. 2.12, while the QCD corrections to the partial decay $\Phi \to \gamma\gamma$ widths relative to the LO result, $\Gamma = \Gamma_{\text{LO}}(1 + \delta)$, are shown in the bottom panel as a function of M_Φ; the scale at which the corrections are evaluated is set to $\mu_Q = \frac{1}{2} m_Q$. As can be seen, the corrections can be large in the case of the H and A bosons, in particular near thresholds.
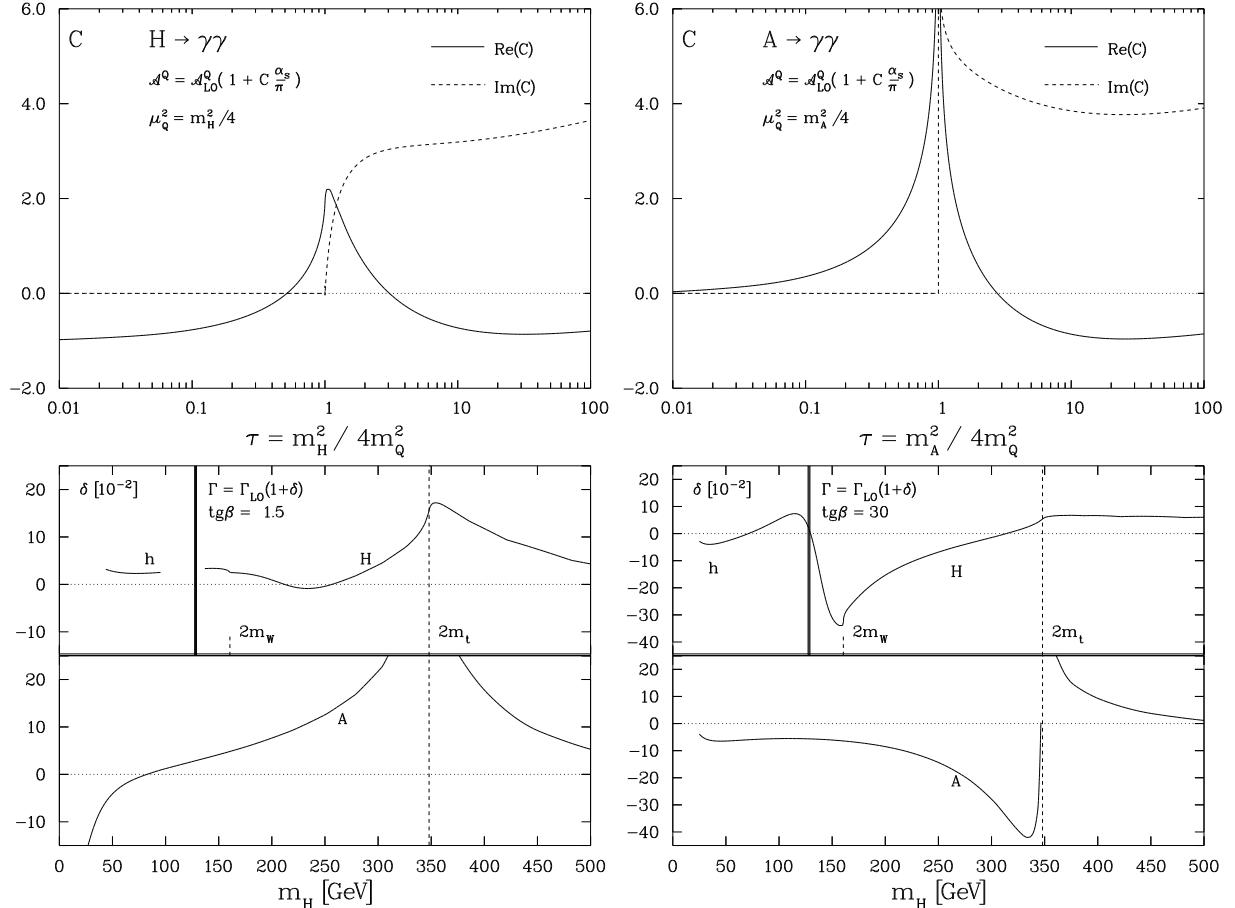
Figure 2.12: Top: The QCD correction factor to the quark amplitude in the two–photon decay of CP–even (left) and CP–odd (right) Higgs bosons as a function of $\tau_Q = M_\Phi^2/4m_Q^2$. Bottom: the size of the QCD correction to the decay widths as a function of the Higgs masses for two values $\tan\beta = 1.5$ (left) and 30 (right). In both cases, the renormalization scale for the quark mass is taken to be $\mu_Q = \frac{1}{2} M_\Phi$; from Ref. [222].

96

The decays $\Phi \to \gamma Z$ and $H^\pm \to \gamma W^\pm, ZW^\pm$

The loop induced couplings of the neutral Higgs bosons to $Z\gamma$ final states [226–230], the Feynman diagrams of which are given in Fig. 2.8 with one photon replaced by a Z boson, are slightly more complicated than the Higgs coupling to two–photons, in particular, when the SUSY particle contributions are taken into account. Ignoring for the time being these additional contributions, the amplitudes for the loop induced $Z\gamma$ decays in the case of the the CP–even $\mathcal{H} = h, H$ bosons, where fermions, W bosons and $H^\pm$ bosons are running in the loops, and in the case of the CP–odd A boson, where only fermions are involved as a consequence of CP–invariance, may be written as

$$\Gamma(\mathcal{H} \to Z\gamma) = \frac{G_\mu^2 M_W^2 \, \alpha \, M_\mathcal{H}^3}{64 \, \pi^4} \left(1 - \frac{M_Z^2}{M_\mathcal{H}^2}\right)^3 \Big| \sum_f g_{\mathcal{H}ff} \frac{Q_f \, \hat{v}_f N_c}{c_W} \mathcal{A}_{1/2}^\mathcal{H}(\tau_f, \lambda_f) \tag{2.33}$$

$$+ g_{\mathcal{H}VV} \mathcal{A}_W^\mathcal{H}(\tau_W, \lambda_W) + \frac{M_W^2 v_{H^\pm}}{2 c_W M_{H^\pm}^2} \lambda_{\mathcal{H}H^+H^-} \mathcal{A}_0^\mathcal{H}(\tau_{H^\pm}, \lambda_{H^\pm}) + \mathcal{A}_{\mathrm{SUSY}}^\mathcal{H} \Big|^2$$

$$\Gamma(A \to Z\gamma) = \frac{G_\mu^2 M_W^2 \, \alpha \, M_A^3}{16 \, \pi^4} \left(1 - \frac{M_Z^2}{M_A^2}\right)^3 \Big| \sum_f g_{Aff} \frac{Q_f \hat{v}_f N_c}{c_W} \mathcal{A}_{1/2}^A(\tau_f, \lambda_f) + \mathcal{A}_{\mathrm{SUSY}}^A \Big|^2$$

where the various couplings, including the radiative corrections, have been given previously except for the Z boson couplings to charged Higgs bosons which reads

$$v_{H^\pm} = \frac{2 c_W^2 - 1}{c_W} \tag{2.34}$$

The reduced variables are $\tau_i = 4M_i^2/M_\Phi^2$, $\lambda_i = 4M_i^2/M_Z^2$ and the amplitude for spin–$\frac{1}{2}$ and spin–one particles have been given in §I.2.3, while the amplitude for spin–zero particles is

$$\mathcal{A}_0^\mathcal{H}(\tau_{H^\pm}, \lambda_{H^\pm}) = I_1(\tau_{H^\pm}, \lambda_{H^\pm}) \tag{2.35}$$

with the form factor I_1 again given in §I.2.3.

These decays follow approximately the same pattern discussed in the case of the Higgs decay into two–photons. For large loop particle masses, when one can neglect the Z–boson mass, the form factors approach the photonic amplitudes modulo the couplings. In the case of the lighter Higgs boson h, the contributions of the charged Higgs particles will decouple as a result of the $M_W^2/M_{H^\pm}^2$ loop factor suppression and we are left with the SM Higgs boson decay rate. This needs not to be the case of the $Z\gamma$ decays of the heavier CP–even Higgs boson but the $H^\pm$ contributions are further suppressed by the coefficient of the amplitude I_1 for spin–zero particles which is also small in this case. In any case, these decays are in general not very important in the MSSM and barely reach branching ratios of order 10^{-3}. The partial decay widths are shown in Fig. 2.13 as a function of the Higgs masses for $\tan\beta = 3, 30$ and compared with the SM Higgs rate.
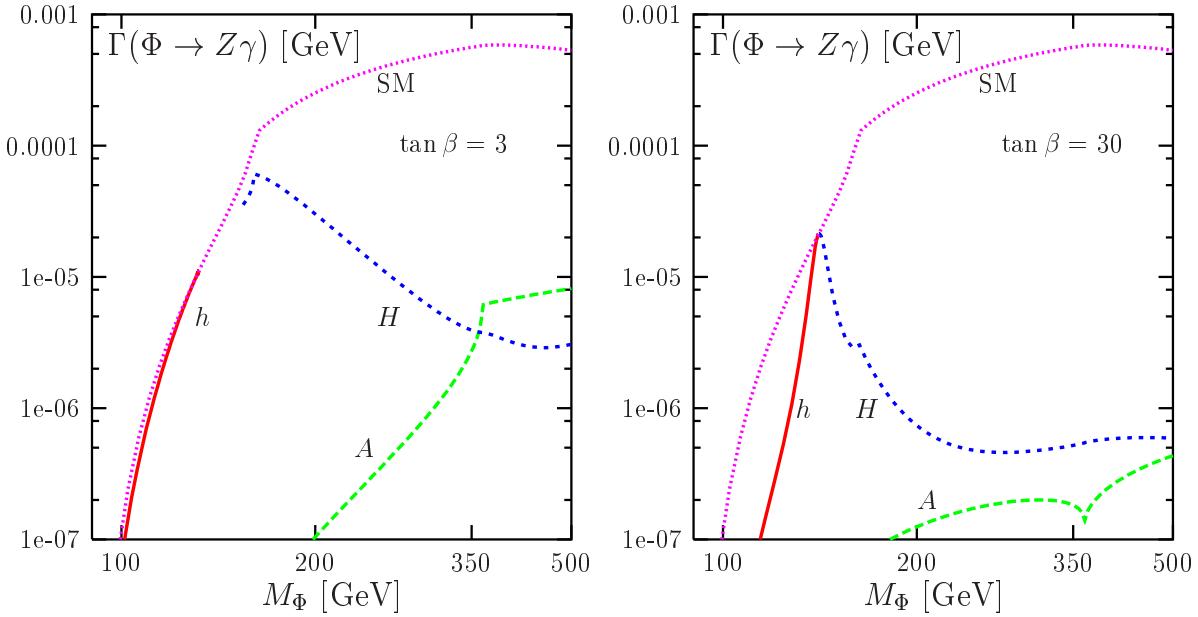
Figure 2.13: The partial decay widths of the MSSM neutral Higgs bosons into a photon and a Z boson as a function of their masses for $\tan\beta = 3$ *(left) and* $\tan\beta = 30$ *(right). For comparison, the width in the SM Higgs case is also displayed.*

Let us now turn to the loop induced decays of the charged Higgs bosons, $H^\pm \to W^\pm \gamma$ [231–234] and $H^\pm \to W^\pm Z$ [98, 99, 233, 235]. They can be generated through the same loop diagrams as in the neutral Higgs case, $\Phi \to \gamma\gamma$ or γZ, but there are also diagrams in which the charged Higgs bosons turn into off–shell W bosons through loops involving charged particles, and the virtual W bosons split then into real γW or ZW states. Besides the top–bottom loop, additional loops involving neutral and charged Higgs bosons together with W/Z bosons [and in a non unitary gauge, Goldstone bosons] occur. In the MSSM, most of the bosonic couplings are however rather small as they do not grow with the masses of the particles. In particular, in the decoupling limit, the $H^\pm$ couplings to the lighter h and the W bosons vanish while the H/A particles, which couple with full strength to the $H^\pm W^\pm$ states, have masses of the same order as $M_{H^\pm}$, implying that these particles do not contribute in a significant way to the loop induced $H^\pm W^\mp \gamma$ and $H^\pm W^\mp Z$ couplings.

Thus, in the MSSM, it is a good approximation to include only the top–bottom quark loop contributions to the partial decay widths. The amplitudes have been derived first in Refs. [98, 99, 231–233] and, more recently, the complicated full expressions including all fermionic and bosonic contributions have been given in a 2HDM in Refs. [234] and [235] for, respectively, the $H^\pm \to W^\pm \gamma$ and $H^\pm \to W^\pm Z$ decays[18]. In the following, we simply write down the two partial decay widths in the limit $m_t \gg M_{H^\pm}, M_W \gg m_b$ which turns out to

---

[18]The contributions of scalar SUSY partners of top and bottom quarks has been also derived in Ref. [233] for large enough squark masses and are small; they will also be ignored in the following discussion.

give an adequate estimate of the full contributions. In this case, one has [233]

$$\Gamma(H^\pm \to W^\pm \gamma) = \frac{\alpha^3 N_c^2 M_{H^\pm}^3}{2^7 \pi^2 M_W^2 c_W^2} \left(1 - \frac{M_W^2}{M_{H^\pm}^2}\right)^3 \left(|\mathcal{M}_2^\gamma|^2 + |\mathcal{M}_3^\gamma|^2\right)$$

$$\Gamma(H^\pm \to W^\pm Z) = \frac{\alpha^3 N_c^2 \lambda^{1/2}}{2^{10} \pi^2 M_W^6 M_{H^\pm}^3} \left[4(\lambda + 12 M_W^2 M_Z^2)|\mathcal{M}_1^Z|^2 + \lambda^2 |\mathcal{M}_2^Z|^2 \right.$$
$$\left. + \quad 8\lambda M_W^2 M_Z^2 |\mathcal{M}_3^Z|^2 + 4\lambda(M_{H^\pm}^2 - M_W^2 - M_Z^2)\mathrm{Re}(\mathcal{M}_1^Z \mathcal{M}_2^{Z*})\right] \quad (2.36)$$

where $\lambda = (M_{H^\pm}^2 - M_W^2 - M_Z^2)^2 - 4M_W^2 M_Z^2$ and the various amplitudes are given by

$$\mathcal{M}_2^\gamma = -\frac{1}{12}\sin 2\theta_W c_+ \;,\;\; \mathcal{M}_3^\gamma = \frac{1}{12}\sin 2\theta_W c_-$$
$$\mathcal{M}_1^Z = \frac{1}{4}m_t^2 c_+ \;,\;\; \mathcal{M}_2^Z = \frac{1}{12}\left(\frac{1}{2} + 2s_W^2\right)c_+ \;,\;\; \mathcal{M}_3^Z = -\frac{1}{4}\left(\frac{1}{2} + \frac{2}{3}s_W^2\right)c_- \quad (2.37)$$

with $c_\pm = \cot\beta \pm \frac{m_b}{m_t}\tan\beta$. The partial widths are significant only for small or large values of $\tan\beta$. The branching ratios for $H^\pm \to W^\pm \gamma$ and the partial decay widths for $H^\pm \to W^\pm Z$ are shown in Fig. 2.14; all contribution are exactly included. In the former case, the figure is in fact in a 2HDM where the angle α and all Higgs masses are free parameters, allowing to enhance the $H^\pm W\gamma$ couplings; the MSSM case is approached only in the example $\sin\alpha = 1$ with $\tan\beta = 40$ where the branching ratio is of order 10^{-6}. In the case of $H^\pm \to WZ$, the partial width is also below the level of 10^{-4} for $\tan\beta$ values in the range 2–60 and for Higgs masses above the tb threshold. Again, in a 2HDM, the rate can be much larger in the presence of sizable Higgs mass splittings which enhance the charged Higgs boson self–couplings. These decays will be ignored in our subsequent discussions.
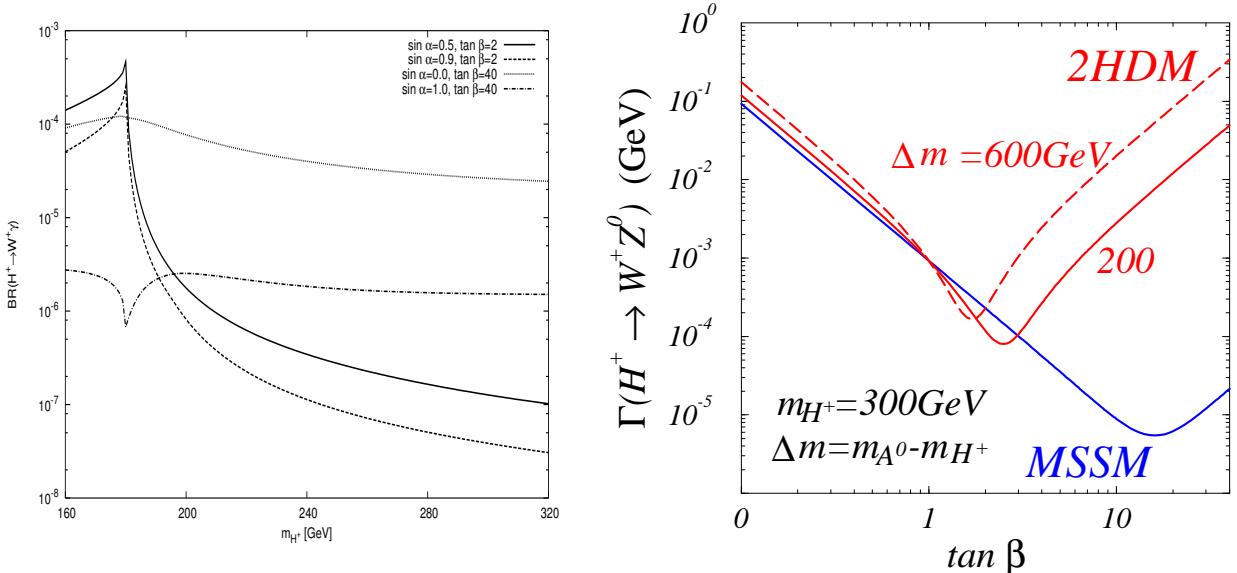
Figure 2.14: The partial decay widths of the charged Higgs boson into γW [234] and ZW [235] final states in a 2HDM and also in the MSSM for the latter case.

Decays into two gluons

The amplitudes for the gluonic decay widths of the CP–even and CP–odd Higgs particles, where only heavy t, b quarks contribute [we will discuss the contribution of squark loops in the CP–even Higgs case at a later stage], are given at leading order by [38, 236–240]

$$\Gamma(\mathcal{H} \to gg) = \frac{G_\mu \alpha_s^2 M_\mathcal{H}^3}{36\sqrt{2}\pi^3}\left|\frac{3}{4}\sum_Q g_{\mathcal{H}QQ}A_{1/2}^\mathcal{H}(\tau_Q) + \frac{3}{4}\mathcal{A}_{\mathrm{SUSY}}^\mathcal{H}\right|^2$$

$$\Gamma(A \to gg) = \frac{G_\mu \alpha_s^2 M_A^3}{36\sqrt{2}\pi^3}\left|\frac{3}{4}\sum_Q g_{AQQ}A_{1/2}^A(\tau_Q)\right|^2 \tag{2.38}$$

with the loop amplitudes and Higgs couplings as given previously. Again, except for the h boson in the decoupling and for the H boson in the anti–decoupling limits, the top quark amplitude is suppressed for values $\tan\beta > 1$ and the b–quark amplitude becomes the dominant component at large $\tan\beta$ values. In the case of the A boson, and for low $\tan\beta$ values when the top quark loop dominates, the $A \to gg$ partial width is smaller than for the H boson at low M_A and comparable at high values, as follows from the variation of the form factors shown in Fig. 2.10. For large $\tan\beta$ values, as a consequence of chiral symmetry, the $A \to gg$ partial width follows that of the lighter h boson at low M_A and that of the heavier H boson at higher M_A, except in the transition and $t\bar{t}$ threshold regions. The partial widths $\Gamma(\Phi \to gg)$ are shown in Fig. 2.15 as a function of the Higgs masses for the two usual values of $\tan\beta$ and compared with the gluonic partial width of the SM Higgs boson.
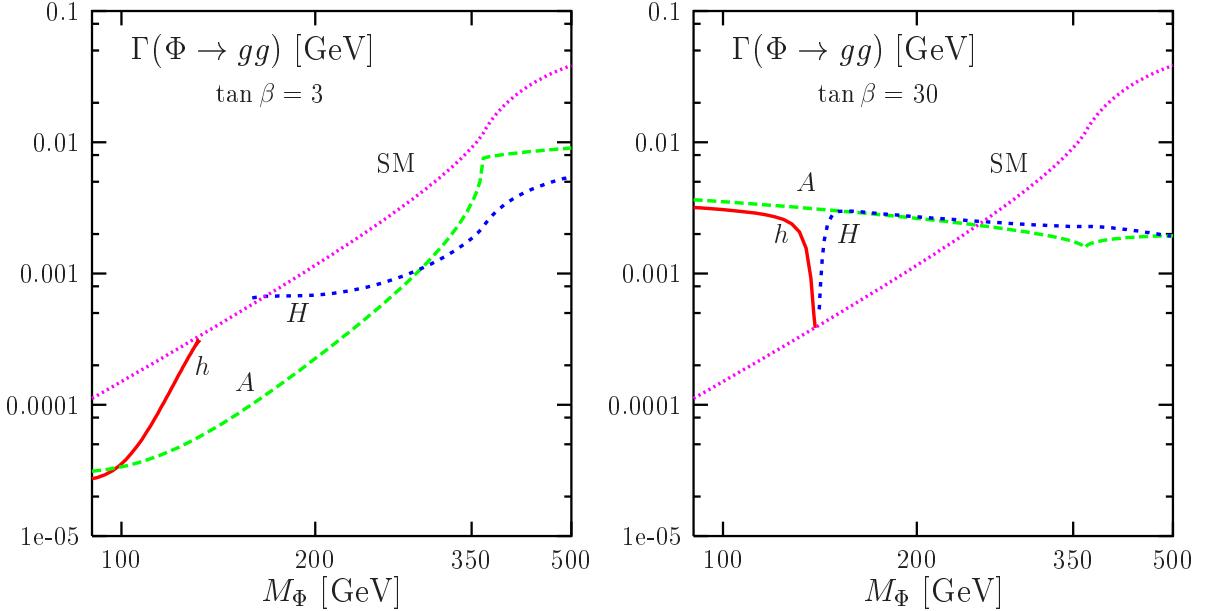
Figure 2.15: The partial decay widths of the MSSM neutral Higgs bosons into two gluons as a function of their masses for $\tan\beta = 3$ *(left) and* $\tan\beta = 30$ *(right). For comparison, the partial width of the SM Higgs boson is also displayed.*

The QCD corrections to the quark loop contribution to the gluonic decay width have been discussed in §2.3.3 and §2.4.3 of Tome I in the CP–even Higgs boson case. At NLO, one has to evaluate two–loop diagrams in which a gluon is exchanged between the quark lines of the triangle [as in the $\Phi \to \gamma\gamma$ case] or between the final gluons or the gluons and quarks and, also, diagrams in which an additional gluon is emitted in the final state, $\Phi \to gg^* \to ggg$ or a gluon splits into a light quark pair $\Phi \to gg^* \to gq\bar{q}$. While for the top quark loops one can use the infinite top quark limit and also include the NNLO corrections in the case of $h \to gg$ decays and, eventually, for $H \to gg$ in the mass range $M_H \lesssim 2m_t$, the full mass dependence or at least the small loop mass expansion has to be used in the case of the bottom quark loop contribution which, as seen previously, is dominant for large values of $\tan\beta$. Of course the NNLO calculation, which has been performed in the heavy quark limit, does not apply in this case. In both limits, the situation is as in the SM Higgs boson case and the corrections are very large, being of the order of 40 to 70%.

The previous discussions do not apply for the decays of the pseudoscalar Higgs boson. In this case, the next–to–leading order QCD corrections have been calculated in Ref. [222] in the full massive quark case. The main features are similar to what has been discussed for the SM Higgs boson, supplemented with the subtleties which occur because of the γ_5 coupling that already appear for the decay $A \to \gamma\gamma$. The corrected gluonic decay widths for the three neutral Higgs particles can be written as

$$\Gamma(\Phi \to gg(g),\ gq\bar{q}) = \Gamma_{\mathrm{LO}}(\Phi \to gg) \left[1 + E_\Phi(\tau_Q)\frac{\alpha_s}{\pi}\right] \tag{2.39}$$

where for the CP–even $\mathcal{H} = h, H$ and CP–odd A bosons, the correction factors are

$$E_{\mathcal{H}}(\tau_Q) = \frac{95}{4} - \frac{7}{6}N_f + \frac{33 - 2N_f}{6}\ \log\frac{\mu^2}{M_{\mathcal{H}}^2} + \Delta E_{\mathcal{H}}(\tau_Q)$$

$$E_A(\tau_Q) = \frac{97}{4} - \frac{7}{6}N_f + \frac{33 - 2N_f}{6}\ \log\frac{\mu^2}{M_A^2} + \Delta E_A(\tau_Q) \tag{2.40}$$

In the heavy quark limit [221, 241], the correction factor E_A is the same as for a scalar particle, except that the constant term 95/4 is replaced by 97/4. For large Higgs masses, the correction factor also approaches $E_{\mathcal{H}}$. The only difference is near the $2m_t$ threshold where, as seen already for the $A \to \gamma\gamma$ decay, the correction has a singularity at the threshold.

The QCD correction factors for the $\mathcal{H}gg$ and Agg amplitudes are shown in Fig. 2.16 as a function of the Higgs masses in the two cases where mostly the top quark loop contributes, $\tan\beta = 3$, and when the bottom quark loop is dominant, $\tan\beta = 30$. In the latter case, no singularity occurs since $M_A \gg 2m_b$, but a small kink is still observable as a result of the large contribution of the imaginary part of the t–contribution to the Agg amplitude.

If the top quark loop provides the dominant contribution to the $\Phi \to gg$ decays and the Higgs masses are below the $t\bar{t}$ threshold, $M_\Phi \lesssim 2m_t$, one can also use the low energy theorem
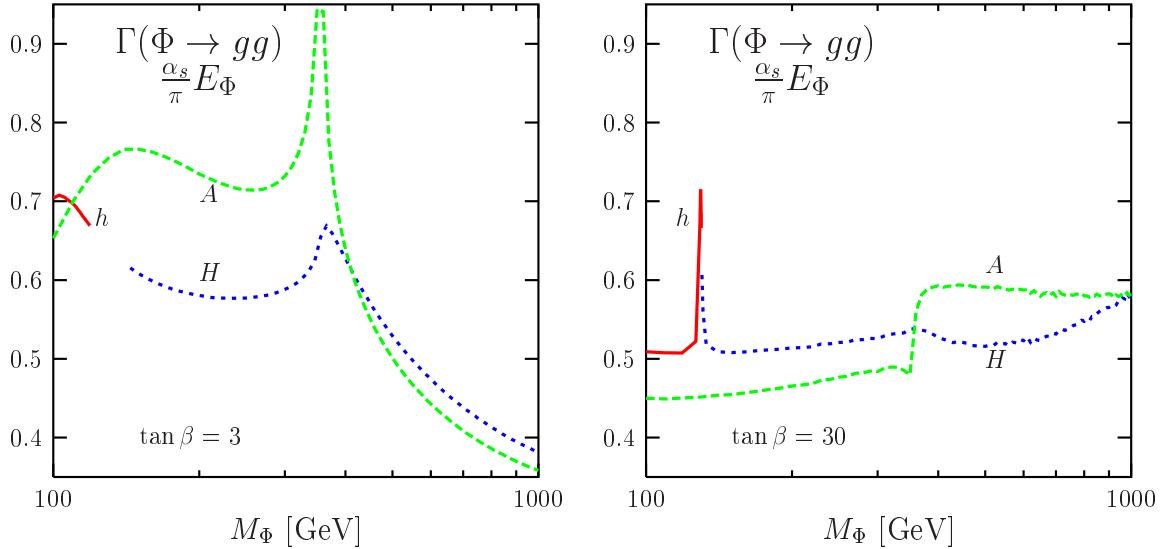
Figure 2.16: The QCD correction factors for the partial widths $\Gamma(\Phi \to gg)$ as a function of the Higgs boson masses for $\tan\beta = 3$ (left) and $\tan\beta = 30$ (right); the contributions of the top quark with $m_t = 178$ GeV and the bottom quark with $m_b = 5$ GeV are included.

discussed in §I.2.4.1 to derive the higher–order QCD corrections to the Φgg couplings in the heavy top quark limit. The NNLO QCD corrections have been also calculated in this case and one finds for the correction factors at this order for $\mathcal{H} \to gg$ [242] and $A \to gg$ [243]

$$
\begin{aligned}
K^{\mathrm{QCD}}_{\mathcal{H} \to gg} &= 1 + \frac{215}{12}\frac{\alpha_s(M_{\mathcal{H}})}{\pi} + \frac{\alpha_s^2(M_{\mathcal{H}})}{\pi^2}\left(156.8 - 5.7\log\frac{m_t^2}{M_{\mathcal{H}}^2}\right) \\
K^{\mathrm{QCD}}_{A \to gg} &= 1 + \frac{221}{12}\frac{\alpha_s(M_A)}{\pi} + \frac{\alpha_s^2(M_A)}{\pi^2}\left(171.5 - 5\log\frac{m_t^2}{M_A^2}\right)
\end{aligned}
\tag{2.41}
$$

where the number of light flavors is taken to be $N_f = 5$ and the renormalization scale is chosen to be $\mu = M_{\Phi}$. In both cases [at NNLO, also, the correction factors are not numerically very different in the scalar and pseudoscalar cases], the three–loop contribution amounts to $\sim 20\%$ of the one–loop (first order) term and $\sim 30\%$ of the two–loop term, therefore showing a good convergence behavior of the perturbative series.

2.1.4 The total decay widths and the branching ratios

The branching ratios of the decays of the four MSSM h, H, A and $H^{\pm}$ bosons into fermions, gauge bosons and other Higgs particles are displayed in Figs. 2.17–2.20 as a function of the decaying particle mass. They have been obtained with the program `HDECAY` where the SM particle masses are set to their world average values given in the Appendix and the values of the strong coupling constant and the electroweak mixing angle taken to be $\alpha_s(M_Z) = 0.1172$ and $s_W^2 = 0.2315$. In the case of the $H^{\pm}$ bosons, the values of some CKM matrix elements need to be fixed in addition and we use also those given in the Appendix.

102

The radiative corrections in the Higgs sector have been evaluated using the program `FeynHiggsFast1.2` for the two values $\tan\beta = 3$ and $\tan\beta = 30$. The various SUSY parameters which enter these corrections have been chosen in the "maximal mixing" benchmark scenario defined in the Appendix [in the "no–mixing" scenario with $X_t = 0$, the trend is similar for the heavier Higgs bosons, but slightly different in the case of the h boson where M_h is smaller]. The mass of the pseudoscalar Higgs boson has been then varied to obtain the masses of the other Higgs particles. The lower range of the h, A masses, $M_{h,A} \sim 90$ GeV, although ruled out by LEP2 constraints is displayed for the sake of completeness.

The branching ratios for the heavier H, A and $H^\pm$ bosons are shown for masses up to 500 GeV only since, for larger mass values, the main features remain essentially the same. In the case of the h boson however, we extended the M_A range up to 1 TeV to fully reach the decoupling limit at low $\tan\beta$ values. Note that only the decays with branching fractions larger than 10^{-3} have been displayed; some important decays which have smaller rates will be discussed later. The total widths of the four Higgs particles are shown in Fig. 2.21 under the same conditions. In what follows, we discuss these decays in the various regimes of the MSSM Higgs sector introduced in §1.3 starting with the simplest one, the decoupling regime.

The decoupling regime

In the decoupling regime, $M_A \gtrsim 150$ GeV for $\tan\beta = 30$ and $M_A \gtrsim 400$–500 GeV for $\tan\beta = 3$, the situation is quite simple. The lighter h boson reaches its maximal mass value and has SM–like couplings and, thus, decays as the SM Higgs boson H_{SM}. Since $M_h^{\mathrm{max}} \lesssim 140$ GeV in the chosen scenarios, the dominant modes are the decays into $b\bar{b}$ pairs and into WW^* final states, the branching ratios being of the same size in the upper mass range [which occurs for the choice $\tan\beta \sim 30$]. The decays into $\tau^+\tau^-, gg, c\bar{c}$ and also ZZ^* final states are at the level of a few percent and the loop induced decays into $\gamma\gamma$ and $Z\gamma$ at the level of a few per mille. The total decay width of the h boson is small, $\Gamma(h) \lesssim \mathcal{O}(10 \text{ MeV})$.

For the heavier Higgs bosons, the decay pattern depends on $\tan\beta$. For $\tan\beta \gg 1$, as a result of the strong enhancement of the Higgs couplings to down–type fermions, the neutral Higgs bosons H and A will decay almost exclusively into $b\bar{b}$ ($\sim 90\%$) and $\tau^+\tau^-$ ($\sim 10\%$) pairs; the $t\bar{t}$ decay when kinematically allowed and all other decays are strongly suppressed for $\tan\beta \sim 30$. The charged $H^\pm$ boson decays mainly into tb pairs but there is also a a significant fraction of $\tau\nu_\tau$ final states ($\sim 10\%$). For low values of $\tan\beta$, the decays of the neutral Higgs bosons into $t\bar{t}$ pairs and the decays of the charged Higgs boson in tb final states are by far dominating. [For intermediate values, $\tan\beta \sim 10$, the rates for the $H, A \to b\bar{b}$ and $t\bar{t}$ decays are comparable, while the $H^\pm \to \tau\nu$ decay stays at the few percent level]. For small and large $\tan\beta$ values, the total decay widths of the four Higgs bosons are, respectively, of $\mathcal{O}(1 \text{ GeV})$ and of $\mathcal{O}(10 \text{ GeV})$ as shown in Fig. 2.21.
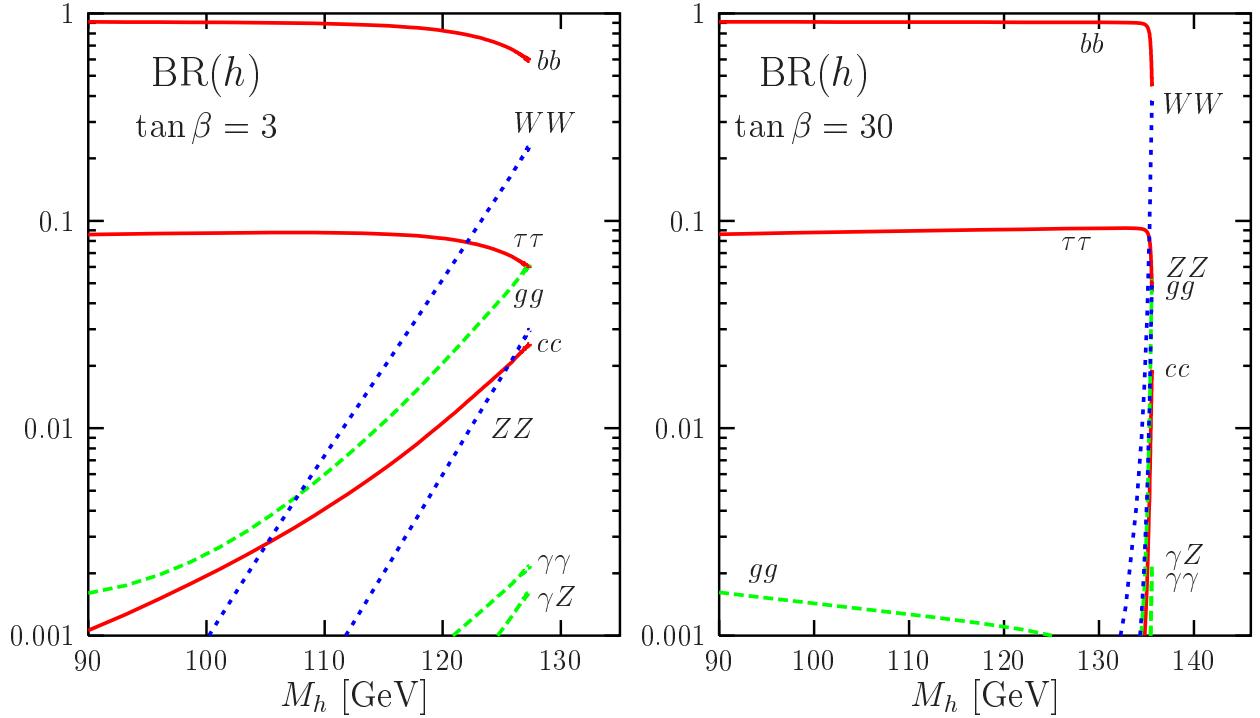
Figure 2.17: The decay branching ratios of the lighter CP–even MSSM h boson as a function of its mass for the two values $\tan\beta = 3$ *(left) and* $\tan\beta = 30$ *(right). The full set of radiative corrections in the Higgs sector has been included as described in the text.*
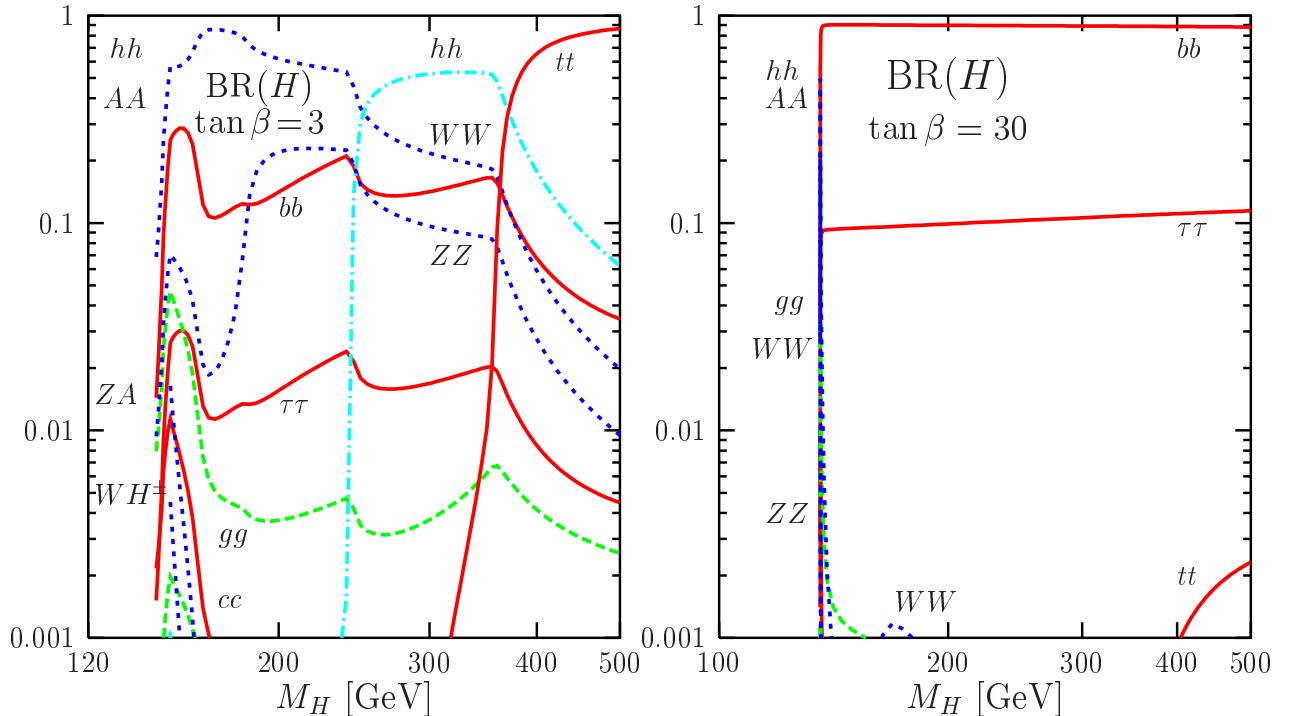

Figure 2.18: The decay branching ratios of the heavier CP–even MSSM H boson as a function of its mass for the two values $\tan\beta = 3$ *(left) and* $\tan\beta = 30$ *(right).*
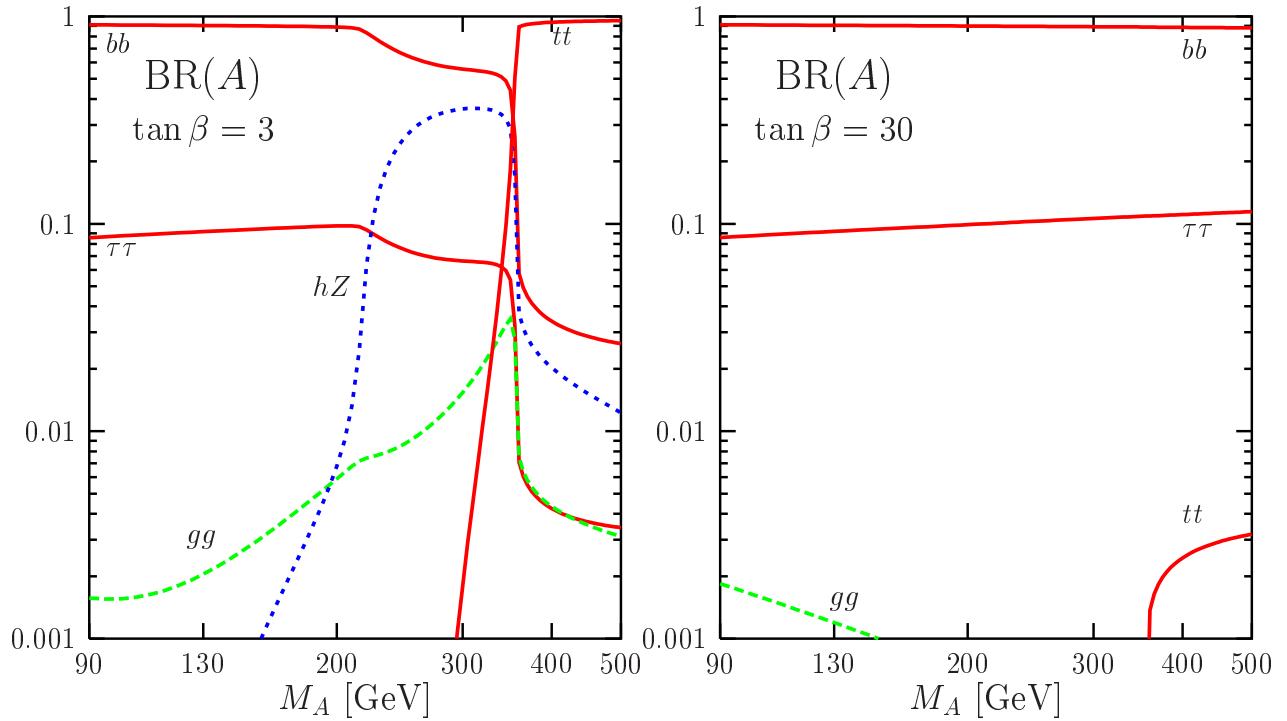
Figure 2.19: The decay branching ratios of the CP–odd MSSM Higgs boson as a function of its mass for the two values $\tan\beta = 3$ *(left) and* $\tan\beta = 30$ *(right).*
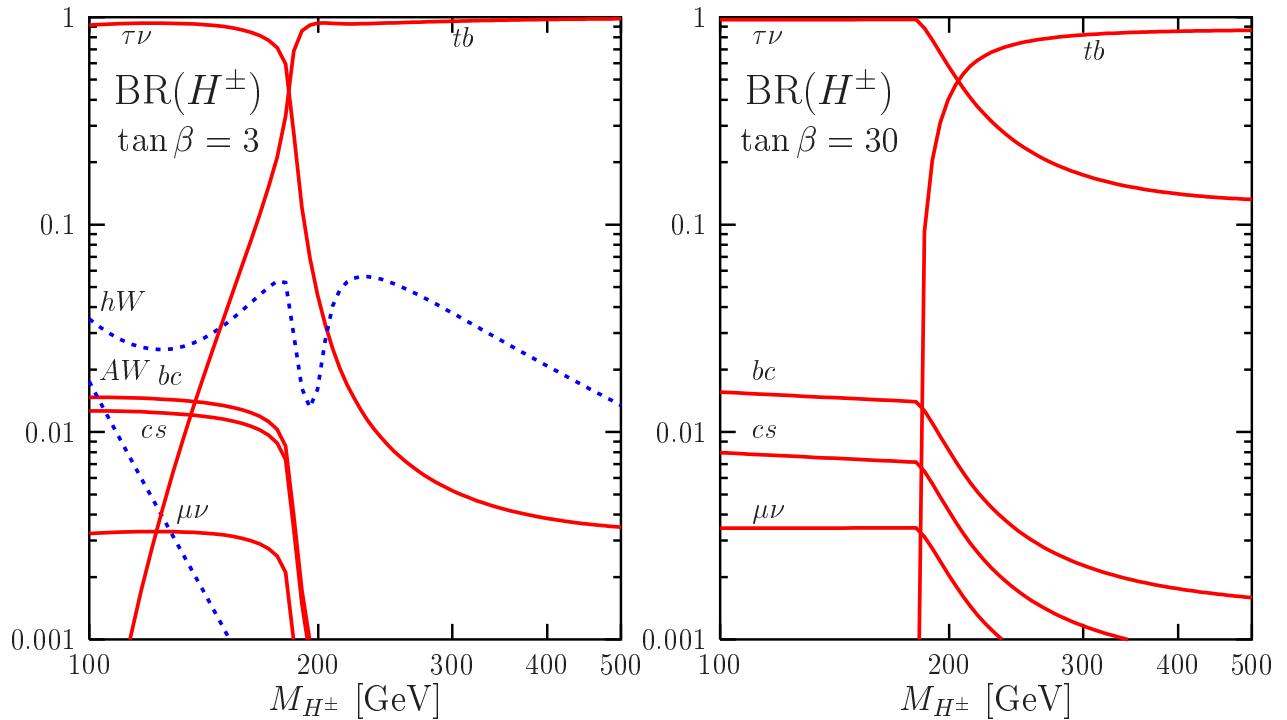
Figure 2.20: The decay branching ratios of the charged MSSM Higgs particles as a function of their mass for the two values $\tan\beta = 3$ *(left) and* $\tan\beta = 30$ *(right).*
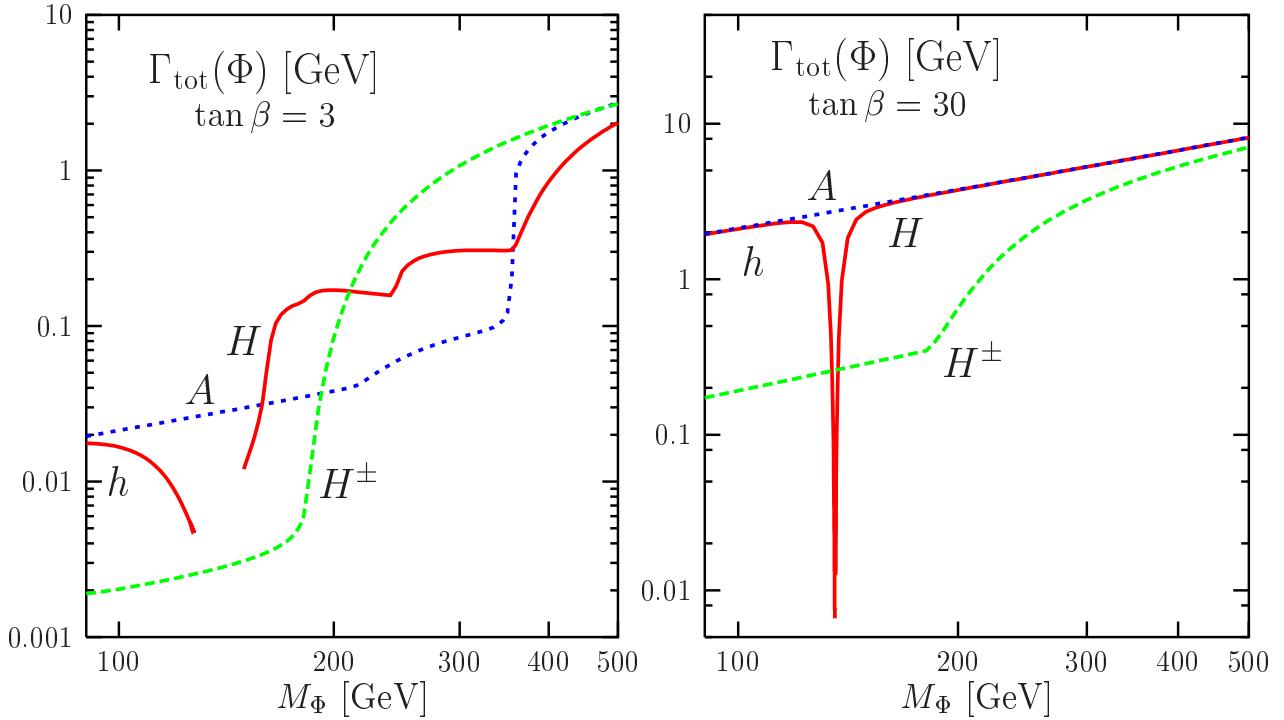
Figure 2.21: The total decay widths in GeV of the four MSSM Higgs particles h, H, A and $H^\pm$ as a function of their masses for the two values $\tan\beta = 3$ (left) and $\tan\beta = 30$ (right).

The anti–decoupling regime

The anti–decoupling regime corresponds in this case to $\tan\beta = 30$ and $M_A \lesssim 130$ GeV and the pattern for the Higgs decays is also rather simple. The lighter CP–even h and the CP–odd A bosons will mainly decay into $b\bar{b}$ ($\sim 90\%$) and $\tau^+\tau^-$ ($\sim 10\%$) pairs, while the charged $H^\pm$ boson decays almost all the time into $\tau\nu_\tau$ pairs ($\sim 100\%$). All other modes are suppressed down to a level below 10^{-3} except for the gluonic decays of the h and A bosons [in which the b–loop contributions are enhanced by the same $\tan\beta$ factor] and some fermionic decays of the $H^\pm$ boson [which, despite of the suppression by the CKM elements can reach the percent level because of the relatively small mass of the τ lepton which dominates the total decay]. Although their masses are small, the three Higgs bosons have relatively large total widths, $\Gamma(h, A, H^\pm) \sim \mathcal{O}(1 \text{ GeV})$ for $\tan\beta = 30$.

The heavier CP–even Higgs boson will have a mass $M_H \sim M_h^{\max}$ and will play the role of the SM Higgs boson or the lighter h boson in the decoupling regime, but with one major difference: in the low M_A range, the h and A particles are light enough for the two–body decays $H \to hh$ and $H \to AA$ to take place. When they occur, these decays are by far the dominant ones and have a branching fraction of $\sim 50\%$ each. However, in view of the LEP2 bound $M_A \sim M_h \gtrsim M_Z$, these channels are now kinematically closed and the three–body decays $H \to hh^* \to hb\bar{b}$ and $H \to AA^* \to Ab\bar{b}$ do not compete with the dominant $H \to b\bar{b}$ and $H \to WW^*$ decay modes. Thus, also the H boson is SM–like in this regime.

106

The intense–coupling regime

In the intense–coupling regime, which corresponds here to the scenario $\tan\beta = 30$ and $M_A \sim 120$–140 GeV, the couplings of both the CP–even h and H particles to gauge bosons and isospin up–type fermions are suppressed, while the couplings to down–type fermions, and in particular b–quarks and τ leptons, are strongly enhanced. Because of this enhancement, the branching ratios of the h and H bosons to $b\bar{b}$ and $\tau^+\tau^-$ final states are the dominant ones, with values as in the pseudoscalar Higgs case, i.e. $\sim 90\%$ and $\sim 10\%$, respectively.

This is exemplified in Fig. 2.22 where we display the branching ratios of the three bosons h, A and H but this time, as a function of the pseudoscalar Higgs mass in the range $M_A = 100$–140 GeV. As can be seen, the decays $H \to WW^*$ do not exceed the level of 1%, already for $M_A \gtrsim 120$ GeV, and in most of the range displayed for M_A, both the decays $H, h \to WW^*$ [and the decays into ZZ^* that are one order of magnitude smaller] are suppressed to the level where they are not useful anymore. The interesting rare decay mode into $\gamma\gamma$ [and the decay into $Z\gamma$ which has not been shown], which is at the level of a few times 10^{-3} in the SM, is very strongly suppressed for the three Higgs particles. Finally, note that the branching ratios for the decays into muons, $\Phi \to \mu^+\mu^-$, which have not been displayed earlier, are constant in the entire exhibited M_A range and are at the level of 3×10^{-4}. The charged Higgs boson in this scenario decays mostly into $\tau\nu$ final states.
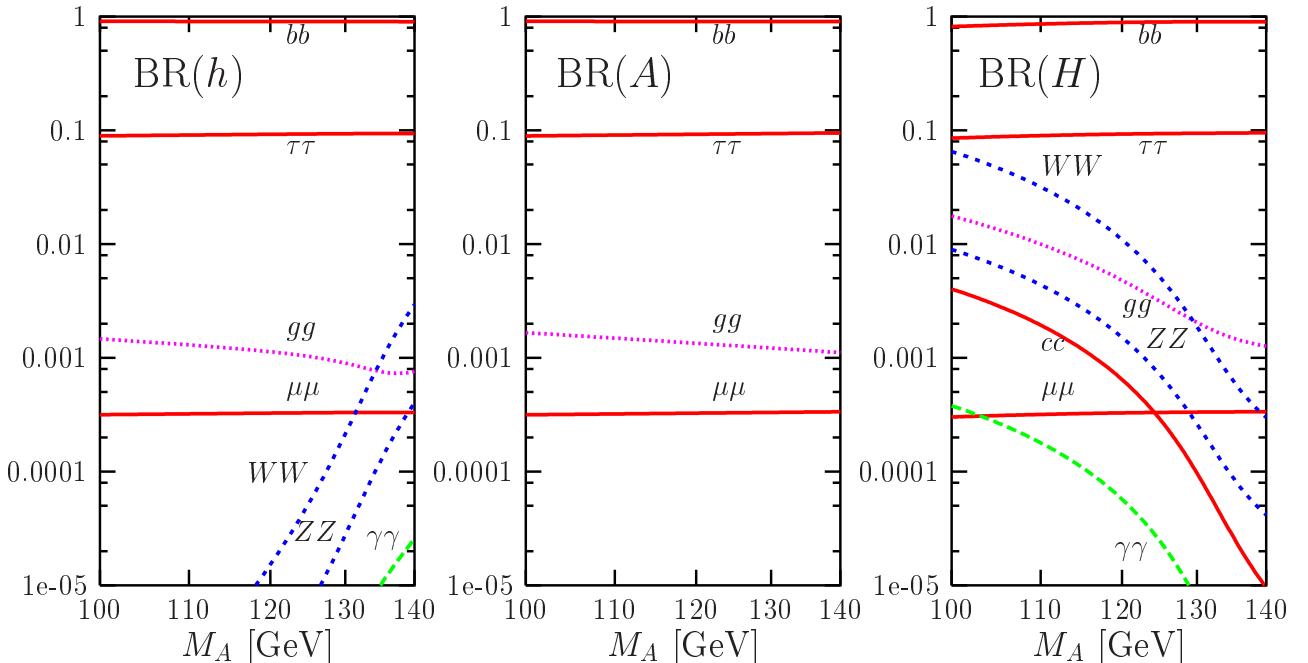
Figure 2.22: The decay branching ratios of the neutral MSSM h, H and A bosons as a function of M_A in the intense–coupling regime with $\tan\beta = 30$.

The intermediate–coupling regime

In the intermediate–coupling regime, i.e. for small values of $\tan\beta$ when the Higgs couplings to bottom quarks and τ leptons are not strongly enhanced, and for H/A masses below 350 GeV when the decays into top quark pairs are kinematically not accessible, interesting decays of the heavier neutral and charged Higgs bosons occur. To highlight the main features, we zoom on this region and display in Fig. 2.23 the branching ratios for the A, H and $H^\pm$ decays as a function of their masses for a value $\tan\beta = 2.5$, lower than previously as to enhance the specific decays. We also increase the value of m_t to evade the experimental bound on the lighter CP–even Higgs boson mass M_h in the low M_A range.

As can be seen, the decay $A \to hZ$ of the pseudoscalar Higgs boson is dominant when it is kinematically accessible, i.e. for masses $M_A \gtrsim 200$ GeV, with a branching ratio exceeding the 50% level. The $b\bar{b}$ and $\tau\tau$ decays are still significant, while the gg mode is visible; the below threshold three–body $A \to tt^*$ decay is also visible. In the case of the H boson, the decay $H \to hh$ is very important, reaching the level of 60% in a significant M_H range, the decays into weak vector bosons and $b\bar{b}$ pairs are still sizable. For the charged Higgs boson, the decay $H^\pm \to hW^\pm$ is at the level of a few percent, the other decay $H^\pm \to AW^\pm$ [which can be observed in Fig. 2.20] is kinematically challenged. Thus, in this intermediate–coupling regime, many interesting Higgs boson decay channels occur.
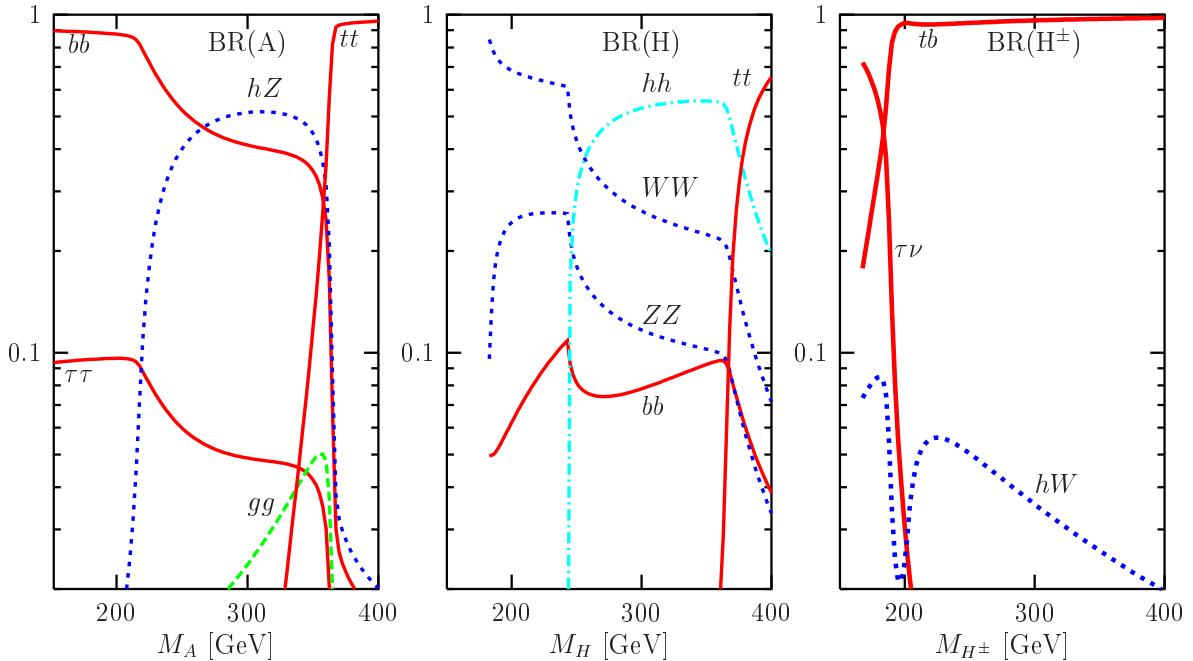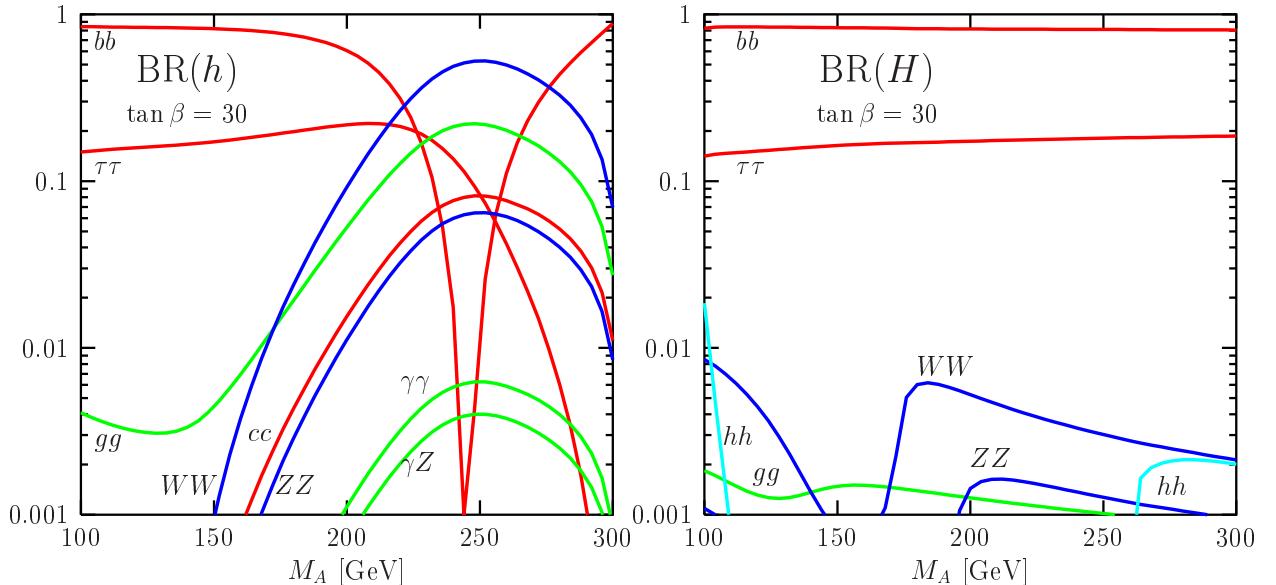
Figure 2.23: The decay branching ratios of the heavier MSSM Higgs particles A, H and $H^\pm$ as a function of their masses in the intermediate–coupling regime with $\tan\beta = 2.5$. The top mass is set to $m_t = 182$ GeV and only the branching ratios larger than 2% are displayed.

The vanishing–coupling regime

Finally, let us say a few words on the regime where the lighter CP–even Higgs couplings to bottom quarks and τ leptons accidentally vanish as a result of cancellations in the Higgs sector radiative corrections. As discussed earlier, this occurs at large values of $\tan\beta$ and moderate to large values of the pseudoscalar Higgs mass, $M_A \sim 150$–300 GeV. The branching ratios in such a scenario are shown in Fig. 2.24 for the CP–even Higgs bosons as a function of M_A for $\tan\beta = 30$; the relevant MSSM parameters are given in the caption. In the case of the H boson, there are a few differences compared to the decoupling regime; they are due to the fact that the b Yukawa coupling is smaller for the chosen large μ value in this scenario, resulting in an enhanced $\tau^+\tau^-$ rate [this will also be the case for the A boson]. In addition, the decays $H \to WW, ZZ$ are not too strongly suppressed and even the decay $H \to hh$ is potentially observable in the higher and lower M_A range.

For the lighter h boson, the decays into $b\bar{b}$ and $\tau\tau$ pairs will be strongly suppressed and, as a result, the other decay modes will be enhanced. In particular, $h \to WW^*$ becomes the dominant mode, reaching branching ratios of more than 50% even for h boson masses below 130 GeV. The decays into gluons and charm quarks will be also boosted reaching values of the order of 20% and 10%, respectively. The rare decays into $\gamma\gamma$ and $Z\gamma$ will be enhanced by $\sim 50\%$, since the total h boson decay width in the absence of the $h \to b\bar{b}$ decay is only approximately a factor of two smaller than in the SM, the $h \to WW^*$ channel being still present.

Figure 2.24: The decay branching ratios of the CP–even h and H bosons as a function of M_A for $\tan\beta = 30$ in the small α scenario. The other MSSM parameters are: $M_S = 0.7$ TeV, $M_2 = M_3 = \frac{1}{5}\mu = 0.5$ TeV, $X_t = 1.1$ TeV and $A_b = A_t$.

2.2 Effects of SUSY particles in Higgs decays

In the previous discussion, we have assumed that the SUSY particles are too heavy to substantially contribute to the loop induced decays of the neutral MSSM Higgs bosons and to the radiative corrections to the tree–level decays of all Higgs particles. In addition, we have ignored the Higgs decay channels into SUSY particles which were considered as being kinematically shut or strongly suppressed because of small couplings. However, as mentioned in the beginning of this chapter and, in view of the experimental limits of eq. (1.53), some SUSY particles such as the charginos, neutralinos and possibly sleptons and third generation squarks, could be light enough to play a significant role in this context. Their contributions to the h, H and A boson decays into $\gamma\gamma$ and gg final states can be large and they can alter significantly the other decay modes through radiative corrections. The decay channels of the MSSM Higgs particles into the various chargino/neutralino and sfermionic states and, eventually, the decays into gravitinos which occur in GMSB models as well as decays into gluinos which, if not ruled out, can occur in small corners of the MSSM parameter space, can be important. These aspects will be discussed in this section.

2.2.1 SUSY loop contributions to the radiative corrections

Besides the radiative corrections to the MSSM Higgs masses and the mixing angle α in the CP–even Higgs sector where, as we have seen previously, third generation sfermion loops play a very important role, the SUSY particles enter directly in the one–loop radiative corrections to the partial decay widths of the neutral and charged Higgs bosons [199–201]. In particular, because of the large value of α_s, squark/gluino loops can dramatically affect the pattern of the hadronic decays. The most important component of these corrections is in fact simply the SUSY threshold effects which alter the relations between the fermion masses and the Higgs Yukawa couplings at the one–loop level, as discussed earlier. There are additional direct contributions which, contrary to the latter and to the corrections to the mixing angle α which disappear when the SM limit is recovered for the lighter h boson, do not decouple in principle. However, and unfortunately, they are very small in general.

In the case of bottom quarks, this can be seen by inspecting the Yukawa Lagrangian of eq. (1.93) where one can notice two different contributions to the bare Higgs–$b\bar{b}$ interaction discussed in §1.2.3

$$
\begin{aligned}
\mathcal{L}_{\text{Yuk}} &\propto \lambda_b^0 \bar{b}_R \left[(1 + \delta\lambda_b/\lambda_b) H_1^0 + (\Delta\lambda_b/\lambda_b) H_2^{0*} \right] b_L \\
&= \lambda_b^0 \bar{b}_R \left[(1 + \Delta_1) H_1^0 + \Delta_2 H_2^{0*} \right] b_L
\end{aligned}
\tag{2.42}
$$

The renormalized Yukawa Lagrangian can be then written as

$$
\mathcal{L}_{\text{Yuk}} \propto \lambda_b \bar{b}_R \left[H_1^0 + \Delta_b H_2^{0*} \right] b_L
\tag{2.43}
$$

110

in terms of the renormalized coupling $\lambda_b = \lambda_b^0(1 + \Delta_1)$ and the already known quantity $\Delta_b = \Delta_2/(1 + \Delta_1)$. Taking into account only strong interactions, while the correction

$$\Delta_2^{\text{QCD}} \approx \frac{2}{3}\frac{\alpha_s}{\pi} m_{\tilde{g}} \mu \tan\beta \,/\, \max(m_{\tilde{b}_1}^2, m_{\tilde{b}_2}^2, m_{\tilde{g}}^2) \tag{2.44}$$

is proportional to $\tan\beta$ and, thus, can take large values for $\tan\beta \gtrsim 10$, the contribution Δ_1 at leading order is simply given by

$$\Delta_1^{\text{QCD}} \approx -\frac{2}{3}\frac{\alpha_s}{\pi} m_{\tilde{g}} A_b \,/\, \max(m_{\tilde{b}_1}^2, m_{\tilde{b}_2}^2, m_{\tilde{g}}^2) \tag{2.45}$$

and does not increase with $\tan\beta$. In fact, as it is proportional to $m_{\tilde{g}} A_b/M_S^2$ for relatively light gluinos, and since A_b cannot take arbitrarily large values compared to M_S because of the CCB constraint $A_b^2 \lesssim 3(2M_S^2 + m_{H_1}^2)$, the correction is in general very small. This is exemplified in Fig. 2.25 where the two corrections Δ_2 (left) and Δ_1 (right) are shown for the three neutral Higgs bosons for $\tan\beta = 30$ as a function of M_A in a scenario where squarks and gluinos are very heavy and the mixing in the sbottom sector is very large, $A_b = -\mu\tan\beta$ with $\mu = -150$ GeV [201]. While Δ_2 is of $\mathcal{O}(10\%)$ in this case and thus of moderate size [note that μ is small in this scenario and the correction will increase with $|\mu|$] the Δ_1 contribution is only of $\mathcal{O}(1\%)$ except in the case of the H boson in the anti–decoupling regime, where it can reach a similar magnitude as Δ_2. Thus, in general, one can neglect the Δ_1 term and simply use the approximation where only the resummed $\Delta_b \sim \Delta_2$ correction is included.
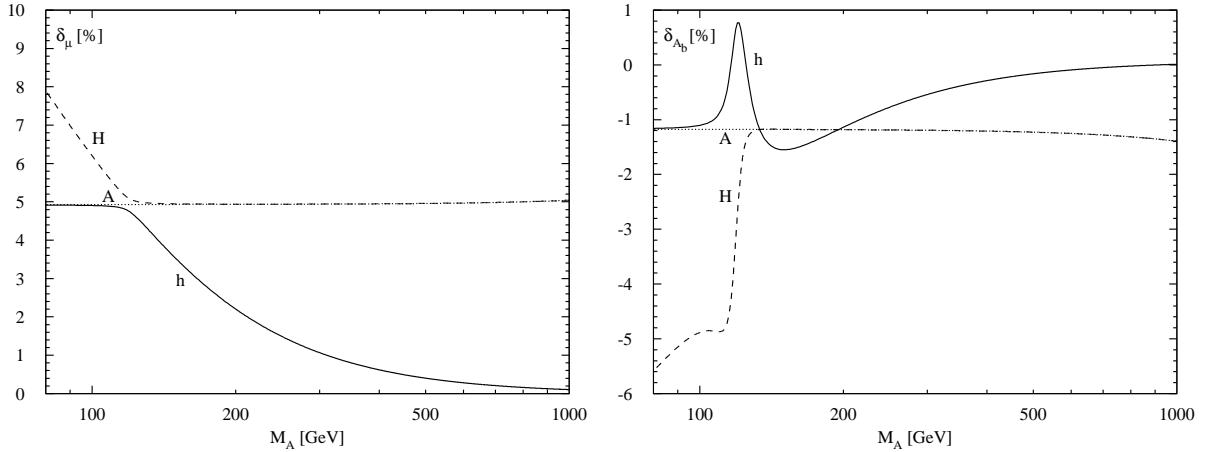
Figure 2.25: Relative corrections due to the Δ_b component including the resummation (left) and to the term Δ_1 (right) as a function of M_A for the three neutral Higgs bosons. The corrections are normalized to the QCD corrected decay widths; from Ref. [201].

The Δ_2 correction generates a strong variation of the $b\bar{b}$ partial widths of the three Higgs bosons which can reach the level of 50% for large μ and $\tan\beta$ values and not too heavy squarks and gluinos [note that gluinos decouple only slowly and their effect can still be felt

for masses of the order of a few TeV]. However, it has only a small impact on the $b\bar{b}$ branching ratios since this decay dominates the total widths of the Higgs particles. In turn, it can have a large influence on the branching ratios for the other decay modes and, in particular, on the $\Phi \to \tau^+\tau^-$ channels. This can be seen in the left–hand side of Fig. 2.26 where the branching ratios for the two modes are shown as a function of M_A in the usual maximal mixing scenario. In the case of the heavier Higgs bosons with masses above the $t\bar{t}$ threshold and for intermediate $\tan\beta$ values when the $b\bar{b}$ and $t\bar{t}$ channels compete with each other, these corrections can be felt by both the $H/A \to b\bar{b}$ and $t\bar{t}$ branching ratios. This is shown in the right–hand side of Fig. 2.26 where the two branching fractions are displayed as a function of M_A in the same scenario as previously but for the value $\tan\beta = 10$.
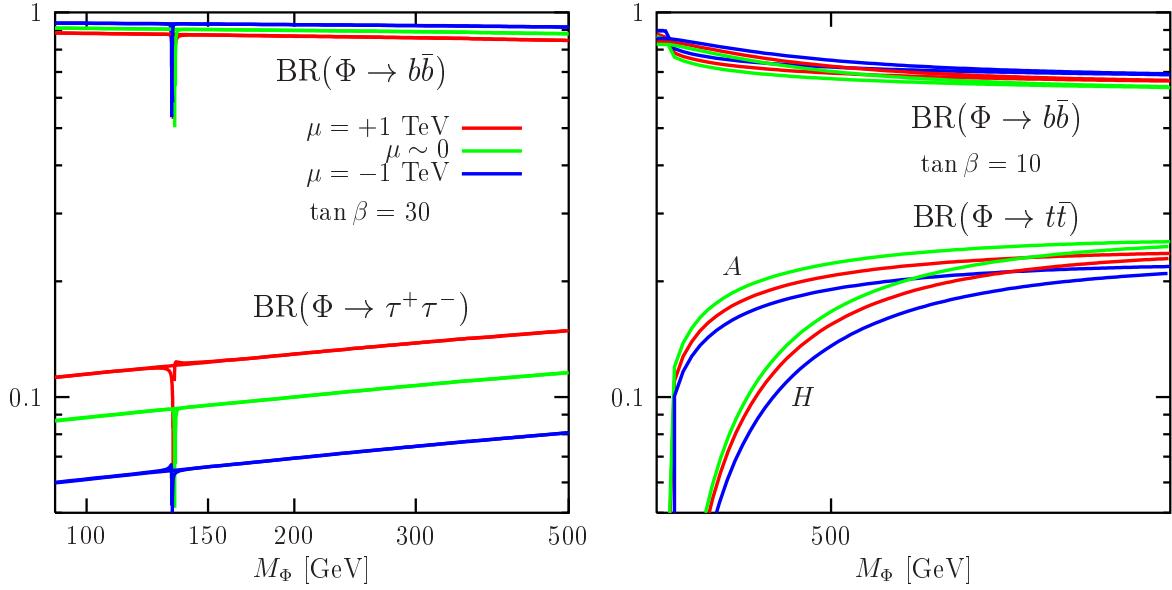
Figure 2.26: The branching ratios for the decays of the three neutral Higgs bosons into $b\bar{b}, \tau\tau$ for $\tan\beta = 30$ (left) and of the heavier H/A bosons into $b\bar{b}, t\bar{t}$ for $\tan\beta = 10$ (right) in the maximal mixing scenario with $M_S = m_{\tilde{g}} = 1$ TeV, including the SUSY–QCD corrections for $\mu = \pm 1$ TeV and without the SUSY–QCD corrections ($\mu \sim 0$).

The same features occur in the case of the charged Higgs boson decays into tb final states [207, 208]. Besides the SUSY–QCD corrections which strongly affect the component of the H^+tb coupling involving the b–quark mass, there are also SUSY–EW corrections which appear through both the top and bottom components of the coupling and which are also potentially large. In particular, the weak correction that is present in the Δ_2 term

$$\Delta_2^{\mathrm{EW}} \approx \frac{h_t^2}{16\pi^2} A_t \mu \tan\beta \,/\, \max(\mu^2, m_{\tilde{t}_1}^2, m_{\tilde{t}_2}^2) \tag{2.46}$$

involves the top–quark Yukawa coupling and is also enhanced at large $\tan\beta$ and μ, as well as for large A_t values. The radiative corrections to the top quark component of the coupling might also be important as they increase with $\alpha_s \mu A_t/M_S^2$ and $\lambda_b^2 \mu^2/M_S^2$, eq. (1.48).

112

The various corrections are shown in the case of the partial width $\Gamma(H^+ \to t\bar{b})$ in Fig. 2.27 as a function of μ for $\tan\beta = 30$ (left) and as a function of $\tan\beta$ for $\mu = -200$ GeV (right); the other parameters are as indicated in the captions [208]. It is apparent that the SUSY–EW corrections reach the level of the SUSY–QCD ones and both of them are of the same size as the standard QCD corrections. The total correction in the MSSM can be either very large or very small, depending on the sign of the SUSY corrections, and more precisely on the sign of μ. The Higgs correction, which is shown separately, is very small.
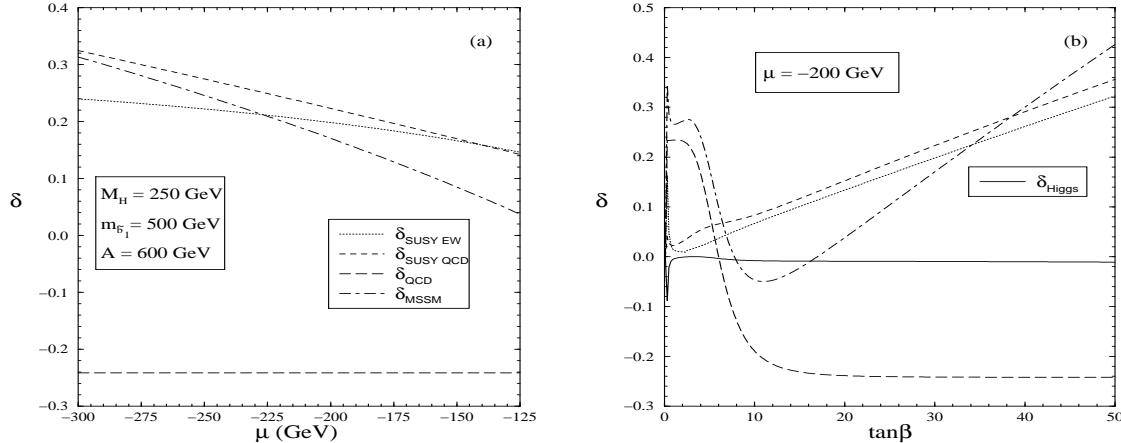
Figure 2.27: The SUSY–EW, SUSY–QCD, standard QCD and the full MSSM contributions as a function of μ with $\tan\beta = 30$ (left) and $\tan\beta$ for $\mu = -200$ GeV where the Higgs contribution is also shown (right); the other inputs are as indicated. From Ref. [208].

Again, these corrections can be more efficiently pinned down by looking at the branching ratio of a decay mode that is not dominant which, in this context, is generally the case of the $H^+ \to \tau^+\nu$ decay. This is exemplified in Fig. 2.28 where one can see that $BR(H^+ \to \tau^+\nu)$ is very sensitive to the SUSY–QCD corrections appearing in the $H^+ \to t\bar{b}$ decay [208].
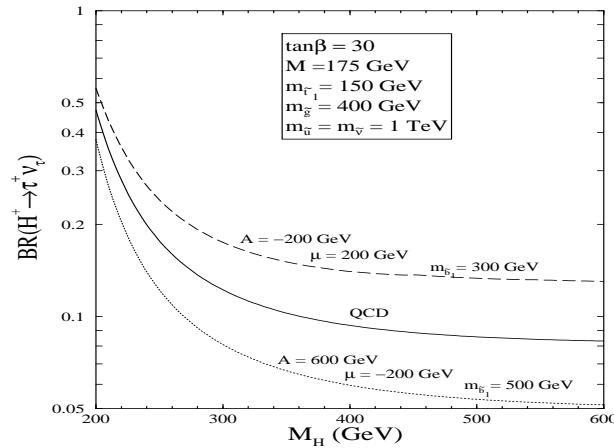
Figure 2.28: $BR(H^+ \to \tau^+\nu_\tau)$ as a function of the $H^\pm$ mass when SUSY–QCD corrections are included in the decay $H^+ \to t\bar{b}$; the various parameters are as listed. From Ref. [208].

113

2.2.2 Sparticle contributions to the loop induced decays

The gluonic decays

If squarks are relatively light, they can induce sizable contributions to the loop induced decays of the CP–even Higgs bosons into two gluons, $\mathcal{H} \rightarrow gg$ with $\mathcal{H} = h, H$. Due to the combined effect of CP–conservation which forbids couplings of the A boson to identical $\tilde{q}_i \tilde{q}_i$ states and SU(3) gauge invariance which forbids gluon couplings to mixed $\tilde{q}_1 \tilde{q}_2$ states, SUSY loops do not contribute to $A \rightarrow gg$ at the one–loop level but only at two–loop when virtual gluinos are exchanged withs squarks; in this case, the contribution is expected to be small. The squark loop contribution to the $\mathcal{H}gg$ amplitude, which has to be added coherently to the standard contribution of heavy quarks, eq. (2.38), is given by [41]

$$\mathcal{A}^{\mathcal{H}}_{\text{SUSY}} \equiv \mathcal{A}^{\mathcal{H}}_{\tilde{Q}} = \sum_{\tilde{Q}_i} \frac{g_{\mathcal{H}\tilde{Q}_i\tilde{Q}_i}}{m^2_{\tilde{Q}_i}} A^{\mathcal{H}}_0(\tau_{\tilde{Q}}) \tag{2.47}$$

where $\tau_{\tilde{Q}} = M^2_{\mathcal{H}}/4m^2_{\tilde{Q}}$ with $m_{\tilde{Q}}$ denoting the loop mass, and where the form factor for spin–zero particles, $A^{\mathcal{H}}_0(\tau_{\tilde{Q}})$, as well as the Higgs couplings to squarks have been given previously. Since squarks, and in general all SUSY particles, do not acquire their masses through the Higgs mechanism and their couplings to the Higgs bosons are not proportional to their masses, the contributions of these scalar particles are damped by loop factors $1/m^2_{\tilde{Q}}$. Thus, contrary to the case of SM quarks, the contributions become very small for high masses and the sparticles decouple completely from the gluonic Higgs couplings if they are very heavy.

However, when they have masses of the order of the Higgs boson masses, squark contributions can be significant. This is particularly true in the case of top squarks in the decays of the lighter h boson, $h \rightarrow gg$. The reason is two–fold:

(i) the mixing in the the stop sector, proportional to the off–diagonal entry $m_t X_t$ of the stop mass matrix, can be very large and could lead to a top squark $\tilde{t}_1$ that is much lighter than all the other scalar quarks and even lighter than the top quark;

(ii) the coupling of top squarks to the h boson in the decoupling regime, for instance $g_{h\tilde{t}_1\tilde{t}_1}$ given in eq. (1.109), involves a component which is proportional to m_t and X_t and for large values of the latter parameter, the coupling can be strongly enhanced.

Combining the two effects, the amplitude for squarks can be of the same order as the one for quarks, despite of the smaller value of the form factors for spin–zero particles, $A^{\mathcal{H}}_0 \sim \frac{1}{3}$, compared to the one of spin–$\frac{1}{2}$ particles, $A^{\mathcal{H}}_{1/2} \sim \frac{4}{3}$, in the limit $\tau \rightarrow 0$. The mixing in the sbottom sector, $m_b X_b = (A_b - m_b \mu \tan\beta)$, can also be sizable for large $\tan\beta$ and μ values and can lead to light $\tilde{b}_1$ states with strong couplings to the h boson. Both $\tilde{t}$ and $\tilde{b}$ states could then dramatically change the rate for the $h \rightarrow gg$ decay even in the decoupling limit where the h boson should in principle behave as the SM Higgs boson [239].

This is exemplified in Fig. 2.29 where, in the left–hand side, the deviation of the branching ratio BR($h \rightarrow gg$) in the MSSM from its SM value, as a result of contributions of top squarks with masses $m_{\tilde{t}_1} = 200$ and 400 GeV, is shown as a function of X_t for $\tan\beta = 2.5$ and $M_A = 1$ TeV. For small values of X_t there is no mixing in the stop sector and the dominant component of the $h t \tilde{t}$ couplings in eq. (1.109) is $\propto m_t^2$. In this case, the t and $\tilde{t}_{1,2}$ contributions interfere constructively in the hgg amplitude and lead to an enhancement of BR($h \rightarrow gg$). With increasing X_t, the two components of $g_{h\tilde{t}_1\tilde{t}_1}$ interfere destructively and partly cancel each other, resulting in a rather small stop contribution. For larger values of X_t, the last component of $g_{h\tilde{t}_1\tilde{t}_1}$ becomes the most important one and the $\tilde{t}_1$ loop contribution interferes destructively with the t–loop one leading to a reduction of BR($gg \rightarrow h$). For very large values, $X_t \sim 1.5$ TeV, the branching can be reduced by an order of magnitude if the stop is light enough, $m_{\tilde{t}_1} \sim 200$ GeV.
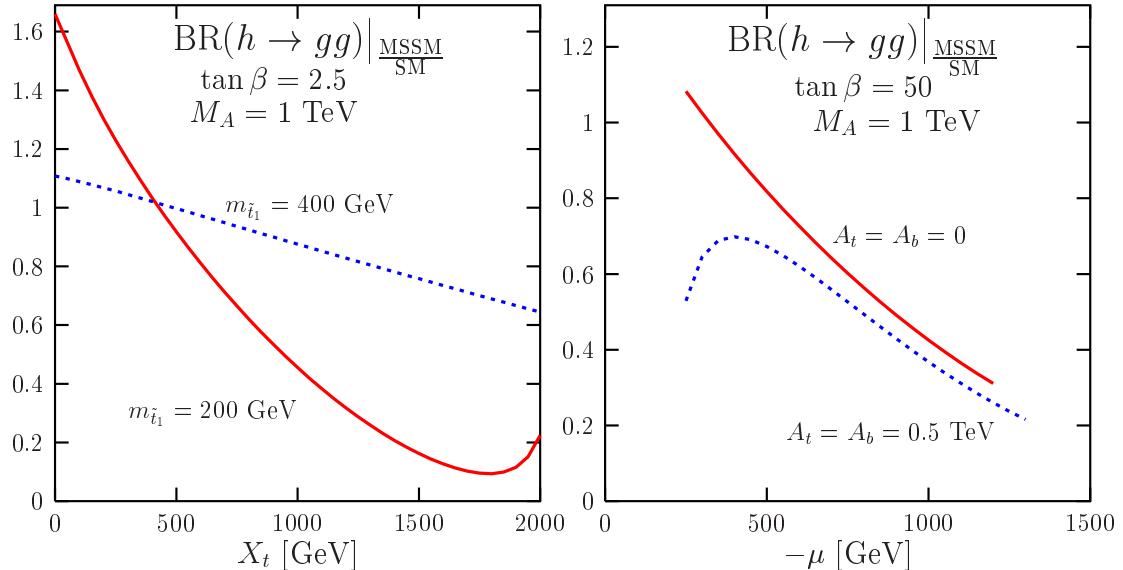
Figure 2.29: The branching ratio for the gluonic decay of the h boson in the MSSM relative to its SM value, BR($h \rightarrow gg$)|$_{\mathrm{MSSM/SM}}$, in various scenarios where the top and bottom squarks contribute. The choice of the SUSY parameters is as listed in the figures.

In the right–hand side of Fig. 2.29, the deviation BR($h \rightarrow gg$) from its SM value, as a result of the contributions of a light sbottom with $m_{\tilde{b}_1} = 200$ GeV, is shown as a function of $-\mu$ for $\tan\beta = 50$ and again $M_A = 1$ TeV; the trilinear couplings have been chosen to be $A_t = A_b = 0$ or 0.5 TeV. As can be seen, the effects can be sizable for large μ values, leading to a reduction of BR($h \rightarrow gg$) by a factor up to 5. Thus, both stop and sbottom contributions can render the gluonic width and branching ratio of the h boson very small, even in the decoupling regime where it is supposed to be SM–like. This feature is rather important also for the production of the MSSM h boson at hadron colliders since the cross section for the dominant mechanism $gg \rightarrow h$ is proportional to the gluonic width.

The relative weight of the quark and squark loops can be altered by the QCD radiative corrections and those affecting the SUSY loops should be thus considered. In the case of vanishing mixing between the two squark eigenstates [which should give a rough idea on the size of the effect in the general case], these corrections fall into two categories:

i) The standard corrections to the scalar quark loops, where only gluons are exchanged between the internal squark or the external gluon lines; there are also diagrams involving the quartic squark interaction. These are the only corrections which appear in a scalar QCD theory [which is not the case of the MSSM] and they can be calculated in the large squark mass limit using the low–energy theorem discussed in §I.2.4. The squark contribution to the QCD β function [244] and the anomalous squark mass dimension [245] being

$$\beta_{\tilde{Q}}(\alpha_s) = \frac{\alpha_s^2}{12\pi}\left[1 + \frac{11}{2}\frac{\alpha_s}{\pi}\right] \ , \ \ \gamma_{m_{\tilde{Q}}} = \frac{4}{3}\frac{\alpha_s}{\pi} \tag{2.48}$$

the virtual QCD correction to the squark amplitude [the QCD real corrections are the same as for the quark loops, since the squarks are assumed to be too heavy to be produced] is given at NLO by [246]

$$\mathcal{L}_{\text{eff}} = \frac{\alpha_s}{48\pi}G^{a\mu\nu}G^a_{\mu\nu}\frac{\mathcal{H}}{v}\left[1 + \frac{25}{6}\frac{\alpha_s}{\pi}\right] \tag{2.49}$$

The correction factor to the total $\mathcal{H}gg$ amplitude will be then given by eq. (2.40), but with the addition of the $\Delta E_{\mathcal{H}}^{\tilde{Q}}$ contribution of squarks

$$\Delta E_{\mathcal{H}}^{\tilde{Q}} = \frac{17}{6}\text{Re}\frac{\sum_{\tilde{Q}_i} g_{\mathcal{H}\tilde{Q}_i\tilde{Q}_i}A_0^{\mathcal{H}}(\tau_{\tilde{Q}})}{\sum_Q g_{\mathcal{H}QQ}A_{1/2}^{\mathcal{H}}(\tau_Q)} \ \ \text{for } M_{\mathcal{H}}^2 \ll 4m_{Q,\tilde{Q}}^2 \tag{2.50}$$

ii) However, in a SUSY theory where one component of the Higgs coupling to squarks is proportional to the quark masses and another to the trilinear couplings which are both affected by strong interactions, one also needs to perform the QCD renormalization of the coupling. This will induce additional contributions [247, 248] that are ultraviolet divergent and which are canceled only if two–loop diagrams involving the exchange of gluinos are added to the pure squark loop diagrams [as mentioned previously, such diagrams will also induce a coupling of the pseudoscalar A boson to two gluons, which is absent at the one–loop level]. In fact, the gluino gives contributions that are logarithmic in its mass and they decouple only if both squark and gluinos are made very heavy at the same time. Because of the many masses involved in the problem, the analytical expressions of these contributions are rather complicated even for heavy gluinos and squarks. However, in the important case of top squarks in the limit $m_{\tilde{g}} \gg m_{\tilde{t}_L} \sim m_{\tilde{t}_R} \sim m_t$ where large contributions are expected at LO, one finds a simple and compact expression for the NLO correction factor to the amplitude induced by the gluino loops [247]

$$\Delta E_{\mathcal{H}}^{\text{SUSY}} \simeq 2\left(\frac{11}{12} + \frac{4}{9}\log\frac{m_t^2}{m_{\tilde{g}}^2}\right) \tag{2.51}$$

116

This correction is much smaller that the one for the fermion loop, a few percent for $m_{\tilde{g}} \sim 1$ TeV and $m_{\tilde{t}_L} \sim m_{\tilde{t}_R} \lesssim 2m_t$ [247]. The gluonic h decay width is shown in Fig. 2.30 in the case where the SUSY loop contributions are included (thick lines) and when only SM quarks are involved (thin lines) in two scenarios [248]. In the left–hand side, the variation is with respect to the gaugino mass parameter $m_{1/2}$ defined at the GUT scale in the SPS1a mSUGRA scenario [249] with $m_0 = -A_0 = 100$ GeV, $\tan\beta = 10$ and $\text{sign}(\mu) > 0$, while in the right–hand side the variation is with the mass of the heavier stop $m_{\tilde{t}_2}$ in a "gluophobic" scenario where the top and stop loops nearly cancel each other at LO, $m_{\tilde{t}_L} = 200$ GeV, $\theta_t = \frac{\pi}{4}$ and $\tan\beta = 10$. In both cases, we are in the decoupling regime and only the top quark and the top squark loop contributions are relevant. The full NNLO contribution is of course included only for the quark loop since it is not yet available for the squark contribution. As can be seen, in the SPS1a scenario, the stop contributions are in general modest except for relatively small $m_{1/2}$ values which lead to light gluinos, $m_{\tilde{g}} \sim 2.5m_{1/2} \sim 250$ GeV, and light $\tilde{t}$ states. In contrast, the impact of the NLO and NNLO corrections is very important in the gluophobic scenario, when the hgg coupling nearly vanishes, since they change the point at which the cancellation of the squark and quark contributions occurs.
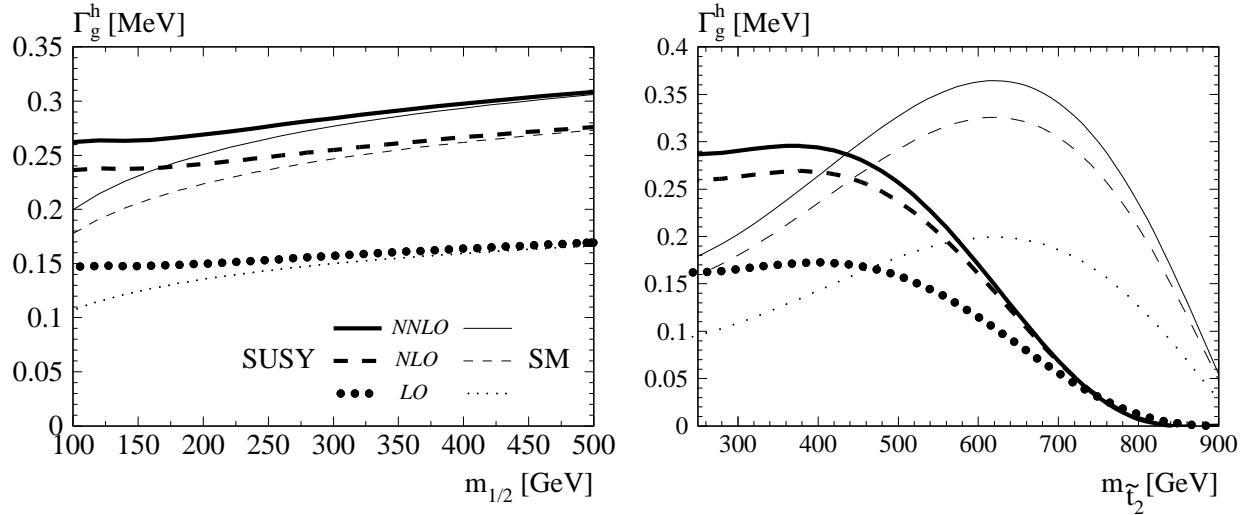
Figure 2.30: *The partial decay width $\Gamma(h \to gg)$ at LO (dotted) NLO (dashed) and NNLO (solid lines) where the thick (thin) lines are with (without) the squark contributions: as a function of $m_{1/2}$ in the SPS1a mSUGRA type model (left) and as a function of $\tilde{t}_2$ in a "gluophobic" Higgs scenario; from Ref. [248].*

The two–photon decays

Besides the loop contributions built up by W bosons, fermions and charged Higgs bosons in the case of the $\mathcal{H} = h, H$ bosons and fermions only in the case of the A boson, the $\gamma\gamma$ couplings of the MSSM neutral Higgs bosons are mediated by sfermion and chargino loops in the $\mathcal{H}\gamma\gamma$ case and chargino loops in the case of the $A\gamma\gamma$ coupling [38, 217, 219]. The partial

decay widths, including the standard contributions, have been given in eq. (2.23) and the amplitudes of the additional SUSY particles are given by [41]

$$
\mathcal{A}_{\mathrm{SUSY}}^{\mathcal{H}} \equiv \mathcal{A}_{\chi^{\pm}}^{\mathcal{H}} + \mathcal{A}_{\tilde{f}}^{\mathcal{H}} = \sum_{\chi_i^{\pm}} \frac{2M_W}{m_{\chi_i^{\pm}}} g_{\mathcal{H}\chi_i^{+}\chi_i^{-}} A_{1/2}^{\mathcal{H}}(\tau_{\chi_i^{\pm}}) + \sum_{\tilde{f}_i} \frac{g_{\mathcal{H}\tilde{f}_i\tilde{f}_i}}{m_{\tilde{f}_i}^2} N_c Q_{\tilde{f}_i}^2 A_0^{\mathcal{H}}(\tau_{\tilde{f}_i})
$$

$$
\mathcal{A}_{\mathrm{SUSY}}^{A} \equiv \mathcal{A}_{\chi^{\pm}}^{A} = \sum_{\chi_i^{\pm}} \frac{2M_W}{m_{\chi_i^{\pm}}} g_{A\chi_i^{+}\chi_i^{-}} A_{1/2}^{A}(\tau_{\chi_i^{\pm}}) \tag{2.52}
$$

In the case of the $h \to \gamma\gamma$ decay, the contributions of the charged sleptons and the scalar partners of the light quarks are, similarly to those of the charged Higgs bosons, extremely small. This is a consequence of the fact that these particles do not couple to the Higgs bosons proportionally to their masses [as the masses are generated by soft SUSY–breaking terms and not through the Higgs mechanism] and the amplitudes are damped by inverse powers $1/m_{\tilde{f}}^2$. In addition, the Higgs couplings to these particles are in general very small and the amplitude for spin–0 particles is much smaller than the dominant W amplitude. In the decoupling regime, these contributions are negligible compared to the largely dominating W boson contribution since the hWW couplings is not suppressed in this case.

A detailed analysis of the contribution of the additional MSSM particles to the two photon decay mode of the lighter CP–even Higgs boson in the decoupling regime has been performed in Ref. [219] with the conclusion that only the lighter chargino and third generation squarks can have a significant effect if their masses are not far above the present experimental bounds. The contributions of the charginos to the partial decay width, which are only damped by powers $1/m_{\chi_i^{\pm}}$ for high loop masses compared to the $1/m_{\tilde{f}}^2$ suppression for sfermions, can exceed the 10% level for masses close to $m_{\chi_1^{\pm}} \sim 100$ GeV, in particular when $\chi_1^{\pm}$ is a mixed gaugino–higgsino state in which case its couplings to the h boson are enhanced. The chargino contributions become rather small for masses above $m_{\chi_1^{\pm}} \gtrsim 250$ GeV.

Because of the same reasons given just previously for the $h \to gg$ case, the top squark and to a lesser extent the bottom squark, can generate sizable contributions to the $h \to \gamma\gamma$ partial width. For stop masses in the ~ 200 GeV range and for large values of X_t, the SUSY contribution could reach the level of the dominant W boson contribution and the interference is constructive increasing significantly the decay width. In the no–mixing case, the stop contributions is smaller because of the smaller $g_{h\tilde{t}_1\tilde{t}_1}$ coupling but leads to a destructive interference. This is shown in the left–hand side of Fig. 2.31 where the deviation of the branching ratio BR($h \to \gamma\gamma$) in the MSSM from its SM value is displayed in the same scenario as for the $h \to gg$ case discussed above.

In the right–hand side of the figure, the effects of a light sbottom are shown for, again, the same scenario as in the $h \to gg$ decay. In this case, the effects are much smaller than in the previous scenario, where stop contributions where dominant, because of the smaller

118

$g_{h\tilde{b}_1\tilde{b}_1}$ coupling compared to $g_{h\tilde{t}_1\tilde{t}_1}$ and the smaller electric charge $Q_b = -\frac{1}{2}Q_t$ and, of course, because of the dominance of the W contribution. Note that in this figure, both the stop and chargino contributions are included; the latter can be visualized for $A_t = A_b = 0.5$ where it leads to a $\sim 10\%$ deviation from unity, as discussed earlier.
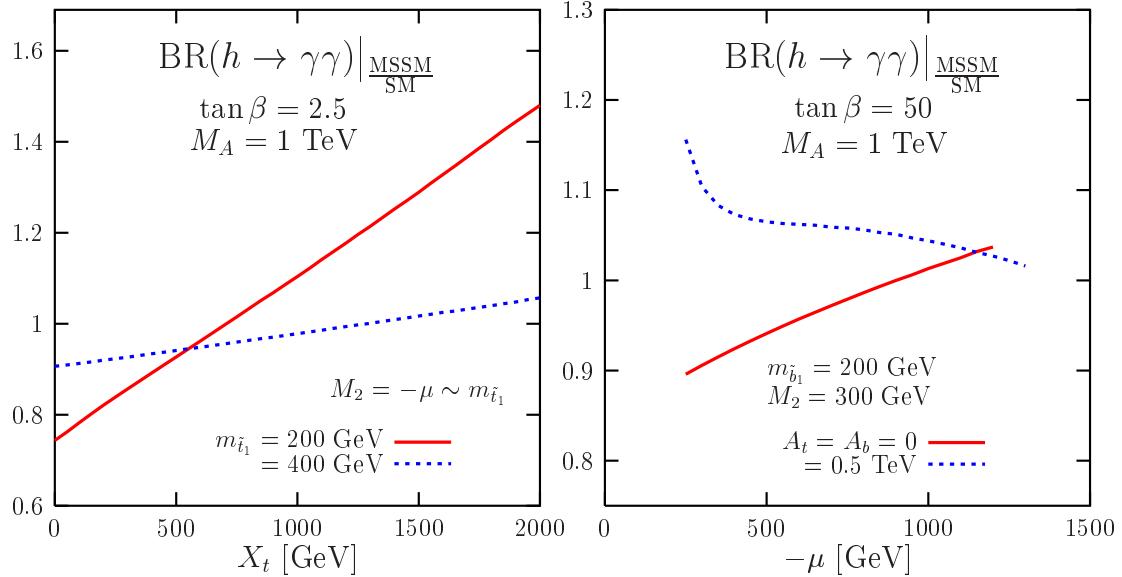

Figure 2.31: *The branching ratio for the two–photon decay of the h boson in the MSSM relative to its SM value, $BR(h \to \gamma\gamma)|_{\mathrm{MSSM/SM}}$, in various scenarios where the SUSY particles contribute. The choice of the SUSY parameters is as listed in the figures.*

For the heavier CP–even and CP–odd Higgs bosons [for the H boson in the anti–decoupling regime, the previous discussion for the lighter h particle approximately holds], the contributions of the SUSY particles can be rather large. Indeed, charginos and sfermions can have masses that are comparable to the Higgs masses and, therefore, do not decouple and the W contribution is absent or strongly suppressed. The top quark contribution is also suppressed and the bulk of the coupling can be provided by the SUSY loop contributions. However, for large $\tan\beta$ values, the b–quark loop contribution will be strongly enhanced and the SUSY contributions will then hardly compete.

Finally, the QCD corrections to the squark loops for the $\mathcal{H} \to \gamma\gamma$ decays are available only in a purely scalar QED. In this case, they are similar to the corresponding component of the $\mathcal{H} \to gg$ decays discussed earlier except that, here, the heavy squark contribution to the QED β function is $\beta_\alpha^{\tilde{Q}} = \frac{\alpha}{2\pi}[1 + 4\frac{\alpha_s}{\pi}]$ [244] which leads to an effective NLO Higgs–$\gamma\gamma$ coupling [and in the limit $M_Z \ll m_{\tilde{Q}}$, Higgs–$Z\gamma$ coupling] [219]

$$\mathcal{L}_{\mathrm{eff}} = g_{\mathcal{H}\tilde{Q}\tilde{Q}} Q_{\tilde{Q}}^2 \frac{\alpha}{8\pi} F^{\mu\nu} F_{\mu\nu} \frac{\mathcal{H}}{v} \left[1 + \frac{8}{3}\frac{\alpha_s}{\pi}\right] \tag{2.53}$$

This component of the QCD correction is small, increasing the amplitude by a mere 10%.

The decays into $Z\gamma$ final states

In principle, the contributions of the SUSY particles [228, 229] to the loop induced Higgs couplings to $Z\gamma$ final states [to our knowledge, the full sparticle contributions to the $H^\pm \to \gamma W^\pm$ and $ZW^\pm$ decays have not been discussed in the literature] lead to slightly more involved analytical expressions than for the two–photon coupling. This is due to the mixing in the sfermion sector and the possibility of having a non diagonal $Z\tilde{f}_1\tilde{f}_2$ coupling [which is absent in the two–photon case as a result of electromagnetic gauge invariance] and Higgs–$\tilde{f}_1\tilde{f}_2$ transitions; this is also the case in the chargino sector where couplings of Higgs and Z bosons to $\chi_1^+\chi_2^-$ mixtures are present. The complete analytical form of the decay amplitudes, including these transitions, can be found in Ref. [229]. However, the effects of the mixing are in general small and can be ignored for most purposes[19]. In this case, only identical sfermions and charginos will be running in the loops and the analytical expressions of the amplitudes of these SUSY particles simplify to [41]

$$
\begin{aligned}
\mathcal{A}_{\text{SUSY}}^{\mathcal{H}} &= \sum_{\tilde{f}_i} \frac{g_{\mathcal{H}\tilde{f}_i\tilde{f}_i}}{m_{\tilde{f}_i}^2} N_c Q_{\tilde{f}_i} v_{\tilde{f}_i} A_0^{\mathcal{H}}(\tau_{\tilde{f}_i}, \lambda_{\tilde{f}_i}) + \sum_{\tilde{\chi}_i^\pm; m,n=L,R} \frac{2M_W}{m_{\chi_i^\pm}} g_{\mathcal{H}\chi_i^+\chi_i^-}^m g_{Z\chi_i^+\chi_i^-}^n A_{1/2}^{\mathcal{H}}(\tau_{\chi_i^\pm}, \lambda_{\chi_i^\pm}) \\
\mathcal{A}_{\text{SUSY}}^{A} &= \sum_{\tilde{\chi}_i^\pm; m,n=L,R} \frac{2M_W}{m_{\chi_i^\pm}} g_{A\chi_i^+\chi_i^-}^m g_{Z\chi_i^+\chi_i^-}^n A_{1/2}^{A}(\tau_{\chi_i^\pm}, \lambda_{\chi_i^\pm})
\end{aligned}
\tag{2.54}
$$

where the not yet defined Z boson couplings to charginos and sfermions are given by

$$
v_{\tilde{f}_1} = \frac{1}{c_W}\left[I_f^{3L}\cos^2\theta_f - Q_f s_W^2\right] \ , \ v_{\tilde{f}_2} = \frac{1}{c_W}\left[I_f^{3L}\sin^2\theta_f - Q_f s_W^2\right]
\tag{2.55}
$$

$$
g_{\chi_i^-\chi_j^+ Z}^L = \frac{1}{c_W}\left[\delta_{ij}s_W^2 - \frac{1}{2}V_{i2}V_{j2} - V_{i1}V_{j1}\right], \ g_{\chi_i^-\chi_j^+ Z}^R = \frac{1}{c_W}\left[\delta_{ij}s_W^2 - \frac{1}{2}U_{i2}U_{j2} - U_{i1}U_{j1}\right]
$$

All other couplings and form factors have been introduced previously.

The SUSY contributions to the $h \to \gamma Z$ decays have been discussed in Ref. [229] in the decoupling limit and we briefly summarize here the main results, referring to the previous article for details. In general, the contribution of sfermions are negligible except again in the case of rather light top squarks with enhanced couplings to Higgs bosons, where contributions at the level of that of the top quark loop can be generated. The chargino contributions which, as in the $h \to \gamma\gamma$ case, are only suppressed by powers of $1/m_{\chi^\pm}$ at large masses, can also be sizable increasing or decreasing [depending on the sign of μ] the total amplitude by as much as the top quark contribution. However, as already discussed, the W boson contribution is by far dominating in this case and the total effects of the additional SUSY loops can never reach the 10% level even for sparticle masses very close to their experimental lower bounds.

---

[19]In the case of sfermions, for instance, the contribution of the mixed states are proportional to $\sin 4\theta_f$ since $g_{\Phi\tilde{f}_1\tilde{f}_2} \propto \cos 2\theta_f$ and $g_{Z\tilde{f}_1\tilde{f}_2} \propto \sin 2\theta_f$ and are therefore very small, being zero in both the no–mixing [$\theta_f = 0$] and the maximal mixing [$\theta_f = \pm\frac{\pi}{4}$] cases.

2.2.3 Decays into charginos and neutralinos

The decay widths of the Higgs bosons H_k, with $k = 1, 2, 3, 4$ corresponding to respectively, $H, h, A, H^\pm$ bosons, into neutralino and chargino pairs are given by [40, 61, 250–252]

$$
\Gamma(H_k \to \chi_i \chi_j) = \frac{G_\mu M_W^2 s_W^2}{2\sqrt{2}\pi} \frac{M_{H_k} \lambda_{ij;k}^{1/2}}{1 + \delta_{ij}} \left[\left((g_{ijk}^L)^2 + (g_{jik}^R)^2 \right) \left(1 - \frac{m_{\chi_i}^2}{M_{H_k}^2} - \frac{m_{\chi_j}^2}{M_{H_k}^2} \right) \right.
$$
$$
\left. - 4\epsilon_i \epsilon_j g_{ijk}^L g_{jik}^R \frac{m_{\chi_i} m_{\chi_j}}{M_{H_k}^2} \right] \tag{2.56}
$$

where $\delta_{ij} = 0$ unless the final state consists of two identical (Majorana) neutralinos in which case $\delta_{ii} = 1$; $\epsilon_i = \pm 1$ stands for the sign of the ith eigenvalue of the neutralino mass matrix [the matrix Z is defined in the convention of eq. (1.27), and the eigenvalues of the mass matrix can be either positive or negative] while $\epsilon_i = 1$ for charginos; $\lambda_{ij;k}$ is the usual two–body phase space function given previously[20].

The left– and right–handed couplings of the Higgs bosons to charginos and neutralinos are given in eqs. (1.110–1.112). From these couplings, one can see that the Higgs bosons mainly couple to mixtures of higgsino and gaugino components. Therefore, in the limits $|\mu| \gg M_{1,2}, M_Z$ or $|\mu| \ll M_{1,2}$, i.e. in the gaugino or higgsino regions for the lightest ino states, the decays of the neutral Higgs bosons into pairs of identical neutralinos and charginos, $H_k \to \chi_i \chi_i$, will be strongly suppressed. For the same reason, the charged Higgs decays $H^+ \to \chi_{1,2}^0 \chi_1^+, \chi_{3,4}^0 \chi_2^+$ will be suppressed. In these limiting situations, the mixed decay channels $H/A \to \chi_{1,2}^0 \chi_{3,4}^0, \chi_1^\pm \chi_2^\mp$ and $H^+ \to \chi_1^+ \chi_{3,4}^0, \chi_2^+ \chi_{1,2}^0$ will be the dominant ones for the heavy Higgs particles. In the mixed region, $|\mu| \sim M_2$, all decay channels occur at comparable rates when they are kinematically allowed. An exception to these rules occurs, however, for the neutral Higgs boson decays into neutralinos when the couplings accidentally vanish for certain values of $\tan\beta$ and M_A.

In mSUGRA type models, there is a significant portion of the parameter space in which $|\mu|$ [as well as M_A] turns out to be very large, $|\mu| \gg M_2, M_1, M_Z$, and it is worth discussing the heavier Higgs boson decay widths into charginos and neutralinos in this limit. In addition to the fact that decays into pairs of identical states are suppressed by the small couplings, there is an additional suppression by phase–space for decays into higgsino–like states since M_A is of the same order as $|\mu|$. The partial widths of the dominant decay channels of the H, A and $H^\pm$ bosons in this case [61] are displayed in Table 2.1 for M_A values sufficiently larger than $|\mu|$, so that phase–space effects can be ignored in a first approximation. Since we are in the decoupling limit, the relation $\sin 2\alpha = -\sin 2\beta$ has been used.

---

[20]The radiative corrections to these decays have been calculated in Ref. [253] and found to be moderate, being at most at the level of $\sim 10\%$.

	$\Gamma(H \to \chi\chi)$	$\Gamma(A \to \chi\chi)$		$\Gamma(H^\pm \to \chi\chi)$
$\chi_1^0\chi_3^0$	$\frac{1}{2}\tan^2\theta_W(1+\sin 2\beta)$	$\frac{1}{2}\tan^2\theta_W(1-\sin 2\beta)$	$\chi_1^\pm\chi_3^0$	1
$\chi_1^0\chi_4^0$	$\frac{1}{2}\tan^2\theta_W(1-\sin 2\beta)$	$\frac{1}{2}\tan^2\theta_W(1+\sin 2\beta)$	$\chi_1^\pm\chi_4^0$	1
$\chi_2^0\chi_3^0$	$\frac{1}{2}(1+\sin 2\beta)$	$\frac{1}{2}(1-\sin 2\beta)$	$\chi_2^\pm\chi_1^0$	$\tan^2\theta_W$
$\chi_2^0\chi_4^0$	$\frac{1}{2}(1-\sin 2\beta)$	$\frac{1}{2}(1+\sin 2\beta)$	$\chi_2^\pm\chi_2^0$	1
$\chi_1^\pm\chi_2^\mp$	1	1	–	–

Table 2.1: The partial widths of neutralino/chargino decays of the heavier Higgs bosons H, A and $H^\pm$ in units of $G_\mu M_W^2 M_{H_k}/(4\sqrt{2}\pi)$ in the limit $M_A \gg |\mu| \gg M_2$.

The sum of the branching ratios for the heavier H, A and $H^\pm$ boson decays into all possible combinations of neutralino and chargino states are shown in Fig. 2.32 as a function of the Higgs masses for the values $\tan\beta = 3$ and 30. To allow for such decays, we have departed from the benchmark scenario used in previous instances to adopt a scenario in which we have still $M_S = 2$ TeV with maximal mixing in the stop sector, but where the parameters in the ino sector have been chosen to be $M_2 = -\mu = 150$ GeV while M_3 is still large. This choice leads to rather light ino states, $m_{\chi_i} \lesssim 200$–250 GeV depending on the value of $\tan\beta$, but which still satisfy the experimental bounds of eq. (1.53), e.g. $m_{\chi_1^+} \gtrsim 110$–130 GeV.
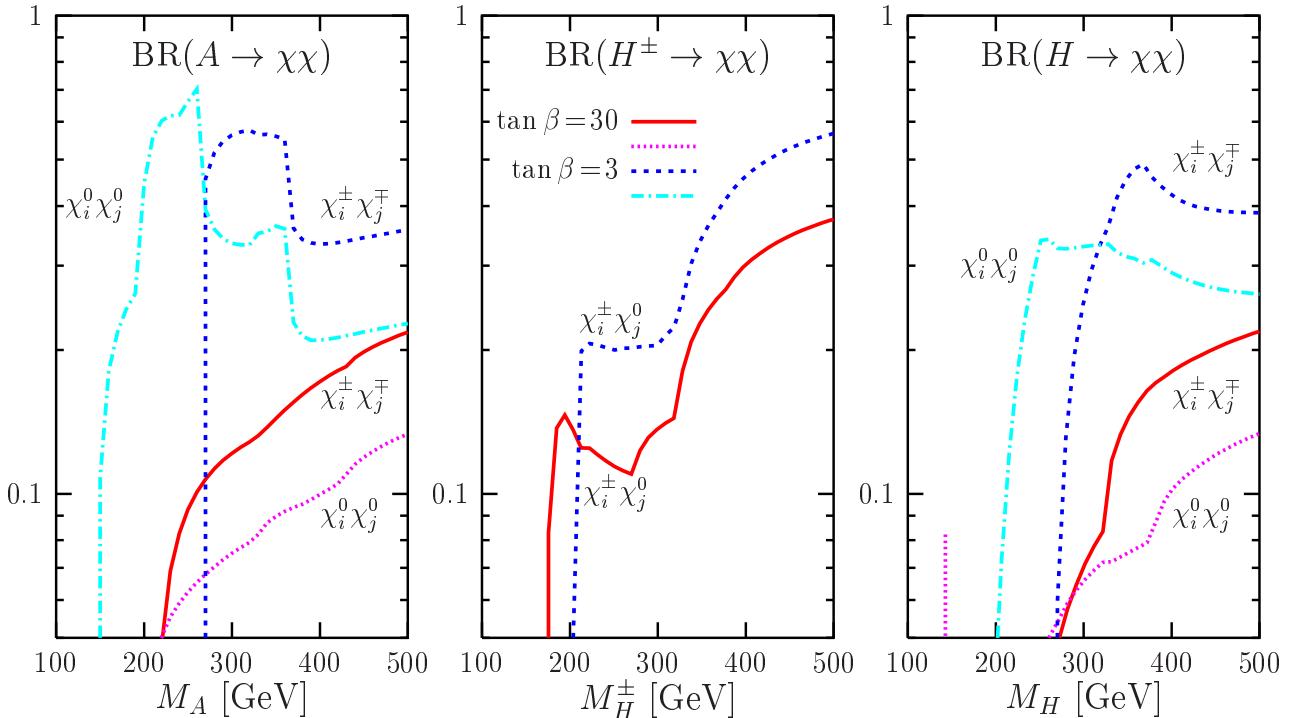
Figure 2.32: The branching ratios for the decays of the heavier MSSM $A, H^\pm$ and H bosons into the sum of charginos and/or neutralinos as a function of their masses for $\tan\beta = 3$ and 30. The relevant SUSY parameters are $M_S = 2$ TeV and $M_2 = -\mu = 150$ GeV.

122

In general, the sum of these branching ratios is always large except in a few cases: (i) for small A masses when the phase space is too penalizing and does not allow for the decay into (several) ino states to occur; (ii) for the H boson in the mass range $M_H \sim 200$–350 GeV and small $\tan\beta$ values when the branching fraction for the decay $H \to hh$ is too large; and (iii) for $H^{\pm}$ just above the $t\bar{b}$ threshold if not all the decay channels into the heavy χ states are open. This is exemplified in the figure, where some of these qualitative features can be seen [here, the inos are light and the phase space is thus favorable; one can even see the decay $H \to \chi_1^0\chi_1^0$ at low M_H]. Note that when kinematically open, the decays of the neutral Higgs bosons into charginos dominate over the decays into neutralinos.

In fact, even above the thresholds of decay channels including top quarks and even for large $\tan\beta$ values, the branching ratios for the decays into charginos and neutralinos are sizable. For very large Higgs masses, they reach a common value of approximately 30% for $\tan\beta \sim 2$ and $\tan\beta \sim 30$. Indeed, as a consequence of the unitarity of the diagonalizing chargino and neutralino mixing matrices, the total widths of the three Higgs bosons decaying into inos do not depend on the parameters M_2 and μ and only mildly on $\tan\beta$. In the asymptotic regime $M_\Phi \gg m_\chi$, this gives rise to the branching ratio [250]

$$\mathrm{BR}(\Phi \to \sum_{i,j} \chi_i\chi_j) = \frac{\left(1 + \frac{1}{3}\tan^2\theta_W\right)M_W^2}{\left(1 + \frac{1}{3}\tan^2\theta_W\right)M_W^2 + \bar{m}_t^2\cot^2\beta + (\bar{m}_b^2 + m_\tau^2)\tan^2\beta} \tag{2.57}$$

where only the leading $t\bar{t}$, $b\bar{b}$ and $\tau\tau$ modes for the neutral and the $t\bar{b}$ and $\tau\nu$ modes for the charged Higgs bosons need to be included in the total widths. The branching ratios are shown in Fig. 2.33 as a function of $\tan\beta$ with M_A fixed to 500 GeV.
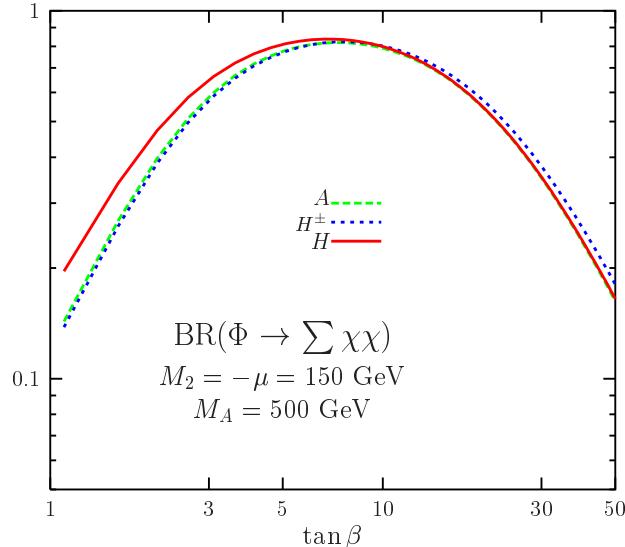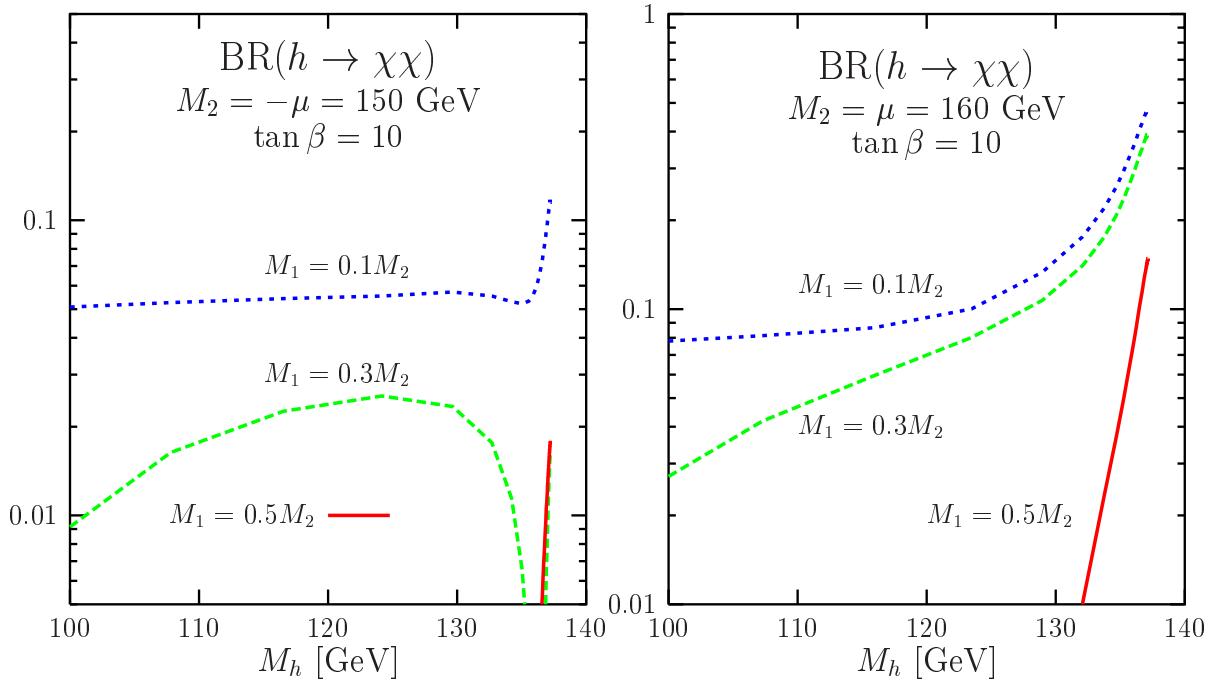
Figure 2.33: *The sum of the branching ratios for the $A, H, H^{\pm}$ boson decays into charginos and neutralinos as a function of $\tan\beta$ for $M_A = 500$ GeV.*

They are always large, even for extreme values of $\tan\beta \sim 1$ or 50 where they are still at the 20% level. They are dominant for values $\tan\beta \sim 10$ when the Higgs coupling to top quarks are suppressed while the $b\bar{b}$ couplings are not too strongly enhanced.

The experimental bounds on the lightest chargino mass, $m_{\chi_1^\pm} \gtrsim 104$ GeV, does not allow for chargino/neutralino decay modes of the lightest CP–even Higgs boson h since $M_h \lesssim 140$ GeV, except for the invisible decays into a pair of the lightest neutralinos, $h \to \chi_1^0\chi_1^0$ [254, 255]. This is particularly true when the universality of the gaugino masses at the GUT scale, which gives $M_1 \sim \frac{1}{2}M_2$ at the low scale, is relaxed leading to light LSPs while the bound on $m_{\chi_1^\pm}$ is still respected [255]. In general, when the $\chi_1^0\chi_1^0$ decay is kinematically allowed, the branching ratio is sizable, in particular, for positive μ and small $\tan\beta$ values; for $\mu < 0$, the branching ratios are much smaller since the inos are less mixed in this case. The rates become smaller for increasing $\tan\beta$, except for $M_h \sim M_h^{\max}$ when the coupling $g_{hb\bar{b}}$ is no longer enhanced.

This discussion is illustrated in Fig. 2.34 where the invisible h branching ratios are shown for $\tan\beta = 10$ as a function of M_h. In the left–hand side, the same scenario with negative μ values as above has been adopted, while the right–hand side is for a scenario with positive μ values, $\mu = M_2 = 160$ GeV. The chosen parameters lead to masses for the h boson and the $\chi_1^\pm$ states that are larger than the respective experimental bounds.

Figure 2.34: The branching ratio of the decay of the lighter h boson into the lightest neutralinos as a function of M_h for $\tan\beta = 10$ and positive (left) and negative (right) μ values. The relevant SUSY parameters are as described in the text.

When the universality condition $M_2 \simeq 2M_1$ is assumed, the phase space allowed by the constraint $m_{\chi_1^\pm} \gtrsim 104$ GeV is rather narrow and the invisible decay occurs only in a small M_h range near the maximal value. However, in the $\mu > 0$ case, the branching fraction can reach the level of 10% when the decay takes place. When the universality assumption is relaxed, $M_1 = 0.3M_2$ and $0.1M_2$ for instance, the LSP is lighter and the invisible decay $h \to \chi_1^0 \chi_1^0$ occurs in a much larger portion of the parameter space. Despite of the fact that in this case, χ_1^0 is bino–like and its coupling to the h boson is not very strong [in particular, for $\mu < 0$, it even vanishes for $M_1 = 0.3M_2$ in a small M_h range near the decoupling limit], the branching ratios are rather large, especially for the maximal M_h value when the partial width of the $h \to b\bar{b}$ decay is SM–like. Thus, large rates for the invisible decays of the h boson are still possible in the MSSM.

2.2.4 Decays into sfermions

The partial decay widths of the neutral and charged Higgs bosons, $H_k = h, H, A, H^\pm$ for $k = 1, .., 4$, into sfermion pairs can be written as [61, 256]

$$\Gamma(H_k \to \tilde{f}_i \tilde{f}_j) = \frac{N_c G_\mu}{2\sqrt{2}\pi M_{H_k}} \lambda^{1/2}_{\tilde{f}_i \tilde{f}_j; H_k} \, g^2_{H_k \tilde{f}_i \tilde{f}_j} \tag{2.58}$$

where the two–body phase space function $\lambda^{1/2}_{\tilde{f}_i \tilde{f}_j; H_k}$ is as defined previously and the neutral and charged Higgs boson couplings to sfermions are given in eq. (1.103).

For the first two generations of sfermions, the decay pattern is rather simple. Because the fermion partners are almost massless, the A boson which couples only to $\tilde{f}_1 \tilde{f}_2$ mixtures with couplings $\propto m_f$, does not decay into sfermions. Because of the experimental lower limits on the sfermion masses from LEP2 and Tevatron, the sfermionic decays of the lighter h boson are kinematically closed. In the asymptotic regime, $M_{H,H^\pm} \gg m_{\tilde{f}}$, the decay widths of the H and $H^\pm$ bosons into sfermions are proportional to $\sin^2 2\beta M_Z^2/M_{H_k}$ and can be significant only for low values $\tan\beta$ for which $\sin^2 2\beta \sim 1$. However, in this regime, the partial widths of the decays $H \to WW, ZZ, hh, t\bar{t}$ and $H^\pm \to Wh, tb$ as well as of the decays into charginos and neutralinos, $H_k \to \chi\chi$, are very large and the sfermion decays do not compete. In particular, since they are inversely proportional to M_{H_k}, the sfermion decays are suppressed for large Higgs masses compared to $f\bar{f}$ and $\chi\chi$ decays which increase with M_{H_k}. Thus, these decay channels are unlikely to be important [61]. Note that due to the isospin and charge assignments, the coupling of the H boson to sneutrinos is approximately a factor of two larger than the coupling to the charged sleptons. Since the sleptons of the three generations are approximately mass degenerate [if one ignores the mixing in the $\tilde{\tau}$ sector which is very small for low values of $\tan\beta$], the small decay widths into sleptons are given by the approximate relation $\Gamma(H \to \tilde{\nu}\tilde{\nu}) \simeq 4\Gamma(H \to \tilde{\ell}_L \tilde{\ell}_L) \simeq 4\Gamma(H \to \tilde{\ell}_R \tilde{\ell}_R)$.

In the case of third generation squarks[21], the Higgs decay widths can be much larger [61]. For instance, the partial decay width of the H boson into identical top squarks is proportional to $m_t^4/(M_H M_Z^2) \times \cot^2\beta$ in the asymptotic region and, for small $\tan\beta$, it will be strongly enhanced compared to decays into first/second generation squarks. Conversely, the decay widths into bottom squarks can be important at large $\tan\beta$. Furthermore, the decays of the H, A bosons into mixed stop and sbottom states will be proportional [up to mixing angle suppression for H] in the asymptotic region to respectively, $m_t^2/M_{H_k} [\mu + A_t \cot\beta]^2$ and $m_b^2/M_{H_k} [\mu + A_b \tan\beta]^2$. For μ and A_Q values of the order of the Higgs boson masses or larger, these decay widths will be competitive with the chargino/neutralino and the standard fermionic decays. The same remarks can be made for the stop plus sbottom decays of the charged Higgs boson which increases as $\tan^2\beta$. Note that for large values of A_Q and/or μ, the mixing in the squark sector becomes very strong and generates a mass splitting between the two squark eigenstates, making one of them possibly much lighter than the other and lighter than the first/second generation squarks. These decays will be thus more favored by phase space, in addition.
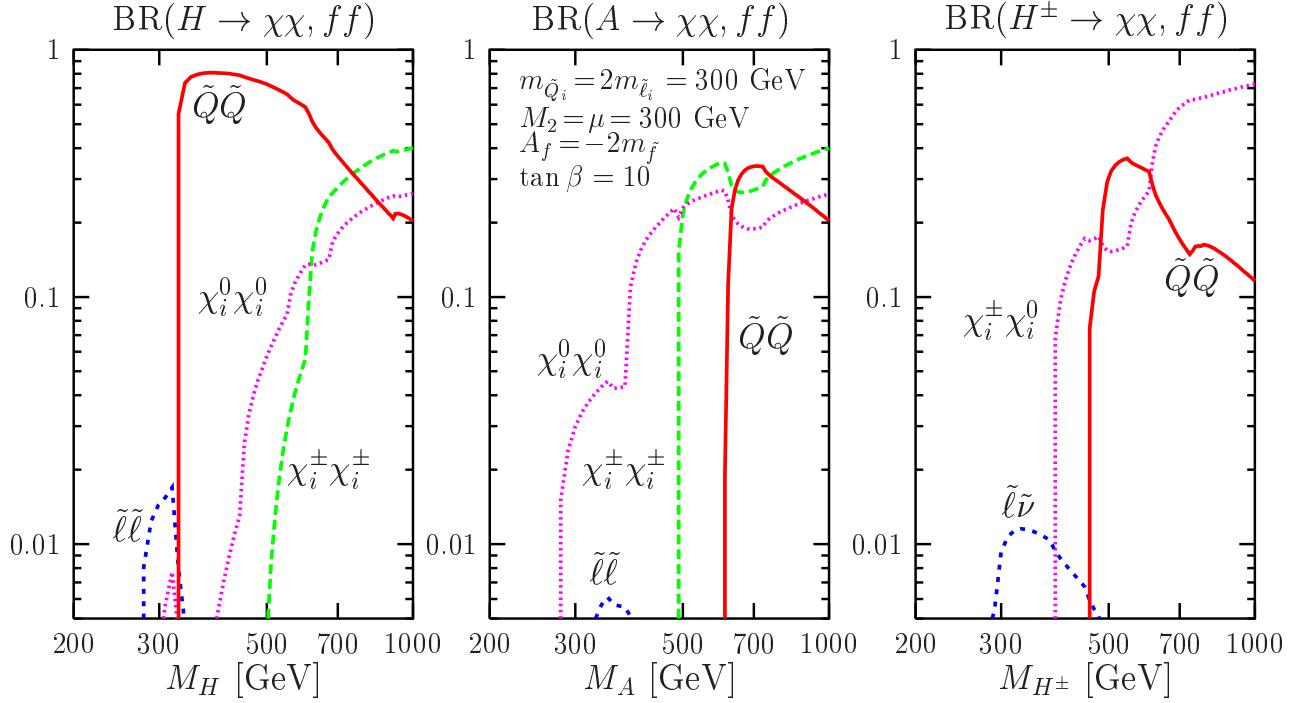
The previous discussion on bottom squarks can be translated to the case of τ sleptons. However, since m_τ is smaller compared to m_b and the color factor is missing, Higgs decays into staus will be suppressed compared to the $\tilde{t}, \tilde{b}$ decays. Nevertheless, the phase space is in general more favorable in the slepton case and, at large $\tan\beta$, the lighter stau state can be the next–to–lightest SUSY particle (NLSP). In some regions of the MSSM parameter space, only Higgs decays into tau sleptons could be therefore kinematically allowed.

To illustrate this discussion, we show in Fig. 2.35 the branching ratios for the decays of the heavier Higgs bosons A, H and $H^\pm$ into third generation sleptons and squarks, as well as into the competing chargino and neutralino final states, as a function of the Higgs masses. The individual decays have been summed up and we have chosen a scenario with $\tan\beta = 10$ and where the sfermions are rather light [but where χ_1^0 is still the LSP and the LEP lower bound on M_h is evaded]: the sfermion masses are $m_{\tilde{Q}_i} = 2m_{\tilde{\ell}_i} = 300$ GeV with trilinear couplings $A_f = -2m_{\tilde{f}}$, while the parameters in the ino sector are $M_2 = \mu = \frac{1}{2}M_1 = 2M_3 = 300$ GeV. In this scenario, the lighter stop and stau states have masses of the order of $m_{\tilde{t}_1} \sim 160$ GeV and $m_{\tilde{\tau}_1} \sim 140$ GeV, slightly above the LSP mass $m_{\chi_1^0} \sim 135$ GeV, while the lighter sbottom mass is larger, $m_{\tilde{b}_1} \sim 280$ GeV. As can be seen, the decay rates for sleptons are rather tiny, although the channels open up earlier. For intermediate Higgs masses, the decays of the H boson into squarks are by far the dominant ones, reaching branching ratios of the order of 80%. The decay channels $A \to \tilde{t}_1 \tilde{t}_2$ and $H^\pm \to \tilde{t}\tilde{b}$ open up later since the $\tilde{t}_2$ and $\tilde{b}_1$ states

---

[21]The QCD corrections for squark decays and the electroweak corrections for all sfermion decays have been calculated in Refs. [257, 258] and have been found to be potentially very large. As in the case of the fermionic decays, the bulk of the corrections can, however, be mapped into running masses and couplings and the remaining corrections are then rather small in general [70].

are heavier and, again, they are sizable. In this regime, $M_\Phi \gtrsim 500\text{--}600$ GeV, the decays into ino states become competitive and, eventually, dominate at higher Higgs masses since their partial widths increase with M_{H_k}.


Figure 2.35: *The branching ratios for the decays of the $A, H, H^\pm$ bosons into third genera-tion sleptons and squarks and into charginos and neutralinos as a function of their masses.* $\tan\beta = 10$ *has been chosen and the various SUSY parameters are as listed in the figure.*

2.2.5 Decays into gravitinos and possibly gluinos

In gauge mediated SUSY–breaking models [58], the gravitino $\tilde{G}$ is rather light [259] with a mass which can be as small as $m_{\tilde{G}} \leq 10^{-4}$ eV. The neutral and charged MSSM Higgs bosons can therefore decay into light gravitinos and, respectively, neutralinos and charginos [260]. The couplings of the "longitudinal" spin–$\frac{1}{2}$ components of the gravitino to ordinary matter are enhanced by the inverse of the gravitino mass and, if $m_{\tilde{G}}$ is sufficiently small, this can compensate the suppression by the inverse Planck mass, $M_P = 2.4 \cdot 10^{18}$ GeV, that appears in all gravitational interactions. In fact, a longitudinal gravitino is [259, 261] simply the goldstino that signals the spontaneous breakdown of global SUSY and whose coupling are inversely proportional to the SUSY–breaking scale $M_S^2 \sim m_{\tilde{G}} M_P$. Since goldstino couplings contain momenta of the external particles, the partial widths for decays into final states containing longitudinal gravitinos depend very strongly on the mass of the decaying particle, $\Gamma_{H_k} \propto M_{H_k}^5$, and can be the dominant decay modes for large values of M_{H_k}.

The partial decay widths of the MSSM Higgs bosons $H_k = h, H, A, H^{\pm}$ into gravitinos and neutralinos or charginos χ_i are given by [260]

$$\Gamma(H_k \to \chi_i \tilde{G}) = \frac{|g_{\tilde{G}\chi_i H_k}|^2}{48\pi} \frac{M_{H_k}^5}{m_{\tilde{G}}^2 M_P^2} \left(1 - \frac{m_{\chi_i}^2}{M_{H_k}^2}\right)^4 \qquad (2.59)$$

where the coupling factors $|g_{\tilde{G}\chi_i H_k}|$ have been given in eq. (1.114) and are sizable only when the charginos and neutralinos have large higgsino components.

It would appear from the previous equation that the partial widths for Higgs to gravitino decays could be made arbitrarily large by making $m_{\tilde{G}}$ very small if $M_{H_k} > m_{\chi_i}$. However, a very small gravitino mass corresponds to a small SUSY–breaking scale and present lower bounds on sparticle masses imply that M_S should be of the order of several hundred GeV at least, which corresponds to a gravitino mass of a few times 10^{-4} eV. In fact, $m_{\tilde{G}} \sim 10^{-4}$ eV corresponds to $M_S = 650$ GeV, which is already quite close to its lower bound in realistic models. We thus adopt the value $m_{\tilde{G}} = 2 \cdot 10^{-4}$ eV in the numerical illustration below.
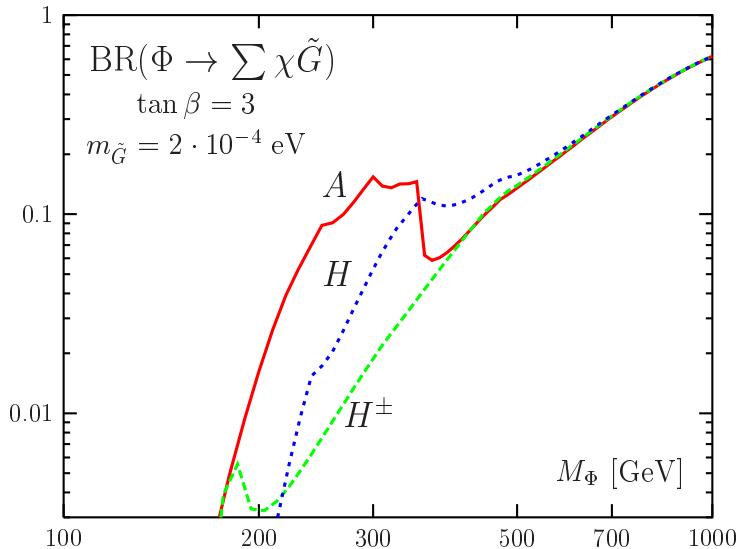
Figure 2.36: The branching ratios for the decays of the $A, H, H^{\pm}$ bosons into gravitinos and all possible chargino and/or neutralino states as a function of their masses. $m_{\tilde{G}} = 2 \cdot 10^{-4}$ eV and the other relevant SUSY parameters are $\tan\beta = 3$ and $M_2 = -\mu = 150$ GeV.

The branching ratios of the H, A and $H^{\pm}$ boson decays into light gravitinos and all possible combinations of χ_i^0 and $\chi_i^{\pm}$ states are shown in Fig. 2.36 as a function of the Higgs masses. Besides $m_{\tilde{G}} = 2 \cdot 10^{-4}$ eV, we have used the value $\tan\beta = 3$ and fixed the parameters in the ino sector to $M_2 = -\mu = 150$ GeV. As can be seen, the decays of the three heavy MSSM Higgs bosons into light gravitinos and inos could be larger than the decays into standard particles and into chargino/neutralino pairs for large Higgs masses, $M_A \gtrsim 700$ GeV in this case. For Higgs bosons with masses in the intermediate range, $M_A = 300$–600

128

GeV, the branching ratios can also be sizable, a few percent. For the lighter h boson and for the pseudoscalar A boson when $M_A \lesssim 150$ GeV, the branching ratios cannot exceed the level of a few per mille for such a value of $m_{\tilde{G}}$, the Higgs masses being not large enough to benefit from the $M_{H_k}^5$ enhancement.

Finally, let us briefly discuss the possibility of Higgs boson decays into light gluinos. The existence of very light gluinos is very unlikely [262] but the mass range $3\,\text{GeV} \lesssim m_{\tilde{g}} \lesssim 6\,\text{GeV}$, has not been definitely ruled out experimentally in a very convincing way. Gluinos can be produced in two–body decays of Z bosons, $Z \to \tilde{g}\tilde{g}$ [263, 264], but the maximal branching ratio is very small, $\sim 5 \cdot 10^{-4}$, if reasonable assumptions are made. With such a small rate, the mass range can be probed only by a dedicated search for gluino final states in four–jet events which are difficult. If by any (lack of?) chance it were the case, the existence of light gluinos could also substantially complicate the search for the MSSM Higgs bosons.

There are two vertex diagrams contributing to the loop induced gluino decays of neutral Higgs bosons: one with two quark and one squark propagators and the other with two squark and one quark propagators. Since gluinos are identical Majorana fermions, one has to antisymmetrize the decay amplitude. As a result, in the absence of squark mixing, i.e. in the limit where either X_q or m_q are set to zero, the amplitudes are proportional to $m_{\tilde{g}}$ and, hence, very small [265]. Thus, only the contributions of the top and bottom quarks and their SUSY scalar partners have to be taken into account. Considering the gluinos as massless, summing over colors and taking into account the fact that there are two identical particles in the final state, the partial decay widths of the CP–even $\mathcal{H} = h, H$ and the CP–odd A bosons into a pair of gluinos are given by

$$\Gamma(\Phi \to \tilde{g}\tilde{g}) = \frac{\alpha}{8s_W^2 M_W^2} M_\Phi \left(\frac{\alpha_s}{\pi}\right)^2 \left(\sum_{q=t,b} \mathcal{A}_q^\Phi\right)^2 \tag{2.60}$$

The amplitudes $\mathcal{A}_q^\Phi$ can be written as

$$
\begin{aligned}
\mathcal{A}_q^{\mathcal{H}} &= \frac{1}{2} m_q^2 g_{\mathcal{H}qq} \sin 2\theta_q \left[(m_q^2 + m_{\tilde{q}_2}^2) C_0(m_q, m_q, m_{\tilde{q}_2}) - (m_q^2 + m_{\tilde{q}_1}^2) C_0(m_q, m_q, m_{\tilde{q}_1})\right] \\
&\quad - m_q \sin 2\theta_q \Big[g_{\mathcal{H}\tilde{q}_1\tilde{q}_1} C_0(m_{\tilde{q}_1}, m_{\tilde{q}_1}, m_q) - g_{\mathcal{H}\tilde{q}_2\tilde{q}_2} C_0(m_{\tilde{q}_2}, m_{\tilde{q}_2}, m_q) \\
&\quad + 2 g_{\mathcal{H}\tilde{q}_1\tilde{q}_2} \cot 2\theta_q C_0(m_{\tilde{q}_1}, m_{\tilde{q}_2}, m_q) \Big]
\end{aligned}
\tag{2.61}
$$

$$
\begin{aligned}
\mathcal{A}_q^A &= \frac{1}{2} m_q^2 g_{Aqq} \sin 2\theta_q \left[(m_q^2 - m_{\tilde{q}_2}^2) C_0(m_q, m_q, m_{\tilde{q}_2}) - (m_q^2 - m_{\tilde{q}_1}^2) C_0(m_q, m_q, m_{\tilde{q}_1})\right] \\
&\quad + 2 g_{A\tilde{q}_1\tilde{q}_2} m_q C_0(m_{\tilde{q}_1}, m_{\tilde{q}_2}, m_q)
\end{aligned}
\tag{2.62}
$$

where all couplings involved have been already given and the Passarino–Veltman scalar function $C_0(m_1, m_2, m_3)$ [74], in the limit where $m_1 = m_2 \gg M_\Phi$ is given by

$$C_0(m, m, m_3) = \frac{1}{m_3^2 - m^2} + \frac{m_3^2}{(m_3^2 - m^2)^2} \log \frac{m^2}{m_3^2} \tag{2.63}$$

As discussed in many instances, in the case of large mixing in the stop sector, top squarks can be lighter than all the other squarks and their couplings to the Higgs bosons strongly enhanced. The $\tilde{g}\tilde{g}$ final state can then completely dominate the decay of the lighter scalar h boson and might be a significant fraction of the decays of the heavier neutral CP–even and CP–odd Higgs bosons. This is exemplified in Fig. 2.37 where the branching ratio for the $h \to \tilde{g}\tilde{g}$ decay is shown as a function of the mass of the lighter stop eigenstate $m_{\tilde{t}_1}$ for $\tan\beta = 25$ (left) and 2 (right) and several values of M_A. The common squark soft SUSY–breaking mass parameter is fixed to $M_S = 400$ GeV with $\mu = 200$ GeV for most cases. The curves have been obtained by varying the common $A \equiv A_{t,b}$ parameter in the region $A < 0$ from the points where the stop mass is minimized and maximized. As can be seen, the branching ratio for $h \to \tilde{g}\tilde{g}$ can reach almost unity in the decoupling limit and for not too heavy stop masses. For small M_A values, the branching ratio is smaller, in particular at large $\tan\beta$ when the partial width of the decay $h \to b\bar{b}$ is enhanced.
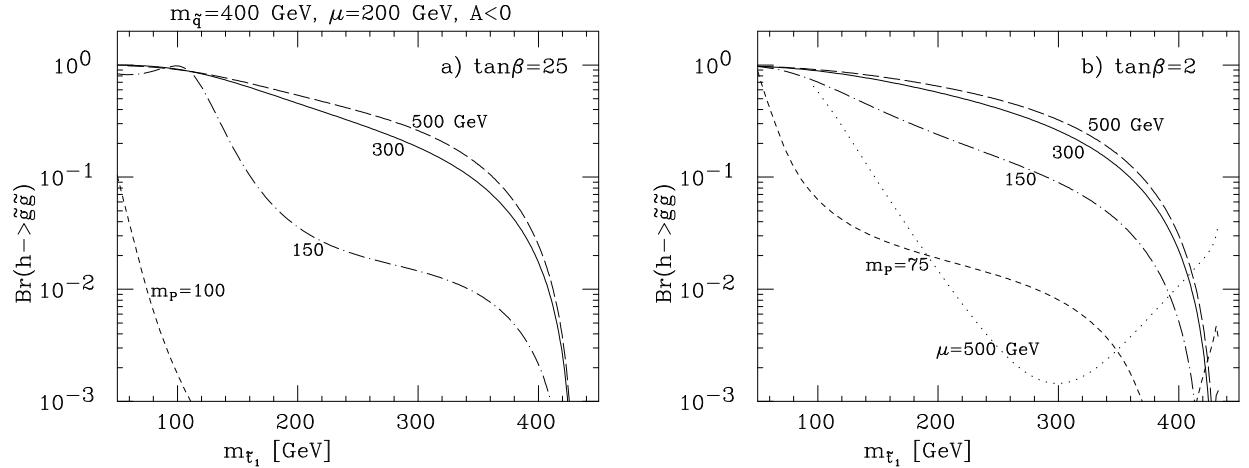
Figure 2.37: The branching ratio of the lighter h boson decay into very light gluinos as a function of the lighter stop mass for $\tan\beta = 25$ (left) and 2 (right). The values of M_A, M_S and μ are as indicated and the trilinear coupling A is varied as discussed in the text.

For the heavier CP–even and CP–odd Higgs bosons, the branching ratios for the decays into gluinos can be also important for low values of $\tan\beta$ and for Higgs masses below the $t\bar{t}$ threshold. At high $\tan\beta$ values, these decays will be superseded by the enhanced decays into $b\bar{b}$ final states.

Finally, in the more realistic case of heavy gluinos, for which the experimental bound $m_{\tilde{g}} \gtrsim 200$–$300$ GeV from Tevatron searches holds, the decays $h \to \tilde{g}\tilde{g}$ are of course kinematically forbidden, while the branching ratios for $A/H \to \tilde{g}\tilde{g}$ decays are negligible because of the loop suppression factor and, for low $\tan\beta$ values, the opening of channels where the Higgs particles have tree–level decays into other heavy states such as top quarks which are dominant; see Ref. [264] for details on these decays.

130

2.3 Decays of top and SUSY particles into Higgs bosons

2.3.1 Top quark decays into charged Higgs bosons

The standard $t \to bW$ decay in the MSSM

The main decay channel of the top quark should be the standard mode $t \to bW$ with a branching ratio which has been measured at the Tevatron to be [1]

$$\mathrm{BR}(t \to Wb) = 0.94^{+0.31}_{-0.24} \tag{2.64}$$

The partial decay width, retaining the dependence on the b-quark mass, is given by

$$\Gamma(t \to bW^+) = \frac{G_\mu}{8\pi\sqrt{2}} \frac{|V_{tb}|^2}{m_t} \lambda^{1/2}(x_W^2, x_b^2; 1) \left[M_W^2(m_t^2 + m_b^2) + (m_t^2 - m_b^2)^2 - 2M_W^4 \right] \tag{2.65}$$

where as usual $\lambda(x, y; z) = (1 - x/z - y/z)^2 - 4xy/z^2$ and $x_W = M_W/m_t, x_b = m_b/m_t$. For a top quark mass $m_t \simeq 180$ GeV, the partial width which is proportional to m_t^3, is of the order of $\Gamma_t \simeq 1.8$ GeV. Since this value is much larger than the QCD scale Λ_{QCD}, the top quark will decay long before it hadronizes, allowing to make reliable perturbative calculations.

The radiative corrections to eq. (2.65) are well known. The standard QCD corrections have been calculated up to two loops [266, 267] and decrease the partial width by approximately 10%. The one–loop electroweak corrections [267, 268], when the naive improved Born approximation is used [that is, when the partial width at the Born level is expressed in terms of G_μ as in eq. (2.65)], are positive but small, hardly reaching the level of 2%.

In the MSSM, the additional QCD and electroweak corrections due to virtual SUSY particles have been calculated in Ref. [269]. The SUSY–QCD corrections, when gluino and top squarks are exchanged, are negative and small in general, being at most a few percent; they do not depend on $\tan\beta$. In turn, the SUSY–EW corrections are negative and can reach the level of -10% depending on the various SUSY parameters and in particular on the value of $\tan\beta$ [since they involve the exchange of stops and neutralinos or sbottoms and charginos which can have enhanced couplings to the top quark when the inos are higgsino like]. The MSSM Higgs exchange contributions are extremely tiny, being less than 0.1%. Note that in a 2HDM, that is, without the exchange of SUSY particles and when only additional Higgs contributions are present, the radiative corrections have been derived in Ref. [270].

Despite the experimental measurement eq. (2.64), in which the central value of $\mathrm{BR}(t \to bW)$ is very close to unity, there is still a large room for non–standard decays of the top quark. First, the value has been obtained from the measurement of the $p\bar{p} \to t\bar{t} \to bWbW$ cross sections and thus includes all the channels which can mimic $WbWb$ final states. In addition, the error on the measurement is rather large and at the 2σ level, the branching ratio can be as low as $\mathrm{BR}(t \to Wb) \sim 50\%$. New decay channels, such as $t \to H^+b$, are thus still allowed provided that they are not dominating over the standard $t \to bW$ mode.

The $t \to bH^+$ decay in the MSSM

If the $H^\pm$ bosons are relatively light, $M_{H^\pm} \lesssim m_t - m_b$, they can be produced in the decays of to quarks [178, 179], Fig. 2.38a,

$$t \to H^+ b \ , \ \ \bar{t} \to H^- \bar{b} \tag{2.66}$$

The couplings of the $H^\pm$ bosons to tb states haven been given in eq. (1.96) where one can observe that they are proportional to the combination

$$g_{H^+ \bar{t} b} \ \propto \ m_b \tan\beta (1 + \gamma_5) + m_t \cot\beta (1 - \gamma_5) \tag{2.67}$$

Thus, for small $\tan\beta \sim 1$ or large $\tan\beta \sim 30$ values, the couplings are strong enough to make this decay compete with the standard $t \to bW^+$ channel discussed above. For intermediate values of $\tan\beta$, the t–quark component of the coupling is suppressed while the b–quark component is not yet strongly enhanced and the overall couplings is small; the minimal value of the coupling occurs at the point $\tan\beta = \sqrt{m_t m_b} \sim 6$.
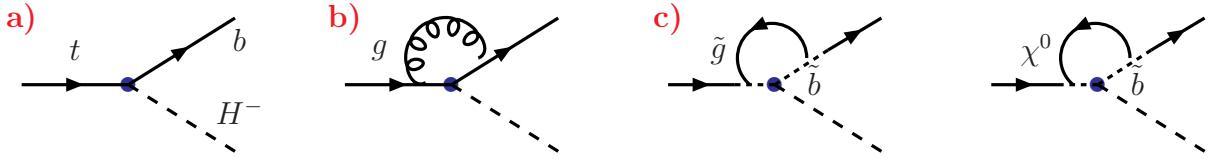
Figure 2.38: Tree level and generic one–loop diagrams for the $t \to bH^+$ decay.

In the Born approximation, keeping the explicit dependence on the bottom quark mass, the partial width of the $t \to H^+ b$ decay is given by [178]

$$\Gamma_{\rm LO} = \frac{G_\mu m_t}{8\sqrt{2}\pi} |V_{tb}|^2 \lambda(x_H^2, x_b^2; 1)^{\frac{1}{2}} [(m_t^2 \cot^2\beta + m_b^2 \tan^2\beta)(1 + x_b^2 - x_H^2) + 4m_t^2 m_b^2] \tag{2.68}$$

where $\lambda(x, y; z)$ has been defined before and $x_H = M_{H^\pm}/m_t, x_b = m_b/m_t$. At least the standard QCD corrections need to be incorporated in this partial width. Neglecting the non enhanced effects of the b–quark mass [i.e. keeping m_b only in the Higgs coupling], the standard gluonic corrections at NLO, Fig. 2.38b, may be written as [271]
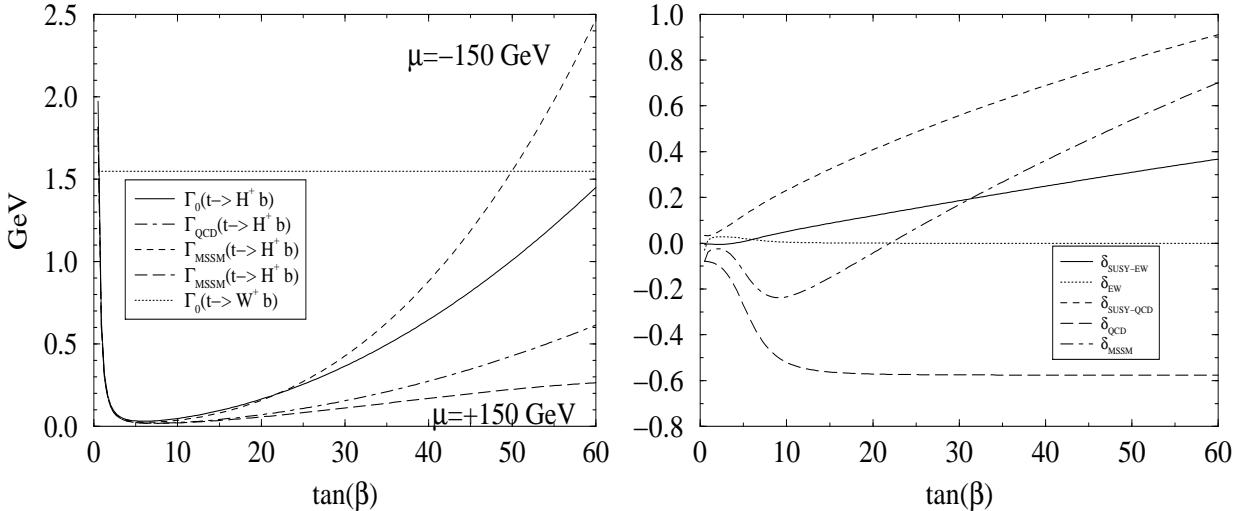
$$\Gamma_{\rm NLO}^{\rm QCD} = \frac{G_\mu m_t}{8\sqrt{2}\pi} |V_{tb}|^2 (1 - x_H^2)^2 \frac{8}{3} \frac{\alpha_s}{\pi} \left[m_t^2 \cot^2\beta (G_+ + G_-) + m_b^2 \tan^2\beta (G_+ - G_-) \right]$$

$$G_+ = {\rm Li}_2(1 - x_H^2) - \frac{x_H^2}{1 - x_H^2} {\rm Li}_2(x_H) + \log(x_H) \log(1 - x_H^2) + \frac{1}{2x_H^2} \left(1 - \frac{5}{2} x_H^2 \right) \log(1 - x_H^2)$$

$$- \frac{\pi^2}{3} + \frac{9}{8} + \frac{3}{4} \log(x_b) \ , \quad G_- = -\frac{3}{4} \log(x_b) \tag{2.69}$$

As can be seen, there are large logarithms, $\log(m_b/m_t)$, in these expressions. For low $H^\pm$ masses, where one can use the approximation $x_H \to 0$, one has $G_+ \to \frac{5}{4} - \frac{\pi^2}{6} + \frac{3}{4} \log \frac{m_b}{m_t}$

and $G_- = -\frac{3}{4} \log \frac{m_b}{m_t}$. Thus, at low $\tan\beta$ values where the component $\propto m_t^2$ is dominant, the logarithms in $G_+ + G_-$ cancels out as expected and the correction is small. In turn, for $\tan\beta \gg 1$, the logarithm remains, $G_+ - G_- \to +\frac{3}{2} \log \frac{m_b}{m_t}$, leading to large and negative corrections, $\sim -60\%$, to the partial decay width. However, these logarithmic corrections can be mapped again into the running b–quark mass defined at the scale m_t.

In the MSSM, there are additional corrections stemming from SUSY–QCD where squarks and gluinos are exchanged or from SUSY–EW contributions where weakly interacting particles with strong couplings are involved; see Fig. 2.38c. These corrections can also be very large, in particular, for large values of $\tan\beta$. These important corrections have been discussed in many instances [272] and we refer to the review of Ref. [273] for details. Here, we simply note that the bulk of these corrections is in fact originating from the threshold corrections to the bottom quark mass, eq. (1.45), and can readily be included by using the corrected b–quark Yukawa coupling given in eq. (1.140).

In the left–hand side of Fig. 2.39, borrowed from Ref. [273], shown is the partial decay width $\Gamma(t \to H^+ b)$ at the tree–level and including the standard as well as the MSSM radiative corrections as a function $\tan\beta$ for two sets of SUSY parameters indicated in the caption. In the right–hand side of the figure, shown are the individual corrections normalized to the Born term for the set of parameters with $\mu > 0$. As can be seen, the corrections can be extremely large reaching $\sim 80\%$ for the SUSY–QCD corrections [which have the same sign as μ] and $\sim 40\%$ for the SUSY–EW ones [which have the opposite sign of $A_t \mu$].

Figure 2.39: The top quark partial decay width $\Gamma(t \to H^+ b)$ compared with the SM one as a function of $\tan\beta$ for $M_{H^\pm} = 120$ GeV. Shown are the tree-level and corrected widths for two sets of the SUSY parameters $\mu, m_{\tilde{t}_1}, m_{\tilde{b}_1}, m_{\tilde{g}}, A_t = -150, 100, 150, 300, +300$ GeV and $+150, 200, 600, 1000, -300$ GeV (left) and the relative corrections from various sectors of the MSSM for the set with $\mu > 0$ (right); from Ref. [273].

The $t \to bH^+$ branching ratio

The branching ratio for the $t \to bH^+$ decay, defined as[22] $\mathrm{BR}(t \to bH^+) = \Gamma(t \to bH^+)/[\Gamma(t \to bW) + \Gamma(t \to bH^+)]$, has been already displayed in Fig. 1.20 of §1.4.2. It is shown again in Fig. 2.40 but as a function of the charged Higgs boson mass for three values, $\tan\beta = 3, 10$ and 30. We have included only the standard QCD corrections to the two decays. One notices the small value of the branching ratio at intermediate $\tan\beta$ where the m_t component of the coupling is suppressed while the m_b component is not yet enhanced, and the clear suppression near the threshold: for $M_{H^\pm} \gtrsim 160$ GeV, the branching ratio is below the per mille level even for $\tan\beta = 3$ and 30.
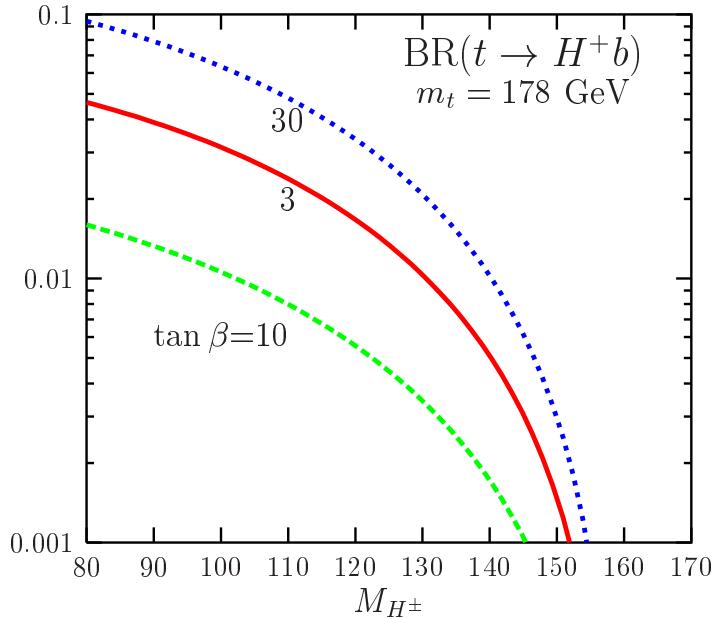
Figure 2.40: The branching ratio for the decay of the top quark into a charged Higgs boson and a bottom quark as a function of $M_{H^\pm}$ for three values $\tan\beta = 3, 10$ and 30; only the standard QCD corrections have been implemented.

Note finally that charged Higgs bosons can also be produced in SUSY cascade decays via the pair production of gluinos [at hadron colliders] and/or top and bottom squarks [at both hadron and lepton colliders], followed by their cascades into top quarks, which subsequently decay into charged Higgs bosons. Another possibility is $H^\pm$ production from SUSY cascades involving the decays of heavier chargino and neutralino states, $\chi \to t + X$, followed by the decay $t \to H^+b$. In fact, the most copious source of $H^\pm$ bosons in a SUSY process could be the decays of heavier charginos and neutralinos into lighter ones and a charged Higgs particle, to which we turn our attention now.

---

[22]We assume of course that only the two decay channels $t \to Wb$ and $t \to H^+b$ are kinematically accessible. However, in view of the lower bounds on the SUSY particles eq. (1.53), the possibility that the top quark decays into a top squark and a neutralino, $t \to \tilde{t}\chi_1^0$ [274], is not entirely ruled out.

2.3.2 Decays of charginos and neutralinos into Higgs bosons

Charginos and neutralinos can be copiously produced at the LHC in the cascade decays of squarks and gluinos $\tilde{g} \to q\tilde{q}^{(*)} \to qq\chi_i$ and $\tilde{q} \to q\chi_i$ [275] and can be accessed directly at e^+e^- colliders through pair or mixed pair production, $e^+e^- \to \chi_i\chi_j$ [276]. If the mass splitting between the heavier $\chi^0_{3,4}, \chi^\pm_2$ states and the lighter $\chi^0_{1,2}, \chi^\pm_1$ states is substantial, the heavier inos can decay into the lighter ones and neutral and/or charged Higgs bosons

$$\chi^\pm_2, \chi^0_3, \chi^0_4 \quad \to \quad \chi^\pm_1, \chi^0_2, \chi^0_1 + h, H, A, H^\pm \tag{2.70}$$

In fact, even the next–to–lightest neutralino can decay into the LSP neutralino and a neutral Higgs boson and the lighter chargino into the LSP and a charged Higgs boson,

$$\chi^0_2 \to \chi^0_1 + h, H, A \quad \text{and} \quad \chi^\pm_1 \to \chi^0_1 + H^\pm \tag{2.71}$$

These decay processes will be in direct competition with decays into gauge bosons, $\chi_i \to \chi_j V$, and if sleptons are light [we assume that squarks are rather heavy, being the main source of heavy inos at the LHC for instance], decays into leptons and their slepton partners, $\chi_i \to \ell\tilde{\ell}_j$. The partial decay widths of these possible two–body decays are given by [277, 278]

$$\Gamma(\chi_i \to \ell\tilde{\ell}_j) = \frac{\alpha}{8} m_{\chi_i} g^2_{\chi_i \ell\tilde{\ell}_j} \left(1 - \mu_{\tilde{\ell}_j} + \mu_\ell\right) \lambda^{\frac{1}{2}}(0, \mu_{\tilde{\ell}_j}) \tag{2.72}$$

$$\Gamma(\chi_i \to \chi_j V) = \frac{\alpha}{8c^2_W} m_{\chi_i} \lambda^{\frac{1}{2}}(\mu_{\chi_j}, \mu_V) \left\{ -12\sqrt{\mu_{\chi_j}} g^L_{\chi_i\chi_j V} g^R_{\chi_i\chi_j V} \right. \tag{2.73}$$

$$\left. + \left[(g^L_{\chi_i\chi_j V})^2 + (g^R_{\chi_i\chi_j V})^2\right](1 + \mu_{\chi_j} - \mu_V) + (1 - \mu_{\chi_j} + \mu_V)(1 - \mu_{\chi_j} - \mu_V)\mu_V^{-1} \right\}$$

$$\Gamma(\chi_i \to \chi_j H_k) = \frac{\alpha}{8} m_{\chi_i} \lambda^{\frac{1}{2}}(\mu_{\chi_j}, \mu_{H_k}) \left\{ \left[(g^L_{\chi_i\chi_j H_k})^2 + (g^R_{\chi_i\chi_j H_k})^2\right](1 + \mu_{\chi_j} - \mu_{H_k}) \right.$$

$$\left. + 4\sqrt{\mu_{\chi_j}}\, g^L_{\chi_i\chi_j H_k} g^R_{\chi_i\chi_j H_k} \right\} \tag{2.74}$$

where $\lambda(x, y) = 1 + x^2 + y^2 - 2(xy + x + y)$ is the usual two–body phase space function with the reduced masses $\mu_X = m^2_X/m^2_{\chi_i}$ and we have neglected the lepton mass and, hence, slepton mixing. The couplings among charginos, neutralinos and the Higgs bosons $H_k = h, H, A$ and $H^\pm$ for $k = 1, 2, 3, 4$ have been given previously, eqs. (1.110–1.112), as were given the couplings of the Z boson to chargino pairs, eq. (2.56). The other ino couplings to W/Z bosons which are needed, using the same normalization, are given by

$$g^L_{\chi^0_i \chi^+_j W} = \frac{c_W}{\sqrt{2}s_W}[-Z_{i4}V_{j2} + \sqrt{2}Z_{i2}V_{j1}] \quad , \quad g^R_{\chi^0_i \chi^+_j W} = \frac{c_W}{\sqrt{2}s_W}[Z_{i3}U_{j2} + \sqrt{2}Z_{i2}U_{j1}]$$

$$g^L_{\chi^0_i \chi^0_j Z} = -\frac{1}{2s_W}[Z_{i3}Z_{j3} - Z_{i4}Z_{j4}] \quad , \quad g^R_{\chi^0_i \chi^0_j Z} = +\frac{1}{2s_W}[Z_{i3}Z_{j3} - Z_{i4}Z_{j4}] \tag{2.75}$$

while the couplings among neutralinos/charginos, leptons and sleptons $\tilde{\ell}_i = \tilde{\ell}_L, \ell_R$ are

$$g_{\chi^0_i \ell\tilde{\ell}_j} = \sqrt{2}\left[Q_\ell(Z_{i1}c_W + Z_{i2}s_W) + \left(I^{3j}_\ell - Q_\ell s^2_W\right)\frac{Z_{i2}c_W - Z_{i1}s_W}{c_W s_W}\right]$$

$$g_{\chi^+_i e\tilde{\nu}_L} = \frac{V_{j1}}{s_W} \ , \ g_{\chi^+_i \nu\tilde{e}_L} = \frac{U_{j1}}{s_W} \ , \ g_{\chi^+_i \nu\tilde{e}_R} = 0 \tag{2.76}$$

135

The decay branching ratios of the heavier chargino $\chi_2^\pm$ and neutralino $\chi_{3,4}^0$ states into the lighter ones $\chi_1^\pm$ and $\chi_{1,2}^0$ and gauge or Higgs bosons are shown in Fig. 2.41 for $\tan\beta = 10$ and $M_A = 180$ GeV in two scenarios. In the left–hand (right–hand) panel, μ_0 (M_2) is fixed at a small value, 150 GeV, which means that the lighter inos are higgsino (gaugino) like, and the other parameter M_2 (μ) is varied with the mass of the decaying ino. The sleptons and squarks are assumed to be too heavy to play a role here.

Since the Higgs bosons couple preferentially to mixtures of gauginos and higgsinos, the Higgs couplings to mixed heavy and light chargino/neutralino states are maximal in the two regions, while the couplings involving only heavy or light ino states are suppressed by powers of M_2/μ for $|\mu| \gg M_2$ or powers of $|\mu|/M_2$ for $|\mu| \ll M_2$. To the contrary, the gauge boson couplings to inos are important only for higgsino– or gaugino–like states. Thus, in principle, the (higgsino or gaugino–like) heavier inos $\chi_2^\pm$ and $\chi_{3,4}^0$ will dominantly decay, if phase space allowed, into Higgs bosons and the lighter χ states. However, in the asymptotic limit where the heavier ino masses are very large, $m_{\chi_i} \gg m_{\chi_j}, M_{H_k}, M_V$, the decay widths into Higgs bosons grow as m_{χ_i}, while the decay widths into gauge bosons grow as $m_{\chi_i}^3$. This is due to the longitudinal component of the gauge boson propagators which introduce extra powers of the χ_i four–momentum in the decay amplitudes. The suppression of the $(g_{\chi_i\chi_j V}^{L,R})^2$ squared coupling by powers of $(\mu/M_2)^2$ or $(M_2/\mu)^2$ depending on whether we are in the gaugino or higgsino region, will be compensated by the power m_χ^2/M_Z^2 from the amplitude squared. Therefore, the branching ratios for the decays of heavy χ particles into lighter ones and Higgs or gauge bosons will have the same order of magnitude. Of course, as usual, the charged current decay modes will be more important than the neutral modes.

This is exemplified in Fig. 2.41. In both the higgsino and gaugino regions, the decays of $\chi_2^\pm$ and $\chi_{3,4}^0$ into lighter charginos and neutralinos and Higgs bosons are not the dominant ones. Still, decays into Higgs bosons, in particular to the lighter h and charged $H^\pm$ bosons, will have substantial branching fractions, of the order of 20 to 30% in this scenario. Note that in mSUGRA type models and as discussed in §2.2.3, we are very often in the gaugino region for the lighter χ states, $|\mu| \sim M_A \gg M_2$ and the $A, H, H^\pm$ bosons are quite heavy. In this case, the charginos and neutralinos decay only into the lighter h boson and W/Z bosons, if the sfermion channels $\chi \to f\tilde{f}$ are also kinematically closed. In this scenario, the partial decay widths of the heavier charginos and neutralinos are given Table 2.2 where we ignore, again, the phase–space suppression and assume the decoupling limit for simplicity. In these limits, the partial widths for the decays of the lighter states χ_2^0 and χ_1^+ into the LSP neutralino and Higgs or gauge bosons [again in units of $G_\mu M_W^2 |\mu|/(8\sqrt{2}\pi)$] are simply

$$\begin{aligned}
\Gamma(\chi_1^+ \to \chi_1^0 W^+) &\sim \Gamma(\chi_2^0 \to \chi_1^0 h) \sim \sin^2 2\beta \\
\Gamma(\chi_2^0 \to \chi_1^0 Z) &\sim \cos^2 2\beta \left[(M_2 - M_1)/2\mu\right]^2
\end{aligned} \tag{2.77}$$

136
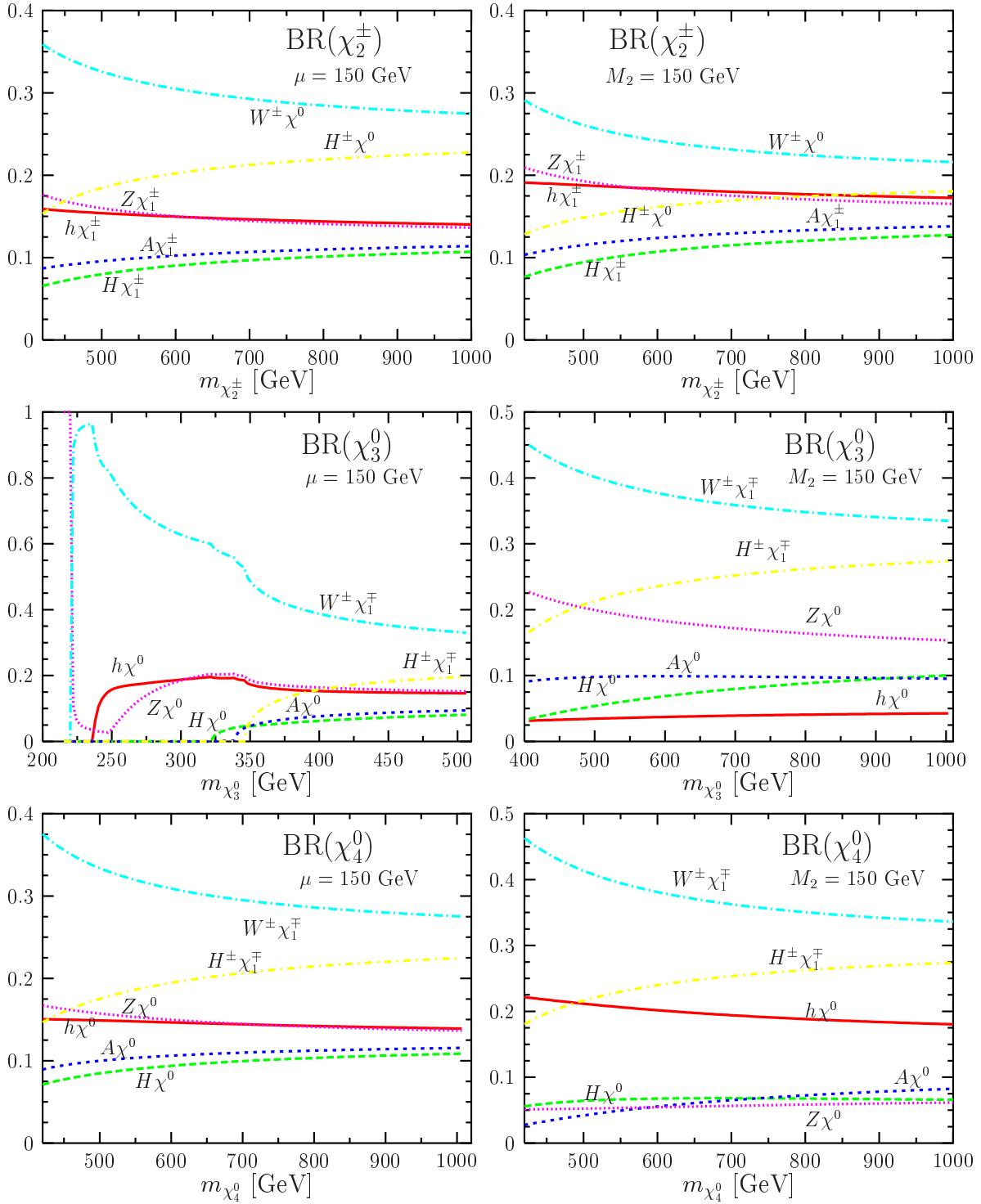
Figure 2.41: Branching ratios of heavier chargino and neutralino decays into the lighter ones and gauge/Higgs bosons as functions of their masses for $\tan\beta = 10$ and $M_A = 180$ GeV. In the left (right) panel, μ (M_2) is fixed while M_2 (μ) varies with the heavy ino mass; χ^0 represents the lighter χ_1^0 and χ_2^0 neutralinos for which the rates are added; from [278].

	$\Gamma(\chi_3^0 \to \chi X)$	$\Gamma(\chi_4^0 \to \chi X)$		$\Gamma(\chi_2^\pm \to \chi X)$
$\chi_1^0 Z$	$\frac{1}{2}\tan^2\theta_W(1 + \sin 2\beta)$	$\frac{1}{2}\tan^2\theta_W(1 - \sin 2\beta)$	$\chi_1^\pm Z$	1
$\chi_1^0 h$	$\frac{1}{2}\tan^2\theta_W(1 - \sin 2\beta)$	$\frac{1}{2}\tan^2\theta_W(1 + \sin 2\beta)$	$\chi_1^\pm h$	1
$\chi_2^0 Z$	$\frac{1}{2}(1 + \sin 2\beta)$	$\frac{1}{2}(1 - \sin 2\beta)$	$W^\pm \chi_1^0$	$\tan^2\theta_W$
$\chi_2^0 h$	$\frac{1}{2}(1 - \sin 2\beta)$	$\frac{1}{2}(1 + \sin 2\beta)$	$W^\pm \chi_2^0$	1
$\chi_1^\pm W^\mp$	2	2	–	–

Table 2.2: *The partial widths of neutralino/chargino decays into the lighter Higgs boson and into massive gauge bosons in units of* $G_\mu M_W^2 |\mu|/(8\sqrt{2}\pi)$ *in the limit* $M_A \sim |\mu| \gg M_2$.

Before closing this discussion, let us make a few brief remarks: i) in the case where the inos are mixed states, that is $|\mu| \sim M_2$, the mass difference between the heavy and light inos will be rather small and the decays into Higgs bosons will be phase–space suppressed. (ii) As already seen in the reverse processes $H_k \to \chi_i\chi_j$, the branching ratios do not depend in a very strong way on the value of $\tan\beta$. (iii) Decays of the inos into sleptons, which can be lighter than squarks, are relevant only if the former particles are gaugino–like since the higgsino couplings to ℓ–$\tilde{\ell}$ states, $\propto m_\ell$, are rather tiny unless $\tan\beta \gg 1$ in which case the decays into $\tilde{\tau}$'s could play a role. (iv) Finally, there is also the possibility of decays of the lighter χ_2^0 and $\chi_1^\pm$ into the LSP and a Higgs boson, eq. (2.71). These "small cascades" are possible only if these states are gaugino like or gaugino–higgsino mixtures; only for small Higgs masses [which is the case of the h boson] are these decays important.

2.3.3   Direct decays of sfermions into Higgs bosons

If the mass splitting between two squarks of the same generation is large enough, as is generally the case of the $(\tilde{t}, \tilde{b})$ isodoublet, the heavier squark can decay into the lighter one plus a neutral or charged Higgs bosons $H_k = h, H, A, H^\pm$ for $k = 1, \cdots, 4$ [279, 280]. The partial decay widths are given at tree–level by [see Ref. [278] for instance]

$$\Gamma(\tilde{q}_i \to \tilde{q}_j' H_k) = \frac{\alpha}{4} m_{\tilde{q}_i} g^2_{\tilde{q}_i\tilde{q}_j'H_k} \lambda^{1/2}(\mu^2_{H_k}, \mu^2_{\tilde{q}_j'}) \tag{2.78}$$

with the phase space function and the Higgs couplings to squarks given previously. These decays have to compete with the corresponding channels where $V = W, Z$ gauge bosons are produced instead of Higgs bosons. In this case, the partial decay widths are given by

$$\Gamma(\tilde{q}_i \to \tilde{q}_j' V) = \frac{\alpha}{4M_V^2} m_{\tilde{q}_i} g^2_{\tilde{q}_i\tilde{q}_j'V} \lambda^{3/2}(\mu^2_V, \mu^2_{\tilde{q}_j'}) \tag{2.79}$$

where the off–diagonal couplings of squarks to the W and Z bosons including mixing are

$$g_{\tilde{q}_1\tilde{q}_2 Z} = g_{\tilde{q}_2\tilde{q}_1 Z} = \frac{2I_q^3 s_{2\theta_q}}{4 s_W c_W} \quad , \quad g_{\tilde{q}_i\tilde{q}_j'W} = \frac{1}{\sqrt{2}s_W} \begin{pmatrix} c_q c_{q'} & -c_q s_{q'} \\ -s_q c_{q'} & s_q s_{q'} \end{pmatrix} \tag{2.80}$$

138

The usually dominant decay modes of the top and bottom squarks are decays into quarks and charginos or neutralinos. In both cases, the partial decay widths can be written as

$$\Gamma(\tilde{q}_i \to q^{(')}\chi_j) = \frac{\alpha \lambda^{\frac{1}{2}}(\mu_q^2, \mu_{\chi_j}^2)}{4} m_{\tilde{q}_i} \left[(a_{ij}^{\tilde{q}\,2} + b_{ij}^{\tilde{q}\,2})(1 - \mu_q^2 - \mu_{\chi_j^0}^2) - 4 a_{ij}^{\tilde{q}} b_{ij}^{\tilde{q}} \mu_q \mu_{\chi_j} \epsilon_{\chi_j} \right] \quad (2.81)$$

The couplings among neutralinos, quarks and squarks are

$$\left\{ \begin{array}{c} a_{j1}^{\tilde{q}}/b_{j1}^{\tilde{q}} \\ a_{j2}^{\tilde{q}}/b_{j2}^{\tilde{q}} \end{array} \right\} = -\frac{m_q r_q}{\sqrt{2} M_W s_W} \left\{ \begin{array}{c} s_{\theta_q}/c_{\theta_q} \\ c_{\theta_q}/-s_{\theta_q} \end{array} \right\} - e_{Lj}^q/e_{Rj}^q \left\{ \begin{array}{c} c_{\theta_q}/s_{\theta_q} \\ -s_{\theta_q}/c_{\theta_q} \end{array} \right\} \quad (2.82)$$

with $r_u = Z_{j4}/\sin\beta$ and $r_d = Z_{j3}/\cos\beta$ for up–type and down–type fermions and

$$e_{Lj}^q = \sqrt{2} \left[e_q (Z_{j1}c_W + Z_{j2}s_W) + \left(I_q^3 - e_q s_W^2 \right) \frac{1}{c_W s_W} \left(-Z_{j1}s_W + Z_{j2}c_W \right) \right]$$

$$e_{Rj}^q = -\sqrt{2}\, e_q \left[(Z_{j1}c_W + Z_{j2}s_W) - \frac{s_W}{c_W} \left(-Z_{j1}s_W + Z_{j2}c_W \right) \right] \quad (2.83)$$

while for the couplings among charginos, fermions and sfermions, $\tilde{q}_i - q' - \chi_j^+$, one has for up–type sfermions:

$$\left\{ \begin{array}{c} a_{j1}^{\tilde{u}} \\ a_{j2}^{\tilde{u}} \end{array} \right\} = \frac{V_{j1}}{s_W} \left\{ \begin{array}{c} -c_{\theta_u} \\ s_{\theta_u} \end{array} \right\} + \frac{m_u V_{j2}}{\sqrt{2}\, M_W s_W s_\beta} \left\{ \begin{array}{c} s_{\theta_u} \\ c_{\theta_u} \end{array} \right\}$$

$$\left\{ \begin{array}{c} b_{j1}^{\tilde{u}} \\ b_{j2}^{\tilde{u}} \end{array} \right\} = \frac{m_d U_{j2}}{\sqrt{2}\, M_W s_W c_\beta} \left\{ \begin{array}{c} c_{\theta_u} \\ -s_{\theta_u} \end{array} \right\} \quad (2.84)$$

and the couplings for down–type fermions can be obtained from the above by performing the changes $u \leftrightarrow d$ and $V \leftrightarrow U$ where U, V are the diagonalizing matrices for the charginos.

When allowed by phase space, the dominant decay modes of these particles are in fact decays into their partner quarks and gluinos with partial widths

$$\Gamma(\tilde{q}_i \to q\tilde{g}) = \frac{2\alpha_s \lambda^{\frac{1}{2}}(\mu_q^2, \mu_{\tilde{g}}^2)}{3} m_{\tilde{q}_i} \left[1 - \mu_q^2 - \mu_{\tilde{g}}^2 - 4 a_{i\tilde{g}}^{\tilde{q}} b_{i\tilde{g}}^{\tilde{q}} \mu_q \mu_{\tilde{g}} \right] \quad (2.85)$$
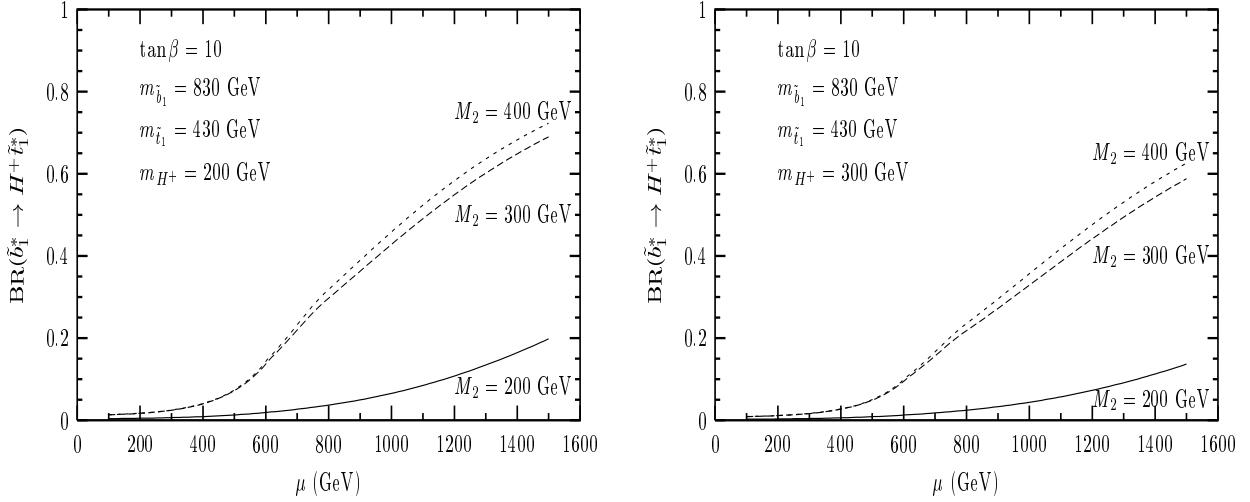
with the same notation as previously and the squark–quark–gluino coupling

$$a_{1\tilde{g}}^q = b_{2\tilde{g}}^q = \sin\theta_q \quad , \quad a_{2\tilde{g}}^q = -b_{1\tilde{g}}^q = \cos\theta_q \quad (2.86)$$

Note that QCD corrections to all these decay modes have been calculated and can be found in Refs. [257,281,282] for, respectively, the decays into Higgs/gauge boson, chargino/neutralino and gluino states. Except possibly when gluinos are involved, the bulk of the radiative corrections can also be mapped into running parameters.

In Fig. 2.42, we display for illustration the branching ratios for the decays of a bottom squark into the lightest top squark and a charged Higgs boson, $\tilde{b}_1 \to \tilde{t}_1 H^-$ or $\tilde{b}_1^* \to \tilde{t}_1^* H^+$, as
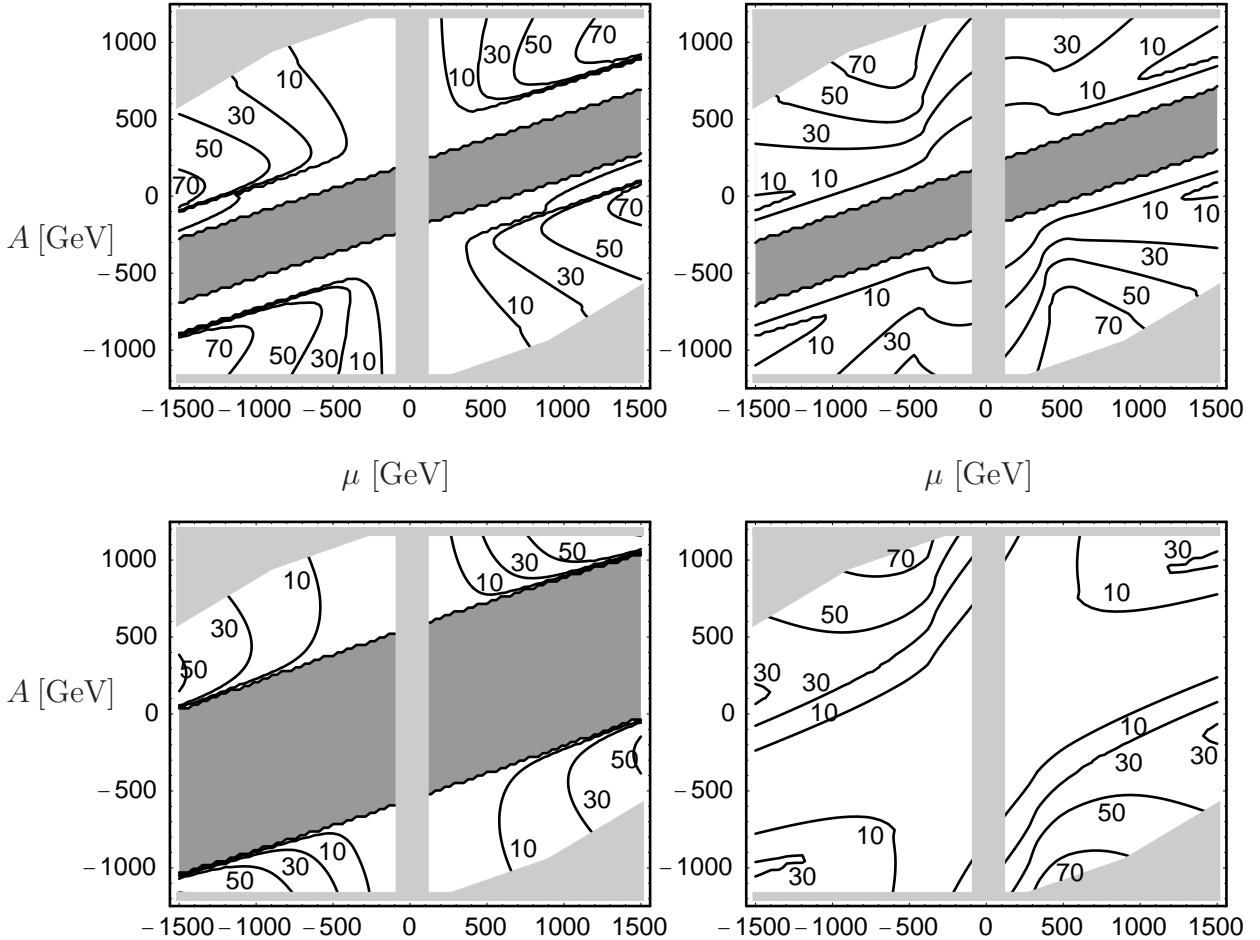
a function of the parameter μ with three values of the wino mass parameter M_2. We have fixed $\tan\beta = 10$ and the sbottom and stop masses to the values indicated in the caption, while the charged Higgs mass is chosen to be $M_{H^\pm} = 200\,(300)$ GeV in the left (right) panel. The other competing neutralino/chargino decays of the sbottom, $\tilde{b} \to b\chi^0$ and $t\chi^-$, are open while the $\tilde{b} \to b\tilde{g}$ decay is open only for $M_2 = 200$ GeV [the universality of the gaugino masses is assumed so that $m_{\tilde{g}} \sim 3M_2$] and dominates in this case.

Figure 2.42: The branching ratios for bottom squarks decaying into top squarks and charged Higgs bosons as a function of μ for $\tan\beta = 10$ and $M_2 = 200, 300$ and 400 GeV. The charged Higgs mass is taken to be $M_{H^\pm} = 200$ and 300 GeV in the left and right panels, respectively. The two squark masses are taken to be $m_{\tilde{b}_1} = 830$ GeV and $m_{\tilde{t}_1} = 430$ GeV [278].

As can be seen, for $M_2 \geq 300$ GeV, $\mathrm{BR}(\tilde{b}_1 \to \tilde{t}_1 H^-)$ can be substantial for large μ values, $\mu \gtrsim 700$ GeV, possibly exceeding the level of 50%. The reason for this feature, besides the fact that for $\mu \gtrsim 800$ GeV the $\tilde{b}_1$ decays into the heavier chargino and neutralinos are kinematically closed, is that the sbottom–stop–$H^\pm$ coupling is strongly enhanced and becomes larger than the sbottom–bottom–gaugino coupling which controls the sbottom decays into the lighter chargino and neutralinos. For smaller values of M_2, as pointed out earlier, the decay $\tilde{b}_1 \to b\tilde{g}$ becomes accessible and would be the dominant decay channel.

The decays of the heavier top squark into the lighter one and neutral Higgs bosons, $\tilde{t}_2 \to \tilde{t}_1 + h/H/A$ can also be substantial in some areas of the MSSM parameter space. In Fig. 2.43, the contour lines for the sum of the branching ratios for the decay modes into Higgs and gauge bosons are shown for $\tan\beta = 3$, $M_A = 150$ GeV and the set of SUSY–breaking parameters specified in the caption. We see that these $\tilde{t}_2$ and $\tilde{b}_2$ decays are dominant in large regions of the MSSM parameter space. In particular, the decays into Higgs bosons can reach the 70% level for large $|\mu|$ and/or $|A|$ values. Note, here, the dependence on the signs of A and μ. Similar results can be obtained for larger values of $\tan\beta$ [280].

Figure 2.43: Branching ratios (in %) of $\tilde{t}_2$ and $\tilde{b}_2$ decays in the μ–A plane for $A_t = A_b \equiv A$, $m_{\tilde{t}_L} = 500$ GeV, $m_{\tilde{t}_R} = 444$ GeV, $m_{\tilde{b}_R} = 556$ GeV, $M_2 = 300$ GeV, $M_A = 150$ GeV and $\tan\beta = 3$. Top–left: $\sum \mathrm{BR}[\,\tilde{t}_2 \to \tilde{t}_1 + h, H, A,\ \tilde{b}_{1,2} + H^+\,]$; top–right: $\sum \mathrm{BR}[\,\tilde{t}_2 \to \tilde{t}_1 + Z,\ \tilde{b}_{1,2} + W^+\,]$; bottom–left: $\mathrm{BR}[\tilde{b}_2 \to \tilde{t}_1 + H^-\,]$; bottom–right: $\mathrm{BR}[\tilde{b}_2 \to \tilde{t}_1 + W^-\,]$. In the dark grey areas the decays are kinematically not allowed; the light grey areas are excluded by the experimental constraints on the chargino, neutralino, Higgs boson and stop/sbottom masses as well as by the constraint on the ρ parameter $\Delta^{\mathrm{SUSY}}\rho \lesssim 10^{-3}$ and the CCB constraint on the trilinear couplings, $A_{t,b} \leq 3(m_{\tilde{t}_L}^2 + m_{\tilde{t}_L,\tilde{b}_L}^2 + m_{H_2,H_1}^2)$; from Ref. [280].

In mSUGRA–type models, where one is very often in the decoupling limit with a large value of $|\mu|$, the only sfermion decay into Higgs a boson which in general possible is $\tilde{t}_2 \to \tilde{t}_1 h$. When stop mixing is large, the partial width is proportional to the square of $\sin 2\theta_t m_t X_t$ with $\sin 2\theta_t \sim 1$ [maximal sfermion mixing], where there is an enhancement at large μ values and low $\tan\beta$ since $X_t = A_t - \mu/\tan\beta$. This decay has to compete with the channel $\tilde{t}_2 \to \tilde{t}_1 Z$ which has a partial width that is also proportional to $\sin 2\theta_t$, as well as with the decays $\tilde{t}_2 \to \chi_{1,2}^0 t$ and $\tilde{t}_2 \to \chi_1^+ b$ which are in general the dominant ones.

2.3.4 Three body decays of gluinos into Higgs bosons

Finally, there are direct decays of gluinos into top squarks, bottom quarks and charged Higgs bosons [278] which are mediated by virtual top quark or bottom squark exchanges as shown in Fig. 2.44. The same type of processes is possible for neutral Higgs production.
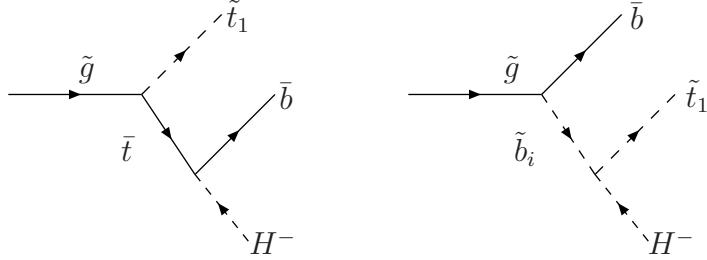
Figure 2.44: The Feynman diagrams contributing to the three–body decay $\tilde{g} \to \tilde{t}_1 \bar{b} H^-$.

The Dalitz density for this decay mode, taking into account all the masses of the final state particles except for the bottom quark, is given by [278]

$$\frac{\mathrm{d}\Gamma}{\mathrm{d}x_1 \mathrm{d}x_2}(\tilde{g} \to H^- \bar{b} \tilde{t}_1) \;=\; \frac{\alpha \alpha_s}{64\pi} m_{\tilde{g}} \left[\mathrm{d}\Gamma_t + \mathrm{d}\Gamma_{\tilde{b}} + 2\mathrm{d}\Gamma_{t\tilde{b}} \right] \tag{2.87}$$

In terms of $x_1 = 2E_{H^\pm}/m_{\tilde{g}}$, $x_2 = 2E_b/m_{\tilde{g}}$ and the reduced masses $\mu_X = m_X^2/m_{\tilde{g}}^2$, the squared t, $\tilde{b}$ contributions and the $t\tilde{b}$ interference amplitude are given by

$$
\begin{aligned}
\mathrm{d}\Gamma_t &= \frac{\mu_t x_2 [y_t^2 c_\beta^2 (b_{1\tilde{g}}^{\tilde{t}})^2 + y_b^2 s_\beta^2 (a_{1\tilde{g}}^{\tilde{t}})^2] + [y_t^2 c_\beta^2 (a_{1\tilde{g}}^{\tilde{t}})^2 + y_b^2 s_\beta^2 (b_{1\tilde{g}}^{\tilde{t}})^2][x_1 x_0 + x_2 \mu_{H^+}]}{(x_1 + x_2 - 1 + \mu_{\tilde{t}_1} - \mu_t)^2} \\[2mm]
\mathrm{d}\Gamma_{\tilde{b}} &= \sum_{i,j=1}^{2} \frac{g_{\tilde{t}_1 \tilde{b}_i H^+} g_{\tilde{t}_1 \tilde{b}_j H^+} [a_{i\tilde{g}}^{\tilde{b}} a_{j\tilde{g}}^{\tilde{b}} + b_{i\tilde{g}}^{\tilde{b}} b_{j\tilde{g}}^{\tilde{b}}] x_2}{(1 - x_2 - \mu_{\tilde{b}_i})(1 - x_2 - \mu_{\tilde{b}_j})} \\[2mm]
\mathrm{d}\Gamma_{t\tilde{b}_1} &= \sum_{i=1}^{2} \frac{g_{\tilde{t}_1 \tilde{b}_H^+} \left[-\sqrt{\mu_t} x_2 \left(y_t c_\beta b_{i\tilde{g}}^{\tilde{b}} b_{1\tilde{g}}^{\tilde{t}} + y_b s_\beta a_{i\tilde{g}}^{\tilde{b}} a_{1\tilde{g}}^{\tilde{t}} \right) - x_0 (y_t c_\beta b_{i\tilde{g}}^{\tilde{b}} a_{1\tilde{g}}^{\tilde{t}} + y_b s_\beta a_{i\tilde{g}}^{\tilde{b}} b_{1\tilde{g}}^{\tilde{t}}) \right]}{(1 + \mu_b - x_2 - \mu_{\tilde{b}_i})(x_1 + x_2 - 1 + \mu_{\tilde{t}_1} - \mu_t)}
\end{aligned}
\tag{2.88}
$$

where we have used, in addition, the abbreviation $x_0 = 1 - x_1 - x_2 - \mu_{\tilde{t}_1} - \mu_{H^+}$. The Yukawa couplings of top and bottom quarks are given in this case by $y_t = m_t/(\sqrt{2}s_W M_W s_\beta)$ and $y_b = m_b/(\sqrt{2}s_W M_W c_\beta)$ and the squark–quark–gluino coupling have been given in eq. (2.86). To obtain the partial decay width, one has to integrate over x_1 and x_2 with the usual three–particle phase space boundary conditions [see for instance §I.2.1].

The branching fraction for the three–body decay, BR$(\tilde{g} \to \tilde{t}_1 \bar{b} H^- + \tilde{t}_1^* b H^+)$, is illustrated in Fig. 2.45 as a function of μ for $\tan\beta = 10$. We have chosen squark masses of $m_{\tilde{q}} = m_{\tilde{b}_i} = 1$ TeV, a gluino mass that is slightly lower, $m_{\tilde{g}} = 900$ GeV, and the lighter stop mass to be $m_{\tilde{t}_1} = 430$ GeV; for the charged Higgs boson mass we take three values: $M_{H^\pm} = 190, 230$ and

310 GeV. In this scenario, all squarks [including bottom squarks] will decay into gluinos and almost massless quarks and the former will dominantly decay into the lighter top squarks and top quarks. The three–body decays $\tilde{g} \to \tilde{t}_1 \bar{b} H^-$ and $\tilde{g} \to \tilde{t}_1^* b H^+$ have therefore to compete with a strong interaction two–body decay, which has a large phase space in this case. This is the reason why the branching ratio hardly exceeds the one percent level, which occurs for large μ values when the $\widetilde{tb}H^\pm$ couplings are enhanced.

Note that the smallness of the branching ratio is also due to the smallness of the tbH^+ coupling for the chosen value of $\tan\beta$; for larger or smaller values of $\tan\beta$, the branching ratio might be significantly larger. Note also that in spite of the small branching ratio, the number of $H^\pm$ final states due to this process can be rather large at the LHC in the chosen kinematical configuration, since the cross section for gluino production can be quite large, in particular, in scenarios where all squarks except for $\tilde{t}_1$ are heavier than gluinos and decay mostly into $\tilde{q} \to q\tilde{g}$ final states.
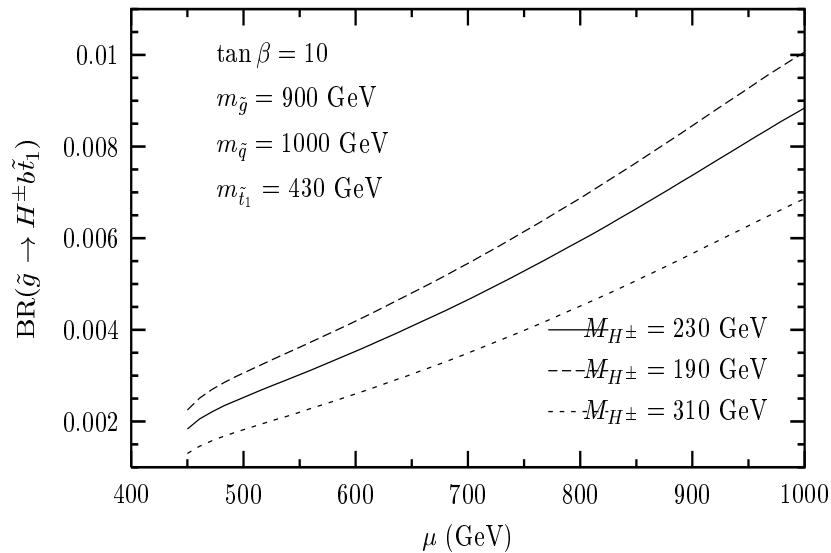
Figure 2.45: The branching ratios for direct decays of gluinos into b–quarks, top squarks and charged Higgs bosons as a function of μ for $\tan\beta = 10$ and $M_{H^\pm} = 190, 230$ and 310 GeV. The squark masses are $m_{\tilde{q}} = 1$ TeV and $m_{\tilde{t}_1} = 430$ GeV while $m_{\tilde{g}} = 900$ GeV [278].

In the case of neutral Higgs bosons, the decays $\tilde{g} \to \tilde{t}_1 t h$ can be quite frequent if phase space allowed, in particular in the decoupling limit where the htt coupling is strong and for large stop mixing where the $h\tilde{t}_1\tilde{t}_1$ coupling is enhanced. The decays $\tilde{g} \to \tilde{b}_1 b H$ and $\tilde{g} \to \tilde{b}_1 b A$ can be also important at high values of $\tan\beta$ where the H/A couplings are enhanced. These decays are under study [283].

2.4 Cosmological impact of the MSSM Higgs sector

2.4.1 Neutralino Dark Matter

As deduced from the WMAP satellite measurement of the temperature anisotropies in the Cosmic Microwave Background, in combination with data on the Hubble expansion and the density fluctuations in the universe, cold Dark Matter (DM) makes up $\approx 25\%$ of the energy of the universe [12]. The DM cosmological relic density is precisely measured to be

$$\Omega_{\mathrm{DM}}\, h^2 = 0.113 \pm 0.009 \tag{2.89}$$

which leads to $0.087 \leq \Omega_{\mathrm{DM}}\, h^2 \leq 0.138$ at the 99% confidence level. In these equations, $\Omega \equiv \rho/\rho_c$, where $\rho_c \simeq 2 \cdot 10^{-29} h^2 \mathrm{g/cm}^3$ is the "critical" mass density that yields a flat universe, as favored by inflationary cosmology and as verified by the WMAP satellite itself; $\rho < \rho_c$ and $\rho > \rho_c$ correspond, respectively, to an open and closed universe, i.e. a metric with negative or positive curvature. The dimensionless parameter h is the scaled Hubble constant describing the expansion of the universe.

In the MSSM with R–parity conservation, there is an ideal candidate for the weakly interacting massive particle (WIMP) which is expected to form this cold Dark Matter [24, 25][23]: the lightest neutralino χ_1^0 which is absolutely stable, electrically neutral and massive. Furthermore, it has only weak interactions and, for a wide range of the MSSM parameter space, its annihilation rate into SM particles fulfills the requirement that the resulting cosmological relic density is within the range measured by WMAP. This is particularly the case in the widely studied mSUGRA scenario [286–288] and in some of its non–universal variants [289, 290].

In this section, we discuss the contribution of the LSP neutralino to the overall matter density of the universe and highlight the role of the MSSM Higgs sector which is prominent in this context[24]. We will follow the standard treatment [11], with the modifications outlined in Ref. [292] [we will closely follow Ref. [287] to which we refer for details and references]. The treatment is based on the assumption [besides that the LSP should be effectively stable, i.e. its lifetime should be long compared to the age of the Universe, which holds in the MSSM with conserved R–parity that is discussed here] that the temperature of the Universe after the last period of entropy production must exceed $\sim 10\%$ of $m_{\chi_1^0}$. This assumption is quite

---

[23]One should mention that there are viable SUSY DM candidates other than the lightest neutralino, examples are the gravitino which is present in all SUSY models and the axino. These two possibilities will not be discussed here; see for instance Ref. [284, 285] for reviews. In addition, the possibility that the sneutrinos form the DM is excluded as their interactions are too strong and these particles should have been already detected in direct WIMP searches [25].

[24]Another cosmological aspect in which the MSSM Higgs sector plays an important role is electroweak baryogenesis [291]. However, for this to be achieved, a fair amount of CP–violation in the MSSM is needed, and this topic is thus beyond the boundaries that have been set for this review.

natural in the framework of inflationary models, given that analyses of structure formation determine the scale of inflation to be $\sim 10^{13}$ GeV in simple models [11].

In the early universe, all particles were abundantly produced and were in thermal equilibrium through annihilation and production processes. The time evolution of the number density of the particles is governed by the Boltzmann equation

$$\frac{dn_{\chi_1^0}}{dt} + 3Hn_{\chi_1^0} = -\langle v\,\sigma_{\mathrm{ann}}\rangle(n_{\chi_1^0}^2 - n_{\chi_1^0}^{\mathrm{eq}\,2}) \tag{2.90}$$

where v is the relative LSP velocity in their center–of–mass frame, σ_{ann} is the LSP annihilation cross section into SM particles and $\langle\ldots\rangle$ denotes thermal averaging; $n_{\chi_1^0}$ is the actual number density, while $n_{\chi_1^0}^{\mathrm{eq}}$ is the thermal equilibrium number density. The Hubble term takes care of the decrease in number density due to the expansion, while the first and second terms on the right–hand side represent, respectively, the decrease due to annihilation and the increase through creation by the inverse reactions. If the assumptions mentioned above hold, χ_1^0 decouples from the thermal bath of SM particles at an inverse scaled temperature $x_F \equiv m_{\chi_1^0}/T_F$ which is given by [11]

$$x_F = 0.38 M_P \langle v\sigma_{\mathrm{ann}}\rangle c(c+2) m_{\chi_1^0}\,(g_* x_F)^{-1/2} \tag{2.91}$$

where $M_P = 2.4 \cdot 10^{18}$ GeV is the (reduced) Planck mass, g_* the number of relativistic degrees of freedom which is typically $g_* \simeq 80$ at T_F, and c a numerical constant which is taken to be $\frac{1}{2}$; one typically finds $x_F \simeq 20$ to 25. Today's LSP density in units of the critical density is then given by [11]

$$\Omega_\chi h^2 = \frac{2.13 \cdot 10^8/\mathrm{GeV}}{\sqrt{g_*}M_P J(x_F)}\,, \quad \text{with} \ \ J(x_F) = \int_{x_F}^{\infty} \frac{\langle v\sigma_{\mathrm{ann}}\rangle(x)}{x^2}dx \tag{2.92}$$

Eqs. (2.91)–(2.92) provide an approximate solution of the Boltzmann equation which has been shown to describe the exact numerical solution very accurately for all known scenarios [after some extensions which will be discussed shortly].

Since χ_1^0 decouples at a temperature $T_F \ll m_\chi$, in most cases it is sufficient to use an expansion of the LSP annihilation rate in powers of the relative velocity between the LSPs

$$v\,\sigma_{\mathrm{ann}} \equiv v\,\sigma(\chi_1^0\chi_1^0 \to \mathrm{SM\,particles}) = a + bv^2 + \mathcal{O}(v^4) \tag{2.93}$$

The entire dependence on the parameters of the model is then contained in the coefficients a and b, which essentially describe the LSP annihilation cross section from an initial S– and P–wave, since the expansion of the annihilation cross section of eq. (2.93) is only up to $\mathcal{O}(v^2)$. S–wave contributions start at $\mathcal{O}(1)$ and contain $\mathcal{O}(v^2)$ terms that contribute to eq. (2.93) via interference with the $\mathcal{O}(1)$ terms. In contrast, P–wave matrix elements start at $\mathcal{O}(v)$, so

145

that only the leading term in the expansion is needed. There is no interference between S– and P–wave contributions and hence no $\mathcal{O}(v)$ terms. Note that Fermi statistics forces the S–wave state of two identical Majorana fermions to have CP$= -1$, while the P–wave has CP$= +1$; the same argument implies that the S–wave has to have total angular momentum $J = 0$. The calculation of the thermal average over the annihilation cross section, and of the annihilation integral eq. (2.92), is then trivial, allowing an almost completely analytical calculation of $\Omega_{\chi_1^0}$ [eq. (2.91) still has to be solved iteratively]. Expressions for the a and b terms for all possible two–body final states are collected in Ref. [293]. In these expressions, one should use running quark masses at the scale $Q \sim m_{\chi_1^0}$, in order to absorb leading QCD corrections and implement the other potentially large radiative corrections.

In generic scenarios the expansion eq. (2.93) reproduces exact results to $\sim 10\%$ accuracy [294], which is in general quite sufficient. However, it has been known for some time [292] that this expansion fails in some exceptional cases, all of which can be realized in some part of the MSSM parameter space, and even in constrained models such as mSUGRA:

i) The expansion breaks down near the threshold for the production of heavy particles, where the cross section depends very sensitively on the c.m. energy $\sqrt{s}$. In particular, due to the non–vanishing kinetic energy of the neutralinos, annihilation into final states with mass exceeding twice the LSP mass ("sub–threshold annihilation") is possible. This is particularly important in the case of neutralino annihilation into W^+W^- and hh pairs, for relatively light higgsino–like and mixed LSPs, respectively.

ii) The expansion eq. (2.93) also fails near $s-$channel poles, where the cross section again varies rapidly with $\sqrt{s}$. In the MSSM, this happens if twice the LSP mass is near M_Z, or near the mass of one of the neutral Higgs bosons [293, 295]. In models with universal gaugino masses, the $Z-$ pole region is now excluded by chargino searches at LEP2 and we are left only with the Higgs pole regions which are important as will be seen later.

iii) If the mass splitting between the LSP and the next–to–lightest superparticle NLSP is less than a few times T_F, co–annihilation processes involving one LSP and one NLSP, or two NLSPs, can be important. As will be discussed later, co–annihilation is important in three cases: higgsino– or SU(2) gaugino–like LSPs [293, 296] and when the LSP is degenerate in mass with $\tilde{\tau}_1$ [297] or with the lightest top squark [298, 299].

2.4.2 Neutralino annihilation and the relic density

In the following, we will discuss the annihilation cross section of two LSP neutralinos into a pair of ordinary SM particles: fermions, gauge and Higgs bosons. Since our aim here is simply to highlight the impact of the MSSM Higgs sector in this particular context, we will make a rather qualitative discussion of the various annihilation rates, following Ref. [293] and assuming in most cases the LSP to be nearly either a bino or a higgsino, and give only

symbolic expressions for the matrix elements which allow to estimate the magnitude of the various contributing channels. The co–annihilation processes will also be discussed and a few numerical examples, borrowed from Refs. [288, 290, 298, 300], will be given for illustration.

Annihilation into fermions

The annihilation of neutralinos into a fermion pair proceeds through t/u–channel sfermion exchange and s–channel Z or Higgs boson exchange; Fig. 2.46. Since both the $Zf\bar{f}$ and $f\tilde{f}$–gaugino couplings conserve chirality, the sfermion and Z exchange contributions to the S–wave matrix element $\mathcal{M}_S$ are proportional to the mass of the final fermion m_f; the contributions due to Higgs boson exchange, the ones from the $f\tilde{f}$–higgsino Yukawa interactions and from sfermion mixing violate chirality, but have an explicit factor of m_f. The coefficient a in the expansion eq. (2.93) of the annihilation cross section is therefore always proportional to m_f^2. In addition, because the CP quantum number of the exchanged Higgs particles must match that of the initial state, only A boson exchange contributes to $\mathcal{M}_S$ while h and H exchange contribute to $\mathcal{M}_P$. Since $\mathcal{M}_P$ only contributes to the coefficient b in eq. (2.93), which is suppressed by a factor $3/x_F \simeq 0.1$–0.2, pseudoscalar A exchange is in general much more important than the contribution from the CP–even Higgs bosons.
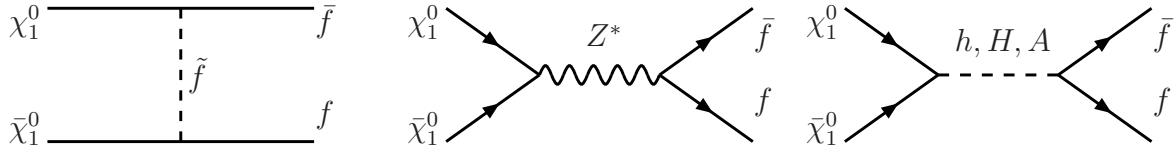
Figure 2.46: Feynman diagrams for LSP neutralino annihilation into a fermion pair.

For a bino–like LSP, that is when $|\mu| \gg M_2$ [hereafter, we assume the universality of the gaugino masses, which leads to the relation $M_1 = \frac{5}{3}\tan^2\theta_W M_2 \simeq \frac{1}{2}M_2$ at the weak scale], the matrix elements for the reaction $\chi_1^0\chi_1^0 \to f\bar{f}$, where the summation over all fermion final states that are kinematically allowed is implicitly assumed, has the form

$$\mathcal{M}_S(\chi\chi \to f\bar{f})\big|_{\tilde{B}} \propto g_1^2 m_f \left[\frac{c_1 m_\chi}{m_{\tilde{f}}^2 + m_\chi^2} Y_f^2 + \frac{c_2 M_Z^2}{M_1^2 - \mu^2} \frac{m_\chi}{M_Z^2} + \frac{c_3}{M_1 + \mu} \frac{m_\chi^2}{4m_\chi^2 - M_A^2 + iM_A\Gamma_A} \right] \quad (2.94)$$

$$\mathcal{M}_P(\chi\chi \to f\bar{f})\big|_{\tilde{B}} \propto g_1^2 v \left[\frac{d_1 m_\chi^2}{m_{\tilde{f}}^2 + m_\chi^2} Y_f^2 + \frac{d_2 M_Z^2}{M_1^2 - \mu^2} \frac{m_\chi^2}{4m_\chi^2 - M_Z^2 + iM_Z\Gamma_Z} + \Sigma_{i=1}^2 \frac{d_{3,i} m_f}{M_1 + \mu} \frac{m_\chi^2}{4m_\chi^2 - M_{H_i}^2 + iM_{H_i}\Gamma_{H_i}} \right]$$

where c_i, d_i are numerical constants of $\mathcal{O}(1)$ and $c_3, d_{3,i}$ contain the $f\bar{f}$ couplings of the $H_i = H, h$ bosons which can be enhanced/suppressed by powers of $\tan\beta$; g_1 is the U(1)$_Y$ gauge coupling. From this equation, one sees that the s–channel diagrams are all suppressed by small couplings. As discussed earlier, the Higgs bosons couple to mixtures of higgsinos and gauginos and the couplings are thus suppressed only by one power of the small higgsino component. The Z boson couples to neutralinos only via their higgsino components and for

a bino–like LSP, this coupling is doubly suppressed. The sfermion exchange contribution in this case is small only if $m_{\tilde{f}}^2 \gg m_\chi^2$. For LSP masses close to $\frac{1}{2} M_Z$ [which is ruled out in mSUGRA type models, eq. (1.54)] or $\frac{1}{2} M_\Phi$, the matrix elements become very large.

In turn, for a higgsino–like LSP, $|\mu| \ll M_2$, the matrix elements have the form

$$\mathcal{M}_S(\chi\chi \to f\bar{f})\big|_{\tilde{H}} \propto (g_1^2 + g_2^2) m_f \left[\left(\frac{c_1' M_Z}{\mu + M_2} + \frac{c_1'' m_f}{M_Z}\right)^2 \frac{m_\chi}{m_{\tilde{f}}^2 + m_\chi^2} + \frac{c_2' M_Z^2}{\mu M_2} \frac{m_\chi}{M_Z^2} + \frac{c_3'}{M_1 + \mu} \frac{m_\chi^2}{4 m_\chi^2 - M_A^2 + i M_A \Gamma_A}\right]$$

$$\mathcal{M}_P(\chi\chi \to f\bar{f})\big|_{\tilde{H}} \propto (g_1^2 + g_2^2) v \left[\left(\frac{d_1' M_Z}{\mu + M_2} + \frac{d_1'' m_f}{M_Z}\right)^2 \frac{m_\chi^2}{m_{\tilde{f}}^2 + m_\chi^2} + \frac{c_2' M_Z^2}{\mu M_2} \frac{m_\chi^2}{4 m_\chi^2 - M_Z^2 + i M_Z \Gamma_Z}\right.$$

$$\left. + \sum_{i=1}^2 \frac{d_{3,i}' m_f}{M_1 + \mu} \frac{m_\chi^2}{4 m_\chi^2 - M_A^2 + i M_A \Gamma_A}\right] \tag{2.95}$$

We see that the sfermion exchange contribution is now suppressed by either the small gaugino component of the LSP or by a power of the Yukawa coupling [for $f = t/b$ this could be an enhancement for small/large values of $\tan\beta$]; one notices also that there are SU(2) gauge contributions which can be sizable as they are suppressed only by $M_Z/(M_2 + \mu)$ terms. The Higgs boson exchange contribution is at the same order in $M_Z/(M_1 + \mu)$ as in the bino–like case. Finally, the Z exchange contribution is now suppressed only linearly with the mass of the heavier neutralinos being $\propto M_Z^2/(\mu M_2)$ contrary to the bino case.

The direct QCD corrections to the channels $\chi_1^0 \chi_1^0 \to q\bar{q}$, which include virtual corrections and the emission of an additional gluon in the final state, were calculated in Refs. [301, 302] and found to be rather important in many regions of the parameter space. Another related QCD channel, calculated in the same references, is $\chi_1^0 \chi_1^0 \to gg$ which occurs through s– channel Z and Higgs exchange with triangle diagrams involving quarks and squarks and box diagrams involving these particles. Although suppressed by a power of α_s^2, this channel might be comparable or even larger than the annihilation into light quarks and leptons, which are helicity suppressed in the non–relativistic limit as seen previously. These channels are in fact more important for the indirect detection of the LSP neutralinos to be discussed later.

In Fig. 2.47, we show the m_0–$m_{1/2}$ parameter space of the mSUGRA model which is compatible with the WMAP measurement of the relic density as obtained from the program `micrOMEGAs1.3` [303] linked to the RGE code `SOFTSUSY` [127]. A point with $\tan\beta = 50$, $A_0 = 0$ and $\text{sign}(\mu) = +$ has been choosen and a scan over the two remaining parameters has been performed. The obtained relic density is given by the dashed line, while the green [light grey] band is the region where $0.94 \le \Omega_{\chi_1^0} h^2 \le 0.129$, that is, within 2σ from the central WMAP value; the hatched area is the region that is excluded since there, $\tilde{\tau}_1$ is the LSP. The required relic density is obtained from the annihilation rate into fermions and, in fact, $\chi_1^0 \chi_1^0 \to b\bar{b}$ and $\tau^+ \tau^-$ represent 98% of $\Omega_{\chi_1^0} h^2$ in this example.

The region below $m_{1/2} \sim m_0 \lesssim 500$ GeV is the "bino–like LSP" region where both the LSP and the $\tilde{\tau}_1$ are light enough for the annihilation $\chi_1^0 \chi_1^0 \to \tau^+ \tau^-$ cross section, through

t–channel $\tilde{\tau}_1$ exchange, to be sizable. For larger values of $m_{1/2}$ and m_0, we enter in the "Higgs funnel" region, where $2m_{\chi_1^0}$ is close the pseudoscalar A boson or scalar H boson s–channel poles. Indeed, for $\tan\beta \gg 1$, M_A [and thus also M_H] become smaller in mSUGRA type models, and their Yukawa couplings to b quarks and τ leptons are strongly enhanced. The resulting large $\tilde{\chi}_1^0 \tilde{\chi}_1^0 \to b\bar{b}, \tau^+\tau^-$ annihilation cross sections reduce the relic density to the required level. When the QCD corrections to the bottom Yukawa coupling are properly included, these Higgs pole regions open up only for values $\tan\beta \gtrsim 40$–50; the corrections to the physical Higgs masses are also of some importance here. The A and H masses are very close to each other in this region of parameter space but the dominant contribution is due to the A boson exchange, since H boson exchange occurs in the P–wave and is suppressed. At zero–velocity, the main contribution can be in fact written as [288]

$$\langle v\,\sigma_{\text{ann}}\rangle_{v=0}^{-1} \propto \frac{4m_{\chi_1^0}\Gamma_A^{\text{tot}}}{g_{\chi_1^0\chi_1^0 A}^2}\left[4\left(\frac{M_A - 2m_{\chi_1^0}}{\Gamma_A^{\text{tot}}}\right)^2 + 1\right] \tag{2.96}$$

Thus, a precise calculation of the mass of the pseudoscalar A boson, its total decay width and its couplings to the LSP are required to obtain the proper relic density, which is given by the full line in the right–hand side of Fig. 2.47 which shows $\Omega_{\chi_1^0}h^2$ as a function of M_A [the range is obtained by varying $m_{1/2}$ in the range 250–1100 GeV] in various approximations. As can be seen, if for instance the resummation of eq. (1.47) for the b–quark mass [which enters in the $Ab\bar{b}$ Yukawa coupling and in the determination of M_A] is not performed or if the two–loop RGEs for the soft SUSY–breaking Higgs masses are not included, the obtained relic density goes outside the WMAP range. The WMAP measurement is in fact so precise, that even the two–loop QCD corrections to the top quark mass [which enters at various places in the RGEs] and the two–loop RGEs for the gaugino masses are important.

Annihilation into gauge and Higgs bosons

The WW and ZZ final states can be produced via t–channel chargino and t/u–channel neutralino exchange, respectively, and s–channel exchange of the CP–even Higgs bosons; in the case of $\chi_1^0\chi_1^0 \to W^+W^-$, s–channel Z exchange also contributes [Fig. 2.48]. As already seen in the decays of inos [and as can be understood from the equivalence theorem discussed in §I.1.1, when the gauge bosons are replaced by Goldstone bosons], the trend is different for longitudinal and transverse gauge bosons: in the former case, the amplitude receives an enhancement factor $\sim m_{\chi_1^0}/M_V$ for each V_L state, which gives finite matrix elements in the limit $m_{\chi_1^0} \to \infty$ even if the $\chi\chi V$ couplings vanish [in this case, unitarity requires strong cancellations between the various contributions to the matrix elements]. Since $V_L V_L$ and $V_L V_T$ pairs cannot be produced in a $J = 0$ state with CP $= -1$, these final states are only accessible through the P–wave which has a suppressed contribution.
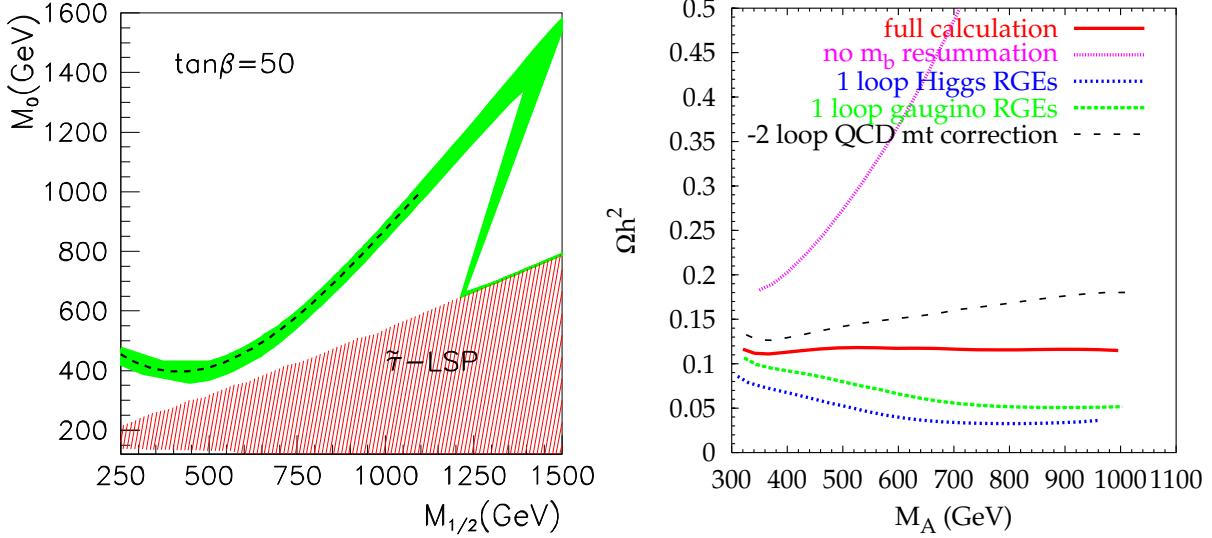
Figure 2.47: The WMAP central value (dashed line) and allowed region (green/light grey) in the m_0–$m_{1/2}$ plane for $\tan\beta = 50$, $A_0 = 0$ and $sign(\mu) = +$; the red/hatched area is ruled out by the constraint that the LSP is neutral (left). The effect of different approximations in the calculation of various parameters on the relic density (right). From Ref. [288].

For a bino–like LSP, the matrix element involves only the P–wave contribution of V_L's

$$\mathcal{M}_P(\chi\chi \to VV)|_{\tilde{B}} \propto g_1^2 v \left[\frac{d_4 M_Z^2}{M_1^2 + \mu^2} \frac{m_\chi}{\mu} + \sum_{i=1}^{2} \frac{d_{5,i} M_Z}{M_1 + \mu} \frac{m_\chi M_V}{4m_\chi^2 - M_{H_i}^2 + iM_{H_i}\Gamma_{H_i}} \right] \frac{m_\chi^2}{M_V^2} \qquad (2.97)$$

which displays the enhancement factor m_χ^2/M_V^2 and does not vanish for $m_{\chi_1^0} \to \infty$, unless one has $|M_1| \ll |\mu|$, as mentioned earlier. The coefficient $d_{5,1} \sim \cos(\beta - \alpha)$ due to the heavier H boson exchange is small in general, and the exchange of the lighter h boson with $d_{5,2} \sim \sin(\beta - \alpha)$, provides the dominant contribution in the bino limit.

For a higgsino–like LSP, the form of the matrix elements is

$$\mathcal{M}_S(\chi\chi \to VV)|_{\tilde{H}} \propto (g_2^2 + g_1^2)c_4'$$
$$\mathcal{M}_P(\chi\chi \to VV)|_{\tilde{H}} \propto (g_2^2 + g_1^2)v \left[d_4' + \sum_{i=1}^{2} \frac{d_{5,i}' M_Z}{M + \mu} \frac{m_\chi M_V}{4m_\chi^2 - M_{H_i}^2 + iM_{H_i}\Gamma_{H_i}} \frac{m_\chi^2}{M_V^2} \right] \qquad (2.98)$$

For the dominant S–wave contribution, there is no propagator suppression of the t/u–channel diagrams for annihilation into [transverse] VV final states as the exchanged inos can also be higgsinos with approximately the same mass as the LSP. Again, the P–wave matrix element exhibits the m_χ^2/M_V^2 enhancement when Higgs bosons are exchanged.

$\chi_1^0\chi_1^0 \to V +$ Higgs final states can be produced via neutralino t/u–channel exchange and s–channel exchange of Z and Higgs bosons. Specializing into the Zh final state, the exchanged particle is the pseudoscalar A boson. In this case, one has for a bino–like LSP

$$\mathcal{M}_S(\chi\chi \to Zh)|_{\tilde{B}} \propto g_1^2 \frac{m_\chi}{M_1 + \mu} \frac{M_Z^2}{M_A^2 + M_Z^2} \left[c_6 + c_7 \frac{m_\chi^2}{4m_\chi^2 - M_A^2 + iM_A\Gamma_A} \right]$$
$$\mathcal{M}_P(\chi\chi \to Zh)|_{\tilde{B}} \propto g_1^2 v \frac{d_6 m_\chi^2}{M_1^2 + \mu^2} \qquad (2.99)$$

150
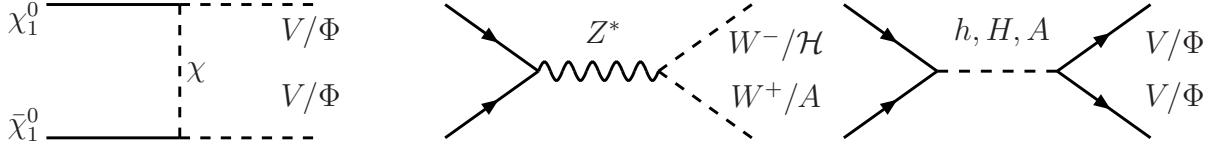
Figure 2.48: Diagrams for LSP neutralino annihilation into Higgs/gauge boson pairs.

where c_6 and d_6 get contributions from neutralino as well as Z exchange diagrams and c_7 is proportional to the ZhA coupling. In the decoupling limit $M_A \gg M_Z$, $\mathcal{M}_S$ is strongly suppressed; the A exchange contribution is further suppressed as $g_{ZhA} \sim \cos(\beta - \alpha)$ is very small. In this limit, only the P–wave amplitude survives but is small for $M_1 \ll |\mu|$.

For a higgsino–like LSP, the $\chi_1^0 \chi_1^0 \to Zh$ amplitudes become

$$\mathcal{M}_S(\chi\chi \to Zh)|_{\tilde{H}} \propto (g_2^2 + g_1^2)\frac{m_\chi}{M_2 + \mu}\left[c_6' + \frac{c_7' M_Z^2}{M_A^2 + M_Z^2}\frac{m_\chi^2}{4m_\chi^2 - M_A^2 + i\Gamma_A M_A} \right]$$

$$\mathcal{M}_P(\chi\chi \to Zh)|_{\tilde{H}} \propto (g_2^2 + g_1^2)v\frac{d_7' m_\chi^2}{M_2^2 + \mu^2} \tag{2.100}$$

and one can see that in this case the $\mathcal{O}(1)$ term from t–channel and Z exchange diagrams survives also in the decoupling limit $M_A \gg M_Z$. As in the bino–LSP case, the total amplitude is suppressed only if $M_1 \gg |\mu|$.

Finally, for $\chi_1^0 \chi_1^0 \to$ Higgs–Higgs annihilation, only t/u–channel neutralino (chargino) exchange and s–channel CP–even Higgs exchange diagrams contribute for hh, HH, Hh, AA ($H^+ H^-$) final states; the final states hA and HA also occur through Z boson exchange. In the case of hh final states on which we will focus, since two identical scalars cannot be in a state with $J = 0$ and CP $= -1$, annihilation can only proceed from the P–wave. The amplitude has the same general form for bino– and higgsino–like LSP neutralinos
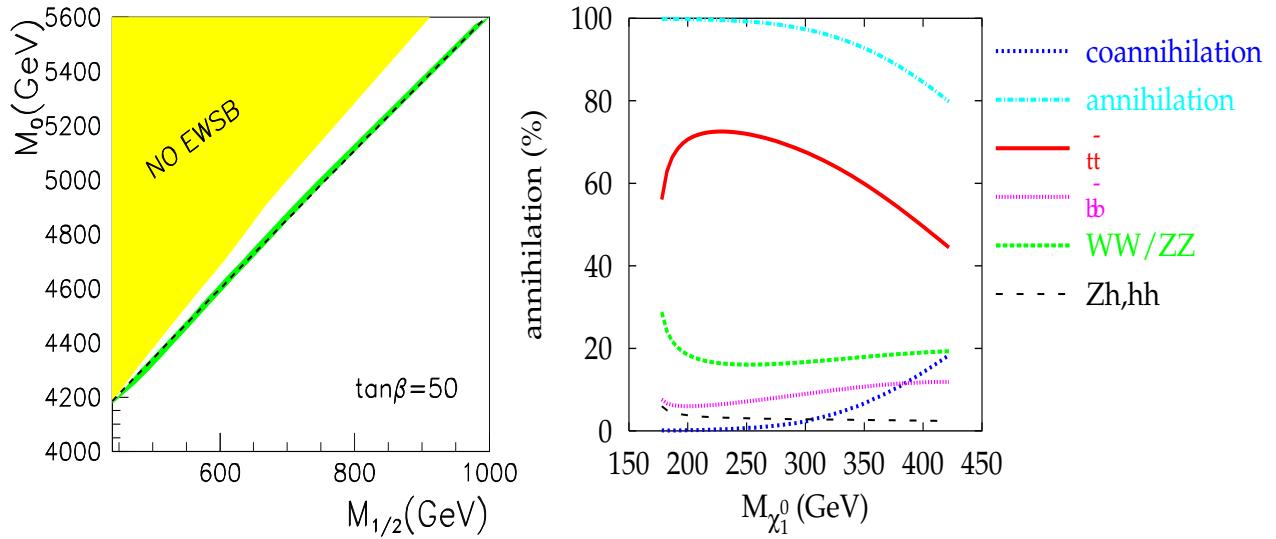
$$\mathcal{M}_P(\chi\chi \to hh) \propto g_1^2 v \left[\frac{d_8 m_\chi}{M_2 + \mu} + \frac{d_9 M_Z^2}{M_2^2 - \mu^2} + \sum_{i=1}^2 \frac{d_{10,i} M_Z}{M_2 + \mu}\frac{M_Z m_\chi}{4m_\chi^2 - M_{H_i}^2 + iM_{H_i}\Gamma_{H_i}} \right] \tag{2.101}$$

The first term is due to the exchange of the heavier neutralinos, which occurs with full strength but is suppressed by small propagators, while the second term is due to neutralino mixing. In the case of a bino–like LSP the coefficient d_8 is suppressed if $\tan\beta \gg 1$, unlike for higgsino–like LSP where the amplitude has contributions from SU(2) gauge interactions. The last term involves the trilinear Higgs interactions and in the decoupling limit, only $H_2 = h$ exchange is important if the LSP is not a pure bino or higgsino.

To illustrate the impact of all these channels, we show in Fig. 2.49, the m_0–$m_{1/2}$ parameter space which is compatible with WMAP as in Fig. 2.47, for $\tan\beta = 50$, $A_0 = 0$, sign$(\mu) = +$ and a very large m_0 value. Here, we are in the "focus point" [304] region where the neutralinos and charginos are mixtures of higgsino and gaugino states, close to the "no EWSB" region where no consistent value of μ is obtained from radiative EWSB [colored/dark region in the left–hand side of the figure].

151

The main channels which contribute to $\chi_1^0\chi_1^0$ annihilation and thus to the relic density, are shown in the right–hand side of the figure. The most important channel in this scenario is $\chi_1^0\chi_1^0 \to t\bar{t}$ annihilation which proceeds mainly through Z boson [or rather, through neutral Goldstone boson] exchange which receives a contribution from the large top quark Yukawa coupling. Another contribution is due to $\chi_1^0\chi_1^0 \to b\bar{b}$ annihilation which proceeds through the exchange of the pseudoscalar A boson which takes advantage of a sizable $Ab\bar{b}$ Yukawa for the chosen high value of $\tan\beta$; however, the contribution is smaller than in the previous example as a result of the propagator suppression by the large value of M_A that one obtains in this particular scenario. Although in the chosen scenario the LSP has a significant Higgsino fraction, the annihilation channels into WW and ZZ final states account for only 20% of the relic density. The reason is that all channels are P–wave suppressed and the S–wave contribution of the t–channel neutralino/chargino exchange for $V_T V_T$ production, does not involve enhanced couplings. The annihilation into Zh and hh final states gives also a rather small contribution, a few percent, in this case.

For values $m_{\chi_1^0} \sim 350$ GeV, the next–to–lightest sparticles, the neutralino χ_2^0 and the chargino $\chi_1^\pm$ have masses that become comparable to that of the LSP and "co–annihilation" with these states starts to contribute significantly to the relic density. The "co–annihilation" mechanism is discussed in the following.

Figure 2.49: The central value (dashed line) and the WMAP allowed region (green/light grey) in the m_0–$m_{1/2}$ parameter space for $\tan\beta = 50, A_0 = 0$ and $\mathrm{sign}(\mu) = +$; the yellow (grey) area is ruled out be the requirement of proper EWSB (left). The contribution of the various channels to the relic density; "annihilation" stands for all the channels which are given individually such as $t\bar{t}, b\bar{b}, W^+W^-, ZZ, Zh$ and hh, and "co-annihilation" stands for $\chi_1^0\chi_2^0, \chi_1^0\chi_1^\pm$ initiated processes. From Ref. [288].

Co–annihilation processes

As mentioned in the beginning of this section, $\chi_1^0 \chi_1^0$ annihilation is not the only process that changes the number of superparticles at temperatures around $T_F \simeq m_\chi/20$. If the mass splitting between the LSP and the next–to–lightest supersymmetric particle $\tilde{P}$ is small, the reactions of the type $\chi_1^0 + X \leftrightarrow \tilde{P} + Y$, where X, Y are SM particles, occur much more frequently at a temperature $T \sim T_F$ than $\chi_1^0 \chi_1^0$ annihilation reactions do. The rate of the latter kind of process is proportional to two powers of the Boltzmann factor $\exp(-m_\chi/T_F) \simeq \exp(-20)$, whereas for $m_\chi \simeq m_{\tilde{P}}$ the rate for the reaction written above is linear in this factor. These reactions will therefore maintain relative equilibrium between the LSP states and the particles $\tilde{P}$ until long after all superparticles decouple from the SM plasma. The total number of superparticles can then not only be changed by $\chi_1^0 \chi_1^0$ annihilation, but also by the "co–annihilation" processes [292]

$$\chi_1^0 + \tilde{P} \leftrightarrow X + Y \quad \text{and} \quad \tilde{P} + \tilde{P}^{(*)} \leftrightarrow X + Y \tag{2.102}$$

Eventually all particles $\tilde{P}$ and $\tilde{P}^*$ will decay into the LSP plus SM particles. To calculate the present LSP relic density, one therefore has to solve the Boltzmann equation for the sum $n_{\tilde{P}}$ of densities n_i of all relevant species of superparticles. One thus has [292]

$$\frac{dn_{\tilde{P}}}{dt} = -3H n_{\tilde{P}} - \sum_{i,j} \langle \sigma_{ij} v \rangle \left(n_i n_j - n_i^{\text{eq}} n_j^{\text{eq}} \right) = -3H n_{\tilde{P}} - \langle \sigma_{\text{eff}} v \rangle \left(n_{\tilde{P}}^2 - n_{\tilde{P}}^{\text{eq}^2} \right) \tag{2.103}$$

where in the second step we made use of the fact that all relevant heavier superparticles maintain relative equilibrium to the neutralino LSP until long after the temperature T_F, which allows to sum all sparticle annihilation processes into an "effective" cross section [292]

$$\sigma_{\text{eff}} \propto g_{\tilde{\chi}\tilde{\chi}} \sigma(\chi_1^0 \chi_1^0) + g_{\tilde{\chi}\tilde{P}} B_{\tilde{P}} \sigma(\chi_1^0 \tilde{P}) + g_{\tilde{P}\tilde{P}} \left(B_{\tilde{P}} \right)^2 \sigma(\tilde{P}\tilde{P}^{(*)}). \tag{2.104}$$

where the g_{ij} are multiplicity factors and $B_{\tilde{P}} = (m_{\tilde{P}}/m_{\chi_1^0})^{3/2} e^{-(m_{\tilde{P}} - m_{\chi_1^0})/T}$ is the temperature dependent relative Boltzmann factor between the $\tilde{P}$ and χ_1^0 densities. The final LSP relic density $\Omega_\chi h^2$ is then inversely proportional to $\langle \sigma_{\text{eff}} v \rangle$ at $T_F \simeq m_\chi/20$. Co–annihilation can therefore reduce the LSP relic density by a large factor, if $\delta m \equiv m_{\tilde{P}} - m_\chi \ll m_\chi$ and $\sigma(\chi_1^0 \tilde{P}) + \sigma(\tilde{P}\tilde{P}^{(*)}) \gg \sigma(\chi_1^0 \chi_1^0)$.

If the LSP is higgsino– or wino–like, co–annihilation has to be included with both χ_2^0 and $\chi_1^\pm$ [296]; one can assume SU(2) invariance to estimate co–annihilation cross sections for final states with two massive gauge bosons from $\sigma(\chi\chi \to VV)$. As shown in Fig. 2.49, in mSUGRA type–models, Higgsino co–annihilation can be important in the "focus point" region $m_0^2 \gg m_{1/2}^2$ and the impact can be even larger in other cases. Since LEP searches imply $m_{\chi_1^0} > M_W$ for higgsino–like LSP, so that $\sigma(\chi_1^0 \chi_1^0 \to W^+ W^-)$ is large, co–annihilation in this case can reduces the relic density by a factor $\lesssim 3$.

The co–annihilation with $\tilde{\tau}_1$ [297] is important near the upper bound on $m_{1/2}$ for a fixed value of m_0, which comes from the requirement that χ_1^0 is indeed the LSP, $m_{\tilde{\tau}_1} > m_{\chi_1^0}$; it can reduce the relic density by an order of magnitude. This is exemplified in Fig. 2.50, where we show the WMAP central value and the allowed range of the relic density in the m_0–$m_{1/2}$ parameter space of the mSUGRA model for $\tan\beta = 10$, $A_0 = 0$ and $\text{sign}(\mu) = +$ (left). In the right–hand side of the figure, shown are the various channels which contribute to the relic density for a given value of $m_{1/2}$ as a function of the lightest stau mass. As can be seen, for $m_{\tilde{\tau}_1} \gtrsim 200$ GeV, $\chi_1^0 \chi_1^0$ annihilation contributes less than 10% of Ωh^2 and the bulk of the contribution originates from $\chi_1^0 \tilde{\tau}_1$ and $\tilde{\tau}_1 \tilde{\tau}_1$ annihilation. The co–annihilation involving the other sleptons, $\tilde{\ell} = \tilde{e}, \tilde{\mu}$, can also be very important when $m_{\tilde{\ell}} \sim m_{\chi_1^0}$.
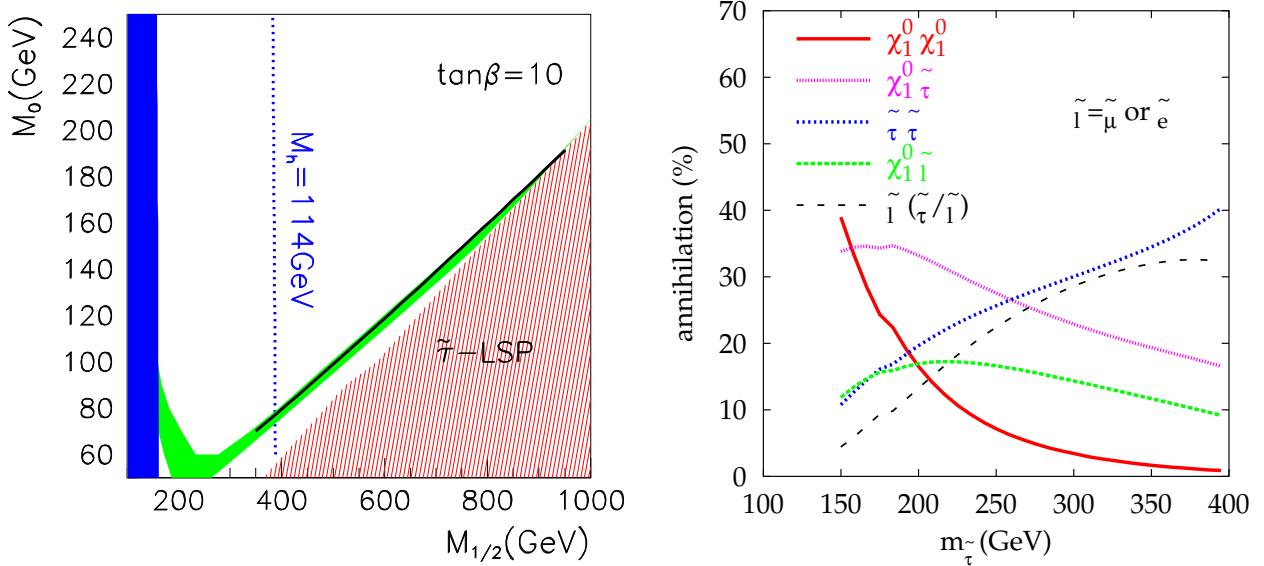
Figure 2.50: *The central value (solid line) and the allowed WMAP range (green/light grey) in the m_0–$m_{1/2}$ parameter space for $\tan\beta = 10$, $A_0 = 0$ and $\text{sign}(\mu) = +$; the red/hatched area is ruled out by the requirement $m_{\chi_1^0} > m_{\tilde{\tau}_1}$ and the vertical band by the LEP2 constraints on the sparticle masses (left). The contribution of the various channels to the relic density in % (right). From Ref. [288].*

Finally, co–annihilation with a top squark that is almost degenerate with the LSP neutralino LSP [298, 299] can be important in some scenarios with non universal scalar masses and/or large $|A_0|$ values. In fact, this is the best example to highlight the effect of the MSSM Higgs sector on the cosmological relic density with co–annihilation processes. We will briefly discuss this case below, taking for illustration an mSUGRA type model but where the universality of the soft scalar masses for sfermions and Higgs doublets is relaxed [which, in practice, means that μ and M_A are assumed to be free parameters]; as discussed in previous instances, for large stop mixing, the state $\tilde{t}_1$ can be rather light and will have strong couplings to the Higgs bosons.
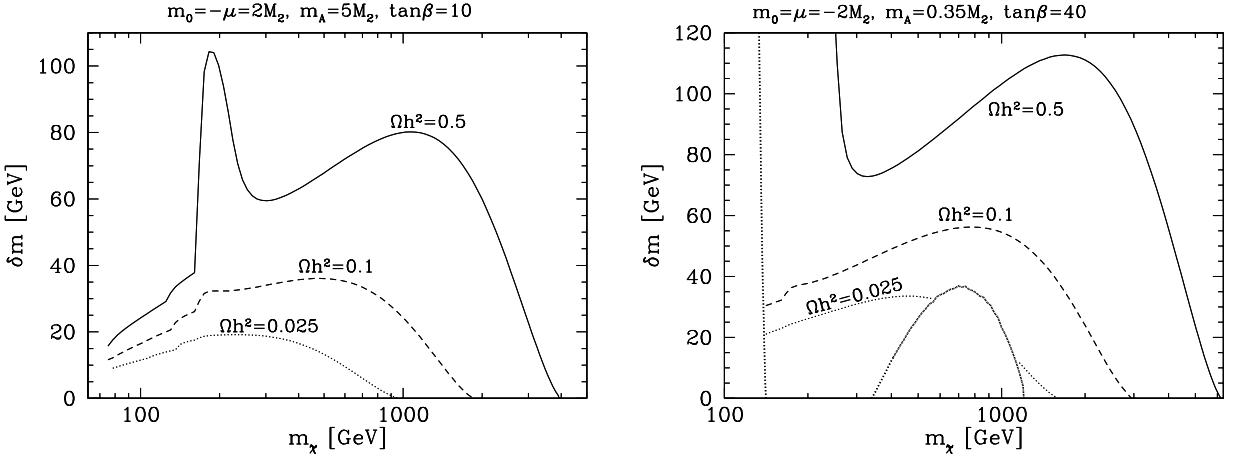
Figure 2.51: Contours of constant $\Omega h^2 = 0.5$ (solid), 0.1 (dashed) and 0.025 (dotted) in the $(m_\chi, \delta m)$ plane, where $\delta m = m_{\tilde{t}_1} - m_\chi$; μ, m_0 and M_A are taken to be fixed multiples of $M_2 \simeq 2m_\chi$ while $\tan\beta = 10$ is kept fixed and A_0 varies between $2.5 m_0$ and $3.2 m_0$, with larger A_0 values corresponding to smaller values of δm. The left–hand side is for $\tan\beta = 10$ and $M_A = 5M_2$ and the right–hand side for $\tan\beta = 40$ and $M_A = 0.35 M_2$; from [298].

In this case, a fairly good approximation of the relic density [298] is to include exactly all $\chi_1^0 \chi_1^0$ annihilation processes, while for stop co–annihilation, one includes only the leading S–wave contributions and ignores all reactions that involve more than the minimal required number of electroweak gauge couplings; however, one should treat the top and bottom quark Yukawa couplings on the same footing as the strong coupling since they can become rather large. [Note that due to the exponential dependence of σ_{eff} on δm, the bounds on the $\tilde{t}_1$–χ_1^0 mass splitting that can be inferred from upper or lower bounds on Ωh^2 should nevertheless be fairly accurate.] One should therefore calculate the cross sections for the following processes, where $H_i^0 \equiv h, H, A$ is one of the three MSSM neutral Higgs bosons:

$$
\begin{aligned}
\chi_1^0 \tilde{t}_1 &\rightarrow t\,g,\; t\,H_i^0,\; b\,H^+ \;;\; \chi_1^0 \tilde{t}_1^* \rightarrow \bar{t}\,g,\; \bar{t}\,H_i^0,\; \bar{b}\,H^- \\
\tilde{t}_1 \tilde{t}_1 &\rightarrow t\,t \qquad\qquad\qquad\quad ;\; \tilde{t}_1^* \tilde{t}_1^* \rightarrow \bar{t}\,\bar{t} \\
\tilde{t}_1 \tilde{t}_1^* &\rightarrow g\,g,\; H_i^0 H_j^0,\; H^+ H^-,\; b\,\bar{b},\; t\,\bar{t}
\end{aligned} \tag{2.105}
$$

In Fig. 2.51, we show contours of constant Ωh^2 in the $(m_\chi, \delta m)$ plane for $-\mu = 2M_2 \simeq 2m_\chi$, which implies that the LSP is bino–like; in the absence of co–annihilation this choice is incompatible with the upper bound on the LSP relic density[25]. In the left–hand side of the figure, a moderate value of $\tan\beta$ has been chosen, $\tan\beta = 10$, and the Higgs spectrum is assumed to be heavy, $M_A = 5M_2$. This minimizes the number of final states contributing

---

[25]In the present discussion we use some pre–WMAP requirements for the relic density: $0.1 \leq \Omega_{\text{DM}} h^2 \leq 0.3$ and the more conservative range $0.025 \leq \Omega_{\text{DM}} h^2 \leq 0.5$ where the lower bound comes from the requirement that χ_1^0 should at least form galactic Dark Matter, and the upper bound is a very conservative interpretation of the lower bound on the age of the Universe.

in eqs. (2.105) and leads to a small $\chi_1^0\chi_1^0$ annihilation cross section. We see that scenarios with very large δm are indeed excluded by the upper bound on Ωh^2 [the peak for $\Omega h^2 = 0.5$ at $m_\chi \simeq m_t$ is due to the $\chi_1^0\chi_1^0 \to t\bar{t}$ process, while the smaller bumps at $m_\chi \simeq 130$ GeV are due to hh final states becoming accessible]. On the other hand, for very small δm and m_χ [in the range indicated by naturalness arguments, $m_\chi \lesssim 0.3$ TeV for which $m_{\tilde{g}} \lesssim 2$ TeV if gaugino mass universality is assumed], the relic density is too small. One needs a $\tilde{t}_1$–χ_1^0 mass splitting of at least 10 to 20 GeV to satisfy the bound $\Omega h^2 \gtrsim 0.025$.

In the right–hand side of the figure, we show analogous results but for $\tan\beta = 40$ and a light Higgs spectrum, $M_A = 0.35M_2 \simeq 0.7m_\chi$, which ensures that all Higgs pair final states will be accessible for $m_\chi \gtrsim 100$ GeV. We see that for natural values of m_χ, requiring $\Omega h^2 > 0.025$ now implies $\delta m > 20$ GeV. Moreover, the LSP makes a good DM candidate, i.e. $\Omega h^2 \sim 0.1$, only for $\delta m \gtrsim 40$ GeV and for $\delta m \to 0$, cosmology now allows an LSP mass up to 6 TeV, corresponding to a gluino mass of about 30 TeV. Thus, the upper bound on Ωh^2 does not necessarilly imply that the LHC must find superparticles if the MSSM is correct and the LSP is bino–like.

2.4.3 Higgs effects in neutralino DM detection

The strength of the expected signal in the two most promising search strategies for neutralino Dark Matter is directly proportional to the neutralino–nucleon scattering cross section $\sigma_{\chi N}$; these are the search for high–energy neutrinos originating from the annihilation of neutralinos in the center of the Sun or Earth, the so–called "indirect detection" [305], and the search of the elastic scattering of ambient neutralinos off a nucleus in a laboratory detector, the "direct search" [306]. An accurate calculation of $\sigma_{\chi N}$ for given model parameters is thus essential for the interpretation of the results of these searches.

The matrix element for χN scattering, mediated by squark and Z–boson exchange [Fig. 2.52a] and Higgs exchange [Fig. 2.52b] diagrams, receives both spin–dependent and spin–independent contributions [307–309]. The former are important for neutralino capture in the Sun, but are irrelevant for capture in the Earth, and play a subdominant role in most direct search experiments, which employ fairly heavy nuclei. The spin–independent contribution in turn is usually dominated by Higgs exchange diagrams, where the Higgs bosons couple either directly to light (u, d, s) quarks in the nucleon, or couple to two gluons through a loop of heavy (c, b, t) quarks or squarks. Only scalar Higgs couplings to neutralinos contribute in the non–relativistic limit and therefore, in the absence of significant CP–violation in the Higgs sector, one only has to include contributions of the two neutral CP–even Higgs particles. The contribution of the heavier Higgs boson often dominates, since its couplings to down–type quarks are enhanced for $\tan\beta \gg 1$. In the following, we discuss these two types of couplings [the direct and the loop induced ones] and their radiative corrections, relying

on some material presented in the preceding sections.
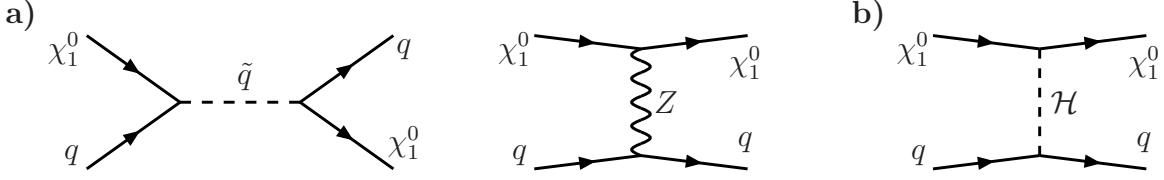
Figure 2.52: Feynman diagrams for χ_1^0 LSP quark scattering.

The leading contribution to the $\mathcal{H}gg$ couplings comes from heavy quark triangle diagrams as discussed previously and can be described by the effective Lagrangian

$$\mathcal{L}_{\mathcal{H}gg}^Q = \frac{1}{4}\,\mathcal{H}\,F_{\mu\nu a}F^{\mu\nu a}\sum_{Q=c,b,t}\frac{c_{iQ}}{M_W}\,C_g^Q \qquad (2.106)$$

where $F_{\mu\nu a}$ is the gluon field strength tensor with a the color index. At the relevant hadronic scale, only the c, b, t quark contributions need to be included and the dimensionless coefficients c_{iQ} are the result of the loop integrals and are independent of m_Q since the factor m_Q in the $\mathcal{H}\bar{Q}Q$ coupling is canceled by a factor $1/m_Q$ from the loop integral; explicit expressions for these coefficients can be found e.g. in Ref. [309]. C_g describes the interactions of the heavy quark and has been discussed at length in §I.2.4; in terms of the quark contribution to the QCD β function and the anomalous quark mass dimension, it reads

$$C_g^Q = \frac{\beta_Q(\alpha_s)}{1+\gamma_Q(\alpha_s)} = -\frac{\alpha_s(m_Q)}{12\pi}\left[1+\frac{11}{4}\frac{\alpha_s(m_Q)}{\pi}+\cdots\right] \qquad (2.107)$$

where $\cdots$ stand for the known higher orders discussed in §I.2.4 and which we refrain from including here since the other effects to be discussed later will only be at $\mathcal{O}(\alpha_s)$. Note that because α_s has to be evaluated at the scale of the heavy quark, the contributions of the coefficient is larger for the c quark than for the top quark. The effective Lagrangian eq. (2.106) gives rise to the $\mathcal{H}\bar{N}N$ couplings, through hadronic matrix elements [309, 310]

$$\frac{\alpha_s}{4\pi}\langle N|F_{\mu\nu a}F^{\mu\nu a}|N\rangle = -\frac{2}{9}m_N\left(1-\sum_{q=u,d,s}\frac{m_q}{m_N}\langle N|\bar{q}q|N\rangle\right) \qquad (2.108)$$

Note that the general result eq. (2.106) can also be used for squark loop contributions to the Higgs–gluon coupling, and one finds the contribution given in eq. (2.49). However, the overall contributions of squark loops to the effective $\mathcal{H}gg$ couplings at vanishing external momenta are always much smaller than the quark loop contributions.

The other important ingredient of the LSP–nucleon cross section is the CP–even Higgs couplings to light quarks. In this context, only the strange quark contribution is important

and one has: *i*) to use the relevant Higgs Yukawa coupling to *s*–quarks at the given scale and thus, one should apply the sophisticated treatments for the running quark masses at higher orders discussed in §I.1.1.4, and *ii*) use the improved Yukawa couplings of down–type fermions given in eq. (1.140) to incorporate the corrections coming from gluino–squark loops, that are closely related to the SUSY loop corrections discussed in §2.2.1 and which can become extremely large at high $\tan\beta$, for which the cross section $\sigma_{\chi N}$ is appreciable.

Note that the squark–gluino loop corrections to the couplings of down–type type quarks also affect the leading $\mathcal{O}(m_{\tilde{q}}^{-2})$ spin–independent contributions from squark exchange, which are proportional to m_q, either through the interference of gauge and Yukawa contributions to the $\chi q\tilde{q}$ couplings [when the LSP is a gaugino–higgsino mixture], or through $\tilde{q}_L - \tilde{q}_R$ mixing. These corrections can again be understood in terms of an effective $f_q\bar{q}q\bar{\chi}\chi$ interaction, where the coefficient f_q is determined by matching to the full theory at a scale $Q \simeq m_{\tilde{q}}$ [309].

The effects of these higher–order corrections are extremely important. This is exemplified in Fig. 2.53 which shows examples for the ratio R of the neutralino scattering rate on ^{76}Ge with and without these corrections as a function of $\tan\beta$ [300]. If the small difference between the χn and χp scattering amplitudes is neglected, R is simply the ratio of the corrected and uncorrected χN scattering cross sections.
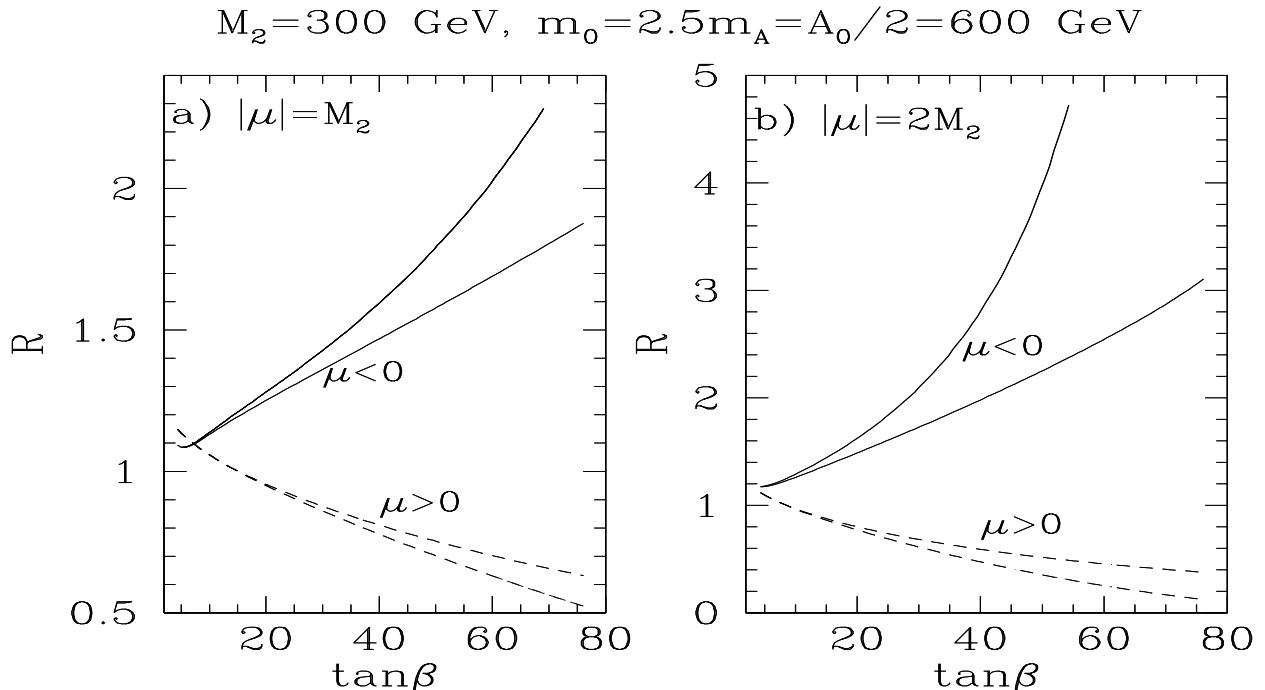
Figure 2.53: The ratio R of corrected to uncorrected χN rates in an MSSM scenario. The upper (lower) curve of a given pattern uses the quark mass with (without) sparticle loop corrections when computing the squark L–R mixing angle. From Ref. [300].

We have chosen a scenario with common soft SUSY–breaking scalar masses $m_0 = 600$ GeV and trilinear coupling $A_0 = 1.2$ TeV at the weak scale and $M_A = 240$ GeV $\simeq 1.6\, m_{\chi_1^0}$. We assume the usual unification conditions for gaugino masses, with $M_2 \sim \frac{1}{3} M_3 \sim \frac{1}{2} M_1 = 300$ GeV and $|\mu| = M_2$ (left) and $|\mu| = 2M_2$ (right), and show the results for both positive (dashed) and negative (solid) μ values. The upper (lower) curves with a given pattern are obtained using the corrected MSSM (SM) running quark masses when calculating the squark mixing angles θ_q. As can be seen, at high $\tan\beta$, the correction factor can easily reach values of the order of two, and can be much larger in some cases. The QCD corrections, in particular the squark–gluino contribution, have thus to be taken into account for a proper prediction of both the relic density and the χN scattering cross section.

Finally, let us make a few remarks on indirect neutralino Dark Matter detection which is also very actively pursued; see Ref. [25] for a review. In the LSP neutralino annihilation into pairs of SM particles, the stable decay and fragmentation products are neutrinos, photons, protons, antiprotons, electrons and positrons. While electrons and protons are undetectable in the sea of matter particles in the universe, neutrinos, photons, positrons and anti-protons could be detected over the background due to ordinary particle interactions. In the detection cross sections, the MSSM Higgs sector thus also plays an important role and the sophisticated treatment of the Higgs masses, total decay widths and couplings discussed for the relic density should also be applied in this case.

Since Majorana LSPs cannot annihilate at rest into massless neutrino pairs [unless CP is violated in the neutralino sector], the neutrinos which could be detected from LSP annihilation should come from the decay of heavier particles. The best source of neutrinos is usually due to LSP annihilation into $\tau^+\tau^-$ pairs for $m_{\chi_1^0} < M_W$ and for heavier LSPs, W^+W^-, ZZ and $t\bar{t}$ final states. The sophisticated treatment of the $\chi_1^0 \chi_1^0$ annihilation cross section discussed for the neutralino relic density should therefore be applied in this case too. Note that, in equilibrium, the annihilation rate of the LSP is half the rate for their capture in celestial bodies, which is given by the LSP–nucleus cross section discussed above.

In the case of indirect detection of LSPs annihilating in the halo, three channels appear to have some potential: positrons, antiprotons and gamma rays. Since positrons are also light, they cannot again be produced from direct LSP annihilation at rest and must come from decays of heavy particles such as W and Z bosons. Antiprotons originate from LSP annihilation into quark pairs, $\chi_1^0 \chi_1^0 \to c\bar{c}, b\bar{b}$ and $t\bar{t}$ [in particular, at high $\tan\beta$ values, annihilation into $b\bar{b}$ pairs is the dominant source]; the large QCD corrections to these channels must therefore be included. Annihilation into two gluons, $\chi_1^0 \chi_1^0 \to gg$, which is mediated by triangle diagrams involving the Zgg and more importantly the Higgs–gg vertices[26] as well

---

[26]This vertex has to be treated as discussed previously for direct neutralino detection, with the difference that, here, the momentum transfer is $Q^2 = 4m_{\chi_1^0}^2$ instead near zero.
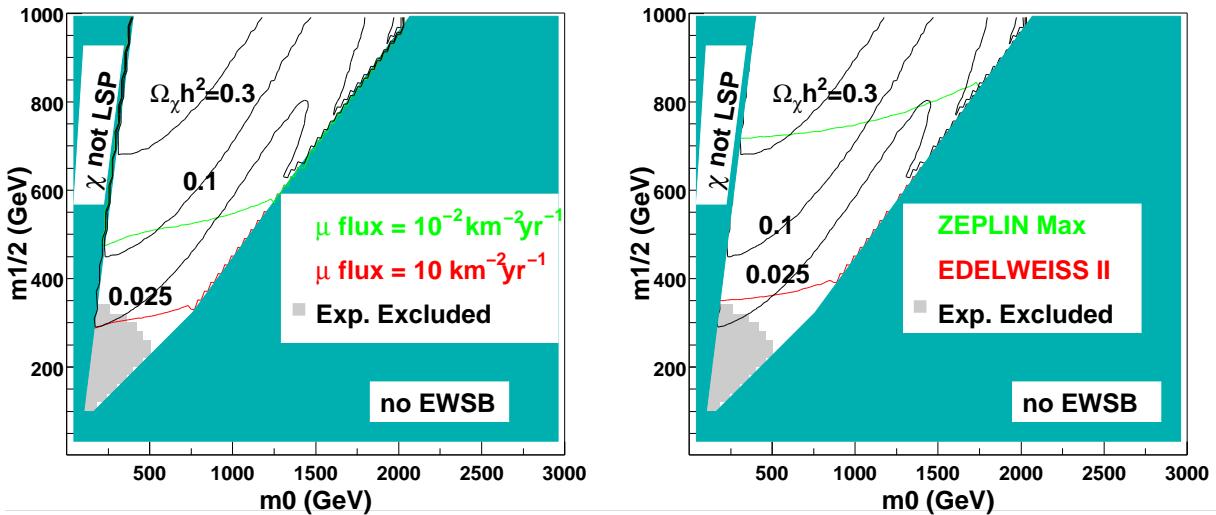
Figure 2.54: Neutralino detection potential in the m_0–$m_{1/2}$ parameter space for an mSUGRA type model but with non–universal Higgs masses, $m_{H_2} = 2m_{H_1} = m_0, A_0 = 0, \tan\beta = 45$ and $\mu > 0$. Indirect detection of muon fluxes pointing toward the Sun for neutrino telescopes (left) direct detection (right). Also shown are constant relic density lines $\Omega_{\chi_1^0} h^2 = 1, 0.3, 0.1, 0.025$, as well as the regions excluded by the requirement of proper EWSB and χ_1^0 LSP; the small grey areas are excluded by current experimental data. From Ref. [290].

as box diagrams, need to be taken into account [301, 302].

Finally, monochromatic gamma rays can be detected from the annihilation $\chi_1^0\chi_1^0 \to \gamma\gamma$ [302, 311] and $Z\gamma$ [312]. These processes are mediated partly by the loop induced Higgs–$\gamma\gamma$ vertices, where all charged standard and SUSY particles are exchanged, and which have been discussed in detail in the previous sections; box diagrams are also involved. Since the annihilation occurs mainly through S–wave, the channel $\chi_1^0\chi_1^0 \to \gamma\Phi$ with $\Phi = h, H, A$, is forbidden by helicity conservation.

To summarize, we show in Fig. 2.54, the potential of LSP detection at near future experiments: indirect detection of muon fluxes due to ν_μ neutrinos coming from the Sun for neutrinos telescopes such as ANTARES and ICECUBE with two values of the muon flux (left) and direct detection in the EDELWEISS II and ZEPPELIN Max (right) experiments. We assume an mSUGRA scenario where the soft SUSY–breaking scalar Higgs masses are not universal, $m_{H_2} = m_0$ and $m_{H_1} = \frac{1}{2}m_0$ and a large value of $\tan\beta$. As can be seen, the sensitivity of these experiments in the m_0–$m_{1/2}$ plane is rather high, and it is hoped that the lightest neutralino should be detected in the near future if it represents indeed the Dark Matter in the universe. If it is the case, the measured detection rate, besides the determined value of the cosmological relic density of the neutralino LSP, will provide a very important constraint on the MSSM parameter space.

3 MSSM Higgs production at hadron colliders

The most important production mechanisms of the MSSM neutral CP–even Higgs bosons [38, 39, 140, 141, 231, 313–315] are simply those of the SM Higgs particle [237, 316–318] which have been discussed in detail in §3 of the first part of this review. In the decoupling limit, the MSSM Higgs sector effectively reduces to the SM one and all the features discussed earlier for a light SM Higgs boson with a mass of $\sim$ 100–150 GeV will hold for the lighter h particle [in the anti–decoupling regime, they hold for the heavier H boson]. Outside the decoupling regime, however, major quantitative differences compared to the SM case can occur since the cross sections will depend on the specific Higgs mass and coupling patterns which can be widely different. This is, for instance, the case in the large $\tan\beta$ regime when the Higgs boson couplings to down–type fermions are strongly enhanced; the bottom quarks will then play a much more important role than in the SM case. For the pseudoscalar Higgs boson, the two main production processes, the gluon fusion mechanism and the associated production with heavy quarks, will follow closely those of either the h or H boson. Thus, most of the analytical expressions for the cross sections given in §I.3 will hold for the neutral Higgs particles of the MSSM with, however, a few exceptions which will need further material.

The situation is quite different in the case of the charged Higgs particle: new production mechanisms not discussed before [except for charged Higgs production from top decays mentioned at the Tevatron in §1.4.2] occur in this case and additional analytical material and phenomenological analyses will be needed. Another major difference between the SM and MSSM cases is the presence of the additional SUSY particle spectrum. The sparticles, if they are relatively light, can substantially contribute to the processes which are mediated by loops such as the gluon–gluon mechanism, and to the radiative corrections in some other cases. In addition, Higgs bosons could decay into SUSY particles with substantial rates, thus, altering in a significant way the search strategies at hadron colliders. Furthermore, the MSSM Higgs bosons can be produced in the decays of the SUSY particles.

All these new issues will be summarized in this section while, for the aspects that are similar to the SM case, we will rely on the material presented in §I.3 and refer to it whenever appropriate. For the numerical illustrations of the magnitude of the cross sections, we will mostly use the FORTRAN codes of Michael Spira [319–321] for the neutral and of Jean-Loic Kneur [323, 324] for the charged Higgs bosons. Some of these codes have been adapted to deal with new processes or situations discussed here [such as charged Higgs pair production for instance]. For the implementation of the radiative corrections in the Higgs sector, we will again adopt most of the time the benchmark scenario given in the Appendix. However, contrary to the Higgs decays which have been discussed in the previous section and where the routine `FeynHiggsFast` [130] based on the Feynman diagrammatic approach has been used, the corrections will be included in the RG improved effective potential approach with

the routine SUBH of Ref. [131]. This choice is dictated by the wish to discuss all processes within the same approximation to allow for consistent comparisons between them and, in most of the numerical codes mentioned above, only this specific routine is incorporated.

The discussion on the detection of the Higgs particles at the Tevatron and the LHC[27] will be mostly based on the summaries given in Refs. [325–338], where the various details can be found. Some material, in particular a list of the various backgrounds for the SM–like processes and the various tests which can be performed on the properties of the Higgs particles, has been already presented in §I.3 and will not be repeated here.

3.1   The production of the neutral Higgs bosons

The production of the neutral Higgs bosons of the MSSM proceeds essentially via the same processes that have been discussed in the case of the SM Higgs particle, Fig. 3.1, that is:

$$\text{associated } h \text{ and } H \text{ production with } W/Z: \quad q\bar{q} \to V + h/H \tag{3.1}$$

$$\text{vector boson fusion for } h \text{ and } H \text{ production}: \quad qq \to V^*V^* \to qq + h/H \tag{3.2}$$

$$\text{gluon} - \text{gluon fusion}: \quad gg \to h/H/A \tag{3.3}$$

$$\text{associated production with heavy quarks}: \quad gg, q\bar{q} \to Q\bar{Q} + h/H/A \tag{3.4}$$

[The pseudoscalar Higgs boson A cannot be produced in association with gauge bosons or in the weak boson fusion processes at the tree–level, since direct A couplings to gauge bosons are forbidden in the MSSM by CP–invariance.] However, as already mentioned, because of the different couplings of the Higgs particles to fermions and gauge bosons, the pattern for the production rates is significantly different from the SM case. We summarize the main differences in this subsection, channel by channel.
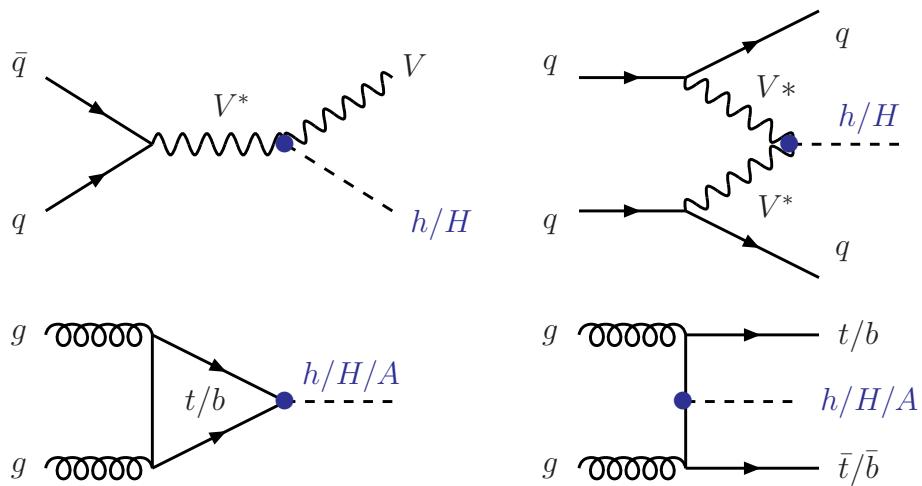
Figure 3.1: The dominant MSSM neutral Higgs production mechanisms in hadronic collisions.

There are also higher–order production mechanisms, as in the case of the SM Higgs boson. In particular, the processes for the production of two Higgs particles

$$\text{Higgs boson pair production}: \qquad q\bar{q}, gg \to \Phi_i \Phi_j \qquad (3.5)$$

are more numerous as a result of the enlarged Higgs sector. Two of these processes, namely hA and HA production, can occur both at the tree level through $q\bar{q}$ annihilation and at one–loop in the $gg \to hA, HA$ mechanisms. The other processes, $pp \to hh, HH, Hh$ and AA, occur only through the loop induced gg mechanism as in the SM Higgs case. We summarize the main features of these processes at the end of this section.

Other higher order mechanisms, such as $gg \to AZ$ and $gg \to g\Phi$, will also be mentioned and most of the remaining ones will be similar to the SM Higgs case and have been discussed in §I.3. Finally, a brief discussion of diffractive Higgs production will be given.

3.1.1   The Higgs–strahlung and vector boson fusion processes

Since, as already stated, the pseudoscalar A boson has no tree–level couplings to $V = W, Z$ bosons, only the CP–even Higgs particles $\mathcal{H} = h, H$ can be produced in association with vector bosons or in the fusion of weak vector bosons[28]. The cross sections are exactly those of the SM Higgs boson but folded with the square of the normalized $g_{\mathcal{H}VV}$ couplings of the $\mathcal{H}$ particles [231, 313]

$$\begin{aligned}
\hat{\sigma}(q\bar{q} \to V\mathcal{H}) &= g_{\mathcal{H}VV}^2 \hat{\sigma}_{\text{SM}}(q\bar{q} \to V\mathcal{H}) \\
\hat{\sigma}(qq \to qq\mathcal{H}) &= g_{\mathcal{H}VV}^2 \hat{\sigma}_{\text{SM}}(qq \to qq\mathcal{H})
\end{aligned} \qquad (3.6)$$
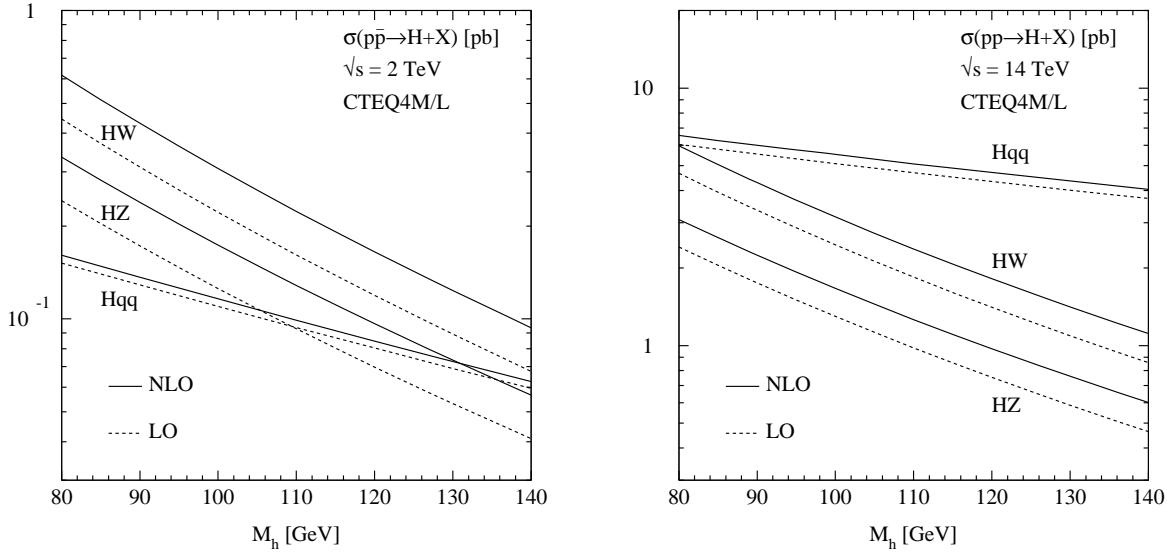
where the cross sections in the SM case have been given in §I.3.2 and §I.3.3. The various distributions are exactly those of the SM Higgs boson and can be found in these sections.

The electroweak radiative corrections [339], discussed in §I.3.2 for $q\bar{q} \to VH_{\text{SM}}$, can be different in the MSSM except in the (anti–)decoupling limit for the $h\,(H)$ bosons when the SUSY loop contributions are ignored. However, since the main contributions such as ISR and light fermion loops are the same, the difference compared to the SM case is expected to be rather small. The QCD corrections to these processes are also essentially the same as in the SM Higgs case [340–342] and, thus, increase the production cross sections by approximately 30% and 10% for, respectively, the Higgs–strahlung and the vector boson fusion processes. The two main differences in the MSSM case, compared to the SM, are as follows.

---

[28]Note, however, that AVV couplings can be induced at higher orders and allow, in principle, such production processes. For instance, the $qq \to Aqq$ mechanism can be induced at one–loop but the expected rates are far too small even at the LHC. The one–loop induced AZ production process will be discussed shortly. Note, also, that an additional source of hZ events will be due to the gg initiated production of the A boson which subsequently decays into these final states, $gg \to A \to hZ$, as will be seen later.

i) There are additional SUSY–QCD corrections originating from the exchange of squarks and gluinos in the Vqq vertices of both processes. These corrections have been calculated at one–loop in Ref. [343] and, for SUSY particle masses beyond the experimental allowed bounds, they have been found to be very small, at most a couple of percent. This is exemplified in Fig. 3.2 where we display the LO and NLO cross sections for the production of the lighter h boson in the decoupling regime in both processes at the Tevatron and the LHC. The rates at NLO include the SUSY–QCD corrections; the CTEQ4 [344] PDFs are used.

Figure 3.2: The LO and NLO cross sections for the production of the lighter MSSM h boson in the strahlung and vector boson fusion processes as a function of M_h at the Tevatron (left) and the LHC (right). The decoupling limit has been assumed and the SUSY–QCD corrections have been included in the NLO rates; from Ref. [343].

ii) In the strahlung process with a Z boson in the final state, $q\bar{q} \to Z\mathcal{H}$, the additional contributions from the heavy quark loop induced $gg \to \mathcal{H}Z$ subprocesses to the cross sections at NNLO [342], will be altered by the different $g_{\mathcal{H}QQ}$ couplings outside the (anti–)decoupling limit for the $h\,(H)$ bosons. In particular, box diagrams involving bottom quarks can give large contributions for $\tan\beta \gg 1$ when the Higgs couplings to $b\bar{b}$ are enhanced, while the contribution of the top quark box diagrams will be suppressed. Additional SUSY particles can also be involved in the loops, thus, altering the production rates. Furthermore, at this order, the pseudoscalar Higgs boson can be produced in this process, $gg \to AZ$, since it can be radiated from the internal quark lines. The cross sections have been calculated in Refs. [345, 346] and are shown in Fig. 3.3 as a function of M_A at the Tevatron and the LHC for the values $\tan\beta = 2, 7$ and 32. As can be seen, they can be rather large at the LHC and, for smaller values of M_A and large values of $\tan\beta$, they can exceed the picobarn level and, hence, surpass the $q\bar{q} \to VH_{SM}$ rate in the SM. In this regime, the cross sections are

large even at the Tevatron. In fact, this conclusion holds also true in the case of the $H(h)$ boson in the (anti–)decoupling regime when these particles have almost the same couplings to b–quarks as the CP–odd Higgs particle, $g_{\mathcal{H}bb} \sim \tan\beta$. The squark contributions have been also evaluated [346] and, as shown in the figure for an mSUGRA–type model, they are in general tiny except for the small and intermediate values $\tan\beta \lesssim 7$ where the standard top quark contribution is suppressed while the bottom quark contribution is not yet enough enhanced. However, the total production rates are small in this case. Note that the QCD corrections have been calculated recently and reduce the LO rate significantly [347]. The process also receives very important contributions from the $b\bar{b} \rightarrow AZ$ subprocess [348].
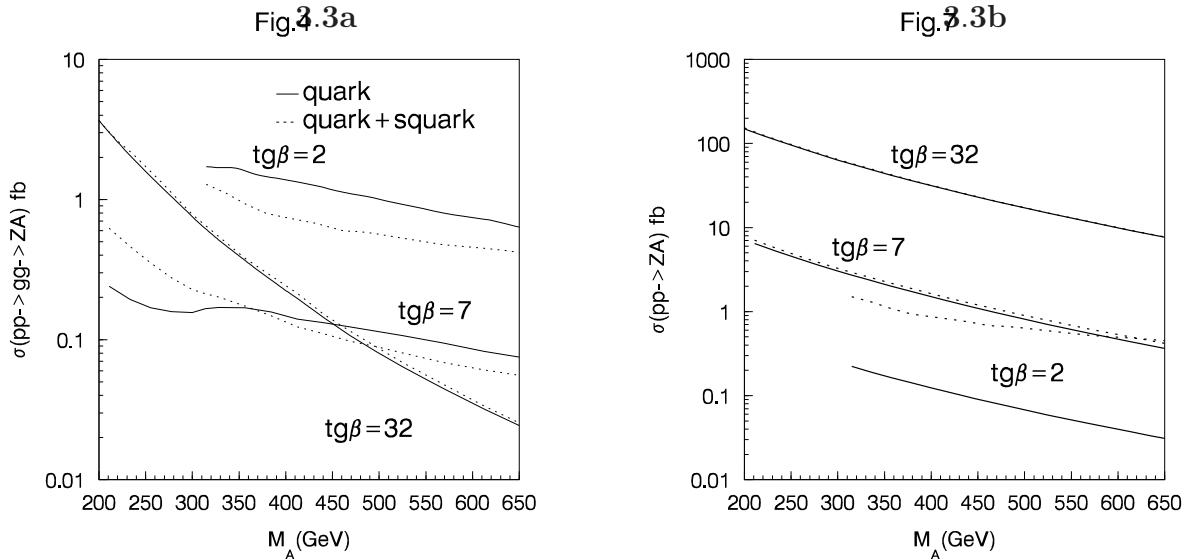
Figure 3.3: *The production cross sections for AZ final states [in fb] in the process $gg \rightarrow AZ$ as a function of M_A at the Tevatron (left) and the LHC (right) for several values of $\tan\beta$. The solid (dashed) lines are without (with) the contributions of squark loops in an mSUGRA scenario with $m_{1/2} = 120$ GeV, $A_0 = 300$ GeV and $\mu > 0$ and with the common scalar mass depending on the variation of M_A; from Ref. [346].*

The total production cross sections for the associated $\mathcal{H}V$ production processes and the weak vector boson fusion $\mathcal{H}qq$ mechanisms are shown at Tevatron and LHC energies as functions of the relevant Higgs masses in Fig. 3.4 and Fig. 3.5, respectively. The two values $\tan\beta = 3$ and 30 are chosen for illustration. As mentioned in the beginning of this chapter, the radiative corrections to the MSSM Higgs masses and couplings have been included in the RG improved effective potential approach using the routine SUBH and the SUSY parameters entering these corrections are in the benchmark scenario given in the Appendix. Only the NLO QCD corrections have been incorporated and, thus, the $gg \rightarrow \mathcal{H}Z$ contributions have been omitted. The renormalization and factorization scales have been chosen as usual [see §I.3] and the default MRST NLO set of PDFs [349] has been adopted.

165
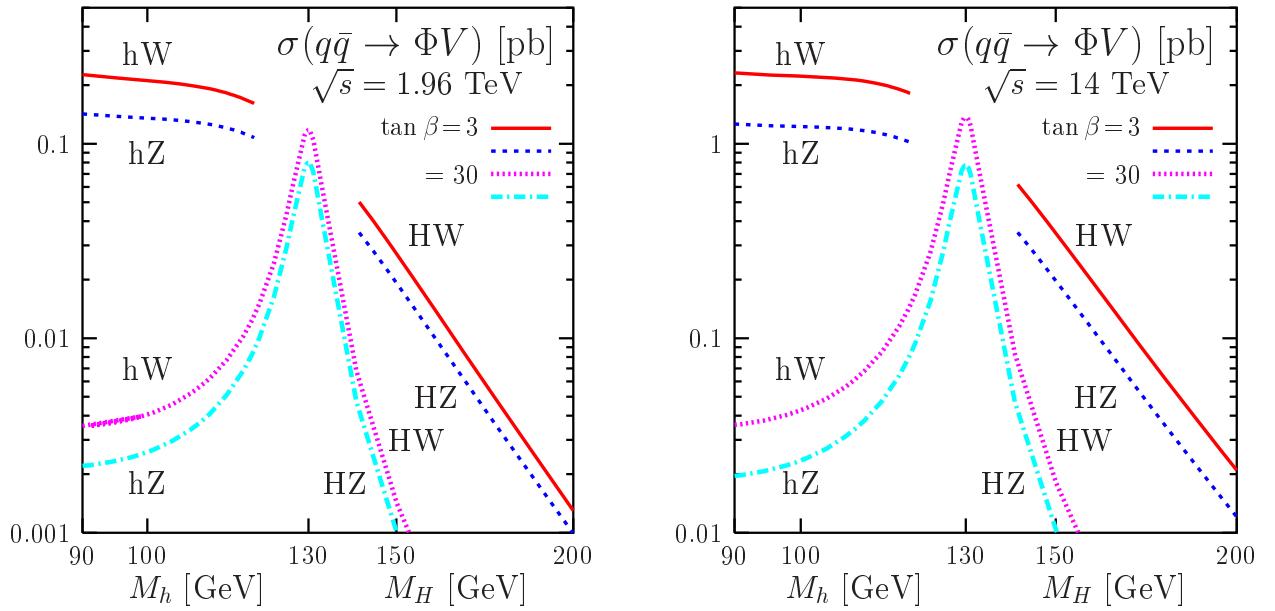
Figure 3.4: The production cross sections for the Higgs–strahlung processes, $q\bar{q} \to V + h/H$ as a function of the respective Higgs masses for $\tan\beta = 3$ and 30 at the Tevatron (left) and LHC (right). They are at NLO with the scales set at the invariant masses of the $\mathcal{H}V$ systems, $\mu_F = \mu_R = M_{V\mathcal{H}}$ and the MRST PDFs have been used. The SUSY parameters are in the scenario given in the Appendix.
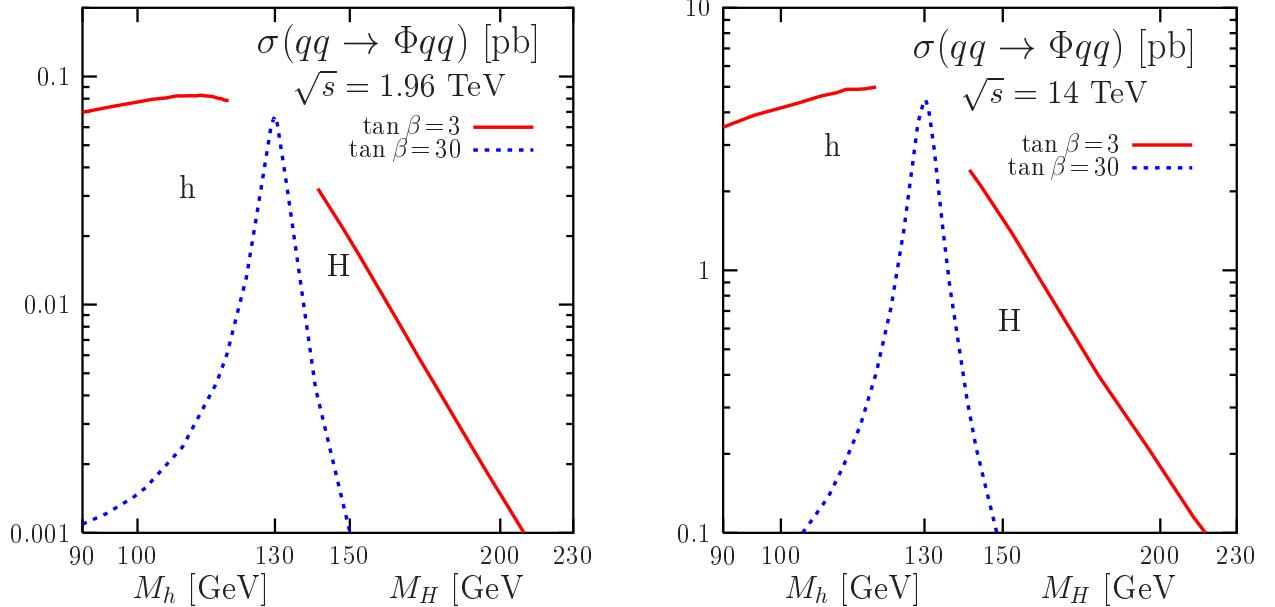
Figure 3.5: The production cross sections for the vector boson fusion processes, $qq \to qq + h/H$, as a function of $M_{h/H}$ for $\tan\beta = 3$ and 30 at the Tevatron (left) and the LHC (right). They are at NLO with $\mu_F^2 = \mu_R^2 = Q_V^2$ at each leg and the MRST PDFs have been used. The SUSY parameters are in the scenario given in the Appendix.

166

The cross sections strongly depend on the couplings $g_{\mathcal{H}VV}$ of the Higgs bosons to vector bosons and one notices the following features, some of which have been already encountered when discussing these couplings. The cross sections for h production are smaller than in the SM case for low values of M_A, when the coupling $g_{hVV} = \sin(\beta - \alpha)$ is suppressed, and get closer to the SM values when the decoupling limit, in which $M_h \simeq M_h^{\mathrm{max}}$ and $\sin(\beta - \alpha) \simeq 1$, is approached. The suppression is much more effective for high values of $\tan\beta$. In fact, as can be seen, there is a steep increase of the cross sections for h production with increasing Higgs mass for $\tan\beta = 30$ while, in the case of $\tan\beta = 3$, the hVV couplings is already almost SM–like for the values $M_h \gtrsim 90$ GeV shown in the figures. Above this mass value, the small increase of the g_{hVV} coupling with increasing M_h [and, hence, M_A], barely counterbalances the decrease of the rate with the smaller phase space.

In turn, in the case of H production, the cross sections are maximal for low M_A values when the H boson is almost SM–like and decrease with increasing M_A when the coupling $g_{HVV} = \cos(\beta - \alpha)$ tends to zero. Eventually, in the decoupling limit the processes are switched off, $\cos(\beta - \alpha) \simeq 0$. On also notices that the plots for h and H production joint for $\tan\beta \gg 1$ where $M_h^{\mathrm{max}} \simeq M_H^{\mathrm{min}}$ while the gap for low $\tan\beta$ values is large. Nevertheless, one can conclude that the processes for h and H production are truly complementary and that the sum of their cross sections is simply the one for the production of a SM Higgs boson with $M_{H_{\mathrm{SM}}} \sim M_h^{\mathrm{max}}$ for any value of M_A and $\tan\beta$, modulo the phase space effects at small $\tan\beta$. This is true also in the intense–coupling regime where $g_{hVV}^2 \simeq g_{HVV}^2 \simeq \frac{1}{2}$.

3.1.2   The gluon–gluon fusion mechanism

The cross sections at the tree level

In the MSSM, the three neutral Higgs bosons can be produced in gg fusion, $gg \to \Phi$ with $\Phi = h, H$ and A, via loops involving mainly the heavy top and bottom quarks. In the Born approximation [which, here, corresponds to the one–loop level] and in the absence of squark loop contributions, the analytical expressions of the cross sections have been given in §I.3.4 for the SM Higgs boson. The cross section in the CP–odd case is the same as for the CP–even Higgs particles, except from the different form factor of the Agg amplitude. The major difference compared to the SM Higgs case is the relative weight of the top and bottom contributions which have to be folded with the normalized couplings to the MSSM Higgs bosons, $g_{\Phi tt}$ and $g_{\Phi bb}$, as discussed when we analyzed the gluonic Higgs decay modes in §2.1.3. In fact, at leading order, the $gg \to \Phi$ production cross sections are directly related to the gluonic decay widths of the Higgs particles $\Gamma(\Phi \to gg)$

$$
\begin{aligned}
\hat{\sigma}_{\mathrm{LO}}(gg \to \Phi) &= \sigma_0^\Phi M_\Phi^2 \, \delta(\hat{s} - M_\Phi^2) \\
&= \frac{\pi^2}{8M_\Phi} \Gamma_{\mathrm{LO}}(\Phi \to gg) \, \delta(\hat{s} - M_\Phi^2)
\end{aligned}
\tag{3.7}
$$

with $\hat{s}$ the partonic c.m. energy and the cross sections at the parton level given by

$$\sigma_0^\Phi = \frac{G_\mu \alpha_s^2(\mu_R^2)}{288\sqrt{2}\pi} \left| \frac{3}{4} \sum_q A_{1/2}^\Phi(\tau_Q) \right|^2 \tag{3.8}$$

where the form factors, $A_{1/2}^{\mathcal{H}}(\tau_Q)$ for $\mathcal{H} = h, H$ and $A_{1/2}^A(\tau_Q)$ for the A boson, in terms of $\tau_Q = M_\Phi^2/4m_Q^2$ have been given earlier and are normalized in such a way that for $m_Q \gg M_\Phi$, they reach the values $\frac{4}{3}$ and 2 in the CP–even and CP–odd Higgs cases, respectively, while they both approach zero in the chiral limit $m_Q \to 0$.

This difference compared to the SM Higgs case can potentially induce huge quantitative changes. Because for $\tan\beta > 1$ the Higgs couplings to top quarks are in general suppressed while those to bottom quarks are enhanced, the b–quark will play a much more important role. For small to intermediate $\tan\beta$ values, the suppression of the $tt\Phi$ coupling is already effective and the $bb\Phi$ coupling is not yet strongly enhanced, resulting in production cross sections that are smaller than in the SM case. For high enough values, $\tan\beta \gtrsim 10$, the b–loop contributions [which are also boosted by large logarithms $\log(m_b^2/M_\Phi^2)$, see §2.1.3] are strongly enhanced, resulting into cross sections which can exceed by far the SM Higgs ones. The latter are recovered only in the (anti–)decoupling limit for $(H)\,h$ production.

At least two other major differences occur in the SUSY case, compared to what has been discussed for the standard Higgs boson. First, there are additional contributions to the Φgg couplings from squark loops as already seen in the gluonic Higgs decay case, §2.1.3 where their analytical expressions have been given. These contributions can be particularly important in scenarios where large mixing effects occur in the stop and sbottom sectors: in this case, the lightest $\tilde{t}_1$ and/or $\tilde{b}_1$ states can be rather light and their couplings to the Higgs bosons strongly enhanced. The discussion of the impact of these additional loops on the production of the lighter h boson will be postponed to §3.4. The second major difference compared to the SM Higgs case is related to the QCD corrections: as the b–loop contribution is generally dominant in the MSSM, the trend will be different from the SM Higgs case. In addition, the corrections to the top quark loop contribution will not be the same for the CP–even and CP–odd Higgs cases and the latter has not been discussed yet.

QCD corrections at NLO

When including the NLO QCD corrections to the gluon–gluon fusion processes, $gg \to \Phi$, besides the virtual corrections where gluons are exchanged between the internal quark and the external gluon lines, the bremsstrahlung of additional gluons, the inelastic quark–gluon process and quark–antiquark annihilation,

$$gg \to \Phi(g) , \quad gq \to \Phi q , \quad q\bar{q} \to \Phi g \tag{3.9}$$

contribute to the production. The diagrams relevant to the various subprocesses are the same as for the SM Higgs boson which has been discussed in detail in §I.3.4; some generic ones are reproduced in Fig. 3.6.
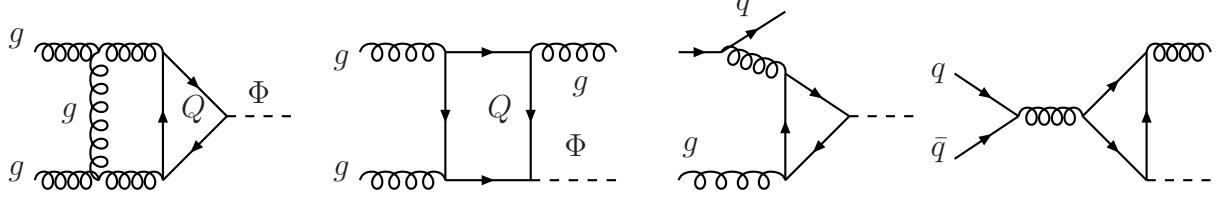
Figure 3.6: Typical diagrams contributing to the NLO QCD corrections to $gg \to \Phi$.

The partonic cross sections may thus be written, in terms of $\hat{\tau} = M_\Phi^2/\hat{s}$, as

$$\hat{\sigma}_{ij}^\Phi = \sigma_0^\Phi \left\{ \delta_{ig}\delta_{jg} \left[1 + C_\Phi(\tau_Q)\frac{\alpha_s}{\pi} \right] \delta(1 - \hat{\tau}) + D_{ij}(\hat{\tau}, \tau_Q)\frac{\alpha_s}{\pi}\Theta(1 - \hat{\tau}) \right\} \quad (3.10)$$

for $i, j = g, q, \bar{q}$. The final result for the pp or $p\bar{p}$ cross sections, after folding with the $\overline{\text{MS}}$ gluon and quark luminosities, can be cast into the compact form

$$\sigma(pp \to \Phi + X) = \sigma_0^\Phi \left[1 + C_\Phi\frac{\alpha_s}{\pi} \right] \tau_\Phi \frac{d\mathcal{L}^{gg}}{d\tau_\Phi} + \Delta\sigma_{gg}^\Phi + \Delta\sigma_{gq}^\Phi + \Delta\sigma_{q\bar{q}}^\Phi \quad (3.11)$$

where $\tau_\Phi = M_\Phi^2/s$ with s the hadronic total c.m. energy and where the partonic cross sections σ_0^Φ have been given previously. The coefficient C_Φ denotes the contribution of the virtual two–loop corrections, in which the infrared singular part is regularized and reads

$$C_\Phi(\tau_Q) = \pi^2 + c^\Phi(\tau_Q) + \frac{33 - 2N_f}{6} \log\frac{\mu_R^2}{M_\Phi^2} \quad (3.12)$$

The regular contributions of the real corrections due to gg, gq scattering and $q\bar{q}$ annihilation, which depend on both the renormalization scale μ_R and the factorization scale μ_F of the parton densities, are given by

$$\Delta\sigma_{gg}^\Phi = \int_{\tau_\Phi}^1 d\tau \frac{d\mathcal{L}^{gg}}{d\tau} \frac{\alpha_s(\mu_R)}{\pi}\sigma_0^\Phi \left\{ -zP_{gg}(z) \log\frac{\mu_F^2}{\tau s} + d_{gg}^\Phi(z, \tau_Q) \right.$$
$$\left. +12 \left[\left(\frac{\log(1 - z)}{1 - z}\right)_+ - z\left[2 - z(1 - z)\right]\log(1 - z) \right] \right\}$$

$$\Delta\sigma_{gq}^\Phi = \int_{\tau_\Phi}^1 d\tau \sum_{q,\bar{q}} \frac{d\mathcal{L}^{gq}}{d\tau} \frac{\alpha_s(\mu_R)}{\pi}\sigma_0^\Phi \left\{ \left[-\frac{1}{2}\log\frac{\mu_F^2}{\tau s} + \log(1 - z) \right] zP_{gq}(z) + d_{gq}^\Phi(z, \tau_Q) \right\}$$

$$\Delta\sigma_{q\bar{q}}^\Phi = \int_{\tau_\Phi}^1 d\tau \sum_q \frac{d\mathcal{L}^{q\bar{q}}}{d\tau} \frac{\alpha_s(\mu_R)}{\pi}\sigma_0^\Phi d_{q\bar{q}}^\Phi(z, \tau_Q) \quad (3.13)$$

with $z = \tau_\Phi/\tau$ and the standard Altarelli–Parisi splitting functions have been given in §I.3.

169

As a result of the factorization theorem, the parity and the specific couplings of the $\Phi = \mathcal{H}/A$ bosons are not relevant for the infrared/collinear form of the cross sections related to interactions at large distances. The specific properties of the Higgs bosons affect only the non–singular coefficient c^Φ in the expression above and also the coefficients d_{ij}^Φ which appear in the parton cross sections for the real corrections. These coefficients have been calculated in Refs. [222, 350] for arbitrary quark masses in both the CP–even and CP–odd Higgs cases.

In the limit of large quark–loop masses compared with the Higgs boson mass, only the coefficients c^Φ depend on the parity of the Higgs particle [222, 241, 351]

$$\tau_Q = M_\Phi^2/4m_Q^2 \to 0 : \quad c^{\mathcal{H}} \to \frac{11}{2} \quad \text{while} \quad c^A \to 6 \tag{3.14}$$

The coefficients d_{ij}^Φ are universal in this limit [the next–to–leading–order term in the mass expansion in the scalar and pseudoscalar cases has also been calculated analytically [352]]

$$d_{gg}^\Phi \to -\frac{11}{2}(1-z)^3 , \;\; d_{gq}^\Phi \to -1 + 2z - \frac{1}{3}z^2 , \;\; d_{q\bar{q}}^\Phi \to \frac{32}{27}(1-z)^3 \tag{3.15}$$

In the opposite limit of small quark–loop masses, $\tau_Q \gg 1$, chiral symmetry is restored for the leading and subleading logarithmic contributions to the c^Φ and d^Φ coefficients which are given by

$$c^\Phi(\tau_Q) \;\; \to \;\; \frac{5}{36}\log^2(-4\tau_Q - i\epsilon) - \frac{4}{3}\log(-4\tau_Q - i\epsilon)$$

$$d_{gg}^\Phi(\hat{\tau}, \tau_Q) \;\; \to \;\; -\frac{2}{5}\log(4\tau_Q)\Big[7 - 7\hat{\tau} + 5\hat{\tau}^2\Big] - 6\log(1-\hat{\tau})\Big[1 - \hat{\tau} + \hat{\tau}^2\Big]$$
$$+ 2\frac{\log\hat{\tau}}{1-\hat{\tau}}\Big[3 - 6\hat{\tau} - 2\hat{\tau}^2 + 5\hat{\tau}^3 - 6\hat{\tau}^4\Big]$$

$$d_{gq}^\Phi(\hat{\tau}, \tau_Q) \;\; \to \;\; \frac{2}{3}\left[\hat{\tau}^2 - \Big(1 + (1-\hat{\tau})^2\Big)\left(\frac{7}{15}\log(4\tau_Q) + \log\left(\frac{1-\hat{\tau}}{\hat{\tau}}\right)\right)\right]$$
$$d_{q\bar{q}}^\Phi(\hat{\tau}, \tau_Q) \;\; \to \;\; 0 \tag{3.16}$$

The only significant difference between the scalar and pseudoscalar cases is for Higgs masses near the threshold, $M_\Phi \simeq 2m_Q$, as already discussed in §2.1.3: there is a singularity in the case of the Agg amplitude and perturbation theory cannot be applied there.

The total K–factors at NLO for the production of the three neutral Higgs particles, defined as the ratios of the NLO to LO cross sections evaluated with the PDFs and α_s at the respective orders, are shown in Fig. 3.7 for the Tevatron and in Fig. 3.8 for the LHC as a function of the respective Higgs mass for the values $\tan\beta = 3$ and 30 [there is a few percent uncertainty from the numerical integrations].
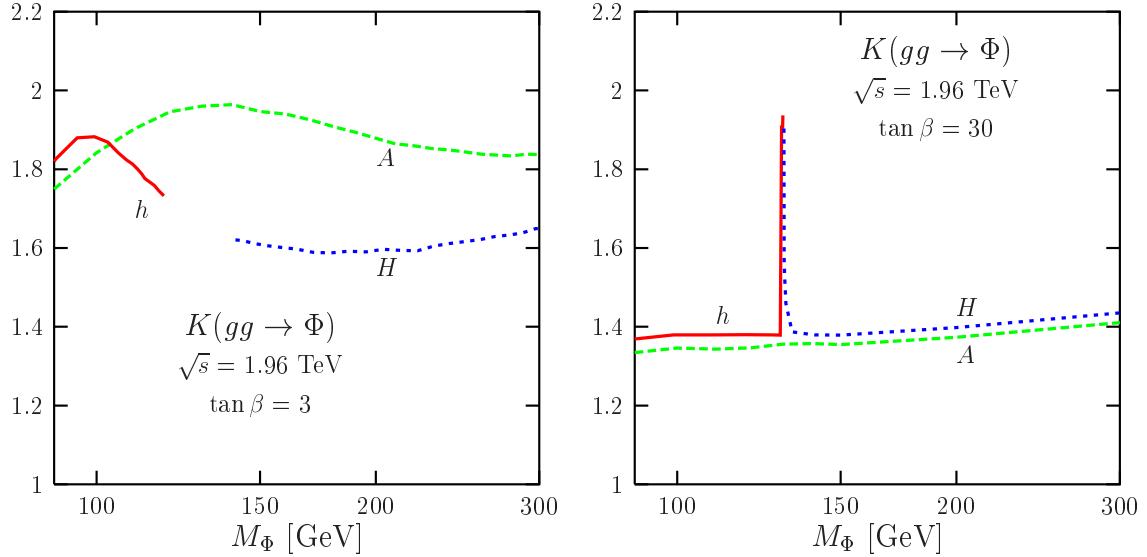
Figure 3.7: The total K–factors at NLO for Higgs production in the $gg \to \Phi$ fusion processes as a function of M_A at the Tevatron for the values $\tan\beta = 3$ (left) and $\tan\beta = 30$ (right). The renormalization and factorization scales have been fixed to $\mu_R = \mu_F = M_\Phi$ and the MRST PDFs have been used.
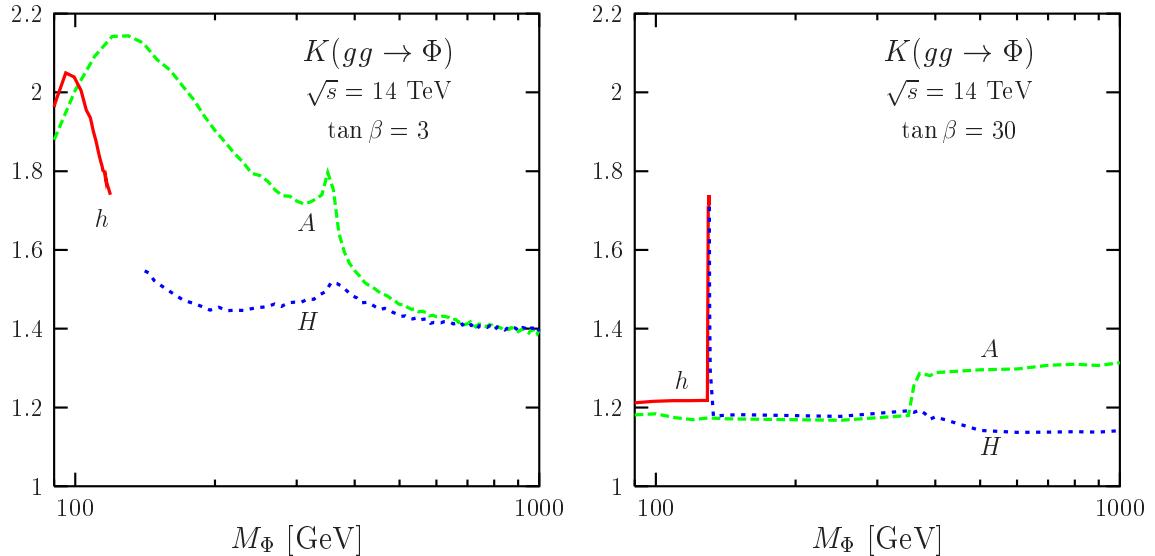
Figure 3.8: The same as Fig. 3.7 for LHC energies.

If the top quark loop were by far dominating, the K–factors would have been as in the SM case: $K \sim 1.8\,(2.2)$ at low Higgs masses and reaching values $K \sim 1.9\,(2.8)$ at high masses, $M_\Phi \sim 1$ TeV (300 GeV) at the LHC (Tevatron). However, because of the additional b–quark contribution which is sizable even for $\tan\beta = 3$, the trend is different and the K–factors are larger at low Higgs masses and smaller at high masses. At large $\tan\beta$, when the bottom quark loop is dominant, the K–factors are almost constant and relatively small, $K \sim 1.4$ at

171

the Tevatron and $K = 1.2$–1.4 at the LHC, except in the range near $M_h^{\max} \sim M_H^{\min}$ when the h or H boson behave as the SM Higgs boson. Note that, except near the $t\bar{t}$ threshold and also above [where the imaginary part of the t–quark contribution plays a role even for $\tan\beta = 30$], the K–factors are almost the same for the A boson and for the pseudoscalar like CP–even Higgs particle.

QCD corrections at NNLO in the heavy top limit

For the production of the CP–even Higgs particles in the gg fusion at NNLO, the results presented for the SM Higgs case in §I.3.4.3 can be straightforwardly translated to the lighter h boson as well as to the heavier H boson for masses below the $t\bar{t}$ threshold, $M_H \lesssim 350$ GeV. These results are, however, only valid when the top quark loop is dominating, that is, for small $\tan\beta$ values and when the $h\,(H)$ particles are in the (anti–)decoupling regime, since the calculation has been performed in the heavy quark limit. Similarly to the SM Higgs case [353], the QCD corrections to the production of the pseudoscalar Higgs boson at NNLO have been also calculated in this limit [354, 355]. The same techniques and procedures have been used and in the following, we will simply summarize the main differences between the CP–even and CP–odd cases, relying on the material already given in §I.3.4.3.

Keeping in mind that the normalization at LO is different from the CP–even case, the results for the corrected partonic cross sections of the process $gg \rightarrow A + X$ at NNLO

$$\sigma_{ij}^{(2)} = \sigma_0^A \Delta_{ijA}^{(2)} \quad \text{with } i, j = g, q, \bar{q} \tag{3.17}$$

can be written in terms of an additional piece to the SM case, $gg \rightarrow H_{\mathrm{SM}} + X$. Retaining again only terms up to order $(1 - \hat{\tau})^1$ [which is a very approximation, see §I.3.4.3 for a discussion], one obtains very simple expressions for the difference between the pseudoscalar and scalar cases [in particular, one can notice the explicit difference at NLO, $\Delta_{ijA}^{(1)} = \Delta_{ijH_{\mathrm{SM}}}^{(1)} + \frac{1}{2}\delta_{ig}\delta_{jg}v\delta(1 - \hat{\tau})$, discussed above] [354]

$$\begin{aligned}
\Delta_{ggA}^{(2)} &= \Delta_{ggH_{\mathrm{SM}}}^{(2)} + (1.97 - 0.71\ell_A)\,\delta(1 - \hat{\tau}) + 6\mathcal{D}_1(\hat{\tau}) - 6\hat{\tau}(\hat{\tau}^2 - \hat{\tau} - 2)\ell + \frac{1}{2}(93 - 96\hat{\tau}) \\
\Delta_{gqA}^{(2)} &= \Delta_{gqH_{\mathrm{SM}}}^{(2)} + \frac{2}{3}(2 - 2\hat{\tau} + \hat{\tau}^2)\ell + \frac{1}{9}(13\hat{\tau} - 60)\;, \\
\Delta_{qqA}^{(2)} &= \Delta_{q\bar{q}A}^{(2)} = \Delta_{qq'A}^{(2)} = 0
\end{aligned} \tag{3.18}$$

with $\ell = \log(1 - \hat{\tau})$, $\ell_A = \log(M_A^2/m_t^2)$ and the $\mathcal{D}_1$ distribution defined in §I.3. For the numerical evaluation of the hadronic cross sections, we follow the same analysis as in the SM case. Assuming that the $At\bar{t}$ coupling has the same magnitude as the $H_{\mathrm{SM}}t\bar{t}$ coupling, $g_t = 1$ [which in practice is equivalent to set $\tan\beta$=1 and to ignore the small contribution of the b–quark loop], the cross section for $gg \rightarrow A$ is shown in Fig. 3.9 at the LHC and at

the Tevatron as a function of M_A at LO, NLO and NNLO. The MRST parton distributions have been again used. The normalization at LO contains the full top mass dependence with $m_t = 175$ GeV. The cross section for different g_t values can be obtained by simply rescaling the curves with $|g_t|^2$, but if the bottom quark loop contribution dominates, the NNLO calculation fails and one has to restrict oneself to the NLO result.

The behavior of the cross sections is qualitatively and quantitatively similar to the one of the SM Higgs boson since we are below the $M_{H/A} = 2m_t$ threshold. The total K–factors are large, with the NNLO contribution significantly smaller than the NLO contribution, indicating a nice converging behavior of the perturbative series. The scale dependence is also the same as in the SM case and varying $\mu_R = \mu_F$ between $\frac{1}{2}M_A$ and $2M_A$ results in a variation of the cross section of 20% (40%) at LO, 15% (25%) at NLO and 10% (15%) at NNLO at the LHC (Tevatron), showing a clear reduction of the scale dependence and, hence, of the theoretical uncertainty when higher–order corrections are included.
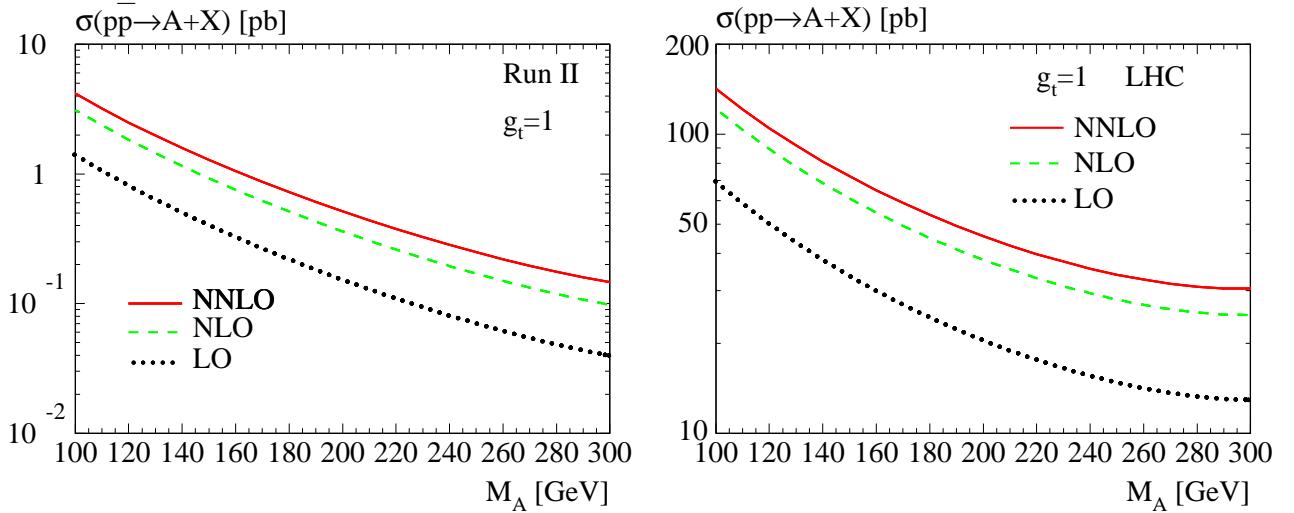
Figure 3.9: The total production cross section for a pseudoscalar Higgs boson at the Tevatron (left) and at the LHC (right) as a function of the Higgs mass at LO, NLO and NNLO. The coupling constant of the A boson to top quarks is as for the SM Higgs boson, $g_t = 1$. The MRST parton distributions are used and the scales are set to M_A; from Ref. [354].

The total cross sections

As mentioned previously, when calculating the total cross sections of the gluon fusion mechanisms in the MSSM, $gg \to \Phi$, one cannot use in general the low energy theorem where the heavy top quark is integrated out to incorporate the higher–order corrections, even for Higgs masses below the $2m_t$ threshold. Because in most cases the b–quark loop gives the dominant contribution, this effective treatment does not apply anymore and one has to incorporate the corrections in the full massive case or at least, when $\tan\beta$ is extremely large and the

bottom loop is by far dominant, in the massless b–quark case when the Yukawa coupling and the large logarithms have been separated out. In the following discussion, we thus ignore the NNLO results discussed previously and implement only the NLO corrections which are known exactly. We also ignore, for the time being, the contribution of the SUSY loops.

The cross sections at NLO for the production of the two CP–even and of the CP–odd Higgs bosons are shown as a function of their respective masses in Figs. 3.10 and 3.11 for, respectively, the Tevatron and the LHC. Again, the two values $\tan\beta = 3$ and 30 have been chosen and the MSSM Higgs sector has been treated in exactly the same way as in the processes involving gauge boson discussed previously. The MRST PDF set has been adopted and the factorization and renormalization scales have been set to $\mu_F = \mu_R = \frac{1}{2}M_\Phi$ to approach the NNLO rates in the decoupling limit or at low $\tan\beta$ values [see §I.3.4].
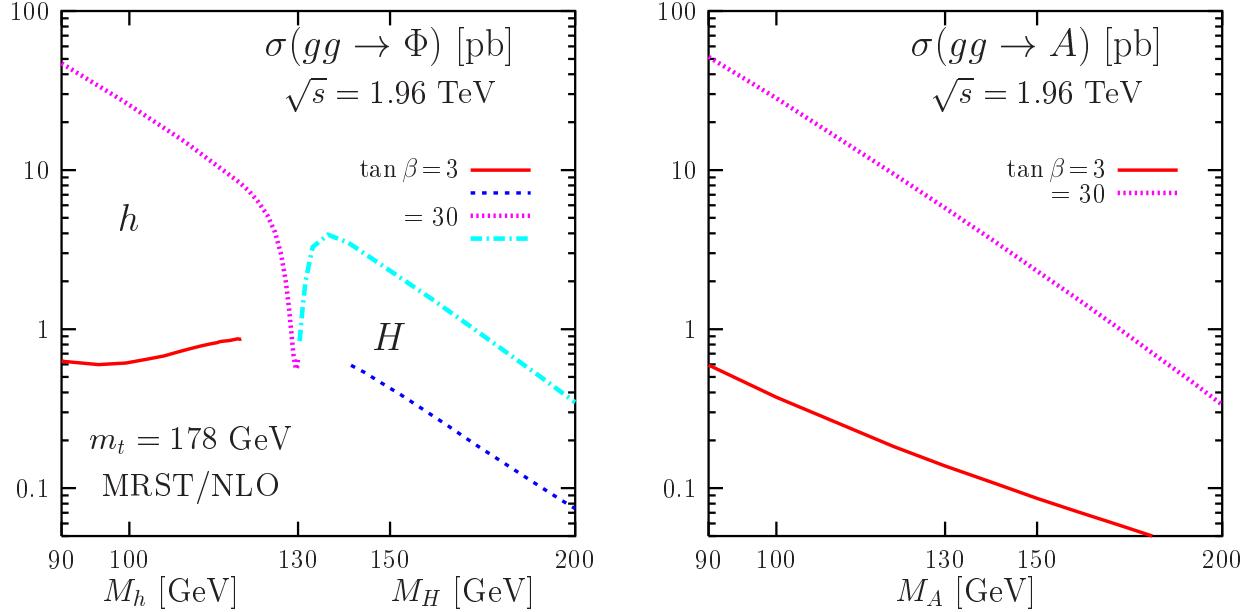
Figure 3.10: The production cross sections of the CP–even h, H bosons (left) and CP–odd A boson (right) in the gluon–gluon fusion mechanism at the Tevatron as a function of the Higgs masses for $\tan\beta = 3$ and 30. They are at NLO, with the scales fixed to $\mu_F = \mu_R = \frac{1}{2}M_\Phi$ with $m_t = 178$ GeV, $m_b = 4.88$ GeV and the MRST set of PDFs has been used.

As can be seen, except for h and H in, respectively, the decoupling and anti–decoupling regimes, the production cross sections for the CP–even Higgs bosons are smaller than in the SM case for low $\tan\beta$ values, when the suppressed top quark loop contribution is still dominant, and very large for high $\tan\beta$ values, when the b–quark loop contribution is strongly enhanced. The cross sections are minimal for values $\tan\beta \sim 6$–8 when we reach the maximal suppression of the coupling $g_{\Phi tt}$ and the minimal enhancement of $g_{\Phi bb}$. For the value $\tan\beta = 30$ used for illustration, the $gg \to h/H$ cross sections are one order of magnitude higher than
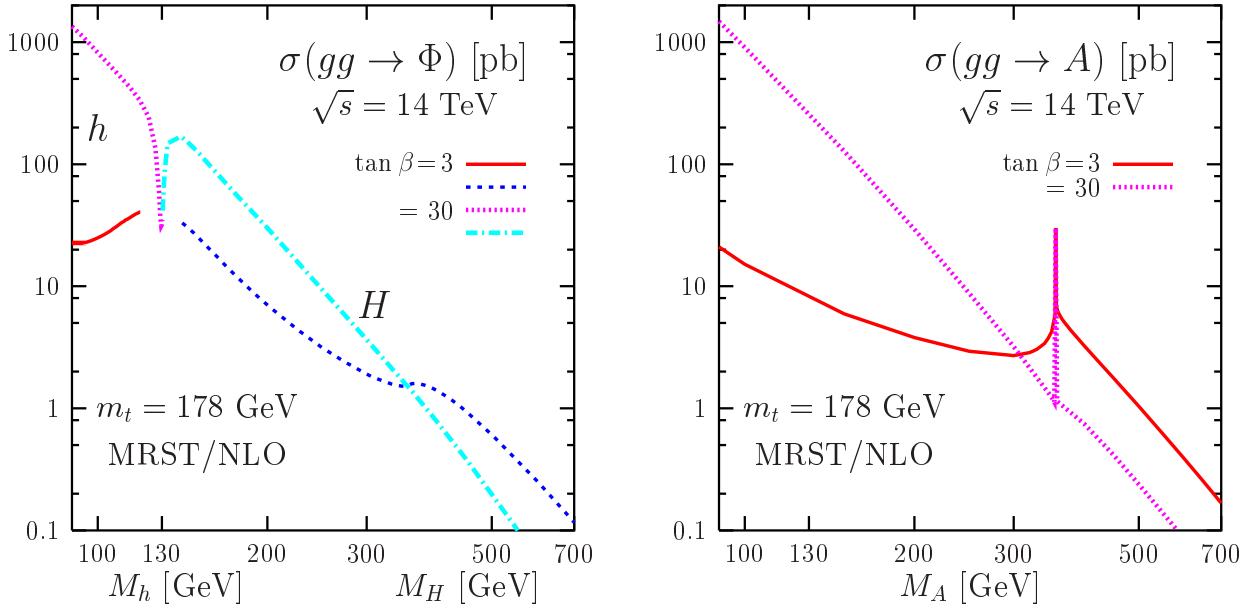
Figure 3.11: The same as Fig. 3.10 but at LHC energies.

in the SM with a dominating top loop contribution. They can be even larger as they grow as $\tan^2 \beta$, possibly exceeding the atobarn level at the LHC for small Higgs masses.
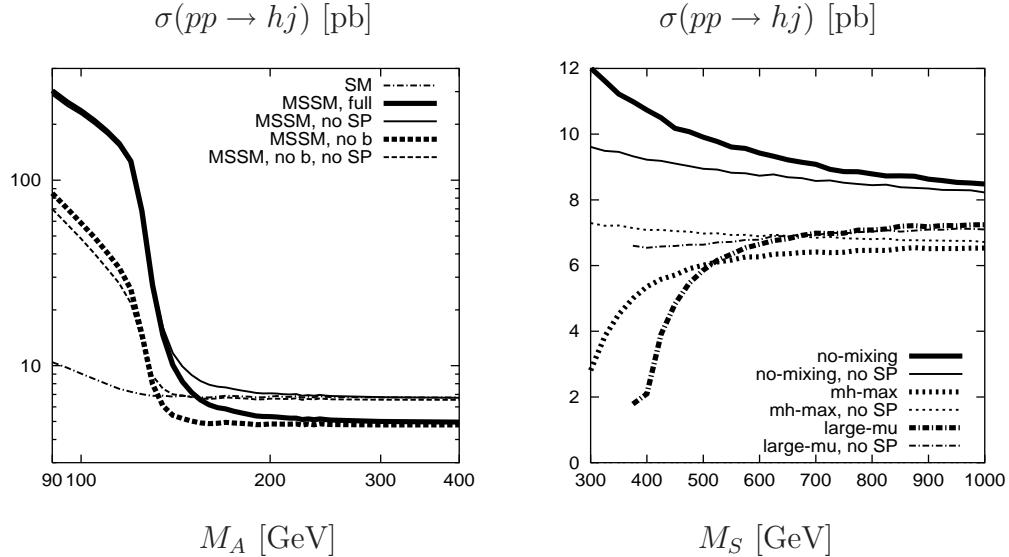
The cross sections in the pseudoscalar Higgs boson case are approximately the same as the ones for h and H production for, respectively, $M_A \lesssim M_h^{\max}$ and $M_A \gtrsim M_h^{\max}$, an approximation which improves with higher $\tan \beta$ values for which the decoupling or anti–decoupling limits are quickly reached and for which the b–quark loop contributions become more important resulting in almost equal $\Phi g g$ amplitudes in the scalar and pseudoscalar cases as a result of chiral symmetry. The only noticeable difference, except of course in the (anti–)decoupling limits for $(H)\,h$, occurs near the $2m_t$ threshold where the amplitude for the CP–odd A boson develops a singularity while the one for the CP–even H boson simply reaches a maximum; these features have been discussed in §2.1.3. For low values of $\tan \beta$, however, the amplitudes are slightly different: first, because the Higgs couplings to top quarks do not reach quickly common values and, second, because the amplitudes are different since the one–loop form factors are such that $A_{1/2}^{\mathcal{H}} \sim \frac{4}{3}$ and $A_{1/2}^{A} \sim 2$ for $m_t \gtrsim M_\Phi$.

Higgs plus jet production

Finally, an additional source of neutral Higgs bosons will be the associated production with a high transverse momentum jet, $gg \rightarrow \Phi + j$. As discussed in the SM case, this is in principle part of the NLO QCD corrections but, since the additional jet can be detected if it is hard enough, this process is interesting [356] as it might have a lower background than the initial process $gg \rightarrow \Phi$. The Feynman diagrams generating this final state are the same

as in the SM but again, one has to include the contributions of the b–quark loops which lead to extremely enhanced cross sections for the production of the pseudoscalar A and the CP–even $h\,(H)$ boson in the (anti–)decoupling limit if the value of $\tan\beta$ is large enough. Additional topologies with initial bg and $b\bar{b}$ initial states are also present for this process and here, again, the possibility that squark loops contribute significantly to the production rates has to be considered.

The cross sections have been calculated in Refs. [357–359] and, as an example of the possible output, we show in Fig. 3.12 borrowed from the first reference, the cross section for the production of the lighter MSSM Higgs boson in association with a jet with a minimum transverse momentum of $p_{Tj}^{\min} = 30$ GeV and a rapidity of $|\eta_j| < 4.5$. In the left–hand side of the figure, the $pp \to hj$ cross section is shown as a function of M_A for $\tan\beta = 30$ at the LHC. The maximal mixing scenario with $M_S = 400$ GeV has been chosen and the cross sections are shown with and without the contribution of SUSY particles (SP) and including or not bottom quark initiated processes. As can be seen, the cross section can be extremely large if the h boson is pseudoscalar like, that is, in the anti–decoupling regime. The initiated b–quark contributions, $b\bar{b} \to hj$ with the initial b–quarks treated as partons, are in fact the dominant ones. Even the contributions of the SUSY particles, when there are light enough, can be significant. This is exemplified in the right–hand side of the figure where the same cross section is shown as a function of M_S with $M_A = 200$ GeV, $\tan\beta = 6$ and in different SUSY scenarios.

Figure 3.12: The cross section for the production of the h boson in association with a hard jet, $pp \to hj$, at the LHC as a function of the pseudoscalar Higgs mass M_A (left) and of the SUSY scale M_S (right) in various scenarios indicated in the figure; from Ref. [357].

3.1.3 Associated production with heavy quarks

The cross sections in an improved Born approximation

The same gross features discussed above for the gg case, appear in the associated production of the neutral Higgs bosons $\Phi = h, H$ and A with top and bottom quark pairs, $pp \to q\bar{q}, gg \to t\bar{t}\Phi$ and $pp \to q\bar{q}, gg \to b\bar{b}\Phi$. These two processes [and in particular, the former process since in the SM, $b\bar{b}$+Higgs production is not very relevant because of the tiny bottom–quark Yukawa coupling] have been analyzed in §I.3.5 and most of the discussion on the analytical aspects holds in the MSSM, at least in the case of the CP–even Higgs bosons. The only difference is, of course, that the cross sections have to be multiplied by the squares of the reduced Higgs Yukawa couplings to fermions [313, 360]

$$\sigma(pp \to Q\bar{Q}\mathcal{H}) \;\; = \;\; g^2_{\mathcal{H}QQ}\, \sigma_{\mathrm{SM}}(pp \to Q\bar{Q}\mathcal{H}) \tag{3.19}$$

The production cross sections for $pp \to t\bar{t} + h/H$ are smaller than the ones of the SM Higgs boson with the same mass except, again, in the decoupling or anti–decoupling limits for, respectively, the h and H bosons and the suppression is drastic at high $\tan\beta$ values. In turn, for these high values, the $pp \to b\bar{b} + h/H$ cross sections are strongly enhanced being proportional to $\tan^2\beta$ outside the two mentioned regimes. In this case, the cross sections for the production of the pseudoscalar Higgs boson are almost identical to those of the h and H bosons for, respectively, $M_A \lesssim M_h^{\mathrm{max}}$ and $M_A \gtrsim M_h^{\mathrm{max}}$, as a result of chiral symmetry which approximately holds in this case since $m_b^2/M_A^2 \ll 1$. For low $\tan\beta$ values, the cross sections for scalar and pseudoscalar Higgs production do not have the same magnitude because of the different ΦQQ couplings [since the decoupling limit is reached very slowly in this case] and, in the case of the $pp \to t\bar{t}\Phi$ process, the amplitudes squared where top quark mass effects are significant for not too large Higgs masses, are not the same.

The total production cross sections are shown at LO as a function of the mass of the relevant Higgs boson in Figs. 3.13 and 3.14 for, respectively, the Tevatron and the LHC. The $pp \to t\bar{t}\Phi$ cross section is displayed for $\tan\beta = 3$ and $m_t = 178$ GeV with the renormalization and factorization scales fixed to $\mu_R = \mu_F = \frac{1}{2}(M_\Phi + 2m_t)$, while the $pp \to b\bar{b}\Phi$ cross section is displayed for $\tan\beta = 30$ using the running b–quark mass at the scale of the Higgs mass in the Yukawa coupling, $\bar{m}_b(M_\Phi^2) \sim 3$ GeV, with the renormalization and factorization scales fixed to $\mu_R = \mu_F = \frac{1}{4}(M_\Phi + 2m_b)$ to absorb the bulk of the higher–order corrections as will be discussed shortly. In both cases, the MRST parton densities have been used and, again, we have adopted the same approximation for the radiative corrections in the MSSM Higgs sector as previously.

As can be seen, while the cross sections for the $pp \to t\bar{t}\Phi$ process become very small, except in the two particular regimes where the h and H bosons are SM–like, they are
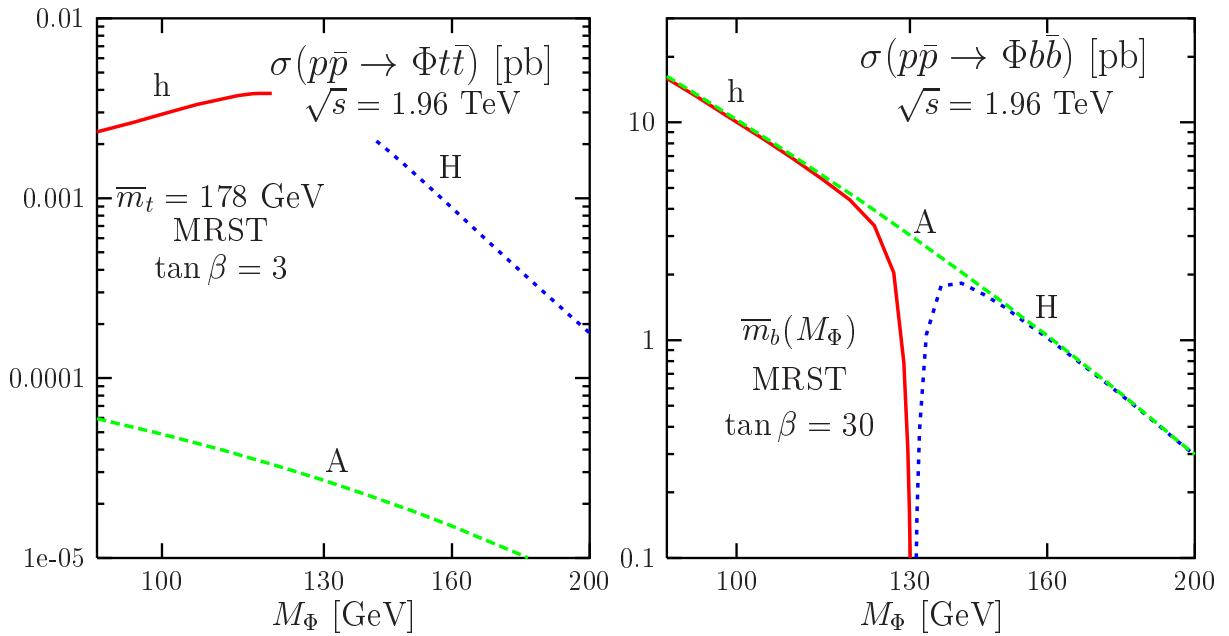
Figure 3.13: The production cross sections of the neutral h, H and A bosons in association with heavy quarks at the Tevatron as a function of the Higgs masses. Shown are the $pp \to t\bar{t}\Phi$ cross sections for $\tan\beta = 3$ with $m_t = 178$ GeV (left) and the $b\bar{b}\Phi$ cross sections for $\tan\beta = 30$ and using the running b–quark mass with the pole mass taken to be $m_b = 4.9$ GeV (right). The renormalization and factorization scales are as described in the text and the MRST PDFs have been used.
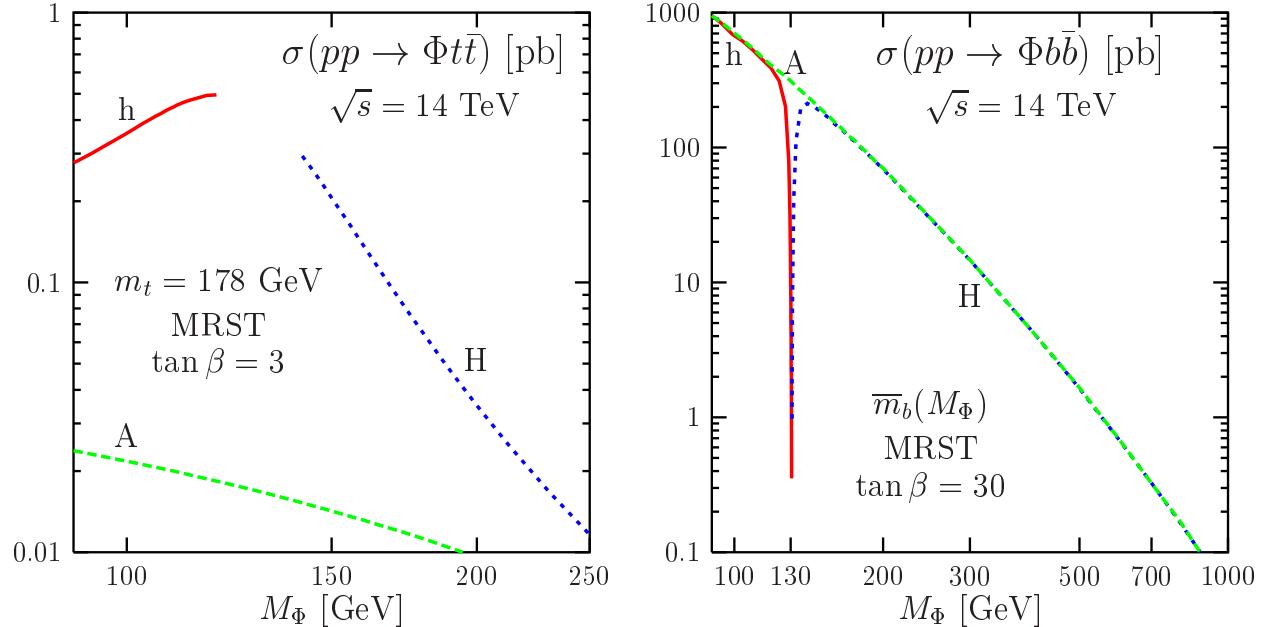
Figure 3.14: The same as Fig. 3.13 but for the LHC.

extremely large in the $pp \to b\bar{b}\Phi$ case with the chosen value $\tan\beta = 30$. In fact, at the LHC, the production rates are approximately the same as in the $gg \to \Phi$ fusion process for low Higgs masses, $M_\Phi = \mathcal{O}(100 \text{ GeV})$, but decrease less steeply with increasing Higgs mass and, at $M_\Phi \sim 200\,(500)$ GeV, they are a factor of $\sim 2\,(5)$ larger than the cross sections of the gg fusion mechanisms. The $pp \to b\bar{b}\Phi$ processes are, thus, the dominant production mechanisms of the MSSM neutral Higgs at the LHC. At the Tevatron also the $p\bar{p} \to b\bar{b}\Phi$ cross sections can be increased to the level where they exceed by orders of magnitude the standard $p\bar{p} \to t\bar{t}H_{\text{SM}}$ cross section and even the one for the $gg \to \Phi$ fusion mechanisms. For the value $\tan\beta = 60$, which is probably the highest value that perturbation theory should allow for this parameter, the huge event rates make it possible to detect the neutral Higgs bosons at the Tevatron in these channels for not too large M_A values.

The NLO QCD corrections

The NLO QCD corrections to the associated production of the CP–even $\mathcal{H} = h, H$ bosons with top quark pairs are the same as in the SM Higgs case [361] which has been discussed in detail in §I.3.5.2. In the mass range where these processes are relevant, in practice in the entire mass range for the lighter h boson and in the range $M_H \lesssim 200$ GeV for the heavier one, these corrections increase (decrease) the total cross sections only by $\sim 20\%$ at the LHC (Tevatron) if the renormalization and factorization scales are chosen to be $\mu_R = \mu_F = \frac{1}{2}(M_\mathcal{H} + 2m_t)$. The NLO QCD corrections in the case of the pseudoscalar Higgs bosons are not yet known but we expect them to be of the same size as for h/H production, at least at the LHC where the mass effects $m_t^2/\hat{s}$ should not be very large. The SUSY–QCD corrections have also not been calculated yet, but they should be relatively small for heavy enough squarks and gluinos, once the leading SUSY threshold corrections to the quark masses have been implemented in the Yukawa couplings.

In the case of the $pp \to b\bar{b}\Phi$ processes, the NLO QCD corrections [362] are also the same as in the SM case and, at least for the calculational part, they follow the same lines as for the associated Higgs production with top quarks. Since the b–quark mass is very small compared to the Higgs masses, chiral symmetry approximately holds and the corrections are the same for the CP–even and CP–odd Higgs bosons. There is, however, a major difference between the $\Phi b\bar{b}$ and $\Phi t\bar{t}$ cases: because of the small b–quark mass, the cross sections $\sigma(gg \to b\bar{b}\Phi)$ develop large logarithms, $\log(Q^2/m_b^2)$, with the scale Q being typically of the order of the factorization scale, $Q \sim M_\Phi \gg m_b$. These logarithms originate from the splitting of gluons into $b\bar{b}$ pairs leading to distributions in the b–quark transverse momentum $d\sigma/dp_{Tb} \propto p_{Tb}/(p_{Tb}^2 + m_b^2)$ which, when integrated over p_{Tb}, give rise to a partonic total cross section $\sigma \propto \log(Q^2/m_b^2)$ where the scale is $Q \sim p_{Tb}^{\max}$. Therefore, while the $gg \to b\bar{b}\Phi$ mechanism gives reliable results at high b–quark transverse momentum, the convergence

of the perturbative series is poor in the opposite case, unless these large logarithms are resummed.

As noted some time ago [360, 363] and discussed more recently [364, 365], this can simply be done via the Altarelli–Parisi equations: by considering the b–quark as a massless parton, these leading logarithms are resummed to all orders in QCD by using heavy quark distribution functions at the factorization scale $\mu_F \sim Q$. In this scheme, the inclusive process where one does not require to observe the b quarks is simply the $2 \to 1$ process $b\bar{b} \to \Phi$ at LO; Fig. 3.15a. If one requires the observation of a high–p_T final b–quark, one has to consider its NLO corrections and in particular the $2 \to 2$ process $gb \to \Phi b$, Fig. 3.15b, which indeed generates the p_T of the b–quark. Requiring the observation of two b quarks, one has to consider the $2 \to 3$ process $gg \to b\bar{b}\Phi$, Fig. 3.15c, which is the leading mechanism at NNLO.
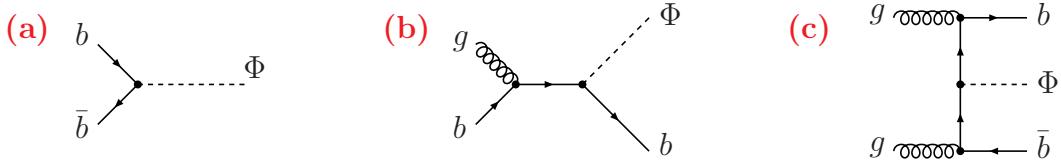
Figure 3.15: Feynman diagrams for $b\bar{b} \to \Phi$, $bg \to b\Phi$ and $gg \to b\bar{b}\Phi$ production.

Let us discuss these three processes at their respective leading orders. For this purpose, it is convenient to follow Ref. [366] and write the partonic cross sections as

$$\hat{\sigma}_{ij}(\hat{\tau}) \;=\; \sigma_0^\Phi \, \Delta_{ij}(\hat{\tau}) \qquad i, j \in \{b, \bar{b}, g, q, \bar{q}\} \tag{3.20}$$

where $\hat{\tau} = M_\Phi^2/\hat{s}$ and $\hat{\sigma}_{ij}$ denotes the cross section for the subprocess $ij \to \Phi + X$ with initial i and j gluons and/or light u, d, s, c, b quarks, and a final state involving the scalar or pseudoscalar Higgs boson Φ and additional quark or gluon jets X. The normalization factor σ_0^Φ is

$$\sigma_0^\Phi = \frac{\pi}{12} \frac{g_{\Phi b\bar{b}}^2}{M_\Phi^2} \tag{3.21}$$

For simplicity, we present the results for the scale choice $\mu_F = \mu_R = M_\Phi$; the results for general values of μ_F and μ_R can be reconstructed from the renormalization scale invariance of the partonic and the factorization invariance of the hadronic cross sections. At LO, the partonic cross section for the $b\bar{b} \to \Phi$ process is simply

$$\Delta_{b\bar{b}}^0(\hat{\tau}) = \delta(1 - \hat{\tau}) \tag{3.22}$$

while for the $bg/\bar{b}g$ subprocesses, one has at LO [366]

$$\begin{aligned}
\Delta_{bg}^0 = \Delta_{\bar{b}g}^0 \;=\; & \frac{1}{2}(\hat{\tau} - 2\hat{\tau}^2 + 2\hat{\tau}^3) \log(1 - \hat{\tau}) - \frac{1}{8}(3\hat{\tau} - 10\hat{\tau}^2 + 7\hat{\tau}^3) \\
& - \frac{1}{4}(\hat{\tau} - 2\hat{\tau}^2 + 2\hat{\tau}^3) \log(\hat{\tau})
\end{aligned} \tag{3.23}$$

For the $gg \to \Phi b\bar{b}$ subprocess, the expressions are much more involved. Defining the variables $\hat{\tau}_\pm = 1 \pm \hat{\tau}$ and using the Spence functions Li_2 and Li_3 with $\zeta_2 = \frac{\pi^2}{6}$, one has [366]

$$
\begin{aligned}
\Delta_{gg}^0 =& \left[-(\hat{\tau} + 2\hat{\tau}^2 - 3\hat{\tau}^3) - \frac{\hat{\tau} + 4\hat{\tau}^2 + 4\hat{\tau}^3}{2} \log(\hat{\tau}) \right] \log^2(\hat{\tau}_-) + \frac{23\hat{\tau} + 52\hat{\tau}^2 - 75\hat{\tau}^3}{8} \log(\hat{\tau}_-) \\
&+ \log(\hat{\tau}_-) \left[\frac{5\hat{\tau} + 16\hat{\tau}^2 - 4\hat{\tau}^3}{4} \log(\hat{\tau}) + \frac{\hat{\tau} + 4\hat{\tau}^2 + 4\hat{\tau}^3}{4} \log^2(\hat{\tau}) - (\hat{\tau} + 4\hat{\tau}^2 + 4\hat{\tau}^3) \text{Li}_2(\hat{\tau}_-) \right] \\
&- \frac{163\hat{\tau} + 1528\hat{\tau}^2 - 1691\hat{\tau}^3}{128} + (\hat{\tau} + 2\hat{\tau}^2 - 3\hat{\tau}^3)\zeta_2 - \frac{54\hat{\tau} + 312\hat{\tau}^2 - 223\hat{\tau}^3}{64} \log(\hat{\tau}) \\
&+ \frac{\hat{\tau} + 4\hat{\tau}^2 + 4\hat{\tau}^3}{2}\zeta_2 \log(\hat{\tau}) - \frac{16\hat{\tau} + 111\hat{\tau}^2 - 43\hat{\tau}^3}{64} \log^2(\hat{\tau}) + \frac{7\hat{\tau} + 25\hat{\tau}^2 + 34\hat{\tau}^3}{48} \log^3(\hat{\tau}) \\
&- \frac{4\hat{\tau} - 15\hat{\tau}^2 - 62\hat{\tau}^3}{16} \text{Li}_2(\hat{\tau}_-) + \frac{11\hat{\tau} + 44\hat{\tau}^2 + 30\hat{\tau}^3}{16} \text{Li}_2(\hat{\tau}_-) \log(\hat{\tau}) + \frac{\hat{\tau}^2 - 6\hat{\tau}^3}{32} \text{Li}_2(\hat{\tau}_-\hat{\tau}_+) \\
&+ \frac{3\hat{\tau} + 6\hat{\tau}^2 + 38\hat{\tau}^3}{64} \text{Li}_2(\hat{\tau}_-\hat{\tau}_+) \log(\hat{\tau}) + \frac{\hat{\tau} + 3\hat{\tau}^2 + 18\hat{\tau}^3}{8} \text{Li}_3(\hat{\tau}_-) \\
&- \frac{15\hat{\tau} + 60\hat{\tau}^2 + 30\hat{\tau}^3}{16} \text{Li}_3\left(-\frac{\hat{\tau}_-}{\hat{\tau}}\right) - \frac{5\hat{\tau} + 10\hat{\tau}^2 + 74\hat{\tau}^3}{128} \text{Li}_3(\hat{\tau}_-\hat{\tau}_+) \\
&- \frac{3\hat{\tau} + 6\hat{\tau}^2 + 70\hat{\tau}^3}{128} \text{Li}_3\left(-\frac{\hat{\tau}_+\hat{\tau}_-}{\hat{\tau}^2}\right) - \frac{\hat{\tau} + 2\hat{\tau}^2 + 2\hat{\tau}^3}{32}\left[\text{Li}_3\left(\frac{\hat{\tau}_-}{\hat{\tau}_+}\right) - \text{Li}_3\left(-\frac{\hat{\tau}_-}{\hat{\tau}_+}\right)\right]
\end{aligned}
\tag{3.24}
$$

However, the LO cross sections of the three processes are plagued with large uncertainties due to the very strong dependence on the renormalization and factorization scales; higher–order corrections have therefore to be included for reliable predictions. These corrections have been completed by now and the three processes or, rather, the two pictures, the one with gg fusion and the one with initial state b–partons, have been recently compared in [367]. We briefly summarize here the results and, for the numerical illustration, we follow Ref. [367] where the observation of the final b quarks is achieved by requiring $p_{Tb,\bar{b}} \geq 20$ GeV and $|\eta_{b,\bar{b}}| \leq 2\,(2.5)$ at the Tevatron (LHC) with an additional jet separation cone of $\Delta R > 0.4$. The renormalization and factorization scales have been set to $\mu_F = \mu_R = \mu_0 = \frac{1}{4}(2m_b + M_\Phi)$ which is expected to reduce the size of the higher–order QCD corrections [364] and the pole b–quark mass is fixed to $m_b = 4.9$ GeV.

In the Higgs + 2–jet case, $q\bar{q}/gg \to b\bar{b}\Phi$, the NLO corrections calculated in Ref. [362] have been already discussed. Although formally the same as for $t\bar{t}\Phi$ production, the corrections are quantitatively different because of the small m_b value compared to m_t. At the central scale, $\mu_0 = \frac{1}{4}(2m_b + M_\Phi)$ which was already used in Figs. 3.13–14, the NLO results modify the cross sections by less than $\sim 30\%$ at the Tevatron and $\sim 50\%$ at the LHC for the numerical values chosen above; Fig. 3.16. The corrections have a strong dependence on the p_{Tb} cut value: they are negative at large p_{Tb}^{cut} and positive and small at low p_{Tb}^{cut}.

In the Higgs + 1–jet case, $gb \to b\Phi$, the cross sections are one order of magnitude larger than in the previous case for the cuts which have been adopted. In the $gg \to b\bar{b}\Phi$ picture,
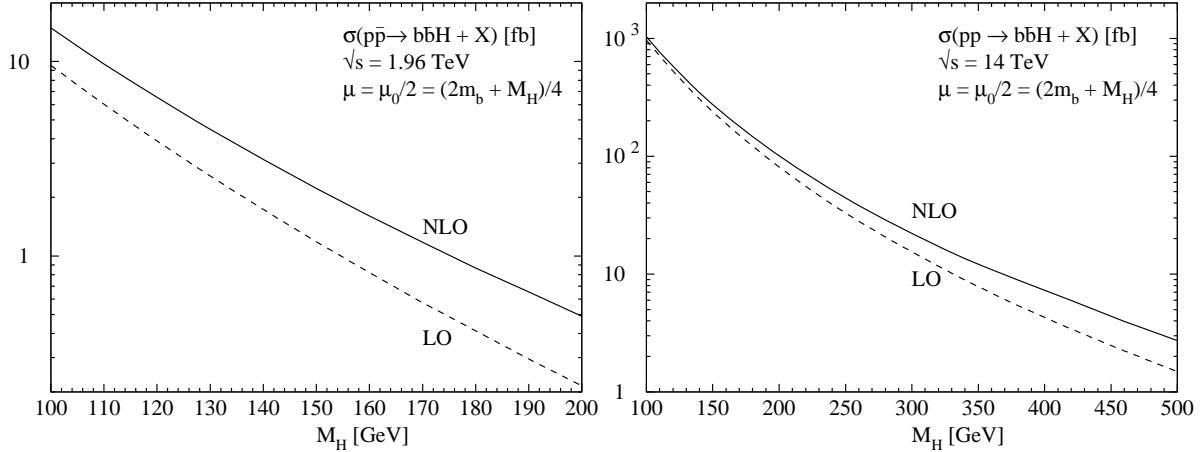
Figure 3.16: The LO and NLO total production cross sections for a SM–like Higgs boson, $\sigma(pp \to b\bar{b}H + X)$, at the Tevatron (left) and the LHC (right) as a function of M_H with two high–p_T b jets identified in the final state. The scales are as indicated; from Ref. [367].

the process has been calculated with the momentum of one b–quark integrated out, leading to a large logarithm, $\log(\mu_0^2/m_b^2)$. The NLO corrections increase the cross section by less than 50% (80%) at the Tevatron (LHC) and the scale, when varied from $2\mu_0$ to $\frac{1}{2}\mu_0$, leads to a significant variation of the cross section; Fig. 3.17. The scale variation is reduced when the b–quark is treated as a parton, the large logarithm being absorbed in the b–density. The NLO corrections to $bg \to b\Phi$ are moderate [368]. One can see from Fig. 3.17 that the two approaches, gg fusion and bottom partons, agree rather well when the scale is chosen to be $\mu_0 = \frac{1}{4}(2m_b + M_\Phi)$, the difference in this case being within the scale uncertainty.
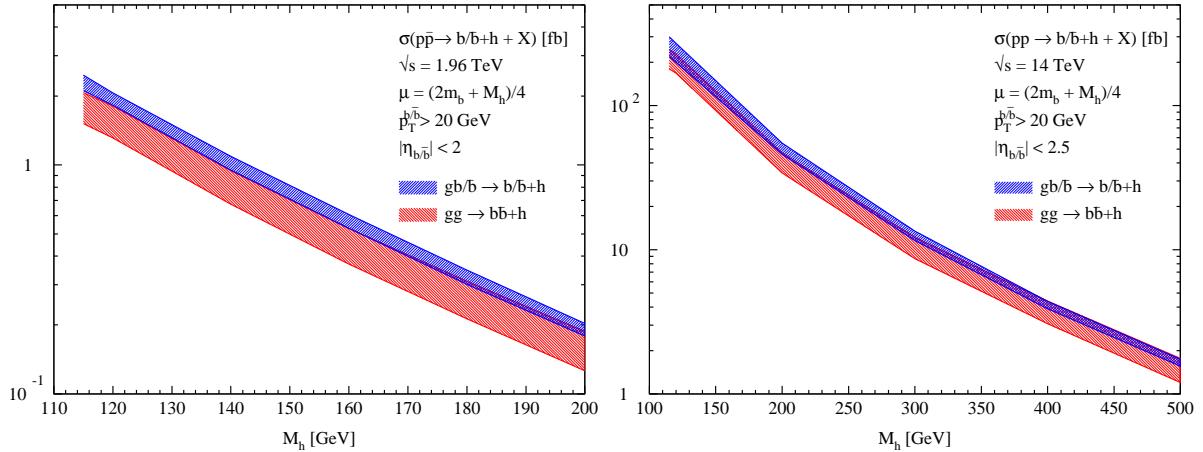
Figure 3.17: The total cross sections for $pp \to b\bar{b}H + X$ at the Tevatron (left) and the LHC (right) as a function of M_H with only one high–p_T b jet identified in the final state. The scale is varied from $\mu_F = \mu_R = 2\mu_0$ to $\frac{1}{2}\mu_0$ around the central scale given [together with the p_T and η cuts] in the figure; from Ref. [367].

Finally, in the case where no final state b–quark is required for identification, i.e. when inclusive Higgs production is considered, there is again an increase in magnitude of the production cross section compared to Higgs plus one b–jet production. The $b\bar{b} \to \Phi$ cross section has been calculated at NLO some time ago [360] and recently at NNLO [366], resulting in a very small scale variation as shown in Fig. 3.18. Note that for the central value μ_0 of the renormalization and factorization scales which has been chosen, the NLO and NNLO results are nearly the same, which justifies this particular choice. The calculation in the $gg \to \Phi b\bar{b}$ picture, despite of the large logarithms which are present, leads to a result which is rather close to the $b\bar{b} \to \Phi$ case. However, the scale dependence is much stronger signaling that the convergence of the perturbative series is worse than in the $pp \to t\bar{t}\Phi$ case[29].
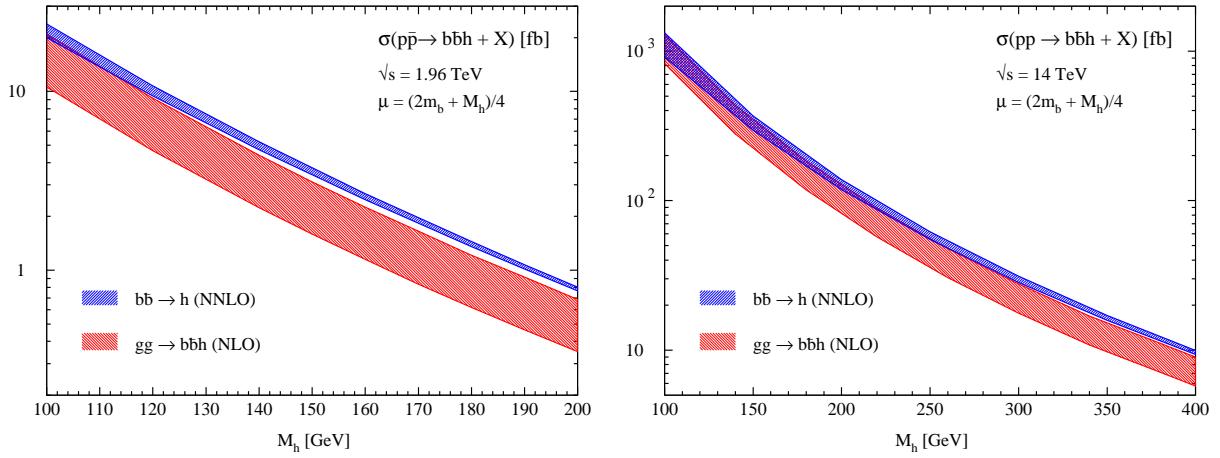
Figure 3.18: The total cross sections for $pp \to b\bar{b}H + X$ at the Tevatron (left) and the LHC (right) as a function M_H with no b jet identified in the final state; Ref. [367]. The error bands correspond to varying the scale from $2\mu_0$ to $\frac{1}{2}\mu_0$. The NNLO curves are from Ref. [366].

Thus, as expected, when including the higher–order QCD corrections the cross sections for $pp \to b\bar{b}\Phi$ in the gg fusion and bottom parton pictures lead to similar results when the scales are appropriately chosen. This agreement gives confidence that the production rates are relatively well under control.

3.1.4 Neutral Higgs boson pair production

The production of pairs of MSSM neutral Higgs bosons in the continuum can be achieved in two main mechanisms: $q\bar{q}$ annihilation, leading to hA and HA final states through the exchange of a virtual Z boson [39], Fig. 3.19a,

$$q\bar{q} \to Z^* \to hA, \ HA \tag{3.25}$$

---

[29]Note that there are closed top loop contributions which in the SM reduce the cross section by approximately 5% (10%) at the Tevatron (LHC) and which are not included in the $gb \to b\Phi$ and $b\bar{b} \to \Phi$ pictures. However, they are smaller in the MSSM where the $\Phi\bar{b}b$ ($\Phi t\bar{t}$) coupling is enhanced (suppressed).

or gg fusion [369–372] induced by heavy quark box and triangle diagrams [the latter being sensitive to the triple Higgs couplings], leading to various Higgs final states, Fig. 3.19b,

$$gg \to hh, \ HH, \ hH, \ AA \ \text{ and } hA, \ HA \tag{3.26}$$

Additional processes [373, 374] are also provided by double Higgs–strahlung, vector boson fusion into two Higgs bosons and triple Higgs boson production [$\mathcal{H}_{i,j} = h, H$]

$$
\begin{aligned}
q\bar{q} &\to V\mathcal{H}_i\mathcal{H}_j, \ VAA \\
qq &\to qq\mathcal{H}_i\mathcal{H}_j, \ qqAA \\
q\bar{q} &\to \mathcal{H}_i\mathcal{H}_jA, \ AAA
\end{aligned}
\tag{3.27}
$$

Because of CP–invariance, the other final states do not occur. As as result of the limited phase space and the low gluon luminosities, these processes will not be relevant at the Tevatron and we thus concentrate on the LHC in the following discussion.
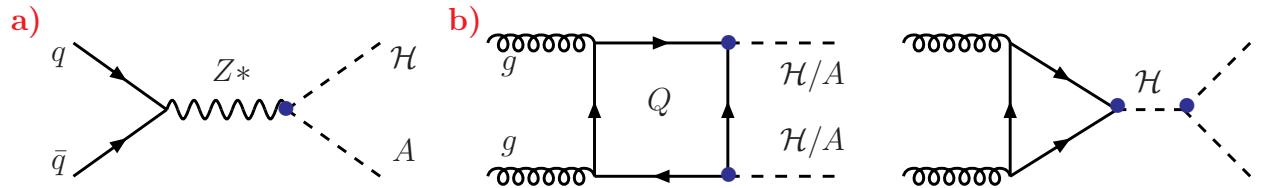
Figure 3.19: Generic diagrams for neutral Higgs pair production in hadronic collisions.

Production in $q\bar{q}$ annihilation

The partonic cross sections for pair production in $q\bar{q}$ annihilation, $q\bar{q} \to \mathcal{H}A$ with $\mathcal{H} = h, H$ are, up to couplings factors, those of the associated $\mathcal{H}$ production with a Z boson

$$\hat{\sigma}(q\bar{q} \to \mathcal{H}A) = g^2_{\mathcal{H}AV} \ \hat{\sigma}_{\mathrm{SM}}(q\bar{q} \to \mathcal{H}Z) \times \frac{\lambda^3_{A\mathcal{H}}}{\lambda_{Z\mathcal{H}}(\lambda^2_{Z\mathcal{H}} + 12M^2_Z/\hat{s})} \tag{3.28}$$

with another difference in the phase space factor to account for the production of two spin–zero particles. The cross sections are shown in Fig. 3.20 as a function of M_A at the LHC for $\tan\beta = 3$ and 30 and the same choice of SUSY parameters as in previous cases. In these plots, the NLO QCD corrections have been implemented: they are, in fact, simply those of the Drell–Yan or, equivalently, the $q\bar{q} \to \mathcal{H}V$ processes with the scales fixed to $\mu_R = \mu_F = M_{A\mathcal{H}}$ and increase the total rates by approximately 30% [375]. When the phase space is favorable, the cross sections can be large. In particular for $M_A \lesssim M_h^{\mathrm{max}}$ when the coupling $g_{hAZ} \equiv g_{HVV} = \cos(\beta - \alpha)$ is almost maximal, the $q\bar{q} \to hA$ cross section is in the range of a fraction of a picobarn. The $q\bar{q} \to HA$ rate is smaller because of phase space suppression and the small $g_{HAZ} \equiv g_{hVV} = \sin(\beta - \alpha)$ coupling for low M_A values.
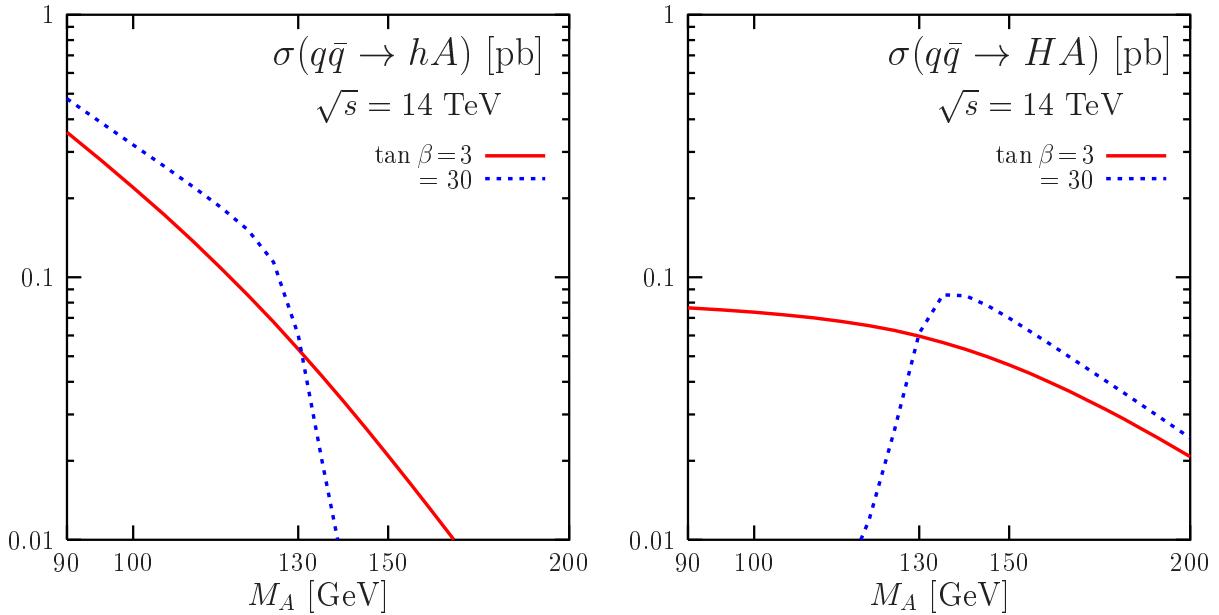
Figure 3.20: The cross sections for associated neutral Higgs pair production in $q\bar{q}$ annihilation, $q\bar{q} \to hA$ and HA, at the LHC as a function of M_A for $\tan\beta = 3$ and 30. They are at NLO with the scales fixed to the invariant mass of the $A\mathcal{H}$ systems, $\mu_R = \mu_F = M_{A\mathcal{H}}$. The MRST PDFs have been used.

Note that $A + h/H$ production, as well as the production of all possible combinations of pairs of Higgs bosons, is also accessible in the fusion of bottom quarks, $b\bar{b} \to \Phi_1\Phi_2$ with $\Phi_i = h, H, A$ [376]. The lower b–quark luminosities may be compensated for by large values of $\tan\beta$ which strongly enhance the cross sections. These processes should, however, be combined with Higgs pair production in association with $b\bar{b}$ pairs in gluon fusion, $gg \to b\bar{b}\Phi_1\Phi_2$ [377] since in the previous process b–quarks also come from gluon splitting. A combined analysis of the two process at the LHC, where there might be relevant, is under way [378].

Production in gg fusion

In the gg fusion mechanism, a plethora of pairs of Higgs particles is accessible. The Feynman diagrams responsible for these processes are drawn in Fig. 3.19b where both top and bottom quark loops [and possibly squark loops when these particles are relatively light] must be included in the box and triangular diagrams and, in the latter case, the two channels involving the virtual exchange of the h and H MSSM states are to be taken into account. The continuum production can be supplemented by the resonant production of the H boson, $gg \to H$, which then decays into two lighter Higgs bosons, $H \to hh$. This channel will be discussed in more details later. In this context, one should also mention the possibility of producing the pseudoscalar A boson, $gg \to A$, which then decays into hZ final states and contributes to the associated AZ production discussed in §3.1.1.

185

For high $\tan\beta$ values, a large ensemble of double Higgs continuum events is generated by gluon fusion. This is shown in Fig. 3.21 where the cross sections for the various processes[30] [including the annihilation $q\bar{q} \to \mathcal{H}A$ processes for comparison] are displayed as a function of M_A for $\tan\beta = 30$. Below the transition limit, $M_A \lesssim M_h^{\max}$, the cross section is dominated by AA, Ah and hh production while, above this limit, AA, AH and HH production dominate. For $M_A \sim M_h^{\max}$, that is, in the intense–coupling regime, all possible Higgs pairs can be generated with sizable rates. The sum of all production cross sections, which is also displayed, can exceed the picobarn level for low M_A values and, at large M_A, it saturates at a level below ~ 50 fb when only the $gg \to hh$ process, with the h boson having a mass $M_h \sim M_h^{\max}$ and SM–like couplings, is at work.
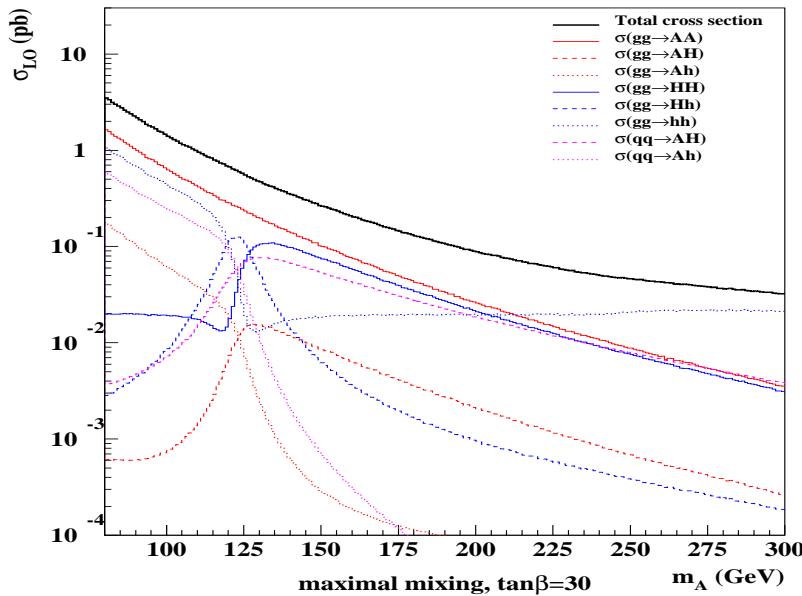
Figure 3.21: The cross sections for the various pair production of the neutral MSSM Higgs bosons at LO in the gg fusion and the $q\bar{q}$ annihilation mechanisms as a function of M_A for $\tan\beta = 30$. The sum of all cross sections is also shown; from Ref. [379].

Except for hh and HH production near, respectively, the decoupling and anti–decoupling limits, in which the situation is similar to the one of the SM Higgs boson discussed in §I.3.6.1, the enhancement is mainly due to the large Yukawa coupling in the b–quark loops connecting the gluons with the Higgs bosons. Since the box diagrams are enhanced quadratically compared to the triangle diagrams, the sensitivity to the trilinear coupling is very small. Thus, except for $gg \to hh\,(HH)$ production when $M_{h(H)} \sim M_h^{\max}$, these processes do not allow to probe these couplings at high $\tan\beta$. Note that the cross sections of the VV fusion and the Higgs–strahlung channels are strongly suppressed except in the two usual limits.

---

[30]The cross sections in gg fusion are shown only at leading order. The NLO QCD corrections are available only in the case where the limit of a very heavy top quark can be taken, leading to a K–factor of $K \sim 2$ [375], which cannot be used here since the b–quark loop contributions are dominating.

The situation is quite different for low values of $\tan\beta$. Focusing first on the production of pairs of the lighter Higgs bosons, the $pp \to hh$ production channels follow the pattern of the SM Higgs boson, with the gluon fusion being dominant, followed by VV fusion and then double Higgs–strahlung. The cross sections [in fb] are shown in the left–hand side of Fig. 3.22 as a function of M_h for $\tan\beta = 3$; they are of moderate size. However, within the cascade decay regions, when the resonant production of an intermediate heavy Higgs boson takes place, the cross sections rise dramatically. Large contributions to the cross sections are generated by H production in the fusion channels, $gg/VV \to H \to hh$, and $H^{\pm} \to W^{\pm}h$ decay in Higgs–strahlung, $W^{\pm*} \to H^{\pm}h \to W^{\pm}hh$. As expected, the $gg \to hh$ cross section becomes very large, ~ 1 pb, in the decaying H region. As will be discussed later, this process provides an interesting channel for searching for MSSM Higgs bosons at the LHC. The sensitivity of the cross sections with regard to a variation of the coupling λ_{hhh} by the rescaling factor $\kappa = 1/2$ to $3/2$ is close to 10% in the continuum while the sensitivity of H cascade decays to a variation of the λ_{Hhh} couplings is indicated by arrows and is significant.
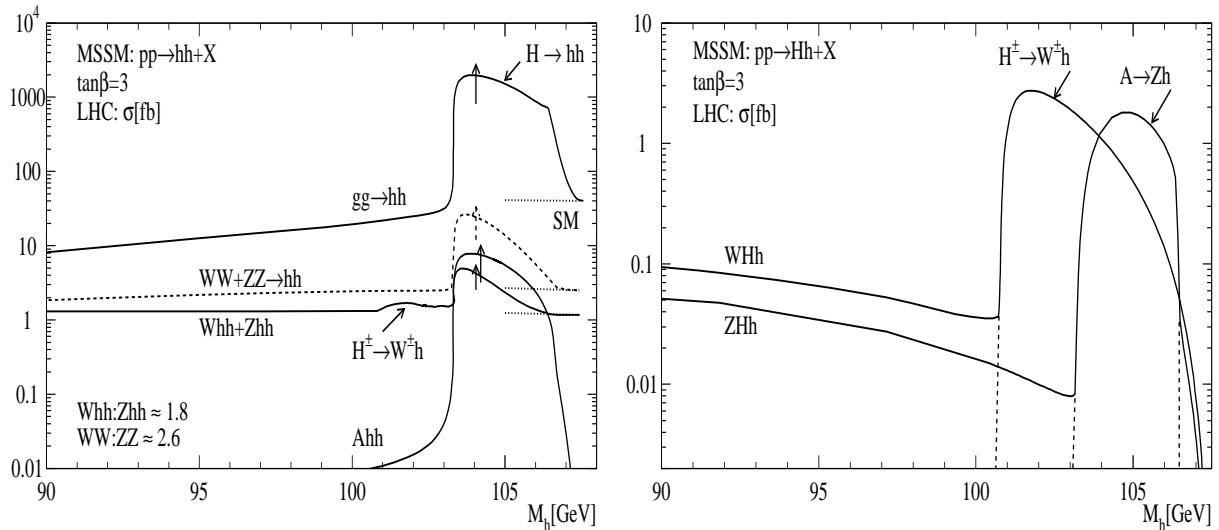
Figure 3.22: The total cross sections at the LHC for hh production via double Higgs–strahlung, VV fusion and gluon fusion (left) and Hh production in the processes $q\bar{q} \to VHh$ (right) as a function of M_h for $\tan\beta = 3$; from Ref. [374].

Finally, turning to the processes involving a light plus a heavy Higgs boson, $pp \to Hh+X$, which is the next favored by phase space, the cross sections in excess of 1 fb at the LHC are shown in the right–hand side of Fig. 3.22 again as a function of M_h and for $\tan\beta = 3$. When the cross section are sizable the final states are in fact generated in cascade decays by gauge interactions, $pp \to Z^* \to AH \to ZhH$ and $pp \to W^* \to H^{\pm}H \to W^{\pm}hH$. These processes are, therefore, not suitable for measuring the trilinear Higgs couplings. The production rates are too small for these final states to be detected anyway.

3.1.5   Diffractive Higgs production

As discussed in §I. 3.6.4, diffractive processes in pp collisions, where two protons are produced at very large rapidities and remain unaltered, lead to centrally produced Higgs particles [380–384]

$$p + p \rightarrow p + \Phi + p \tag{3.29}$$

[the $+$ sign is for the large rapidity gaps] and nothing else in the case of the central exclusive double diffractive process. These events are clean enough to be detected by measuring the missing mass of the system when the protons are tagged. As also discussed in §I.3.6.4 , an interesting feature is that there are selection rules which make that the production of the CP–even Higgs particles is much more favored than CP–odd Higgs production. In the SM, the cross section, which is proportional to the gluonic Higgs width, is rather small [381]. As we have seen in this chapter, the Φgg coupling can be much larger in the MSSM [382,383] as a result of the enhanced b–loop contributions for large $\tan\beta$ values, leading to significantly larger production rates for the process eq. (3.29) compared to the SM. This is exemplified in Fig. 3.23 where the cross sections for the production of the h, H and A bosons at the LHC are shown as a function of the Higgs masses for $\tan\beta = 30$. They are folded with the branching ratios for the decays $\Phi \rightarrow b\bar{b}$ which are at the level of $\sim 90\%$ in most cases.

As can be seen, the rates are rather large in the case of the CP–even Higgs bosons outside the decoupling and anti–decoupling regimes, in which they reduce to the SM values which are shown for comparison. For $M_A \sim 130$ GeV, that is in the intense coupling regime, the cross sections for both h and H are at the 10 fb level. If a missing mass resolution of $\Delta M = 1$ GeV is achieved, one is left with ~ 100 observable events for both particles for a luminosity of $\mathcal{L} = 30$ fb^{-1} and a background of only a few events, after selection cuts and experimental efficiencies are applied [383], resulting in a large discovery significance. [In the SM, a detailed Monte Carlo analysis of the signal, backgrounds and detector effects has been performed in Ref. [384] and it has been shown that a ratio $S/B \sim 1$ can be achieved for $M_{H_{\mathrm{SM}}} = 120$ GeV with a missing mass resolution of 1 GeV.] The small resolution on the missing mass would lead to a nice measurement of the Higgs boson masses.

As a result of the spin–parity selection rules in the process, the cross section for diffractive production of the pseudoscalar Higgs boson is two orders of magnitude smaller than in the CP–even case. This would lead to a clean determination of the 0^{++} quantum numbers of the produced Higgs states. In fact, even if the cross section for the CP–even and CP–odd states Higgs bosons were comparable, the CP–nature of the h, H bosons could be verified by looking at the azimuthal correlation between the outgoing protons. The separation of the almost mass degenerate CP–even and CP–odd states in the decoupling or anti–decoupling regimes could also be made if the mass differences [and the total Higgs widths] are smaller than

Central exclusive diffractive production

Br(h/H/A→bb)·σ   (fb)

MSSM
tanβ = 30

10^2

h

10

H

1

Standard Model

10^{-1}

A

10^{-2}

100   120   140   160   180   200   220   240

$M_{h/H/A}$ **(GeV)**
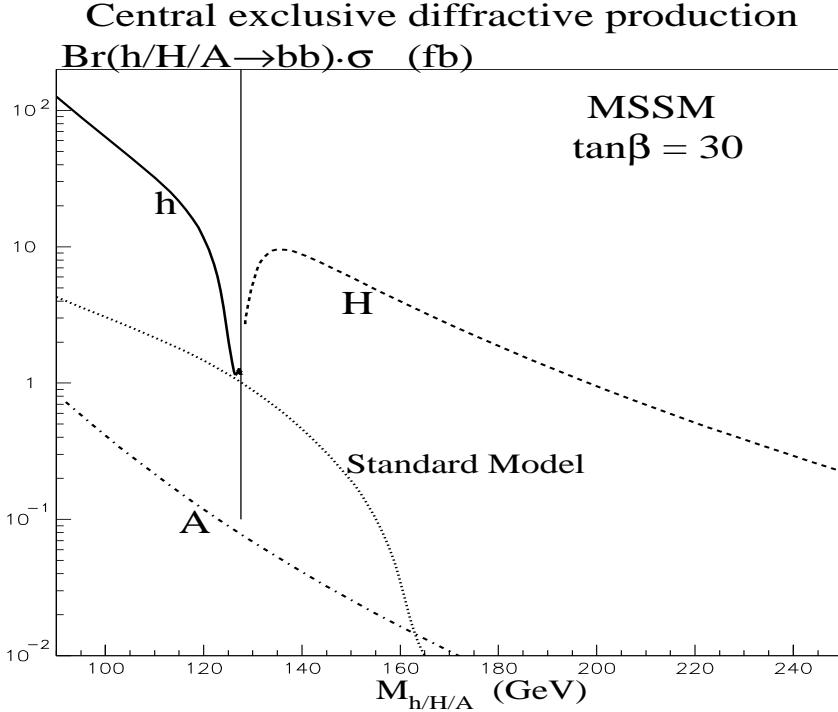
Figure 3.23: The production cross sections times the $b\bar{b}$ branching ratios for the central exclusive production of the neutral MSSM Higgs bosons at the LHC as a function of the Higgs masses for $\tan\beta = 30$. The SM result is shown for comparison; from Ref. [383].

the resolution on the missing mass[31]. Hence, central exclusive diffractive Higgs production might be an interesting channel in the MSSM, in particular in the intense coupling regime.

3.1.6 Higher–order processes

Finally, let us briefly mention some higher order processes for MSSM neutral Higgs production at the LHC. Among the processes of this type, discussed for the SM Higgs in §I.3.5.4 and §I.3.6.2 where details can found, three channels might be relevant in the MSSM:

– CP–even Higgs production in association with gauge boson pairs. As in this process the Higgs bosons are only emitted from the gauge boson lines, the cross sections for $pp \rightarrow VV\mathcal{H}$ with $V = W, Z, \gamma$ and $\mathcal{H} = h, H$ are simply those of the SM Higgs boson folded by the $g^2_{\mathcal{H}VV}$ factors. They are, thus, suppressed in general compared to the SM case except in the (anti–)decoupling regime for the $(H)\,h$ boson. As in Higgs–strahlung and vector boson fusion, one would approximately have $\sigma(VVh) + \sigma(VVH) \approx \sigma(VVH_{\mathrm{SM}})$.

– Higgs production in association a gauge boson and two jets. The vector boson fusion type processes $pp \rightarrow qq\mathcal{H}V$ with $V = W, Z, \gamma$ are also similar to those which occur for the SM Higgs boson and the bulk of the cross section can be obtained by folding the SM rate by the

---

[31]See also the recent discussion of Ref. [385] in the context of almost degenerate Higgs particles in the case of the CP–violating MSSM.

$g^2_{\mathcal{H}VV}$ factors. However, here, there are additional diagrams involving the other MSSM Higgs bosons and in fact even the A and $H^\pm$ particles can be produced in this type of processes [although we expect the rates to be tiny]. These channels are presently under study [386].

– Associated production with a single top quark. In the SM [387], the process is mediated by several channels [see §I.3.5.4] but the total rate is rather small, barely reaching the level of 100 fb for low Higgs masses at the LHC for the most important one: t–channel fusion of a light quark and a bottom parton from the proton sea which, through W exchange, leads to the $qb \to qt\Phi$ final state. In the MSSM [388], the $\Phi b\bar{b}$ couplings are enhanced at large $\tan\beta$, possibly increasing the production cross sections. This is shown in Fig. 3.24 where the production rates for light h and A bosons are shown for this t–channel process as a function of the Higgs masses for several values of $\tan\beta$. The cross section in the SM Higgs case is also shown for comparison. While the rates are indeed enhanced compared to the SM at large enough $\tan\beta$ values [in the case of h, this occurs only in the anti–decoupling regime], the enhancement is not very large: only a factor of ~ 3 for $\tan\beta \sim 50$. The reason is that in the SM, the dominant contribution is originating from the emission of the Higgs boson from the W and top quark lines and these contributions are switched off in the MSSM for the pseudoscalar and pseudoscalar–like Higgs bosons as their couplings to these particles are zero or inversely proportional to $\tan\beta$. The contribution of the diagram where h and A are emitted from the b–quark line [which is negligible in the SM] can only be enhanced to a level where it becomes comparable or only slightly larger, as $m_b \tan\beta \approx m_t$ for $\tan\beta \sim 30$–50. In view of the large backgrounds which affect this final state [388], the detection of the Higgs bosons in this process is, thus, as difficult in the MSSM than in the SM.
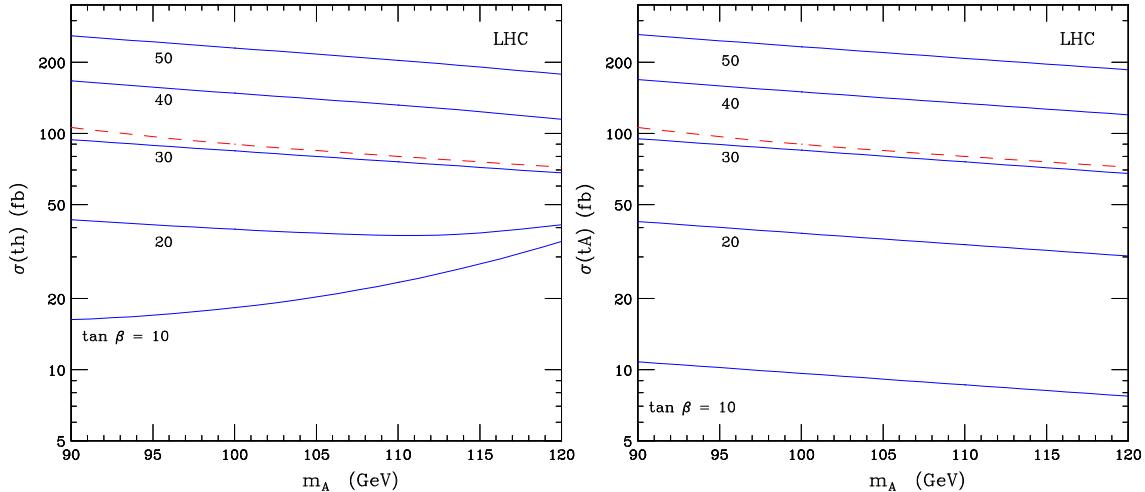
Figure 3.24: The cross sections for the production of CP–even h (left) and CP–odd A (right) bosons in association with a single top quark as a function of M_A and $\tan\beta$ in the maximal mixing scenario with $M_S = 1$ TeV and $\mu = -200$ GeV; only t–channel production is included. The rate for a SM Higgs boson is shown for comparison; from Ref. [388].

190

3.2 The production of the charged Higgs bosons

3.2.1 Production from top quark decays

As discussed in §2.3.1, if the $H^\pm$ bosons are lighter than the top quarks, $M_{H^\pm} \lesssim m_t - m_b \sim$ 170 GeV, they can be produced in the decays $t \to H^+ b$ and $\bar{t} \to H^- \bar{b}$ [178, 389]. The production of top quark pairs results from $q\bar{q}$ annihilation and gg fusion, Fig. 3.25, with the former (latter) process being largely dominant at the Tevatron (LHC). Top quark pair production has been discussed in many places and we refer the reader to e.g. the review of Ref. [390] for details. Here, we simply mention that the cross section is about $\sigma(p\bar{p} \to t\bar{t}) \sim 5$ pb at the Tevatron and increases to $\sigma(pp \to t\bar{t}) \sim \mathcal{O}(1 \text{ nb})$ at the LHC. This means that approximately 10^4 and 10^8 top quark pairs can be produced at integrated luminosities of, respectively, 2 fb^{-1} at the Tevatron Run II and 100 fb^{-1} at the nominal LHC. While the top quark should dominantly decay into a W boson and a bottom quark, the branching ratio being presently measured to be BR$(t \to bW^+) \gtrsim 0.5$ at the 2σ level, the decay $t \to bH^+$ in the MSSM could lead to more than 10^2 (10^6) charged Higgs particles at the Tevatron (LHC) if kinematically allowed and if the branching ratio is larger than 1 percent.
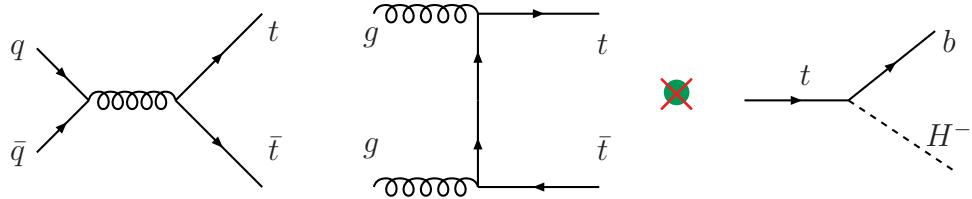
Figure 3.25: Feynman diagrams for top quark production and decay in hadronic collisions.

The branching ratio for the decay $t \to bH^+$ has been discussed in §2.3.1 including the relevant higher–order standard and SUSY corrections and it has been shown that, when kinematically allowed and if not too much suppressed by phase space, it is rather large, in particular, for small and large values of $\tan\beta$ where it can exceed the level of $\sim 20\%$. The cross section[32] times branching ratio, $\sigma(pp \to t\bar{t}) \times \text{BR}(t \to bH^+)$ is displayed in Fig. 3.26 as a function of the $H^\pm$ mass for several values of $\tan\beta$, $\tan\beta = 3, 10$ and 30, at the Tevatron and LHC energies; the CTEQ4 set of PDFs has been used. The rate for H^- production is of course the same and the cross sections for the two processes have to be added.

As can be seen, for small ($\lesssim 3$) or large ($\gtrsim 30$) values of $\tan\beta$, the production rates are huge if the charged Higgs boson is light enough. For intermediate values, $\tan\beta \sim 10$, the $H^\pm tb$ coupling is not enough enhanced and the rates are rather small, in particular at the Tevatron. There is also a strong suppression near the $m_t \sim M_{H^\pm}$ kinematical threshold and,

---

[32]Note that for the $pp \to t\bar{t}$ cross section, we used only the tree–level result. A K–factor of about $K \sim 1.5$ should be applied [391], thereby increasing the production rate.
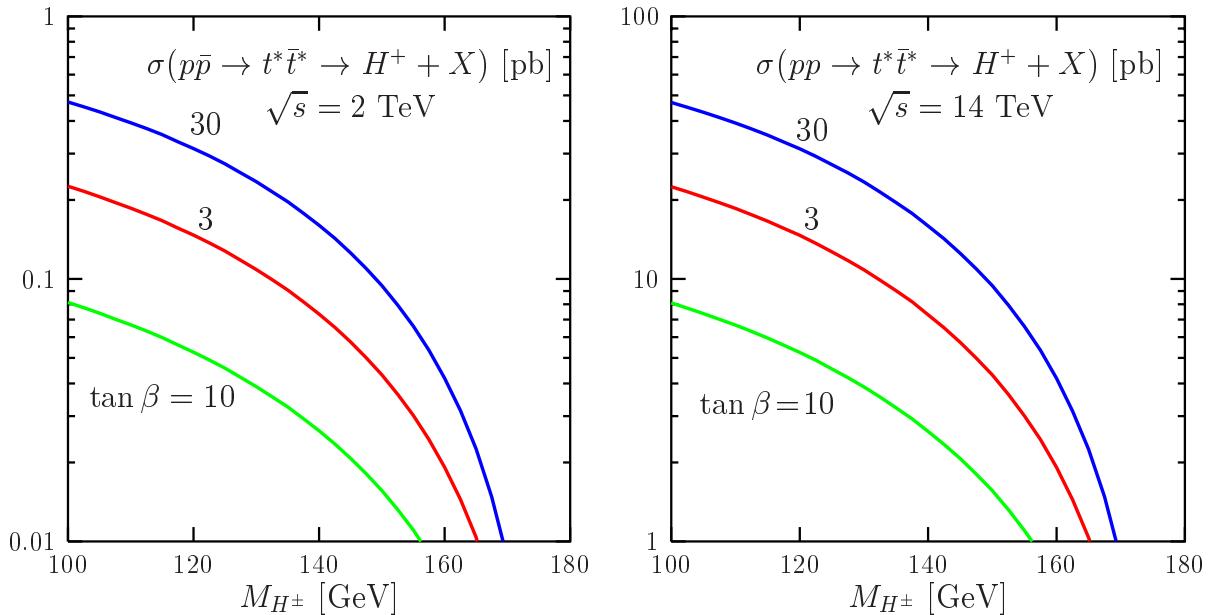
Figure 3.26: The production cross section for the charged Higgs boson from top decays, $pp \to t\bar{t} \to H^{\pm}tb$ in pb, as a function of the $H^{\pm}$ mass for different values of $\tan\beta$ at the Tevatron (left) and the LHC (right). The CTEQ4 PDFs have been used and the pole quark masses are set to $m_t = 178$ GeV and $m_b = 4.9$ GeV.

for $M_{H^{\pm}} = 160$ GeV, the cross section at the Tevatron is only of the order of $20\,(50)$ fb for $\tan\beta = 3\,(30)$. Note that close to this threshold, one should include top quark width effects which allow a smooth transition from the production in top decays, $pp \to t^*\bar{t} \to H^+b\bar{t}$ for $m_t > M_{H^{\pm}} + m_b$, to the production in the continuum, $pp \to H^+\bar{t}b$ for $m_t < M_{H^{\pm}} + m_b$. In the figure, the off–shellness of the top quarks has been, in fact, included in the production rate and this explains the not too fast fall off near threshold. [In this case, other channels might need to be added to have a gauge invariant amplitude; see Ref. [392] for instance.].

3.2.2 The gg and gb production processes

If the charged Higgs bosons are heavier than the top quark, one has to resort to direct production mechanisms [313,324,371,393–406]. At high energies, when the gluon luminosities are large, two mechanisms are relevant for $H^{\pm}$ production: gb fusion [313] and gg fusion [393], with a small contribution from $q\bar{q}$ annihilation in the later case

$$
\begin{aligned}
pp &\to gb\,(g\bar{b}) \to tH^-\,(\bar{t}H^+) \\
pp &\to gg, q\bar{q} \to tH^-\bar{b} + \bar{t}H^+b
\end{aligned}
\tag{3.30}
$$

Examples of Feynman diagrams for these two production processes at leading order are shown in Fig. 3.27. The expression of the partonic cross section for the $2 \to 2$ mechanism $gb \to tH^-$, where the b–quark is treated as a parton inside the proton, is rather simple to
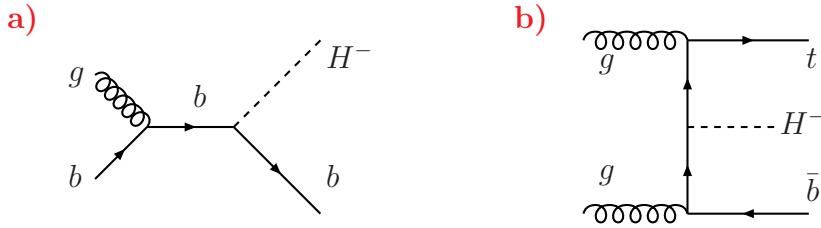
Figure 3.27: Generic Feynman diagrams for the processes $bg \to H^- t$ (a) and $gg \to t\bar{b}H^-$ (b).

write down [324]

$$\hat{\sigma}(g\,b \to H^-\,t) = \frac{G_\mu \alpha_s}{24\sqrt{2}\hat{s}}|V_{tb}|^2 \frac{1}{(1-x_b^2)^3}\left\{8C_- x_b x_t \left[\ell\,(1-x_{ht}^2) - 2\,\lambda\right] + \right.$$

$$\left. C_+ \left[2\ell\left(1 + x_b^4 - 2x_b^2 x_{ht}^2 - 2x_{ht}^2(1-x_{ht}^2)\right) - \lambda\left(3 - 7x_{ht}^2 + x_b^4(3+x_{ht}^2) + 2x_b^2(1-x_{ht}^2)\right)\right]\right\} \quad (3.31)$$

with the abbreviations $x_i \equiv m_i/\sqrt{\hat{s}}$, $x_{ht}^2 = x_h^2 - x_t^2$, $\ell \equiv \log\left[(1 - x_{ht}^2 + \lambda)/(1 - x_{ht}^2 - \lambda)\right]$ and the phase space function $\lambda = [(1 - (x_t + x_h)^2)\,(1 - (x_t - x_h)^2)]^{1/2}$, while the combination of couplings is given by $C_\pm = m_t^2 \cot^2 \beta + m_b^2 \tan^2 \beta \pm 2m_t m_b$. As usual, this partonic cross section has to be folded with the b and g densities to obtain the total hadronic cross section.

The cross sections, evaluated with the program of Ref. [323], are shown at the LHC in the left–hand side of Fig. 3.28 as a function of $M_{H^\pm}$ for the three values $\tan\beta = 3, 10$ and 30 [these processes have negligibly small cross sections at the Tevatron where they will be ignored here]. The running mass have been used in the case of the b–quark, $\bar{m}_b \sim 3$ GeV, and the CTEQ4L parton distributions [344] have been adopted at LO with $\alpha_s^{\mathrm{LO}}(M_Z^2) = 0.132$. However, to absorb part of the NLO corrections and, similarly to $b\bar{b}\Phi$ production discussed earlier, the renormalization and factorization scales have been set to $\mu_F = \mu_R = \frac{1}{3}(m_t + M_{H^\pm})$. For the low and high $\tan\beta$ values, as they scale as $m_t^2 \cot^2 \beta$ and $\bar{m}_b^2 \tan^2 \beta$, respectively, the cross sections exceed the 0.1 pb level only for low Higgs masses, $M_{H^\pm} \sim 300$ GeV, i.e. they are two orders of magnitude smaller than in the production from top decays at $M_{H^\pm} \sim 100$ GeV. The cross sections drop quickly with increasing masses but they are still at the level of 10 fb at $M_{H^\pm} \sim 700$ GeV in the low and high $\tan\beta$ regimes.

For the $2 \to 3$ process $gg/q\bar{q} \to tbH^\pm$, the analytical expression of the partonic cross section is probably too complicated and, to our knowledge, it is not available in the literature [in turn, the amplitudes can be found in Ref. [395], for instance]. The total hadronic cross section is shown as a function of $M_{H^\pm}$ in the right–hand side of Fig. 3.28 for the same inputs, including the scale choice $\mu_F = \mu_R = \frac{1}{3}(m_t + M_{H^\pm})$ as for the $gb \to H^- b$ fusion case. It follows exactly the same trend as the previous process, but it is a factor 2 to 3 smaller as a result of the additional coupling factor.

In this leading order picture, when the dominant decays $H^\pm \to tb$ ($H^\pm \to \tau\nu$) take place, the gb fusion process gives rise to $3\,(1)$ b–quarks in the final state while the gg fusion
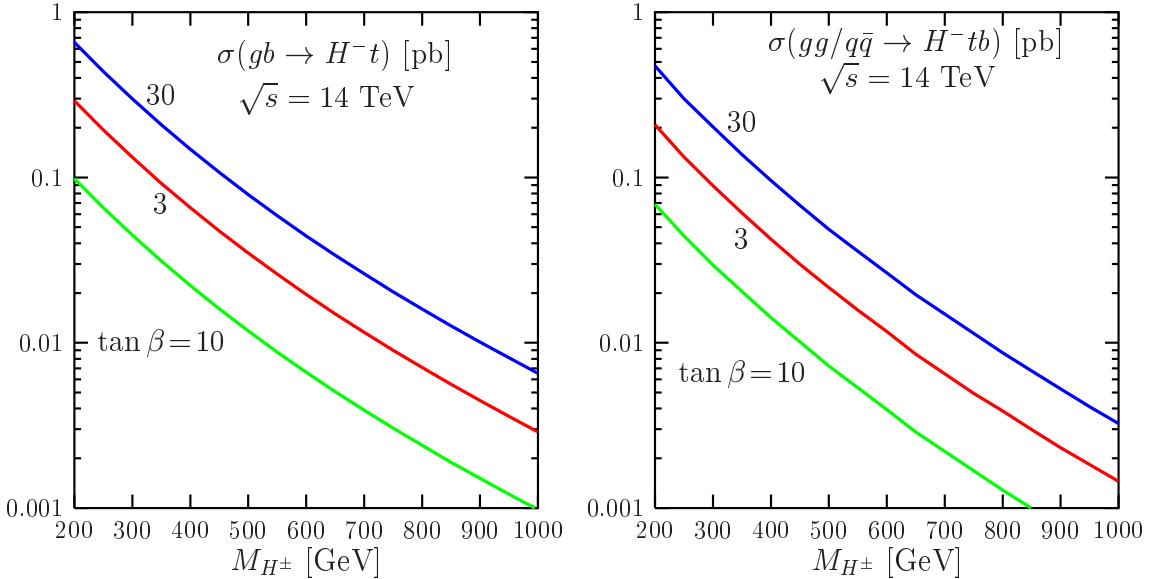
Figure 3.28: The production cross sections for the charged Higgs boson at the LHC as a function of the $H^\pm$ mass for $\tan\beta = 3, 10$ and 30 in the $2 \to 2$ process $gb \to H^- t$ (left) and in the $2 \to 3$ process $q\bar{q}/gg \to H^- tb$ (right). They are at LO with the scales fixed to $\mu_R = \mu_F = \frac{1}{3}(M_{H^\pm} + m_t)$; the CTEQ4 PDFs with $\alpha_s^{LO}(M_Z) = 0.132$ have been used.

process leads to 4 (2) b–quarks. Both processes contribute to the inclusive production where at most 3 (1) final b–quarks are required to be observed. However, in this case, the two processes have to be properly combined to avoid the double counting of the contribution where a gluon gives rise to a $b\bar{b}$ pair that is collinear to the initial proton [324, 360]. The total cross section of the inclusive process in this case is mid–way between those of the two production mechanisms. This, however, might not be the case when additional cuts are applied; a Monte–Carlo implementation of this combination has recently been made [407].

Similarly to what has been discussed in the case of associated Higgs production with $b\bar{b}$ pairs, the process $gg \to H^- tb$ is in fact simply part of the NLO QCD corrections to $gb \to H^- t$ when the momentum of the additional final b–quark is integrated out. Also as in the $b\bar{b}+$ Higgs case, the scale dependence at LO for both processes is rather large, changing the magnitude of the cross sections by $\sim 50\%$ for a reasonable variation of the renormalization and factorization scales. While the NLO corrections to the $2 \to 3$ process [which are even more complicated than in the tt and $b\bar{b}+$ Higgs cases because of the presence of three final state particles with different masses] are not yet available, the NLO QCD corrections to the fusion process $gb \to H^- t$ have been derived recently [365, 408], leading to a huge stabilization of the production rate.

The results of the calculation are summarized in the two [busy] plots of Fig. 3.29 where, in the left–hand side, the cross sections in different approximations are shown and, in the

right–hand side, the K–factors with their scale variation are displayed. The default scale has been chosen to be $m_{av} = \frac{1}{2}(m_t + M_{H^\pm})$. The main features are familiar to us: the use of the pole quark masses at tree–level is inappropriate, the very large scale variation at LO is strongly reduced when including the NLO corrections and almost all these NLO corrections can be absorbed by choosing a low scale $\mu_F \sim \mu_R \sim \frac{1}{3}m_{av}$ for which the K–factor is close to unity. Note that there are also potentially large SUSY–QCD corrections but, again, they essentially consist of the threshold corrections to the bottom and top quark masses and can be thus mapped into the Yukawa couplings.
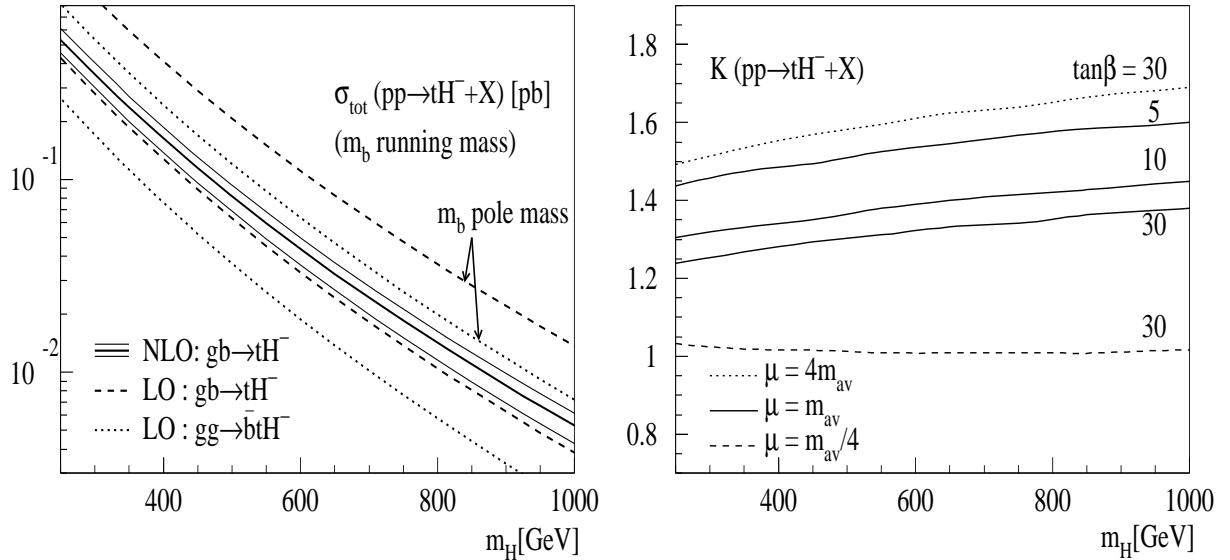
Figure 3.29: Left: the inclusive production cross section $pp \to tH^- + X$ at the LHC as a function of $M_{H^\pm}$ where the dashed and solid lines show the consistent LO and NLO results and the dotted line is the total cross section from the exclusive production process $gg \to H^- t\bar{b}$. The tree–level results are also shown using the pole mass for the b–quark Yukawa coupling. The range for the NLO order result is given for $\mu_F = \mu_R = m_{av}/4$ up to $4m_{av}$ with $m_{av} = \frac{1}{2}(m_t + M_{H^\pm})$. Right: the corresponding consistent K–factors for the three values of $\tan\beta = 5, 10, 30$; in the case of $\tan\beta = 30$, shown are the cross sections for three choices of $\mu = \mu_R = \mu_F$, consistently at LO and NLO. From Ref. [365].

3.2.3 The single charged Higgs production process

The most straightforward process for charged Higgs production at hadron colliders should be, in fact, single production via the annihilation of light quarks [396–398]. Despite of the small couplings of the $H^\pm$ bosons to these fermions, which strongly suppress the cross sections, there is a partial compensation since one is dealing with a $2 \to 1$ process. However, a very large contribution is also coming from the exchange of the W boson and both processes, Fig. 3.30, and their interference should be considered at the same time.
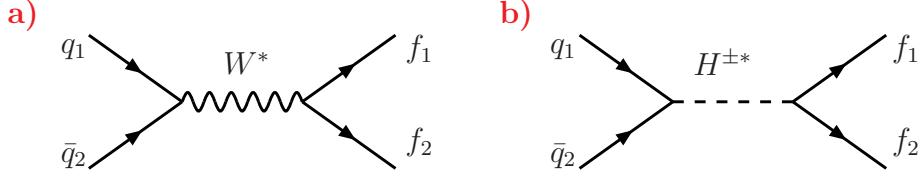
Figure 3.30: Feynman diagrams for the production of two fermions through W and $H^{\pm}$ exchange in light quark annihilation at hadron colliders.

In Ref. [397], the production of tb final states in the annihilation of light quarks

$$q_1(p_1)\,\bar{q}_2(p_2) \rightarrow H^{\pm*},\, W^{\pm*} \rightarrow t(p_t)\,\bar{b}(p_b) \tag{3.32}$$
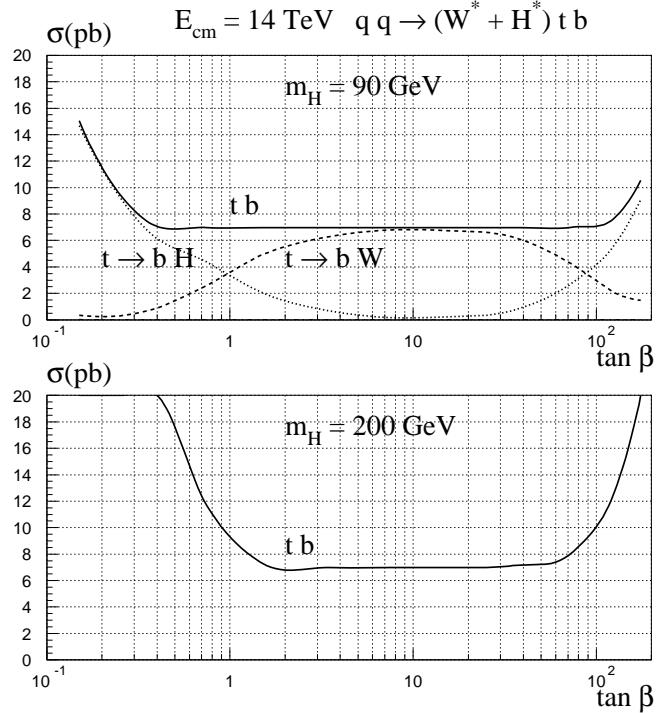
described by the two diagrams of Fig. 3.30 has been discussed in detail. In the general case where one assumes the intermediate particles to be virtual, the matrix element squared for the process, in terms of the momenta of the involved particles defined in the equation above, is given by $|A_{2\rightarrow2}|^2 = |A_{H^{\pm}}|^2 + |A_W|^2 + |A_I|^2$ where the amplitudes squared for $H^{\pm}, W^{\pm}$ exchanges and their interference read

$$
\begin{aligned}
|A_{H^{\pm}}|^2 &= \frac{16 G_\mu^2 |V_{12}|^2 |V_{tb}|^2}{\hat{s}_{H^{\pm}}^2 + \gamma_{H^{\pm}}^2} \left[\left(m_t^2 \cot^2\beta + m_b^2 \tan^2\beta\right)(p_t p_b) - 2 m_b^2 m_t^2\right] \\
&\quad \times \left[\left(m_1^2 \cot^2\beta + m_2^2 \tan^2\beta\right)(p_1 p_2) - 2 m_1^2 m_2^2\right] \\
|A_W|^2 &= \frac{128 M_W^4 G_\mu^2 |V_{12}|^2 |V_{tb}|^2}{\hat{s}_W^2 + \gamma_W^2}(p_t p_2)(p_b p_1) \\
|A_I|^2 &= \frac{32 G_\mu^2 |V_{12}|^2 |V_{tb}|^2 m_t m_b [\hat{s}_W \hat{s}_{H^{\pm}} + \gamma_W \gamma_{H^{\pm}}]}{[\hat{s}_W \hat{s}_{H^{\pm}} + \gamma_W \gamma_{H^{\pm}}]^2 + [\hat{s}_W \gamma_{H^{\pm}} - \hat{s}_{H^{\pm}} \gamma_W]^2} \\
&\quad \times [-m_1^2 \cot^2\beta(p_t p_2) + m_2^2(p_t p_1) + m_1^2(p_b p_2) - m_2^2 \tan^2\beta(p_b p_1)] \tag{3.33}
\end{aligned}
$$

where $\hat{s}_X = \hat{s} - M_X^2$ and $\gamma_X = \Gamma_X M_X$ with $\hat{s}$ being the partonic c.m. energy. The total hadronic cross section is obtained by multiplying the amplitude squared by the flux and phase–space factors and folding the result with the parton luminosities. In the real world, however, the higher–order contributions to this process have to be included and the most important component of these will be simply the gb and gg processes which have been discussed in the previous section and which, because of the large gluon flux at the LHC, can have much larger cross sections if only the charged Higgs contribution is considered. Note that the cross section, including the decay $t \rightarrow bW$, has also been derived in Ref. [397] and is useful for the study of the top quark polarization properties.

The production cross section at the LHC is displayed in Fig. 3.31 as a function of $\tan\beta$ for the two mass values $M_{H^{\pm}} = 90$ and 200 GeV. In the former case, the separate contributions of the W and $H^{\pm}$ exchanges are shown and one can see that, except for very small and very large values of $\tan\beta$ [which are not viable in the MSSM], the W contribution is largely

dominating. In Ref. [397], the $H^{\pm}$ signal and the W background have been analyzed and it has been advocated that, with specific p_T cuts and the study of the top quark polarization, one might be able to distinguish between the two different channels. However, this is true only for small $\tan\beta \lesssim 0.2$ values which are not possible in the MSSM.


Figure 3.31: *The cross section for $pp \to tb$ at the LHC including W and $H^{\pm}$ exchange as a function of $\tan\beta$ for $M_{H^{\pm}} = 90$ and 200 GeV. In the former case, the separate contributions of the two channels is shown. From Ref. [397].*

One can also consider the $\tau\nu$ final states for which the production cross sections can be straightforwardly derived from the expressions of eq. (3.33). This has been done in the detailed simulation of Ref. [398] where it has also been advocated that, at large $\tan\beta$ and for $M_{H^{\pm}} = 200$–400 GeV, one could possibly extract the charged Higgs signal above the huge $q\bar{q}' \to W \to \tau\nu$ background if the τ polarization is exploited and a proper reconstruction of the transverse mass distribution is made. This would allow a measurement of $\tan\beta$ at the 10% level for $\tan\beta \gtrsim 20$. However, the channel is extremely difficult.

3.2.4 Pair and associated production processes

There are also other mechanisms for charged Higgs production at hadron colliders: pair production in $q\bar{q}$ annihilation [399, 403], gg fusion [371, 401, 402] and vector boson fusion [404] as well as associated production with neutral Higgs bosons in $q\bar{q}$ annihilation [39, 399, 400]; there is also the possibility of $H^{\pm}$ production in association with W bosons through gg

fusion and $q\bar{q}$ annihilation [405, 406]; Fig. 3.32. We briefly discuss these processes below, concentrating again on the LHC where the phase space is more favorable.
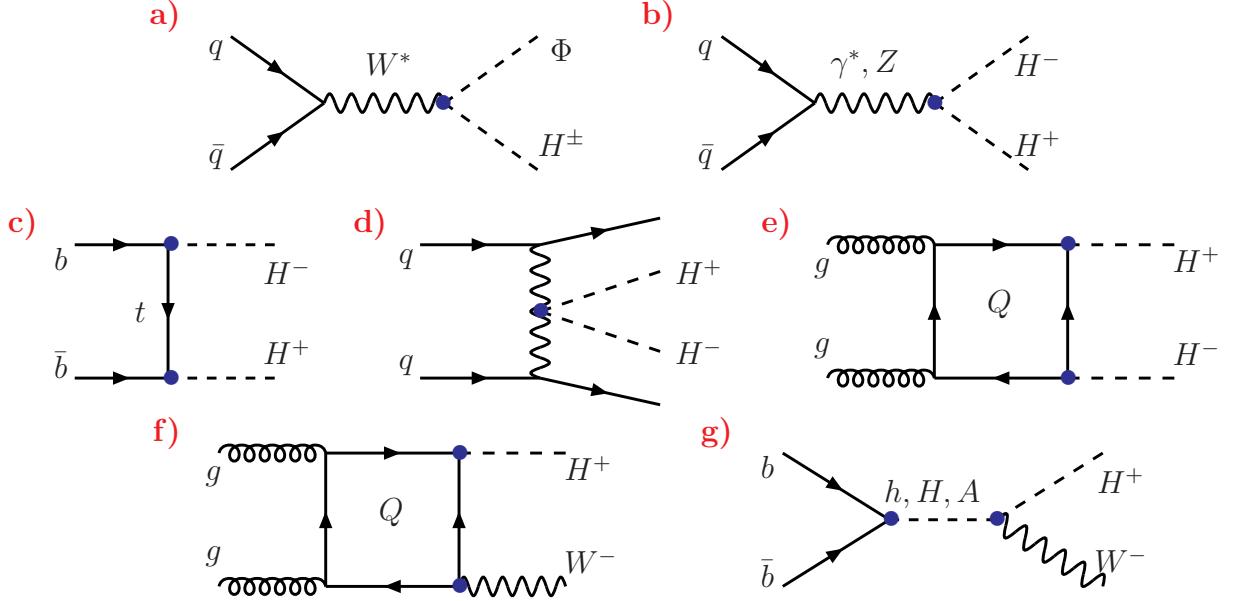
Figure 3.32: Diagrams for $H^{\pm}\Phi$, $H^{+}H^{-}$ and $H^{\pm}W^{\mp}$ production in hadronic collisions.
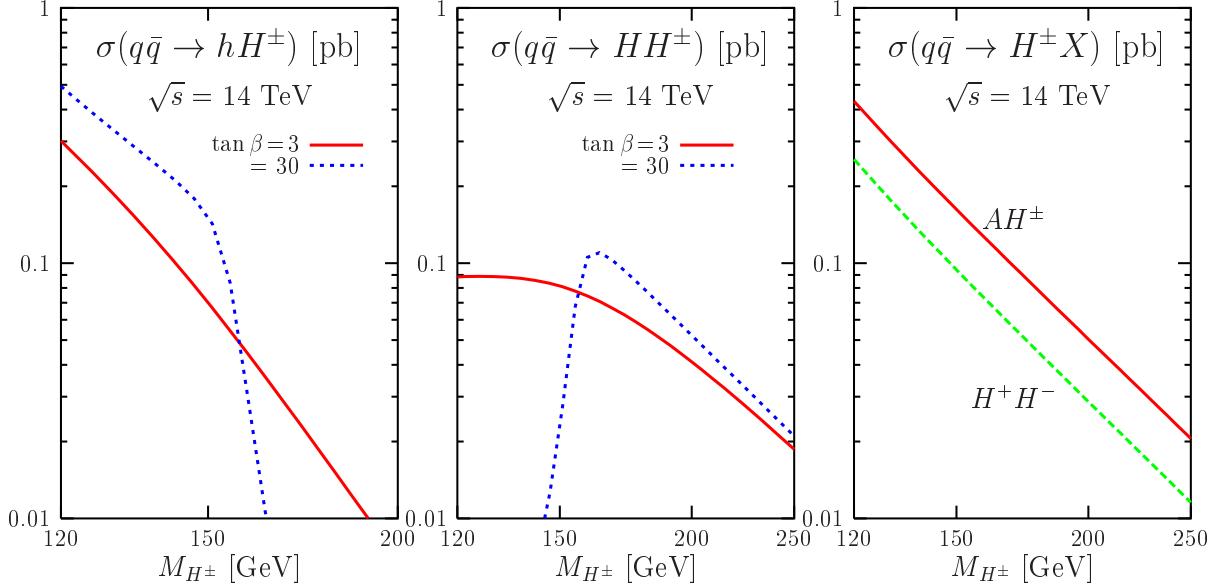
The associated $H^{\pm}$ production with a neutral Higgs boson, $q\bar{q}' \to \Phi H^{\pm}$ with $\Phi = h, H$ and A, Fig. 3.32a, is mediated by virtual W exchange and the cross section is again simply the one in the Higgs–strahlung process for the SM Higgs boson, $q\bar{q} \to H_{\mathrm{SM}}W$, with the proper change of the coupling and phase space factors [39, 399, 400]

$$\hat{\sigma}(q\bar{q}' \to \Phi H^{\pm}) = g^2_{\Phi H^{\pm}W^{\mp}}\, \hat{\sigma}_{\mathrm{SM}}(q\bar{q}' \to W\Phi) \times \frac{\lambda^3_{H^{\pm}\Phi}}{\lambda_{W\Phi}(\lambda^2_{W\Phi} + 12M^2_W/\hat{s})} \qquad (3.34)$$

where the reduced couplings $g_{\Phi H^{\pm}W^{\mp}}$ are given in Table 1.5. For the production with the CP–even Higgs bosons, $q\bar{q}' \to hH^{\pm}$ and $HH^{\pm}$, the cross sections follow exactly the same trend as the corresponding ones for the production of hA and HA pairs [the NLO corrections are also the same] except that the overall normalization is different. In the $AH^{\pm}$ case, once the two charges are summed, the rates are larger by approximately a factor of two for large enough A or $H^{\pm}$ masses when the phase space is almost the same, $M_{H^{\pm}} \sim M_A$.

This is exemplified in Fig. 3.33 where the cross sections at NLO are shown for the LHC as a function of $M_{H^{\pm}}$ for $\tan\beta = 3$ and 30. As can be seen, in the $HH^{\pm}$ case there is no coupling suppression at large masses, $g_{HH^{\pm}W^{\mp}} = \sin(\beta - \alpha) \to 1$, and the cross section is at the level of 10 fb for $M_{H^{\pm}} \sim 250$ GeV. In fact, for large $M_{H^{\pm}}$ values, the $HH^{\pm}$ cross section is approximately the same as for $AH^{\pm}$ production. The latter is not suppressed by the coupling factor since $g_{AH^{\pm}W^{\mp}} = 1$ and, at low $M_{H^{\pm}}$ values, it approaches the cross section

for the $hH^\pm$ process which is then maximal. Thus, for moderate charged Higgs masses, the cross sections for these processes are not that small, after all.


Figure 3.33: The cross sections for associated production of the charged and the three neutral MSSM Higgs bosons, as well as H^+H^- production in $q\bar{q}$ annihilation, at the LHC as a function of $M_{H^\pm}$ for $\tan\beta = 3$ and 30. The NLO QCD corrections are included in all processes and the MRST PDFs have been used.

Charged Higgs bosons can also be produced in pairs. At LO, the mechanism proceeds via $q\bar{q}$ annihilation with the exchange of a virtual photon and Z boson; Fig. 3.22b. As in the case of e^+e^- collisions at LEP2 but with the quark charges implemented and the colors averaged, the partonic cross section reads [399]:

$$\hat{\sigma}(q\bar{q} \to H^+H^-) = \frac{\pi\alpha^2(\hat{s})}{27\hat{s}} \left[Q_q^2 + \frac{2v_q Q_q v_H}{1 - M_Z^2/\hat{s}} + \frac{(a_q^2 + v_q^2)v_H^2}{(1 - M_Z^2/\hat{s})^2} \right] \left(1 - \frac{4M_{H^\pm}^2}{\hat{s}} \right)^{1/2} \quad (3.35)$$

with the couplings already given; the cross section depends only on the charged Higgs mass and on no other MSSM parameter. It is shown in the extreme right–hand side of Fig. 3.33, together with the cross section for $AH^\pm$ production. The trend is similar to the latter process, except that the H^+H^- cross section is approximatively a factor of two smaller.

There are three additional processes for charged Higgs pair production: $b\bar{b}$ fusion through the t–channel exchange of top quarks for instance, Fig. 3.32c, the vector boson fusion process $qq \to V^*V^* \to qqH^+H^-$, Fig. 3.32d, and the gluon fusion process $gg \to H^+H^-$ with the exchange of top and bottom quarks in vertex and box diagrams, Fig. 3.32e. However, because of the relatively low b density in the first process, the additional electroweak factor in the second one and the loop suppression factor in the third case, the production cross sections are rather small. They are shown in the left–hand side of Fig. 3.34 as a function of $M_{H^\pm}$

for the values $\tan \beta = 1.5, 7$ and 30. In the case of the $qq \to V^*V^* \to qqH^+H^-$ process, the cross section does not depend on $\tan \beta$ while, in the case of $q\bar{q} \to H^+H^-$, the contribution from γ, Z exchange [Fig. 3.32b] is included and provides the bulk of the cross section except at high $\tan \beta$ values where the two contributions are comparable. As can be seen, for large values of $\tan \beta$, $\tan \beta \gtrsim 30$ and low $H^\pm$ masses, $M_{H^\pm} \sim 130$ GeV, the cross sections reach the 10 fb level and are larger in the $b\bar{b} \to H^+H^-$ case. On might, therefore, take advantage of these processes at the LHC, although only in the very high luminosity option.
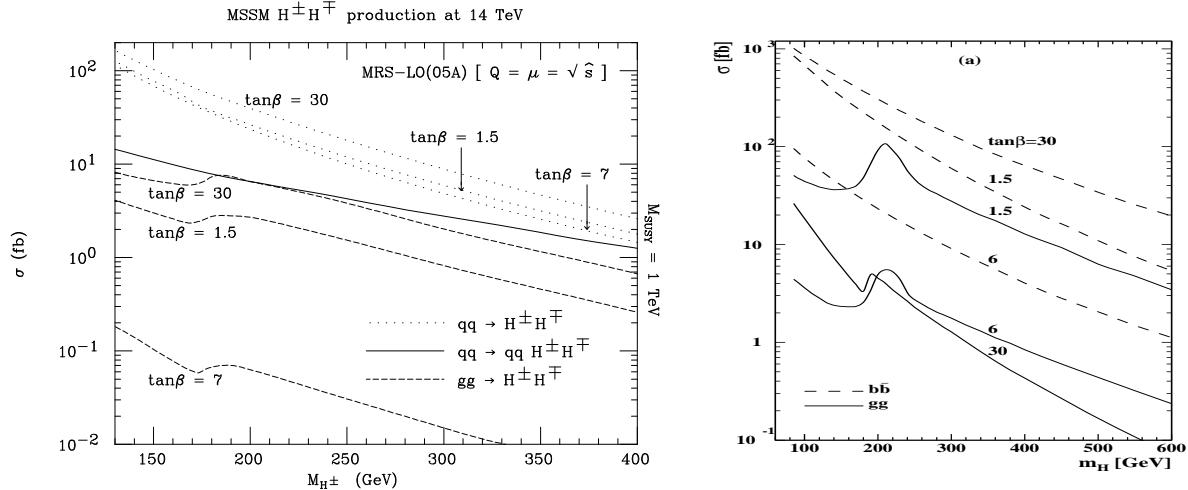
Figure 3.34: The cross sections for charged Higgs pair production at the LHC in $q\bar{q}$ annihilation including $b\bar{b}$, gg fusion and vector boson fusion for $\tan \beta = 1.5, 7$ and 30 (left) and for associated production of charged Higgs bosons with W bosons in gg fusion and $b\bar{b}$ annihilation for $\tan \beta = 6$ and 30 (right); from Refs. [404] and [406], respectively.

Finally, there is also the possibility of producing the $H^\pm$ bosons in association with W bosons, either in gluon fusion, $gg \to H^\pm W^\mp$ [405, 406], Fig. 3.32f, or in $b\bar{b}$ annihilation [406], Fig. 3.32g [recall that the $H^\pm WZ, H^\pm W\gamma$ coupling are absent at the tree level]. The cross sections, shown in the right–hand side of Fig. 3.34 for almost the same values of $\tan \beta$ as before, are approximately one order of magnitude higher than the corresponding ones for charged Higgs pair production. The $b\bar{b} \to H^\pm W^\mp$ process, together with $b\bar{b} \to H^+H^-$, can thus have rather large rates. They possibly need a more sophisticated treatment as one expects a very strong dependence on the input b–quark mass, on the renormalization and factorization scales, rather large QCD corrections and the combination of these channels with the $gg \to b\bar{b}H^+H^-(W^-)$ processes might be required; see e.g. Refs. [409, 410]. Note that in the $gg \to H^+H^-$ and $gg \to H^\pm W^\mp$ processes, additional contributions come from relatively light top/bottom squarks but, for reasonable masses and couplings, the squark loops cannot strongly increase the cross sections in general.

3.3 Detection at the Tevatron and the LHC

3.3.1 Summary of the production cross sections

Before discussing the channels suitable for the detection of the MSSM Higgs bosons at the Tevatron and the LHC, let us first recollect the various cross sections for Higgs boson production in the main processes that have been discussed in the previous sections. In the case of single neutral Higgs production and for charged Higgs production, they are shown in Fig. 3.35 for the Tevatron and in Fig. 3.36 for the LHC as functions of the Higgs boson masses for $\tan\beta = 3$ and 30 in the maximal mixing scenario where $X_t = \sqrt{6}M_S$ with $M_S = 2$ TeV. The pole top and bottom quark masses are set to, respectively, $m_t = 178$ GeV and $m_b = 4.9$ GeV and the NLO QCD radiative corrections have been implemented in all neutral Higgs channels except for associated production with heavy quarks where, however, the renormalization and factorization scales are set to $\mu_R = \mu_F = \frac{1}{2}(M_\Phi + 2m_t)$ for $t\bar{t}\Phi$ and $\frac{1}{4}(M_\Phi + 2m_b)$ for $b\bar{b}\Phi$, as to minimize them. The NLO MRST set of PDFs has been adopted.

As can be seen, at high $\tan\beta$, the largest cross sections are by far those of the $gg \to \Phi_A/A$ and $q\bar{q}/gg \to b\bar{b} + \Phi_A/A$ processes where $\Phi_A = H$ (h) in the (anti–)decoupling regime. The other processes involving these two Higgs bosons have cross sections that are orders of magnitude smaller. The production cross sections for the other CP–even Higgs boson, that is, $\Phi_H = h$ (H) in the (anti–)decoupling regime when $M_{\Phi_H} \simeq M_h^{\max}$, are similar to those of the SM Higgs boson with the same mass and are substantial in all the channels which have been displayed [at least at the LHC]. For small values of $\tan\beta$, the gg fusion and $b\bar{b}$+Higgs cross sections are not strongly enhanced as before and all production channels [except for associated $b\bar{b}$–Higgs production which is only slightly enhanced] have cross sections that are smaller than in the SM Higgs case outside the region where the lighter h boson is SM–like.

For the charged Higgs boson, the only channel that is relevant at the Tevatron is $H^\pm$ production from top quark decays at high and low $\tan\beta$, for masses not too close to $M_{H^\pm} \sim 150$ GeV. At the LHC, this process is also the dominant production channel in this mass range but, for higher masses, the fusion process $gg \to H^\pm tb$ [supplemented by $gb \to H^\pm t$] are the ones to be considered. In the figures, shown are the $q\bar{q}/gg \to H^\pm tb$ process which includes the possibility of on–shell top quarks and, hence, $pp \to t\bar{t}$ with $t \to H^+ b$. Additional sources of $H^\pm$ states for masses below ~ 250 GeV are provided by pair and associated production with neutral Higgs bosons in $q\bar{q}$ annihilation, but the cross sections are not shown.

In the following, we discuss the main Higgs detection channels at the Tevatron and the LHC, relying mostly on Refs. [325–338], where details and additional references can be found. For the neutral Higgs particles, some of these channels are simply those which allow for the detection of the SM Higgs particle discussed in §I.3.7. We thus simply summarize these aspects, referring to the previous discussion for details, and focus on the new features and

signatures which are specific to the MSSM.
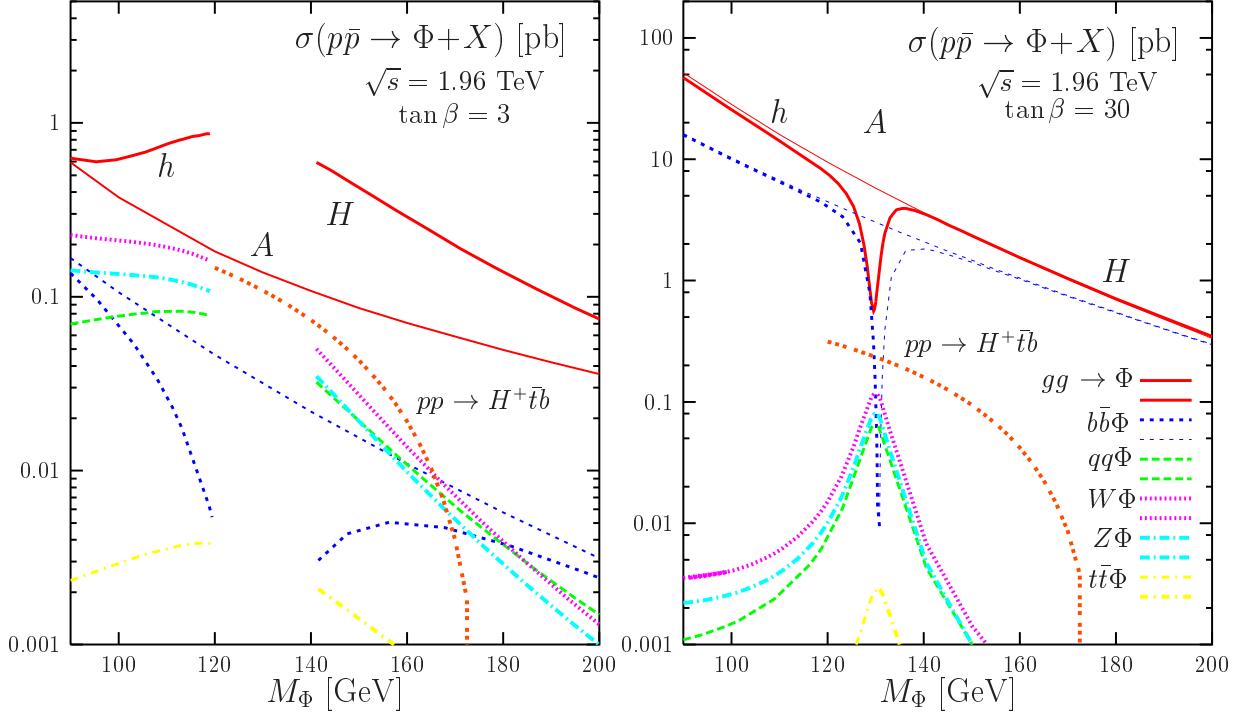
Figure 3.35: *The production cross sections for the neutral and charged MSSM Higgs bosons at the Tevatron as a function of their masses for* $\tan\beta = 3$ *and 30; the thin lines correspond to the production of the A boson. The various parameters are as described earlier.*
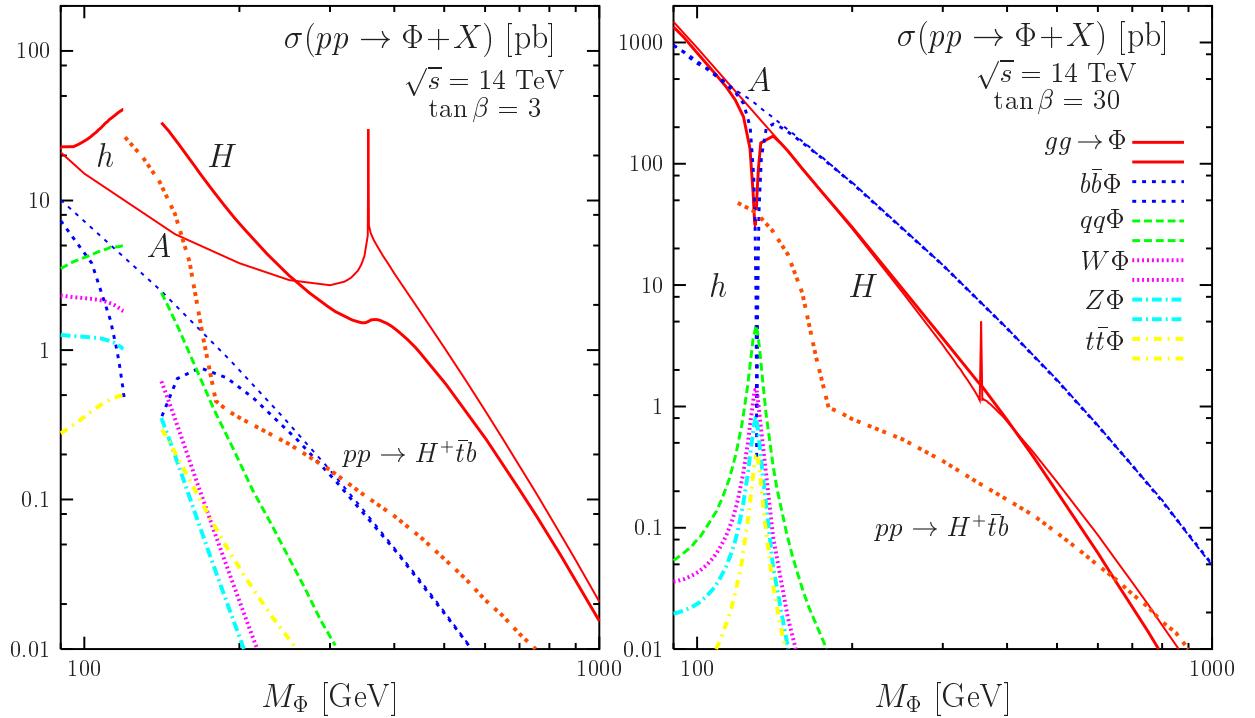

Figure 3.36: *The same as Fig. 3.35 but for the LHC.*

3.3.2 Higgs detection in the various regimes

Detection in the decoupling and anti–decoupling regimes

In the decoupling (anti–decoupling) regime where $\Phi_H = h\,(H)$ is SM–like, the detection techniques of this particle are exactly the same as those of the SM Higgs boson in the mass range below $M_{H_{\rm SM}} \lesssim 140$ GeV. At the Tevatron, the processes $p\bar{p} \to W\Phi_H \to \ell\nu b\bar{b}$ and $Z\Phi_H \to \ell\ell b\bar{b}$ or $\nu\nu b\bar{b}$ discussed in §I.3.7.2 can be exploited [411, 412]. The discovery reach depends on the ratio $R_{\rm exp} \equiv \sigma(q\bar{q}' \to V\Phi){\rm BR}(\Phi \to b\bar{b})/\sigma(q\bar{q}' \to VH_{\rm SM}){\rm BR}(H_{\rm SM} \to b\bar{b})$ which provides the rates in the MSSM for these particular final states, compared to the SM case. In the decoupling or anti–decoupling limits, this ratio is by definition equal to unity for the Φ_H particle. The detailed simulations performed for the Tevatron [325], where many systematic errors such as those from b–tagging efficiency, mass resolution, backgrounds *etc...* have been taken into account, have shown that ~ 30 fb^{-1} luminosity per experiment [that is, the total luminosity delivered by the collider] is needed for a 5σ discovery of the SM–like Higgs particle in this channel in the mass range below $M_{\Phi_H} \approx 130$ GeV; see the left–hand side of Fig. 3.37. However, to exclude at the 95% CL a Higgs boson in this mass range, only a luminosity of 5 fb^{-1} is required since less data is needed for this purpose.
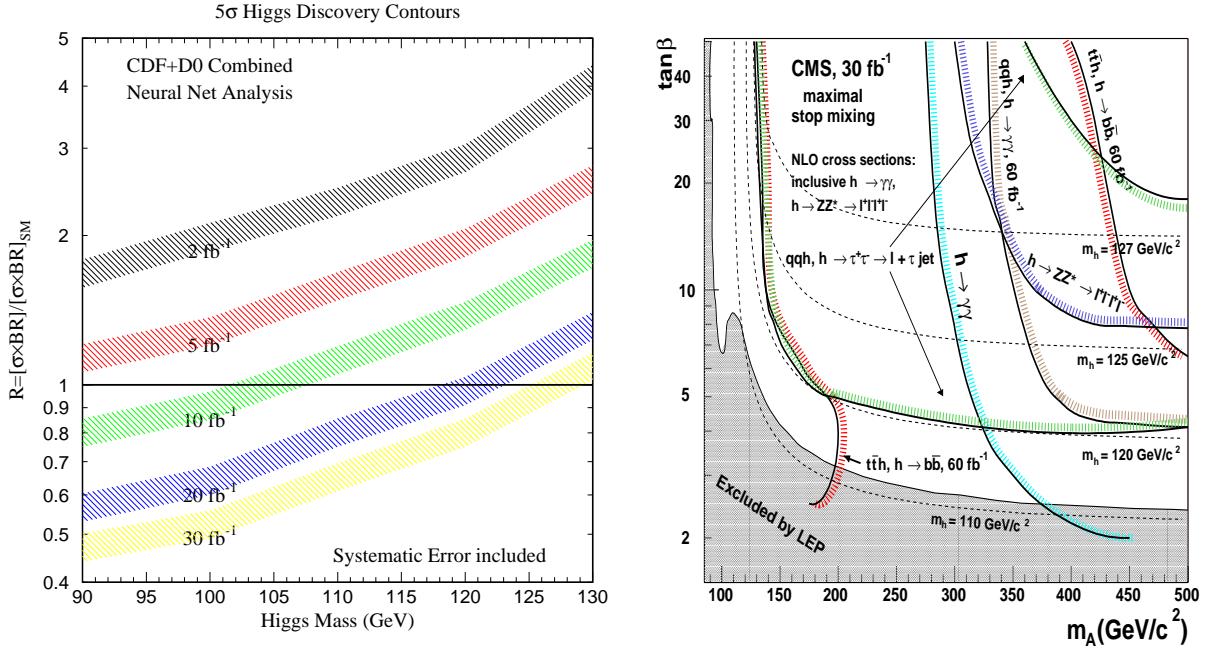
Figure 3.37: Left: the ratio $R_{\rm exp} \equiv \sigma(q\bar{q}' \to V\Phi){\rm BR}(\Phi \to b\bar{b})/\sigma(q\bar{q}' \to VH_{\rm SM}){\rm BR}(H_{\rm SM} \to b\bar{b})$ as a function of M_Φ, that is necessary at the Tevatron to discover a Higgs boson at the 5σ level for the indicated integrated luminosity per experiment; the thickness of the bands indicate the experimental uncertainties; from Ref. [325]. Right: the detection of the lighter MSSM Higgs boson at the LHC in the M_A–$\tan\beta$ plane at CMS in various channels for the maximal mixing scenario and an integrated luminosity of 30 fb^{-1}; from Ref. [413].

At the LHC, the $\Phi_H \to \gamma\gamma$ decays with the Higgs boson produced in the processes $gg \to \Phi_H$ or $pp \to W\Phi_H, t\bar{t}\Phi_H$ and leading to $\gamma\gamma\ell$ events, can be exploited [231, 315, 411, 413, 414]. In the $pp \to t\bar{t}\Phi_H$ processes, also the decays $\Phi_H \to b\bar{b}$ can be used [415, 416], while in the gg fusion mechanisms, the clean decays $\Phi_H \to ZZ^* \to 4\ell$ [231, 411] are also useful for $M_{\Phi_H} \gtrsim 120$ GeV when the ZZ^* branching ratio is large enough. In the vector boson fusion production channel, $qq \to qq\Phi_H$ with $\Phi_H \to \gamma\gamma$ and $\tau^+\tau^-$ [the later mode needs a low luminosity] are accessible [417, 418]. The coverage in the M_A–$\tan\beta$ plane for these various detection channels is shown for the lighter h boson in the right–hand side of Fig. 3.37 for a luminosity of (mainly) 30 fb^{-1} at CMS in the maximal mixing scenario.

At high values of $\tan\beta$, the pseudoscalar and pseudoscalar–like CP–even Higgs boson Φ_A are dominantly produced in the gg and $b\bar{b}$–Higgs mechanisms and decay almost exclusively into $b\bar{b}$ and $\tau^+\tau^-$ pairs. The only channels in which they are accessible are thus the $q\bar{q}/gg \to b\bar{b} + A/\Phi_A$ [132, 148, 149, 419, 420] where at least one b–quark is identified [one can in this case use the cross section for the $bg \to b + A/\Phi_A$ processes as discussed in §3.1.3]. The cross sections for both A and Φ_A are to be summed since the two Higgs bosons are almost degenerate in mass. At the Tevatron, because the initial production rates are not that large and the four jet background not too overwhelming, the $\Phi/A \to b\bar{b}$ signal should be exploited [421]. Again, one can parametrize the discovery reach in terms of the ratio $R_{\mathrm{exp}} \equiv \sigma(p\bar{p} \to b\bar{b}\Phi_A)\mathrm{BR}(\Phi_A \to b\bar{b})/\sigma(p\bar{p} \to b\bar{b}H_{\mathrm{SM}})\mathrm{BR}(H_{\mathrm{SM}} \to b\bar{b})$, which is approximately equal to $\tan^2\beta$ in the mass range below $M_{\Phi_A} = 130$ GeV where $\mathrm{BR}(H_{\mathrm{SM}}) \sim \mathrm{BR}(\Phi_A)$. For such a Higgs mass, a value $\tan\beta \sim 50$, will be needed to achieve a 5σ discovery with 10 fb^{-1} when both A and Φ_A production are added up, as shown in the left–hand side of Fig. 3.38.

At the LHC, the $4b$ signal is too difficult to extract because of the much larger QCD background [422]. One has then to rely on $\Phi_A/A \to \tau^+\tau^-$ decays with a tagging of the two τ leptons decaying either into hadrons or leptons, or in mixed decays [423]. In the right–hand of Fig. 3.38, we show the coverage of the M_A–$\tan\beta$ plane [in the maximal mixing scenario but with $M_S = 1$ TeV and smaller values of μ and M_2 than usual] with these processes as resulting from a CMS simulation with a luminosity of 30 fb^{-1}. At high masses, the best coverage is obtained in the channel $H/A \to \tau^+\tau^- \to jj + X$ which has a larger branching fraction and a better mass reconstruction and which allows to reach values of $M_A \sim 800$ GeV for $\tan\beta \sim 35$. In the lower Higgs mass range, $M_A \lesssim 400$ GeV, and with a higher luminosity, $\mathcal{L} = 60$ fb^{-1}, one can use the $H/A \to \mu^+\mu^-$ decays which, despite of the very small branching ratio $\sim 3 \times 10^{-4}$, are much cleaner than the $\tau^+\tau^-$ final states and allow a more precise Higgs mass reconstruction, thanks to the very good muon resolution [327, 424, 425]. Masses down to $M_A \sim 120$ GeV for $\tan\beta \gtrsim 15$ [where in fact, $\Phi_A \equiv h$] can be probed; for lower M_A values the tail of the $pp \to Z(b\bar{b}) \to \mu^+\mu^-(b\bar{b})$ process becomes too large. One can also notice that for $M_A \lesssim 130$ GeV and $\tan\beta \gtrsim 10$, where we are in the anti–decoupling regime with the heavier H boson being SM–like, the channel $qq \to qqH \to qq\tau^+\tau^-$ has been exploited.
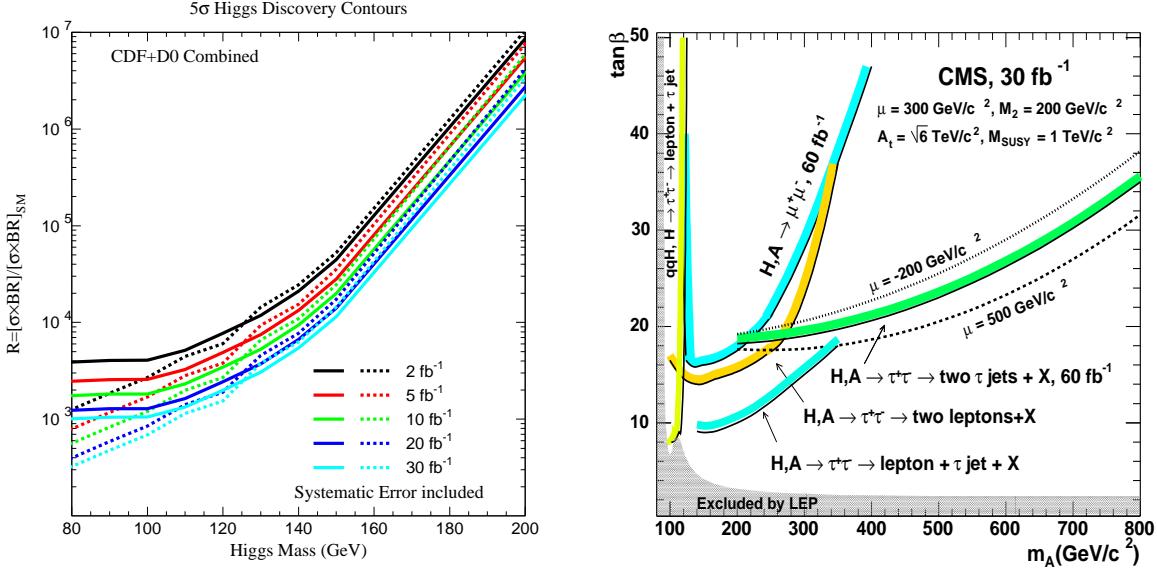
*Figure 3.38: Left: the ratio $R_{\rm exp} \equiv \sigma(p\bar{p} \to \Phi b\bar{b}){\rm BR}(\Phi \to b\bar{b})/\sigma(p\bar{p} \to b\bar{b}H_{\rm SM}){\rm BR}(H_{\rm SM} \to b\bar{b})$ as a function of M_Φ that is necessary at the Tevatron for a 5σ discovery for the indicated luminosities; the solid (dashed) lines are for the CDF (DØ) analyses which include systematical errors; from Ref. [325]. Right: the detection of the heavier MSSM neutral Higgs boson at the LHC in the M_A–$\tan\beta$ plane at CMS in various channels for the maximal mixing scenario with an integrated luminosity of 30 fb^{-1}; from Ref. [332].*

Detection of the charged Higgs boson

If the charged Higgs boson is lighter than the top quark, it can be searched in top decays $t \to H^+ b$, with the subsequent decay $H^+ \to \tau\nu$. The search is in fact restricted to smaller masses than $M_{H^+} \sim m_t - m_b \sim 170$ GeV since, close to this limit, the phase space and also the possibly large $H^\pm$ total width become too problematic. At the Tevatron [426], the indirect or disappearance searches where one looks for an excess of the $p\bar{p} \to t\bar{t}$ cross section is expected to provide better results for luminosities up to $\mathcal{L} = 2$–4 fb^{-1}. For higher luminosities, the direct search for the decays $H^+ \to \tau\nu$ and also for the more challenging channels $H^+ \to c\bar{s}$ at low $\tan\beta$ and $H^+ \to t^*\bar{b} \to Wb\bar{b}$ at high $M_{H^\pm}$ will be superior. From the absence of a signal, one can delineate the 95% CL exclusion range in the $M_{H^\pm}$–$\tan\beta$ plane and the result of the analysis of Ref. [325] is shown in Fig. 3.39 for two possible Run II luminosities, $\mathcal{L} = 2$ fb^{-1} and 10 fb^{-1}. For $M_{H^\pm} \sim 120$ GeV, which corresponds to the present limit in the MSSM, the range $\tan\beta \lesssim 2$ and $\tan\beta \gtrsim 15$ can be excluded, while for $M_{H^\pm} \sim 150$ GeV, only values $\tan\beta \lesssim 1$ and $\tan\beta \gtrsim 40$ can be ruled out. Note that these are only exclusion limits, the regions for $H^\pm$ discovery are significantly smaller.

At the LHC, thanks to the higher $t\bar{t}$ production rate and the larger luminosity, the direct search of the $H^\pm$ boson in $t \to H^+ b$ with $H^+ \to \tau\nu$ can be extended to almost the entire $M_{H^\pm}$–$\tan\beta$ range [427, 428], the two only problematic regions being $M_{H^\pm} \gtrsim 150$ GeV and $\tan\beta \sim \sqrt{m_t/m_b}$, where the $t \to H^+ b$ branching ratio is small; see Fig. 3.40.

205
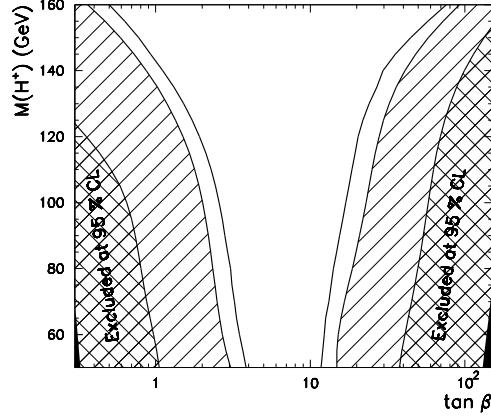
Figure 3.39: The 95% CL exclusion regions in the $M_{H^\pm}$–$\tan\beta$ plane for $m_t = 175$ GeV and luminosity values of 0.1 fb^{-1} (at $\sqrt{s} = 1.8$ TeV, cross–hatched), 2 fb^{-1} (at $\sqrt{s} = 2$ TeV, single–hatched), and 10 fb^{-1} (at $\sqrt{s} = 2$ TeV, hollow); from Ref. [325].

Here, hadronic $H^\pm \to cs$ decays help to increase the discovery reach [428]. For $M_{H^+} > m_t$, the $H^\pm$ particles have to be directly produced in the $q\bar{q}/gg \to t\bar{b}H^-$ or $gb \to tH^-$ and eventually $q\bar{q} \to H^+H^-, AH^\pm, \cdots$ processes and detected in the clean $H^+ \to \tau\nu$ mode [429]. τ–polarization in $\tau \to \pi^{\pm,0}\nu$ decays [430] enormously helps to discriminate these decays from $W \to \tau\nu$ decays [where the pions are softer] and to suppress the huge $t\bar{t}$ background. For very large and small values of $\tan\beta$, the decays $H^+ \to t\bar{b}$ with the top quark being produced in $gb \to bH^+$ could be used in principle [431], if one requires three b–quarks and one lepton from top decays to be identified and reconstruct both top quark as well as the $H^\pm$ masses [a recent study [432] has shown that this channel might be more problematic than expected]. The portion of the M_A–$\tan\beta$ plane which can be covered is shown in Fig. 3.40.
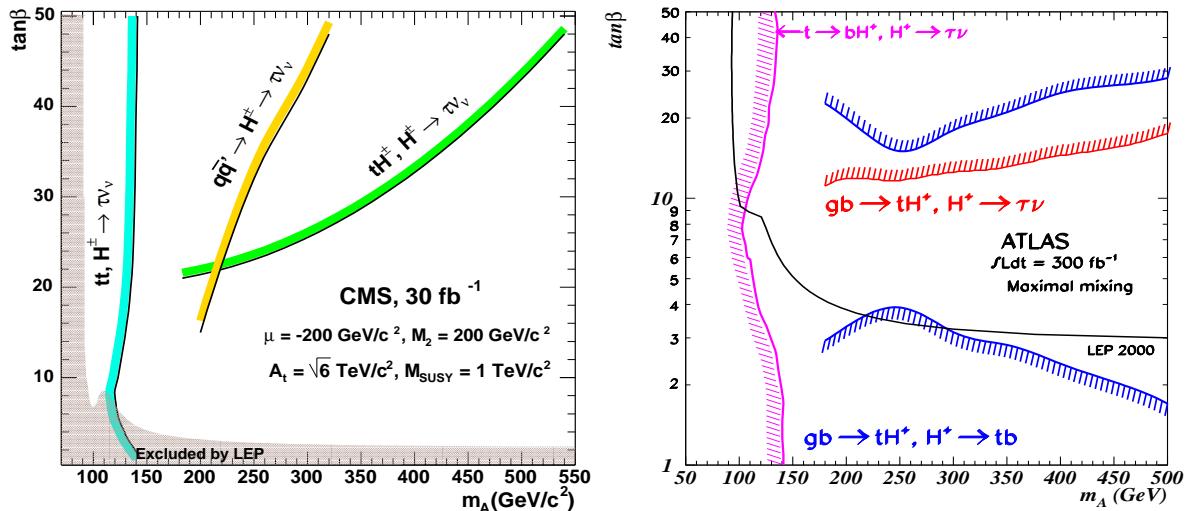

Figure 3.40: The coverage in the M_A–$\tan\beta$ plane in the search for the charged Higgs boson at the LHC in CMS (left) and ATLAS (right) simulations; from Refs. [327, 332].

Detection in the intermediate–coupling regime

In the intermediate–coupling regime, that is, for a not too heavy pseudoscalar boson and for relatively small values of $\tan\beta$, several interesting detection channels of the heavier neutral and charged Higgs bosons are possible and a summary based on Ref. [330] is given below.

For $M_H \lesssim 2m_t$ and $\tan\beta \lesssim 5$, the decays of the heavier Higgs boson H into two lighter ones, $H \to hh$, as well as the decays into gauge bosons $H \to WW, ZZ$ have sizable branching fractions while the $gg \to H$ cross section is still rather large, the suppression by the factor $\cos^2(\beta - \alpha)$ being not yet too drastic. The decays into gauge bosons, with one of them being eventually off–shell, can be detected in much the same way as for the SM Higgs particle but in a Higgs mass range that is narrower because of the smaller cross section times branching ratio. The channel $gg \to H \to hh$ is much more interesting since it would allow first, for the simultaneous discovery of two Higgs particles and second, for the measurement of the very important Hhh trilinear coupling [371, 372, 422, 433]. The most promising detection channel in this context is $H \to hh \to b\bar{b}\gamma\gamma$ with two isolated and high transverse momentum photons and two high p_T b–quark jets. Since the rates are rather low, one requires only one b jet to be tagged. The diphoton mass should be with a couple of GeV of M_h and the dijet mass within $\sim \pm 20$ GeV around M_h; the $\gamma\gamma b\bar{b}$ invariant mass is then required to be within ~ 20 GeV of M_H. The most important backgrounds are the irreducible $\gamma\gamma b\bar{b}$ continuum backgrounds but, since the b–tagging efficiency is only about 50 to 60% depending on the luminosity, one has also to consider the very dangerous $bj, c\bar{c}, cj, jj + \gamma\gamma$ backgrounds which have large uncertainties because of the poor knowledge of the total $b\bar{b}, b\bar{c}$ and jj cross sections.

A simulation using `ATLFAST` [434] has been performed some time ago [330] and the output, shown in Fig. 3.41 (left), is that the process $H \to hh \to b\bar{b}\gamma\gamma$ can be observed in the mass range $m_t \lesssim M_A \lesssim 2m_t$ with $\tan\beta \lesssim 3$–4 if a luminosity of 300 fb^{-1} is collected; only lower values of $\tan\beta$ are accessible for smaller integrated luminosities. The two additional channels $H \to hh \to b\bar{b}\tau^+\tau^-$ and $H \to hh \to b\bar{b}b\bar{b}$ have much larger rates [at least one and two orders of magnitude, respectively], however, the backgrounds are also much larger and the resolution on the τ lepton and b–quark pairs is much worse than in the $\gamma\gamma$ case. In Ref. [433], it has been shown that the channel $H \to hh \to b\bar{b}b\bar{b}$ could be at the edge of observability in a rather small area of the parameter space if enough luminosity is collected. Note also that the continuum production of two Higgs particles, $gg \to hh$, has been considered in Ref. [433] and the observability of the process in the $4b$ channel is possible only at very high values of $\tan\beta$, when the cross section is rather large as a result of the $\tan^4\beta$ enhancement. In this case, however, the contributions of the triangle diagrams involving the Hhh and hhh trilinear couplings are too small and these couplings cannot be measured.

Another interesting channel is $gg \to A \to hZ$ since it also allows the simultaneous discovery of two Higgs bosons [435]. The $hZ \to 4b$ final state has the largest rate and is
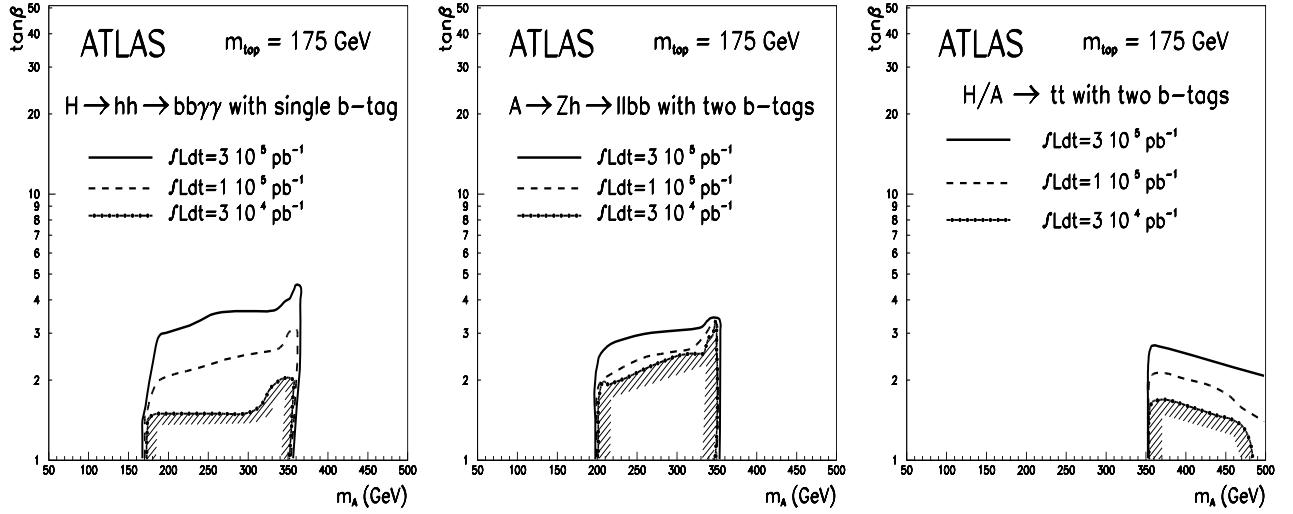
*Figure 3.41: The regions in the M_A–$\tan\beta$ parameter space where the channels $gg \to H \to hh \to b\bar{b}\gamma\gamma$ (left), $gg \to A \to hZ \to b\bar{b}\ell^+\ell^-$ (center) and $gg \to H/A \to t\bar{t} \to \ell\nu jjb\bar{b}$ (right) can be detected at the LHC with three options for the integrated luminosity; from Ref. [330].*

similar to the $H \to hh \to 4b$ case discussed above, while the final state $hZ \to \gamma\gamma\ell\ell$ is the cleanest one but the rates are unfortunately too low to be useful. The channel $A \to hZ \to b\bar{b}\ell^+\ell^-$ has been studied first in Ref. [330]; the final state can be easily triggered upon and the rates are still sizable since $\mathrm{BR}(Z \to \ell\ell) \simeq 6\%$ for $\ell = e, \mu$. Using similar cuts and kinematical constraints as those discussed for the $hh \to \gamma\gamma b\bar{b}$ case, with the two–photon pair replaced by the two–lepton pair [but here, the $\ell\ell$ and $\ell\ell jj$ mass can be required to be within ± 6 GeV of respectively, M_Z and M_A], the process can be singled out of the $\ell\ell jj$ backgrounds [also here, the $Zb\bar{b}$ and $t\bar{t}$ backgrounds are the dominant ones] in a region of the M_A–$\tan\beta$ parameter space that is slightly smaller than for the $H \to hh \to \gamma\gamma b\bar{b}$ process if a high luminosity is collected; see the central plot of Fig. 3.41.

For $M_A \gtrsim 2m_t$, the decays $H/A \to t\bar{t}$ can still have substantial branching ratios for $\tan\beta \lesssim 5$ despite of the coupling suppression; the two channels cannot be disentangled since H and A have comparable masses and are both dominantly produced in the gg fusion mechanism. The detection of this channel has been studied in the $t\bar{t} \to WWb\bar{b} \to \ell\nu jjb\bar{b}$ topology with both top quarks being reconstructed and the two b jets tagged and is possible but only for Higgs masses $M_H \sim M_A \lesssim 500$ GeV and $\tan\beta \lesssim 2.5$ even for very high luminosities, as shown in the right–hand side of Fig. 3.41. Note that, due to a negative interference between the signal and $pp \to t\bar{t}$ which is the main background [Wj can be made much smaller by reasonable cuts], the signal appears as a dip in the $t\bar{t}$ invariant mass spectrum [436].

Finally, for the $H^\pm$ bosons, there is also a chance that the final states $H^\pm \to Wh \to \ell\nu b\bar{b}$ can be observed at low $\tan\beta$ and $M_{H^\pm} \lesssim m_t$ [330,437]. These final states can also originate from $H^\pm \to t^*b \to W\bar{b}b$ and the two channels have to be disentangled; see Ref. [179]

Detection in the intense–coupling regime

The most difficult problem we must face in the intense–coupling regime is to resolve between the three peaks of the neutral Higgs bosons when their masses are close to one another [146]. The only decays with large branching ratios on which one can rely are the $b\bar{b}$ and $\tau^+\tau^-$ modes. At the LHC, the former has a too large QCD background to be useful while, for the latter channel, the expected resolution on the invariant mass of the $\tau^+\tau^-$ system is only about 10–20 GeV and, thus, clearly too large. One would then simply observe a relatively wide resonance corresponding to A and h and/or H production. Since the branching ratios of the decays into $\gamma\gamma$ and $ZZ^* \to 4\ell$ are too small, a way out [see also Ref. [438] e.g.] is to use the decays into muons: although rare, $\mathrm{BR}(\Phi \to \mu^+\mu^-) \sim 3.3 \times 10^{-4}$, the resolution is expected to be as good as 1 GeV, i.e. comparable to the Higgs total widths for $M_\Phi \sim 130$ GeV.

Since the Higgs–strahlung and vector boson fusion processes, as well as $pp \to t\bar{t}\Phi$, will have smaller cross sections [418], the Higgs couplings to the involved particles being suppressed, the three Higgs bosons will be produced mainly in the gluon–gluon process, $gg \to \Phi = h, H, A \to \mu^+\mu^-$, which is dominantly mediated by b–quark loops, and the associated production with $b\bar{b}$ pairs, $gg/q\bar{q} \to b\bar{b} + \Phi \to b\bar{b} + \mu^+\mu^-$. The dominant background to $\mu^+\mu^-$ production is the Drell–Yan process $pp \to \gamma^*, Z^* \to \mu^+\mu^-$ but, for the $pp \to \mu^+\mu^- b\bar{b}$ final state, one has to include the full 4–fermion background which is mainly due to the process $pp \to b\bar{b}Z$ with $Z \to \mu^+\mu^-$. An analysis of the signal and backgrounds in this case has been performed in Ref. [146] and we summarize below the main conclusions.

The differential cross sections for $pp(\to h, H, A) \to \mu^+\mu^-$ are shown as a function of the invariant dimuon mass in the left–hand side of Fig. 3.42 for the scenario $M_A = 125$ GeV and $\tan\beta = 30$, which leads to $M_h \sim 124$ GeV and $M_H \sim 134$ GeV. As can be seen, the signal rate is fairly large but when put on top of the huge Drell–Yan background, it becomes completely invisible. Thus, already with a parton–level simulation, the Higgs signal will probably be very difficult to extract in this process for $M_\Phi \lesssim 140$ GeV. In the right–hand side of Fig. 3.42, we display, again for the same scenario, the signal from $pp \to \mu^+\mu^- b\bar{b}$ and the complete 4–fermion SM background as a function of the dimuon system mass. The number of signal events is an order of magnitude smaller than in the previous case, but one can still see the two peaks, corresponding to h/A and H production, on top of the background.

In a realistic analysis, the signal and background events have been generated using `CompHEP` [439] and detector effects have been simulated taking the example of CMS; the details have been given in Ref. [146] to which we refer. The result for a luminosity of 100 fb^{-1} are shown in Fig. 3.43 where the number of $\mu^+\mu^- b\bar{b}$ events in bins of 0.25 GeV is shown as a function of the mass of the dimuon system. The left–hand side shows the signal with and
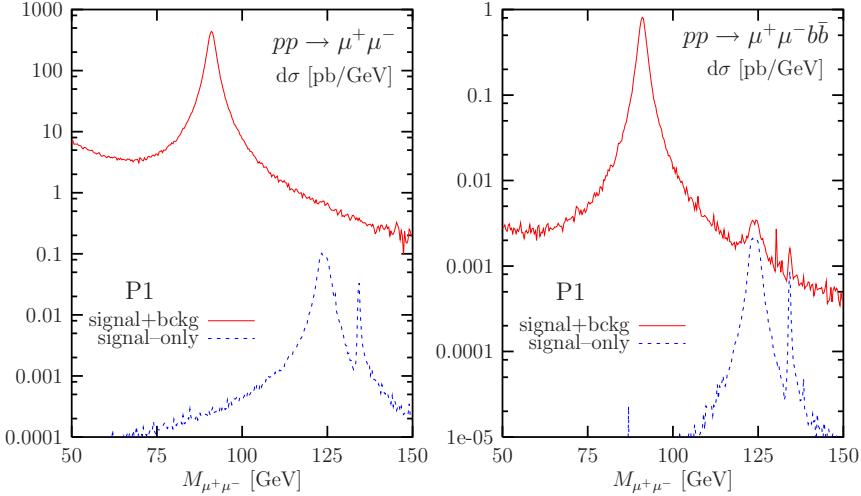
Figure 3.42: The differential cross section in pb/GeV as a function of the dimuon mass for both the signal and signal plus background in the processes $pp(\to \Phi) \to \mu^+\mu^-$ (left figure) and $pp(\to \Phi b\bar{b}) \to \mu^+\mu^- b\bar{b}$ (right figure); $M_A = 125$ GeV and $\tan\beta = 30$. From Ref. [146].

without the resolution smearing as obtained in the Monte Carlo analysis, while the figure in the right–hand side shows also the backgrounds, including the detector effects.

In this scenario, the signal cross section for the H boson is significantly smaller that from the h and A bosons; the latter particles are too too close in mass to be resolved and only one single broad peak for h/A is clearly visible. To resolve also the peak for the H boson, the integrated luminosity should be increased by at least a factor of 3. The analysis has also been performed for points with $M_A = 130$ and 135 GeV and the same values of $\tan\beta$. In the former case, it would be possible to see also the second peak, corresponding to the H boson signal with a luminosity of 100 fb^{-1} but, again, the h and A peaks cannot be resolved. In the latter case, all three h, A and H bosons have comparable signal rates and the mass differences are large enough to hope isolating the three different peaks, although with some difficulty. Thus, in the intense–coupling regime, the detection of the individual Higgs boson peaks is very challenging at the LHC and dedicated studies are needed.

Higgs detection summary in the M_A–$\tan\beta$ plane

Combining the search in the various MSSM Higgs detection channels, the coverage in the M_A–$\tan\beta$ parameter space is summarized in Fig. 3.44 for the Tevatron and in Fig. 3.45 for the LHC, in the maximal mixing scenario where $A_t = \sqrt{6}$ TeV and $M_S = 1$ TeV. At the Tevatron, shown are the 95% CL exclusion plane from the absence of any Higgs signal and the 5σ range for the discovery of one Higgs particle when the statistics of both CDF and DØ are combined. The analysis is based on an average of the expected CDF and DØ performances improved by neural network techniques. The assumed integrated luminosities are indicated in the figure and, for the color coding, as $\mathcal{L}$ increases, the corresponding

210
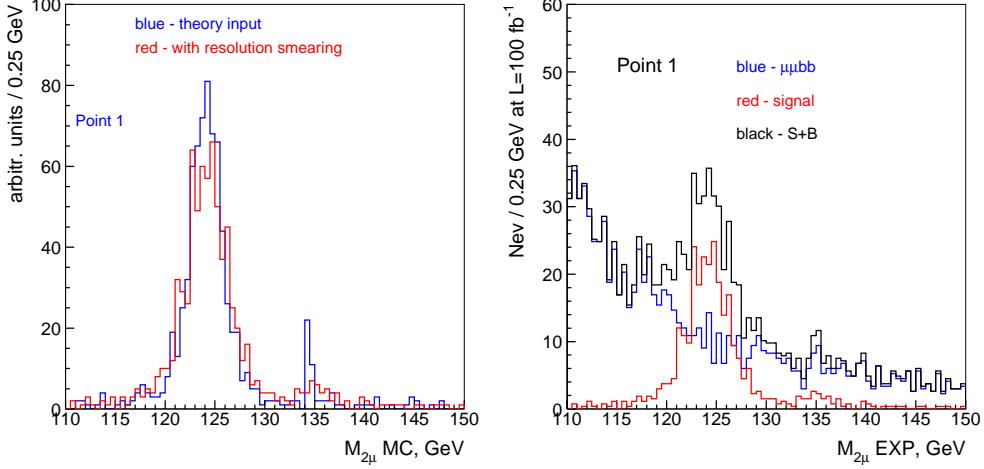
Figure 3.43: The $\mu^+\mu^-$ pair invariant mass distributions for the signal before and after detector resolution smearing (left) and for the signal and the background (right); from Ref. [146].

shaded areas successively cover the plane; the darker shading of a given color corresponds to a degradation in the coverage of the plane due to the experimental uncertainties in b–tagging efficiency, background, mass resolution and other effects.
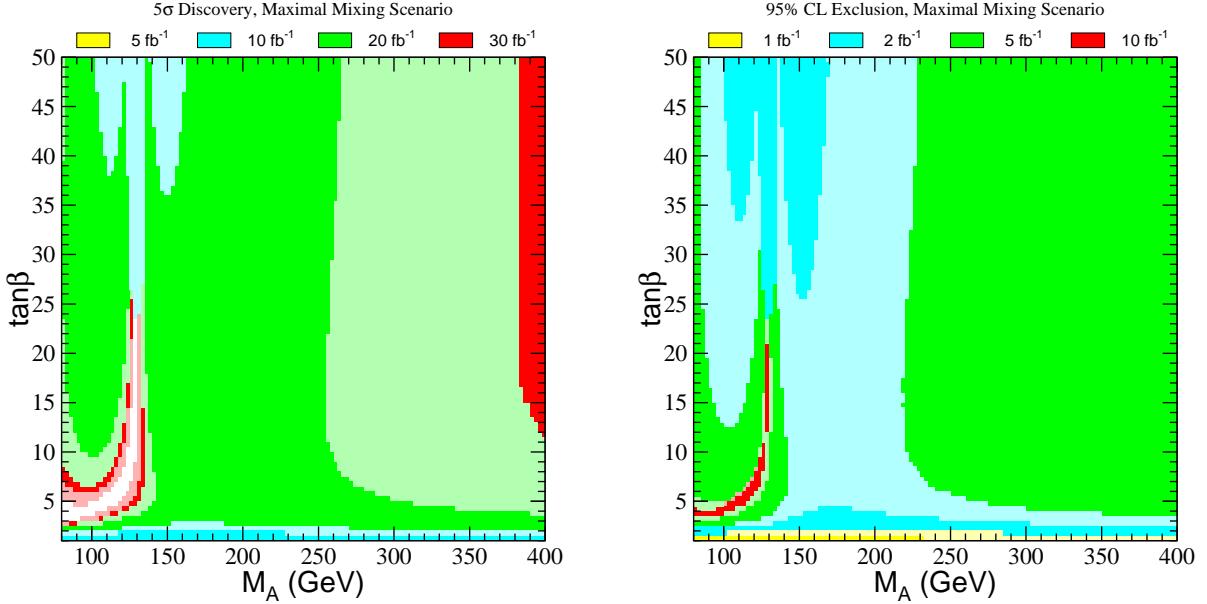

Figure 3.44: Regions of the M_A–$\tan\beta$ parameter space corresponding to the discovery a Higgs boson at the 5σ level (left) and the exclusion of a Higgs signal at 95% CL (right) for various values of the integrated luminosity; from the simulation of Ref. [325].

As can be seen, in the maximal mixing scenario, there is a significant region of the parameter space where a Higgs signal can be observed for a luminosity of 20 fb^{-1}, or excluded at the 95% CL with a luminoisty of 5 fb^{-1} [in the no–mixing scenario the coverage is of course larger, but most of the plane is, however, already ruled out by LEP2 searches]. There are, nevertheless, still regions with low M_A values which cannot be accessed. In fact, the worst

scenario at the Tevatron is the vanishing–coupling regime where $g_{hbb} \ll 1$, since the analysis mostly relies on the $h \to b\bar{b}$ decays. Other problematic regions are the intermediate–coupling regime where g_{hVV} is suppressed and g_{Hbb}, g_{Abb} not strong enough and also the decoupling regime but where the value of $\tan\beta$ is not too large to make that the Φ_A and A are not degenerate in mass as to contribute to the same signal peak.

At the LHC, many channels allow to discover an MSSM Higgs boson as shown in the left–hand side of Fig. 3.45 where the result of an ATLAS simulation with 300 fb^{-1} of luminosity is displayed. Most of the M_A–$\tan\beta$ parameter space is covered by the search for the lighter h boson in $\gamma\gamma$, $\gamma\gamma\ell$ and $t\bar{t}h \to t\bar{t}b\bar{b}$ events or from the search of the H/A and $H^{\pm}$ bosons in respectively, $pp \to b\bar{b} + H/A$ with $H/A \to \tau\tau \to jjX$ and $gb \to tH^{\pm}$ with $H^{\pm} \to \tau\nu$. The channels with vector boson fusion have not been included, although they also lead to visible signals. As can be seen, the whole MSSM parameter range can be covered at the LHC. Even the intermediate–coupling regime with $\tan\beta \lesssim 3$ can be probed for the heavier Higgs particles and the interesting decays $H \to hh, A \to hZ$ and $H/A \to t\bar{t}$ can be observed as shown in the lower part of the figure.

Nevertheless, in large parts of the parameter space, only one Higgs boson which corresponds in general if not always to the lighter h, can be observed. As shown in the right–hand side of Fig. 3.45, where the regions in which the number of accessible Higgs particles in AT-LAS is delineated for 300 fb^{-1} of luminosity, for $M_A \gtrsim 200$ GeV and not too large values of $\tan\beta$, only the h boson is accessible [note, again, that vector boson fusion processes have not been used here]. In fact, it is even the case in a "hole" in the plane, namely for $M_A \sim 150$ GeV and $\tan\beta \sim 5$. Thus, there is a relatively high probability that at the LHC, only one Higgs particle is observed with SM–like properties but with a mass below ~ 140 GeV.

3.3.3 Higgs parameter measurements at the LHC

<u>Measurements for a SM–like h boson</u>

In the decoupling regime when the pseudoscalar Higgs boson is very heavy, only the lighter MSSM boson with SM–like properties will be accessible. In this case, the measurements which can be performed for the SM Higgs boson with $M_{H_{\rm SM}} \lesssim 140$ GeV and that we discussed in some detail in §I.3.7.4 will also be possible. The h mass can be measured with a very good accuracy, $\Delta M_h/M_h \sim 0.1\%$, in the $h \to \gamma\gamma$ decay which incidentally, verifies the spin–zero nature of the particle. However, the total decay width is very small and it cannot be resolved experimentally. The parity quantum numbers will be very challenging to probe, in particular since the $h \to ZZ^* \to 4\ell^{\pm}$ decay in which some correlations between the final state leptons can characterize a $J^{\rm PC} = 0^{++}$ particle, might be very rare. This will be also the case of the trilinear Higgs–self coupling which needs extremely high luminosities.
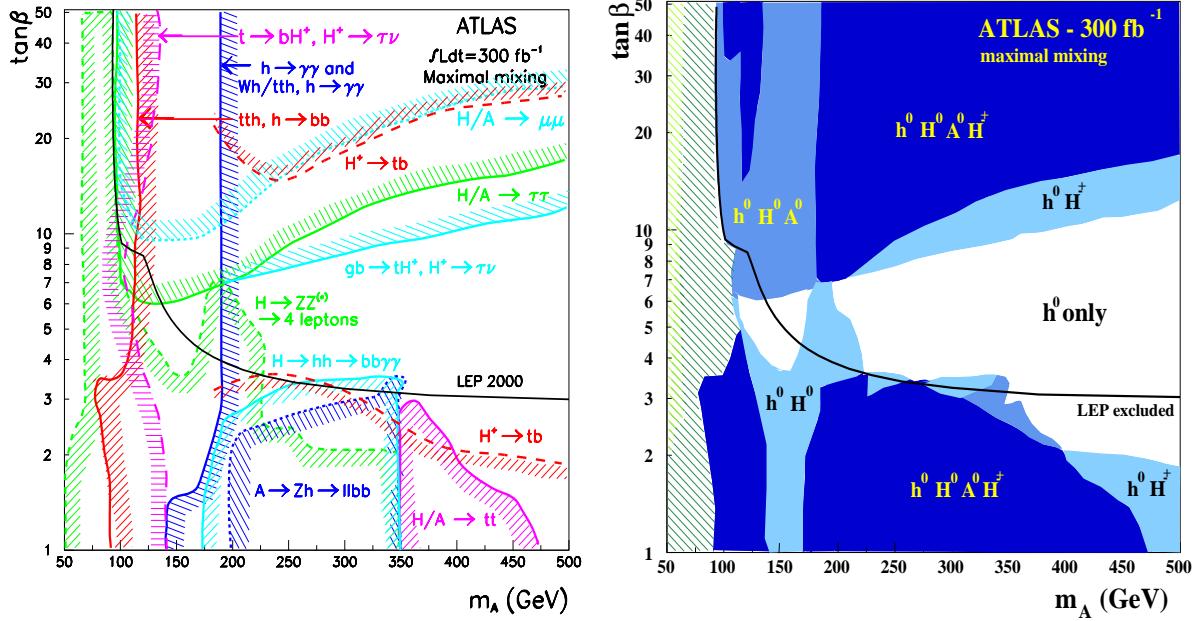
Figure 3.45: The coverage of the M_A–$\tan\beta$ parameter space using various Higgs production channels in ATLAS with a luminosity of 300 fb^{-1} (left) and the number of MSSM Higgs bosons that can be observed in ATLAS with a luminosity of 300 fb^{-1} (right) [327].

Nevertheless, combinations of Higgs production cross sections and decay branching ratios can be measured with a relatively good accuracy [440] as summarized in §I.3.7.4. The Higgs couplings to fermions and gauge bosons can be then determined from a fit to all available data. However, while in the SM one could make reasonable theoretical assumptions to improve the accuracy of the measurements, in the MSSM the situation is made more complicated by several features, such as the possibility of invisible decay modes, the radiative corrections in the Higgs sector which can be different for b, τ and W/Z couplings, etc...

In some cases, the distinction between a SM and an MSSM Higgs particle can be achieved. The extent to which this discrimination can be performed has been discussed in Ref. [441] for instance, where a χ^2 analysis of the deviation of the Higgs couplings expected for a given MSSM scenario, compared to the SM case, has been made. The contours in the M_A–$\tan\beta$ plane where the two scenarios are different with a 3σ and 5σ significance is shown in Fig. 3.46 for three possible luminosities; in the areas at the left of the contours, the SM scenario can be ruled out. With 300 fb^{-1} data, on can distinguish an MSSM from a SM Higgs particle at the 3σ level for pseudoscalar Higgs masses up to $M_A =$ 300–400 GeV.

Measurements for decoupled heavier Higgs bosons

The heavier Higgs particles H, A and $H^\pm$ are accessible mainly in, respectively, the $gg \rightarrow b\bar{b} + H/A$ and $gb \rightarrow H^\pm t$ production channels for large $\tan\beta$ values. The main decays of the particles being $H/A \rightarrow b\bar{b}, \tau^+\tau^-$ and $H^+ \rightarrow t\bar{b}, \tau^+\nu$, the Higgs masses cannot be determined
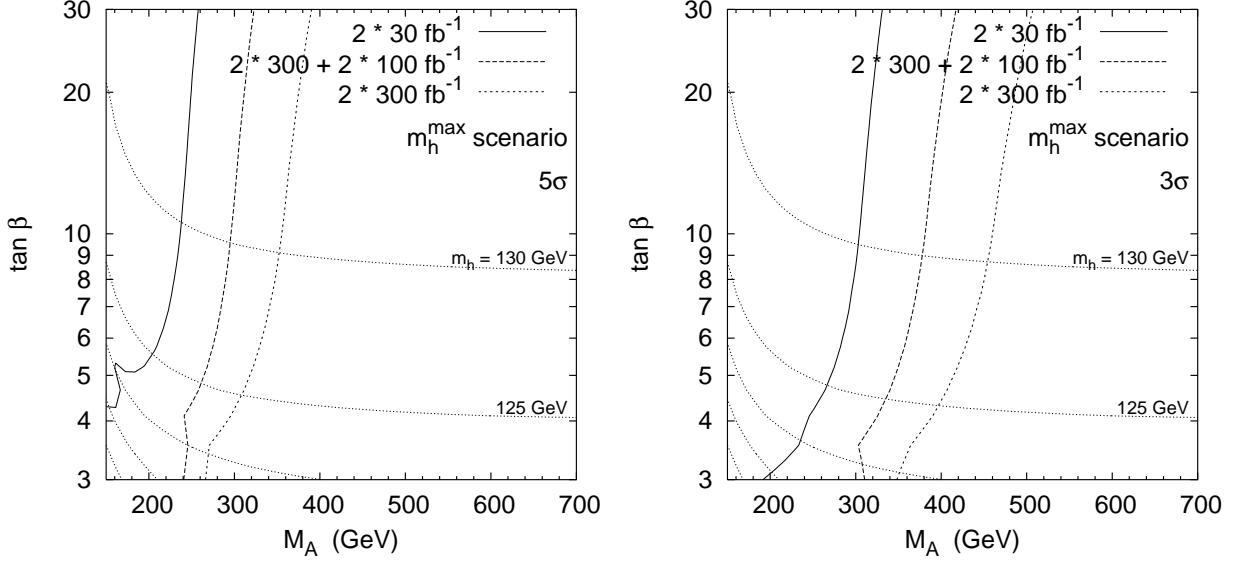
Figure 3.46: Fit within the MSSM M_h^{max} scenario in the M_A–$\tan\beta$ plane for three luminosity scenarios at the LHC. The left–hand parts of the curves show the regions where a $\geq 5\sigma$ (left panel) and $\geq 3\sigma$ (right panel) discrepancy from the SM case can be observed. The mostly–horizontal dotted lines are contours of M_h in steps of 5 GeV; from Ref. [441].

with a very good accuracy as a result of the poor resolution. However, for $M_A \lesssim 300$ GeV and with high luminosities, the H/A masses can be measured with a reasonable accuracy by considering the decays $H/A \to \mu^+\mu^-$ for which the mass resolution is about $\Delta M_\Phi = 2\%$. This resolution is nevertheless not sufficient to distriminate between the particles since in general, the mass difference $M_H - M_A$ is much smaller. The situation is made more complicated by the large total decay widths of the particles which, again, cannot be directly measured with a very good accuracy. The spin–parity quantum numbers of the Higgs particles cannot be probed in these fermionic decays, too. The τ polarization, which helps in discriminating the signals from the backgrounds, cannot be exploited in the complicated hadronic environment of the LHC to disentangle between the H and A bosons for instance.

There is, however, one very important measurement which can be performed in these channels. As the production cross sections above are all proportional to $\tan^2\beta$ and, since the ratios of the most important decays fractions are practically independent of $\tan\beta$ for large enough values [when higher–order effects are ignored], one has an almost direct access to this parameter. In Ref. [442], a detailed simulation of the two production channels $gb \to H^-t$ and $q\bar{q}/gg \to H/A + b\bar{b}$ at CMS has been performed. In the latter process, all final states in τ decays, $jj/j\ell/\ell\ell + X$, have been considered. The result for the accuracy of the $\tan\beta$ measurement when these three channels are combined is shown in Fig. 3.47 for three values $\tan\beta = 20, 30, 40$ at a luminosity of 30 fb^{-1}. In the three lower curves, only the statistical errors have been taken into account and, as can be seen, one can make a rather precise

measurement, $\Delta \tan\beta/\tan\beta \lesssim 10\%$ for $M_A \lesssim 400$ GeV.
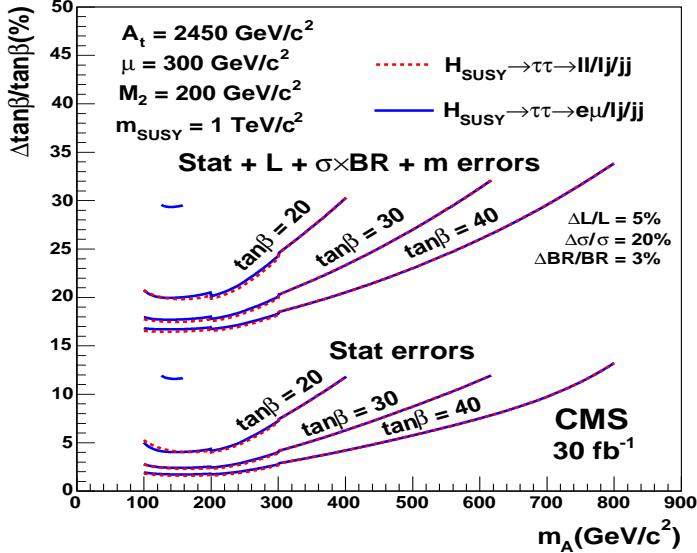
Figure 3.47: *The uncertainty in the measurement of $\tan\beta$ in the channel $gg \to H/A + b\bar{b}$ with the combined $H/A \to \tau\tau$ decays at CMS with 30 fb^{-1} data. The three lower curves show the uncertainty when only statistical errors are taken into account, while the upper curves include the uncertainties from the mass (a few %) and luminosity (5%) measurements and the theoretical uncertainty (23%); from Ref. [442].*

However, besides the statistical uncertainties of the event rates, there are systematical errors from e.g. the luminosity measurement [443] as well as theoretical errors due to the uncertainties on the PDFs [444] and from higher–order effects in the production cross sections [367]. In particular, since the latter are also proportional to m_b^2 and because the bottom quark mass receives radiative corrections that are themselves proportional to $\tan\beta$, the interpretation of the measurement is rather ambiguous. A possible approach that has been adopted in Ref. [442], is to define an effective $\tan\beta$ parameter in which these higher–order corrections are mapped, leaving aside the theoretical interpretation of the measurement. The remaining theoretical error is estimated to be $\sim 20\%$ for the production cross section and $\sim 3\%$ for the decay branching ratio. In the upper curves of the figure, the effect of including some of these systematical error is displayed. The accuracy of the measurement worsens then to the level of $\sim 30\%$ for $M_A \sim 400$ GeV and $\tan\beta = 20$ with 30 fb^{-1} data.

Measurements in the other regimes

In the anti–decoupling regime, it is the heavier CP–even H boson which is SM–like and for which the previously discussed measurements for a SM Higgs particle apply. In this case, the h boson is degenerate in mass with the pseudoscalar Higgs boson and both can be detected in the decays $h/A \to \mu^+\mu^-$ for large enough values of $\tan\beta$ and $M_A \gtrsim 110$ GeV.

In the intense–coupling regime, as discussed earlier, the three Higgs bosons will be difficult to disentangle and the situation will be somewhat confusing. In the intermediate–coupling regime, there will be a hope to measure the trilinear Hhh coupling and to have a direct access to part of the scalar potential which breaks the electroweak symmetry.

3.4 The MSSM Higgs bosons in the SUSY regime

In this section, we discuss the effects of light SUSY particles on the production and the detection of the MSSM Higgs bosons. We first analyze the loop effects of these particles and then their direct effects in Higgs production in association with squarks, Higgs decays into SUSY particles and Higgs production from cascade decays of heavier sparticles.

3.4.1 Loop effects of SUSY particles

As already discussed, the Higgs–gluon–gluon vertex in the MSSM is mediated not only by heavy top and bottom quark loops but, also, by loops involving squarks in the CP–even Higgs case. If the top and bottom squarks are relatively light, the cross section for the dominant production mechanism of the lighter h boson in the decoupling regime, $gg \to h$, can be significantly altered by their contributions, similarly to the gluonic decay $h \to gg$ that we have discussed in §2.2.2. In addition, in the $h \to \gamma\gamma$ decay which is considered as one of the most promising detection channels, the same stop and sbottom loops together with chargino loops, will affect the branching rate as also discussed in §2.2.2. One can conclude from these discussions that the cross section times branching ratio $\sigma(gg \to h) \times \mathrm{BR}(h \to \gamma\gamma)$ for the lighter h boson at the LHC, Fig. 3.48, can be very different from the SM, even in the decoupling limit in which the h boson is supposed to be SM–like [239].
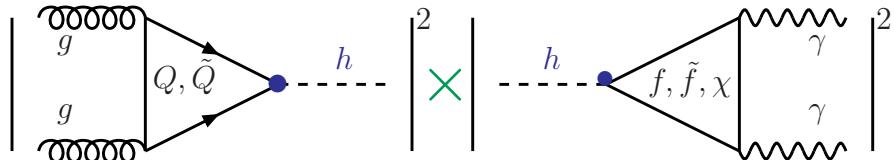

Figure 3.48: Loop contributions to the $gg \to h$ cross section times $h \to \gamma\gamma$ branching ratio.

This is shown in Fig. 3.49 where we have simply adopted the scenarios of Figs. 2.29 and 2.31 for $\mathrm{BR}(h \to gg)$ and $\mathrm{BR}(h \to \gamma\gamma)$, respectively, and multiplied the two rates. In the left–hand side, we show the gg cross section times the $\gamma\gamma$ branching ratio including the contribution of top squarks, relative to its SM value. As expected, while the effects are small for small $X_t = A_t - \mu \cot\beta$ mixing and large stop masses, they can be extremely large for $m_{\tilde{t}_1} \sim 200$ GeV and large A_t values. In this case, the loop suppression is not effective and the stop coupling to the h boson, $g_{h\tilde{t}_1\tilde{t}_1} \propto m_t X_t$, is strongly enhanced. Since here, the

$\tilde{t}_1$ loop contribution interferes destructively with that of the top–quark loop, it leads to an enhancement of BR($h \to \gamma\gamma$) and a reduction of $\sigma(gg \to h)$. However, the reduction of the latter is much stronger than the enhancement of the former and the product $\sigma(gg \to \gamma\gamma)$ decreases with increasing X_t. For X_t values of about 1.5 TeV, the signal for $gg \to h \to \gamma\gamma$ in the MSSM is smaller by a factor of ~ 5 compared to the SM in such a scenario.
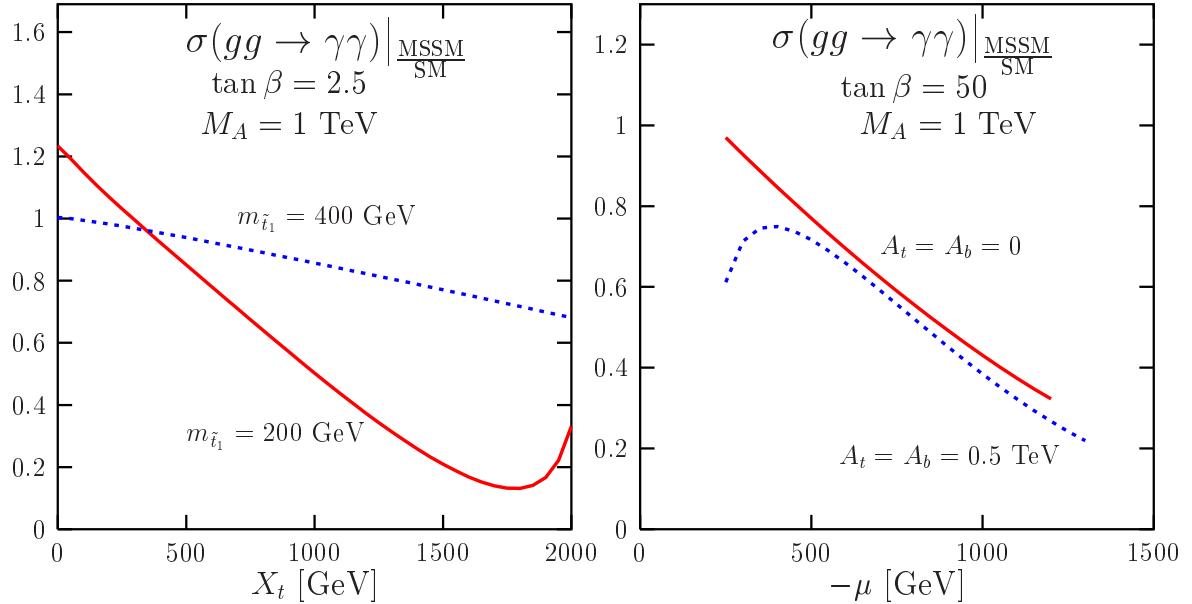

Figure 3.49: The gg–fusion cross section times the photonic branching ratio for the production of the h boson in the MSSM relative to its SM value, $\sigma(gg \to h \to \gamma\gamma)|_{MSSM/SM}$ in scenarios where relatively light top and bottom squarks as well as charginos contribute.

In the no mixing case, $X_t \sim A_t \sim 0$ case, the stop contribution interferes constructively with the one of the top quark, but since the coupling $g_{h\tilde{t}_1\tilde{t}_1}$ is smaller, the cross section $\sigma(gg \to h \to \gamma\gamma)$ increases only moderately, up to $\sim 20\%$ in the light stop case. The deviations become of course smaller for increasing stop mass and, also, for moderate mixing $X_t \sim 0.5$ TeV where the two components of the $g_{h\tilde{t}_1\tilde{t}_1}$ couplings, eq. (1.109), almost cancel each other. In the right–hand side of Fig. 3.49, we also show the effect of a light sbottom with $m_{\tilde{b}_1} = 200$ GeV and large $\tan\beta$ and μ values on the $gg \to h \to \gamma\gamma$ cross section, following the scenarios already presented when we discussed the decays $h \to gg$ and $h \to \gamma\gamma$. Here, again, the effects can be drastic leading to a strong suppression of the cross section $\sigma(gg \to h \to \gamma\gamma)$ compared to the SM case. An experimental (CMS) analysis of this situation has recently appeared [413] and higher luminosities are needed to overcome the suppression.

We note that in the cross sections times branching ratios for the other decay modes of the lighter h boson when produced in the gluon–gluon fusion mechanism, such as the process $gg \to h \to WW^*$, the deviations due to stop and sbottom loops compared to the SM case are simply the ones shown in Fig. 2.29 for the decay rate $\Gamma(h \to gg)$, as a result of the

proportionality of the Higgs gluonic decay width and the $gg \to h$ production cross section. In this case, the rates can be even smaller in some cases since they do not gain from the possible enhancement of the $h \to \gamma\gamma$ amplitude.

Finally, let us discuss the SUSY QCD corrections to this process. In the MSSM, in addition to the standard QCD corrections to the quarks loops, one needs to evaluate the QCD corrections to the squark loops for the CP–even Higgs bosons. In this case, since squarks are expected to be rather massive, the heavy loop mass expansion can be used for $M_{\mathcal{H}} \lesssim 2m_{\tilde{Q}}$ [in the opposite case, $M_{\mathcal{H}} > 2m_{\tilde{Q}}$ the decay of the Higgs boson into squarks will occur and would be dominating if squarks have any impact in the loop]. These corrections [246–248] are the same as those discussed in §2.2.2 when we analyzed the Higgs decays into gluons. The only difference is in the overall normalization since the QCD corrections to the quark loops are different in the production and decay processes and, in the former case, one has to include the contributions of $q\bar{q}$ and qg initial states. Again, this part of the NLO calculation has been discussed in the SM case and reanalyzed in the MSSM in §3.1.2.

The impact of these SUSY QCD corrections is illustrated in Fig. 3.50 where we show the K–factors for the production of the lighter h boson in $gg \to h$ at LHC energies. We have again adopted the same two scenarios of Fig. 2.30 of §2.2.2 for the gluonic decay width, that is, the SpS1a scenario with a varying gaugino mass $m_{1/2}$ and the scenario in which the $\tilde{t}_1$ state is rather light and its contribution almost cancels the top quark contribution, resulting in a nearly vanishing rate. In both cases, the mass of the pseudoscalar Higgs boson is large so that we are in the decoupling limit where the h boson has SM couplings to top quarks [and, thus, one can also include the NNLO corrections] and the b–quark loop contribution can be neglected. As can be seen, the SUSY corrections are small and negative, except in the "gluophobic" Higgs case where the resulting total rate production is nevertheless small.

3.4.2 Associated Higgs production with squarks

If one of the top squarks is light and its coupling to the h boson is enhanced, an additional process might provide a new source for Higgs particles in the MSSM: the associated production with $\tilde{t}$ states [445–447]. Since the associated production of the heavier H and A bosons with stop pairs is, together with h production with heavier stops, phase space suppressed, while the associated production with bottom squarks leads to smaller cross sections in general [448] we will, in the following, consider only the associated production of the h boson with a pair of lightest top squarks at the LHC:

$$pp \to gg, q\bar{q} \to \tilde{t}_1 \tilde{t}_1 h \tag{3.36}$$

At lowest order, i.e. at $\mathcal{O}(G_\mu \alpha_s^2)$, the process is initiated by diagrams that are similar to the ones which occur in the $pp \to t\bar{t}h$ process, Fig. 3.51, with additional diagrams provided by
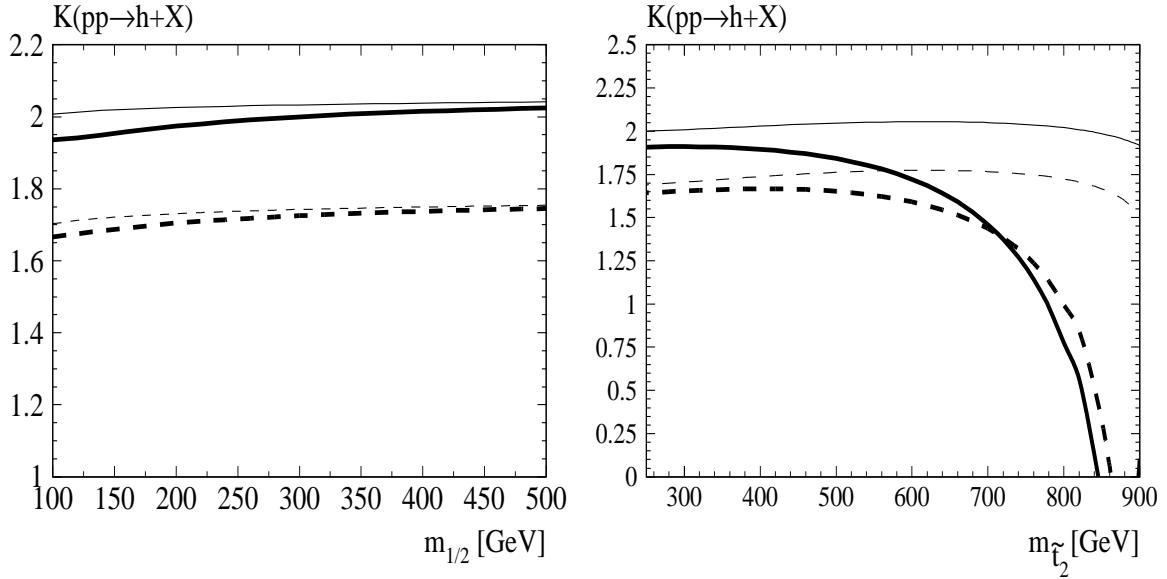
Figure 3.50: The K–factors for $gg \to h$ at the LHC at NLO (dashed lines) and NNLO (for the quark contribution, solid lines) in the case where the squark loop contributions are included (thick lines) or excluded (thin lines). They are as a function of $m_{1/2}$ in the SPS1a mSUGRA scenario with $m_0 = A_0 = 100$ GeV, $\tan\beta = 10$ and $\mu > 0$ (left) and as a function of $\tilde{t}_2$ in a "gluophobic" Higgs scenario where $m_{\tilde{t}_L} = 200$ GeV and $\theta_t = \frac{\pi}{4}$; from Ref. [248].

the quartic $gg\tilde{t}\tilde{t}$ interaction. Due to the larger gluon flux at the LHC, the contribution of the gg–fusion diagrams is much larger than the one of the $q\bar{q}$ annihilation diagrams.
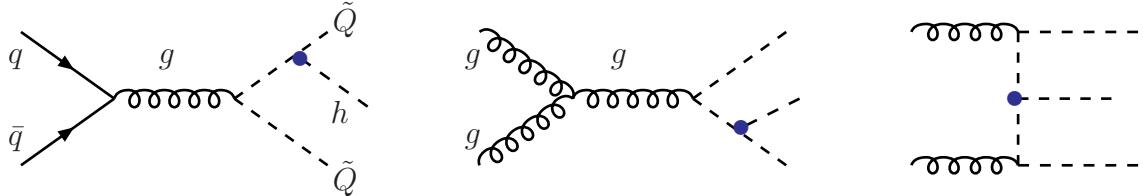

Figure 3.51: Generic Feynman diagrams for the associated Higgs production with squarks in hadronic collisions, $pp \to q\bar{q}, gg \to \tilde{Q}\tilde{Q}h$.

Except for the overall strength and the impact of phase space, the main features of the production cross sections follow, in fact, those discussed in the case of the loop contributions of the top squarks to the hgg vertex amplitude. In the right–hand side of Fig. 3.52, the $pp \to \tilde{t}_1\tilde{t}_1 h$ production cross section is displayed as a function of $m_{\tilde{t}_1}$ for $\tan\beta = 2$ or 30, in the case of no stop mixing $[A_t = 200 GeV, \mu = 400$ GeV], moderate mixing $[A_t = 500$ GeV and $\mu = 100$ GeV] and large mixing $[A_t = 1.5$ TeV and $\mu = 100$ GeV]. We have, in addition, used the usual simplifying assumption $m_{\tilde{t}_L} = m_{\tilde{t}_R} \equiv M_S$.

In the no–mixing case, $\tilde{t}_1$ and $\tilde{t}_2$ have the same mass and approximately the same couplings to the h boson since the m_t^2/M_Z^2 components are dominant, eq. (1.109). The cross section, which should be then multiplied by a factor of two to take into account both squarks,
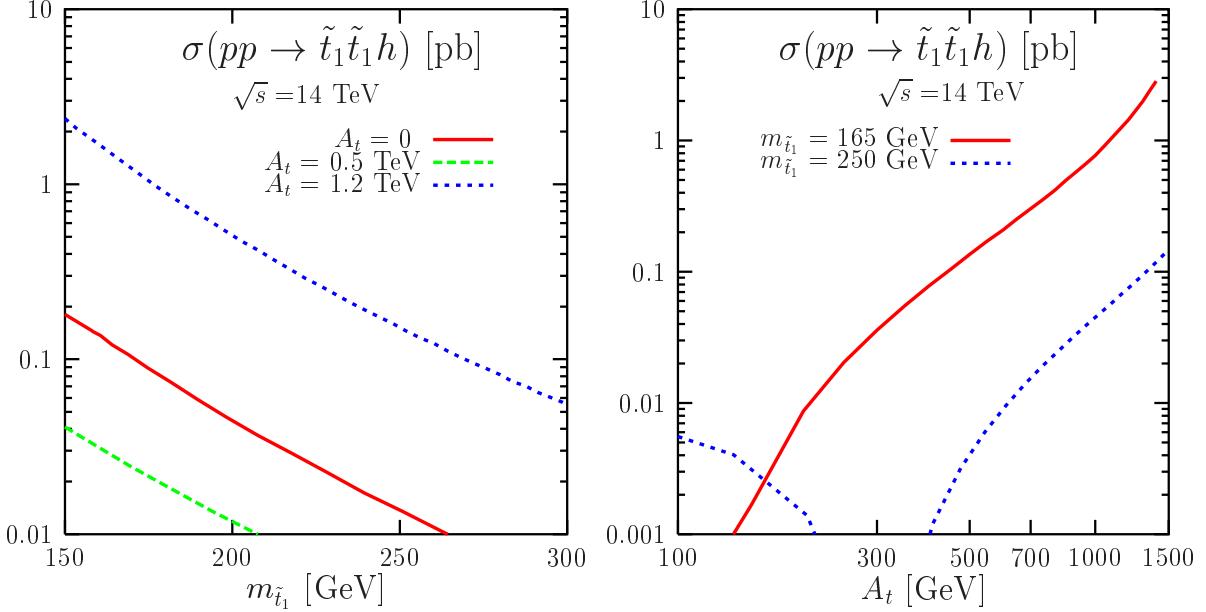
Figure 3.52: The production cross section for the process $\sigma(pp \to \tilde{t}_1\tilde{t}_1 h)$ [in pb] at the LHC as a function of $m_{\tilde{t}_1}$ and three sets of A_t values (left) and as a function of A_t for two values of the stop mass $m_{\tilde{t}_1} = 165$ and 250 GeV. The CTEQ4 parton densities have been used and $m_t = 175$ GeV; adapted from Ref. [445].

is comparable to $\sigma(pp \to t\bar{t}h)$ in the low stop mass range, $m_{\tilde{t}} \lesssim 200$ GeV. For intermediate values of A_t, the two components of the $h\tilde{t}_1\tilde{t}_1$ coupling interfere destructively and partly cancel each other resulting in a rather small cross section, unless $m_{\tilde{t}_1} \sim \mathcal{O}(100)$ GeV. In the strong mixing case $A_t \sim 1.5$ TeV, $\sigma(pp \to \tilde{t}_1\tilde{t}_1 h)$ can be very large: it is above the rate for the standard process $pp \to t\bar{t}h$ for values of $m_{\tilde{t}_1}$ smaller than ~ 200 GeV. If $\tilde{t}_1$ is lighter than the top quark, the $\tilde{t}_1\tilde{t}_1 h$ cross section significantly exceeds the one for $t\bar{t}h$ final states. For instance, for $m_{\tilde{t}_1} = 140$ GeV [which, nevertheless, could lead to a too light h boson, $M_h \lesssim 90$ GeV], $\sigma(pp \to \tilde{t}_1\tilde{t}_1 h)$ is an order of magnitude larger than $\sigma(pp \to t\bar{t}h)$. The same features can be seen in the right–hand side of the figure, where we fix the stop mas to $m_{\tilde{t}_1} = 165$ GeV and 250 GeV and display the $pp \to \tilde{t}_1\tilde{t}_1 h$ cross section as a function of A_t.

In the interesting region where $\sigma(pp \to \tilde{t}_1\tilde{t}_1 h)$ is large, i.e. for light stop eigenstates, $\tilde{t}_1 \to b\chi^+$ is the dominant decay mode of the top squark and χ_1^+ will mainly decay into bW^+ plus missing energy leading to $\tilde{t}_1 \to bW^+$ final states. This is the same topology as the decay $t \to bW^+$ except that, in the case of the $\tilde{t}$, there is a large amount of missing energy. The only difference between the final states generated by the $\tilde{t}\tilde{t}h$ and $t\bar{t}h$ processes will be due to the softer energy spectrum of the charged leptons coming from the chargino decay in the former case, because of the energy carried by the invisible LSP. The Higgs boson can be tagged through its $h \to \gamma\gamma$ decay mode. As discussed previously, this mode can be substantially enhanced compared to the SM case for light top squarks and large $\tilde{A}_t$ values. Therefore, $\gamma\gamma+$ charged lepton events can be more copious than in the SM and the

contributions of the $pp \to \tilde{t}\tilde{t}h$ process to these events can render the detection of the h boson easier than with the process $pp \to t\bar{t}h$ alone. For the other possible decays of $\tilde{t}_1$, that is, decays into $c\chi_1^0$ or three or four–body body into $\tilde{t}_1 \to b\chi_1^0 f\bar{f}'$ states [449], the situation might be more complicated. Dedicated analyses need to be performed to assess to which extent the lighter MSSM Higgs boson is observable in this channel.

3.4.3 Higgs decays into SUSY particles

A feature which might drastically affect the phenomenology of the MSSM Higgs bosons at the LHC is the possibility of decays into SUSY particles if they are light enough. The rates for these decays in various situations have been discussed in §2.2.3. Here, we summarize the main consequences of these decays and briefly comment on two possibilities: the invisible Higgs decays of a SM–like Higgs boson and the decays of the heavier neutral H/A bosons into neutralinos which lead to multi–lepton final states.

Invisible Higgs boson decays

We have seen in §2.2.3 that invisible decays of the lighter MSSM Higgs boson, $h \to \chi_1^0\chi_1^0$, are still possible for small values of M_2 and μ and, even more, when the gaugino mass universality, which leads to the relation $M_2 \sim 2M_1$, is relaxed allowing for small M_1 values and, hence, lighter LSPs, without being in conflict with the experimental limits on the chargino mass. However, because the $h\chi_1^0\chi_1^0$ couplings are in general small, the branchings ratios are sizable only in rather special situations. For the heavier H and A bosons, the invisible decays are important only for low $M_{H,A}$ and $\tan\beta$ values when the standard decay modes are not too enhanced and when the other ino decays are not yet kinematically open. One should, therefore, not expect in general fully invisible Higgs decays in the MSSM.

A possible channel in the search of an invisible CP–even $\mathcal{H}$ boson at the LHC is the associated production with a gauge boson, $q\bar{q} \to \mathcal{H}V$, with $V = W, Z$ decaying leptonically [240, 450–452]. The signature is then a high p_T lepton and a large amount of $\slashed{E}_T$ in $\mathcal{H}W$ production and two hard leptons peaking at M_Z and large $\slashed{E}_T$ in $Z\mathcal{H}$ production. The backgrounds to these processes, mainly due to VV, Vjj and $t\bar{t}$, are very large. Parton level analyses [240, 451] have shown that a Higgs boson $\mathcal{H}$ coupling with full strength to the gauge bosons, $g_{\mathcal{H}VV} = 1$, and decaying invisibly with 100% probability can be detected in these channels with a significance that slightly exceeds 5σ if a high luminosity is collected and if $M_{\mathcal{H}} \lesssim 150$ GeV. The mass reach can be extended to $M_{\mathcal{H}} \sim 250$ GeV using the process $pp \to t\bar{t}\mathcal{H}$ [453], if the same conditions are met. However, recent realistic simulations [454] show that these conclusions were too optimistic.

Another possibility for searching for invisible MSSM Higgs boson decays is the vector boson fusion production channel, $qq \to \mathcal{H}qq \to qq + \slashed{E}_T$ [455]; see also the recent analysis of

Ref. [452]. Again, in a parton level analysis, it has been shown in Ref. [455] that only 10 fb^{-1} data are needed for a 5σ observation of a Higgs boson with a SM $\mathcal{H}VV$ coupling and decaying 100% of the time invisibly, for masses up to $M_{\mathcal{H}} \sim 500$ GeV. Recently, two fast simulations have been performed for this channel by ATLAS and CMS [454], taking into account the various backgrounds [the important most one, Vjj, can be estimated from data] as well as trigger and detector efficiencies.

The output is that a SM–like Higgs boson with a mass up to $M_{\mathcal{H}} \sim 250$ GeV and an invisible decay branching ratio of $\sim 50\%$ can be probed at the 95% CL with a luminosity of 10 fb^{-1} only. This is shown in the left–hand side of Fig. 3.53 where the sensitivity parameter $\zeta^2 = \mathrm{BR}(\mathcal{H} \to \mathrm{inv}) \times g^2_{\mathcal{H}VV}$ is plotted against $M_{\mathcal{H}}$. In the MSSM, the previous conclusion thus holds for the $h\,(H)$ boson in the (anti–)decoupling limit only. In this case, the region of parameter space in the M_2–μ plane in which invisible h decays with $M_h \sim 120$ GeV can be probed, is shown in the right–hand side of Fig. 3.53 for $\tan\beta = 5$ and $M_1 = 0.2M_2$. In the region above the line for the ATLAS sensitivity, the invisible branching ratio is too small and the h boson can be detected in other decay channels.
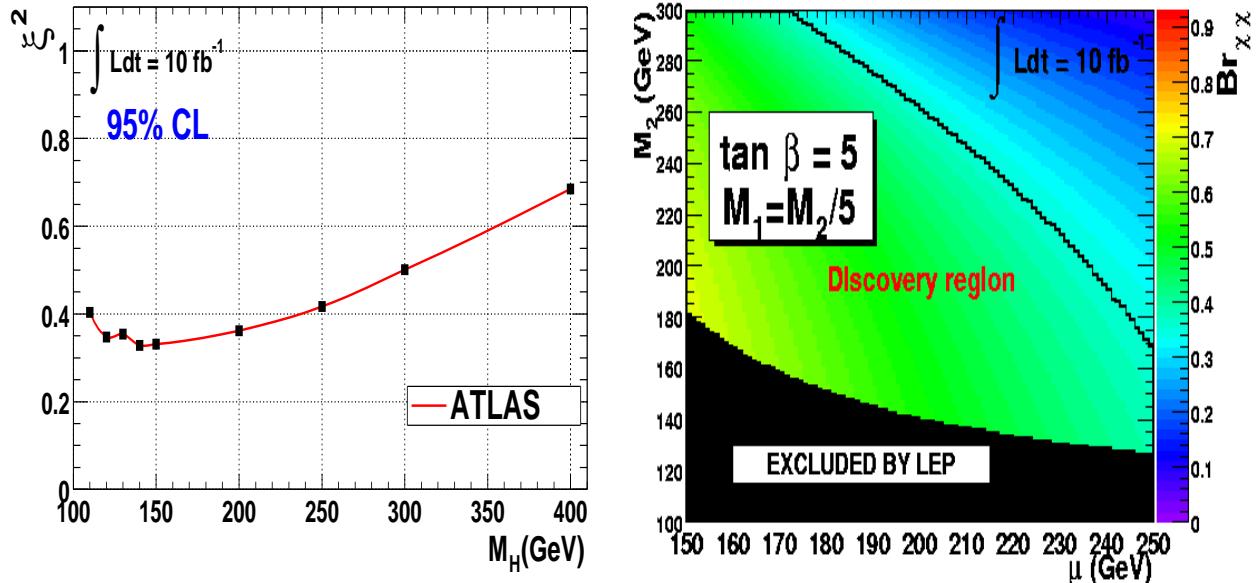

Figure 3.53: The sensitivity to the invisible decay signal of a CP–even MSSM Higgs boson at the 95% CL at the LHC as a function of the Higgs mass for $\mathcal{L} = 10$ fb^{-1} in an ATLAS simulation with $\zeta^2 = BR(\mathcal{H} \to inv.) \times g^2_{\mathcal{H}VV}$ (left) and the branching ratio for the invisible decay in the M_2–μ plane in the case where gaugino mass universality is relaxed, with the line indicating the ATLAS sensitivity limit; from Ref. [454].

Heavier Higgs decays into inos

The decays of the H, A and $H^{\pm}$ bosons into heavier charginos and neutralinos, when they occur, have in general much larger rates than the invisible decays and can even dominate over the SM modes in some favorable situations; see Figs. 2.32–33. These decays, although theoretically discussed since a long time [456], have been considered for some time as being devastating for the MSSM Higgs boson searches at hadron colliders, the main problem being the huge background generated by SUSY itself. However, there are favorable regions of the parameter space where the signals are clean enough to be detected at the LHC. One of the possibilities is that the heavier neutral Higgs bosons decay into pairs of the second lightest neutralinos, $H/A \to \chi_2^0 \chi_2^0$, with the subsequent decays of the latter into the LSP and leptons, $\chi_2^0 \to \tilde{\ell}^* \ell \to \chi_1^0 \ell \ell$ with $\ell^{\pm} = e^{\pm}, \mu^{\pm}$, through the exchange of relatively light sleptons. This leads to four charged leptons and missing energy in the final state. If the H/A bosons are produced in the gg–fusion processes, there will be little hadronic activity and the $4\ell^{\pm}$ final state is clean enough to be detected.

A simulation for this processes has been made in Ref. [457], taking into account the performance of the CMS detector and the various SM and SUSY backgrounds. The latter is largely dominating but with suitable cuts it can be reduced to the level where a convincing signal is standing above it in favorable regions of the MSSM parameter space. This is exemplified in the left–hand side of Fig. 3.54 where the $4\ell^{\pm}$ invariant mass spectrum is shown for $M_A = 350$ GeV, $\tan\beta = 5$ and the SUSY parameters set to $M_2 = 2M_1 = 120$ GeV, $\mu = -500$ GeV, $m_{\tilde{\ell}} = \frac{1}{4}m_{\tilde{q}} = 250$ GeV, which leads to relatively light χ_2^0 neutralino states and not too heavy sleptons.

In fact, because $\mathrm{BR}(H/A \to \chi_2^0 \chi_2^0) \to 4\ell^{\pm}$ is large, the observation of the signal can be extended to larger $\tan\beta$ and M_A values and even to higher M_2 values which lead to heavier neutralinos. This is shown in the right–hand side of Fig. 3.54 where the discovery reach at the LHC in the M_A–$\tan\beta$ plane is displayed. With high luminosities, a sizable portion of the plane is covered and, interestingly enough, this range includes the wedge $M_A \sim 150$ GeV and $\tan\beta \sim 5$ where the H, A bosons are very difficult to detect through the standard processes, while the h boson is almost SM–like. Thus, SUSY decays of Higgs bosons could not only be an additional means to detect the MSSM Higgs particles but they can allow for their discovery in areas where the standard searches are inefficient.

A more complete study of the 4ℓ channel for other combinations of $H/A \to \chi_i\chi_j$ final states, including the possibility of light sleptons in which the Higgs bosons can also decay, has appeared recently [458]. Note, however, that too optimistic conclusions that could be drawn from the previous discussion should be tempered: in other [larger] portions of the MSSM parameter space, small $m_{\tilde{\ell}}$ values lead to rather light τ sleptons [in particular at high $\tan\beta$] implying that τ final states are dominant in chargino and neutralino decays [92, 459]
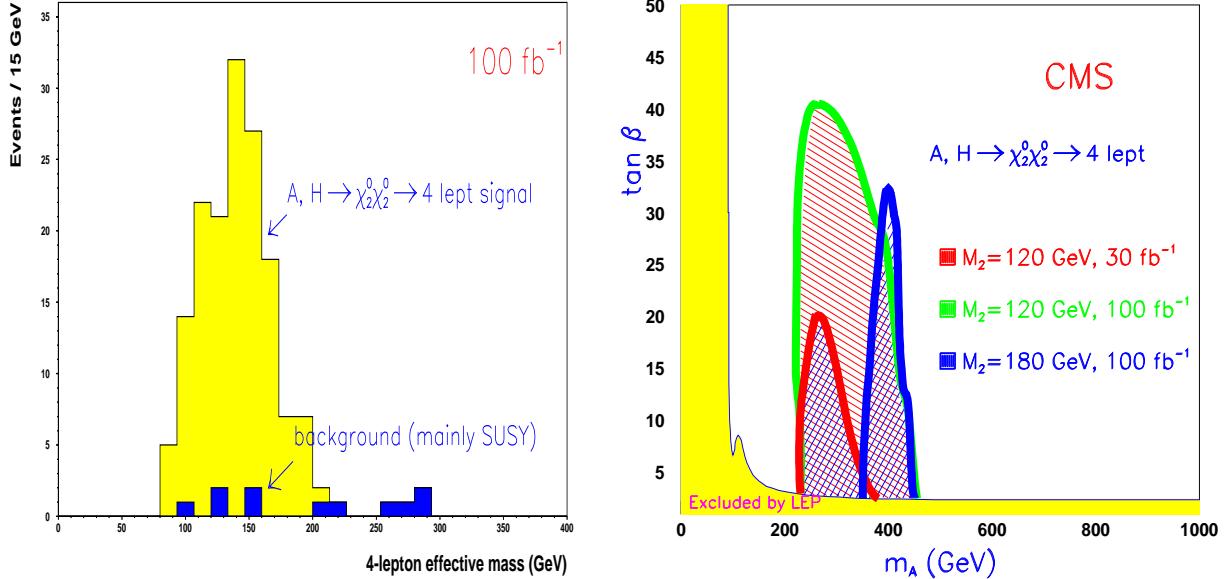
Figure 3.54: *The invariant $4\ell^{\pm}$ mass spectrum for $A/H \to \chi_2^0 \chi_2^0 \to 4\ell^{\pm} + X$ decays and the total SM and SUSY backgrounds (left) and the expected discovery reach for H/A bosons through this decay in the M_A–$\tan\beta$ plane for $\mathcal{L}=30$ and $100~fb^{-1}$ (right). The plots result from a CMS simulation performed in Ref. [457].*

and they are more difficult to detect. In addition, the decays into third generation squarks, which tend to dominate over all other decays when kinematically accessible, are far more difficult to observe. Thus, SUSY decays are still a potentially dangerous situation in the MSSM and more studies are needed in this area.

3.4.4 Higgs production from cascades of SUSY particles

A potential source of MSSM Higgs bosons at the LHC is the cascade decays of squarks and gluinos [278, 460–462] which are copiously produced in hadronic collisions via strong interactions. These particles could then decay into the heavy inos $\chi_2^{\pm}$ and $\chi_{3,4}^0$ and, if enough phase space is available, the latter decay into the lighter ones $\chi_1^{\pm}$ and $\chi_{1,2}^0$ and Higgs bosons

$$
\begin{aligned}
pp \to \tilde{g}\tilde{g}, \tilde{q}\tilde{q}, \tilde{q}\tilde{q}^*, \tilde{q}\tilde{g} &\to \chi_2^{\pm}, \chi_{3,4}^0 + X \\
&\to \chi_1^{\pm}, \chi_{1,2}^0 + h, H, A, H^{\pm} + X
\end{aligned}
\tag{3.37}
$$

Another possibility is the direct decay of squarks and gluinos into the lightest charginos $\chi_1^{\pm}$ and the next–to–lightest neutralinos χ_2^0 which then decay into the LSP and Higgs bosons

$$
\begin{aligned}
pp \to \tilde{g}\tilde{g}, \tilde{q}\tilde{q}, \tilde{q}\tilde{q}^*, \tilde{q}\tilde{g} &\to \chi_1^{\pm}, \chi_2^0 + X \\
&\to \chi_1^0 + h, H, A, H^{\pm} + X
\end{aligned}
\tag{3.38}
$$

224

In Ref. [462], the decay chain in eq. (3.37) was dubbed the "big cascade" and the one in eq. (3.38) the "little cascade" [462]. Generic Feynman diagrams for these two cascades, starting with either a gluino or a squark, are shown in Fig. 3.55.

Other possibilities for Higgs production in SUSY processes are the direct decays of heavier top and bottom squarks into the lighter ones and Higgs bosons, if large enough squark mass splitting is available [278, 462], $pp \to \tilde{t}_2 \tilde{t}_2^*, \tilde{b}_2 \tilde{b}_2^*$ with $\tilde{t}_2(\tilde{b}_2) \to \tilde{t}_1(\tilde{b}_1) + h/H/A$ or $\tilde{b}_1(\tilde{t}_1) + H^\pm$, as well as top quarks originating from SUSY particle cascades decaying into $H^\pm$ bosons, $pp \to \tilde{g}\tilde{g}, \tilde{q}\tilde{q}, \tilde{q}\tilde{q}^*, \tilde{q}\tilde{g} \to t/\bar{t} + X \to H^\pm + X$. These sfermionic decays have been discussed in §2.3 where the various partial widths have been given. No realistic simulation has been performed for these channels and we will not discuss them further here.
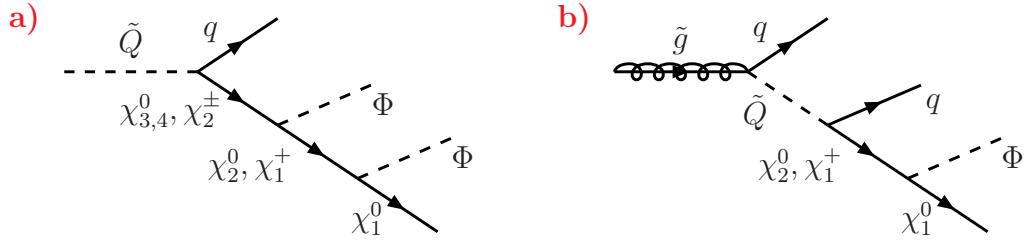

Figure 3.55: Generic Feynman diagrams for MSSM Higgs production through squark decays in the chargino/neutralino "big cascade" (a) and gluino decays in the "little cascade" (b).
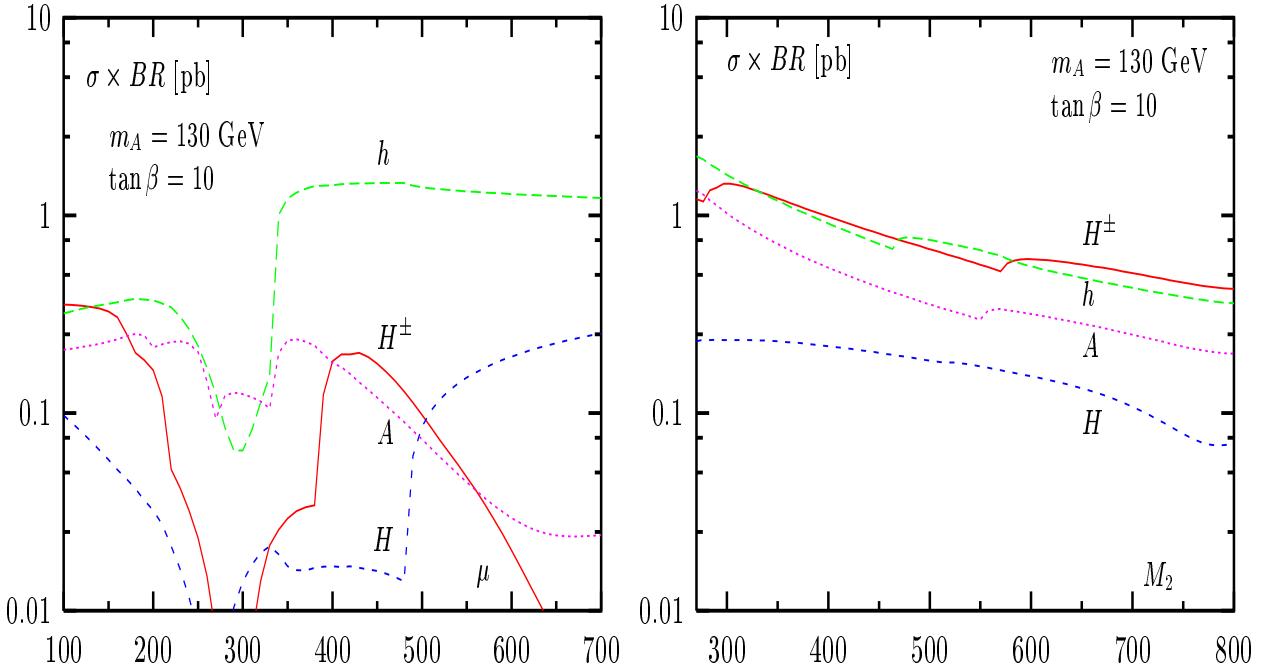
These SUSY cascade decays are interesting for at least two reasons, besides the fact that they provide a new source of MSSM Higgs bosons which must be considered anyway: i) the couplings involved in the cascades are important ingredients of the weak scale SUSY Lagrangian and their measurement would provide essential informations on EWSB in the MSSM; and ii) since the ino couplings to Higgs bosons do not depend strongly on $\tan\beta$, they could allow for the detection of the heavier H, A and $H^\pm$ in the hole region 130 GeV $\lesssim M_A \lesssim$ 250 GeV and $\tan\beta \sim$ 5–10 in much the same was as Higgs boson decays into inos. The little cascades have been discussed some time ago [460, 461] for h and relatively light A, H and $H^\pm$ bosons and recently reanalyzed in a somewhat broader perspective, with the big cascades included [462]. We briefly summarize this study below.

The rates for MSSM Higgs production in squark and gluino cascades depends on several ingredients: the relative mass between squarks and gluinos and the mixing in the stop/sbottom sectors which determine the starting point of the cascade and the amount of heavy inos from the two–body decays of squarks and the three–body decays of gluinos, the parameters in the gaugino sector which control the mass splitting between the inos and their couplings to Higgs and gauge bosons, and the parameters in the Higgs sector which give

the Higgs masses and couplings. A full analysis in the pMSSM is therefore very involved. Two scenarios allow however to highlight the main features:

– Sc2: $M_2 = 2M_1 = 300$ GeV, $\mu = 450$ GeV, $m_{\tilde{g}} = 900$ GeV and $m_{\tilde{q}} = 1080$ GeV $\sim \frac{1}{2}m_{\tilde{l}}$.

– Sc3: $M_2 = 2M_1 = 350$ GeV, $\mu = 150$ GeV, $m_{\tilde{g}} = 1200$ GeV and $m_{\tilde{q}} = 800$ GeV $\sim \frac{1}{2}m_{\tilde{l}}$.

In Sc2 (Sc3), the squarks are heavier (lighter) than gluinos while the heavier inos have dominant higgsino (gaugino) components, implying gaugino (higgsino) like light charginos and neutralinos. The variation of the cross sections times branching ratios to obtain at least one neutral or charged Higgs boson in the final state from the big or little cascades, or from both, is shown in Fig. 3.56 as a function of μ for Sc2 and of M_2 for Sc3 for the choice $M_A = 130$ GeV and $\tan\beta = 10$. As one can see, in both scenarios the cross sections times branching ratios for the four Higgs bosons can be rather large, exceeding the level of 0.1 pb in large areas of the parameter space and, even, reaching the picobarn level in some cases. These conclusions hold in, fact, even for larger pseudoscalar Higgs mass values, $M_A \sim 200$ GeV, and for different $\tan\beta$ values, $\tan\beta \lesssim 20$.


Figure 3.56: The cross sections times branching ratios for the production of at least one neutral or one charged MSSM Higgs boson in cascades of squarks and gluinos in the two scenarios Sc2 (left) and Sc3 (right) discussed in the text for the values $M_A = 130$ GeV and $\tan\beta = 10$; from Ref. [462].

A Monte–Carlo study that takes into account the various signals as well as the SM and SUSY backgrounds at the LHC, using ISAJET [463], and includes a fast simulation of some important aspects of the response of the CMS detector [464] has been performed. For neutral

226

Higgs bosons decaying into $b\bar{b}$ pairs, the SM and the more important SUSY backgrounds can be efficiently suppressed by rather simple selection criteria. In the two scenarios above, but with slightly different inputs in the Higgs sector, $M_A = 150$ GeV and $\tan\beta = 5$ [which leads to smaller cross sections than in Fig. 3.56], it has been shown that the neutral Higgs bosons are visible after a few years of low luminosity running at the LHC. This is shown in Fig. 3.57 where the $b\bar{b}$ invariant mass spectrum is displayed. One can see that in Sc2, a large signal peak is visible, corresponding to the h boson that is abundantly produced in the little cascades, and a smaller and broader peak can be observed, signaling the presence of A and H bosons coming from the big cascades. The latter peaks are more clearly visible in Sc3.
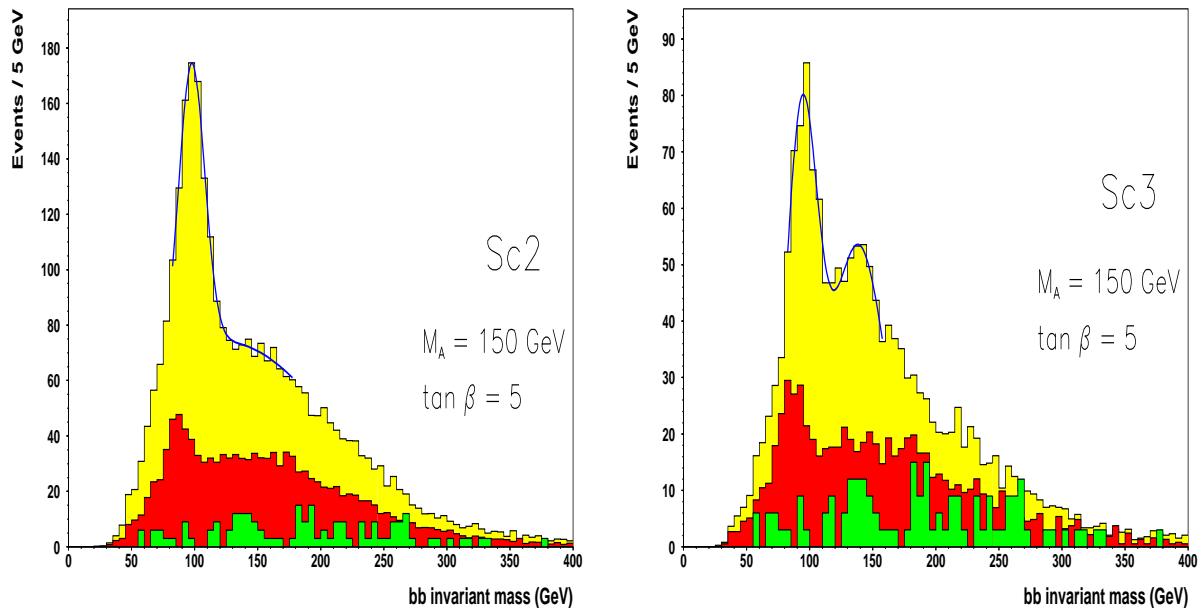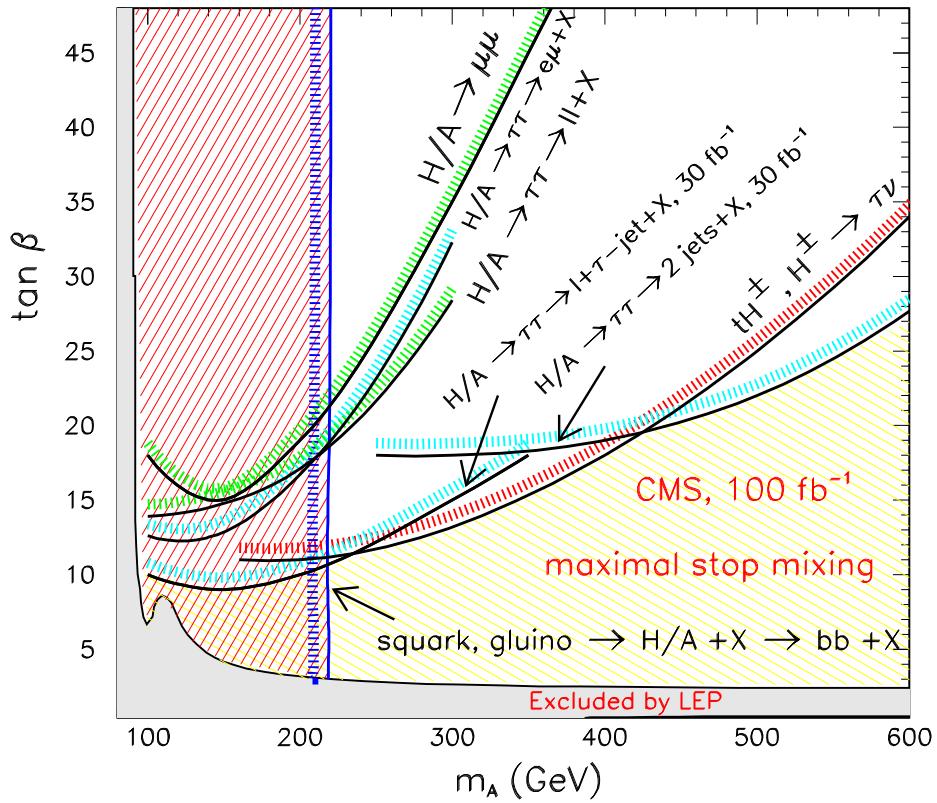

Figure 3.57: Distribution of the $b\bar{b}$ invariant mass for the SUSY signal events on top of the SUSY cascade (red) and SM (green) backgrounds assuming scenarios Sc2 and Sc3 discussed in the text for $M_A = 150$ GeV and $\tan\beta = 5$ and with 30 fb^{-1} integrated luminosity, as a result of a simulation performed in Ref. [462].

The evidence in the $H^{\pm}$ case, where the decay $H^- \to \tau\nu$ has also been studied, is less convincing as the mass peak cannot be reconstructed. But with the use of τ–polarization and with the help of the MSSM relation between $M_{H^{\pm}}$ and M_A, one could attribute the observed excess in τ–jet events, if it is large enough, to the production of charged Higgs particles in these cascades.

This analysis of the Higgs bosons produced in SUSY cascades shows that the search in this alternative mechanism looks very promising and could be complementary to the standard searches. This is exemplified in Fig. 3.58, which shows the usual M_A–$\tan\beta$ plane with the contours for which the MSSM Higgs particles can be observed in various search

channels and where we have added the region $M_A \lesssim 200$ GeV in which the neutral Higgs bosons can be detected in the scenario Sc3. This area also includes the wedge region at low M_A and moderate $\tan\beta$ values where only the h boson can be observed at the LHC. Similar contours can be drawn for other cases and more studies are, however, needed to cover the many possible scenarios. We stress, again, that these cascade processes are important not only because they represent a new source of Higgs bosons but, also, because they will be very useful to measure the sparticle–Higgs couplings which are essential ingredients to reconstruct the SUSY Lagrangian. More detailed studies, some of which have already started [465], are therefore needed in this context.


Figure 3.58: The areas in the M_A–$\tan\beta$ parameter space where the MSSM Higgs bosons can be discovered at CMS in the scenario Sc3 described in the text with an integrated luminosity of 100 fb^{-1}. Various detection channels are shown in the case of the standard searches for the maximal stop mixing scenario. The right–hatched and cross–hatched regions show the areas where only the lightest h boson can be observed in these production channels. The left–hatched area is the region where the heavier CP–even H and pseudoscalar A bosons can be observed through the (big) cascade decays of squarks and gluinos in the scenario Sc3 with $M_2 = 350$ GeV. From Ref. [462].

4 MSSM Higgs production at lepton colliders

At e^+e^- colliders [466–473], the main production mechanisms for the CP–even neutral Higgs bosons of the MSSM are simply those of the SM Higgs boson: Higgs–strahlung [160–162] and WW fusion [162,317,474]. The only difference is the range taken by the masses of the h and H particles and their couplings to the gauge bosons [250,475,476]. Most of the analytical expressions presented for the SM Higgs boson in §4 of the first part of this review will thus hold and will not be repeated here. There is, however, an additional channel which is very important in the MSSM context: the associated production of the CP–even Higgs particles h and H with the pseudoscalar Higgs boson A [163,164]. This channel has been already encountered when we discussed the limits from the neutral MSSM Higgs boson searches at LEP2, §1.4.2. For the charged Higgs particles, the two main production mechanisms, direct pair production in e^+e^- collisions [163,173] and production from top quark decays [178] have been also briefly discussed when we summarized the experimental constraints on the charged Higgs mass in §1.4.2.

These main production channels for the neutral and charged Higgs bosons will be discussed in detail in respectively, §4.1 and §4.3, including the electroweak radiative corrections [not only those involved in the Higgs masses and couplings but also the direct corrections to the processes, which have been almost completed recently] and their experimental detection at e^+e^- colliders. The production cross sections will be updated and, for the numerical analyses, we will use the FORTRAN code HPROD [477]. To incorporate the radiative corrections in the MSSM Higgs sector we will use, as usual, the benchmark scenario of the Appendix for illustration with the corrections implemented, again, in the RG improved effective potential approach using the routine SUBH [131]. The direct radiative corrections to these processes have been evaluated in various approximations in Refs. [478–491].

There also higher–order production processes for the neutral Higgs bosons, some of which are important when it comes to the study their fundamental properties: the ZZ fusion mechanism, the associated production with heavy fermions [492–494], the double Higgs–strahlung [144,495,496] as well as some other subleading mechanisms [229,485,486,497–499]; they will be discussed in §4.2. The higher–order processes for charged Higgs production [492, 500–506] will be presented in §4.3.4. Finally, some production channels involving relatively light SUSY particles [446,507–510] will be analyzed in §4.4.

At the end of this chapter, we will briefly discuss MSSM neutral Higgs production as s–channel resonances at $\gamma\gamma$ and $\mu^+\mu^-$ colliders. Most of material needed for this purpose has been already presented in the relevant sections of the first part of this review, namely, §I.4.5 and §I.4.6. Here, we will simply summarize the additional information which can be obtained in these modes for the aspects of MSSM Higgs physics that cannot be probed in a

satisfactory way in the e^+e^- option of future linear colliders. Detailed reviews on the other physics potential of these two collider modes can be found in Refs. [511–514] and [515, 516] for, respectively, the $\gamma\gamma$ and $\mu^+\mu^-$ options. Finally, in the last section of this chapter, we will discuss the tests and consistency checks of the MSSM Higgs sector that one can achieve via the high–precision measurements which can be performed at lepton colliders in the various options. The complementarity of the searches and measurements at the lepton colliders with those which will be performed at the LHC will be summarized. Here, also, we will be rather brief as a very detailed review on the subject has appeared only recently [517].

4.1 Neutral Higgs production at e^+e^- colliders

4.1.1 The main production mechanisms

The main production mechanisms of the MSSM neutral Higgs bosons at e^+e^- colliders are the Higgs–strahlung [158, 160, 161] and the pair production [163, 164] processes [Fig. 4.1]:

$$\text{Higgs} - \text{strahlung} : \quad e^+e^- \; \longrightarrow \; (Z^*) \longrightarrow Z + h/H \qquad (4.1)$$

$$\text{pair production} : \quad e^+e^- \; \longrightarrow \; (Z^*) \longrightarrow A + h/H \qquad (4.2)$$

as well as the WW fusion processes for the CP–even Higgs bosons [474]:

$$\text{WW fusion process} : \quad e^+e^- \; \longrightarrow \; \nu \, \bar\nu \; (W^*W^*) \longrightarrow \nu \, \bar\nu \; + h/H \qquad (4.3)$$

Because of CP–invariance, the CP–odd Higgs boson A cannot be produced in the strahlung and fusion processes at leading order, as has been noticed previously.
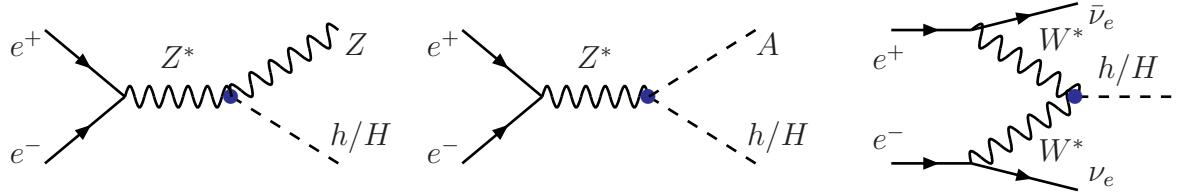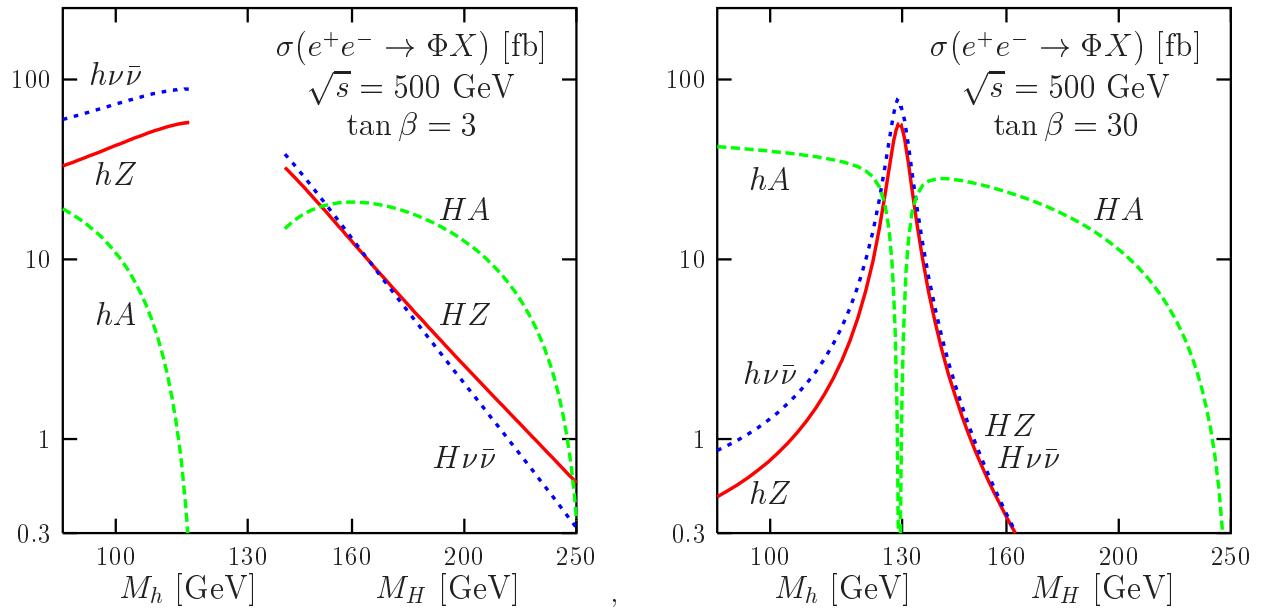

Figure 4.1: The main channels for MSSM neutral Higgs production in e^+e^- collisions.

Denoting as usual the CP–even Higgs particles by $\mathcal{H} = h, H$, the cross sections for the four bremsstrahlung and pair production processes are given, in terms of the SM cross section for Higgs–strahlung $\sigma_{\rm SM}(e^+e^- \to \mathcal{H}Z)$, the reduced couplings of the Higgs bosons to gauge bosons $g_{\mathcal{H}VV}$, and the phase–space factor which accounts for the correct suppression of the P–wave cross sections near the threshold for $\mathcal{H}A$ production, by [250, 475, 476]

$$
\begin{aligned}
\sigma(e^+e^- \to Z\mathcal{H}) &= g_{\mathcal{H}VV}^2 \, \sigma_{\rm SM}(e^+e^- \to \mathcal{H}Z) \\
\sigma(e^+e^- \to A\mathcal{H}) &= g_{\mathcal{H}AV}^2 \, \sigma_{\rm SM}(e^+e^- \to \mathcal{H}Z) \times \frac{\lambda_{A\mathcal{H}}^3}{\lambda_{Z\mathcal{H}}(\lambda_{Z\mathcal{H}}^2 + 12M_Z^2/s)}
\end{aligned}
\qquad (4.4)
$$

230

The cross sections for the strahlung and pair production processes, as well as the cross sections for the production of the light and the heavy CP–even Higgs bosons h and H, are mutually complementary to each other coming either with a coefficient $\sin^2(\beta - \alpha)$ or a coefficient $\cos^2(\beta - \alpha)$ [88]. Since $\sigma_{\rm SM}(e^+e^- \to \mathcal{H}Z)$ is large, at least one of the CP–even Higgs bosons should be detected. The cross sections are shown in Figs. 4.2 and 4.3 as functions of the CP–even Higgs masses for the values $\tan\beta = 3$ and 30 at c.m. energies $\sqrt{s} = 500$ GeV and 1 TeV, respectively. The usual maximal mixing scenario with $M_S = 2$ TeV is adopted for the implementation of the radiative corrections in the MSSM Higgs sector.

In the Higgs–strahlung processes, the production cross section for the h boson is large for small values of $\tan\beta$ and/or large values of M_A where $\sin^2(\beta - \alpha)$ approaches its maximal value. In these two cases, the cross sections are of the order of ~ 50 fb at $\sqrt{s} = 500$ GeV which, for an integrated luminosity of $\mathcal{L} = 500$ fb^{-1}, corresponds to ~ 25.000 events. In contrast, the cross section for the heavier H boson is large for large $\tan\beta$ and a light A boson, implying small M_H. As anticipated, for the associated production channels $e^+e^- \to Ah$ and AH, the situation is opposite to the previous case: the cross section for Ah is large for light A and/or large values of $\tan\beta$, whereas AH production is preferred in the complementary region. At $\sqrt{s} = 500$ GeV, the sum of the two cross sections decreases from ~ 50 fb to ~ 10 fb if M_A increases from ~ 90 to 200 GeV.


Figure 4.2: *The production cross sections of the neutral h, H, A bosons in the main mechanisms in e^+e^- collisions, Higgs–strahlung, associated pair production and WW fusion, as a function of the CP–even Higgs masses for the values $\tan\beta = 3$ (left) and 30 (right). The c.m. energy is fixed to $\sqrt{s} = 500$ GeV and the radiative corrections are implemented in the maximal mixing scenario $X_t = \sqrt{6}M_S$ with $M_S = 2$ TeV. The direct radiative corrections to the processes, ISR and beamstrahlung effects have not been included.*
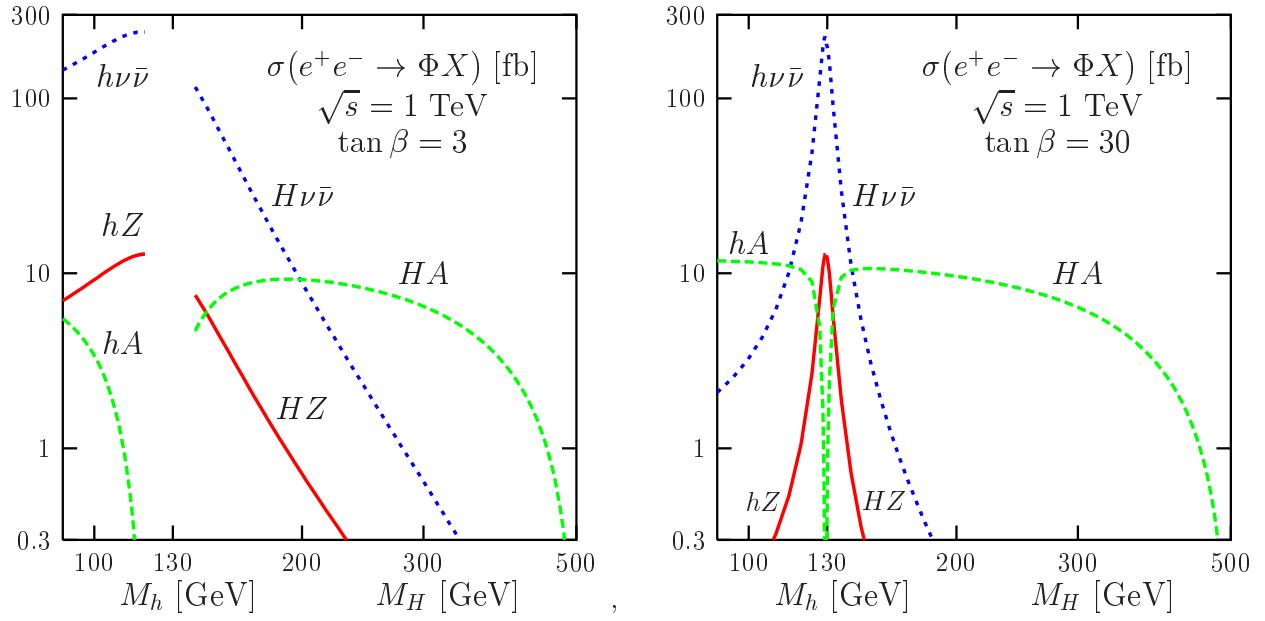
Figure 4.3: The same as Fig. 4.2 but for a c.m. energy of $\sqrt{s} = 1$ TeV.

Note that for a fixed Higgs mass and far from the production threshold, the cross sections are smaller at higher energies in both the Higgs–strahlung and the associated pair production channels, as the two processes are mediated by s–channel Z boson exchange and the cross sections drop like $1/s$. In fact, since $M_h \lesssim 140$ GeV, the lighter h boson is accessible in these channels even for c.m. energies as low as $\sqrt{s} \sim 250$ GeV. Because of this $1/s$ behavior of the cross sections, it is in general more appropriate to operate at low center of mass energies where the rates are larger [recall that the maximum cross section in the Higgs–strahlung process is obtained for $\sqrt{s} \simeq \sqrt{2}M_{\mathcal{H}} + M_Z$; see §I.4.2.1].

At energies beyond LEP2, the WW fusion process which leads to associated Higgs bosons and $\nu\bar{\nu}$ pairs in the final state, provides an additional mechanism for the production of the CP–even neutral Higgs bosons. The cross sections can again be expressed in terms of the corresponding SM Higgs boson cross section [250, 475]

$$\sigma(e^+e^- \to W^*W^* \to \mathcal{H}\nu\bar{\nu}) \;\; = \;\; g_{\mathcal{H}VV}^2 \, \sigma_{\mathrm{SM}}(e^+e^- \to \mathcal{H}\nu\bar{\nu}) \tag{4.5}$$

The cross sections are also shown in Figs. 4.2 and 4.3 for, respectively, $\sqrt{s} = 500$ GeV and 1 TeV and, as in the case of the Higgs–strahlung process, the production of the lighter h and the heavier H bosons are complementary. As a result of the $M_W^{-2} \log(s/M_W^2)$ enhancement of the fusion cross section for low Higgs masses, the production rate in the $e^+e^- \to h\nu\bar{\nu}$ process is always larger than the corresponding rate in Higgs–strahlung at c.m. energies higher than $\sqrt{s} \gtrsim 400$ GeV. For H boson production, this is in general also the case for $\sqrt{s} = 500$ GeV and when M_H is small enough to allow for large production rates. As discussed earlier, see §I.4.2.2, WW fusion and Higgs–strahlung followed by the decay $Z \to \nu\bar{\nu}$ lead to the same

final state. However, the two processes can be disentangled by looking at the mass spectrum of the $\nu\bar{\nu}$ pair which, in the latter case, should peak at M_Z.

In the decoupling limit, $M_A \sim M_H \gg M_Z$, similarly to what has been discussed in several instances, only the h boson is accessible in Higgs–strahlung and vector boson fusion

$$M_A \gg M_Z \quad : \quad e^+e^- \to hZ \ \text{ and } \ e^+e^- \to h\nu\bar{\nu} \tag{4.6}$$

with cross sections that are very close to the SM–Higgs production cross section. The other processes are suppressed by the $\cos^2(\beta-\alpha) \to 0$ factor, leading to negligible rates. The only exception is the pair production of the heavier CP–even and CP–odd Higgs bosons

$$M_A \gg M_Z \quad : \quad e^+e^- \to HA \ \text{ if } \ \sqrt{s} > M_A + M_H \tag{4.7}$$

which, being proportional to the factor $\sin^2(\beta - \alpha) \to 1$, is not suppressed and is thus accessible if the c.m. energy of the collider is high enough. As usual, in the anti–decoupling limit, $M_H \sim M_h^{\max}$, the role of the CP–even h and H bosons are reversed.

4.1.2 Radiative corrections to the main channels

Higgs–strahlung and associated production

The one–loop radiative corrections to Higgs–strahlung and associated Higgs production have been first calculated in Refs. [479,480] and have been updated and completed more recently in Ref. [481]. The main component of these corrections is due to the Higgs boson propagators which, as discussed earlier, can be mapped in the RGE improved renormalization of the angle α which enters in the couplings of the MSSM Higgs bosons to the Z boson. This renormalization has been performed not only at $\mathcal{O}(\alpha)$, but at two–loop order in the strong and third generation Yukawa coupling constants as discussed in detail in §1.3. For a complete calculation, however, one has to consider in addition to the corrections to the CP–even and CP–odd Higgs boson propagators, where the momentum dependence should be included, the following set of corrections [see the generic Feynman diagrams shown in Fig. 4.4].
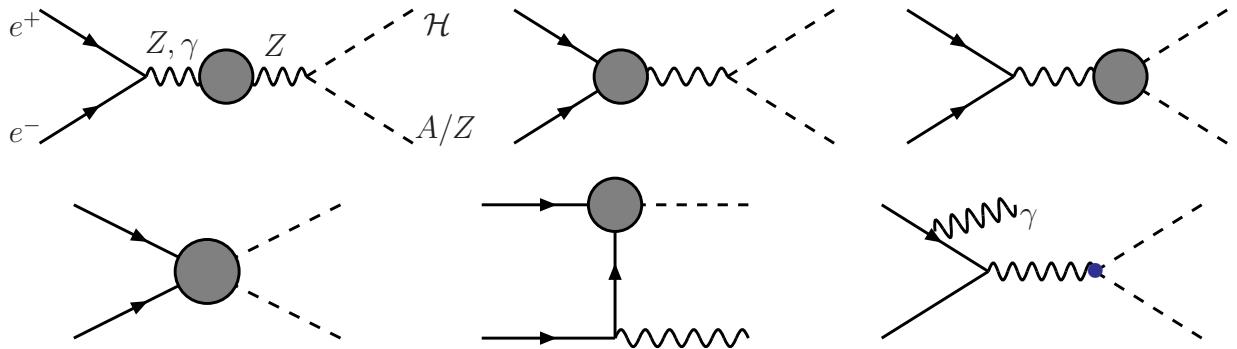

Figure 4.4: Generic Feynman diagrams for the $\mathcal{O}(\alpha)$ corrections to $e^+e^- \to \mathcal{H}Z$ and $\mathcal{H}A$.

233

i) One–loop corrections to the electron and Z boson self–energies, as well as the $Z\gamma$ mixing, and corrections to the initial Ze^+e^- vertex. These corrections are similar to those occurring in the SM and are, typically, at the level of a few percent. The SUSY particle contributions are in general rather small in this context.

ii) Corrections to the $ZZ\mathcal{H}$ and $Z\mathcal{H}A$ final vertices. These are qualitatively the same as those which affect the ZZH_{SM} vertex discussed in §I.2.4.2. They are also small in general but they can reach the level of 10% for very small or very large values of $\tan\beta$ when the Higgs Yukawa couplings to top or bottom quarks become very strong.

iii) Box diagrams and t–channel contributing diagrams, which depend strongly on the c.m. energy. They are rather small at LEP2 energies where they stay at the level of a few percent, but can be extremely large at higher c.m. energies, reaching the level of several 10% at $\sqrt{s} = 1$ TeV, as in the case of the $e^+e^- \to ZH_{\text{SM}}$ process discussed in §I.4.2.3.

iv) Finally, electromagnetic corrections to the initial state with virtual photonic corrections and initial state photon radiation. These corrections are exactly the same as those affecting the $e^+e^- \to ZH_{\text{SM}}$ cross section and can be implemented using the structure function approach discussed in §I.1.2. The corrections are in general large and positive [except near the kinematical production threshold] since they decrease the effective c.m. energy, which thus increases the cross sections, $\sigma \propto 1/s$.
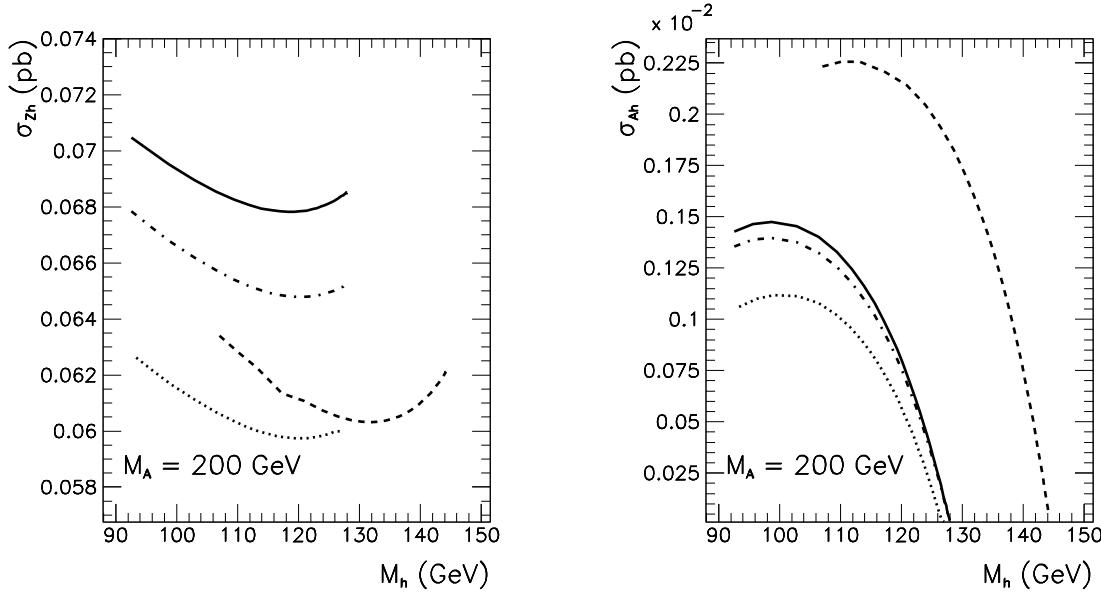
The effect of the full set of radiative corrections on the cross sections is exemplified in Fig. 4.5 for $e^+e^- \to hZ$ and hA production at a c.m. energy of $\sqrt{s} = 500$ GeV as a function[33] of M_h in the maximal mixing scenario with $M_A = 200$ GeV; the squark masses are set to $M_S = 1$ TeV while the slepton masses are chosen to be $m_{\tilde{\ell}} = 300$ GeV. The results are shown for the case [481] where the full one–loop corrections are included in the Feynman diagrammatic approach (dashed lines) and are compared to the case where the two–loop improved calculation of the mixing angle α is performed including and excluding the box contributions (solid and dot–dashed lines, respectively) and to the case where only the one–loop RG improved angle $\bar{\alpha}$ is used (dooted lines). Except in the latter case, the radiative corrections to the Higgs boson masses are included up to two loops. The differences in the cross section predictions are, first, due to the different values of M_h and $\bar{\alpha}$ and, second, to the inclusion or not of the vertex and box corrections.

As a general trend, the difference between the full one–loop and the RGE corrected cross sections can be rather large, being of the order of 10 to 15% for $\sigma(e^+e^- \to hZ)$ and 20% for $\sigma(e^+e^- \to hA)$. The inclusion of the two–loop corrections in $\bar{\alpha}$ increases (decreases)

---

[33]This parametrization of the cross sections in terms of two Higgs boson masses, M_A and M_h (or M_H), instead of the formal quantity $\tan\beta$, is more physical. Although leading to more involved expressions, this parametrization has the advantage of using physically well defined input quantities avoiding possible confusions from different renormalization schemes.

the $e^+e^- \to hZ\,(hA)$ cross section by more than 10%. The box contributions, which are more important at high energies, are at the level of 5 to 10% with the dominant component being the exchange of W and Higgs bosons. As can be seen from the figure, the main effect is, in fact, due to the different shift in the CP–even Higgs boson mass in the Feynman diagrammatic and RGE approaches which also alters the phase space. For high M_A values and at large $\tan\beta$, a sizable difference also occurs in the $e^+e^- \to hA$ channel when the box contributions are included. This is due to the fact that in this limit, the tree–level cross section is very small because of the $\cos^2(\beta - \alpha) \to 0$ decoupling, while the box diagrams induce contributions that are not proportional to the g_{hAZ} coupling and can be thus relatively much larger. However, in this case, the total cross section is anyway very small.


Figure 4.5: The production cross sections $\sigma(e^+e^- \to Zh)$ and $\sigma(e^+e^- \to Ah)$ as a function of M_h at $\sqrt{s} = 500$ GeV for $M_A = 200$ GeV in the maximal mixing scenario. The other input parameters are $M_S = \mu = M_2 = A_t = A_b = 1$ TeV while $m_{\tilde{\ell}} = 300$ GeV. The meaning of the various lines is described in the text; from Ref. [481].

In the case of the heavier CP–even Higgs production, the difference between the effective potential and the Feynman diagrammatic approaches is summarized in Fig. 4.6 where the cross sections $\sigma(e^+e^- \to HZ)$ and $\sigma(e^+e^- \to HA)$ are shown as a function of M_H, again, at $\sqrt{s} = 500$ GeV [480]. Similar conclusions as previously can be drawn in this case: the typical size of the differences between the two methods is in general 10–20% for this energy, but they can become quite large (60%) for the process $\sigma(e^+e^- \to ZH)$. The difference between the two approaches becomes more important with increasing energies, exceeding the level of 40% at $\sqrt{s} = 1$ TeV. Note also that the effect of the additional form factors in the Feynman diagrammatic approach grows and modifies the angular dependence of the cross sections compared to the effective Born approximation where they behave as $\sim \sin^2\theta$.

235
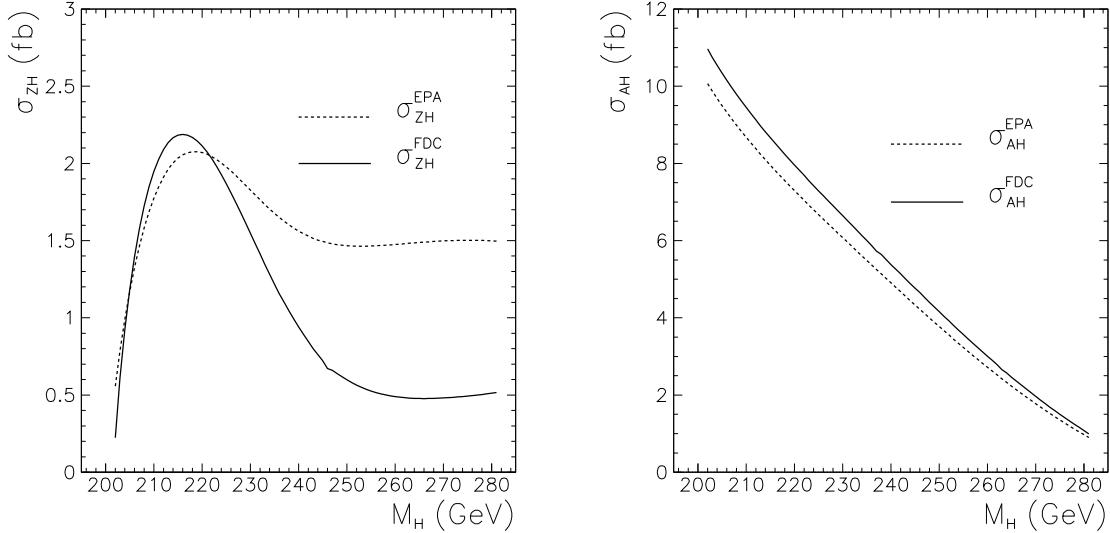
Figure 4.6: The cross sections $\sigma(e^+e^- \to ZH)$ and $\sigma(e^+e^- \to AH)$ as functions of M_H at a 500 GeV e^+e^- collider where the effective potential approach (EPA) is compared to the Feynman diagrammatic one (FDC); the other inputs are as in Fig. 4.5; from Ref. [480].

The fusion production processes

In the case of the fusion processes, $e^+e^- \to \mathcal{H}\nu\bar{\nu}$, the full set of one–loop radiative corrections is not yet available. While some important corrections, such as ISR, the external lepton and internal W boson propagator corrections as well as the $We\nu$ vertex corrections, should be the same as in the SM Higgs case [since the contribution of the SUSY particles is in general very small], the corrections to the $\mathcal{H}WW$ vertices and the box corrections should be different outside the decoupling regime when the case of the h boson is considered. The dominant corrections are expected to be those involving closed loops of fermions and sfermions, in particular those of the third generation which may have strong Yukawa couplings. These one–loop corrections have been calculated recently [483, 484] and we briefly summarize the main effects here; some generic Feynman diagrams are displayed in Fig. 4.7.
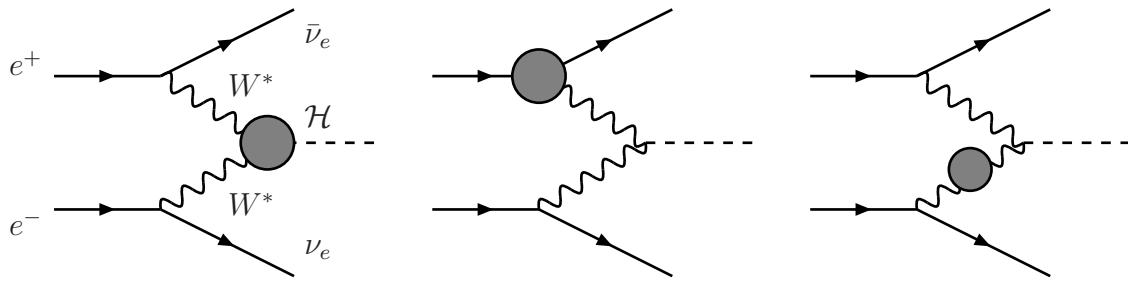

Figure 4.7: Generic diagrams for the corrections from (s)fermion loops to $e^+e^- \to \nu\bar{\nu}\mathcal{H}$.

236

As expected from what we have learned in the SM Higgs case, §I.4.2.3, the fermionic corrections to $\sigma(e^+e^- \to \nu\bar{\nu}h)$ are rather small if the renormalization of the mixing angle α is left aside [i.e. when the tree–level cross section is calculated with $\bar{\alpha}$ and the Higgs mass is radiatively corrected at the same order]. They are at the level of 1 to 5% in the entire range of M_A and $\tan\beta$ values and the SUSY loop contributions are in general very small, except for large values of the trilinear SUSY–breaking parameter A_t for which the $h\tilde{t}\tilde{t}$ couplings are strongly enhanced; in this case the sfermion correction become of the same size as the fermionic corrections. In the decoupling limit, one recovers the SM result, that is, a negative correction of approximately -2% at high enough c.m. energy, when the tree–level cross section is expressed in terms of G_μ and the corrected h boson mass is used.

The production cross sections for the process $e^+e^- \to \nu\bar{\nu}h$ at tree–level and at one–loop [483] are shown in Fig. 4.8 as a function of the c.m. energy for $M_A = 500$ GeV and the two values $\tan\beta = 3, 40$ in four benchmark scenarios: the maximal– and no–mixing scenarios, a gluophobic Higgs scenario where the squark loops are important [reducing drastically the Higgs coupling to gluons] and the vanishing–coupling scenario where the angle α is small. The main effect is, again, due to the Higgs propagator corrections which affect both the value of M_h and the coupling to gauge bosons. These corrections can change the cross section by up to $\sim 25\%$ but the other loop corrections are small staying, typically, below 2%.

In fact, the one–loop corrections are more interesting to investigate in the case of the production of the heavier CP–even H boson. Indeed, since for high M_H values one is close to the decoupling limit where the $e^+e^- \to \nu\bar{\nu}H$ cross section vanishes, the inclusion of the one–loop corrections in the HWW vertex will induce contributions that are not proportional to the tree–level coupling $g_{HWW} = \cos(\beta-\alpha) \to 0$, thus generating a non–zero production cross section. The situation is even more interesting if the H boson is too heavy to be produced in association with the CP–odd Higgs boson, $M_H \gtrsim \sqrt{s} - M_A$, but is still light enough to be produced in the fusion process with sizable rates. In most of the MSSM parameter space, this is obviously not the case, in particular, when SUSY particles are too heavy. However, there are scenarios where sfermions are light enough and couple strongly to the H boson to generate contributions which lead to sizable cross sections. This is, for instance, the case of the "enhanced $H\nu\bar{\nu}$ cross section" scenario of Ref. [483] where the squark masses are set at $M_S = 350$ GeV and the higgsino mass parameter to $\mu = 1$ TeV, while the trilinear couplings are such that $A_b \sim A_t$ with $X_t \sim 2M_S$ [which in the on–shell scheme corresponds to the maximal mixing scenario].

The effect of the fermion/sfermion radiative corrections to the $e^+e^- \to H\nu\bar{\nu}$ process is exemplified in Fig. 4.9 where the tree–level, the $\bar{\alpha}$ improved and the full one–loop cross sections are shown in the M_A–$\tan\beta$ parameter space in the unpolarized case (upper row) and with 100% longitudinal polarization of both the e_L^- and e_R^+ beams which increases the
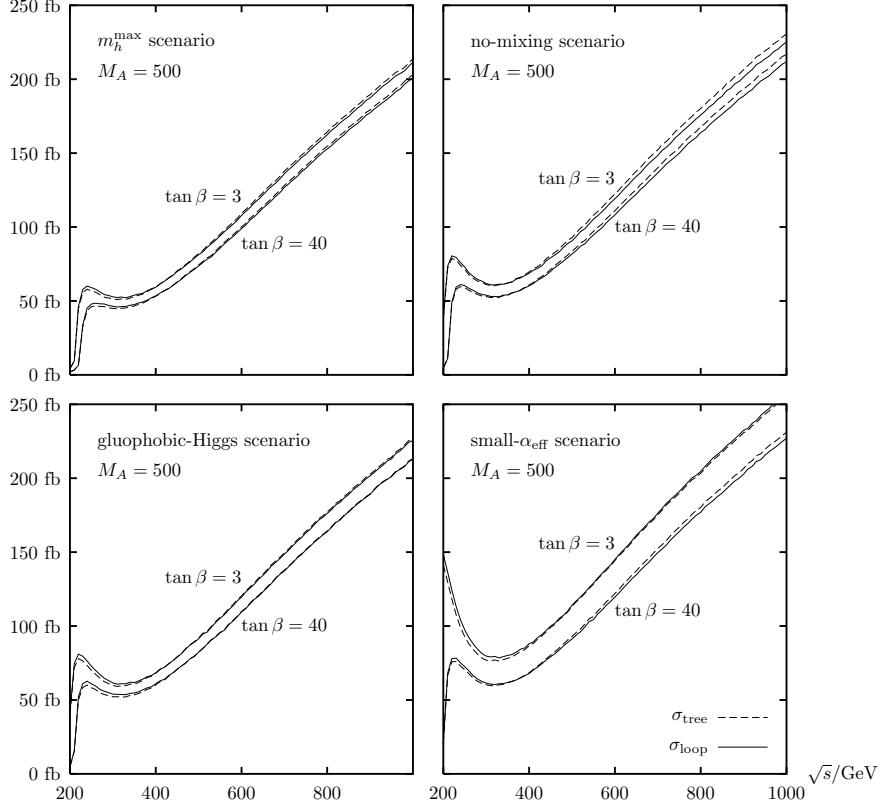
Figure 4.8: The tree–level and the one–loop corrected production cross sections for the process $e^+e^- \rightarrow \nu\bar{\nu}h$ *as a function of* $\sqrt{s}$ *for* $M_A = 500$ *GeV and* $\tan\beta = 3, 40$ *in four benchmark scenarios: maximal mixing [$X_t = 2M_S$ with $M_S = 1$ TeV, $m_{\tilde{g}} = 0.8M_S$ and $\mu = M_2 = 200$ GeV], no–mixing [$X_t = 0$ with $M_S = 2$ TeV, $m_{\tilde{g}} = 0.8M_S$ and $\mu = M_2 = 200$ GeV], gluophobic [$X_t = -2M_S$ with $M_S = 300$ GeV, $m_{\tilde{g}} = 500$ GeV and $\mu = M_2 = 300$ GeV] and small–α [$X_t = -1.1$ TeV with $M_S = 0.8$ TeV, $m_{\tilde{g}} = M_2 = 500$ GeV and $\mu = 2.5M_S$]; from Ref. [483].*

production rate by a factor of four (lower row). As can be seen, the effect of the radiative corrections is quite drastic. While the area where the cross section is larger than $\sigma \geq 0.02$ fb [which corresponds to 20 events for $\mathcal{L} = 1$ ab^{-1}] is rather small at tree–level and even smaller when only the renormalization of the angle α is included, it becomes rather large as a result of the fermion/sfermion contributions to the HWW vertex. The longitudinal polarization of the initial beams vastly improves the situation and the areas where the cross sections make the process observable are much larger than in the unpolarized case.

Note that the same type of discussion can be made in the case of the production of the pseudoscalar Higgs particle in the WW fusion mechanism, $e^+e^- \rightarrow A\nu\bar{\nu}$. The AWW coupling, which is absent at tree–level, is generated at a higher level [485, 486] by loop diagrams allowing the process to take place [additional contributions to the process might come from other sources such as box or pentagonal diagrams for instance]. This possibility will be discussed in the next section.
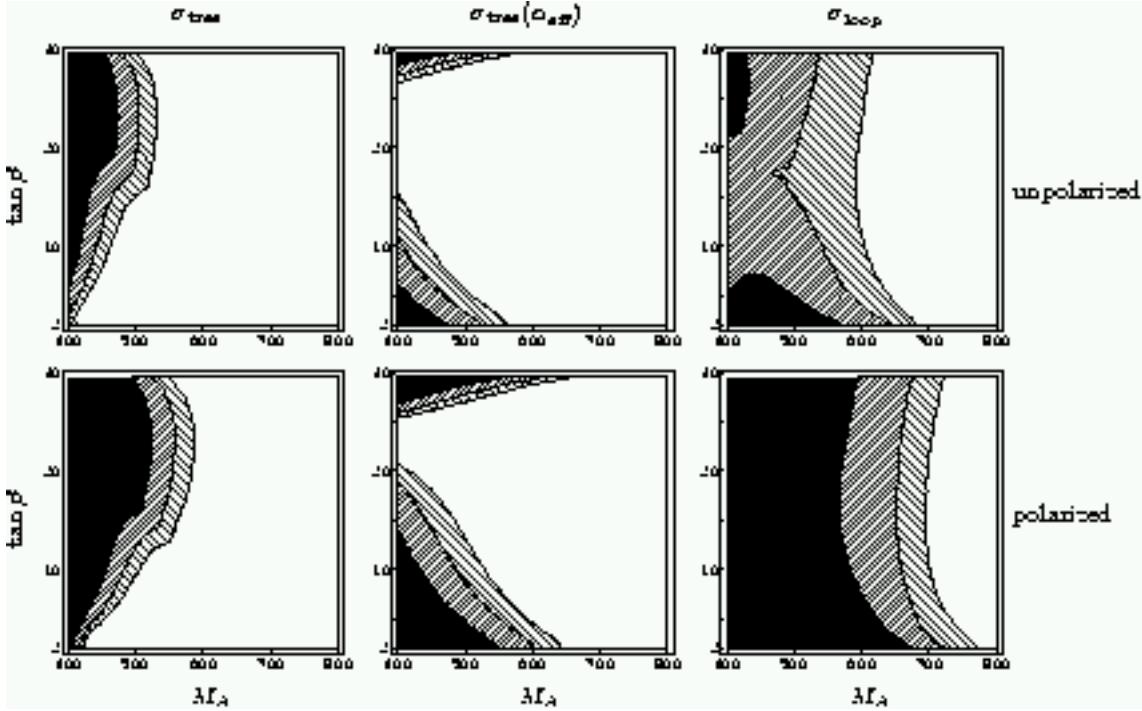
Figure 4.9: The cross sections for the process $e^+e^- \rightarrow \nu\bar{\nu}H$ in the M_A–$\tan\beta$ plane for $M_S = 350$ GeV and $\mu = 1$ TeV in the maximal mixing scenario at $\sqrt{s} = 1$ TeV. The tree–level cross section (left) including the finite wave–function corrections is compared to the $\bar{\alpha}$ approximation (middle) and the one–loop corrected cross section (right column). The upper (lower) row is for unpolarized (100% polarized) $e^\pm$ beams. The different shadings correspond to: white: $\sigma \leq 0.01$ fb, light shaded: $0.01 \leq \sigma \leq 0.02$ fb, dark shaded: $0.02 \leq \sigma \leq 0.05$ fb, black: $\sigma \geq 0.05$ fb. From Ref. [483].

4.1.3 Neutral Higgs boson detection

Decoupling and anti–decoupling regimes

In the decoupling and anti–decoupling regimes where, respectively, the lighter h and heavier H particle has SM–like couplings to weak vector bosons and to fermions, the search for the $\Phi_H = h$ or H boson follows exactly the same lines as the search for the SM Higgs boson [518, 519] in the low mass range, $M_{\Phi_H} \lesssim 140$ GeV, discussed in §I.4.4. The particle is produced in the Higgs–strahlung and WW fusion mechanisms with large cross sections and decays into $b\bar{b}$ pairs [and in the upper mass range, $M_{\Phi_H} \gtrsim 130$ GeV, into pairs of W bosons with one of them being off–shell] with large branching fractions. In fact, the recoil mass technique in the Higgs–strahlung process, $e^+e^- \rightarrow Z\Phi_H$, allows to detect the particle independently of its decay modes [and in particular, if it decays invisibly as will be discussed in a forthcoming section]. As mentioned previously, it would be more appropriate to search for this particle at relatively low center of mass energies, $\sqrt{s} \sim \sqrt{2}M_{\Phi_H} + M_Z \sim 250$–300 GeV, where the Higgs–strahlung cross section is maximal.

In the two regimes, the only accessible additional process will be the associated production of the pseudoscalar–like Higgs boson, $\Phi_A = H\,(h)$ in the (anti–)decoupling case, and the CP–odd A boson, $e^+e^- \to \Phi_A A$. The $Z\Phi_A A$ coupling has full strength, $g_{Z\Phi_A A} \simeq 1$, and the cross section is large except near the kinematical threshold $\sqrt{s} = M_A + M_{\Phi_A} \sim 2M_A$ where it drops sharply, being suppressed by the usual β^3 factor for spin–zero particle production. For large $\tan\beta$ values, both Φ_A and A decay mostly into $b\bar{b}$ and $\tau^+\tau^-$ pairs with branching ratios of approximately 90% and 10%, respectively. The final states will thus consist mainly into $b\bar{b}b\bar{b}$ and $b\bar{b}\tau^+\tau^-$ events. b–tagging is thus important, in particular in the $4b$ final state signature, to reduce the large four–jet and $t\bar{t}$ backgrounds. In the anti–decoupling limit with $M_{A,h} \gtrsim \mathcal{O}(M_Z)$ that is, slightly above the LEP2 bounds, one can simply extend the LEP2 analyses but with a much higher energy and luminosity; the only additional complication will be the larger $e^+e^- \to ZZ \to 4b$ background which has to be rejected by suitable cuts.
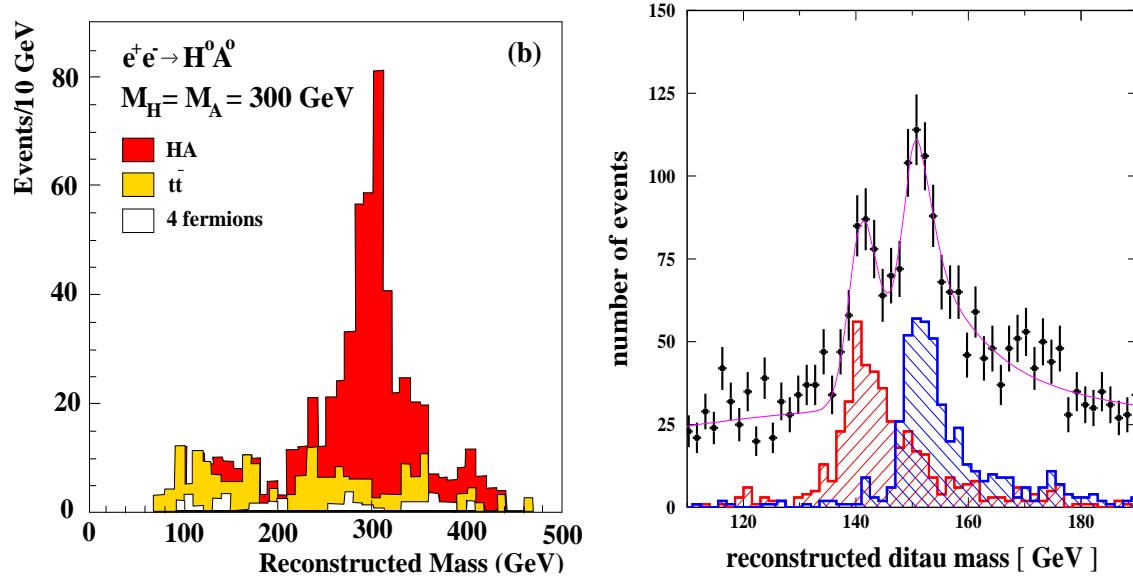

Figure 4.10: The Higgs boson mass peaks in the process $e^+e^- \to HA \to b\bar{b}b\bar{b}$ for $50\,fb^{-1}$ at $\sqrt{s} = 800$ GeV (left) and the reconstructed $\tau\tau$ invariant mass from a kinematic fit in the process $e^+e^- \to HA \to b\bar{b}\tau^+\tau^-$ for $M_A = 140$ GeV and $M_H = 150$ GeV at $\sqrt{s} = 500$ GeV with $500\,fb^{-1}$ data (right); from Refs. [470, 520].

In Refs. [470, 521], it has been shown with a full simulation that only 50 fb^{-1} data are sufficient to observe the $4b$ Higgs signal for $M_A = M_H = 350$ GeV at $\sqrt{s} = 800$ GeV. In the left–hand side of Fig. 4.10, the mass peak for $e^+e^- \to HA \to b\bar{b}b\bar{b}$ is shown for this energy and luminosity, but for Higgs boson masses $M_A = M_H = 300$ GeV; it is chiefly standing above the $t\bar{t}$ and 4–fermion backgrounds. More recently, another detailed study [520], including detector simulation and all SM backgrounds, has been performed for the associated Higgs pair production process in both the $b\bar{b}b\bar{b}$ and $b\bar{b}\tau^+\tau^-$ channels. A very good mass reconstruction is achieved using a kinematical fit which imposes energy momentum conservation. This

is exemplified in the right–hand side of Fig. 4.10 where the reconstructed $\tau^+\tau^-$ invariant mass from the fit is shown on top of the SM backgrounds for AH production with masses $M_A = 140$ GeV and $M_H = 150$ GeV at $\sqrt{s} = 500$ GeV with 500 fb^{-1} data.

Besides the possibility of measuring the production sections in the two channels, the kinematical fit allows a rather precise measurement of the masses of the CP–even and CP–odd Higgs bosons [473]. Representative values for two c.m. energies and some combinations of Higgs masses, of the measured sum and difference of the masses, as well as the $b\bar{b}b\bar{b}$ and $b\bar{b}\tau^+\tau^-$ cross sections are shown in Tab. 4.1 with a luminosity of 500 fb^{-1}. As can be seen, accuracies of the order of $\Delta M_\Phi/M_\Phi \sim 0.2\%$ can be achieved on the Higgs masses, while the production cross sections can be measured at the level of a few percent in the $b\bar{b}b\bar{b}$ channel and $\sim 10\%$ in the $b\bar{b}\tau^+\tau^-$ channel.

$\sqrt{s}$	M_A	M_H	$(M_A + M_H)$	$(|M_A - M_H|)$	$\sigma(b\bar{b}b\bar{b})$	$\sigma(b\bar{b}\tau\tau)$
500 GeV	140 GeV	150 GeV	0.2 GeV	0.2 GeV	1.5%	$\simeq 7\%$
500 GeV	200 GeV	200 GeV	0.4 GeV	0.4 GeV	2.7%	8%
800 GeV	250 GeV	300 GeV	0.5 GeV	0.7 GeV	3.0%	$\simeq 13\%$
800 GeV	300 GeV	300 GeV	0.6 GeV	0.7 GeV	3.5 %	10%

Table 4.1: Expected precision on the masses [in GeV] and cross sections [in %] of the heavier MSSM Higgs bosons produced in $e^+e^- \to HA$ at two c.m. energies $\sqrt{s} = 500$ GeV and 800 GeV with 500 fb^{-1} data for various Higgs boson masses; from Ref. [473].

The intense coupling regime

The intense-coupling regime, where $\tan\beta$ is rather large and the three neutral MSSM h, H and A bosons have comparable masses close to $M_h^{\max} \sim 110$–140 GeV, is possibly one of the most difficult scenarios to be resolved completely at future colliders. As discussed in §3.3.2, the detection of the individual Higgs boson signals is very challenging at the LHC. In e^+e^- collisions, thanks to the clean environment and the complementarity of the available production channels, the separation of the three Higgs bosons is possible.

The Higgs-strahlung processes first allow to probe the h and H bosons and to measure their masses from the recoiling mass spectrum against the Z boson. A detailed simulation of the signal and all main background processes has been performed in Ref. [522] at a c.m. energy $\sqrt{s} = 300$ GeV, including ISR and beamstrahlung effects as well as a simulation of a detector response. It was found that the most promising way of measuring M_h and M_H is to select first the $\ell^+\ell^-b\bar{b}$ event sample with $\ell = e/\mu$ and then apply the recoil Z boson mass technique to single out the $e^+e^- \to Zh/ZH$ processes. If some realistic b–tagging and kinematical cuts are applied, the discrimination of the two Higgs signal peaks is possible as shown in Fig. 4.11 (left) for the MSSM parameter point P1 introduced in §3.3.2, where

$M_A = 125$ GeV and $\tan\beta = 30$ leading to $M_h \simeq 124$ GeV and $M_H \simeq 134$ GeV. As indicated in the figure, with 500 fb^{-1} data, the h and H masses can be determined with a precision of the order of 100 MeV for h and 300 MeV for H at this energy.
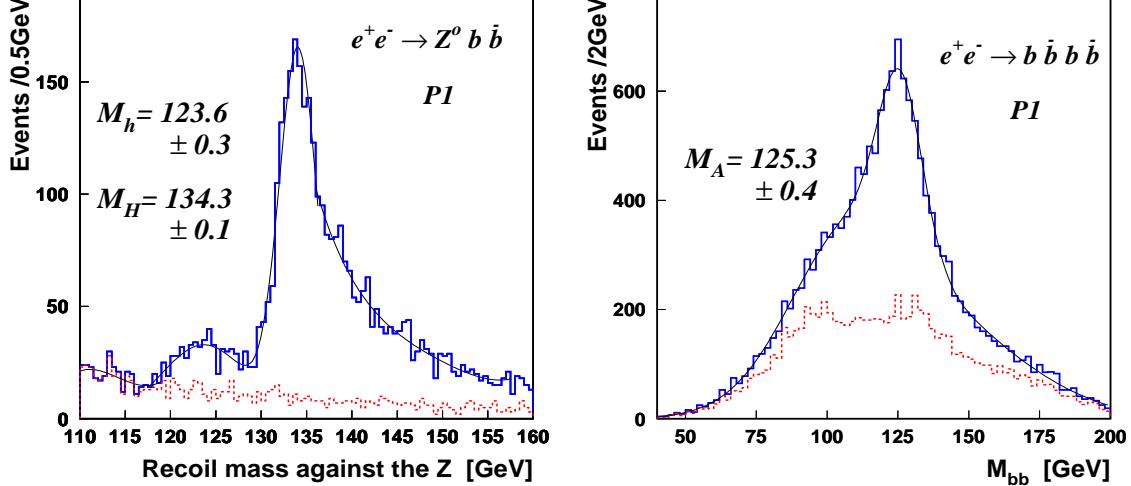

Figure 4.11: The recoil mass distributions for the signal and backgrounds including ISR, beamstrahlung and detector smearing for the parameter points P1 (M_A=125 GeV, $\tan\beta = 30$) after cuts and b–tagging (left), and the invariant mass of two b jets from the A boson after cuts and selection procedures for the same parameter point P1 (right); from Ref. [522].

The complementary pair production channels, $e^+e^- \to A + h/H$, allow to probe the CP–odd A boson. Since the h and H masses will be known from the recoil mass technique, the determination of the mass of the A boson can be made either via the reconstruction of the $b\bar{b}$ and/or $\tau^+\tau^-$ invariant masses, or through a threshold scan, similarly to what occurs in the decoupling regime [520, 521]. Promising results are obtained when selecting 4 b–jet events by means of b–tagging. A good separation of the "physical" combination of 2 b–jet pairs from the combinatorial background could be achieved with suitable cuts on the separation of the individual b quarks and the $b\bar{b}$ pairs. The selection of the pseudoscalar boson from the (Ah) and (AH) pairing, relies on the "combinatorial mass difference" method discussed in Ref. [522]. Resulting $b\bar{b}$ mass spectra for the MSSM parameter points P1 are shown in the right–hand side of Fig. 4.11. Only the 2 b–jet mass assigned to the A boson is displayed and all 4 b–jet background sources are taken into account. The mass of the pseudoscalar A boson can be measured with an accuracy of less than 400 MeV.

The same analysis has been performed for other scenarios in the intense coupling regime at $\sqrt{s} \simeq 300$ GeV and an integrated luminosity of 500 fb^{-1} and the uncertainties on the mass measurements of the neutral MSSM Higgs bosons are found to be of about 100–300 MeV for the two CP–even Higgs particles and 300–400 MeV for the CP–odd Higgs boson. These values are smaller than the typical mass differences as well as the natural widths of the Higgs bosons, but much worse than the accuracy on $M_{H_{\rm SM}}$, $\Delta M_{H_{\rm SM}} \sim 50$ MeV.

The vanishing and the intermediate–coupling regimes

In the regime where the coupling of the lighter MSSM Higgs particle to isospin down–type fermions is small or vanishing, the h boson will mostly decay into W pairs with one of the W bosons being off–shell and, to a lesser extent, into gluons and charm quarks; in the high mass range, $M_h \sim 130$–140 GeV even the decays into ZZ^* have sizable rates. This can be seen in Fig. 2.24 where the branching ratios for the various decays have been displayed in a particular scenario. Since the cross section for the strahlung process $e^+e^- \to hZ$ is almost not affected by this feature [as long as $\tan\beta > 1$], the h boson can be detected independently of any final state decay using the missing mass technique. Nevertheless, direct searches in the relevant topologies would allow to perform much better measurements [compared to the SM case] of the Higgs couplings to these particles. In particular, the information obtained from the measurement of the gluonic decay mode would be very interesting, as it is sensitive to new particles. In fact, even the other loop induced decays, $h \to \gamma\gamma$ and $Z\gamma$, would be more easily accessible as their branching fractions are increased by a factor of ~ 2.

The decays of the heavier neutral H and A bosons, as well as those of the charged Higgs particles, will not be affected by this scenario and the searches discussed for these particles in the decoupling regime will hold in this case. The only new effect might be that the relative size of the $b\bar{b}$ and $\tau^+\tau^-$ branching ratios of the H and A bosons and the tb and $\tau\nu$ branching ratios of the $H^\pm$ particles are affected. Indeed, as already discussed, the vanishing of the $hb\bar{b}$ coupling occurs in scenarios where both $\tan\beta$ and μ are large. In this case, the SUSY loop corrections to the $Ab\bar{b}, Hb\bar{b}$ and $H^+\bar{t}b$ couplings will be rather large and will affect the branching fractions in a sizable way as has been exemplified in Figs. 2.26–2.28.

Finally, in the intermediate regime where $\tan\beta \lesssim 5$ and $200 \lesssim M_A \lesssim 500$ GeV, both $\cos(\beta - \alpha)$ and $\sin(\beta - \alpha)$ are not too small [by definition of this regime]. In this case, there should be no problem for detecting the lighter h boson since at least the cross sections for $e^+e^- \to hZ$ and $e^+e^- \to h\nu\bar{\nu}$ processes should be large enough. For the heavier H particle, the cross section for $e^+e^- \to HZ$ should also be sizable and the decays $H \to WW$ and potentially $H \to ZZ$, as well as $H \to tt$ for $M_H \gtrsim 350$ GeV, have reasonable branching fractions. One can then use the same techniques for the SM–Higgs search in the high mass range but with lower production cross sections times branching ratios. The large luminosities which will be available ensure that the various final states will be detected.

For the pseudoscalar A particle, the cross section for $e^+e^- \to hA$ is not too suppressed so that one can use at least the $4b$ searches discussed above for the intense–coupling regime. Additional searches could be performed in the $b\bar{b}WW$ channel if the decays $h \to WW^*$ take place with sizable rates as well as in $A \to hZ$ decays for $M_A \lesssim 300$ GeV, which would lead to $e^+e^- \to hA \to hhZ$ final states. If enough c.m. energy is available, the process $e^+e^- \to HA$ will lead to a rich variety of final states. For $M_A \gtrsim 350$ GeV, the decays $H/A \to t\bar{t}$ can be

243

searched for in $t\bar{t}t\bar{t}$ or $t\bar{t}b\bar{b}$ final states. For a slightly lower M_A value, the very interesting decay $H \to hh$ [which can also be observed in $e^+e^- \to HZ \to Zb\bar{b}b\bar{b}$ events] as well as the decay $A \to hZ$ can be probed in this process. The production rates can be large enough to allow for the detection of all these topologies as shown in the left–hand side of Fig. 4.12 where the $e^+e^- \to HA$ cross section times the branching ratios for these decays is displayed at a c.m. energy $\sqrt{s} = 1$ TeV as a function of M_A for $\tan\beta = 3$ in the maximal mixing scenario. As can be seen, the rates exceed the femtobarn level in rather large areas allowing, for the planed luminosities, to collect a sample of signal events that is healthy enough to allow for cuts to suppress the various backgrounds and/or for detection efficiency losses.
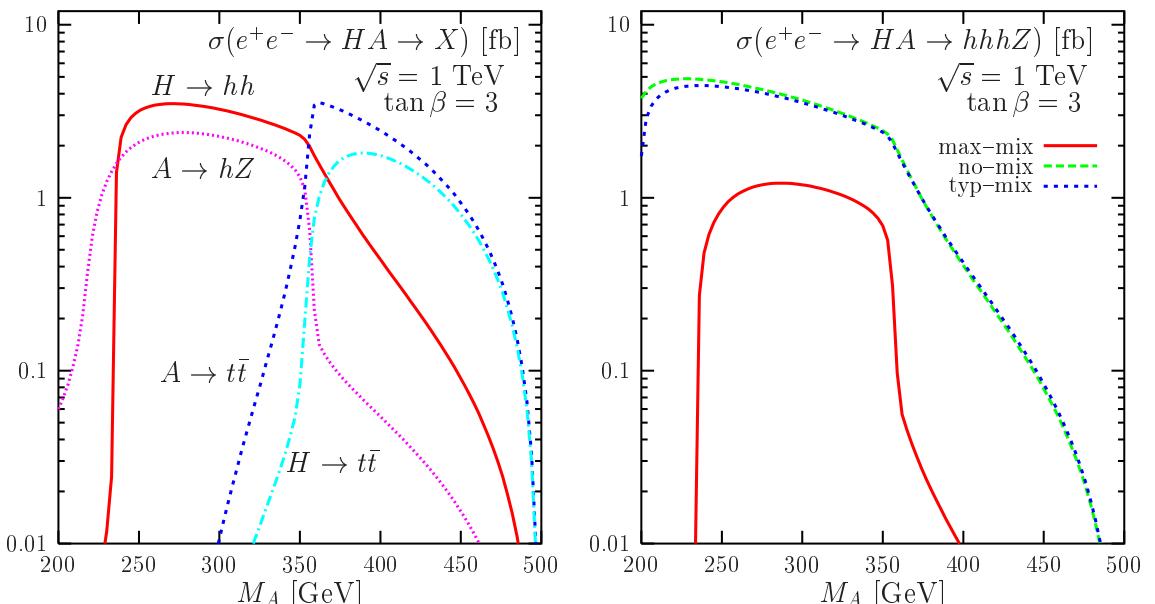

Figure 4.12: *Left: the cross section $\sigma(e^+e^- \to HA)$ times the branching ratios for the decays $H \to hh$, $A \to hZ$ and $H/A \to t\bar{t}$ as a function of M_A in the maximal mixing scenario. Right: $\sigma(e^+e^- \to HA) \times BR(H \to hh) \times BR(A \to hZ)$ as a function of M_A and three mixing scenarios $X_t = 0$ (no–mixing), $X_t = M_S$ (typical–mixing) and $X_t = \sqrt{6}M_S$ (maximal mixing) with $M_S = 2$ TeV. Both figures are for $\tan\beta = 3$ and $\sqrt{s} = 1$ TeV.*

However, the most spectacular process is undoubtedly associated $e^+e^- \to HA$ production with the subsequent Higgs decays $H \to hh$ and $A \to hZ$, leading to three Higgs particles and a Z boson in the final state. The rates for this process are not that small as shown in Fig. 4.12 where the cross section $\sigma(e^+e^- \to HA)$ times the branching ratios $BR(H \to hh) \times BR(A \to hZ)$ are shown again at $\sqrt{s} = 1$ TeV as a function of M_A for $\tan\beta = 3$ in the maximal, typical and no–mixing scenarios. In the mass range $230 \lesssim M_A \lesssim 350$ GeV, the rate is larger than 1 fb, leading to a thousand events for a luminosity $\mathcal{L} = 1$ ab^{-1}. The resulting $6b+Z$ final states will have little background and their detection should not be very problematic [except from combinatorial problems] with efficient b–tagging and once some of the many mass constraints are imposed.

244

4.2 Neutral Higgs production in higher–order processes

4.2.1 The ZZ fusion mechanism

As in the case of the SM Higgs particle, the ZZ fusion production channels which at tree–level occur only for the CP–even neutral Higgs bosons,

$$\text{ZZ fusion process} \qquad e^+e^- \ \longrightarrow \ e^+e^- \ (Z^*Z^*) \longrightarrow e^+e^- + h/H \tag{4.8}$$

follow the same trend as the corresponding WW fusion channels, $e^+e^- \to \nu\bar{\nu} + h/H$, but with cross sections that are approximately a factor of ten smaller as a result of the reduced neutral current couplings compared to the charged current couplings. This is shown in Fig. 4.13 at the two c.m. energies $\sqrt{s} = 500$ GeV and 1 TeV as a function of the Higgs masses for $\tan\beta = 3$ and 30. Nevertheless, when they are not suppressed by the coupling factors $\cos^2(\beta - \alpha)$ or $\sin^2(\beta - \alpha)$ and by phase space in the case of the H boson, the rates are still significant allowing to collect a few thousand events with the planed luminosities.
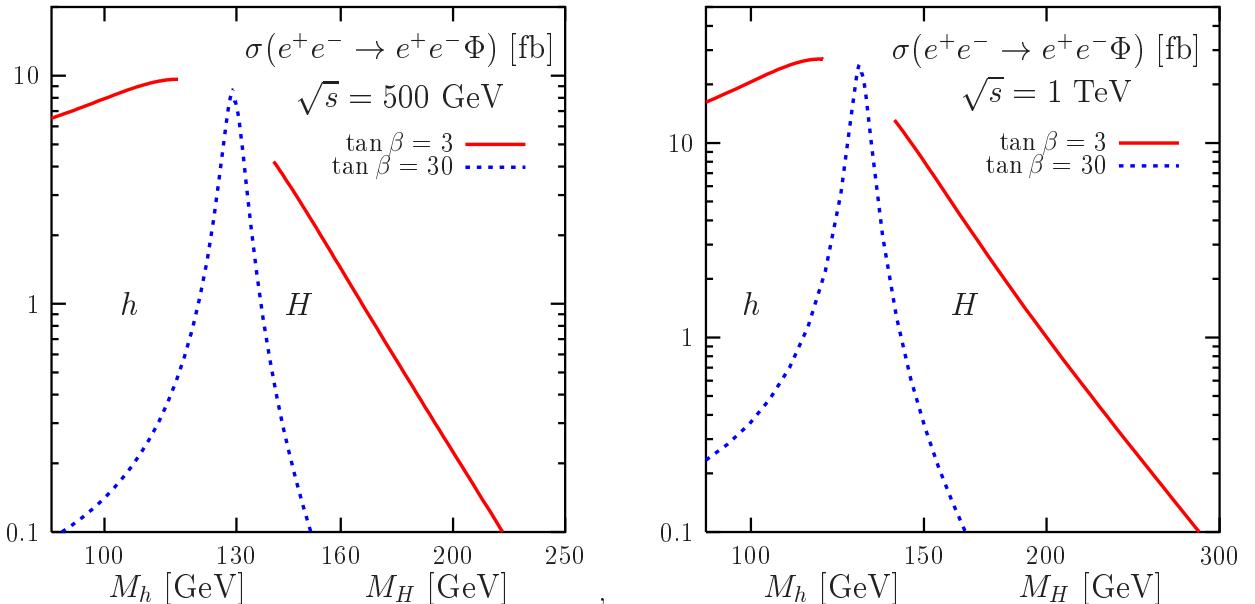

Figure 4.13: The production cross sections in the ZZ fusion channels $e^+e^- \to e^+e^- + h/H$ for $\tan\beta = 3$ and 30 as a function of the Higgs masses for two values of the c.m. energy, $\sqrt{s} = 500$ GeV (left) and 1 TeV (right).

Since the entire final states can be reconstructed, these processes allow for measurements that are cleaner than those which can be performed in the WW fusion channel. In addition, because at high energies the cross sections are not suppressed, as they grow as $\log(s/M_{\mathcal{H}}^2)$, in contrast to the Higgs–strahlung process whose cross section drops like $1/s$, one can use in the ZZ fusion process the missing mass technique familiar from Higgs–strahlung, as it was discussed in the case of the SM Higgs at the CLIC multi–TeV collider; see §I.4.4.4.

4.2.2 Associated production with heavy fermions

In the continuum, the associated production of the neutral MSSM Higgs particles with heavy top and bottom quarks, as well as with τ leptons [492],

$$\text{association with heavy fermions}: \quad e^+e^- \longrightarrow \gamma^*, Z^* \longrightarrow f\bar{f} + h/H/A \qquad (4.9)$$

proceeds primarily through the radiation off the heavy fermion lines as in the SM Higgs case. For these specific contributions, the cross sections are simply those discussed for the SM Higgs boson in §I.4.3.2 [in particular since we have also considered the case of a CP–even Higgs particle for comparison] damped by the square of the Higgs couplings to fermions

$$\sigma(e^+e^- \to f\bar{f}\Phi) \sim g_{\Phi ff}^2 \, \sigma_{\mathrm{SM}}(e^+e^- \to f\bar{f}\Phi) \qquad (4.10)$$

This is particularly the case for $b\bar{b}$ and $\tau^+\tau^-$ final states which, because of their strongly enhanced couplings to the Higgs bosons for large $\tan\beta$ values, should be considered in the MSSM. Indeed, since the fermion masses can be neglected in the amplitudes, there is no difference between the CP–even and CP–odd cases. Nevertheless, in the MSSM, there are additional Feynman diagrams which contribute to these final state topologies as shown in Fig. 4.14: besides the familiar $e^+e^- \to \mathcal{H}Z^* \to \mathcal{H}f\bar{f}$ diagram, one has also associated $\mathcal{H}A$ production, with one of the Higgs bosons splitting into the $f\bar{f}$ pair. In the case of b–quark and τ–lepton final states, as well as in the case of top quarks for $M_{H,A} \gtrsim 2m_t$, these processes might provide the leading contribution when the cross sections for the $2 \to 2$ processes $e^+e^- \to hA$ or HA are not suppressed by the mixing angle factors. Note also that the diagram where the fermion pair originates from the virtual Z boson is absent in the case of the pseudoscalar A boson since there is no ZZA coupling at the tree–level.
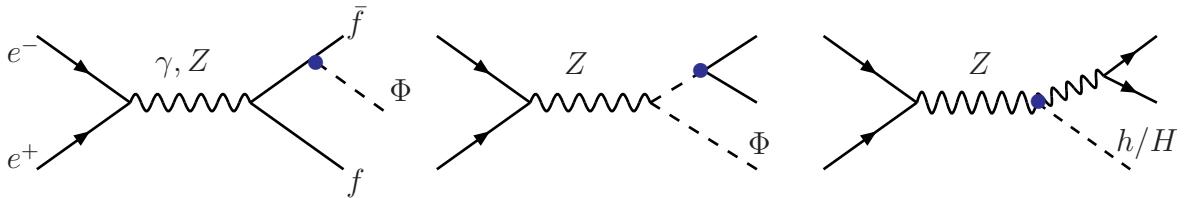
Figure 4.14: Diagrams for the associated production of Higgs bosons with a fermion pair.

For Higgs production in association with top quarks, $e^+e^- \to t\bar{t} + h/H/A$, and for $\tan\beta \gtrsim 3$, the cross sections are strongly suppressed for the pseudoscalar and pseudoscalar–like Higgs boson, $\Phi_A = H$ or h depending on whether we are in the anti–decoupling or the decoupling regimes and are sizable only for the Φ_H boson which has almost SM–like couplings to the top quarks. At $\sqrt{s} = 500$ GeV, the cross sections are very small, barely reaching the level of 0.2 fb even for the SM–like Higgs boson since at this energy, there is only a little amount of phase–space available for the process. At higher energies, e.g. $\sqrt{s} = 1$ TeV, the

cross sections can reach the level of ~ 1 fb as shown in the left–hand side of Fig. 4.15 for $\tan\beta = 3$. This would allow for the measurement of the $\Phi_H t\bar{t}$ couplings [493] since most of the cross section is coming from Higgs radiation off the top quarks as discussed earlier.

In the case of Higgs production in association with bottom quarks, $e^+e^- \to b\bar{b} + h/H/A$, one should take into account only the gauge invariant contribution coming from Higgs radiation off the b–quark lines since a much larger contribution would come from the associated production process, $e^+e^- \to Ah$ or AH, with one of the Higgs bosons decaying into $b\bar{b}$ pairs, or from the Higgs–strahlung process, $e^+e^- \to Zh$ or ZH with $Z \to b\bar{b}$. These resonant processes have been discussed earlier and can be separated from the Higgs radiation off b–quarks by demanding that the invariant mass of a $b\bar{b}$ pair does not coincide with that of a Z boson or another Higgs boson. Because of the strong enhancement of the b–quark Yukawa coupling, the cross sections can exceed the level of $\sigma(e^+e^- \to \bar{b}bA + \bar{b}b\Phi_A) \gtrsim 1$ fb for $\tan\beta \gtrsim 30$ and small to moderate Higgs masses, as shown in the right–hand side of Fig. 4.15 where a c.m. energy of $\sqrt{s} = 500$ GeV has been assumed and $\tan\beta$ is fixed to 30.

Note that the cross cross section for associated Higgs production with $\tau^+\tau^-$ pairs, $e^+e^- \to \tau^+\tau^-\Phi$, is not significantly smaller than the $b\bar{b}\Phi$ cross section. Indeed, despite of the smaller τ mass and the missing color factor, there is a compensation due to the larger electric charge, the square of which multiplies the dominant photon exchange contribution, and there is only a factor of two to three difference between $\sigma(e^+e^- \to \tau^+\tau^-\Phi)$ and $\sigma(e^+e^- \to b\bar{b}\Phi)$.
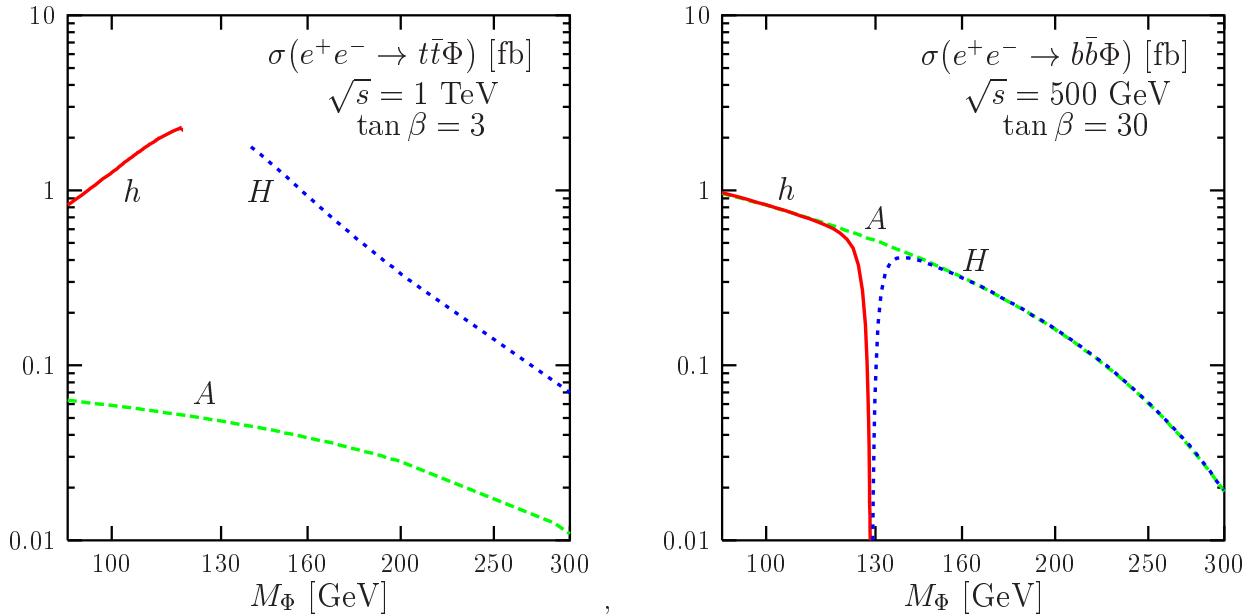
Figure 4.15: The production cross sections of the three neutral MSSM Higgs bosons in association with heavy quarks as a function of the respective Higgs masses: $e^+e^- \to t\bar{t} + h/H/A$ at $\sqrt{s} = 1$ TeV and $\tan\beta = 3$ (left) and $e^+e^- \to b\bar{b} + h/H/A$ at $\sqrt{s} = 500$ GeV and $\tan\beta = 30$ (right). The pole quark masses are set to $m_t = 178$ GeV and $m_b = 4.9$ GeV.

247

Since the cross section for $e^+e^- \to b\bar{b}\Phi$ is directly proportional to $\tan^2\beta$, this process has been advocated as a means to perform a measurement of $\tan\beta$ when it takes large enough values, in much the same way as the $gg \to b\bar{b}\Phi$ process at the LHC but with much less uncertainties. In Ref. [494], a simulation has been performed for the $e^+e^- \to b\bar{b}A \to b\bar{b}b\bar{b}$ signal [where cuts have been applied to discard the resonant production of Higgs boson pairs which is less sensitive to $\tan\beta$] and the background processes, $e^+e^- \to eW\nu, e^+e^-Z, WW, q\bar{q}, t\bar{t}$ besides HA/hA production, including the effects of ISR and beamstrahlung as well as the response of a detector that is similar to the one expected for the TESLA machine. At $\sqrt{s} = 500$ GeV, the $b\bar{b}\Phi$ signal cross section is sizable at low M_A and high $\tan\beta$ values, Fig. 4.15. The b quarks have to be tagged and the efficiency for one b–tag is assumed to be $\sim 80\%$ for a purity of $\sim 80\%$. The expected background rate for a given efficiency of the signal is displayed in the left–hand side of Fig. 4.16.

Although relatively small, the background from the $\Phi_A A$ resonant process is very important since it interferes with the signal; for $M_A = 100$ GeV and $\tan\beta = 50$, the interference is positive and is about 30% of the signal after cuts. If only this background process is included, one would have a statistical error on the $\tan\beta$ measurement, $\Delta\tan^2\beta/\tan^2\beta = \sqrt{S+B}/S \approx 0.14$ for the previous choice of parameters, leading to an error of 7%. When all backgrounds are included, the statistical accuracy on the $\tan\beta$ measurement for three values of M_A is shown in the right–hand side of Fig. 4.16 for a selection efficiency of 10% and a luminosity of 2 ab^{-1}. Note that if the channel $b\bar{b}\Phi_A$ is added, the precision will be improved since the signal is doubled. However, this gain will be lost if the running b–quark mass, $\bar{m}_b(M_A) \simeq 3$ GeV, is used as the signal rate drops then by a factor of two.
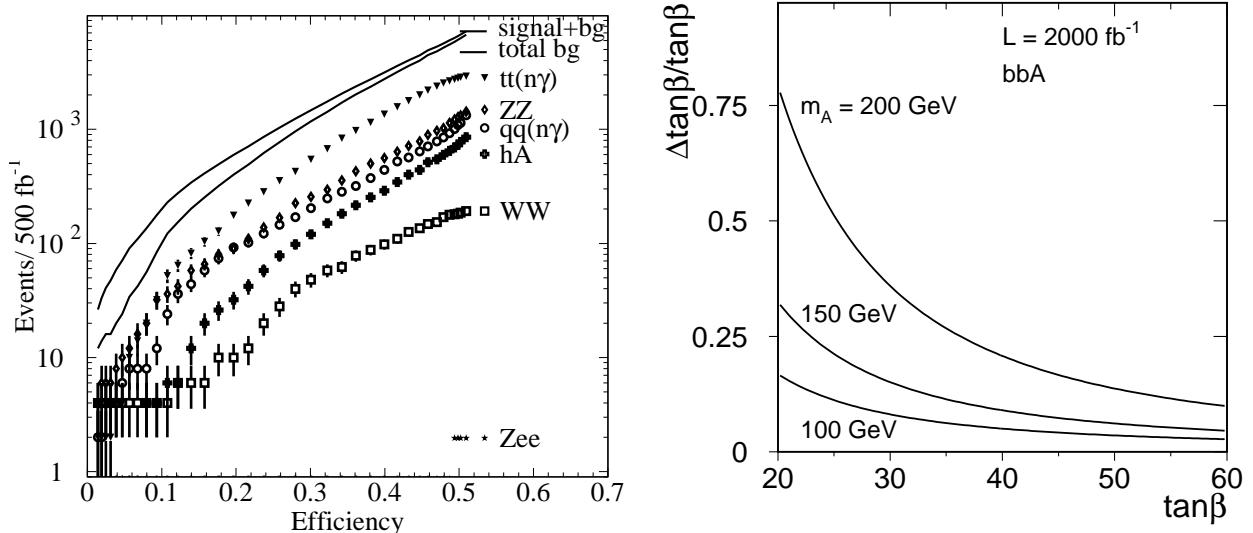
Figure 4.16: Left: the final background rate versus the $b\bar{b} + A$ signal efficiency for $M_A = 100$ GeV, $\sqrt{s} = 500$ GeV and $\mathcal{L} = 500$ fb^{-1}. Right: the corresponding $\tan\beta$ statistical error for $\mathcal{L} = 2$ ab^{-1} and three values $M_A = 100, 150$ and 200 GeV. For both plots, the value of the b–quark pole mass is fixed to $m_b = 4.9$ GeV; from Ref. [494].

248

4.2.3 Multi–Higgs boson production

As discussed in §1.2.3, a large ensemble of Higgs couplings is present in the MSSM: six different trilinear couplings hhh, Hhh, HHh, HHH, hAA, HAA are generated among the neutral particles and many more quadrilinear couplings. In e^+e^- collisions, these couplings can be accessed through Higgs pair production in the strahlung and WW fusion processes as in the case of the SM Higgs boson [144, 495]:

$$e^+e^- \to Z + hh/HH/Hh/AA \quad \text{and} \quad e^+e^- \to \nu\bar{\nu} + hh/HH/Hh/AA \qquad (4.11)$$

but also in triple Higgs production involving one or three CP–even Higgs particles [144]:

$$e^+e^- \to A + hh/HH/Hh/AA \qquad (4.12)$$

Some examples of Feynman diagrams leading to these processes in the $e^+e^- \to Z\Phi_1\Phi_2$ or $A\Phi_1\Phi_2$ channels and involving the trilinear Higgs couplings are shown in Fig. 4.17. The channels in which the various couplings can be probed have been cataloged in Table 4.2.
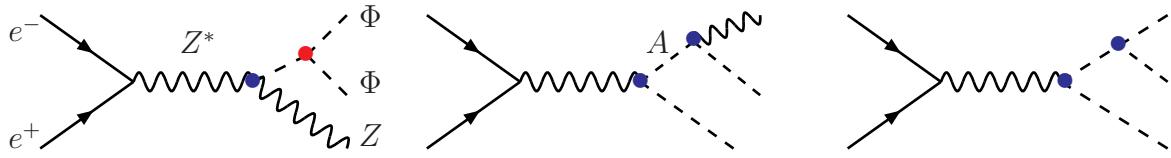

Figure 4.17: The double–strahlung and associated triple Higgs boson production processes.

λ	Double Higgs$-$strahlung				Triple Higgs$-$production			
	Zhh	ZHh	ZHH	ZAA	Ahh	AHh	AHH	AAA
hhh	$\times$				$\times$			
Hhh	$\times$	$\times$			$\times$	$\times$		
HHh		$\times$	$\times$			$\times$	$\times$	
HHH			$\times$				$\times$	
hAA				$\times$	$\times$	$\times$		$\times$
HAA				$\times$		$\times$	$\times$	$\times$

Table 4.2: The trilinear Higgs couplings which can generically be probed in double Higgs–strahlung and associated triple Higgs–production are marked by a cross.

Since in large parts of the MSSM parameter space the H, A and $H^\pm$ bosons are quite heavy, their couplings will be accessible only at high energies. In contrast, those of the lighter h boson can be accessed already at a 500 GeV collider since $M_h \lesssim 140$ GeV. We will first discuss the production of hh pairs and mention briefly later the production of heavy Higgs

bosons. Because light A bosons have been ruled out, λ_{Hhh} is the only trilinear coupling that may be measured in resonance decays, $H \to hh$, while all the other couplings must be accessed in continuum pair or triple production. The analytical expression of the cross sections for all these processes can be found in Ref. [144].

The total cross sections for the double Higgs strahlung process $e^+e^- \to hhZ$ are shown at a c.m. energy $\sqrt{s} = 500$ GeV in Fig. 4.18 where $\tan\beta$ is chosen to be 3 and 50 with the mixing parameters being $A_t = 1$ TeV and $\mu = -1$ TeV and 1 TeV. Since the vertices are suppressed by sin / cos functions of the mixing angles β and α, the continuum hh cross sections are in general suppressed compared to the SM Higgs case. The size of the cross sections increases for moderate $\tan\beta$ by nearly an order of magnitude if the hh final state can be generated in the chain $e^+e^- \to ZH \to Zhh$ via resonant H–strahlung. If M_h approaches the upper limit for a given $\tan\beta$ value, the decoupling drives the cross section back to its SM value. Note that for $\tan\beta = 50$, the cross section is extremely small except in the decoupling limit and even the resonance production is not effective.
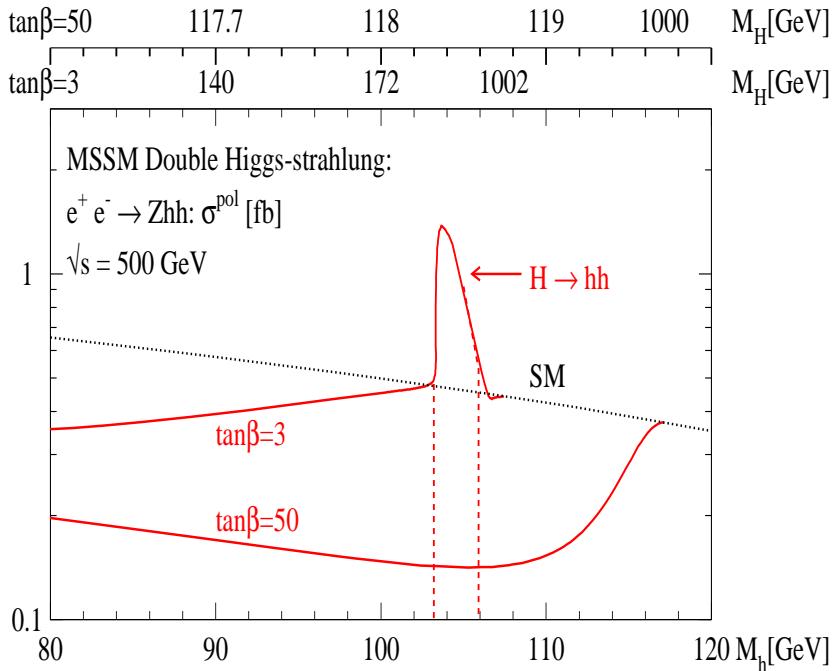
Figure 4.18: The total cross sections for MSSM hh production via double Higgs–strahlung at a 500 GeV e^+e^- collider for $\tan\beta = 3$ and 50, including mixing effects ($A_t = 1$ TeV, $\mu = -1/1$ TeV for $\tan\beta = 3/50$). The dotted line is for the SM cross section; from [144].

In fact, the reduction of the Zhh cross section outside the decoupling limit is partly compensated by the ZHh and ZHH production cross sections so that their sum adds up approximately to the SM value, if kinematically possible. This is demonstrated in the left–hand side of Fig. 4.19 which shows the cross sections for the hh, Hh and HH final states at $\sqrt{s} = 500$ GeV for $\tan\beta = 3$ [opposite helicities for the initial electrons and positrons are
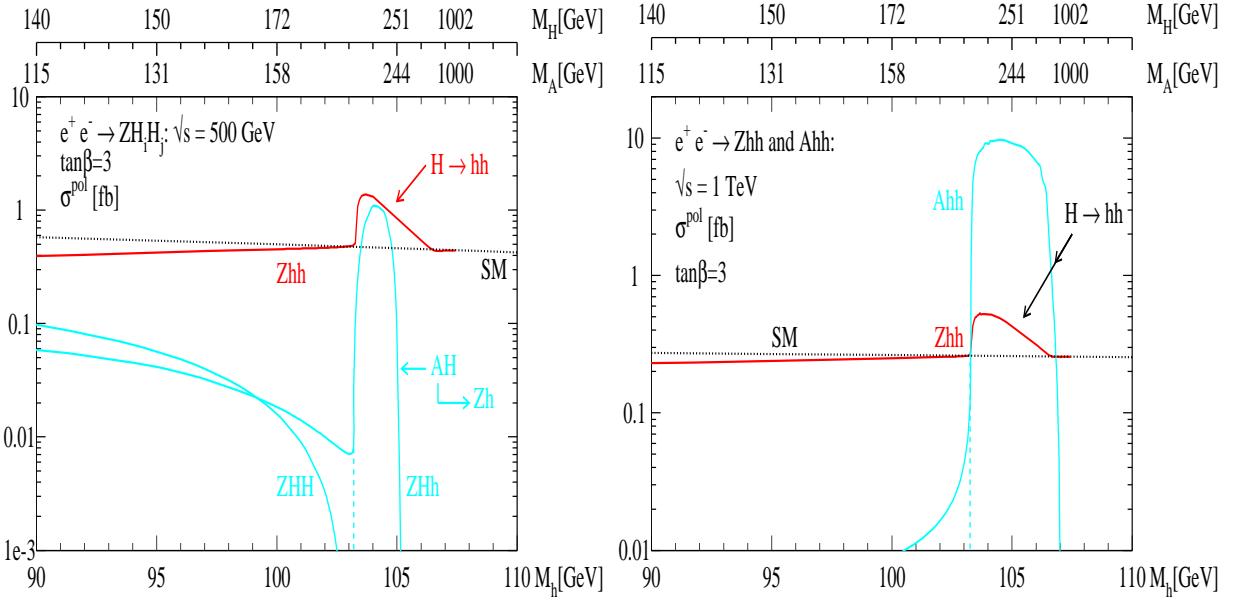
*Figure 4.19: The production cross sections for the processes Zhh, ZHh and ZHH for $\sqrt{s} = 500$ GeV (left) and Zhh and Ahh for $\sqrt{s} = 1$ TeV (right) for and $\tan\beta = 3$ and including mixing effects ($A = 1$ TeV, $\mu = -1$ TeV); from Ref. [144].*

assumed so that the cross section doubles compared to the unpolarized case]. One can notice that the $e^+e^- \to HhZ$ cross section, which is rather small in the lower M_h [and, hence, lower M_A] range, increases by two orders of magnitude for moderately large values of M_A. In this case, the $A \to hZ$ decay channel opens up leading to the familiar resonance production of HA followed by the decay $A \to hZ$ which results in hHZ final states. This channels disappears for larger values of M_A when the dominant decay channel $A \to t\bar{t}$ becomes accessible.

In the case of triple Higgs production, the first process that is accessible kinematically is $e^+e^- \to Ahh$. The size of the cross section $\sigma(e^+e^- \to Ahh)$ is compared with double Higgs–strahlung $\sigma(e^+e^- \to Zhh)$ in the right–hand side of Fig. 4.19 for $\tan\beta = 3$ at $\sqrt{s} = 1$ TeV. The cross section involving the pseudoscalar Higgs boson is small in the continuum. The effective coupling in the chain $Ah^* \to Ahh$ is $\cos(\beta - \alpha)\lambda_{hhh}$ while in the chain $AH^* \to Ahh$ it is $\sin(\beta - \alpha)\lambda_{Hhh}$; both products are small either in the first or in the second coefficient. Only for resonance H decays, $AH \to Ahh$, the cross section becomes very large.

Based on these cross sections, one can construct sensitivity areas for the trilinear MSSM Higgs couplings; WW double–Higgs fusion can provide additional information on the self–couplings, in particular for large collider energies. In Refs. [144, 523], the sensitivity areas have been defined in the M_A–$\tan\beta$ plane with the criteria for accepting a point in the plane as accessible for the measurement of a specific trilinear coupling being: (*i*) $\sigma[\lambda] > 0.01$ fb, meaning that 20 events are produced with a luminosity of 2 ab^{-1}, and (*ii*) eff$\{\lambda \to 0\} > 2$ st.dev., that is, on demands at least a 2 standard deviation effect of the non–zero trilinear

coupling away from zero. A slight tightening of these two criteria does not have a large impact on the size of the sensitivity areas.
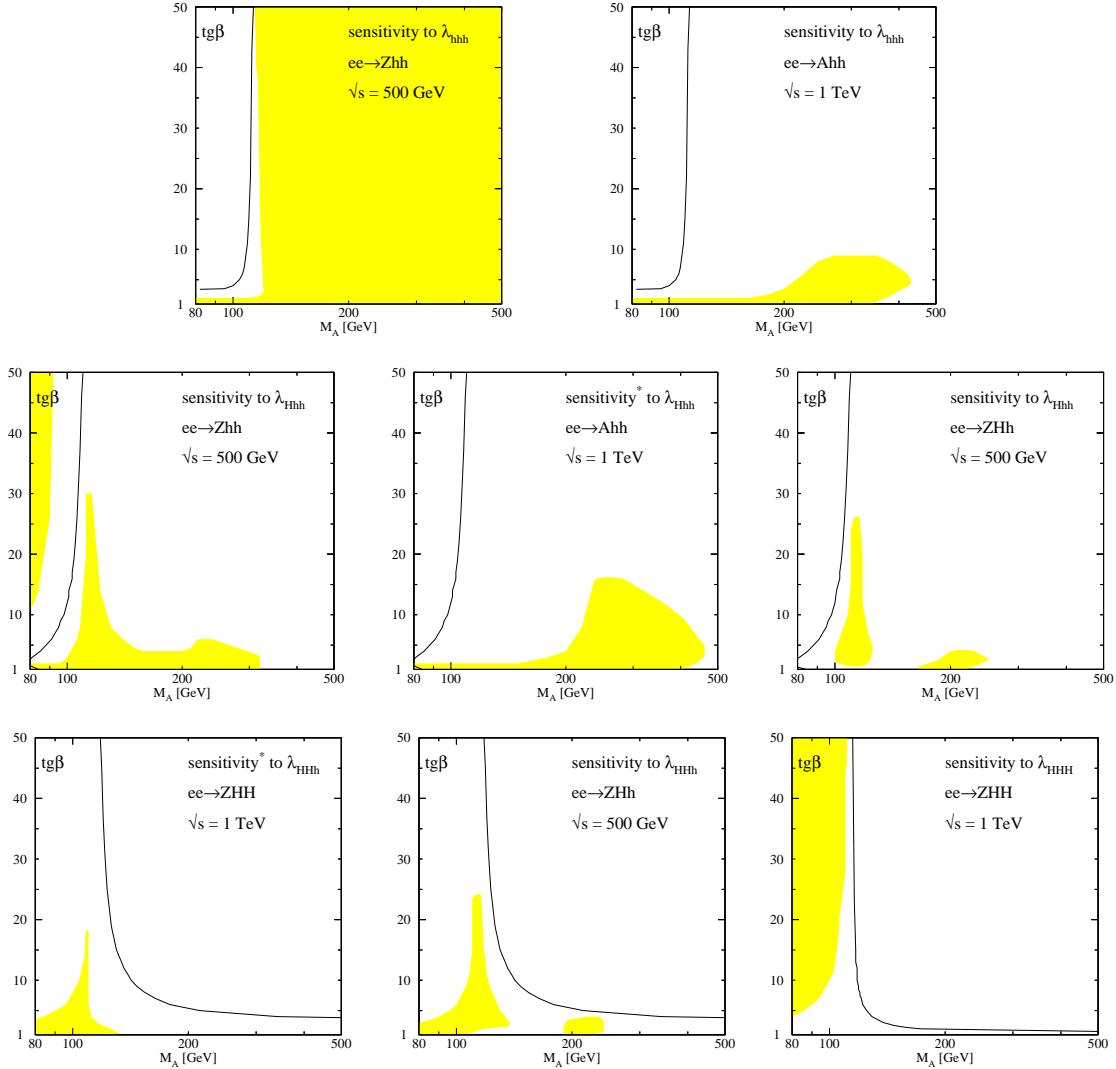

Figure 4.20: Sensitivity to the couplings λ_{hhh}, λ_{Hhh}, λ_{HHh} and λ_{HHH} in double Higgs–strahlung and triple Higgs production for collider energies of 500 GeV and 1 TeV in the no–mixing scenario. Vanishing trilinear couplings are indicated by contour lines; from Ref. [144].

Sensitivity areas of the trilinear couplings among the scalar Higgs bosons h and H in the matrix Table 4.2 are depicted in Fig. 4.20. If at most one heavy Higgs boson is present in the final state, the lower energy $\sqrt{s} = 500$ GeV is more preferable in the case of double Higgs–strahlung. HH final states in this process and triple Higgs production including A give rise to larger sensitivity areas at the high energy $\sqrt{s} = 1$ TeV. Apart from small regions in which interference effects play a major role, the magnitude of the sensitivity regions in the parameter $\tan\beta$ is readily explained by the magnitude of the parameters $\lambda \sin(\beta - \alpha)$ and $\lambda \cos(\beta - \alpha)$. For large M_A, the sensitivity criteria cannot be met anymore either as a result

of phase space effects or due to the suppression of the H/A propagators for large masses. While the trilinear coupling of the light h boson is accessible in nearly the entire MSSM parameter space, the regions for the λ's involving heavy Higgs bosons are rather restricted.

Note finally, that one is also sensitive to the trilinear couplings involving the CP–odd Higgs boson λ_{hAA} and λ_{HAA} in the process $e^+e^- \rightarrow ZAA$. In the case of λ_{hAA}, this is shown in the left–hand side of Fig. 4.21 in the M_A–$\tan\beta$ plane using the same criteria as previously. For $M_A \lesssim 200$ GeV, the sensitivity is rather high.

The pair production of two A bosons in Higgs strahlung, as well as in double WW fusion, has been advocated [102,496] as among the few mechanisms [together with associated production with fermions] which would allow for the detection of the pseudoscalar Higgs particle in the case where both the h and H bosons are too heavy and decouple [this can occur, for instance in non SUSY 2HDMs]. The maximal and minimal values of the cross sections for the two processes, after scanning on $1 \leq \tan\beta \leq 50$, are shown in this case in the right–hand side of Fig. 4.21 as a function of M_A. The contributions of the h/H bosons have been almost removed [the variation with $\tan\beta$ is due to the small remaining contributions] by setting $M_h = M_H = M_{H^\pm} = 1$ TeV. At $\sqrt{s} = 500$ GeV and with 1 ab^{-1}, 20 events can be produced for $M_A \lesssim 160$ GeV in the two channels AAZ and $AA\nu\bar{\nu}$ when only the quartic $AAVV$ interactions are included. As expected, at higher energies, there is more sensitivity in the WW fusion channel and the mass reach is $M_A \lesssim 300$ GeV at $\sqrt{s} = 800$ GeV.
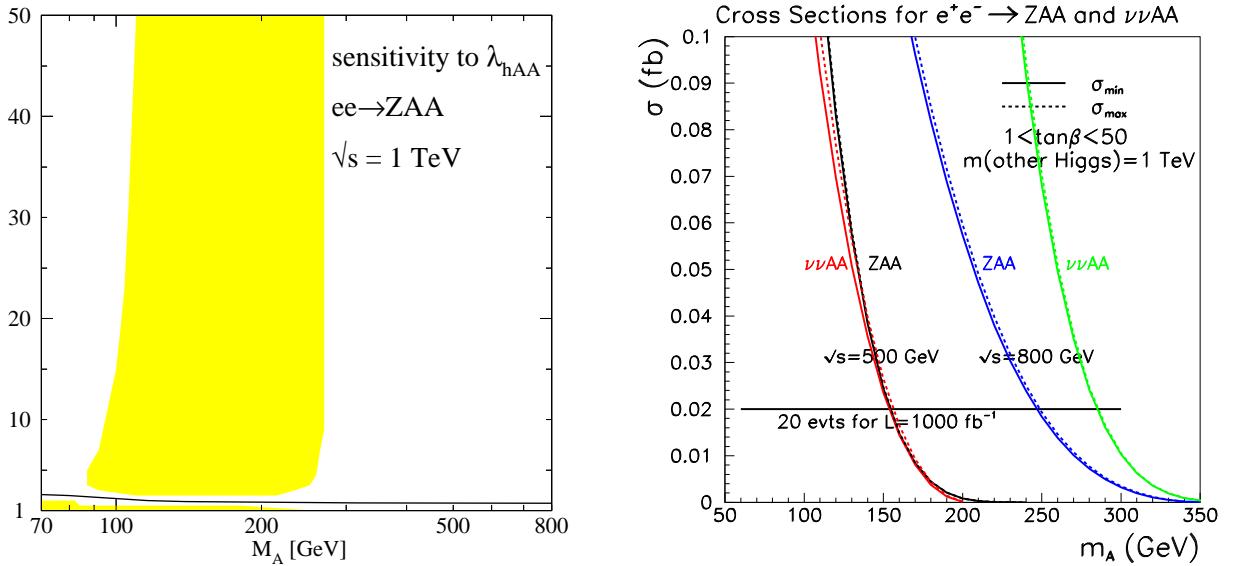
Figure 4.21: Left: sensitivity to the couplings λ_{hAA} in $e^+e^- \rightarrow ZAA$ at $\sqrt{s} = 1$ TeV using the same criteria as in Fig. 4.20; from Ref. [144]. Right: the cross sections for $e^+e^- \rightarrow ZAA$ and $e^+e^- \rightarrow \nu\bar{\nu}AA$ as a function of M_A at $\sqrt{s} = 500$ and 800 GeV; shown are the maximal and minimal values after scanning on $1 \leq \tan\beta \leq 50$ and without the contributions of the h/H bosons; the 20 event level for 1 ab^{-1} is indicated; from Ref. [486].

4.2.4 Loop induced higher–order processes

There are several processes for the production of the MSSM neutral Higgs bosons[34] that are induced by loops involving the SM particles as well as the SUSY and Higgs particles. Two of these processes have been discussed in the context of the SM Higgs boson and that one can generalize to the MSSM: the associated production with a photon, $e^+e^- \to \gamma + h/H/A$ [229, 498], and the pair production of Higgs bosons, $e^+e^- \to hh/HH/Hh/AA$ [497]. In the case of the pseudoscalar Higgs particle, which has no tree–level couplings to vector bosons, the associated production with a Z boson, $e^+e^- \to AZ$ [499], and the associated production with a neutrino pair in WW fusion, $e^+e^- \to \nu\bar{\nu}A$ [485, 486], can be generated radiatively. As one would expect, the cross sections for these processes are rather small as a result of the additional electroweak coupling. We summarize below the main features of these processes.

Loop induced Higgs pair production: As in the SM case, because of CP–invariance, the process $e^+e^- \to \Phi_i\Phi_j$ are mediated only by box diagrams involving W/ν and Z/e virtual states and, in the MSSM, additional contributions originate from their SUSY partners, charginos/sneutrinos and neutralinos/selectrons. The latter contributions are in general extremely small since no enhanced coupling is involved and the cross sections are even smaller than in the SM Higgs case because of the suppressed ΦVV couplings. Only in the (anti–)-decoupling limit for $(HH)\,hh$ production that the rates are comparable. At $\sqrt{s} = 500$ GeV and for $M_{h(H)} \sim 140$ GeV, they reach the level of $\sigma[hh\,(HH)] \sim 0.2$ fb, when left (right)–handed polarized $e^-(e^+)$ beams are used to enhance the cross section by a factor of four, since the W boson loop is dominating. The cross sections $\sigma[hH\,(AA)]$ are in general much smaller since A and one of the h or H bosons does not couple to the W boson.

Associated Higgs production with a photon: The process $e^+e^- \to \gamma\Phi$ occurs through s–channel $\gamma^*\gamma\Phi$ and $Z^*\gamma\Phi$ vertex diagrams involving charged particles [$f, W^\pm, H^\pm, \tilde{f}, \chi^\pm$ for the CP–even Higgs bosons and only $f, \chi^\pm$ for the CP–odd A boson] as well as t–channel vertex and box diagrams involving W/neutrino and Z/electron and their corresponding SUSY partners [$\chi^+/\tilde{\nu}$ and $\chi^0/\tilde{e}$; only the former diagrams contribute in the case of $A\gamma$ production]. The processes are possibly detectable, with $\sigma[\gamma\Phi] \sim 0.1$ fb, only in the case of h or H bosons, when they have SM–like couplings to the W boson, which again provides the dominant contribution [as in $h/H \to \gamma\gamma(Z\gamma)$ decays]. In the $e^+e^- \to A\gamma$ case, the production cross section is shown in Fig. 4.22 as a function of M_A for several values of $\tan\beta$ at $\sqrt{s} = 500$ GeV and 800 GeV. As can be seen, for $\tan\beta > 1$, it is below the 0.1 fb level.

---

[34]Note that there are also higher–order processes but which occur at the tree–level, in particular for the CP–even Higgs particles. Two examples are: associated production with two gauge bosons, $e^+e^- \to VV + h/H$ and associated production with a gauge boson in vector boson fusion, $e^+e^- \to V\ell\ell + h/H$. These processes have been discussed in the SM Higgs case in §I.4.3.4 and in §3.1.6 in the pp case, and the bulk of the cross sections can be obtained by folding the one of the SM Higgs boson by factors $g^2_{\mathcal{H}VV}$. There are additional diagrams involving the MSSM Higgs bosons, but we expect their contributions to be tiny.
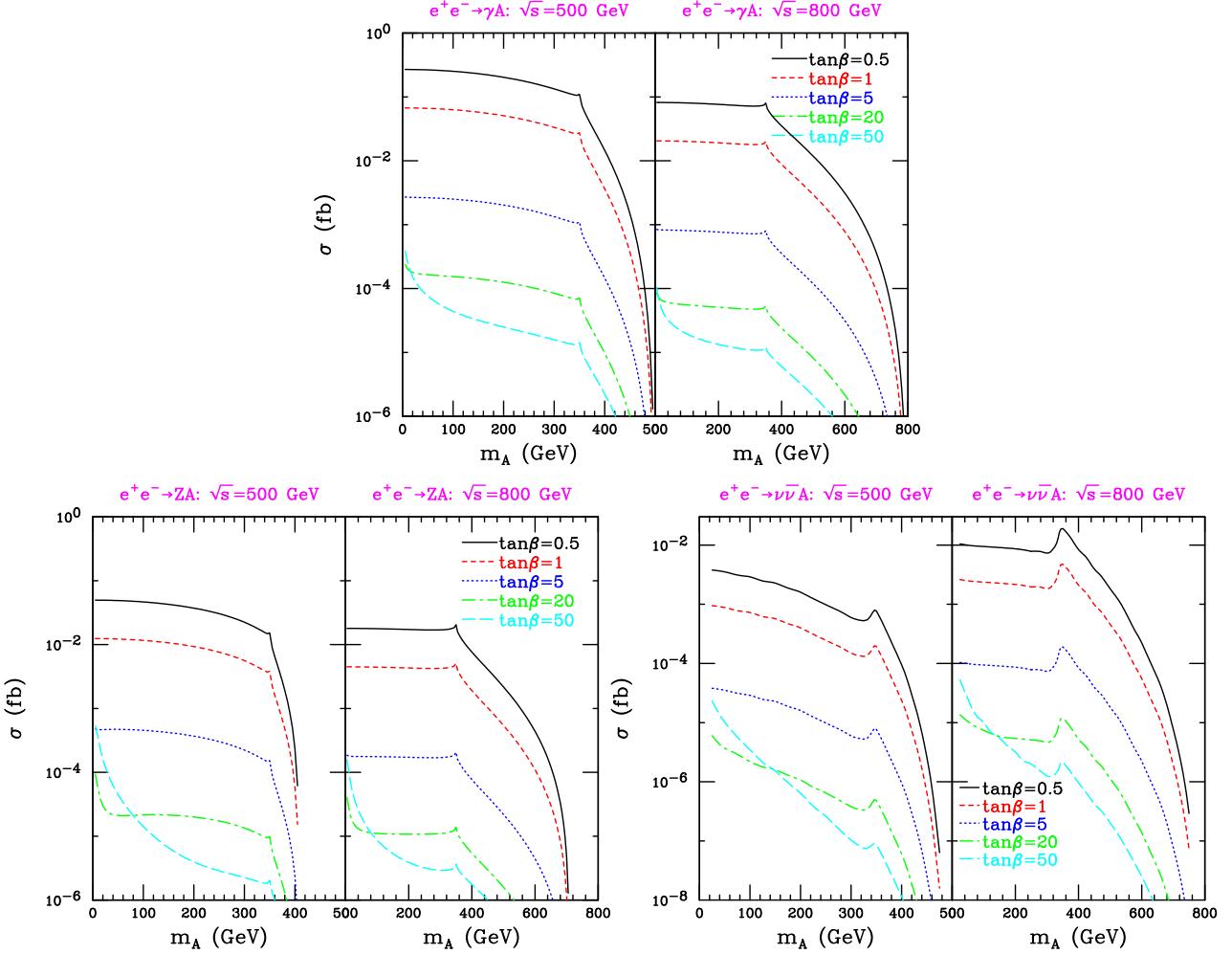
Figure 4.22: The $e^+e^- \to \gamma A$, ZA and $\nu\bar{\nu}A$ cross sections as a function of M_A for $\sqrt{s} = 500$ GeV and 800 GeV and for $\tan\beta = 0.5, 1, 5, 20, 50$; from Ref. [486].

<u>Associated CP–even Higgs production with a Z boson</u>: The process $e^+e^- \to ZA$, which does not occur at the tree–level in CP–conserved theories, is generated by exactly the same loops which are present in the $e^+e^- \to A\gamma$ process, supplemented by diagrams involving neutral particles [such as neutral Higgs bosons and neutralinos in the vertex diagrams] which couple to the Z boson and not to the photon. However, these extra contributions do not enhance the cross sections and the production rates are even smaller than in the $A\gamma$ case [which in addition is more favored by phase space]; see Fig. 4.22.

<u>CP–even Higgs production in WW fusion</u>: As mentioned when we discussed the radiative corrections to the $e^+e^- \to \nu\bar{\nu}H$ process, one can mediate the production of the CP–even Higgs production, $e^+e^- \to \nu\nu A$, by the same type of loop diagrams except that the W loop contributions are absent. It turns out again that the cross section, which is of $\mathcal{O}(\alpha^5)$, is extremely small; Fig. 4.22. Note that, in principle, one has to add to this channel the contribution of the $e^+e^- \to AZ$ channel discussed above with $Z \to \nu\bar{\nu}$.

4.3 Charged Higgs production in e^+e^- collisions

4.3.1 Production in the main channels

In e^+e^- collisions, charged Higgs bosons can be pair produced through the exchange of a virtual photon and Z boson in the s channel, Fig. 4.23a, [163, 173]

$$e^+e^- \to \gamma^*, Z^* \to H^+H^- \tag{4.13}$$

Since the coupling of the charged Higgs boson to photons is simply proportional to the electric charge and its couplings to the Z boson are $v_H = (-1 + 2s_W^2)/(2s_W c_W)$ and $a_H = 0$, the production cross section will depend, again, only on the $H^\pm$ mass and on no other MSSM parameter. The analytical expression at tree–level has been given in eq. (1.162).
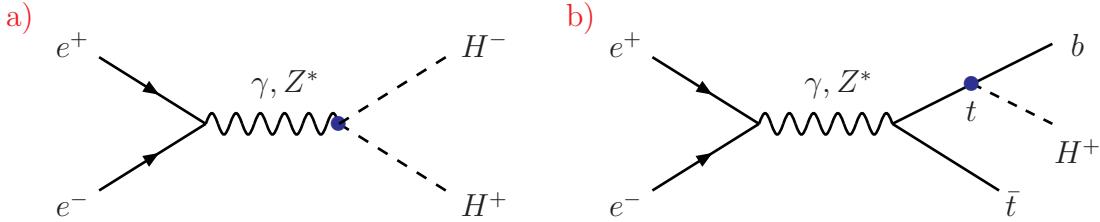

Figure 4.23: Feynman diagrams for charged Higgs production in e^+e^- collisions.

The cross section is shown in Fig. 4.24 at two c.m. energies, $\sqrt{s} = 500$ GeV and 1 TeV as a function of $M_{H^\pm}$. For small masses, $M_{H^\pm} \lesssim 200$ GeV, it is higher at lower c.m. energies being proportional to $1/s$. At $\sqrt{s} = 500$ GeV, it lies between 100 and 50 fb in the mass range $M_{H^\pm} = 100$–200 GeV, which means that for an integrated luminosity of 500 fb^{-1}, about 50.000 to 25.000 pairs can be created. For higher Higgs masses, the production cross section drops very quickly due to the P–wave suppression factor β^3 near the kinematical threshold; higher energies are thus necessary in this case. The angular distribution of the charged Higgs bosons follows the $\sin^2\theta$ law typical for spin–zero particle production.

The charged Higgs bosons, if lighter than ~ 170 GeV, can also be produced in decays of top quarks, with the latter being produced in pairs in e^+e^- collisions, $e^+e^- \to \gamma^*, Z^* \to t\bar{t}$; Fig. 4.23b. The $t \to bH^+$ decay branching ratio, compared to that of the expected dominant standard mode $t \to bW^+$, has been discussed in §2.3.1 and can be significant for low and large values of $\tan\beta$ when the $H^\pm tb$ coupling is enhanced. The cross section for top quark pair production is of the order of $\sigma(e^+e^- \to t\bar{t}) \sim 0.5$ pb at $\sqrt{s} = 500$ GeV and approximately a factor of four lower at $\sqrt{s} = 1$ TeV. The $t\bar{t}$ production cross section at these two c.m. energies, multiplied by $\mathrm{BR}(t \to H^+b, \bar{t} \to H^-\bar{b})$ [that is, the rate for producing one charged Higgs boson] is also shown in Fig. 4.24 for the two values $\tan\beta = 3$ and 30. As can be seen, if $M_{H^\pm}$ is not to close to m_t, the rates are substantial being of the same order of magnitude as the rates for direct charged Higgs pair production for low $M_{H^\pm}$ values.
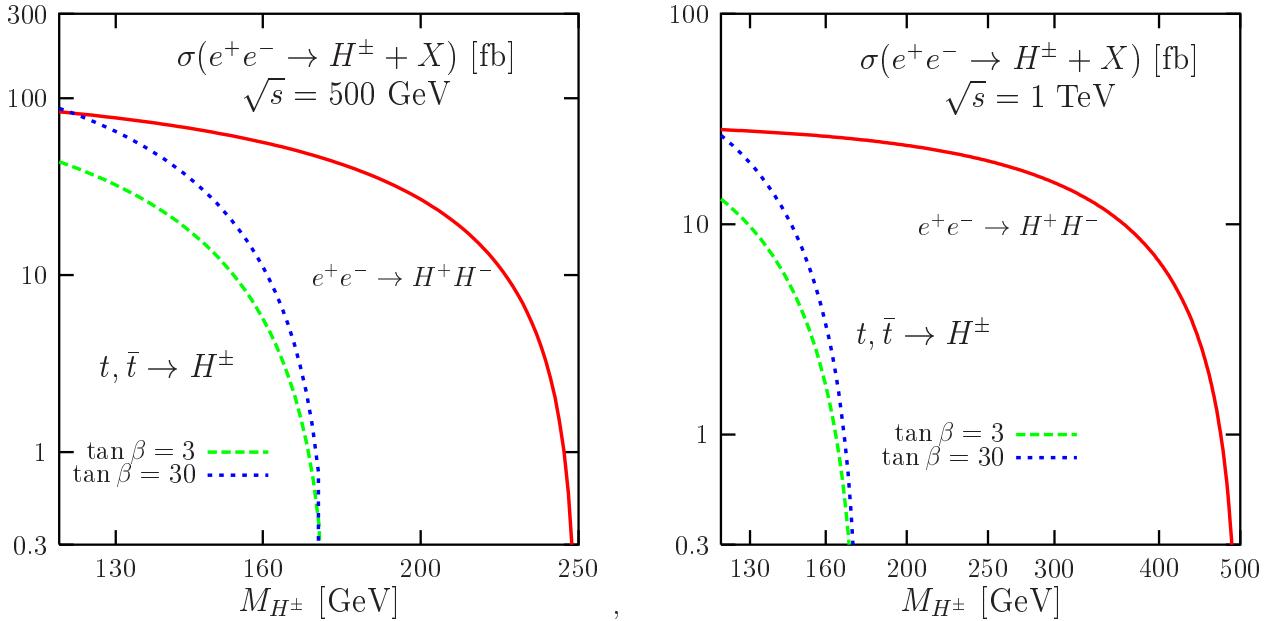
Figure 4.24: The production cross sections of the charged Higgs boson in direct e^+e^- collisions and in decays of the top quark (for $\tan\beta = 3$ and 30 in this case) as a function of the $H^\pm$ mass for two values of the c.m. energy, $\sqrt{s} = 500$ GeV (left) and 1 TeV (right).

The signature for $H^\pm$ production can be read off the graphs displaying the branching ratios in §2.1.4. If $M_{H^\pm} \lesssim m_t$, the charged Higgs boson will decay mainly into $\tau\nu_\tau$ and $c\bar{s}$ pairs, the $\tau\nu_\tau$ mode being always dominating for $\tan\beta$ larger than unity. This results in a surplus of τ final states over e, μ final states, an apparent breaking of the lepton universality which has been verified at the 1% level in Z decays at LEP1. For large $M_{H^\pm}$ values, the dominant mode is the decay $H^+ \to t\bar{b}$, leading to $Wb\bar{b}$ final states. In some parts of the parameter space [in fact, in the intermediate–coupling regime] also the decays $H^\pm \to W^\pm h$ and potentially $H^\pm \to AW^\pm$, with the W boson being possibly off–shell, are allowed leading to cascades with heavy τ and b fermions in the final state. In a narrow mass range below $2m_t$ and for small values of $\tan\beta$, the three–body decay $H^+ \to t^*\bar{b} \to b\bar{b}W$ is also possible.

4.3.2 Radiative corrections to the pair production

The one–loop radiative corrections[35] to $e^+e^- \to H^+H^-$ pair production have been calculated in a two–Higgs doublet model [i.e. without the SUSY particle contributions] in Ref. [487] and completed in the MSSM first in Ref. [488] and later in Refs. [489, 490]. Some generic Feynman diagrams contributing to these corrections are shown in Fig. 4.25. These are, in fact, the same corrections that appear in the case of the associated $e^+e^- \to hA/HA$ processes except that, here, the final spin–zero state is electrically charged.

---

[35]The radiative corrections to top quark decays into charged Higgs bosons have been discussed in §2.3.1. The radiative corrections to $t\bar{t}$ production have been discussed in Refs. [524, 525] in the SM and the MSSM.
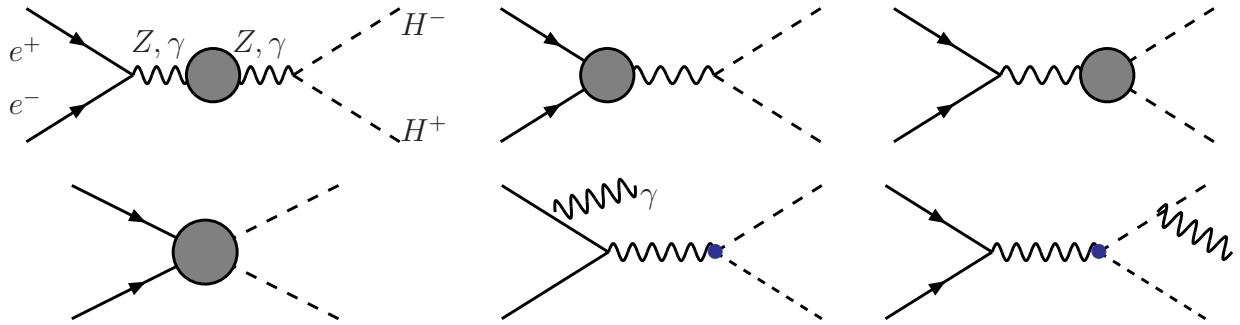
Figure 4.25: Generic diagrams for the $\mathcal{O}(\alpha)$ corrections to $e^+e^- \to H^+H^-$.

The subclass of photonic QED corrections including ISR, can be calculated using the structure function approach but, in this case, final state electromagnetic corrections [as well as photonic box diagrams] are present. The interference between initial and final state corrections generate a charge or forward–backward asymmetry that is absent at tree–level, since the angular distribution behaves as $\sin^2\theta$. The QED radiative corrections can decrease the cross section by several 10% depending on the cut on the photon energy and the $H^\pm$ mass. Being large, they have to be resummed for the leading terms using the usual techniques. The pure weak corrections, similarly to the $e^+e^- \to \mathcal{H}Z$ and $\mathcal{H}A$ processes discussed previously [although, here, the renormalization of the mixing angle α is not needed since the angle does not occur at the tree–level; however, to absorb the large corrections at higher orders, the renormalized α and the corrected MSSM Higgs masses should be used when they appear in the one–loop corrections], consist of:

i) Loops which contain gauge bosons, together with electrons and neutrinos, and Higgs bosons which contribute to the initial and final state vertices [Higgs bosons contribute significantly only to the final state vertices], as well as self–energy and box diagrams. The induced corrections are of similar nature as those affecting neutral Higgs boson production and are moderate in general, except at high energies where corrections that are proportional to $\log^2(s/M_W^2)$ and $\log(s/M_W^2)$ appear.

ii) Loops of top and bottom quarks and their SUSY partners which contribute to the final state corrections. These corrections can be very large, in particular when $\tan\beta$ is small or large giving rise to enhanced Higgs couplings to, respectively, top and bottom quarks. In addition, top squark loop contributions can be significant for large values of the mixing parameter A_t which can strongly enhance the Higgs couplings to top squarks. Strong Higgs couplings to bottom squarks can also be present for large $\tan\beta$ and μ values.

iii) Finally, there are many diagrams involving the contributions of charginos, neutralinos, selectrons and sneutrinos in self–energy, vertex and box corrections. They lead in general to small corrections to the total cross sections, at most a few percent, but they generate a forward–backward asymmetry.
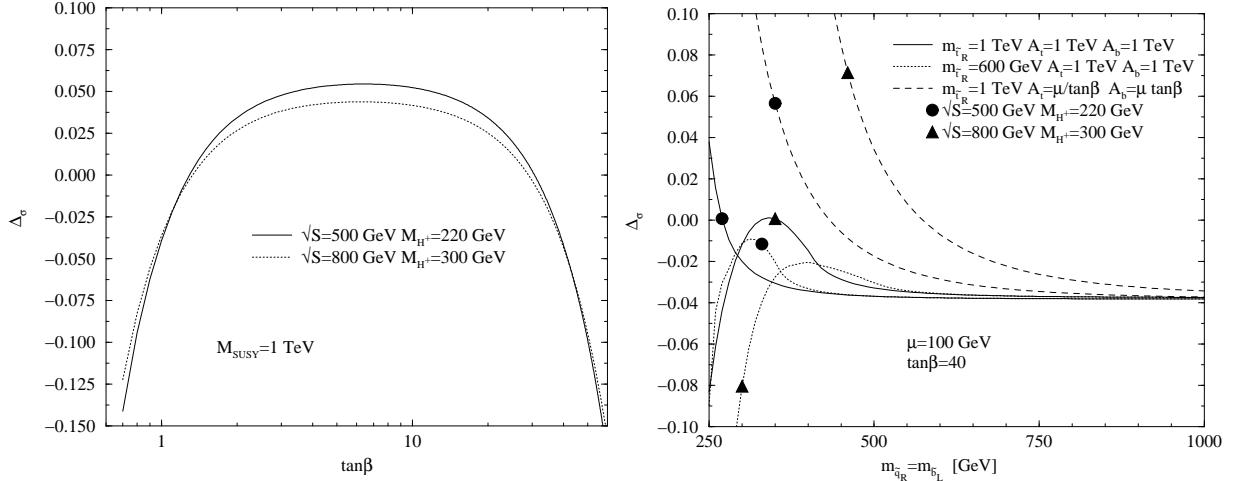
Figure 4.26: The one–loop weak corrections to $\sigma(e^+e^- \to H^+H^-)$ in the MSSM for $M_{H^\pm} = 220$ GeV at $\sqrt{s} = 500$ GeV and $M_{H^\pm} = 300$ GeV at $\sqrt{s} = 800$ GeV; from Ref. [489]. Left: as a function of $\tan\beta$ for $\mu = M_S = A_q = M_1 = M_2 = 1$ TeV and right: as a function of the bottom squark mass parameter with the other parameters as given in the frame.

The impact of the pure electroweak corrections to the $e^+e^- \to H^+H^-$ cross section in the MSSM is exemplified in Fig. 4.26 at two c.m. energies and charged Higgs masses, $\sqrt{s} = 500$ GeV for $M_{H^\pm} = 220$ GeV and $\sqrt{s} = 800$ GeV for $M_{H^\pm} = 300$ GeV. In the left–hand side, they are shown as a function of $\tan\beta$ when all the SUSY particles are heavy, with masses of about 1 TeV, and almost decouple. The corrections are moderate for $\tan\beta$ values in the range $1 \lesssim \tan\beta \lesssim 30$ where they are mostly driven by the gauge couplings and the Higgs self–couplings and they do not exceed the $\pm 5\%$ level. However, for larger values of $\tan\beta$ when the $H^\pm tb$ is strongly enhanced, they are significant and reach the level of -15% for $\tan\beta \sim 50$ in this scenario. In the right–hand side of the figure, the relative corrections are shown as a function of the sbottom soft SUSY–breaking mass parameter for $\tan\beta = 40$ and different choices of the other SUSY parameters. For relatively low squark masses, $m_{\tilde{q}} \lesssim 500$ GeV, the corrections are positive and rather large even for SUSY particles that are too heavy to be directly produced at the given e^+e^- c.m. energy. In all cases, the generated forward–backward asymmetries are at the level of a few percent.

In fact, the large electroweak corrections are of the Sudakov type [490,491], quadratically as well as linearly proportional to the logarithm of the c.m. energy, $\log(s/M_W^2)$, and in principle can be resummed to all orders. In the TeV energy range, one can perform for the radiative correction $\Delta(s) = \sigma^{1-\mathrm{loop}}/\sigma^{\mathrm{Born}} - 1$, the following asymptotic Sudakov expansion including all the double and single logarithms [490]

$$\Delta(s) = -\frac{\alpha}{2\pi s_W^2(1+4s_W^4)}\left[(1+2s_W^4)\log^2\frac{s}{M_W^2} - \frac{1}{2}(1+2s_W^4+8s_W^6)\log^2\frac{s}{M_Z^2}\right] \quad (4.14)$$

$$-\frac{2}{3c_W^2}(11-16s_W^2+32s_W^4+72s_W^6)\log\frac{s}{M_Z^2} + \frac{3}{2}\left(\frac{m_t^2}{M_W^2}\cot^2\beta + \frac{m_b^2}{M_W^2}\tan^2\beta\right)\log\frac{s}{m_t^2} + \Delta_{\mathrm{rem}}(s)$$

where the last term $\Delta_{\rm rem}(s)$, called the next–to–subleading correction in Ref. [490], encapsulates the remaining corrections. A detailed study of this correction shows that, except near kinematical thresholds, it is practically constant and depends only very mildly on the SUSY parameters and on the c.m. energy [at very high masses, this is obvious since the SUSY particles should decouple from the cross section].

Thus, by subtracting the known double and single logarithms which depend only on s, and measuring the production cross section at different c.m. energies, one obtains the slope of the cross section which depends essentially on the logarithmic term that is proportional to $\tan\beta$, allowing for an indirect determination of this important parameter. Assuming a statistical error of the order of 1% on the cross section and, including also an error from the small variation of the remaining correction $\Delta_{\rm rem}(s)$, a measurement of $\tan\beta$ can be performed at the level of a few 10%. This is shown in Fig. 4.27 where the percentage error on the determination of $\tan\beta$ for various $\tan\beta$ values is shown in the scenarios where the SUSY particles are very light, relatively light and when the parameter μ is large. The error bars are for the statistical and remaining theoretical error on the cross section and the vertical line corresponds to the point where the radiative correction starts to exceed the level of 10%. As can be seen, under these assumptions, a determination of $\tan\beta$ with an accuracy of less than 10% is possible for $\tan\beta \gtrsim 30$. Note that the same procedure can be applied in the case of associated HA production close to the decoupling limit since the Sudakov expansion of the $e^+e^- \to HA$ cross section is essentially the same.
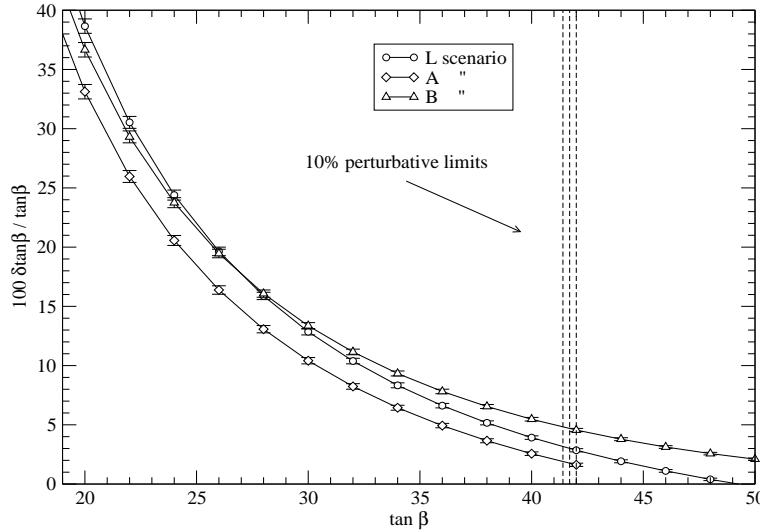
*Figure 4.27: Percentage error on the determination of* $\tan\beta$ *as a function of* $\tan\beta$ *for the production of charged Higgs boson pairs with masses* $M_{H^\pm} \sim 260$ *GeV in the energy range* $\sqrt{s} = 0.8$–1 *TeV in the three scenarios:* $\mu = 300$ *GeV and* $M_2 = 100$ *GeV (L),* $\mu = 300$ *GeV and* $M_2 = 200$ *GeV (A) and* $\mu = 400$ *GeV and* $M_2 = 200$ *GeV (B); from Ref. [490].*

4.3.3 Detection and measurements in e^+e^- collisions

In the low mass range, $M_{H^\pm} \lesssim m_t$, the charged Higgs particles can be produced both directly, $e^+e^- \to H^+H^-$, and in top quark decays, $t \to bH^+$. In the latter case, the search can be performed in the channels $e^+e^- \to t\bar{t} \to b\bar{b}W^\mp H^\pm$ or $b\bar{b}H^+H^-$, the first channel leading to more statistics since the standard decay mode $t \to bW$ is expected to be dominant. As at the Tevatron and the LHC, the signal consists into a surplus of $\tau\nu$ final states compared to $e\nu$ and $\mu\nu$ final states since the decay $H^- \to \tau\nu$ is dominant in this mass range. In direct pair production, the final state consists of $\tau^+\tau^- + \not{E}$ and, to a lesser extent [for rather low values of $\tan\beta$], $c\bar{s}\tau + \not{E}$ and $c\bar{s}\bar{c}s$ final states. The search is a straightforward extension of the one performed at LEP2 and discussed in §1.4.2. In Ref. [526], it has been shown that if its mass is not too close to the two kinematical thresholds, $M_{H^\pm} = m_t - m_b$ and/or $M_{H^\pm} = \frac{1}{2}\sqrt{s}$, a charged Higgs boson cannot escape detection in e^+e^- collisions, even for integrated luminosities as low as 10 fb^{-1}.

For larger masses, $M_{H^\pm} \gtrsim m_t$, the relevant process is charged Higgs pair production with their subsequent decays into tb pairs, $e^+e^- \to H^+H^- \to t\bar{t}b\bar{b} \to b\bar{b}b\bar{b}WW$. Eventually, one could in addition use the decays $H^\pm \to hW^\pm$ which lead to the same final states and, also, still the decay channel $H^+ \to \tau\nu$ which, as discussed in §2.1.4, has a branching ratio of the order of 10% for large enough $\tan\beta$. In Ref. [527], a detailed simulation has been performed in the main channel $e^+e^- \to H^+H^- \to t\bar{b}\bar{t}b$ for a charged Higgs boson with a mass $M_{H^\pm} = 300$ GeV at a c.m. energy $\sqrt{s} = 800$ GeV; the possible events from the $H^\pm \to hW^\pm$ decays with $M_h \sim 120$ GeV have been included. By using b–tagging and the mass constraints on the intermediate t, W and eventually h states, the background can be reduced to a low level. The combinatorial background due to jet–jet pairing ambiguities in the signal can also be resolved, since the b–tagged jets cannot come from W decays. From the m_t and M_W constraints, the resolution on the charged Higgs boson mass is estimated to be of the order of 10 GeV. With a luminosity of 500 fb^{-1}, the analysis gives 120 signal events on an estimated background of 50 events. This is shown in Fig. 4.28 where the dijet invariant mass distribution for the candidate signal events is displayed.

The product $\sigma(e^+e^- \to H^+H^-) \times \mathrm{BR}(H^+H^- \to t\bar{b}\bar{t}b)$ and the charged Higgs mass $M_{H^\pm}$ can be then obtained from a likelihood fit to the reconstructed mass distribution with the number of signal events, the mass resolution and $M_{H^\pm}$ as free parameters. The resulting statistical uncertainty on the charged Higgs mass is $\Delta M_{H^\pm} \sim \pm 1$ GeV and that on the production cross–section times branching ratio is $\Delta\sigma(e^+e^- \to H^+H^- \to t\bar{b}\bar{t}b) \lesssim 15\%$. Note that in the same analysis, it has been shown that a 5σ discovery will be possible for $H^\pm$ masses up to $M_{H^\pm} \sim 350$ GeV for the assumed energy, $\sqrt{s} = 800$ GeV, and integrated luminosity, $\mathcal{L} = 500$ fb^{-1}. Above this mass value, the statistics become too small since the cross section drops as a result of the β^3 suppression near the production threshold.
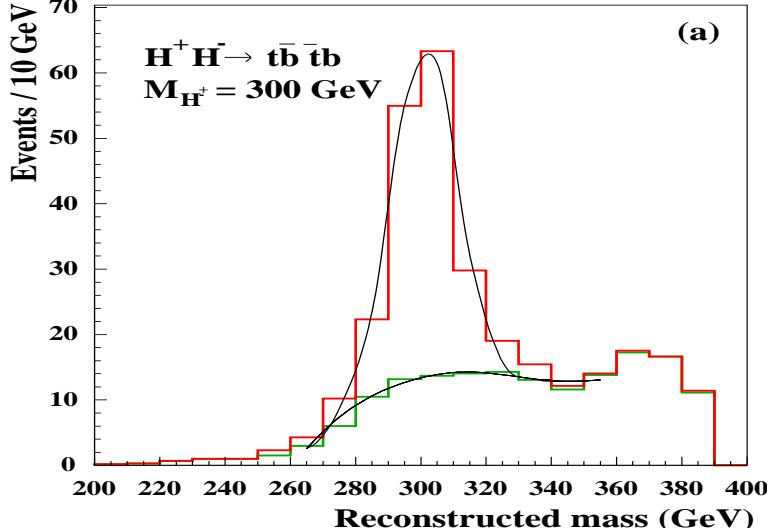
Figure 4.28: The dijet invariant mass distribution for $e^+e^- \to H^+H^- \to t\bar{b}\bar{t}b$ candidates for $M_{H^\pm} = 300$ GeV after applying the intermediate W and t mass and the equal mass final state constraints for 500 fb^{-1} data at $\sqrt{s} = 800$ GeV; from Ref. [470].

The process $e^+e^- \to H^+H^- \to t\bar{b}\bar{t}b$ can also be used for the determination of the value of $\tan\beta$. Indeed, while the production cross section is independent of $\tan\beta$ at the tree–level, the branching ratio $t \to bH^+$ has a significant dependence on this parameter, in particular for low values $\tan\beta \lesssim 5$ where there is a competition between the $t\bar{b}$ and $\tau\nu$ decay modes. At higher $\tan\beta$ values, the ratio of the two previous branching fractions is approximately given by $3\bar{m}_b^2/m_\tau^2 \sim 10$ and does not depend on this parameter. Instead, the total decay width of the charged Higgs boson is very sensitive to $\tan\beta$ in this case, being proportional to the combination $\Gamma(H^\pm) \propto \bar{m}_b^2 \tan^2\beta + m_t^2 \cot^2\beta$. One can thus combine the $t \to bH^+$ decay branching ratio measurement that is given by the event rate in $e^+e^- \to H^+H^- \to t\bar{b}\bar{t}b$ and the measurement of the total decay width which can be resolved experimentally to probe this parameter in the entire possible range $1 \lesssim \tan\beta \lesssim 60$.

In Ref. [494], a simulation of this process has been performed for a c.m. energy $\sqrt{s} = 500$ GeV along the same lines discussed for the associated $e^+e^- \to b\bar{b}A$ process where some details for the treatment of the backgrounds have been given. It has been shown that for $M_{H^\pm} \sim 200$ GeV, the signal process can be isolated with an efficiency of $\sim 2\%$ with almost negligible backgrounds. For the measurement of the total decay width, each $t\bar{b}\bar{t}b$ event is counted twice, since one looks at both H^+ and H^- decays and only 75% of the events are accepted, the remaining ones which lie in the wings of the mass distributions, lead to wrong jet–pairing. The resolved width is the quadratic average of the natural width and the detector resolution, which is estimated to be $R_{\rm res} = 5$ GeV with a 10% systematical error.

In the left–hand side of Fig. 4.29, shown are the 1σ bounds on $\tan\beta$ that are based on the measurement of the resolved $H^\pm$ decay width and the $e^+e^- \to t\bar{b}\bar{t}b$ event rate; an

integrated luminosity of 2 ab^{-1} has been assumed. The expected accuracy is also shown for $M_{H^\pm} \sim M_A \sim 200$ GeV and maximal mixing in scenarios where all SUSY particles are too heavy for H^+ to decay into (I) and $M_S = 0.5$ TeV and $\mu \sim 2M_2 \sim 250$ GeV, leading to light charginos and neutralinos so that the decay $H^\pm \to \chi^\pm\chi^0$ occurs with significant rates (II). As expected, in the low $\tan\beta$ range, a better measurement is provided by the $t\bar{b}\bar{t}b$ rate while, in the high range, a good precision is achieved from $\Gamma_{H^\pm}^R$. In both cases, the accuracy is at the level of $\Delta\tan\beta/\tan\beta \sim 10$–$20\%$. In the intermediate range, $10 \lesssim \tan\beta \lesssim 50$, the accuracy is much worse, except in scenario (II) where the decays into SUSY particles allow for a reasonable measurement of BR($H^+ \to t\bar{b}$) up to values $\tan\beta \lesssim 30$.
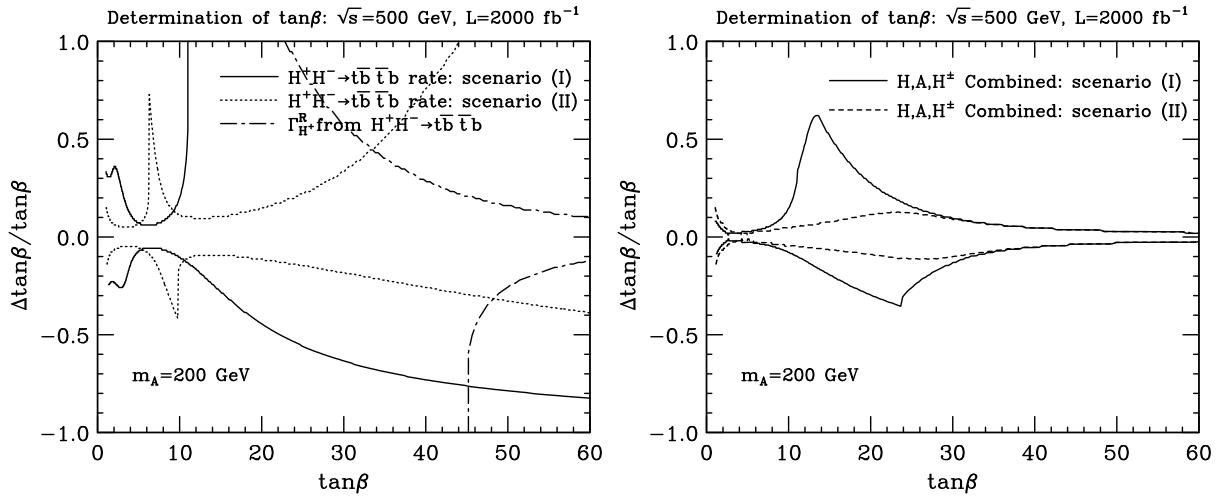
Figure 4.29: Left: Expected precision on $\tan\beta$ (1σ bounds) based on $\Gamma(H^\pm)$ and the $t\bar{b}\bar{t}b$ rate for a scenario $M_S = 1$ TeV, $\mu = M_2 = 250$ GeV (I) and $M_S = 0.5$ TeV, $\mu \sim 2M_2 \sim 250$ GeV (II) with $M_{H^\pm} \sim M_A = 200$ GeV, $\sqrt{s} = 500$ GeV and $\mathcal{L} = 2$ ab^{-1}. Right: the precision when the measurements in $e^+e^- \to H^+H^- \to t\bar{b}\bar{t}b$ are combined with those made in $e^+e^- \to HA \to b\bar{b}b\bar{b}$ and $e^+e^- \to b\bar{b}+A/H$ under the same conditions as above; from Ref. [494].

In fact, one can perform the same analysis for the $e^+e^- \to HA \to b\bar{b}b\bar{b}$ channel which is also sensitive to $\tan\beta$ through the A/H total decay widths [but only at high $\tan\beta$ in this case when they are proportional to $\bar{m}_b^2 \tan^2\beta$] and through the event rate [for rather low $\tan\beta$ values]. Except from the slight complication due to the small $M_A - M_H$ difference at low $\tan\beta$, the analysis is essentially the same as in the charged Higgs case. One can also add in the combination, the measurement which can be performed in the $e^+e^- \to b\bar{b}+A/H$ channels discussed in §4.2.2. The overall result on the accuracy on $\tan\beta$, when all measurements and channels are combined, is shown in the right–hand side of Fig. 4.29 with the same assumptions as previously. One can see that an error of a few percent can be achieved in the low and high $\tan\beta$ regions, while the precision is at the level of 10 to 30% for $10 \lesssim \tan\beta \lesssim 30$, except if new decay modes are allowed. Note that theoretical errors due to the different $\tan\beta$ dependence of the processes at higher orders have to be considered too.

263

4.3.4 Higher–order processes

There are also several higher–order mechanisms for the production of the charged Higgs bosons in e^+e^- collisions. These processes, some of which are similar to those occurring for MSSM neutral Higgs production at higher orders, are summarized below.

Associated production with heavy fermions

As in the case of neutral Higgs bosons, the associated production of a charged Higgs particle with a fermion–antifermion pair is primarily generated by the radiation off the heavy fermion lines [492]. However, there are two possibilities in this case since in the parent process, $e^+e^- \to f\bar{f}$, both isospin–type fermions can be initially produced, Fig. 4.30, and a Higgs boson with a given charge cannot be radiated from the two legs of the same diagram. In addition, the diagram where the fermion pair originates from the splitting of a charged Higgs particle into a $u\bar{d}$ pair contributes substantially since the initial $e^+e^- \to H^+H^-$ cross section is large. These process are interesting since they allow for the single production of a charged Higgs boson which is kinematically more accessible than the pair production process. Among the final states that are possible, the production in association with tb and $\tau\nu$ [492, 500–503] leads to the largest rates as a result of the enhanced Yukawa couplings of third generation fermions. The cross sections for the two processes are shown in Figs. 4.31 and 4.32 as a function of $M_{H^\pm}$ for $\tan\beta = 40$ with the c.m. energy fixed to $\sqrt{s} = 1$ TeV.
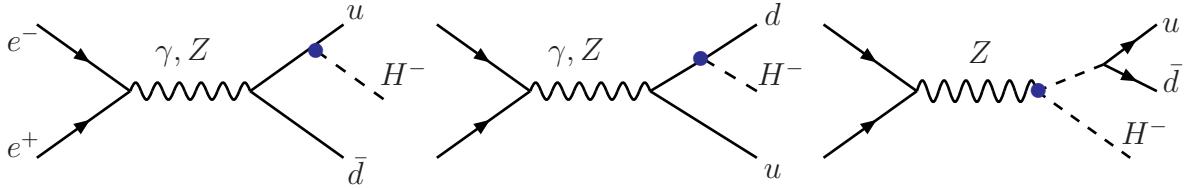
Figure 4.30: Diagrams for the associated production of H^- with a $u\bar{d}$ quark pair.

In the left–hand side of Fig. 4.31, shown are the $t\bar{b}\bar{t}b$ rates originating from the total $e^+e^- \to H^+H^-$ cross section folded with $\mathrm{BR}(H^+ \to t\bar{b})$ where the top quark is allowed to be off–shell, the rate for the $\bar{t}bH^+$ signal when all involved heavy particles $[t, W, H^+]$ are on–shell, the complete set of contributions where all particles are allowed to be off–shell and, finally, the main background events originating from $e^+e^- \to t\bar{t}g^* \to t\bar{t}b\bar{b}$. The main differences arise at the two thresholds: for $M_{H^\pm} \sim m_t$, where one can notice the effect of the finite widths of the heavy particles and for $M_{H^\pm} \sim \frac{1}{2}\sqrt{s}$ where the main effect is due to the $H^\pm$ total width, $\Gamma(H^\pm) \sim 10$ GeV, and the additional events from associated production.

In Ref. [502], a parton–level analysis of the signal and the background has been performed in the final state topology $b\bar{b} + t\bar{t} \to b\bar{b} + b\bar{b}W^+W^- \to b\bar{b} + b\bar{b}jj\ell\nu$, with the signature being four b–quarks to be tagged, two jets, a charged lepton and the missing energy due to the
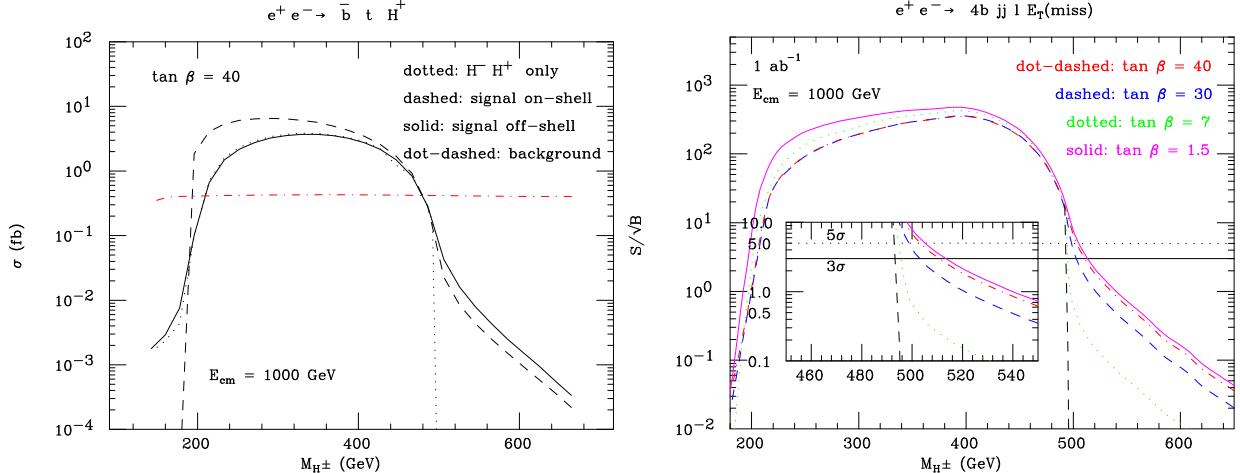
Figure 4.31: Left: The total cross sections for $e^+e^- \to H^+H^- \to t\bar{b}\bar{t}b$ in various approximation as a function of $M_{H^\pm}$ for $\tan\beta = 40$ at $\sqrt{s} = 1$ TeV. Right: Statistical significance of the signal yielding the $4b\,jj\,\ell\not{E}$ signatures after cuts, with a luminosity of $1\,ab^{-1}$ and several $\tan\beta$ values; the 3σ evidence and the 5σ discovery thresholds are shown and, in the insert, the threshold region $M_{H^\pm} \sim \frac{\sqrt{s}}{2}$ is enlarged. From Ref. [502].

escaping neutrino [for which one can in fact reconstruct the longitudinal momentum, even in the presence of ISR]. The statistical significance of the signal is shown in the right–hand side of Fig. 4.31 as a function of $M_{H^\pm}$ at the same energy but for various $\tan\beta$ values. As can be seen, it drops sharply from the otherwise large values near the two kinematical thresholds. However, as shown in the insert to the figure which zooms on the $\sqrt{s} = 2M_{H^\pm}$ threshold region, a 5σ discovery or a 3σ evidence for the signal is still possible for $M_{H^\pm}$ values slightly above the threshold if the value of $\tan\beta$ is either large, $\tan\beta \sim 40$, or small, $\tan\beta \sim 1$.

The situation is slightly more encouraging in the case of associated production with $\tau\nu$ pairs [503], although the process is relevant only for high values of $\tan\beta$. While the cross section, shown in the left–hand side of Fig. 4.32 in the same configuration as previously, is smaller than in the $t\bar{b}$ case for the associated production part, there is a compensation due to the choice of the signal topology. In this case, the signal is $e^+e^- \to \tau^-\nu H^+ \to \tau^-\nu t\bar{b} \to \tau^-\nu b\bar{b}W$ leading to a final state consisting of 4 jets [when the W boson is required to decay hadronically and no b–tagging is assumed], a τ lepton which is tagged as narrow jet in its one prong hadronic decay and missing transverse momentum. The main background will be due to top quark pair production where one of the W bosons decays hadronically while the other one decays into $\tau\nu$ pairs. Again, in a parton level simulation which takes advantage of the τ polarization, it has been shown that the background can be reduced at a low level. The significance of the signal, shown in the right–hand side of Fig. 4.32, extends by 20–30 GeV beyond the kinematical reach of Higgs pair production. Combining this channel with the $t\bar{b}H^+$ channel discussed above should lead to better results. In fact, one should also include the $e^+e^- \to H^\pm W^\mp$ process to which we turn now.
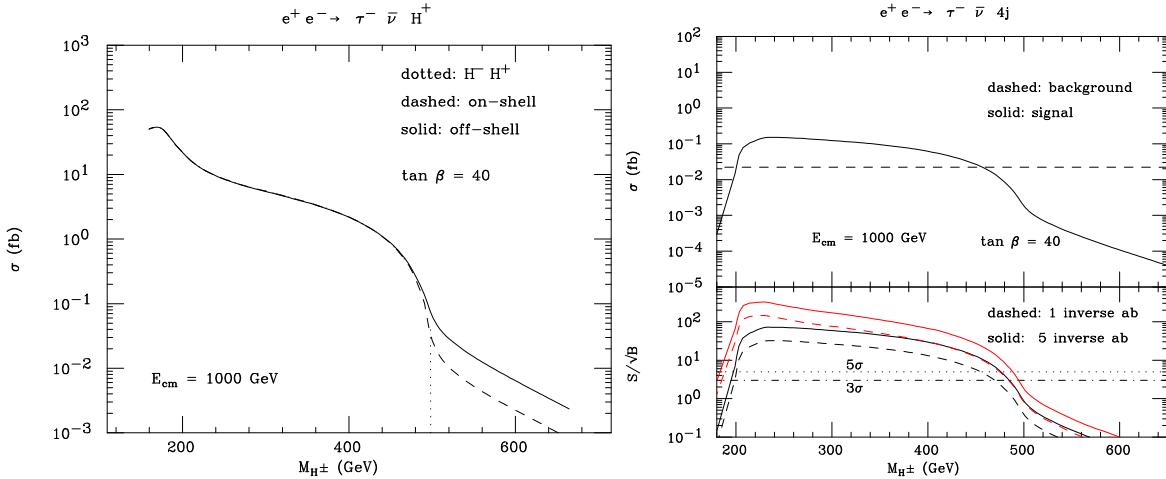
Figure 4.32: Left: the cross sections for $e^+e^- \rightarrow H^+H^- \rightarrow t\bar{b}\tau\nu$ production in various approximation as a function of $M_{H^\pm}$ for $\tan\beta = 40$ at $\sqrt{s} = 1$ TeV. Right: statistical significance of the signal yielding the $4j\,\tau E\!\!\!/$ signatures after cuts, with luminosities of 1 and 5 ab^{-1} with the 3σ evidence and the 5σ discovery thresholds; from Ref. [503].

Associated production with a W boson

The process $e^+e^- \rightarrow H^\pm W^\mp$ is mediated by loop diagrams involving both SM and MSSM particles. There are diagrams where W^+W^- pairs are produced with one of the W bosons turning into an $H^\pm$ boson via a self–energy insertion, $\gamma(Z)W^\mp H^\pm$ vertex diagrams as well as box diagrams; Fig. 4.33. The calculation has been performed some time ago [504] in a a two–Higgs doublet like model (2HDM), that is, including only the contributions of the SM and MSSM Higgs particles, and completed more recently [505] by evaluating the additional contributions of the SUSY particles.
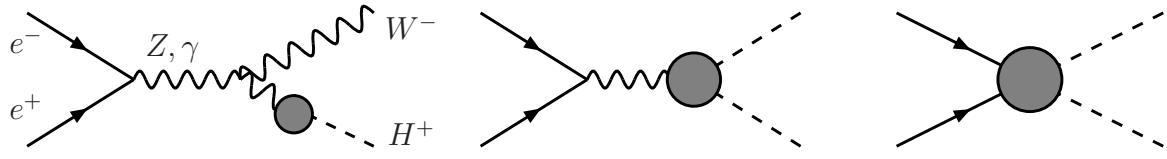
Figure 4.33: Generic diagrams for the $\mathcal{O}(\alpha^3)$ process $e^+e^- \rightarrow H^\pm W^\mp$.

It turns out that the largest contributions are due to the vertex diagrams in which loops of third generation quarks and squarks that couple strongly to the charged Higgs boson are involved. In particular, top/bottom loops have a large impact at low and large $\tan\beta$ values when the H^-tb coupling is strong, since the cross section scales as $\sigma \propto m_t^4 \cot^2\beta$ or $m_b^4 \tan^2\beta$; the rates might also be enhanced by threshold effects as shown in the 2HDM curve of Fig. 4.34. If SUSY particles are light, they can enhance the cross sections by several orders of magnitude as shown by the MSSM curve which includes the SUSY contributions with rather low squark masses, $M_S = 350$ GeV, and large stop mixing, $X_t = -800$ GeV.

266
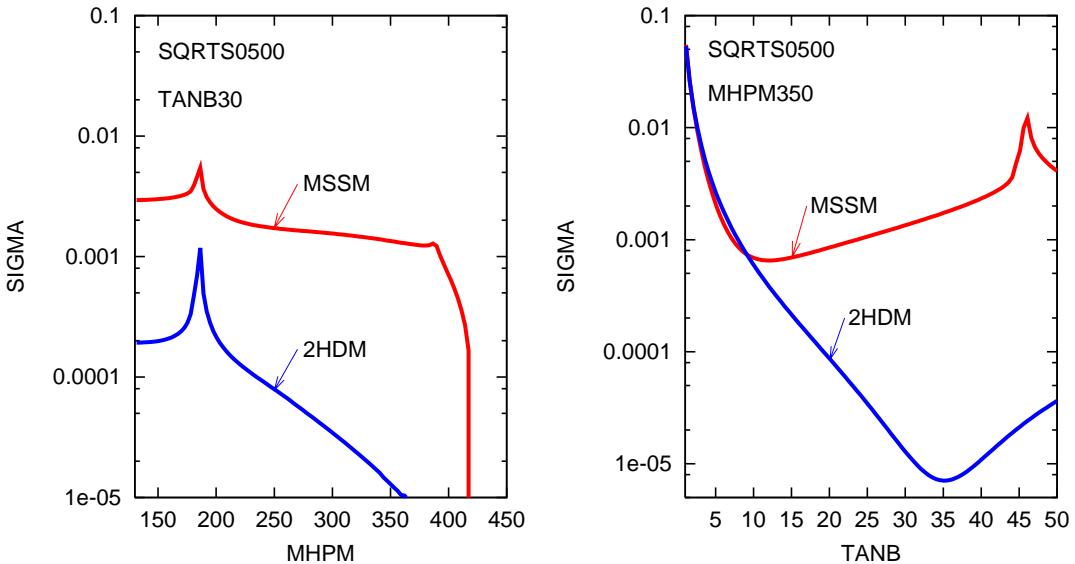
Figure 4.34: The cross section for $e^+e^- \rightarrow H^\pm W^\mp$ [in fb] for a c.m. energy $\sqrt{s} = 500$ GeV as a function of $M_{H^\pm}$ (left) and $\tan\beta$ (right) with the predictions of the MSSM with light SUSY particles and the corresponding MSSM–like 2HDM; from Ref. [505].

Thus, besides the fact that its cross section is not particularly suppressed beyond the kinematical threshold for Higgs pair production, the $H^\pm W^\mp$ channel might allow, in addition, to probe the SUSY quantum effects. The signal essentially consists of $t\bar{b}W \rightarrow b\bar{b}WW$ and the main background will be, thus, $t\bar{t}$ production which can be substantially reduced by kinematical constraints. The strategy to detect the signal has been sketched in Ref. [500] and the prospects are not entirely hopeless provided the rates are not prohibitively small.

Other subleading processes

There are also higher–order processes for single $H^\pm$ production but with cross sections [500] that are even smaller than those of the processes discussed above. Among these, are the associated $W^\mp H^\pm$ production with a Z boson or neutral Higgs bosons $\Phi = h, H$ or A,

$$e^+e^- \rightarrow W^\mp H^\pm Z, \ W^\mp H^\pm \Phi \tag{4.15}$$

which leads to a surplus of $b\bar{b}W^\pm H^\pm$ final states which are discussed in Ref. [500] and associated production with W/Z and Φ bosons in vector boson fusion type processes,

$$e^+e^- \rightarrow W^\mp H^\pm e^+e^-, \ W^\mp H^\pm \nu\bar{\nu}, \ H^\pm Z e^\mp \nu, \ H^\pm \Phi e^\mp \nu \tag{4.16}$$

similarly to the SM Higgs case but with much smaller rates. In addition, there is a process which can be generated through the one–loop $H^\pm W Z$ and $H^\pm W \gamma$ vertices [500, 506],

$$e^+e^- \rightarrow H^\pm e^\mp \nu \tag{4.17}$$

4.4 The SUSY regime

If SUSY particles are light, they can alter in a significant way the physics of the MSSM Higgs bosons at e^+e^- linear colliders, not only indirectly through loop contributions as has been exemplified several times in the preceding sections but, also, directly at the production level. This topic has been touched upon only marginally up to now, except for a handful of examples that we summarize below. We mainly focus on the case of the lighter Higgs boson which will presumably be more favored by phase space considerations but we will also mention a few items for the heavier Higgs particles.

4.4.1 Decays into SUSY particles

Invisible decays of the neutral Higgs bosons

Invisible decays of the h boson in the MSSM, that is, decays into the LSP neutralinos[36] can be searched for in e^+e^- collisions in two ways [470, 528, 529]:

i) The recoil mass technique in the strahlung process, $e^+e^- \to Zh \to \ell^+\ell^- h$, allows to probe the h boson independently of its decays. Thus, by comparing the event rate in the recoil mass peak with the rate of all visible events that have been searched for directly in the relevant topologies, one could extract the invisible decay width.

ii) One can look at the $e^+e^- \to hZ$ process and explicitly ask for missing energy and missing momentum compatible with an invisible Higgs decay. Of course, this direct technique is expected to be highly superior to the indirect method i).

The same techniques hold for the heavier H boson when its couplings to the Z boson are not too strongly suppressed. In the case of the A boson, one has to consider the $e^+e^- \to hA$ or HA processes and look for the visible decays of the CP–even Higgs particles.

In Ref. [528], a detailed simulation has been performed for the process $e^+e^- \to Zh \to Z+ \not{E}$ in the environment expected at the TESLA machine with a c.m. energy of 350 GeV and an integrated luminosity of 500 fb^{-1}. The output of the analysis is shown in Fig. 4.35 where the achievable accuracy of the measurement of the invisible branching ratio BR$(h \to \chi_1^0 \chi_1^0)$ is displayed as a function of the branching ratio itself for three mass values, $M_h = 120, 140$ and 160 GeV. As can be seen, a 2–3% measurement can be performed for an invisible branching ratio that is larger than $\sim 20\%$, while a branching ratio of $\sim 5\%$ can be measured at the level of 10%. The figure also shows that the direct measurement of the rate (dashed lines) gives a much better accuracy than the indirect method (large dots). Note that the invisible

---

[36]Another possible invisible channel of the lighter h boson is the decay into sneutrinos, $h \to \tilde{\nu}\tilde{\nu}$, that are lighter than the charginos and thus would decay exclusively into neutrino and LSP neutralino final states, $\tilde{\nu} \to \chi_1^0 \nu$, which also escape detection. However, in view of the lower limit on the masses of the left–handed sleptons from the negative LEP2 searches, $m_{\tilde{\ell}} \gtrsim 100$ GeV, which are related through SU(2) symmetry to the sneutrino masses, these decays are now kinematically closed in the MSSM.
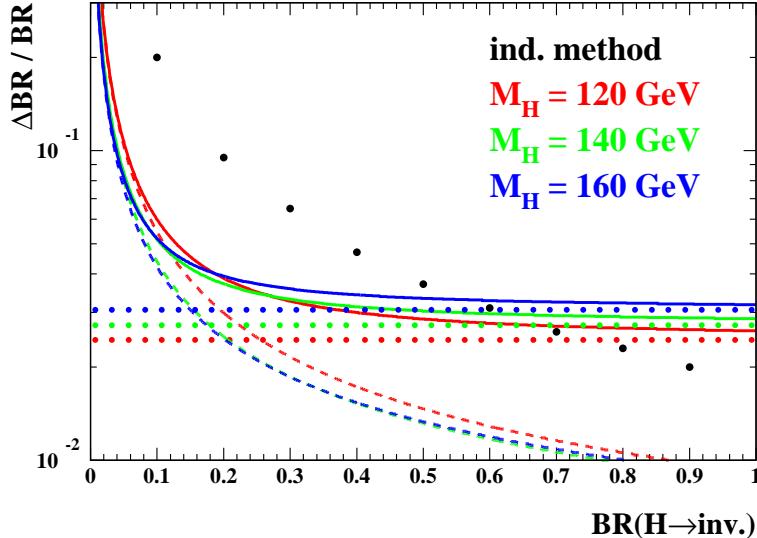
Figure 4.35: The expected accuracy on the invisible branching ratio $BR(h \to \chi_1^0 \chi_1^0)$ as a function of the branching ratio itself for three Higgs mass values, $M_h = 120, 140$ and 160 GeV using 500 fb^{-1} data at a c.m. energy $\sqrt{s} = 350$ GeV (full lines). The other lines indicate the individual contributions to these curves from the measurement of the invisible rate (dashed lines) and from the total Higgs–strahlung cross section measurement (dotted line). The large dots are the result of the indirect method [470]; from Ref. [528].

Higgs decay can be observed at the 5σ level down to a branching ratio of $\sim 2\%$ for this Higgs mass range at the considered energy and luminosity.

Higgs decays into SUSY particles

To investigate the decays of the heavier neutral and charged Higgs bosons into SUSY particles in the main production processes, $e^+e^- \to HA$ and $e^+e^- \to H^+H^-$, one has to look for final states where one of the Higgs bosons decays into standard modes [mainly $t\bar{t}$ and $b\bar{b}$ for the neutral and tb for the charged Higgs particles] while the other one decays into charginos and/or neutralinos as well as into top and/or bottom squarks [40,61]. As discussed previously [see Fig. 2.35], the decays into the other squarks are disfavored either by phase space or by the small couplings, while the branching ratios into sleptons are always small and can be safely neglected in this discussion.

Here, we only briefly comment on the case where one of the Higgs bosons decays into chargino and neutralino pairs,

$$
\begin{aligned}
e^+e^- &\to HA &&\to [t\bar{t} \text{ or } b\bar{b}]\,[\chi^+\chi^- \text{ or } \chi^0\chi^0] \\
e^+e^- &\to H^+H^- &&\to [t\bar{b} \text{ or } b\bar{t}]\,[\chi^-\chi^0 \text{ or } \chi^+\chi^0]
\end{aligned}
\tag{4.18}
$$

The HA production cross sections times the branching ratios for these decays is exemplified in Fig. 4.36 as a function of M_A at a c.m. energy $\sqrt{s} = 1$ TeV in a scenario where the

parameter μ is large such that only decays into the lighter chargino and neutralinos are allowed by phase–space, $\mu = 2M_2 \simeq 4M_1 = 400$ GeV; the squarks and the sleptons are assumed to be very heavy. For the chosen $\tan\beta = 5$ value, both the $b\bar{b}$ and $t\bar{t}$ decays [when kinematically allowed] have substantial branching ratios. In the left–hand (right–hand) side of the figure, shown are the branching ratios for the visible $HA \to b\bar{b}b\bar{b}$ ($HA \to t\bar{t}t\bar{t}$) modes and for the mixed decays $HA \to b\bar{b}\chi\chi$ ($HA \to t\bar{t}\chi\chi$). As can be seen, the cross section times branching ratios for the later decays and, particularly when the $H/A \to b\bar{b}$ modes are selected, can be significant and should be easily detected in the clean environment and for the luminosities $\mathcal{L} \sim \mathcal{O}(1\,\text{ab}^{-1})$ that are expected at these machines. As discussed in §2.2.3, the lightest chargino χ_1^+ and next–to–lightest neutralino χ_2^0 decay into the LSP and [possibly virtual] W, Z and the lightest Higgs boson h. In the limit of large $|\mu|$, the partial widths of these decays have been given in eq. (2.77) in the decoupling limit.
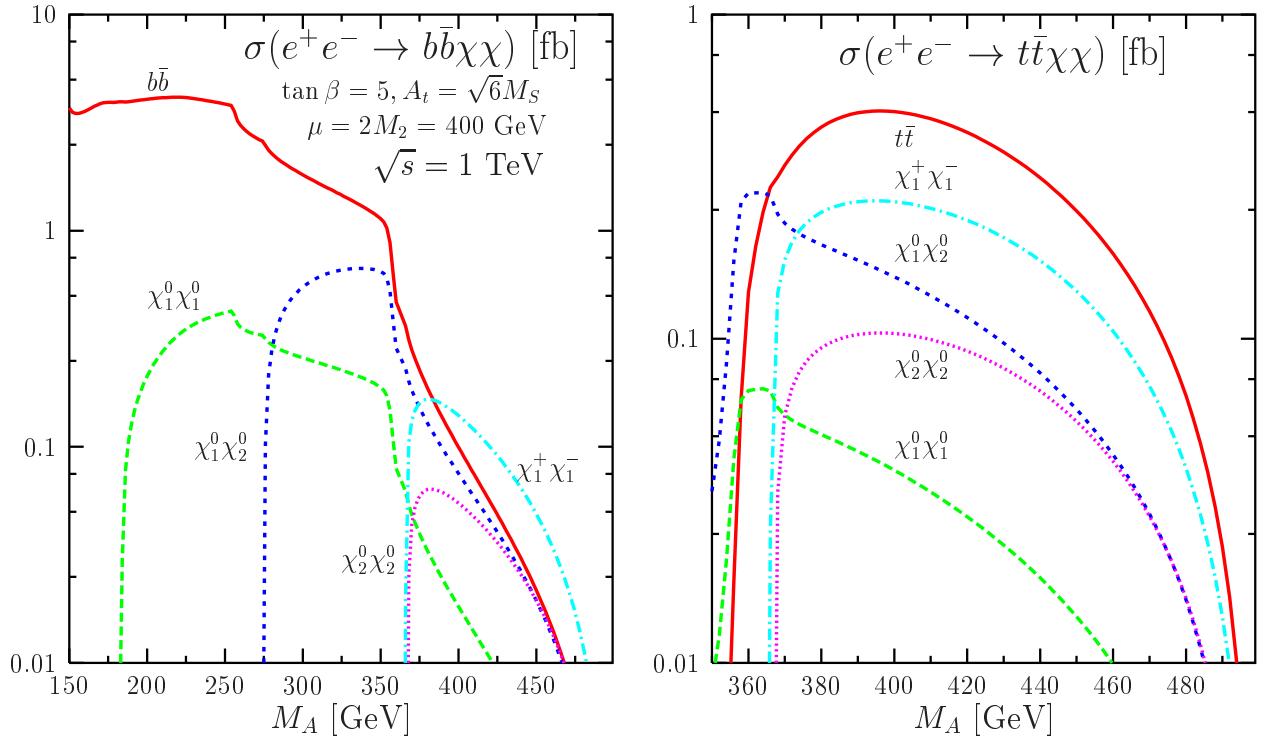
Figure 4.36: The cross sections times branching ratios for the production of HA states with the subsequent decays of one of the Higgs bosons into chargino/neutralino pairs and $b\bar{b}$ (left) and $t\bar{t}$ (right) pairs as a function of M_A at a c.m. energy of 1 TeV; the MSSM parameters are $\tan\beta = 5$, $m_{\tilde{q}} = 1$ TeV with maximal stop mixing and $\mu = 2M_2 = 400$ GeV.

In the case of the $H^\pm$ boson, the cross section times branching ratio for $e^+e^- \to H^+H^- \to tb\chi^\pm\chi^0$ is shown in Fig. 4.37 for the same scenario as previously (solid lines). Because the branching ratio $\mathrm{BR}(H^+ \to t\bar{b})$ is large, only the decay $H^+ \to \chi_1^+\chi_1^0$ has a sizable rate, and the rate exceeds the fb level when the phase space is not too penalizing. The decay $H^+ \to \chi_1^+\chi_2^0$,

although allowed by phase space at large $M_{H^\pm}$, has a too small rate in this case. For negative μ values, the charginos and neutralinos are less mixed than for positive μ and, hence, have couplings to the Higgs bosons that are suppressed. The masses of the states are also larger than for $\mu > 0$, resulting in smaller branching ratios. For lower μ values, $\mu \sim \pm 200$ GeV, the decays into almost all ino species are possible and the cross sections times branching ratios for these decays are larger than in the previous scenario.
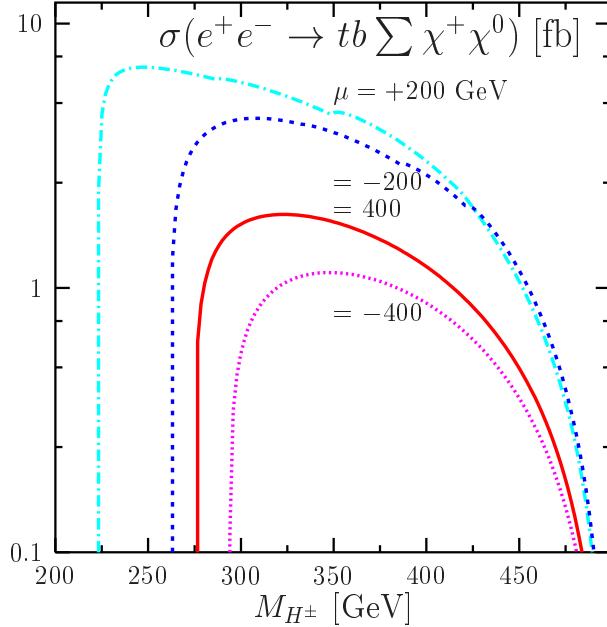

Figure 4.37: *The cross sections times branching ratios for the production of H^+H^- states with the subsequent decays of one of the Higgs bosons into the sum of chargino/neutralino pairs and the other into tb states as a function of $M_{H^\pm}$ at a c.m. energy of 1 TeV; the MSSM parameters are as in the previous figure but with $\mu = 2M_2 = \pm 200, \pm 400$ GeV.*

Note that, as discussed in §2.2.3, when all chargino and neutralino decay channels are open, the branching ratios BR $(\Phi \rightarrow \sum \chi\chi)$ are approximately the same for $\Phi = H, A$ and $H^\pm$. The production rates for H, A bosons decaying into inos [for say, $\mu = \pm 200$ GeV] is simply given by the magnitude of the HA cross section relative to that of H^+H^-.

4.4.2 Associated production with SUSY particles

The neutral h boson can be produced in association with the neutralinos and charginos if the latter particles are light enough to be accessed kinematically. In particular, associated h production with the LSP neutralinos, $e^+e^- \rightarrow h\chi_1^0\chi_1^0$, is the most favored process by phase space. In this process, the Higgs boson can be radiated off the neutralinos and virtual Z lines in the s–channel process $e^+e^- \rightarrow Z^* \rightarrow \chi_1^0\chi_1^0$, as well as from the neutralino and selectron lines in the t/u–channel diagrams. However, all these couplings are rather small and the

271

cross sections never reach the level of 0.1 fb even for sparticle masses with values close to their experimental limits [507]. The production in association with the lighter chargino, $e^+e^- \to h\chi_1^+\chi_1^-$ is more promising [508] because the h couplings to the $\chi_1^\pm$ [and even to the $\tilde{\nu}$s which are exchanged in the t–channel] are larger and the exchange of the photon in the s–channel enhances substantially the cross section of the $e^+e^- \to \chi_1^+\chi_1^-$ parent process.
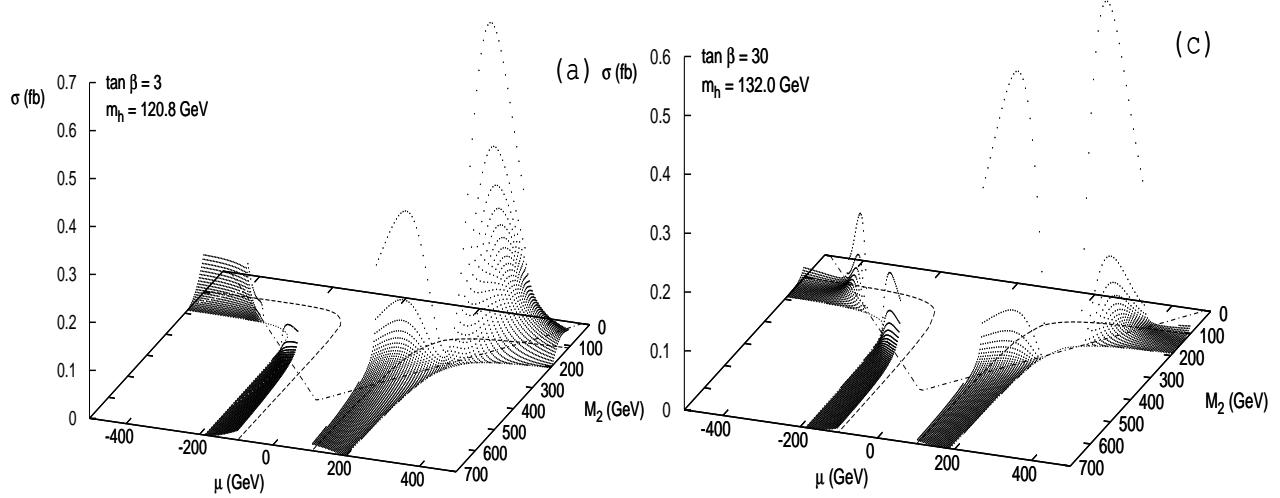
Figure 4.38: The total cross section for the associated production process $e^+e^- \to h\chi_1^+\chi_1^-$ in the μ–M_2 plane at $\sqrt{s} = 500$ GeV for $\tan\beta = 3$ and 30; the maximal mixing scenario with $M_A = 500$ GeV is assumed; from Ref. [508].

This channel has been recently discussed [508] in the case of very large slepton masses, where one has to consider only the s–channel diagrams. In Fig. 4.38, the production cross sections are shown in the μ–M_2 parameter space at a c.m. energy $\sqrt{s} = 500$ GeV for two values $\tan\beta = 3$ and 30 in the maximal mixing scenario and in the decoupling limit, $M_A = 500$ GeV. The shaded areas in the μ–M_2 plane are those in which non–resonant $e^+e^- \to h\chi_1^+\chi_1^-$ production is kinematically possible at this energy. As can be seen, for moderate and positive values of μ and small to moderate value of M_2, for which the charginos $\chi_1^\pm$ are mixtures of gaugino and higgsino states and not too heavy, the cross sections can almost reach the fb level.

Much larger cross sections can be obtained in associated Higgs production with third generation sfermions [446, 507, 509]. As discussed in §1.2.4, for large mixing in the stop [in particular, for large values of $X_t = A_t - \mu\cot\beta$] and sbottom/stau [large values of $X_{b,\tau} = A_{b,\tau} - \mu\tan\beta$] sectors, there is a strong enhancement of the h couplings to these particles. The mixing, incidentally, induces a large splitting between the sfermion eigenstates, allowing one of them to be light and potentially accessible kinematically.

The cross sections for the processes $e^+e^- \to h\tilde{t}_1\tilde{t}_1$ at $\sqrt{s} = 800$ GeV and $e^+e^- \to h\tilde{\tau}_1\tilde{\tau}_1$ at
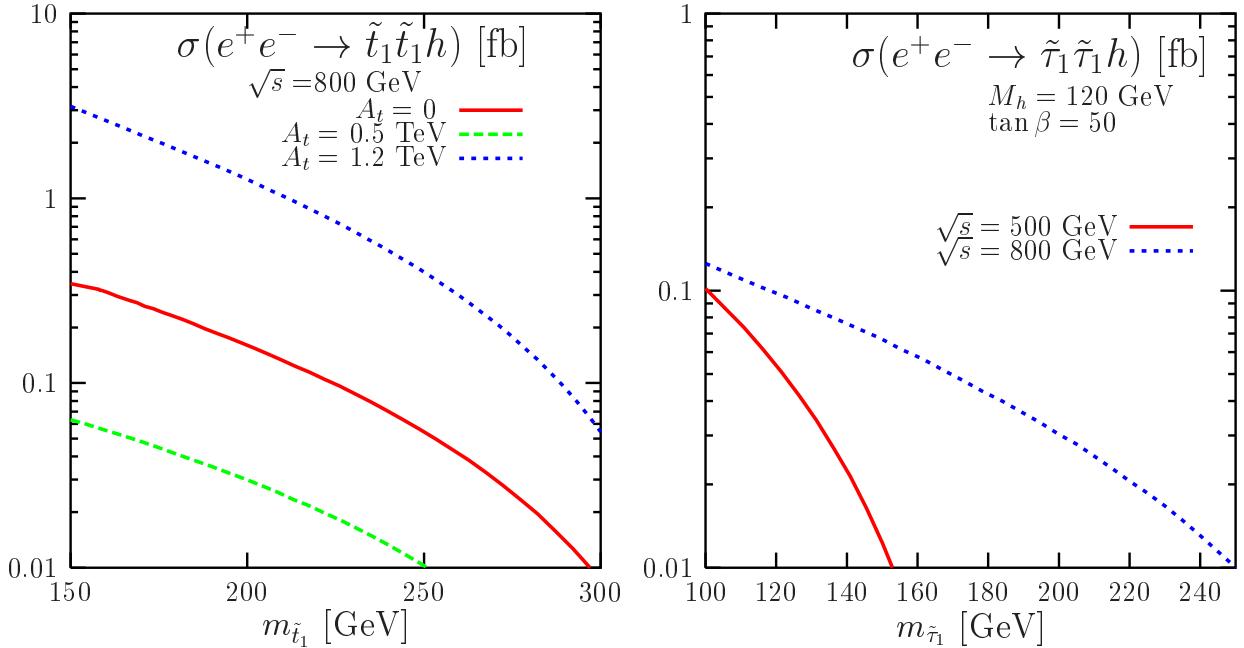
Figure 4.39: *The associated production cross sections of the lighter h boson with sfermions as a function of their masses: $\sigma(e^+e^- \to h\tilde{t}_1\tilde{t}_1)$ for several values of A_t at $\sqrt{s} = 800$ GeV [446] (left) and $\sigma(e^+e^- \to h\tilde{\tau}_1\tilde{\tau}_1)$ for $\mu = -A_\tau = 500$ GeV and $\tan\beta = 50$ at $\sqrt{s} = 500$ and 800 GeV [507] (right). In both cases, the decoupling limit has been assumed.*

$\sqrt{s} = 500$ and 800 GeV are shown in, respectively, the left– and right–hand sides of Fig. 4.39 as a function of the sfermion masses in various scenarios that are indicated in the captions. As in the case of $pp \to h\tilde{t}_1\tilde{t}_1$ at the LHC, the cross sections for associated Higgs production with the lighter top squarks, can be significant for large values of A_t and small $m_{\tilde{t}_1}$. For stop masses below ~ 200 GeV they can exceed the femtobarn level for $A_t \sim 1$ TeV and are thus comparable to the $ht\bar{t}$ cross section. For associated production with $\tilde{\tau}$'s, the cross sections are smaller; still, for $m_{\tilde{\tau}_1} \lesssim 140$ GeV and $\tan\beta \gtrsim 50$, they can reach the level of 0.1 fb.

4.4.3 Production from the decays of SUSY particles

The lighter Higgs boson can also be produced in the decays of SUSY particles if the latter are kinematically accessible at the collider. As discussed in §2.3, if the splitting between the two third generation sfermion eigenstates is large, it could allow for the decays of the heavier sfermion into the lighter one plus a Higgs boson. In the case of the top squark for instance, mixed $e^+e^- \to \tilde{t}_1\tilde{t}_2$ production can take place through Z–boson exchange [photon exchange is forbidden by $U(1)_{\text{QED}}$ symmetry], with the subsequent decay $\tilde{t}_2 \to \tilde{t}_1$ plus a Higgs boson. In fact, this process is the resonant counterpart of the associated $e^+e^- \to \tilde{t}_1\tilde{t}_1h$ process discussed above and can provide much larger event rates.

Such a situation is illustrated in Fig. 4.40, where the cross section $\sigma(e^+e^- \to \tilde{t}_1\tilde{t}_2)$ times the branching ratio $\mathrm{BR}(\tilde{t}_2 \to \tilde{t}_1 h)$ is shown as a function of the $\tilde{t}_1$ mass at a c.m. energy of $\sqrt{s} = 800$ GeV in an mSUGRA scenario with $\tan\beta = 30$, $m_{1/2} = 100$ GeV, $A_0 = -600$ GeV and $\mathrm{sign}(\mu) = +$. As can be seen, the cross section can reach the level of 1 fb for relatively small $m_{\tilde{t}_1}$ values, leading to more than one thousand events in the course of a few years, with the expected integrated luminosity of $\int \mathcal{L} \sim 500$ fb^{-1}. The dotted lines show the contribution of the non–resonant contributions which is very small in this case.
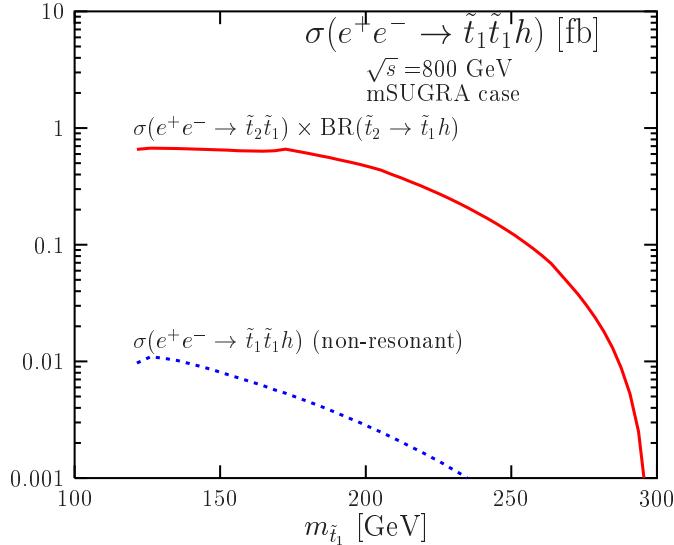
Figure 4.40: The cross section $\sigma(e^+e^- \to \tilde{t}_1\tilde{t}_1 h)$ at $\sqrt{s} = 800$ GeV as a function of $m_{\tilde{t}_1}$ in an mSUGRA scenario with $\tan\beta = 30$, $m_{1/2} = 100$ GeV and $A_0 = -600$ GeV. Shown are the resonant piece and the cross section in the continuum; from Ref. [446].

Finally, a copious source of Higgs particles might be provided by the cascade decays of charginos and neutralinos which can be produced in e^+e^- collisions with large rates. Indeed, the production of identical chargino pairs is mediated by photon as well as Z boson exchange, and has always a large cross section, even in presence of the possible negative interference of the t–channel sneutrino exchange. Neutralino production proceeds only through s–channel Z boson exchange [as is the case for mixed chargino pairs] and t/u–channel selectron exchange and the cross section is in general smaller, in particular, for gaugino like states [which have very small couplings to the Z bosons] and heavy sleptons [which suppresses the contribution of the t/u–channel diagrams]. In addition, as discussed in §2.3, charginos and neutralinos can have large decay branching ratios into Higgs bosons.

To our knowledge, a detailed study of this possibility has not been performed for e^+e^- colliders. We have thus started a study of this possibility [510] and we show in Fig. 4.41 some preliminary results of the possible production rates for such mechanisms. Fixing the two Higgs sector parameters to $M_A = 120$ GeV and $\tan\beta = 5$, we show the cross sections

times branching ratios for the processes that are allowed by phase space as a function of μ when the other relevant parameters are set to $M_2 = 2M_1 = 250$ GeV at $\sqrt{s} = 500$ GeV (left) $M_2 = 2M_1 = 300$ GeV at $\sqrt{s} = 800$ GeV (right); the common squark and slepton masses are taken to be 1 TeV and 300 GeV and maximal stop mixing is assumed.
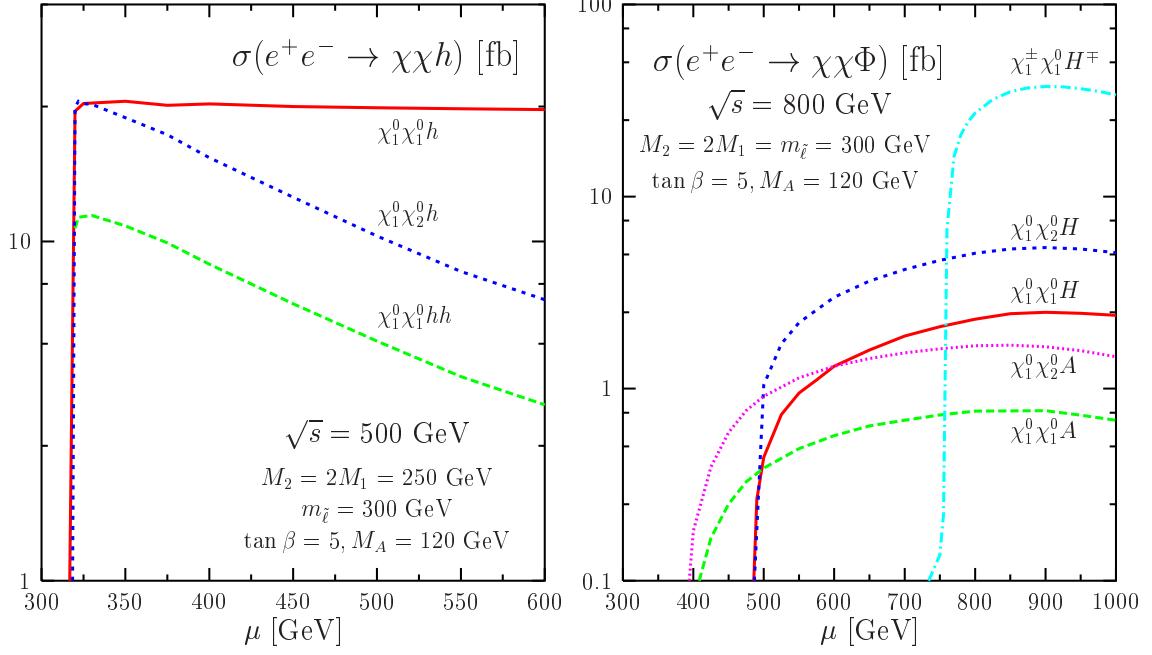
Figure 4.41: The cross sections times branching ratios for the production of MSSM Higgs bosons from the decays of χ_2^0 and $\chi_1^\pm$; the MSSM parameters are $M_A = 120$ GeV, $\tan\beta = 5$, $m_{\tilde{q}} = 1$ TeV and maximal mixing is assumed. Left: h production for $M_2 = 2M_1 = 250$ GeV, $m_{\tilde{\ell}} = 250$ GeV and $\sqrt{s} = 500$ GeV and right: H, A and $H^\pm$ production for $M_2 = 2M_1 = m_{\tilde{\ell}} = 300$ GeV and $\sqrt{s} = 800$ GeV; from Ref. [510].

In the left–hand side of the figure, $\sqrt{s}$ is fixed to 500 GeV and only the processes involving χ_1^0 and χ_2^0 are kinematically possible. In addition, only the decay $\chi_2^0 \to h\chi_1^0$ is allowed since $M_h \lesssim m_{\chi_2^0} - m_{\chi_1^0} \lesssim M_A$ and the branching ratio is close to unity since the other two–body decay mode, $\chi_2^0 \to Z\chi_1^0$, is suppressed the two neutralinos being gaugino–like. The $e^+ e^- \to \chi_2^0 \chi_1^0$ cross section leads to an almost constant and large $\sigma \times \mathrm{BR}(\chi_1^0 \chi_1^0 h)$. In turn, $\sigma(e^+ e^- \to \chi_2^0 \chi_2^0)$ is suppressed for increasing μ values as χ_2^0 approaches the phase–space limit $m_{\chi_2^0} \sim 250$ GeV. Still, $\sigma \times \mathrm{BR}(\chi_1^0 \chi_2^0 h)$ and even $\sigma \times \mathrm{BR}(\chi_1^0 \chi_1^0 hh)$ have significant rates. In the right–hand side of the figure, the c.m. energy is increased to $\sqrt{s} = 800$ GeV and the value of M_2 is slightly larger, allowing for the decays into the heavier Higgs bosons to take place as well. The rates are also large, exceeding the fb level in most of the cases that are displayed. The highest rate is originating from $\sigma(e^+ e^- \to \chi_1^+ \chi_1^-)$ as the process is mediated by photon exchange which occurs with full strength. Thus, when the chargino is accessible and the decay $\chi_1^+ \to H^+ \chi_1^0$ is kinematically allowed, the rate for H^+ production from chargino decays can be comparable to the one from direct production in $e^+ e^-$ collisions.

275

4.5 s–channel Higgs production at $\gamma\gamma$ and $\mu^+\mu^-$ colliders

4.5.1 Strengths and weaknesses of e^+e^- colliders for MSSM Higgs bosons

As should be clear from the preceding discussions, e^+e^- linear colliders with energies in the range 300–500 GeV to be extended to 1 TeV, and a luminosity a few times $10^{34}\mathrm{cm}^{-2}\mathrm{s}^{-1}$, are ideal instruments to search for the Higgs bosons of the MSSM. As far as the direct searches of the particles are concerned [we will comment on the impact of the precision measurements in the forthcoming section], the discussion can be summarized as follows.

The lighter CP–even Higgs particle h can be detected in the entire range of the MSSM parameter space either through the Higgs–strahlung process, $e^+e^- \to hZ$, or through pair production, $e^+e^- \to hA$. In fact, this conclusion holds true even at a c.m. energy of 300 GeV, independently of the other parameters of the MSSM such as the squark masses and $\tan\beta$ and also if invisible neutralino decays are allowed for. The missing mass technique in Higgs–strahlung plays a key role in this context and, since the cross section scales as $1/s$, it is preferable to operate the collider at low energies, $\sqrt{s} \sim M_Z + \sqrt{2}M_h$, where the event rate is maximal. The properties of this particle can be measured with a very high degree of accuracy, as was shown for a SM–Higgs boson in the mass range 100–150 GeV.

There is a substantial area of the MSSM parameter space where all the neutral and charged Higgs bosons can be discovered at these colliders. This is possible if the mass of the pseudoscalar A boson which, at this stage, is approximately equal to the masses of the heavier neutral CP–even and charged Higgs bosons, $M_A \sim M_H \sim M_{H^\pm}$, is less than the collider beam energy, $M_A \lesssim \frac{1}{2}\sqrt{s}$. This is because the only two channels which are relevant at high masses, in particular for high $\tan\beta$ values, are the pair production processes $e^+e^- \to HA$ and $e^+e^- \to H^+H^-$. Again, when these channels are kinematically accessible, it is preferable to operate the e^+e^- collider at not too high energies since the production cross sections also drop like $1/s$. In turn, when the particles are heavier than $\frac{1}{2}\sqrt{s}$, one simply needs to raise the energy of the collider up to the kinematical threshold.

If the SUSY particles are not too heavy, they could affect in a significant way the phenomenology of at least the heavier $H, A, H^\pm$ bosons [and that of the h boson, but only indirectly except for very light LSPs]. The production cross sections and the decay branching ratios can be altered via loop contributions of SUSY particles and, potentially, Higgs decays into and/or associated production with these particles might be observed. This would provide a unique opportunity to access the Higgs couplings to superparticles which are of special importance since they probe both the electroweak symmetry and the Supersymmetry breaking mechanisms. The possible determination of these couplings in the clean environment of e^+e^- colliders would help to reconstruct the SUSY Lagrangian at the EWSB scale which would then allow the structure of the fundamental theory at high scales to be derived.

However, there are also a few situations which cannot be addressed and some questions which cannot be answered in a satisfactory way at e^+e^- machines and either at the LHC:

i) The total decay widths of the Higgs particles cannot be measured with a very good accuracy. The width of the h boson in the decoupling regime is too small to be resolved experimentally while the widths of the $H, A, H^\pm$ bosons can be probed only at relatively high masses and for small or large values of $\tan\beta$ since they rise as $\Gamma_\Phi \propto (m_t^2 \cot^2\beta + m_b^2 \tan^2\beta)M_\Phi$. This is shown in Fig. 4.42 where the H/A total widths are displayed in the range $M_A = 250$–500 GeV for several $\tan\beta$ values. Since for heavy SUSY particles, these Higgs bosons decay mostly into t, b and eventually τ states, the width measurements [in particular when they are small, $i.e.$ for the intermediate values $5 \lesssim \tan\beta \lesssim 15$] suffer from the poor experimental resolution on these fermions. In fact, this problem is a sequel of the usual difficulty of measuring $\tan\beta$ with a satisfactory accuracy in its entire range.

ii) Close to the decoupling limit, the difference between the masses of the scalar H and the pseudoscalar A bosons is rather tiny, as shown also in Fig. 4.42 where the $M_H - M_A$ difference is displayed as a function of M_A for selected $\tan\beta$ values. The same problem arises in the anti–decoupling regime, where the lighter h particle will play the role of the H boson. At high $\tan\beta$, as well as at low $\tan\beta$ when the H/A masses are beyond the $t\bar{t}$ threshold, the two Higgs particles will have essentially the same decay modes and total widths. Since they are generally produced in pairs, the two Higgs bosons cannot be discriminated.

iii) The fact that in the decoupling limit, the H/A bosons can only be produced in pairs generates an additional problem: the mass reach of the e^+e^- collider is $M_A \lesssim \frac{1}{2}\sqrt{s}$. In this regime, this is also the case for the charged Higgs boson as $M_{H^\pm} \sim M_A$ and for these M_A values, single H production in WW fusion is suppressed by the small g_{HVV} coupling while associated $H/A/H^\pm$ production with heavy fermions does not allow to significantly exceed the beam energy. At the first stage of the planned e^+e^- colliders, the mass reach is thus limited to $M_A \sim 250$ GeV. In §3.3.2, we have seen that at the LHC, there is a significant range of $\tan\beta$ values, $3 \lesssim \tan\beta \lesssim 10$–$20$, in which only the lighter h boson is accessible for $M_A \sim 250$–500 GeV, even after collecting a large luminosity. The $H/A/H^\pm$ bosons could be thus only slightly heavier than 250 GeV without being observed at the LHC or at a 500 GeV e^+e^- collider. Of course, for such Higgs mass and $\tan\beta$ values, the effects of these particles would be visible in the couplings of the lighter h boson, but one would have to wait for the SLHC or for the higher–energy stage of the e^+e^- collider to probe directly this range.

iv) If SUSY particles are light, the measurement of the Higgs couplings to these particles would provide important informations on the MSSM Lagrangian. However, the loop induced decays [which involve sparticles] are in general very rare and the rates for direct Higgs decays into sparticles or decays of sparticles into Higgs bosons might be too small to be detected at e^+e^- colliders in some areas of the MSSM parameter space.
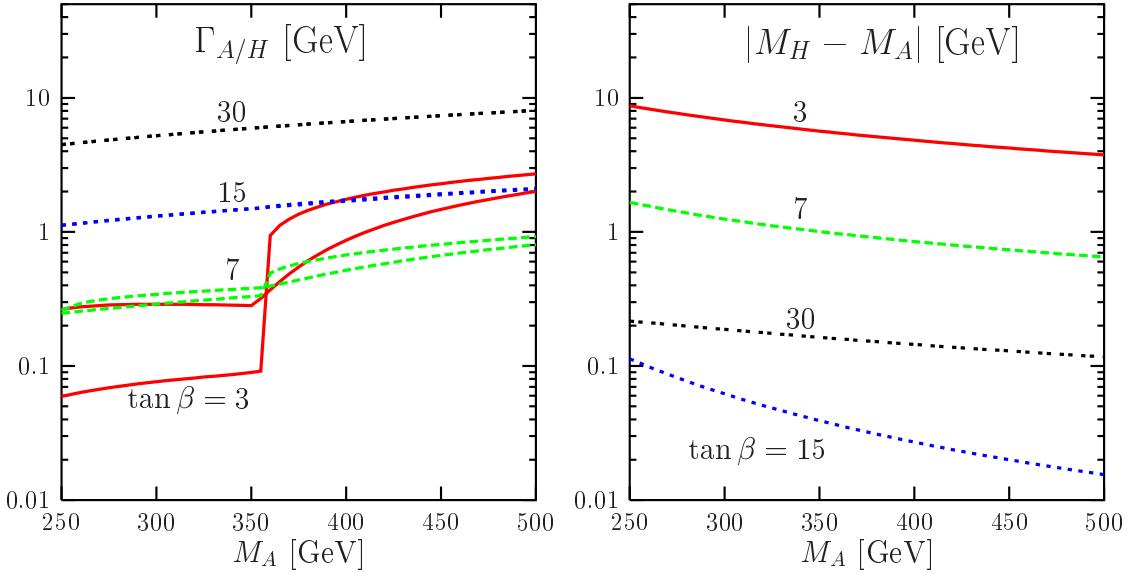
Figure 4.42: The total decay widths of the H and A bosons (left) and their mass difference (right) as function of M_A for several values $\tan\beta = 3, 7, 15$ and 30.

The s–channel production of the MSSM neutral Higgs bosons at $\gamma\gamma$ and $\mu^+\mu^-$ colliders can address some of these issues. Indeed, the energy reach of $\gamma\gamma$ colliders is expected to be $\sim 80\%$ of that of the original e^+e^- collider and, thus, they can in principle probe higher masses in single production, $\gamma\gamma \to H/A$, potentially solving problem *iii*). For instance, the mass reach of a 500 GeV LC in the $\gamma\gamma$ option is expected to be $M_A \sim 400$ GeV and, if precision measurements of the h boson properties indicate that such a light A particle is likely, one could immediately operate in the $\gamma\gamma$ option rather than waiting for the higher stage of the e^+e^- machine. In addition, $\gamma\gamma$ colliders might help improving the determination of $\tan\beta$ in *i*), e.g. using the $\tau\tau$ fusion process $\gamma\gamma \to \tau\tau + H/A$ as recently pointed out. Muon colliders can also address these two points, if they operate at high enough energy and luminosity [and for *iii*), before the 1 TeV e^+e^- collider, which seems unlikely]. However, it is for point *ii*) that they provide a unique opportunity: because of the very good energy resolution which can be achieved, one could perform a separation of the almost overlapping A and H resonances if their intrinsic widths are not much larger than their mass difference. For point *iv*) SUSY loop effects can be probed in the measurement of the Higgs–$\gamma\gamma$ couplings while direct Higgs decays into SUSY particles could be studied in detail at $\mu^+\mu^-$ colliders.

In the following two subsections, we briefly discuss the main benefits which can be obtained at $\gamma\gamma$ and $\mu^+\mu^-$ colliders, restricting to the four topics *i*)–*iv*) listed above. Many other physics issues can also be studied at these colliders and a very important one, the verification of the Higgs CP properties, has been already discussed in the SM–Higgs case and we have little to add. The measurement of the Higgs couplings to SM particles has been also discussed in §I.4.5 and §I.4.6 and a few additional remarks will be made later in §4.6.

278

4.5.2 Production at $\gamma\gamma$ colliders

Detection of the H/A bosons in the range $M_A = 250$–500 GeV

The production of Higgs bosons in $\gamma\gamma$ collisions has been discussed in §I.4.5 where all the basic ingredients have been given. The study of MSSM H/A production in the M_A range beyond the kinematical reach of the e^+e^- collider has been performed in detail in Ref. [512] on which the subsequent material will be based. However, in this study, the c.m. energy of the initial e^+e^- collider was assumed to be $\sqrt{s} = 650$ GeV so that Higgs bosons with masses up to $M_A \sim M_H \sim 500$ GeV can be probed and the wedge of Fig. 3.43, where only the SM–like h boson can be discovered at the LHC, is entirely covered[37].

The study assumes the NLC machine and detector designs discussed in Ref. [514] for an e^+e^- center of mass energy up to $\sqrt{s} \approx 630$ GeV; the expectations for the TESLA machine [513] are obtained by simply multiplying the luminosity by a factor of ~ 2. The beam spectra and, hence, the luminosity and the polarization, are obtained with the Monte–Carlo event generator `CAIN` [530]. For the broad spectrum, the obtained luminosity is large even below the peak at $E_{\gamma\gamma} \sim 500$ GeV, while the average photon polarization $\langle\lambda_1\lambda_2\rangle$ is large only for $E_{\gamma\gamma} \gtrsim 450$ GeV. For the peaked spectrum, the luminosity is large near the peak, $E_{\gamma\gamma} \gtrsim 400$ GeV and the product $\langle\lambda_1\lambda_2\rangle$ is of moderate size for $250 \lesssim E_{\gamma\gamma} \lesssim 400$ GeV.

Since the masses of the H and A bosons will not be precisely known, one cannot immediately tune the energy of the machine to sit on the resonances. Therefore, one has either to scan in the c.m. energy of the $e^+e^-/\gamma\gamma$ collider using a peaked $E_{\gamma\gamma}$ luminosity spectrum or run at a fixed c.m. energy with a broad spectrum and then switch to a peaked spectrum. In Ref. [512], it has been suggested that for the problem that we are concerned with here, it is more convenient to run at a fixed energy but with a peaked spectrum half of the time and with a broad spectrum the rest of the time.

The effective production cross sections for the $\gamma\gamma \to H/A \to b\bar{b}$ processes, as defined in §I.4.5.1 [but without the polarization factors $(1 + \lambda_1\lambda_2)$ and the δ function replaced by $\sqrt{s}$], are shown in Fig. 4.43 as a function of M_A for several values of $\tan\beta$; the maximal mixing scenario has been assumed with $M_S = 1$ TeV so that the loop induced $\gamma\gamma$ width and the total decay width are not affected by the heavy SUSY particles.

As for the backgrounds, the average $\langle\lambda_1\lambda_2\rangle$ obtained with `CAIN` is not close enough to unity to suppress strongly the $J_Z = 2$ events from $\gamma\gamma \to b\bar{b}$ by the $1 - \langle\lambda_1\lambda_2\rangle$ factor. Cuts similar to those discussed in §I.4.5 are needed to further suppress these backgrounds. In Ref. [512] an angular cut $\cos\theta_{b,\bar{b}} \lesssim 0.5$ has been applied and a cut of 10 GeV on the $b\bar{b}$ mass distribution has been chosen [the total Higgs widths in the range that is relevant here,

---

[37]Of course, stopping the variation of M_A at 500 GeV in these figures was arbitrary. The wedge is much larger if the value of M_A is pushed to 1 TeV and the additional range will not be covered by this analysis.
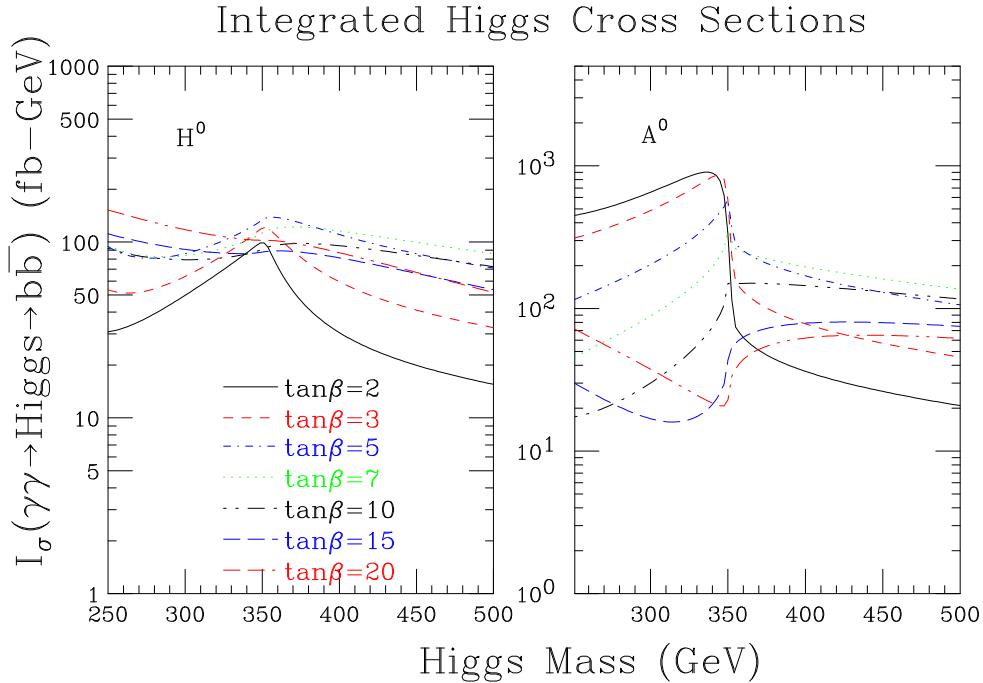
Figure 4.43: Effective cross sections for the production of the heavier CP–even (left) and the CP–odd (right) Higgs bosons in $\gamma\gamma$ collisions, $\sigma(\gamma\gamma \to H/A \to b\bar{b})$, as a function of M_A for several $\tan\beta$ values in the maximal mixing scenario with $M_S = 1$ TeV; from Ref. [512].

$250 \lesssim M_A \lesssim 500$ GeV and $3 \lesssim \tan\beta \lesssim 20$, is smaller than 5 GeV but the $M_H - M_A$ difference can be also of a few GeV; see Fig. 4.42] with assumptions that half of the Higgs events will fall into the 10 GeV bin centered around M_A. In this case, the obtained signal events for $\tan\beta = 3, 7, 15$ and for the $b\bar{b}/c\bar{c}$ background events are shown in Fig. 4.44 as a function of the jet–jet invariant masses for the broad and peaked spectra.
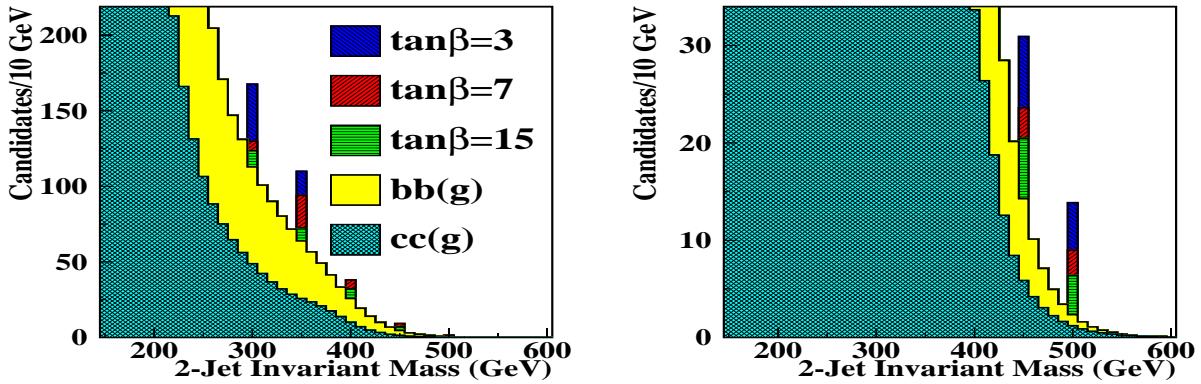
Figure 4.44: Signal and background rates for the considered M_A–$\tan\beta$ range as a function of the jet–jet invariant mass for a broad spectrum (left) and a peaked spectrum (right) for one year operation at $\sqrt{s} = 630$ GeV. The cuts are as described in the text; from Ref. [512].
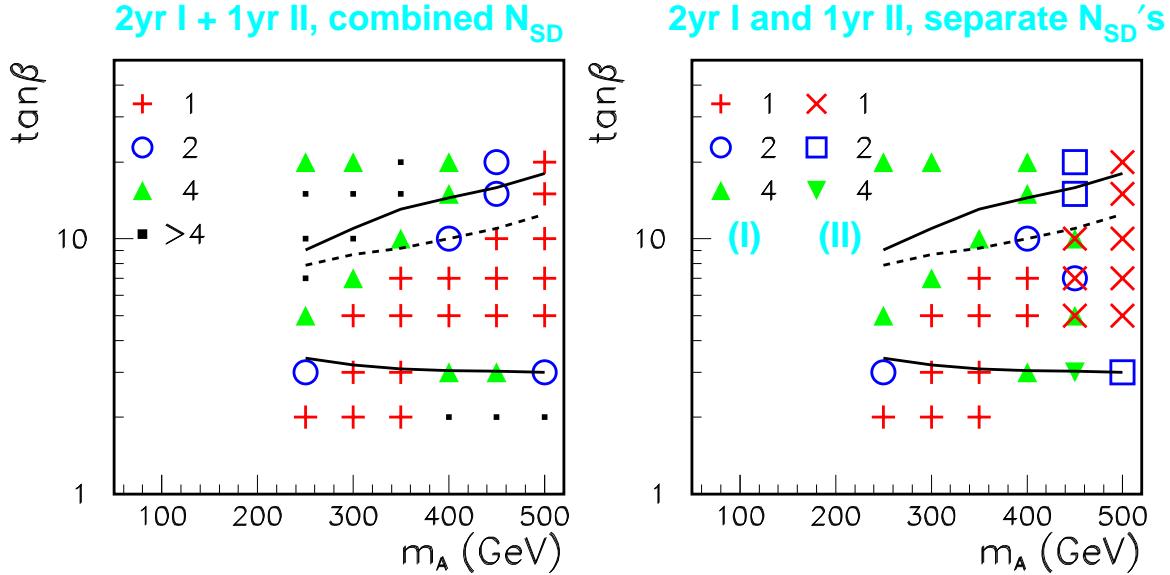
Figure 4.45: The M_A–$\tan\beta$ points for which two years of broad spectrum operation plus one year of peaked spectrum operation at $\sqrt{s} = 630$ GeV will yield a significance $S/\sqrt{B} \geq 4$. Shown are the combined significance from both the broad and peaked spectra running (left) and the separate significances from the broad and peaked spectra running (right). Also shown are the additional points for which a 4σ signal is achieved if the total luminosity is doubled ('2') or quadrupled ('4') relative to the assumed luminosity. The small black squares in the left figure indicate additional points sampled for which even a luminosity increase by a factor of four for both spectra does not yield a 4σ signal. The solid curves show the boundaries of the LHC wedge region of Fig. 3.45; from Ref. [512].

The ability of a $\gamma\gamma$ collider, based on the NLC design and running at this energy, to cover the LHC wedge is illustrated in Fig. 4.45 where the range of the M_A–$\tan\beta$ parameter space in which a 4σ detection of the H/A bosons is possible under specific assumptions on the available luminosity as indicated in the caption. A significant portion of the parameter space can be probed with the nominal luminosity and a three year running of the machine. If the luminosity is a factor of four larger [a factor of two in a TESLA–like design] only a few points [$7 \lesssim \tan\beta \lesssim 15$ with $300 \lesssim M_A \lesssim 400$ GeV, since the lower part of the M_A range up to ~ 300 GeV can be probed in the process $e^+e^- \to HA$ in the original mode of the collider] would be left out. A further improvement in the luminosity and/or in the mass resolution would allow to probe these remaining points and to cover the entire wedge. Thus, the $\gamma\gamma$ option of future linear e^+e^- colliders can indeed allow the coverage of a larger part of the MSSM Higgs sector parameter space.

Determination of $\tan\beta$

The measurement of the $\gamma\gamma \to H/A \to b\bar{b}$ rate as discussed above can be used for a determination of $\tan\beta$. Again, for an NLC based 630 GeV $\gamma\gamma$ collider with a two years and one year operation with, respectively, a broad and a peaked spectrum, one can measure $\tan\beta$ with the accuracies shown in Table 4.3 for selected values of M_A and $\tan\beta$ [512]. The accuracies, at most of the order of 30% in the favorable cases, are clearly worse than those which can be achieved at a 1 TeV e^+e^- collider; see Fig. 4.29.

M_A [GeV]	250	300	350	400	450	500
$\tan\beta = 3$	0.51	0.27	–	0.45	0.30	0.32
$\tan\beta = 7$	–	0.66	0.23	0.62	0.67	0.87
$\tan\beta = 15$	0.46	0.67	–	–	–	–

Table 4.3: Uncertainties on the parameter $\tan\beta$ as determined from measurements of the $\gamma\gamma \to H/A \to b\bar{b}$ production rate associated with the Higgs discovery in the LHC wedge as discussed in the text; errors larger than 100% are not shown.

It has been recently pointed out that there is a much better way to measure this parameter in $\gamma\gamma$ collisions: the fusion of τ leptons, $\gamma\gamma \to \tau^+\tau^-\Phi$ with $\Phi = h, H, A$ [531]. The cross section, which can be easily derived in the equivalent particle approximation, is proportional to the square of the $g_{\Phi\tau\tau}$ coupling which is enhanced at large $\tan\beta$ for the CP–odd A boson and for the CP–even H (h) boson in the (anti–)decoupling regime. A further enhancement of the cross section is provided by $\log^2(M_\Phi^2/m_\tau^2)$ terms.

The cross section for the signal $\gamma\gamma \to \tau^+\tau^-\Phi \to \tau^+\tau^-b\bar{b}$ and for the background processes $\gamma\gamma \to \tau^+\tau^-b\bar{b}$ are shown in Fig. 4.46 at a $\gamma\gamma$ collider based on the TESLA design for h production at $\sqrt{s_{\gamma\gamma}} = 400$ GeV (left) and for H/A production at $\sqrt{s_{\gamma\gamma}} = 600$ GeV (right). Cuts have been applied to suppress the diffractive γ–exchange process and the invariant $b\bar{b}$ mass has been constrained to be in the range $\Delta = 0.05M_\Phi$. The τ leptons are required to be in opposite hemispheres and visible with energies and polar angles larger than, respectively, 5 GeV and 130 mrad. As can be seen, for $\tan\beta = 30$, the signal cross sections are very large, exceeding the femtobarn level in most of the range displayed for M_h and M_H, while the irreducible background is much lower after applying the cuts.

With the expected luminosity of 100 and 200 fb^{-1} per year in, respectively, the low and high energy options, and assuming efficiencies of 70% for b–quark tagging and 50% for τ–identification, one obtains the statistical errors on the measurement of $\tan\beta$ which are shown in Table 4.4 for various $\tan\beta$ and M_A values when CP–even and CP–odd Higgs production are combined. In the entire displayed mass range, $M_A = 100$–500 GeV, the accuracy is at
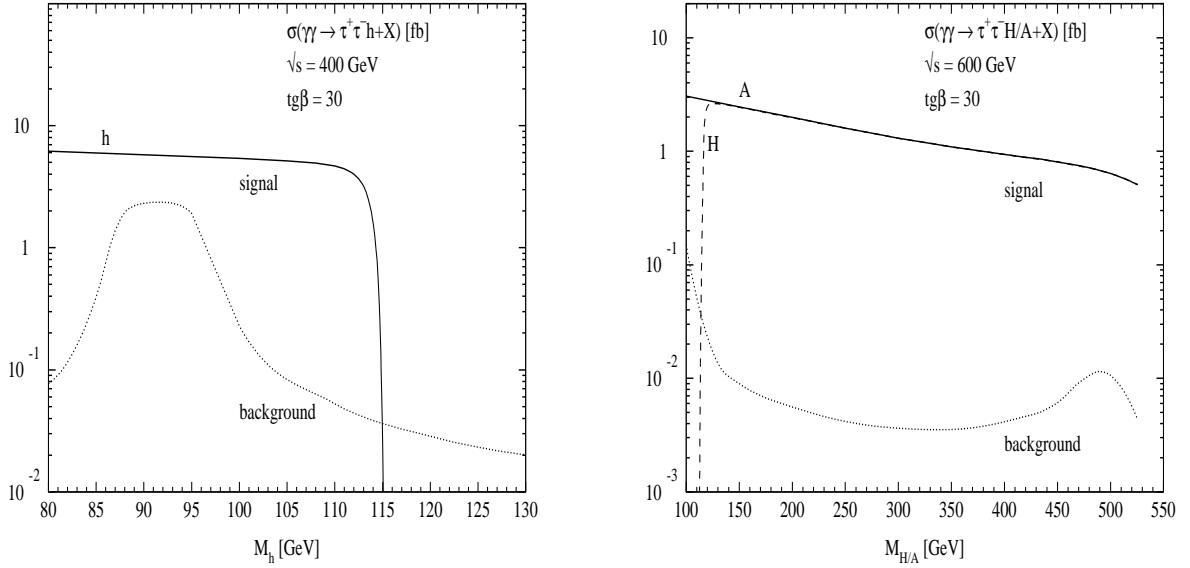
Figure 4.46: The cross sections for the production of the h boson (left) and the H/A bosons (right) in the ττ fusion process at a γγ collider for $\tan\beta = 30$. *Also shown is the background cross section after applying the cuts specified in the text; from Ref. [531].*

the level of 10% for $\tan\beta = 10$ and a few percent for $\tan\beta \gtrsim 30$. This is clearly one of the best individual $\tan\beta$ measurements that can be performed. Detailed simulations, including the detector response are, however, required to confirm these values.

	$E_{\gamma\gamma} = 400$ GeV, $\mathcal{L} = 100$ fb^{-1}			$E_{\gamma\gamma} = 600$ GeV, $\mathcal{L} = 200$ fb^{-1}				
	$A \oplus h$	$A \oplus H$		$A \oplus h$	$A \oplus H$			
M_A [GeV]	100	200	300	100	200	300	400	500
$\tan\beta = 10$	8.4%	10.7%	13.9%	8.0%	9.0%	11.2%	13.2%	16.5%
$\tan\beta = 30$	2.6%	3.5%	4.6%	2.4%	3.0%	3.7%	4.4%	5.3%
$\tan\beta = 50$	1.5%	2.1%	2.7%	1.5%	1.8%	2.2%	2.6%	3.2%

Table 4.4: Relative errors $\Delta\tan\beta/\tan\beta$ *for various values of* $\tan\beta$ *and* M_A *based on combined* $A \oplus h$ *and* $A \oplus H$ *production in* ττ *fusion at* γγ *colliders, with the specified* γγ *energies and luminosities; from Ref. [531].*

Effects of light SUSY particles

Finally, let us briefly comment on the impact of light SUSY particles on Higgs physics in $\gamma\gamma$ collisions by taking two examples. The first effect of such light particles is to alter the $\gamma\gamma$ widths of the Higgs bosons and to modify the value of the $H/A \to b\bar{b}$ branching ratios since these particles can also end up as Higgs decay products. The effective $\gamma\gamma \to H/A \to b\bar{b}$ cross sections will be then increased or decreased depending on the sign of the interference between

283

the SM and superparticle contributions and the magnitude of the branching ratios for the decays into SUSY particles [532]. This is exemplified in the left–hand side of Fig. 4.47 where the $\gamma\gamma \to b\bar{b}$ cross sections are shown as a function of $\sqrt{s_{\gamma\gamma}} \simeq M_A$ for $\tan\beta = 7$ in a scenario where charginos and neutralinos are light, $M_2 = 2M_1 = \pm\mu = 200$ GeV, but sfermions are heavy, $M_S = 1$ TeV. The familiar cuts allowing to enhance the signal to background ratio have been used as indicated.
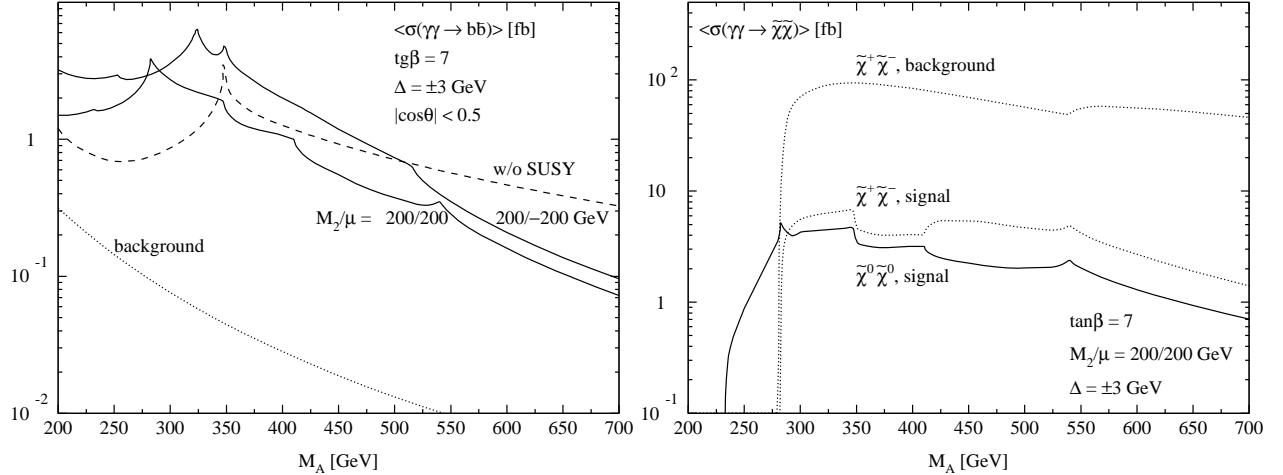
Figure 4.47: Left: Cross sections for the resonant production $\gamma\gamma \to H/A \to b\bar{b}$ as a function of M_A and for the background [with cuts as indicated] with and without SUSY contributions. Right: the same as previously but for chargino and neutralino final states [532].

Another implication is that one could search for final states involving the SUSY particles. This is exemplified in the right–hand side of Fig. 4.47 where the production of $\chi_1^+\chi_1^-$ and $\chi_1^0\chi_2^0$ pairs is shown in the same scenario. The signal cross sections are significant but the chargino continuum background is one order of magnitude higher. Since neutralinos cannot be produced directly at leading order, the decay $H/A \to \chi^0\chi^0$ could be observed in topologies where the final state is different from the one present in chargino pair production [532].

Finally, let us note that there are rare but interesting processes which have larger cross sections in $\gamma\gamma$ that in e^+e^- collisions and which might be more accessible at $\gamma\gamma$ colliders despite of the reduced energy and luminosity[38]. This is exemplified in the case of associated h production with $\tilde{t}_1\tilde{t}_1$ and $\tilde{\tau}_1\tilde{\tau}_1$ pairs, Fig. 4.48. The cross sections are to be compared with those obtained in the e^+e^- option, Fig. 4.39, where the relevant scenarios are described. While the cross section for associated production with stop pairs is only slightly above the one in e^+e^- collisions, the rate for associated production with $\tilde{\tau}$ pairs is an order of magnitude larger. These cross sections have still to be folded with the photon luminosities, though, and might be thus reduced. The backgrounds might also be larger than in e^+e^- collisions.

---

[38]Charged Higgs particles can be pair produced in two–photon collisions, $\gamma\gamma \to H^+H^-$, with rates which can be larger than those of the e^+e^- option. However, the mass reach is smaller as $\sqrt{s_{\gamma\gamma}} < \sqrt{s_{e^+e^-}}$.
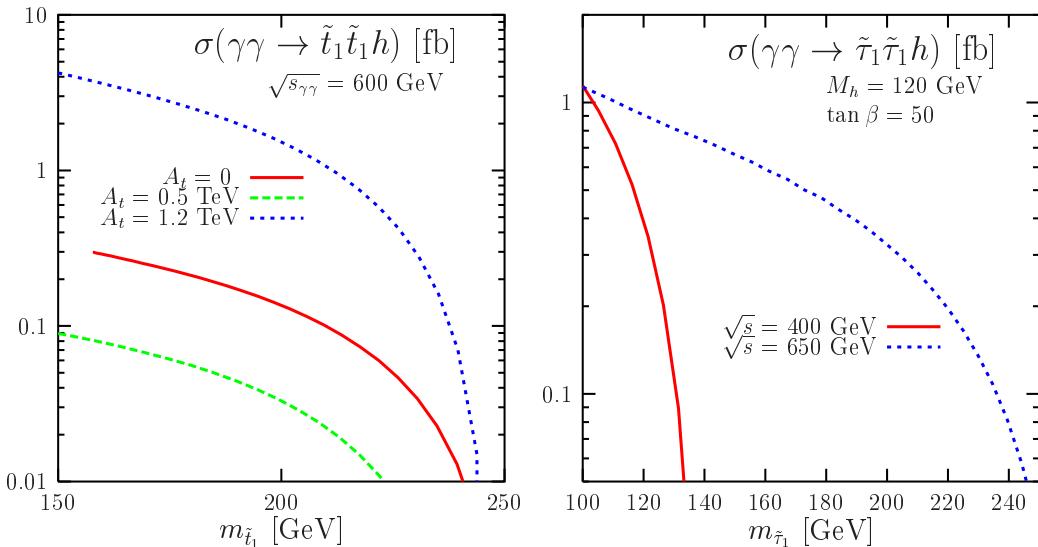
Figure 4.48: Associated h production with stop (left) and stau (right) pairs in $\gamma\gamma$ collisions at various c.m. energies in the scenarios presented in Fig. 4.39; from Refs. [446, 507].

4.5.3 Production at $\mu^+\mu^-$ colliders

Higgs lineshape measurements

Physics at muon colliders in the context of MSSM Higgs particles has been discussed in numerous reviews [515]. Here, we will simply address the question of how well the masses and the total decay widths of the s–channel produced Higgs particles can be measured, that is, what is the benefit of a $\mu^+\mu^+$ collider to improve on the points i)–iii) discussed in §4.5.1 and which are not covered at the LHC or at a first stage e^+e^- collider in a satisfactory way.

In Ref. [533], the production of the heavier neutral H/A bosons has been investigated at a Higgs factory with a luminosity of a few 100 pb^{-1} based on the machine and detector performances of a [second stage] muon collider that is discussed at CERN [516]. Taking, as an example, a scenario in which $M_A = 300$ GeV and $\tan\beta = 10$ [i.e. again in the wedge region in which the LHC sees only the lighter h boson, Fig. 3.45], the common total decay widths of the Higgs bosons are $\Gamma_A \sim \Gamma_H \sim 0.6$ GeV while the mass difference, $M_H - M_A \sim 0.7$ GeV, is only slightly larger. The total cross section for $\mu^+\mu^- \to H, A \to b\bar{b}$ production is of the order of 100 pb at the resonance peaks.

Assuming that the value of M_A is predicted with a 20% accuracy from the high precision measurements of the properties of the h boson at an e^+e^- collider or at the first stage of the muon collider running at the h resonance [we will see in the next section that this is possible in this M_A–$\tan\beta$ scenario], a wide scan over the ± 60 GeV window for $M_A = 300$ GeV with steps of 1 GeV and luminosities of 1 pb^{-1} per step, would allow to discover the A and H bosons in less than one year running at the muon collider. A finer scan of the two resonances

would allow the overall lineshape to be measured. With six energy points at a luminosity of 25 pb^{-1} per point, the average mass and the mass difference, the two peak cross sections and the two total decay widths can be determined with a very high accuracy for the energy spread of 3×10^{-5} that is expected to be achieved. This is exemplified in Fig. 4.49 where the total cross sections for $\mu^+\mu^- \to H/A \to b\bar{b}$ production are displayed in the previously discussed scenario and with the assumed resolution of 3×10^{-5}. As can be seen, the H and A resonant peaks can be resolved for this $\tan\beta$ choice, as shown by the six small triangles with errors bars. The production cross sections can be measured with an accuracy of 1%, the Higgs masses with a precision of $\Delta M_{H,A} = \pm 10$ MeV and the total Higgs decay widths with an accuracy $\Delta\Gamma_{H,A} = \pm 50$ MeV. The latter measurement would allow a determination of $\tan\beta$ at the percent level, if theoretical errors are ignored.
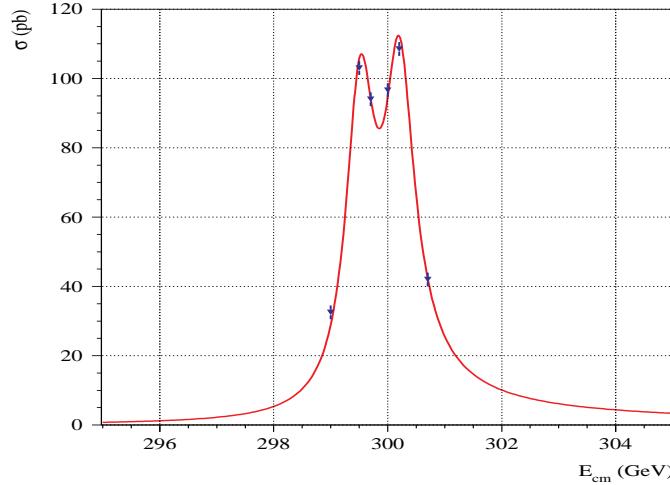
Figure 4.49: *Simulated measurements of s–channel $\mu^+\mu^- \to H/A \to b\bar{b}$ production at a muon collider for $M_A = 300$ GeV and $\tan\beta = 10$, with six energy points at 25 pb^{-1} of integrated luminosity per point and a beam energy spread of 3×10^{-5}; from Ref. [533].*

Thus, clearly, the muon collider is a unique tool and would allow very precise measurements of the Higgs lineshape parameters. However, this is possible only in favorable regions of the MSSM parameter space where the H/A total decay widths are smaller than the Higgs mass difference. In Ref. [534], a relation between these two quantities for which the separation between the two resonant peaks can be achieved, has been proposed. With a resolution $R = 0.01\%$ and with ~ 10 energy scans separated by 100 MeV around the Higgs resonances at an integrated luminosity of 10 pb^{-1} per point, and assuming a 50% efficiency for b–tagging, its has been shown that the two resonance peaks can be separated provided that $|M_H - M_A| > \frac{1}{3}(\Gamma_A + \Gamma_H)$. Using the program HDECAY, the range of the M_A–$\tan\beta$ parameter space in which this rule is obeyed is shown in Fig. 4.50. Values of up to $\tan\beta = 20$ can be probed for $M_A \lesssim 200$ GeV, while for $\tan\beta \lesssim 6$–8, the separation can be made for mass values up to $M_A \sim 700$ GeV.
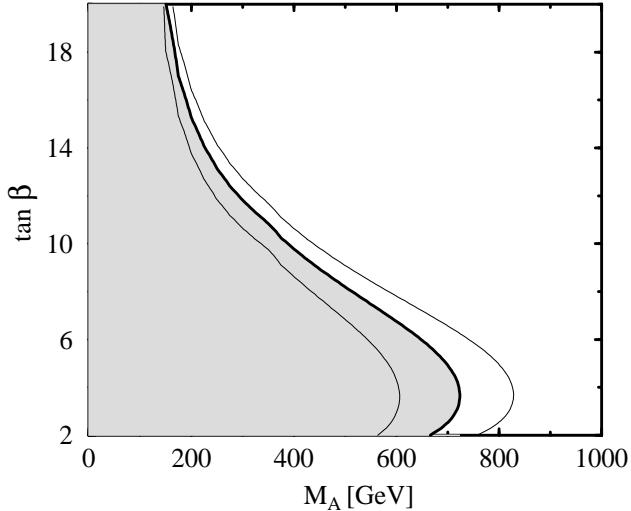
Figure 4.50: The region of the M_A–$\tan\beta$ parameter space in which the Higgs mass difference is sufficiently large $|M_H - M_A| > \frac{1}{3}(\Gamma_A + \Gamma_H)$ that a scan over the H and A boson resonances can measure the two masses (shaded area). Also shown are the $|M_H - M_A| = \frac{1}{2}(\Gamma_A + \Gamma_H)$ (leftmost) and $|M_H - M_A| = \frac{1}{4}(\Gamma_A + \Gamma_H)$ (rightmost) contours for comparison [534].

Decays into SUSY particles

If SUSY particles are light, they can end up as final decay products of at least the heavier CP–even and CP–odd s–channel Higgs boson resonances. These processes would provide a very good opportunity to probe the couplings between the Higgs and SUSY particles which, as discussed previously, are essential ingredients of the MSSM Lagrangian as they involve many soft SUSY–breaking terms. In the following, we will discuss such a possibility restricting ourselves to two examples which are in principle more favored by phase space considerations: Higgs decays into the lightest and next–to–lightest neutralinos and Higgs decays into a pair of $\tilde{\tau}$ slepton eigenstates [at high $\tan\beta$ values, $\tilde{\tau}_1$ appears often to be the next–to–lightest SUSY particle]; other related studies can be found in Ref. [515] for instance.

At muon colliders, the process $\mu^+\mu^- \to \chi_1^0\chi_2^0$ proceeds through s–channel Z boson exchange, t–channel $\tilde{\mu}$ exchange and through the decays $H/A \to \chi_1^0\chi_2^0$ if the c.m. energy of the collider is tuned to sit on the Higgs resonances. However, since the H, A particles are nearly degenerate in mass in large parts of the MSSM parameter space, the determination of the resonance lineshape parameters would be a difficult task in some cases, as seen previously. In Ref. [535], it has been suggested to use the dependence of the production process on the polarizations of the initial muons and on that of the final neutralinos, to disentangle between the contributions of the two different resonances.

Indeed, the interference of the CP eigenstates H and A is known to be sizable if the mass difference between the particles is of the order of their total decay widths [536]. Since the neutralinos are of Majorana nature, their polarizations averaged over the scattering angles

vanish in the s–channel Z and t–channel $\tilde{\mu}$ exchange contributions and results only from the interference of the two Higgs channel contributions. For decays of the heavier neutralino into a lepton and a slepton, $\chi_2^0 \to \ell \tilde{\ell}_{L,R}$, the energy distribution of the final lepton depends on the longitudinal polarization of the neutralino χ_2^0 which is correlated with the longitudinal polarization of the initial muon beams, $P_\pm^L$, when the interference effects are present. The distributions can be used to probe the Higgs–neutralino couplings and, in particular, one can define the asymmetry in the $\ell^\pm = e, \mu, \tau$ energies $E_\ell, \bar{E}_\ell$

$$\mathcal{A}_\ell^n = \frac{1}{2}(\mathcal{A}_{\ell^-}^n - \mathcal{A}_{\ell^+}^n) \ , \ \text{with} \ \mathcal{A}_{\ell^\pm}^n = \frac{\sigma_{\ell^\pm}^n(E_\ell > \bar{E}_\ell) - \sigma_{\ell^\pm}^n(E_\ell < \bar{E}_\ell)}{\sigma_{\ell^\pm}^n(E_\ell > \bar{E}_\ell) + \sigma_{\ell^\pm}^n(E_\ell < \bar{E}_\ell)} = \pm \frac{1}{2}\eta_\ell^n \frac{\bar{\Sigma}}{\bar{P}} \qquad (4.19)$$

with $n = L, R$, $\eta_\ell^{L/R} = \mp 1$ in the absence of slepton mixing and where $\bar{P} \propto 1 + P_+^L P_-^L$, $\Sigma \propto P_+^L - P_-^L$ are functions of the Higgs couplings to the neutralinos, with the latter being directly proportional to the interference between the H/A couplings.
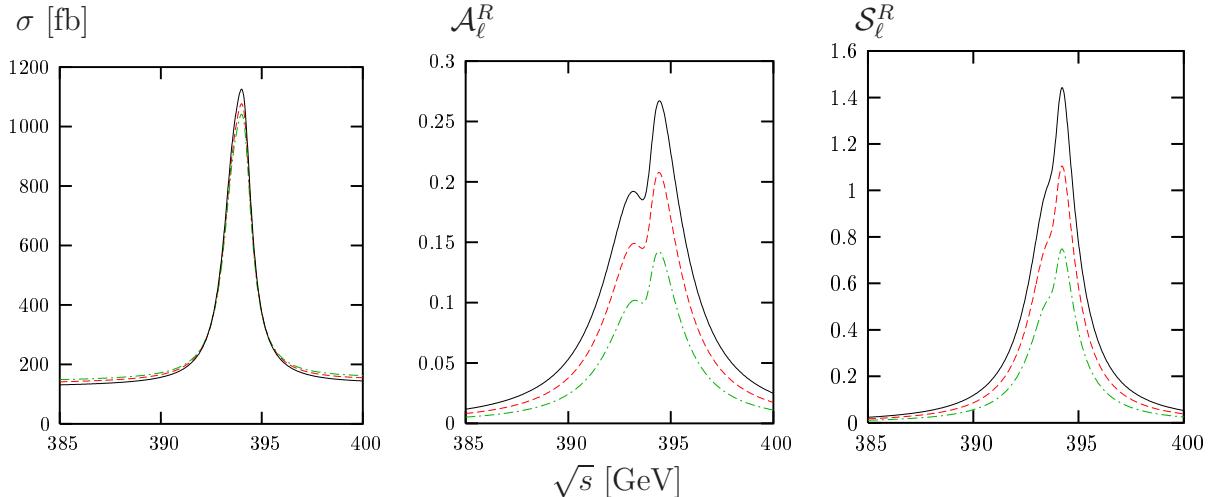
Figure 4.51: The neutralino production cross section, $\sigma(\mu^+\mu^- \to \chi_1^0\chi_2^0)$, the asymmetry $\mathcal{A}_\ell^R$ in the lepton energy distribution in the decay $\chi_2 \to \ell^- \tilde{\ell}_R^+$ with $\ell = e, \mu$, and the significance with luminosity times detection efficiency $\epsilon\mathcal{L} = \mathcal{L}_{eff} = 0.5\,fb^{-1}$ as a function of the c.m. energy in the scenario SPS1a for various beam polarizations: $P_+^L = P_-^L = -0.2$ (dash–dotted), -0.3 (dashed) and -0.4 (solid); from Ref. [535].

Fig. 4.51 displays the cross section $\sigma(\mu^+\mu^- \to \chi_1^0\chi_2^0)$, the asymmetry $\mathcal{A}_\ell^R$ and its statistical significance $\mathcal{S}_\ell^R = |\mathcal{A}_\ell^R|\sqrt{2\sigma \times \text{BR}(\chi_2^0 \to \ell^- \tilde{\ell}_n^+)\mathcal{L}_{\text{eff}}}$ as a function of the c.m. energy around the Higgs resonances for different values of the longitudinal beam polarization. The chosen SUSY scenario is the SPS1a point which leads to $M_A = 393.6$ GeV and $M_H = 394.1$ GeV with $\Gamma_A \approx \Gamma_H \approx 1$ GeV while $m_{\chi_2^0} \sim 2m_{\chi_1^0} \sim 180$ GeV. The production cross section is large, in particular near $\sqrt{s} \sim M_A$, and does not significantly depend on the polarization since $\sigma \propto 1 + P_-^L P_+^L \sim 1$ in this case. In turn, the asymmetry is largest for $\sqrt{s} \sim M_H$ where the CP–even and CP–odd amplitudes are of the same order and depends significantly on

the beam polarizations, $\mathcal{A}_\ell^n \propto P_-^L + P_+^L$. The statistical significance follows the trend of the asymmetry. The lepton energy asymmetry is very sensitive to a variation of the parameters which enter in the Higgs couplings, namely, $\tan\beta, M_1, M_2$ and μ. Similar studies have been performed for chargino pair production at muon colliders [537].

A powerful probe of the couplings of the Higgs bosons to SUSY particles is through the production of third generation sleptons at muon colliders. The processes occur through s–channel γ, Z and h, H boson exchange for unmixed pairs, $\mu^+\mu^+ \to \tilde{\tau}_i\tilde{\tau}_i$ with $i = 1, 2$ [as a consequence of CP–invariance, the A boson does not couple to diagonal states] and for mixed pairs, $\mu^+\mu^+ \to \tilde{\tau}_1\tilde{\tau}_2$, through the exchange of the Z boson [as the $\gamma\tilde{\tau}_1\tau_2$ coupling is forbidden by $\mathrm{U(1)_{QED}}$ gauge invariance] and the three Higgs particles h, H, A. As mentioned previously, these states might be light enough to be accessible and third generation sfermions have in general much stronger Higgs couplings than first/second generation sfermions. To study these couplings and to check, for instance, the absence or presence of CP–violation in the vertices, one has to construct as many asymmetries as possible. In this respect, $\tilde{\tau}$ sleptons are ideal objects since their charges can be easily identified [as it must be the case in most asymmetries allowing to probe CP–violation for instance] in contrast to the case of $\tilde{t}$ and $\tilde{b}$ production [which, in any case, are expected to be heavier than $\tilde{\tau}$s].

If the H and A resonances can be separated, running at c.m. energies close to the pole of the pseudoscalar Higgs particle and producing pairs of diagonal states $\mu^+\mu^- \to A \to \tilde{\tau}_i\tilde{\tau}_i$ in excess of the continuum background, $\mu^+\mu^- \to \gamma, Z \to \tilde{\tau}_i\tilde{\tau}_i$, is a definite sign of CP–violation in the Higgs sector. Unfortunately, this is generally not the case and the H/A poles are overlapping at high $\tan\beta$. This is shown in the left–hand side of Fig. 4.52 where the cross sections for $\tilde{\tau}_1\tilde{\tau}_1, \tilde{\tau}_2\tilde{\tau}_2$ and $\tilde{\tau}_1\tilde{\tau}_2$ production are shown in the scenario described in the caption, where all states are kinematically accessible. While the cross section for the diagonal states is dominated by gauge boson exchange, the production of the mixed states is essentially due to the Higgs exchange diagrams and, in this case, both H and A contribute and the two peaks cannot be resolved as the $M_H - M_A$ difference is small compared to Higgs total widths.

Thus, for the probing of the couplings, one has to resort to distributions and asymmetries. Assuming the possibility of longitudinally and transversally initial beams and allowing for CP–violation, the most general matrix element for the production amplitude $\mu^+\mu^- \to \tilde{\tau}_i\tilde{\tau}_j$ involves 15 terms, out of which 9 terms are CP–even and 6 terms are CP–odd. This would allow, for a single final state, to define 9 rate asymmetries R and for a given final state 6 polarization and angle asymmetries P [leading to a total of 27 asymmetries when all final states are considered]. The number of asymmetries which can be measured depends on the number of kinematically accessible final states but, more importantly, on the availability or not of the beam polarization. Without polarization, only one rate asymmetry is measurable, while with longitudinal polarization, another rate and polarization asymmetries are
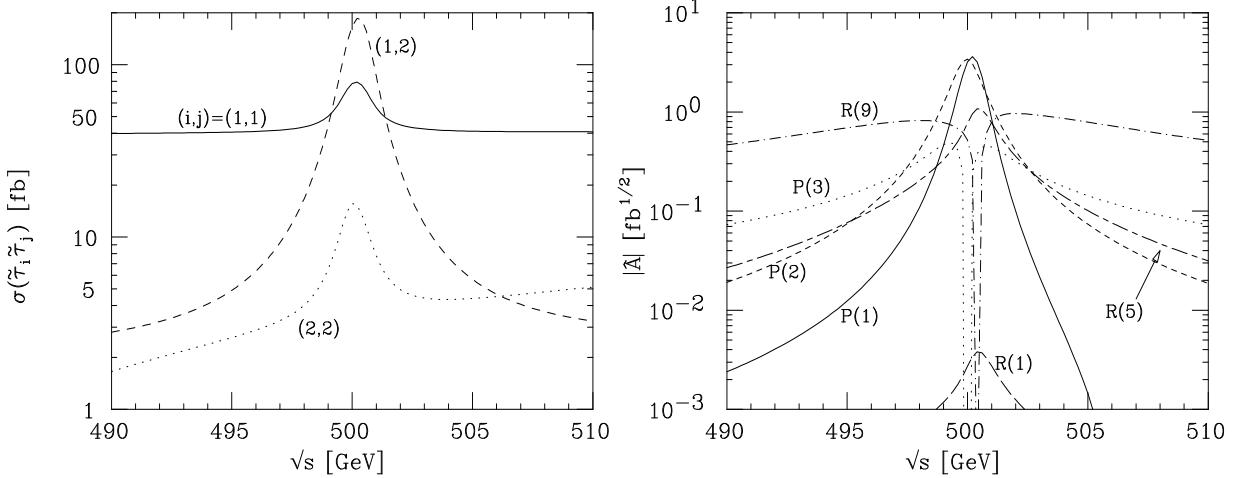
Figure 4.52: The total cross sections for $\mu^+\mu^- \to \tilde{\tau}_i^- \tilde{\tau}_j^+$ with the curve labeled '(1,2)' refers to the sum of $\tilde{\tau}_1^- \tilde{\tau}_2^+ + \tilde{\tau}_1^+ \tilde{\tau}_2^-$ production as a function of the c.m. energy (left) and absolute values of selected asymmetries times square root of the cross section the labels 'R' and 'P' refer to rate and polarization/azimuthal angle asymmetries, respectively. The set of SUSY parameters is: $M_A = |\mu| = |A_\tau| = \frac{3}{5}M_2 = 500$ GeV, $m_{\tilde{\tau}_L} = 230$ GeV, $m_{\tilde{\tau}_R} = 180$ GeV and $\tan\beta = 10$; all phases are zero, except for that of A_τ which is taken to be 1; from [538].

measurable. All other asymmetries are accessible only if, at least, one beam is transversally polarized. Note that these asymmetries need the reconstruction of the $\tilde{\tau}$ azimuthal angles.

In the right–hand side of Fig. 4.52, we show in $\tilde{\tau}_1^+ \tilde{\tau}_1^-$ production a number of rate and polarization effective asymmetries, defined as the product of asymmetries times the square–root of the relevant cross sections which determine the luminosity times reconstruction efficiencies that are needed to observe the asymmetries. The total rate asymmetry $R(1)$ in the figure is entirely due to the interference between the CP–even h and H boson contributions and is thus very small. In contrast, near the Higgs peaks the effective polarization asymmetries $P(1)$ and $P(2)$ are both very large: the former is measurable with longitudinally polarized beams, while the latter is only accessible if at least one beam is transversely polarized. $R(5)$ and $R(9)$ can also reach the level of 1 fb$^{1/2}$ and the latter, which is accessible with one longitudinally and one transversely polarized beam, goes through zero at $\sqrt{s} = M_H$ while the effective polarization asymmetry $P(3)$ goes through zero at $\sqrt{s} = M_A$.

Hence, the contributions of the H and A bosons can be separated out. However, in the figure, a 100% beam polarization is assumed so that these asymmetries will be diluted in practice. In turn, the corresponding asymmetries in the case $\tilde{\tau}_1^\pm \tilde{\tau}_2^\pm$ production can be much larger in some cases. In addition, if the mass difference $M_H - M_A$ is large, as would be the case if CP–violation is present in the Higgs sector, some of these asymmetries would be completely different, thereby probing this violation and allowing to measure the Higgs mass difference. Thus, many aspects can be investigated in these processes and more detailed discussions can be found in Ref. [539].

4.6 MSSM consistency tests and the LHC/LC complementarity

As highlighted at several places in this report, lepton colliders are very high precision instruments in the context of Higgs physics. In the MSSM, a number of very important measurements can be performed at these machines as is briefly summarized below.

4.6.1 Precision measurements at lepton colliders

If the heavier H, A and $H^\pm$ states are kinematically accessible, one can measure their masses and their cross sections times decay branching with a relatively good accuracy. This has been discussed in §4.1.3 for the neutral Higgs bosons in the decoupling regime where it has been shown that in the pair production process $e^+e^- \to HA$, a precision of the order of 0.2% can be achieved on the H and A masses, while a measurement of the cross sections can be made at the level of a few percent in the $b\bar{b}b\bar{b}$ channel and ten percent in the $b\bar{b}\tau^+\tau^-$ channel; see Table 4.1. For the charged Higgs boson, statistical uncertainties of less than 1 GeV on its mass and less than 15% on its production cross section times branching ratio in the channel $e^+e^- \to H^+H^- \to t\bar{b}\bar{t}b$ can be achieved for $M_{H^\pm} \sim 300$ GeV with high enough energy and luminosity; §4.3.3. The spin–zero nature of the particles can be easily checked by looking at the angular distributions which should go as $\sin^2\theta$ at tree–level.

These measurements allow the determination of the most important branching ratios, $b\bar{b}$ and $\tau^+\tau^-$ for the neutral and tb and $\tau\nu$ for the charged Higgs particles, as well as the total decay widths which can be turned into a determination of the value of $\tan\beta$, with an accuracy of 10% or less. These measurements can be improved by turning to the $\gamma\gamma$ mode of the collider, where one can reach a precision of a few percent on $\tan\beta$ in τ–lepton fusion, or moving to a $\mu^+\mu^-$ collider, where a very good measurement of the H/A lineshapes is possible. Several other measurements, such as the spin–parity of the Higgs particles and in a favorable region of the parameter space, some trilinear Higgs couplings, can be made.

The profile of the lighter Higgs boson can be entirely determined. This is particularly the case close to the decoupling regime where the h boson behaves as the SM Higgs particle but with a mass below $M_h \lesssim 140$ GeV. This is, in fact, the most favorable range for precision measurements as the Higgs boson in this mass range has many decay channels that are accessible. This has been shown in great details in §I.4.4 when we reviewed the precision studies for a SM Higgs boson at e^+e^- colliders, as well as in §I.4.5 and §I.4.6 at, respectively, the photon and the $\mu^+\mu^-$ colliders. The mass of the Higgs particle can be determined with an accuracy of about 50 MeV and its couplings to W, Z bosons, to bottom/charm quarks and to τ–leptons, as well as the couplings to gluons, can be measured with a precision of a few percent. The important Yukawa couplings to top quarks and the trilinear Higgs self–couplings can also be determined with a precision of less than 10% and 20%, respectively. The two–photon width can be measured at the level of a couple of percent at $\gamma\gamma$ colliders and

the total decay width [which can be determined indirectly with a precision of a few percent in e^+e^- collisions] can be accessed directly at muon colliders where a measurement at the level of 5 to 10%, depending on the luminosity, can be made. The spin–parity quantum numbers of the particles can be also pinned down in e^+e^- collisions either in distributions in the Higgs–strahlung production process or by looking at correlations in the decays into W/Z bosons or τ leptons. Additional checks of the spin–parity assignments can be made at $\gamma\gamma$ and $\mu^+\mu^-$ colliders if suitable polarizations of the beams are available as has been shown in §I.4.5 and §I.4.6.

As discussed in §I.4.4, a dedicated program called `HFITTER`, based on the code `HDECAY` for the calculation of the Higgs boson branching ratios, has been developed by the authors of Ref. [540]. It uses as inputs the various cross section and branching ratio measurements which can be performed in e^+e^- collisions for the SM–Higgs boson and gives the accuracies with which the Higgs couplings to the SM particles can be determined, including the full correlation matrix in the measurements. The output for the accuracies on the SM Higgs couplings to fermions, gauge bosons and the self–coupling are displayed in Table 4.5 for $M_{H_\mathrm{SM}} = 120$ GeV and 140 GeV at $\sqrt{s} = 500$ GeV with $\mathcal{L} = 500$ fb^{-1}. Although already shown in §I.4.4.3, we reproduce this table for the sake of completeness and to make the subsequent discussion more transparent.

Quantity	$M_H = 120$ GeV	$M_H = 140$ GeV
ΔM_H	$\pm\ 0.00033$	$\pm\ 0.0005$
Γ_H	$\pm\ 0.061$	$\pm\ 0.045$
ΔCP	$\pm\ 0.038$	$-$
λ_{HHH}	$\pm\ 0.22$	$\pm\ 0.30$
g_{HWW}	$\pm\ 0.012$	$\pm\ 0.020$
g_{HZZ}	$\pm\ 0.012$	$\pm\ 0.013$
g_{Htt}	$\pm\ 0.030$	$\pm\ 0.061$
g_{Hbb}	$\pm\ 0.022$	$\pm\ 0.022$
g_{Hcc}	$\pm\ 0.037$	$\pm\ 0.102$
$g_{H\tau\tau}$	$\pm\ 0.033$	$\pm\ 0.048$

Table 4.5: Relative accuracy on the couplings of a SM–like Higgs boson obtained from a global fit using the program `HFITTER`. A luminosity $\mathcal{L} = 500\,fb^{-1}$ at $\sqrt{s} = 500$ GeV is assumed except for the measurement of $g_{Htt}(\lambda_{HHH})$, which assume $1000\,fb^{-1}$ at $\sqrt{s} = 800$ (500) GeV in addition. On top of the table, we display the accuracies on the Higgs mass, the total width and its CP–component as obtained at $\sqrt{s} = 350$ GeV with $\mathcal{L} = 500$ fb^{-1}.

In Fig. 4.53 are shown the 1σ and 95% confidence level contours for the fitted values of various pairs of ratios of couplings for a SM–like Higgs boson with a mass of 120 GeV, assuming the experimental accuracies which can be achieved at the TESLA machine with the energy and luminosity quoted above.
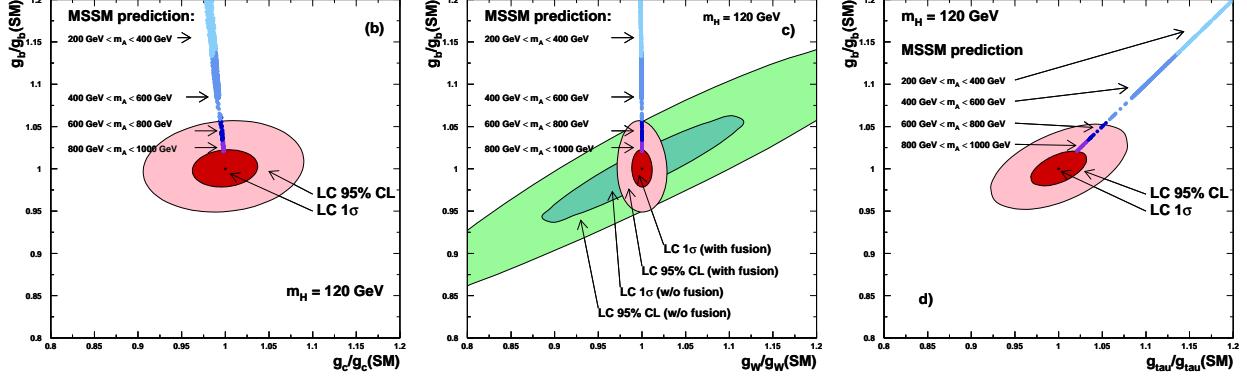
Figure 4.53: Determination of the couplings of a SM–like Higgs boson at TESLA and the interpretation within the MSSM. The contours are for g_{hbb} vs. g_{hcc}, g_{hbb} vs. g_{hWW} and g_{Hbb} vs. $g_{h\tau\tau}$ for a 120 GeV Higgs boson as measured with $500\,fb^{-1}$ data at $\sqrt{s} = 350$ GeV; the full covariance matrix has been used for the correlated measurements; from Ref. [470].

4.6.2 Discriminating between a SM and an MSSM Higgs boson

In the [unlikely] case were no genuine SUSY particle has been produced at the LHC or at the LC, the discovery of a neutral Higgs boson with a mass $\lesssim 140$ GeV will raise the question of whether the observed particle is the SM Higgs boson or the lightest h boson of the MSSM extension. In particular, since there is a large area of the MSSM parameter space in which only the lighter Higgs particle can be produced at the LHC, Fig. 3.45, and since the particle has almost the SM–Higgs properties, it will be very difficult to discriminate between the SM and MSSM Higgs bosons. Also, for non MSSM enlarged Higgs sectors [such as non SUSY two–Higgs doublet models or SUSY extensions with additional singlet and/or doublet fields] where decoupling occurs, there is a possibility that the produced Higgs particle looks as the SM Higgs or the lightest MSSM h boson. In this case, the precision measurements of the Higgs couplings at the linear collider will be a powerful means to disentangle between the various possible scenarios.

A detailed analysis of the deviations of the couplings of a Higgs boson with a mass of 120 GeV, assumed to be the MSSM h boson, from the predictions in the SM [as discussed earlier, the profile of H_{SM} is entirely determined once its mass is fixed] has been performed in Ref. [470] based on a complete scan of the MSSM parameter space, including the full set of radiative corrections. For each set of M_A and $\tan\beta$ values leading to a Higgs mass of $M_h = 120 \pm 2$ GeV [where 2 GeV corresponds to an optimistic estimate of the theoretical error], the h boson branching ratios into various final states have been calculated and compared

to the SM predictions. From a χ^2 test which compares the deviations, 95% of all MSSM solutions can be distiguished from the SM case for $M_A \lesssim 600$ GeV and this number reduces to only 68% for $M_A \lesssim 750$ GeV. This is also shown in Fig. 4.53 where the fitted values of the pairs of measurements for a SM–like Higgs boson are compared to the changes induced in the MSSM for M_A values in various ranges. As can be seen, at the 1σ level, the MSSM effects can be observed even for pseudoscalar masses of 1 TeV.

If large deviations of the Higgs couplings from the SM predictions have been observed, one could go further and use the available high–precision observables to estimate the mass of the MSSM CP–odd Higgs boson. By varying the A boson mass, together with the other MSSM parameters, within the range compatible with the experimental and theoretical uncertainties, it has been shown in the same analysis discussed above that an indirect determination of M_A in the mass range 300–600 GeV is possible with an accuracy of 70–100 GeV.
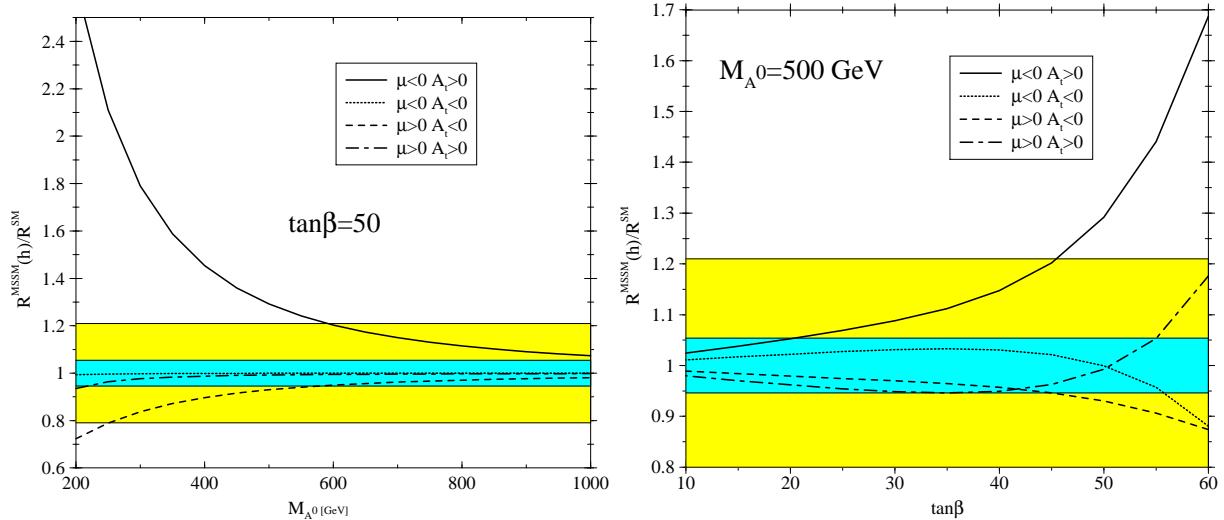
Figure 4.54: The deviation of the ratio $BR(h \to b\bar{b})/BR(h \to \tau\tau)$ from its SM value as a function of M_A for $\tan\beta = 50$ (left) and $\tan\beta$ for $M_A = 500$ GeV (right) for fixed values of A_t and μ; from [200]. The inner small (blue/dark) and large (yellow/light) bands represent the expected measurement error of the ratio at, respectively, the LC and the LHC.

The same exercise can be performed using the ratio of branching ratios $\mathrm{BR}(h \to b\bar{b})/\mathrm{BR}(h \to \tau\tau)$ [200]. In the MSSM, this ratio should be constant at tree–level, $\propto 3\bar{m}_b^2/m_\tau^2$. However, slightly outside the decoupling regime, the ratio is very sensitive to the SUSY loop contributions as discussed in §2.2.1. In particular, for large values of $\tan\beta$ [and μ], the gluino/sbottom contributions to the $h \to b\bar{b}$ partial widths can be rather large. This ratio is thus sensitive not only to M_A as seen above but also to the value of $\tan\beta$ and, even, to the parameters μ and A_t. This is exemplified in Fig. 4.54 where the ratio is displayed as a function of M_A for $\tan\beta = 50$ (left) and as a function of $\tan\beta$ for $M_A = 500$ GeV (right) for given values and signs of the parameters μ and A_t. The inner small bands represent the expected accuracy in the measurement of the ratio at the linear collider.

As can be seen from the figure, this type of indirect determination cannot be made in a convincing way at the LHC as the experimental errors in the various measurements are much worse than at the LC. This is also exemplified in Fig. 4.55 where the contours for the pair of couplings g_{hWW} and g_{htt}, similarly to those of Fig. 4.53, are displayed for $M_h = 120$ GeV. As can be seen, while the 1σ LC contour is sensitive to pseudoscalar Higgs masses up to almost 1 TeV, there is practically no sensitivity at the LHC.
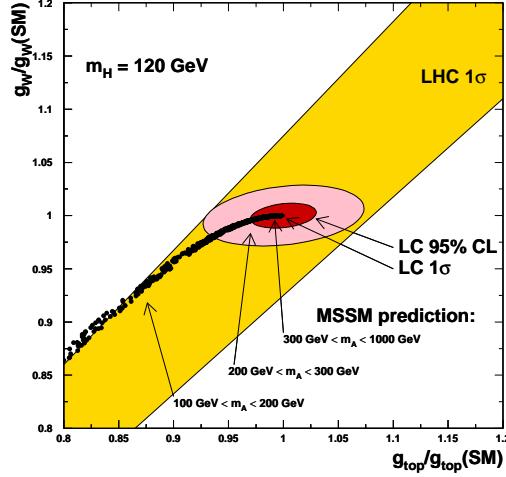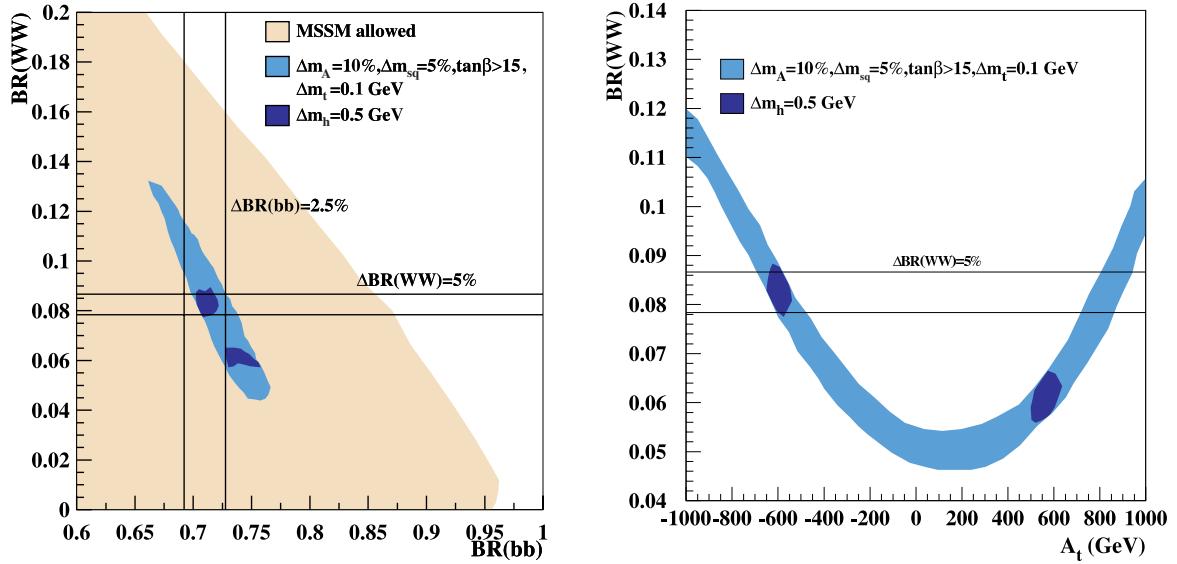
Figure 4.55: A comparison of the accuracy in the determination of the g_{htt} and g_{hWW} couplings at TESLA [with the same assumptions as in Fig. 4.53] and at the LHC, compared to the MSSM predictions for different values of M_A; from Ref. [470].

4.6.3 Complementarity between the LHC and the LC

However, the precision measurements at the LC can gain enormously from other measurements that can be performed only at the LHC. Indeed, the various Higgs couplings are not only sensitive to the input parameters M_A and $\tan\beta$ which enter at the tree level but, also, on parameters of the SUSY sector that enter through the large radiative corrections. Some of these SUSY parameters, in particular the stop and sbottom masses which contribute through large logarithms, will probably be measured only at the LHC where the energy reach is much higher than at the LC. If, in addition, the pseudoscalar Higgs boson is discovered at the hadron machine, which means that $\tan\beta$ is probably large, $\tan\beta \gtrsim 15$ for the dominant production and detection channels $gg \to A/H + b\bar{b} \to \tau\tau b\bar{b}$ to be effective, and its mass is measured at the level of 10% which, as we have seen in §3.3.3 is possible, the only other important parameter entering the Higgs sector at one–loop is the trilinear coupling A_t [and to a lesser extent, A_b and μ] which will be only loosely constrained at the LHC. Nevertheless, using this knowledge and the fact that the top quark mass, which is also a very important ingredient of the radiative corrections in the MSSM Higgs sector, can be measured with a precision of 100 MeV at the LC, one can vastly improve the tests of the MSSM Higgs sector that can be performed at the LHC or at the LC alone.

This statement is exemplified in the left–hand side of Fig. 4.56 where the contours for the branching ratios of the decays of a Higgs boson into W bosons and b quarks is shown for $M_h = 116$ GeV. Also shown are the accuracies with which these branching ratios can be measured at the LC, typically, 2.5% and 5% for $\mathrm{BR}(h \to b\bar{b})$ and $\mathrm{BR}(h \to WW^*)$, respectively. Here, we are in the mSUGRA SPS 1b benchmark scenario [249] in which the value of $\tan\beta$ is large, $\tan\beta = 30$, and the value of the pseudoscalar Higgs mass is $M_A = 550$ GeV while the stop and sbottom masses are in the range of 600–800 GeV. All these particles can be discovered at the LHC and their masses can be measured; in particular an accuracy of $\sim 5\%$ can be obtained on the squark masses. While the region of the MSSM parameter space that is allowed for these decay branching ratios is in principle very large, it shrinks to a very narrow range when the available experimental information from the LHC and the top quark measurement at the LC is included. If, in addition, one assumes that a theoretical error of only 0.5 GeV can be achieved for the prediction of M_h at the time the LC is running [the experimental error is very small, $\Delta M_h \approx 50$ MeV], the allowed parameter space for the MSSM prediction reduces to two extremely small regions which correspond to the sign ambiguity in the trilinear coupling A_t.

Figure 4.56: Left: the experimental accuracies for the branching ratios $BR(h \to b\bar{b})$ and $BR(h \to WW^*)$ at the LC [the vertical and horizontal bands] compared with the prediction in the MSSM. The light shaded (yellow) region is for the full allowed parameter space, the medium shaded (light blue) region is for the range of predictions in the MSSM when compatible with the assumed experimental information from LHC and LC, $\Delta M_A = 10\%$, $\tan\beta > 15$, $\Delta m_{\tilde{t}}, \Delta m_{\tilde{b}} = 5\%$, $\Delta m_t = 0.1$ GeV and the dark shaded (dark blue) region is when a measurement of the light h boson mass, including a theoretical uncertainty of $\Delta M_h = 0.5$ GeV, is assumed. Right: the branching ratio of the decay $h \to WW^*$ as a function of the trilinear coupling A_t; the light shaded (light blue) region is the range of MSSM predictions compatible with the experimental information given above; from Ref. [541].

These two regions can be discriminated by the experimental measurements. This can be seen from the right–hand side of Fig. 4.56 where the branching ratio for the decay $h \to WW^*$ is shown as a function of A_t under the same conditions as above. Not only the sign ambiguity A_t is removed but the parameter itself, which is notoriously known to be very difficult to probe at hadron colliders, can be determined with a reasonable precision. This additional information will be very important, particularly in constrained models in which the trilinear coupling defined at the high scale is among the few basic input parameters.

Thus, an agreement between the precise measurements of the various branching ratios which can be performed at the linear collider, supplemented by the information on the masses of the heavy states that is provided by the LHC, with the theoretical prediction will constitute a highly non trivial test of the MSSM at the quantum level. This is a typical example of the LHC/LC complementarity which has been discussed in detail in the review of Ref. [517] to which we refer for other examples.

4.6.4 Discriminating between different SUSY–breaking mechanisms

The high–precision measurements in the Higgs sector would allow to perform consistency tests of a given model of Supersymmetry breaking. In the context of mSUGRA type models, for instance, the measurement of the many branching ratios of the lighter h boson can tell an mSUGRA model with universal boundary conditions at the GUT scale for all scalar particles from the less constrained models in which, e.g., the sfermion and the Higgs soft SUSY–breaking mass parameters are different at this high scale. The ability of the measurements, via their sensitivity to variations of the parameter M_A and μ for example, to test the universality assumption of mSUGRA models and to verify the presence of non–universal scalar masses for the Higgs fields is demonstrated in Fig. 4.57. The number of standard deviations of the cross sections times branching ratios of the lighter h boson for several final states from their values as predicted in the SM, as well as from the values predicted in an mSUGRA scenario in which the chosen input parameters lead in principle to a pseudoscalar Higgs mass of $M_A \approx 440$ GeV, is shown when this parameter is varied around the mSUGRA point. In the left–hand side, only the measurements performed at the e^+e^- collider [with a c.m. energy between 350 and 500 GeV] are displayed while, in the right–hand side, the additional information from measurements performed at the $\gamma\gamma$ mode of the machine and at $\mu^+\mu^-$ colliders, is displayed.

As can be seen, the variations with M_A is quite substantial, in particular in the $h \to b\bar{b}$ and $h \to WW^*$ channels at the LC where deviations from the mSUGRA prediction $M_A = 440$ GeV could be as large as $\sim 2.5\sigma$ or more for $\Delta M_A = 100$ GeV; the $h \to b\bar{b}$ measurement at photon and muon colliders is also very sensitive to this variation. Thus, a distinction of the two scenarios can be performed at a very high level. [The variation with μ, the other
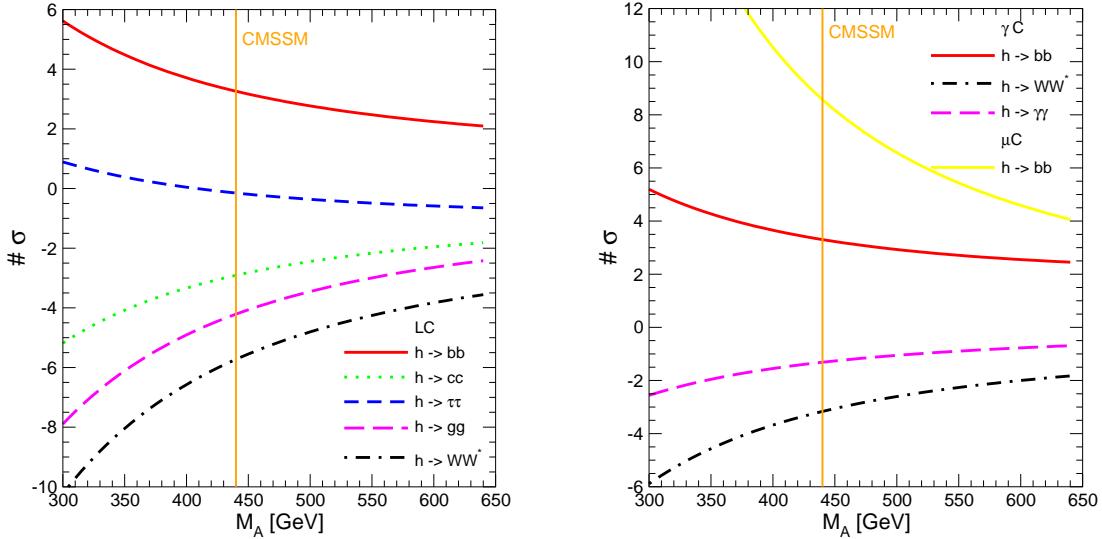
Figure 4.57: The number of standard deviations of the predictions in non–universal Higgs mass mSUGRA–type models as compared to the SM are shown in the different $\sigma \times BR$ channels as functions of M_A for the LC (left) and at $\gamma\gamma$ and $\mu^+\mu^-$ colliders (right); the corresponding cMSSM values of M_A are indicated by light vertical (orange) lines. The other parameters are $m_{1/2} = 300$ GeV, $m_0 = 100$ GeV, $\tan\beta = 10$ and $A_0 = 0$; from Ref. [156].

parameter which is affected by the non–universality of the Higgs mases, is rather weak as it enters the Higgs sector observables only at the loop level in contrast to M_A.]
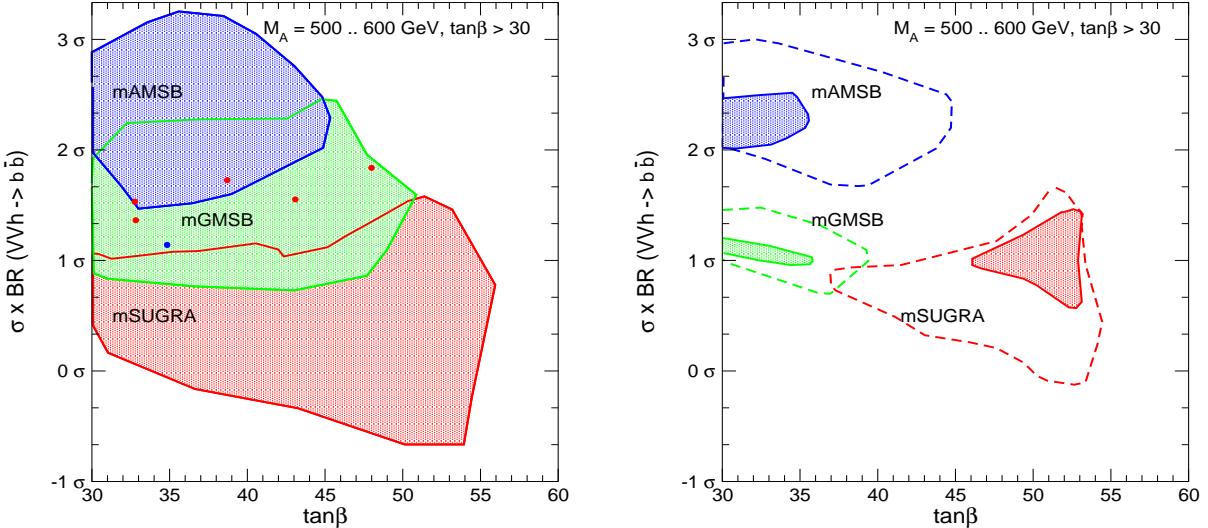
Figure 4.58: Left: comparison of $BR(h \to b\bar{b})$ in the three soft SUSY–breaking scenarios, mSUGRA, AMSB and GMSB, via measurements at a linear collider. Right: the same as previously, but assuming direct input on the SUSY spectrum from the LHC. The areas surrounded by dashed lines correspond to the parameter regions in the three scenarios where the stop mass is the range $m_{\tilde{t}_1} = 850 \pm 50$ GeV, while the shaded areas surrounded by full lines correspond to the case where, in addition, one has $m_{\tilde{g}} = 950 \pm 50$ GeV [156].

The possibility of precision measurements in the Higgs sector at lepton colliders could allow to distinguish between different scenarios for soft SUSY–breaking. This is particularly true when the measurements of the various cross sections and branching ratios of the h boson are combined with measurements of the SUSY spectrum at the LHC. This is exemplified in Fig. 4.58 where, in the left–hand side, the range allowed for BR($h \to b\bar{b}$) is displayed as a function of $\tan \beta \gtrsim 30$ for a small variation of M_A around 550 GeV, in three popular scenarios of SUSY–breaking: mSUGRA and minimal AMSB and GMSB. The three possibilities can be discriminated in some cases but the overlapping regions are quite large. In turn, if some information from measurements of the squark and gluino masses at the LHC is added, the three possibilities can be disentangled with a high confidence. This is another example of the complementarity between the LHC and future lepton colliders.

4.6.5 The connection with cosmological issues

Finally, the measurements that could be performed at both the LHC and the LC will be undoubtedly needed for a precise prediction of the cosmological relic density of the LSP neutralino which is supposed to make the Dark Matter of the universe in SUSY models. As discussed in §2.4, the WMAP measurement of $\Omega_{\mathrm{DM}}h^2$ is so accurate and the forthcoming measurement by the Planck satellite will be even more accurate that a very precise knowledge of the physical parameters of the MSSM will be required. This is particularly true in mSUGRA–type models where, in most of the parameter space, the LSP neutralino turns out to be bino–like and does not annihilate efficiently enough into fermions [through t–channel sfermion exchange] to satisfy the tight WMAP constraint. One therefore has to resort to additional mechanisms, such as rapid annihilation via s–channel exchange which occurs near Higgs boson poles and co–annihilation with sfermions which needs a near mass degeneracy of the lightest neutralino with the NLSP. All these mechanisms [in addition to the "focus point" scenario where the LSP has a large higgsino component and annihilates efficiently into gauge and Higgs bosons] occur only in very narrow strips of the parameter space and need a fine adjustment of several SUSY parameters to take place.

Examples of accuracies which are needed on the weak scale parameters of the MSSM [either the physical or the soft SUSY–breaking parameters] to match the WMAP measurement are displayed in Fig. 4.59 in the various scenarios which have been discussed in §2.4.2. The fractional quantities $a = \Delta P/P$ are defined as the accuracies that are required on each MSSM parameter P to obtain a 10% shift in the value of $\Omega_{\chi_1^0}h^2$, which corresponds to the uncertainty of the WMAP measurement, $\Omega_{\mathrm{DM}} h^2 = 0.113 \pm 0.009$. Here, a point in the constrained mSUGRA model is chosen but for the calculation of the accuracy $a(P)$ the more general pMSSM model is assumed. This allows to relax the strong assumptions of mSUGRA and to perform a less model dependent analysis.
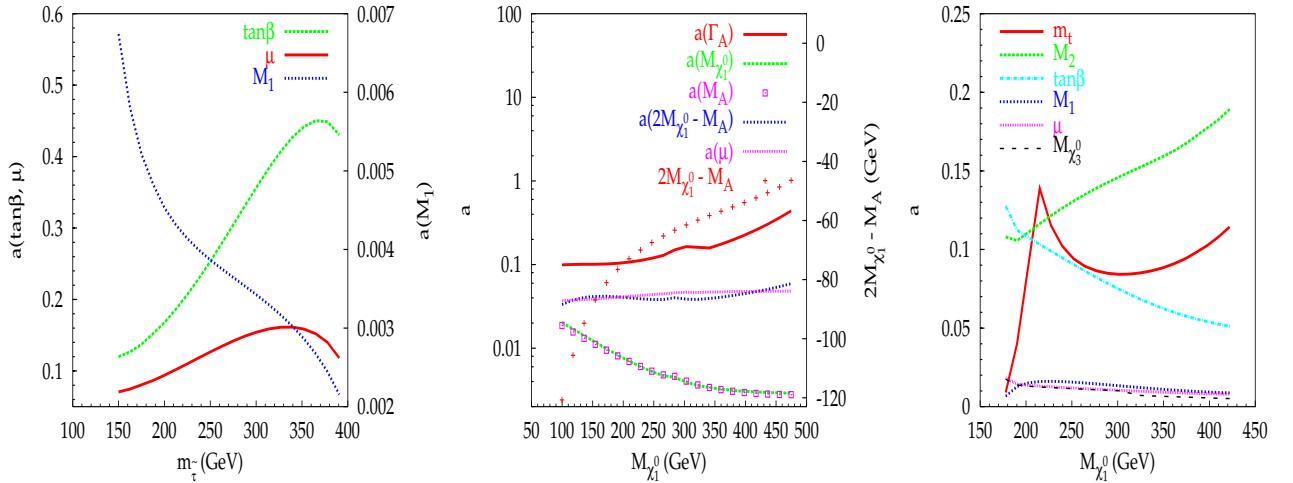
Figure 4.59: Required fractional accuracies $a(P)$ upon various MSSM parameters P in the pMSSM to match the WMAP accuracy for the neutralino relic density obtained in an mSUGRA scenario. The left, central and right figures correspond to the scenarios which have been given in respectively, Figures 2.50, 2.49 and 2.48; from Ref. [288].

In the left–hand side of Fig. 4.59, shown are the fractional accuracies a which are needed on the parameters $\tan\beta, \mu$ and M_1 to arrive at the small mass difference between the lightest $\tilde{\tau}_1$ and the LSP neutralino which gives the correct $\Omega_{\chi_1^0}h^2$ in the scenario where $\tilde{\tau}_1$–χ_1^0 co–annihilation is the main ingredient; Fig. 2.50. The central figure shows the accuracies a of the various parameters, in particular the total width of the pseudoscalar A boson and the $2m_{\chi_1^0} - M_A$ difference, which are needed for a rapid LSP annihilation to take place in the "Higgs funnel" scenario of Fig. 2.48, through the s–channel A boson pole. Finally, the figure in the right–hand side shows the accuracies which are needed for several parameters which allow the LSP to have a large higgsino component and adequate couplings to the Higgs boson to make the required relic density in the "focus–point" scenario of Fig. 2.49.

As can be seen, the experimental information which is needed to arrive at a precise prediction of $\Omega_{\chi_1^0}h^2$ is very demanding, since some MSSM parameters should be measured at the percent, if not a the per mille, level [a very high–precision measurement of some SM parameters, such as the top quark mass, will also be needed in this context]. Some parameters of the MSSM Higgs sector such as $\tan\beta, M_A$ and $\Gamma(A)$ could play a key role in this context. The combination of the complementary informations that will be obtained at the LHC and at a future linear collider will be crucial to arrive at such a precision. Note, also, that theoretical uncertainties in the prediction of the neutralino relic density [which can be estimated for instance through scale dependence, etc..] are also large at the present time. A large theoretical effort will be, thus, also necessary in order to match the WMAP and the forthcoming PLANCK measurements.

Appendix

A1: SM input parameters

Except when it is explicitly mentioned, we use the following default values for the pole masses of the SM gauge bosons, leptons and quarks

$$M_Z = 91.187 \text{ GeV} , \ M_W = 80.425 \text{ GeV} , \tag{A.1}$$

$$m_\tau = 1.777 \text{ GeV} , \ m_\mu = 0.105 \text{ GeV} , \tag{A.2}$$

$$m_t = 178 \pm 4.3 \text{ GeV} , \ m_b = 4.88 \pm 0.07 \text{ GeV} , \ m_c = 1.64 \pm 0.07 \text{ GeV} \tag{A.3}$$

For the quark masses, we have included the experimental errors. In most cases [except, eventually, for the top quark], we use the running $\overline{\text{MS}}$ or $\overline{\text{DR}}$ quark masses defined at the scale of the Higgs mass as described in §1.1.6 and §I.1.1.4 of the first part of this review. The electron and the light quark masses are too small to be relevant. An exception is provided by the strange quark mass for which we will use the value $\bar{m}_s(1 \text{ GeV}) = 0.2 \text{ GeV}$.

In the case of the $H^\pm$ bosons, the values of some CKM matrix elements need to be fixed in addition and we use

$$V_{us} = 0.22 , \ \ V_{cb} = 0.04 , \ \ V_{ub}/V_{cb} = 0.08 \tag{A.4}$$

The values used for the fine structure constant, the Fermi coupling constant and the strong coupling constants are:

$$\alpha^{-1}(M_Z^2) = 127.934 , \ G_\mu = 1.16637 \cdot 10^{-5} \text{ GeV}^{-2} , \ \alpha_s(M_Z^2) = 0.1172 \pm 0.002 \tag{A.5}$$

The value of electroweak mixing angle is derived from the W and Z masses and we use

$$\sin^2 \theta_W \equiv s_W^2 = 1 - c_W^2 = 0.2315 \tag{A.6}$$

A2: The benchmark scenario

In the majority of cases and unless otherwise stated, we have implemented the radiative corrections in the MSSM Higgs sector in the following $M_h^{\max}$ benchmark scenario

$$M_S \equiv m_{\tilde{Q}_i} = \tfrac{1}{2} m_{\tilde{\ell}_i} = 2 \text{ TeV} , \ A_t = A_b = \sqrt{6} \, M_S$$
$$M_2 \simeq 2 \, M_1 = -\mu = 400 \text{ GeV} , \ M_3 = 0.8 \, M_S \tag{A.7}$$

and varied the pseudoscalar Higgs boson mass M_A, for which we take the value $M_A = 1$ TeV for the decoupling limit. The parameter $\tan\beta$ is in general chosen to be $\tan\beta = 3$ or $\tan\beta = 30$.

A3: Notation for the Higgs states

In addition to $H_{\rm SM}$ which denotes the SM Higgs boson, we have used throughout this review, the following notation for the MSSM Higgs particles:

- H_k with $H_1 = H, H_2 = h, H_3 = A$ and $H_4 = H^{\pm}$ for all Higgs bosons.
- $\Phi = h, H, A$ for the three neutral MSSM Higgs bosons.
- $\mathcal{H} = h, H$ for the two CP–even neutral Higgs particles.
- $\varphi = h, A$ for the lighter CP–even and CP–odd neutral particles.
- $\Phi_H = h(H)$ and $\Phi_A = H(h)$ for the SM–like and pseudoscalar–like Higgs boson in the decoupling (anti–decoupling) regime.

References

[1] Particle Data Group, K. Hagiwara *et al.*, Phys. Rev. D66 (2002) 010001; S. Eidelman *et al.*, Phys. Lett. B592 (2004) 1.

[2] The LEP Collaborations (ALEPH, DELPHI, L3 and OPAL), the LEP Electroweak Working Group and the SLD Heavy Flavour Group, *A combination of preliminary Electroweak measurements and constraints on the Standard Model*, hep-ex/0412015; `http://lepewwg.web.cern.ch/LEPEWWG`.

[3] S. Glashow, Nucl. Phys. 22 (1961) 579; S. Weinberg, Phys. Rev. Lett. 19 (1967) 1264; A. Salam, in "Elementary Particle Theory", ed. N. Svartholm, Almqvist and Wiksells, Stockholm (1969), p. 367.

[4] M. Gell-Mann, Phys. Lett. 8 (1964) 214; G. Zweig, CERN-Report 8182/TH401 (1964); H. Fritzsch, M. Gell-Mann and H. Leutwyler, Phys. Lett. B47 (1973) 365; D. Gross and F. Wilczek, Phys. Rev. Lett. 30 (1973) 1343; H.D. Politzer, Phys. Rev. Lett. 30 (1973) 1346; G. 't Hooft, Marseille Conference on Yang–Mills fields (1972).

[5] P.W. Higgs, Phys. Rev. Lett. 13 (1964) 508; *ibid.* Phys. Rev. 145 (1966) 1156; F. Englert and R. Brout, Phys. Rev. Lett. 13 (1964) 321; G.S. Guralnik, C.R. Hagen and T. Kibble, Phys. Rev. Lett. 13 (1965) 585; T. Kibble, Phys. Rev. 155 (1967) 1554.

[6] H. Georgi and S. Glashow, Phys. Rev. Lett. 32 (1974) 438; G. Pati and A. Salam, Phys. Rev. D10 (1974) 275.

[7] For reviews on GUT, see P. Langacker, Phys. Rept. 72C (1981) 185; R. Mohapatra "Unification and Supesrymmetry", Ed. Springer, 1986.

[8] H. Georgi, H. Quinn and S. Weinberg, Phys. Rev. Lett. 33 (1974) 451.

[9] J. Ellis, S. Kelley and D.V. Nanopoulos, Phys. Lett. B260 (1991) 131; U. Amaldi, W. de Boer and H. Fürstenau, Phys. Lett. B260 (1991) 447; P. Langacker and M. Luo, Phys. Rev. D44 (1991) 817; C. Giunti, C.W. Kim and U.W. Lee, Mod. Phys. Lett. A6 (1991) 1745.

[10] F. Zwicky, Hel. Phys. Acta 6 (1933) 110.

[11] For a review, see: E.W. Kolb and M.S. Turner, *The Early Universe*, Addison–Wesley, New York, 1990.

[12] D.N. Spergel *et al.* (WMAP Collaboration), Astrophys. J. Suppl. 148 (2003) 175.

[13] M. Veltman, Acta. Phys. Pol. B8 (1977) 475.

[14] S. Weinberg, Phys. Lett. 82B (1979) 387; M. Veltman, Acta. Phys. Polon. B12 (1981) 437; C.H. Llewellyn Smith and G.G. Ross, Phys. Lett. 105B (1981) 38.

[15] J. Wess and B. Zumino, Nucl. Phys. B70 (1974) 39.

[16] P. Ramond, Phys. Rev. D3 (1971) 2415; A. Neveu and J.H. Schwarz, Nucl. Phys. B31 (1971) 86; J.L. Gervais and B. Sakita, Nucl. Phys. B34 (1971) 632; Yu. A. Gol'fand and E. P. Likhtman, JETP Lett. 13 (1971) 323; D.V. Volkov and V.P. Akulov, Phys. Lett. B46 (1973) 109.

[17] J. Wess and J. Bagger, *Supersymmetry and Supergravity*, Princeton Series in Physics, New Jersey, 1992.

[18] S. Martin, in *Perspectives on Supersymmetry*, Ed. G.L. Kane, World Scientific, Singapore, 1998, hep-ph/9709356.

[19] P. Fayet, Nucl. Phys. B90 (1975) 104; *ibid.* Phys. Lett. B64 (1976) 159; *ibid.* Phys. Lett. B69 (1977) 489; *ibid.* Phys. Lett. B84 (1979) 416.

[20] K. Inoue, A. Komatsu and S. Takeshita, Prog. Theor. Phys 68 (1982) 927; (E) *ibid.* 70 (1983) 330.

[21] J. Hisano, H. Murayama and T. Yanagida, Nucl. Phys. B402 (1993) 46; Y. Yamada, Z. Phys. C60 (1993) 83; G.G. Ross and R.G. Roberts, Nucl. Phys. B377 (1992) 571.

[22] See for instance: G. Altarelli, F. Feruglio and I. Masina, JHEP 0011 (2000) 040.

[23] G.R. Farrar and P. Fayet, Phys. Lett. B76 (1978) 575.

[24] J. R. Ellis, J. S. Hagelin, D. V. Nanopoulos, K. A. Olive, and M. Srednicki, Nucl. Phys. B238 (1984) 453.

[25] For a detailed review on SUSY Dark Matter, see: G. Jungman, M. Kamionkowski and K. Griest, Phys. Rept. 267 (1996) 195. For more recent reviews, see G. Bertone, D. Hooper and J. Silk, hep-ph/0404175 (to appear in Phys. Rept.); J. Feng, Lectures given at the *2003 SLAC Summer School*, hep-ph/0405215; M. Drees, Plenary talk at *12th International Conference on Supersymmetry and Unification of Fundamental Interactions (SUSY 04)*, Tsukuba, Japan, June 2004, hep-ph/0410113; K. Olive, summary talk at *DARK 2004*, Heidelberg, hep-ph/0412054.

[26] E. Witten, Nucl. Phys. B188 (1981) 513; *ibid* Nucl. Phys. B202 (1982) 253; N. Sakai, Z. Phys. C11 (1981) 153; S. Dimopoulos and H. Georgi, Nucl. Phys. B193 (1981) 150; R.K. Kaul and P. Majumdar, Nucl. Phys. B199 (1982) 36.

[27] L. Girardello and M.T. Grisaru, Nucl. Phys. B194 (1982) 65.

[28] L. Ibañez and G.G. Ross, Phys. Lett. B110 (1982) 227; L. Alvarez–Gaumé, J. Polchinski and M.B. Wise, Nucl. Phys. B221 (1983) 495; J. Ellis, J. Hagelin, D. Nanopoulos and K. Tamkavis, Phys. Lett. B125 (1983) 275; L.E. Ibanez and C. Lopez, Nucl. Phys. B233 (1984) 511; L.E. Ibanez, C. Lopez and C. Munoz, Nucl. Phys. B256 (1985) 218.

[29] For reviews on the MSSM, see: P. Fayet and S. Ferrara, Phys. Rep. 32 (1977) 249; H.P. Nilles, Phys. Rep. 110 (1984) 1; R. Barbieri, Riv. Nuovo Cim. 11N4 (1988) 1; R. Arnowitt and Pran Nath, Report CTP-TAMU-52-93; J. Bagger, Lectures at TASI-95, hep-ph/9604232.

[30] H. E. Haber and G. Kane, Phys. Rep. 117 (1985) 75.

[31] M. Drees and S. Martin, CLTP Report (1995) and hep-ph/9504324.

[32] D.J.H. Chung, L.L. Everett, G.L. Kane, S.F. King, J. Lykken and L.T. Wang, Phys. Rept. 407 (2005) 1.

[33] M. Drees, R.M. Godbole and P. Roy, *Theory and Phenomenology of Sparticles*, World Scientific, Spring 2004.

[34] A.H. Chamseddine, R. Arnowitt and P. Nath, Phys. Rev. Lett. 49 (1982) 970; R. Barbieri, S. Ferrara and C.A Savoy, Phys. Lett. B119 (1982) 343; L. Hall, J. Lykken and S. Weinberg, Phys. Rev. D27 (1983) 2359.

[35] S. Dimopoulos and D. Sutter, Nucl. Phys. B452 (1995) 496; see also the discussion given by H.E. Haber, hep-ph/9709450.

[36] A. Djouadi and S. Rosiers–Lees (conv.) *et al.*, Summary Report of the MSSM Working Group for the "GDR–Supersymétrie", hep-ph/9901246.

[37] Y. Okada, M. Yamaguchi and T. Yanagida, Prog. Theor. Phys. 85 (1991) 1; *ibid.* Phys. Lett. B262 (1991) 54; J.R. Ellis, G. Ridolfi and F. Zwirner, Phys. Lett. B257 (1991) 83; *ibid.* Phys. Lett. B262 (1991) 477; H.E. Haber and R. Hempfling, Phys. Rev. Lett. 66 (1991) 1815.

[38] J.F. Gunion and H.E. Haber, Nucl. Phys. B272 (1986) 1; (E) hep-ph/9301205.

[39] J.F. Gunion and H.E. Haber, Nucl. Phys. B278 (1986) 449.

[40] J.F. Gunion and H.E. Haber, Nucl. Phys. B307 (1988) 445; (E) hep-ph/9301205.

[41] J.F. Gunion, H.E. Haber, G.L. Kane and S. Dawson, *The Higgs Hunter's Guide*, Addison–Wesley, Reading (USA), 1990.

[42] See the various physics notes of the LEP Higgs working groups at the web site: `http://lephiggs.web.cern.ch/LEPHIGGS/papers/index.html`.

[43] F. Abe *et al.* (CDF Collaboration), Phys. Rev. Lett. 74 (1995) 2626; S. Abachi *et al.* (DØ Collaboration), Phys. Rev. Lett. 74 (1995) 2632.

[44] The Tevatron Electroweak Working Group (CDF and DØ Coll.), hep-ex/0404010.

[45] A. Djouadi, *The Anatomy of Electro–Weak Symmetry Breaking, I: The Higgs boson in the Standard Model.*

[46] A. Djouadi, *The Anatomy of Electro–Weak Symmetry Breaking, III: The Higgs sector in models beyond the SM and MSSM benchmarks*, in preparation.

[47] L. O'Raifeartaigh, Nucl. Phys. B96 (1975) 331.

[48] P. Fayet and J. Iliopoulos, Phys. Lett. 51B (1974) 461.

[49] See for instance, F. Gabbiani, E. Gabrielli, A. Masiero and L. Silvestrini, Nucl. Phys. B477 (1996) 321.

[50] R. Arnowitt and P. Nath, Phys. Rev. D46 (1992) 3981; V. Barger, M.S. Berger and P. Ohmann, Phys. Rev. D49 (1994) 4908.

[51] P.H. Chankowski, S. Pokorski and J. Rosiek, Nucl. Phys. B423 (1994) 437. G. Gamberini, G. Ridolfi and F. Zwirner, Nucl. Phys. B331 (1990) 331; B. de Carlos and J.A. Casas, Phys. Lett. B309 (1993) 320; A.B. Lahanas and V.C. Spanos, Eur. Phys. J. C23 (2002) 185.

[52] H.P. Nilles, Phys. Lett. B115 (1982) 193; *ibid.* Nucl. Phys. B217 (1983) 366; S.K. Soni and H.A. Weldon, Phys. Lett. B126 (1983) 215; N. Ohta, Prog. Theor. Phys. 70 (1983) 542.

[53] M. Machacek and M.T. Vaughn, Nucl. Phys. B222 (1983) 83; *ibid.* Nucl. Phys. B236 (1984) 221; *ibid.* Nucl. Phys. B249 (1985) 70; I. Jack, Phys. Lett. B147 (1984) 405; W. de Boer, R. Ehret and D.I. Kazakov, Z. Phys. C67 (1994) 647; Y. Yamada, Phys. Rev. D50 (1994) 3537; I. Jack and D.R.T. Jones, Phys. Lett. B333 (1994) 372; D.J.

Castaño, E.J. Piard and P. Ramond, Phys. Rev. D49 (1994) 4882; V. Barger, M.S. Berger and P. Ohmann, Phys. Rev. D47 (1993) 1093.

[54] I. Jack, D. Jones, S. Martin, M. Vaughn and Y. Yamada, Phys. Rev. D50 (1994) 5481; S. Martin and M. Vaughn, Phys. Lett. B318 (1993) 331; *ibid.* Phys. Rev. D50 (1994) 47.

[55] L. Randall and R. Sundrum, Nucl. Phys. B557 (1999) 79; G. Giudice, M. Luty, H. Murayama and R. Rattazzi, JHEP 9812 (1998) 027; J.A. Bagger, T. Moroi and E. Poppitz, JHEP 0004 (2000) 009.

[56] For a phenomenological review of AMSB models, see for instance: K. Huitu, J. Laamanen and P. N. Pandita, Phys. Rev. D65 (2002) 115003.

[57] M. Dine and A. E. Nelson, Phys. Rev. D48 (1993) 1277; M. Dine, A. E. Nelson and Y. Shirman, Phys. Rev. D51 (1995) 1362; M. Dine, A. E. Nelson, Y. Nir and Y. Shirman, Phys. Rev. D53 (1996) 2658.

[58] For a general review of GMSB models, see: G.F. Giudice and R. Rattazzi, Phys. Rept. 322 (1999) 419.

[59] For phenomenological reviews on GMSB models, see for instance: S. Ambrosanio, G.D. Kribs and S.P. Martin, Phys. Rev. D56 (1997) 1761; C.H. Chen and J.F. Gunion, Phys. Rev. D58 (1998) 075005.

[60] M.M. El Kheishen, A.A. Shafik and A.A. Aboshousha, Phys. Rev. D45 (1992) 4345; M. Guchait, Z. Phys. C57 (1993) 157 and (E) *ibid.* C61 (1994) 178.

[61] A. Djouadi, J. Kalinowski, P. Ohmann and P.M. Zerwas, Z. Phys. C74 (1997) 93.

[62] J. Ellis and S. Rudaz, Phys. Lett. B128 (1983) 248; M. Drees and K. Hikasa, Phys. Lett. B252 (1990) 127.

[63] K.G. Chetyrkin, Phys. Lett. B404 (1997) 161; J.A.M. Vermaseren, S.A. Larin and T. van Ritbergen, Phys. Lett. B405 (1997) 327.

[64] N. Gray, D.J. Broadhurst, W. Grafe and K. Schilcher, Z. Phys. C48 (1990) 673; K.G. Chetyrkin and M. Steinhauser, Phys. Rev. Lett. 83 (1999) 4001; *ibid* Nucl. Phys. B573 (2000) 617; K. Melnikov and T. van Ritbergen, Phys. Lett. B482 (2000) 99.

[65] S.G. Gorishny, A.L. Kataev, S.A. Larin and L.R. Surguladze, Mod. Phys. Lett. A5 (1990) 2703; *ibid.* Phys. Rev. D43 (1991) 1633.

[66] K.G. Chetyrkin and A. Kwiatkowski, Nucl. Phys. B461 (1996) 3; S.A. Larin, T. van Ritbergen and J.A.M. Vermaseren, Phys. Lett. B362 (1995) 134.

[67] T. Banks, Nucl. Phys. B303 (1988) 172; L.J. Hall, R. Rattazzi and U. Sarid, Phys. Rev. D50 (1994) 7048; R. Hempfling, Phys. Rev. D49 (1994) 6168; M. Carena, M. Olechowski, S. Pokorski and C.E. Wagner, Nucl. Phys. B426 (1994) 269; F. Borzumati M. Olechowski and S. Pokorski, Phys. Lett. B349 (1995) 311; T. Blazek, S. Pokorski and S. Raby, Phys. Rev. D52 (1995) 4151; J. Kubo, M. Modragón and G. Zoupanos, Phys. Lett. B389 (1996) 523.

[68] M. Carena, D. Garcia, U. Nierste and C.E. Wagner, Nucl. Phys. B577 (2000) 88.

[69] D.M. Pierce, J.A. Bagger, K.T. Matchev and R.J. Zhang, Nucl. Phys. B491 (1997) 3.

[70] See e.g.: H. Eberl, K. Hidaka, S. Kraml, W. Majerotto and Y. Yamada, Phys. Rev. D62 (2000) 055006.

[71] W. Siegel, Phys. Lett. B84 (1979) 193; D.M. Capper, D.R.T. Jones and P. van Nieuwenhuizen, Nucl. Phys. B167 (1980) 479.

[72] For a review, see: I. Jack and D.R.T. Jones, *Regularization of supersymmetric theories*, hep-ph/9707278.

[73] L.V. Avdeev and M.Yu. Kalmykov, Nucl. Phys. B502 (1997) 419; H. Baer, J. Ferrandis, K. Melnikov and X. Tata, Phys. Rev. D66 (2002) 074007.

[74] G. Passarino and M. Veltman, Nucl. Phys. B160 (1979) 151.

[75] R. Barbieri and G. Giudice, Nucl. Phys. B306 (1988) 63; R. Arnowitt and P. Nath, Phys. Lett. B289 (1992) 368; S. Kelley *et al.*, Nucl. Phys. B398 (1993); Olechowski and S. Pokorski, Nucl. Phys. B404 (1993) 590; B. de Carlos and J.A. Casas, Phys. Lett. B309 (1993) 320; G.G. Ross and R.G. Roberts in Ref. [21]; S. Dimopoulos and G. F. Giudice, Phys. Lett. B357 (1995) 573; K. Agashe and M. Graesser, Nucl. Phys. B507 (1997) 3.

[76] J.M. Frère, D.R.T. Jones and S. Raby, Nucl. Phys. B222 (1983) 11; M. Claudson, L. Hall and I. Hinchliffe, Nucl. Phys. B228 (1983) 501.

[77] See e.g. J. A. Casas, A. Lleyda and C. Munoz, Nucl. Phys. B471 (1996) 3.

[78] M. Veltman, Nucl. Phys. B123 (1977) 89; M.S. Chanowitz, M.A. Furman and I. Hinchliffe, Phys. Lett. B78 (1978) 285.

308

[79] A. Djouadi and C. Verzegnassi, Phys. Lett. B195 (1987) 265; A. Djouadi, Nuov. Cim. A100 (1988) 357; B. Kniehl, Nucl. Phys. B347 (1990) 86; F. Halzen and B. Kniehl, Nucl. Phys. B353 (1991) 567; A. Djouadi and P. Gambino, Phys. Rev. D49 (1994) 3499; M. Awramik, M. Czakon, A. Freitas and G. Weiglein, Phys. Rev. Lett. 93 (2004) 201805.

[80] R. Barbieri and L. Maiani, Nucl. Phys. B224 (1983) 32; C.S. Lim, T. Inami and N. Sakai, Phys. Rev. D29 (1984) 1488; E. Eliasson, Phys. Lett. 147B (1984) 65; Z. Hioki, Prog. Theo. Phys. 73 (1985) 1283; J. A. Grifols and J. Sola, Nucl. Phys. B253 (1985) 47; R. Barbieri, M. Frigeni, F. Giuliani and H.E. Haber, Nucl. Phys. B341 (1990) 309; M. Drees, K. Hagiwara and A. Yamada, Phys. Rev. D45 (1992) 1725; P. Chankowski, A. Dabelstein, W. Hollik, W. Mösle, S. Pokorski and J. Rosiek, Nucl. Phys. B417 (1994) 101; D. Garcia and J. Solà, Mod. Phys. Lett. A9 (1994) 211.

[81] M. Drees and K. Hagiwara, Phys. Rev. D42 (1990) 1709.

[82] A. Djouadi, P. Gambino, S. Heinemeyer, W. Hollik, C. Jünger and G. Weiglein, Phys. Rev. Lett. 78 (1997) 3626; *ibid.* Phys. Rev. D57 (1998) 4179.

[83] J-F. Grivaz, Talk given at the Conference "Physics at the LHC", Vienna, July 2004, hep-ex/0411002.

[84] J. Espinosa and M. Quiros, Phys. Rev. Lett. 81 (1998) 516.

[85] S.L. Adler and W.A. Bardeen, Phys. Rev. 182 (1969) 1517; R. Jackiw, Lectures on "Current Algebra and its Applications", Princeton University Press, 1972.

[86] L. Alvarez-Gaume and E. Witten, Nucl. Phys. B234 (1983) 269.

[87] A. Weldon, Phys. Rev. D30 (1984) 1547.

[88] J.F. Gunion, H.E. Haber and J. Wudka, Phys. Rev. D43 (1991) 904.

[89] S. Glashow and S. Weinberg, Phys. Rev. D15 (1973) 1958.

[90] J.F. Donoghue and L.F. Li, Phys. Rev. 19 (1979) 945.

[91] L.J. Hall and M.B. Wise, Nucl. Phys. B187 (1981) 397.

[92] A. Djouadi, Y. Mambrini and M. Muhlleitner, Eur. Phys. J. C20 (2001) 563.

[93] A. Djouadi, M. Drees, P. Fileviez Perez and M. Muhlleitner, Phys. Rev. D65 (2002) 075016.

[94] For a recent review of 2HDMs including CP–violation, see for instance: I.F. Ginzburg, M. Krawczyk and P. Osland, hep-ph/0211371.

[95] For a recent discussion of CP–conserving 2HDMs and for the Feynman rules, see: S. Kanemura, Y. Okada, E. Senaha and C.P. Yuan, Phys. Rev. D70 (2004) 115002.

[96] H. Georgi, Hadronic J. 1 (1978) 155.

[97] A. Méndez, in Procceddings of the ECFA–DESY Workshops e^+e^- collisions at TeV energies: The physics Potential, DESY-92-123A (1991), p. 103.

[98] J. Grifols and A. Méndez, Phys. Rev. D22 (1980) 1725; A. Méndez and A. Pomarol, Nucl. Phys. B349 (1991) 369.

[99] A. Johansen, N. Ural'tsev and V. Khoze, Yad. Fiz. 36 (1982) 1230; G. Keller and D. Wyler, Nucl. Phys. B274 (1986) 410.

[100] H. Haber, G. Kane and T. Sterling, Nucl. Phys. B61 (1979) 493.

[101] A. Dobado, M.J. Herrero and S. Penaranda, Eur. Phys. J. C17 (2000) 487; J.F. Gunion and H.E. Haber, Phys. Rev. D67 (2003) 075019.

[102] H.E. Haber and Y. Nir, Phys. Lett. B306 (1993) 327.

[103] H.E. Haber, CERN-TH/95-109 and hep-ph/9505240.

[104] M. Carena and H. E. Haber, Prog. Part. Nucl. Phys. 50 (2003) 63.

[105] S. Heinemeyer, hep-ph/0407244.

[106] W. Hollik, S. Heinemeyer and G. Weiglein, hep-ph/0412214.

[107] A. Dedes, G. Degrassi and P. Slavich, Nucl. Phys. B672 (2003) 144.

[108] P.H. Chankowski, S. Pokorski and J. Rosiek, Phys. Lett. B274 (1992) 191; A. Brignole, Phys. Lett. B281 (1992) 284.

[109] A. Dabelstein, Z. Phys. C67 (1995) 495.

[110] M. Drees and M. Nojiri, Phys. Rev. D45 (1992) 2482.

[111] M. Carena, J.R. Espinosa, M. Quiros and C.E. Wagner, Phys. Lett. B355 (1995) 209; M. Carena, M. Quiros and C.E. Wagner, Nucl. Phys. B461 (1996) 407; J.R. Espinosa and I. Navarro, Nucl. Phys. B615 (2001) 82.

[112] H.E. Haber, R. Hempfling and A.H. Hoang, Z. Phys. C75 (1997) 539.

[113] R. Hempfling and A.H. Hoang, Phys. Lett. B331 (1994) 99.

[114] S. Heinemeyer, W. Hollik and G. Weiglein, Phys. Rev. D58 (1998) 091701; Phys. Lett. B440 (1998) 296; Eur. Phys. J. C9 (1999) 343; Phys. Lett. B455 (1999) 179.

[115] R.J. Zhang, Phys. Lett. B447 (1999) 89; J.R. Espinosa and R.J. Zhang, JHEP 0003 (2000) 026.

[116] J.R. Espinosa and R.J. Zhang, Nucl. Phys. B586 (2000) 3.

[117] G. Degrassi, P. Slavich and F. Zwirner, Nucl. Phys. B611 (2001) 403.

[118] A. Brignole, G. Degrassi, P. Slavich and F. Zwirner, Nucl. Phys. B643 (2002) 79.

[119] S. Heinemeyer, W. Hollik, H. Rzehak and G. Weiglein, Eur. Phys. J. C39 (2005) 465.

[120] A. Brignole, G. Degrassi, P. Slavich and F. Zwirner, Nucl. Phys. B631 (2002) 195.

[121] B.C. Allanach, A. Djouadi, J.L. Kneur, W. Porod et P. Slavich, JHEP 0409 (2004) 044.

[122] A. Dedes and P. Slavich, Nucl. Phys. B657 (2003) 333.

[123] S.P. Martin, Phys. Rev. D65 (2002) 116003; *ibid.* Phys. Rev. D66 (2002) 096001.

[124] S.P. Martin, Phys. Rev. D67 (2003) 095012.

[125] S.P. Martin, Phys. Rev. D71 (2005) 016012.

[126] A. Djouadi, J. L. Kneur and G. Moultaka, hep-ph/0211331, available from the web site: `http://www.lpta.univ-montp2.fr/~kneur/Suspect` .

[127] B. Allanach, Comput. Phys. Commun. 143 (2002) 305; available from the web site: `http://allanach.home.cern.ch/allanach/softsusy.html` .

[128] W. Porod, Comput. Phys. Commun. 153 (2003) 275; available at the web site: `http://www-theorie.physik.unizh.ch/~porod/SPheno.html` .

[129] A. Djouadi, J. Kalinowski and M. Spira, Comput. Phys. Commun. 108 (1998) 56.

[130] S. Heinemeyer, W. Hollik and G. Weiglein, Comp. Phys. Commun. 124 (2000) 76; M. Frank, S. Heinemeyer, W. Hollik and G. Weiglein, hep-ph/0202166.

[131] `SUBH`, based on M. Carena, M. Quiros and C.E.M. Wagner in Ref. [111].

[132] M. Carena, S. Mrenna and C. Wagner, Phys. Rev. D60 (1999) 075010.

[133] A. Brignole, Phys. Lett. B277 (1992) 313; A. Brignole, J. Ellis, G. Ridolfi and F. Zwirner, Phys. Lett. B271 (1991) 123.

[134] E. Boos, A. Djouadi, M. Muhlleitner and A. Vologdin, Phys. Rev. D66 (2002) 055004.

[135] M. Carena, S. Heinemeyer, C. E. M. Wagner and G. Weiglein, hep-ph/9912223.

[136] S. Narison, *Light and heavy quark masses, flavor breaking of chiral condensates, meson weak leptonic decay constants in QCD*, hep-ph/0202200.

[137] M. Carena, H.E. Haber, S. Heinemeyer, W. Hollik, C.E.M. Wagner and G. Weiglein, Nucl. Phys. B580 (2000) 29.

[138] A. Brignole and F. Zwirner, Phys. Lett. B299 (1993) 72.

[139] S. Heinemeyer and W. Hollik, Nucl. Phys. B474 (1996) 32.

[140] V. Barger, M. Berger, A. Stange and R. Phillips, Phys. Rev. D45 (1992) 4128.

[141] Z. Kunszt and F. Zwirner, Nucl. Phys. B385 (1992) 3.

[142] W. Hollik and S. Penaranda, Eur. Phys. J. C23 (2002) 163; A. Dobado, M.J. Herrero, W. Hollik and S. Penaranda, Phys. Rev. D66 (2002) 095016; M.V. Dolgopolov and Yu.P. Philippov, Phys. Atom. Nucl. 67 (2004) 590 and hep-ph/0310018.

[143] F. Boudjema and A. Semenov, Phys. Rev. D66 (2002) 095007.

[144] A. Djouadi, W. Kilian, M.M. Muhlleitner and P.M. Zerwas, Eur. Phys. J.C10 (1999) 27; *ibid* hep-ph/0001169.

[145] See for instance, J.F. Gunion, A. Stange, S. Willenbrock (conv.) *et al.* in *Electroweak symmetry breaking and new physics at the TeV scale*, Ed. T. Barklow *et al.*, hep-ph/9602238.

[146] E. Boos, A. Djouadi and A. Nikitenko, Phys. Lett. B578 (2004) 384.

[147] H. Baer and J. Wells, Phys. Rev. D57 (1998) 4446; W. Loinaz and J.D. Wells, Phys. Lett. B445 (1998) 178; K.S. Babu and C.F. Kolda, Phys. Lett. B451 (1999) 77.

[148] J.L. Diaz-Cruz, H.-J. He, T. Tait and C.P. Yuan, Phys. Rev. Lett. 80 (1998) 4641; C. Balázs, J.L. Diaz-Cruz, H.-J. He, T. Tait and C.P. Yuan, Phys. Rev. D59 (1999) 055016.

[149] M. Carena, S. Mrenna and C.E.M. Wagner, Phys. Rev. D62 (2000) 055008.

[150] S. Heinemeyer, W. Hollik and G. Weiglein, Eur. Phys. J. C16 (2000) 139.

[151] See, for instance, F. Zwirner, Plenary talk at the Workshop on *Physics and Experiments with Linear Colliders*, Saariselka, Finland, Sep. 1991, hep-ph/9203204.

[152] M.B. Einhorn and D.R.T. Jones, Nucl. Phys. B196 (1982) 475; J. Ellis, D.V. Nanopoulos and S. Rudaz, Nucl. Phys. B202 (1982) 43.

[153] V.D. Barger, M.S. Berger, P. Ohmann and R.J.N. Phillips, Phys. Lett. B314 (1993) 351; M. Carena, S. Pokorski and C.E.M. Wagner, Nucl. Phys. B406 (1993) 59.

[154] G. Degrassi, S. Heinemeyer, W. Hollik, P. Slavich and G. Weiglein, Eur. Phys. J. C28 (2003) 133.

[155] A. Dedes, S. Heinemeyer, P. Teixeira-Dias and G. Weiglein, hep-ph/9912249; S. Ambrosanio, A. Dedes, S. Heinemeyer, S. Su and G. Weiglein, Nucl. Phys. B624 (2002) 3.

[156] J.R. Ellis, S. Heinemeyer, K.A. Olive and G. Weiglein, JHEP 0301 (2003) 006.

[157] A. Dedes, S. Heinemeyer, S. Su and G. Weiglein, Nucl. Phys. B674 (2003) 271.

[158] B.W. Lee, C. Quigg and H.B. Thacker, Phys. Rev. D16 (1977) 1519.

[159] M. Carena and P.M. Zerwas (conv.) *et al.*, *Higgs Physics at LEP2* in *Physics at LEP2*, CERN Report 96–01, eds. G. Altarelli, T. Sjöstrand and F. Zwirner, Part I, p. 351, hep-ph/9602250.

[160] J. Ellis, M.K. Gaillard and D.V. Nanopoulos, Nucl. Phys. B106 (1976) 292.

[161] J.D. Bjorken, Proc. 1976 SLAC Summer Inst. Part. Phys., SLAC report 198 (1977) 1; B.L. Joffe and V.A. Khoze, Sov. J. Part. Phys. 9 (1978) 50; E. Ma and Y. Okada, Phys. Rev. D20 (1979) 1052; J. Finjord, Physica Scripta 21 (1980) 143; R.L. Kelly and T. Shimuda, Phys. Rev. D23 (1981) 1940; F.A. Behrends and R. Kleiss, Nucl. Phys. B260 (1985) 32.

[162] D.R.T. Jones and S.T. Petcov, Phys. Lett. B84 (1979) 440.

[163] G. Pocsik and G. Zsigmond, Z. Phys. C10 (1981) 367; A. Grau, J. Grifols and N. Lupon, Phys. Rev. D25 (1982) 165; N.G. Deshpande, X. Tata and D.A. Dicus, Phys. Rev. D29 (1984) 1527.

[164] J. Ellis, K. Enqvist, D.V. Nanopoulos and S. Ritz, Phys. Lett. B158 (1985) 417 and (E) *ibid.* 163B (1985) 408; S. Glashow and A. Manohar, Phys. Rev. Lett. 54 (1985) 526; G. Giudice, Phys. Lett. B208 (1988) 315; M. Drees and K. Hikasa, Phys. Rev. D40 (1989) 47.

[165] The LEP Collaboration (ALEPH, DELPHI, L3 and OPAL), Phys. Lett. B565 (2003) 61 [hep-ex/0306033].

[166] The LEP Working Group for Higgs boson searches, hep-ex/0107030.

[167] The LEP Working Group for Higgs boson searches, Contribution to ICHEP, August 2004, Beijing, LHWG-Note 2004-01 in Ref. [42].

[168] M. Drees, hep-ph/0502075; G.L. Kane, T.T. Wang, B. Nelson and L.T. Wang, Phys. Rev. D71 (2005) 035006; A. Sopczak, hep-ph/0112086; B. Tuchming, Doctoral Thesis, Orsay, April 2000.

[169] J. Kalinowski and S. Pokorski, Phys. Lett. B219 (1989) 116; A. Djouadi, P.M. Zerwas and J. Zunft, Phys. Lett. B259 (1991) 175; J. Kalinowski and M. Krawczyk, Phys. Lett. B361 (1995) 66.

[170] J. Abdallah *et al.* (DELPHI Collaboration), hep-ex/0410017.

[171] M. Drees, M. Guchait and P. Roy, Phys. Rev. Lett. 80 (1998) 2047 and (E) *ibid.* 81 (1998) 2394.

[172] W.N. Yao (for the CDF and DØ Collaborations), hep-ex/0411053.

[173] S. Komamiya, Phys. Rev. D38 (1988) 2158.

[174] The LEP Working Group for Higgs boson searches, LHWG-Note 2001-05 in Ref. [42] and hep-ex/0107031.

[175] A. Heister *et al.* (ALEPH Collaboration), Phys. Lett. B543 (2002) 1.

[176] T. Affolder *et al.* (CDF Collaboration), Phys. Rev. D62 (2000) 012004; V.M. Abrazov *et al.* (DØ Collaboration), Phys. Rev. Lett. 82 (1999) 4975.

[177] F. Abe *et al.* (CDF Collaboration), Phys. Rev. Lett. 79 (1997) 357.

[178] E. Golowich and T.C. Yang, Phys. Lett. 80B (1979) 245; L.N. Chang and J.E. Kim, Phys. Lett. 81B (1979) 233; D.R.T. Jones, G. Kane and J.P. Leveille, Phys. Rev. D24 (1981) 2990; I. Bigi, Y.L. Dokshitser, V. Khoze, J. Kühn and P. Zerwas, Phys. Lett. B181 (1986) 157.

[179] For a recent review, see D.P. Roy, Mod. Phys. Lett. A19 (2004) 1813.

[180] L. Moneta (for the CDF and DØ Collaborations), hep-ex/0106050.

[181] A. Denner, R.J. Guth, W. Hollik and J.H. Kuhn, Z. Phys. C51 (1991) 695; A. Djouadi, J.L. Kneur and G. Moultaka, Phys. Lett. B242 (1990) 265; D. Garcia, R.A. Jimenez and J. Sola, Phys. Lett. B347 (1995) 309; H.E. Logan, PhD Thesis, hep-ph/9906332; H.E. Haber and H.E. Logan, Phys. Rev. D62 (2001) 015011.

[182] O. Lebedev, W. Loinaz and T. Takeuchi, Phys. Rev. D62 (2000) 055014.

[183] M. Boulware and D. Finell, Phys. Rev. D44 (1991) 2054; A. Djouadi, G. Girardi, C. Verzegnassi, W. Hollik and F.M. Renard, Nucl. Phys. B349 (1991) 48.

[184] Muon $(g-2)$ Collaboration: H.N. Brown *et al.*, Phys. Rev. Lett. 86 (2001) 2227; G.W. Bennett *et al.*, Phys. Rev. Lett. 89 (2002) 101804 (2002) and (E) *ibid.* 89 (2002) 129903; *ibid.* Phys. Rev. Lett. 92 (2004) 161802.

[185] M. Davier, S. Eidelman, A. Höcker and Z. Zhang, Eur. Phys. J. C31 (2003) 503; K. Hagiwara, A.D. Martin, D. Nomura and T. Teubner, Phys. Rev. D69 (2004) 093003; J.F. de Troconiz and F.J. Yndurain, hep-ph/0402285; M. Passera, hep-ph/0411168.

[186] A. Dedes and H.E. Haber, JHEP 0105 (2001) 006.

[187] S. Bertolini, F. Borzumati, A. Masiero and G. Ridolfi, Nucl. Phys. B353 (1991) 591; R. Barbieri and G. Giudice, Phys. Lett. B309 (1993) 86; F. Borzumati, M. Olechowski and S. Pokorski, Phys. Lett. B349 (1995) 311; M. Ciuchini, G. Degrassi, P. Gambino and G.F. Giudice, Nucl. Phys. B527 (1998) 21; *ibid.* Nucl. Phys. B534 (1998) 3; G. Degrassi, P. Gambino and G.F. Giudice, JHEP 0012 (2000) 009; C. Bobeth, M. Misiak and J. Urban, Nucl. Phys. B567 (2000) 153; F. Borzumati, C. Greub, T. Hurth and D. Wyler, Phys. Rev. D62 (2000) 075005; M. Carena, D. Garcia, U. Nierste and C.E.M. Wagner, Phys. Lett. B499 (2001) 141.

[188] M.S. Alam *et al.* (CLEO Collaboration), Phys. Rev. Lett. 74 (1995) 2885; an update is given in S. Ahmed *et al.*, hep-ex/9908022; K. Abe *et al.* (Belle Collaboration), Phys. Lett. B511 (2001) 151.

[189] P. Koppenburg *et al.* (Belle Collaboration), Phys. Rev. Lett. 93 (2004) 061803.

[190] M. Neubert, hep-ph/0408179.

[191] G. Eilam and A. Soni, Phys. Lett. 215B (1988) 171; S. Choudhury and N. Gaur, Phys. Lett. B451 (1999) 86; K. Babu and C. Kolda, Phys. Rev. Lett. 84 (2000) 228; C. Bobeth, T. Ewerth, F. Krüger and J. Urban, Phys. Rev. D64 (2001) 074014; A. Dedes, H. Dreiner and U. Nierste, Phys. Rev. Lett. 87 (2001) 251804; G. Isidori and A. Retico, JHEP 0111 (2001) 001; A. Dedes and A. Pilaftsis, Phys. Rev. D67 (2003) 015012; A. Buras, P. Chankowski, J. Rosiek and L. Slawianowska, Nucl. Phys. B659 (2003) 3; P. Gambino, U. Haisch and M. Misiak, hep-ph/0410155.

[192] T. Hurth, Rev. Mod. Phys. Lett. A19 (2004) 1813.

[193] W. de Boer and G. Sanders, Phys. Lett. B585 (2004) 276.

[194] L. Resnick, M.K. Sundaresan and P.J.S. Watson, Phys. Rev. D8 (1973) 172.

[195] E. Braaten and J.P. Leveille, Phys. Rev. D22 (1980) 715; N. Sakai, Phys. Rev. D22 (1980) 2220; T. Inami and T. Kubota, Nucl. Phys. B179 (1981) 171; S.G. Gorishny, A.L. Kataev and S.A. Larin, Sov. J. Nucl. Phys. 40 (1984) 329.

[196] M. Drees and K. Hikasa, Phys. Rev. D41 (1990) 1547; *ibid.* Phys. Lett. B240 (1990) 455 and (E) *ibid.* B262 (1991) 497.

[197] A. Djouadi and P. Gambino, Phys. Rev. D51 (1995) 218.

[198] A. Djouadi, M. Spira and P.M. Zerwas, Z. Phys. C70 (1996) 427.

[199] A. Dabelstein, Nucl. Phys. B456 (1995) 25; P.H. Chankowski, S. Pokorski and J. Rosiek, Nucl. Phys. B423 (1995) 497; J.A. Coarasa, R.A. Jiménez and J. Solà, Phys. Lett. B389 (1996) 312; C.S. Li and J.M. Yang, Phys. Lett. B315 (1993) 367; H.E. Haber, M.J. Herrero, H.E. Logan, S. Peñaranda, S. Rigolin and D. Temes, Phys. Rev D63 (2001) 055004.

[200] J. Guasch, W. Hollik and S. Penaranda, Phys. Lett. B515 (2001) 367.

[201] J. Guasch, P. Hafliger and M. Spira, Phys. Rev. D68 (2003) 115001.

[202] R. Harlander and M. Steinhauser, Phys. Rev. D56 (1997) 3980.

[203] A. Djouadi, J. Kalinowski and P.M. Zerwas, Z. Phys. C70 (1996) 435.

[204] S. Moretti and W. Stirling, Phys. Lett. B347 (1995) 291; (E) *ibid.* B366 (1996) 451.

[205] E. Barradas, J.L. Diaz-Cruz, A. Gutierrez and A. Rosado, Phys. Rev. D53 (1996) 1678.

[206] A. Méndez and A. Pomarol, Phys. Lett. B252 (1990) 461; C.S. Li and R.J. Oakes, Phys. Rev. D43 (1991) 855; M. Drees and D.P. Roy, Phys. Lett. B269 (1991) 155.

[207] R.A. Jiménez and J. Solà, Phys. Lett. B389 (1996) 53; A. Bartl, H. Eberl, K. Hikasa, T. Kon, W. Majerotto and Y. Yamada, Phys. Lett. B378 (1996) 167; H. König, Mod. Phys. Lett. A10 (1995) 1113; F. Borzumati, G.R. Farrar, N. Polonsky and S. Thomas, Nucl. Phys. B555 (1996) 53; A. Bartl, K. Hidaka, Y. Kizukuri, T. Kon and W. Majerotto, Phys. Lett. B315 (1993) 360.

[208] For a review, see: J.A. Coarasa, D. Garcia, J. Guash, R.A. Jiménez and J. Solà, hep-ph/9711472.

[209] F.M. Borzumati and A. Djouadi, Phys. Lett. B549 (2002) 170 [hep-ph/9806301]; E. Ma, D.P. Roy and J. Wudka, Phys. Rev. Lett. 80 (1998) 1162; X.J. Bi, Y.B. Dai and X.Y. Qi, Phys. Rev. D61 (2000) 015002.

[210] T.G. Rizzo, Phys. Rev. D22 (1980) 722; G. Pocsik and T. Torma, Z. Phys. C6 (1980) 1; W.-Y. Keung and W.J. Marciano, Phys. Rev. D30 (1984) 248.

[211] R.N. Cahn, Rep. Prog. Phys. 52 (1989) 389; A. Grau, G. Panchieri and R.J.N. Phillips, Phys. Lett. B251 (1990) 293; B. Kniehl, Phys. Lett. B244 (1990) 537.

[212] V. Barger, K. Cheung, A. Djouadi, B. Kniehl and P. Zerwas, Phys. Rev. D49 (1994) 79.

[213] G. Pocsik and G. Zsigmond, Phys. Lett. B112 (1982) 157.

[214] J. Balog and G. Pocsik, Acta Phys. Austriaca 53 (1981) 207; G. Zsigmond, Acta Physiol. Acad. Sci. Hung. 56 (1984) 73.

[215] A. Akeyrod, A. Arhrib and E. Naimi, Eur. Phys. J. C12 (2000) 451; *ibid.* Eur. Phys. J. C20 (2001) 51.

[216] A.I. Vainshtein, M.B. Voloshin, V.I. Zakharov and M.A. Shifman, Sov. J. Nucl. Phys. 30 (1979) 711; L. Okun, *Leptons and Quarks*, Ed. North Holland, Amsterdam, 1982; M. Gavela, G. Girardi, C. Malleville and P. Sorba, Nucl. Phys. B193 (1981) 257.

[217] P. Kalyniak, R. Bates and J. Ng, Phys. Rev. D33 (1986) 755; R. Bates, P. Kalyniak and J. Ng, Phys. Rev. D34 (1986) 172; J.F. Gunion, G. Gamberini and S.F. Novaes, Phys. Rev. D38 (1988) 3481; T.M. Aliev and Yu.M. Kasumzade, Sov. J. Nucl. Phys. 47 (1988) 293.

[218] G.L. Kane, G.D. Kribs, S.P. Martin and J.D. Wells, Phys. Rev. D53 (1996) 213.

[219] A. Djouadi, V. Driesen, W. Hollik and J.I. Illana, Eur. Phys. J. C1 (1998) 149.

[220] H. Zheng and D. Wu, Phys. Rev. D42 (1990) 3760; A. Djouadi, M. Spira, J. van der Bij and P.M. Zerwas, Phys. Lett. B257 (1991) 187; S. Dawson and R.P. Kauffman, Phys. Rev. D47 (1993) 1264; K. Melnikov and O. Yakovlev, Phys. Lett. B312 (1993) 179; M. Inoue, R. Najima, T. Oka and J. Saito, Mod. Phys. Lett. A9 (1994) 1189; J. Fleischer and O.V. Tarasov, Z. Phys. C64 (1994) 413; J. Fleischer, O.V. Tarasov and V.O. Tarasov, Phys. Lett. B584 (2004) 294.

[221] A. Djouadi, M. Spira and P.M. Zerwas, Phys. Lett. B311 (1993) 255.

[222] M. Spira, A. Djouadi, D. Graudenz and P.M. Zerwas, Nucl. Phys. B453 (1995) 17.

[223] G. 't Hooft and M. Veltman, Nucl. Phys. B44 (1972) 189; P. Breitenlohner and D. Maison, Commun. Math. Phys. 52 (1977) 11.

[224] S.A. Larin, Phys. Lett. B303 (1993) 113.

[225] K. Melnikov, M. Spira and O. Yakovlev, Z. Phys. C64 (1994) 401.

[226] R.N. Cahn, M.S. Chanowitz and N. Fleishon, Phys. Lett. 82B (1979) 113; L. Bergstrom and G. Hulth, Nucl. Phys. B259 (1985) 137.

[227] M. Spira, A. Djouadi and P.M. Zerwas, Phys. Lett. B276 (1992) 350.

[228] T.J. Weiler and T.C. Yuan, Nucl. Phys. B318 (1989) 337.

[229] A. Djouadi, V. Driesen, W. Hollik and J. Rosiek, Nucl. Phys. B491 (1997) 68.

[230] For the reverse decay, $Z \rightarrow \gamma +$ Higgs, mainly in 2HDMs and in various approximations, see also: L. Bergstrom, Phys. Lett. B167 (1986) 332; R. Decker, M. Nowakowski and D. Woitschitzky, Phys. Lett. B255 (1991) 605; G. Gamberini, G. Giudice and G. Ridolfi, Nucl. Phys. B292 (1987) 237; A. Barroso, J. Pulido and J. Romao, Nucl. Phys. B267 (1986) 509; J. Romao and A. Barroso, Nucl. Phys. B272 (1986) 693.

[231] J.F. Gunion, G.L. Kane and J. Wudka, Nucl. Phys. B299 (1988) 231.

[232] S. Raychaudhuri and A. Raychaudhuri, Phys. Lett. B297 (1992) 159; *ibid.* Phys. Rev. D50 (1994) 412.

[233] M. Capdequi-Peyranère, H.E. Haber and P. Irulegui, Phys. Rev. D44 (1991) 191.

[234] J. Hernández-Sánchez, M.A. Pérez, G. Tavares-Velasco and J.J. Toscano, Phys. Rev. D69 (2004) 095008; see also, J.L. Diaz-Cruz, J. Hernández-Sánchez and J.J. Toscano, Phys. Lett. B512 (2001) 339.

[235] S. Kanemura, Phys. Rev. D61 (2000) 095001.

[236] F. Wilczek, Phys. Rev. Lett. 39 (1977) 1304; J. Ellis, M. Gaillard, D. Nanopoulos and C. Sachrajda, Phys. Lett. 83B (1979) 339; T. Rizzo, Phys. Rev. D22 (1980) 178.

[237] H. Georgi, S. Glashow, M. Machacek and D. Nanopoulos, Phys. Rev. Lett. 40 (1978) 692.

[238] B. Kileng, Z. Phys. C63 (1994) 87; B. Kileng and P. Osland, Z. Phys. C71 (1996) 87.

[239] A. Djouadi, Phys. Lett. B435 (1998) 101.

[240] G. Bélanger, F. Boudjema, F. Donato, R. Godbole and S. Rosier-Lees, Nucl. Phys. B581 (2000) 3.

[241] R. Kauffman and W. Schaffer, Phys. Rev. D49 (1994) 551.

[242] K.G. Chetyrkin, B.A. Kniehl and M. Steinhauser, Nucl. Phys. B510 (1998) 61.

[243] K.G. Chetyrkin, B.A. Kniehl and M. Steinhauser, Nucl. Phys. B535 (1998) 3.

[244] W. Caswell, Phys. Rev. Lett. 33 (1974) 244; D.R.T. Jones, Phys. Rev. D25 (1982) 581; M. Einhorn and D.R.T. Jones, Nucl. Phys. B196 (1982) 475.

[245] L. Alvarez–Gaumé, J. Polchinski and M. Wise, Nucl. Phys. B221 (1983) 495; J. Derendinger and C. Savoy, Nucl. Phys. B237 (1984) 307; S. Martin and M. Vaughn, Phys. Rev. D50 (1994) 2282.

[246] S. Dawson, A. Djouadi and M. Spira, Phys. Rev. Lett. 77 (1996) 16.

[247] R.V. Harlander and M. Steinhauser, Phys. Lett. B574 (2003) 258; *ibid.* Phys. Rev. D68 (2003) 111701.

[248] R.V. Harlander and M. Steinhauser, JHEP 0409 (2004) 066.

[249] B. C. Allanach *et al.*, Eur. Phys. J. C25 (2002) 113.

[250] A. Djouadi, J. Kalinowski and P.M. Zerwas, Z. Phys. C57 (1993) 569.

[251] A. Djouadi, P. Janot, J. Kalinowski and P. Zerwas, Phys. Lett. B376 (1996) 220.

[252] J.F. Gunion and J. Kelly, Phys. Rev. D56 (1997) 1730.

[253] L.H. Wan, W.G. Ma, R.Y. Zhang and Y. Jiang, Phys. Rev. D64 (2001) 115004; R.Y. Zhang, W.G. Ma, L. Wan and Y. Jiang, Phys. Rev. D65 (2002) 075018; H. Eberl, M. Kincel, W. Majerotto and Y. Yamada, Nucl. Phys. B625 (2002) 372; H. Eberl, W. Majerotto and Y. Yamada, Phys. Lett. B597 (2004) 275.

[254] K. Griest and H.E. Haber, Phys. Rev. D37 (1988) 719; B. Grzadkowski, J. Kalinowski and S. Pokorski, Phys. Lett. B241 (1990) 534.

[255] A. Djouadi, Mod. Phys. Lett. A14 (1999) 359; G. Bélanger, F. Boudjema, A. Cottrant, R.M. Godbole and A. Semenov, Phys. Lett. B519 (2001) 93.

[256] A. Bartl, K. Hidaka, Y. Kizukuri, T. Kon and W. Majerotto, Phys. Lett. B315 (1993) 360; A. Bartl *et al.*, Phys. Lett. B373 (1996) 117; A. Bartl *et al.*, Phys. Lett. B460 (1999) 157.

[257] A. Arhrib, A. Djouadi, W. Hollik and C. Junger, Phys. Rev. D57 (1998) 5860; A. Bartl, H. Eberl, K. Hidaka, S. Kraml, W. Majerotto, W. Porod and Y. Yamada, Phys. Rev. D59 (1999) 115007; *ibid.* Phys. Lett. B419 (1998) 243.

[258] C. Weber, H. Eberl and W. Majerotto, Phys. Rev. D68 (2003) 093011; *ibid.* Phys. Lett. B572 (2003) 56; A. Arhrib and R. Benbrik, hep-ph/0412349.

[259] P. Fayet, Phys. Lett. 70B (1977) 461; *ibid.* Phys. Lett. 86B (1979) 272; *ibid.* Phys. Lett. B175 (1986) 471.

[260] A. Djouadi and M. Drees, Phys. Lett. B407 (1997) 243.

[261] R. Casalbuoni, S. De Curtis, D. Dominici, F. Feruglio and R. Gatto, Phys. Lett. B215 (1988) 313; *ibid.* Phys. Rev. D39 (1989) 2281.

[262] See the recent analysis of P. Janot, Phys. Lett. B564 (2003) 183.

[263] B.A. Campbell, J.A. Scott and M.K. Sundaresan, Phys. Lett. B126 (1983) 376; G.L. Kane and W.B. Rolnick, Nucl. Phys. B217 (1993) 117; B. Kileng and P. Osland, Z. Phys. C66 (1995) 503.

[264] A. Djouadi and M. Drees, Phys. Rev. D51 (1995) 4997.

[265] K. Ng, H. Pois and T.C. Yuan, Phys. Rev. D40 (1989) 1689.

[266] M. Jeżabek and J. H. Kühn, Nucl. Phys. B314 (1989) 1; *ibid.* Nucl. Phys. B320 (1989) 20; A. Czarnecki, Phys. Lett. B252 (1990) 467; C.S. Li, R.J. Oakes and T.C. Yuan, Phys. Rev. D43 (1991) 3759; A. Denner and T. Sack, Nucl. Phys. B358 (1991) 46; A. Czarnecki and K. Melnikov, Nucl. Phys. B544 (1999) 520; K. G. Chetyrkin, R. Harlander, T. Seidensticker and M. Steinhauser, Phys. Rev. D60 (1999) 114015.

[267] G. Eilam, R. Mendel, R. Migneron and A. Soni, Phys. Rev. Lett. 66 (1991) 3105; A. Denner and T. Sack, Nucl. Phys. B358 (1991) 46; T. Kuruma, Z. Phys. C57 (1993) 551.

[268] B. Irwin, B. Margolis and H.D. Trottier, Phys. Lett. B256 (1991) 533; C. P. Yuan and T.-C. Yuan, Phys. Rev. D44 (1991) 3603.

[269] D. Garcia, W. Hollik, R.A. Jiménez and J. Solà, Nucl. Phys. B427 (1994) 53; A. Dabelstein, W. Hollik, C. Jünger, R.A. Jiménez and J. Solà, Nucl. Phys. B454 (1995) 75.

[270] B. Grządkowski and W. Hollik, Nucl. Phys. B384 (1992) 101; A. Denner and A.H. Hoang, Nucl. Phys. B397 (1993) 483.

[271] A. Czarnecki and S. Davidson, Phys. Rev. D47 (1993) 3063; *ibid.* Phys. Rev. D48 (1993) 4183.

[272] J.-M. Yang and C.-S. Li, Phys. Lett. B320 (1994) 117; J. Guasch, R. A. Jiménez and J. Solà, Phys. Lett. B360 (1995) 47; J. A. Coarasa, D. Garcia, J. Guasch, R. A. Jiménez and J. Solà, Eur. Phys. J. C2 (1998) 373; J. A. Coarasa, J. Guasch, J. Solà and W. Hollik, Phys. Lett. B442 (1998) 326.

[273] For a review on top quark production and decay in the MSSM, see: J. Guasch, W. Hollik, J.I. Illana, C. Schappacher and J. Solà, hep-ph/0003109.

[274] J. Ellis and S. Rudaz, Phys. Lett. B128 (1983) 248; H. Baer and X. Tata, Phys. Lett. B167 (1986) 241; H. Baer, M. Drees, R. Godbole, J. Gunion and X. Tata, Phys. Rev. D44 (1991) 725; K. Hidaka, Y. Kizukuri and T. Kon, Phys. Lett. B278 (1992) 155; A. Djouadi, W. Hollik and C. Junger, Phys. Rev. D54 (1996) 5629; C.S. Li, R.J. Oakes and J.M. Yang, Phys. Rev. D54 (1996) 6883; Y.S. Yang, C.S. Li, Q.H. Cao and H.X. Liu, Commun. Theor. Phys. 33 (2000) 21.

[275] H. Baer, J. Ellis, G. Gelmini, D.V. Nanopoulos and X. Tata, Phys. Lett B161 (1985) 175; G. Gamberini, Z. Phys. C30 (1986) 605; H.A. Baer, V. Barger, D. Karatas and X. Tata, Phys. Rev. D36 (1987) 96; R.M. Barnett, J.F. Gunion amd H.A. Haber, Phys. Rev. D37 (1988) 1892; A. Bartl, W. Majerotto and N. Oshimo, Phys. Lett. B216 (1989) 233.

[276] A. Bartl, H. Fraas and W. Majerotto, Nucl. Phys. B278 (1986) 1.

[277] J.F. Gunion and H.E. Haber, Phys. Rev. D37 (1988) 2515.

[278] A.K. Datta, A. Djouadi, Y. Mambrini and M. Guchait, Phys. Rev. D65 (2002) 015007.

[279] A. Bartl, W. Majerotto and W. Porod, Z. Phys. C64 (1994) 499; A. Bartl, H. Eberl, K. Hidaka, T. Kon, W. Majerotto and Y. Yamada, Phys. Lett. B389 (1996) 538.

[280] A. Bartl, H. Eberl, K. Hidaka, S. Kraml, T. Kon, W. Majerotto and Y. Yamada, Phys. Lett. B435 (1998) 118.

[281] S. Kraml, H. Eberl, A. Bartl, W. Majerotto and W. Porod, Phys. Lett. B386 (1996) 175; A. Djouadi, W. Hollik and C. Junger, Phys. Rev. D55 (1997) 6975.

[282] W. Beenakker, R. Hopker and P.M. Zerwas, Phys. Lett. B378 (1996) 159; W. Beenakker, R. Hopker, T. Plehn and P.M. Zerwas, Z. Phys. C75 (1997) 349.

[283] A. Djouadi, Y. Mambrini and M. Muhlleitner, in preparation.

[284] For recent discussions on gravitino DM, see for instance: W. Buchmuller, K. Hamaguchi and M. Ratz, Phys. Lett. B574 (2003) 156; J. Ellis, K. Olive, Y. Santoso and V. Spanos, Phys. Lett. B588 (2004) 7; J.L. Feng, S. Su and F. Takayama, hep-ph/0404231 and hep-ph/0404198; L. Roszkowski and R. Ruiz de Austri, hep-ph/0408227.

[285] For recent discussions on axino DM, see for instance, L. Covi, L. Roszkowski, R. Ruiz de Austri and M. Small, JHEP 0406 (2004) 003.

[286] For recent analyses, see: H. Baer, C. Balazs, A. Belyaev, J.K. Mizukoshi, X. Tata and Y. Wang, JHEP 0207 (2002) 050; H. Baer and C. Balazs, JCAP 0305 (2003) 006; U. Chattopadhyay, A. Corsetti and P. Nath, Phys. Rev. D68 (2003) 035005; J. Ellis, K. Olive, Y. Santoso and V.C. Spanos, Phys. Lett. B565 (2003) 176; M. Battaglia, A. De Roeck, J.R. Ellis, F. Gianotti, K.A. Olive and L. Pape, Eur. Phys. J. C33 (2004) 273 (2004); R. Arnowitt, B. Dutta and B. Hu, hep-ph/0310103; J.R. Ellis, K.A. Olive, Y. Santoso and V.C. Spanos, Phys. Rev. D69 (2004) 095004; M.E. Gomez, T. Ibrahim, P. Nath and S. Skadhauge, Phys. Rev. D70 (2004) 035014; J. Ellis, S. Heinemeyer, K.A. Olive and G. Weiglein, hep-ph/0411216.

[287] A. Djouadi, M. Drees and J.L. Kneur, JHEP 0108 (2001) 055.

[288] B.C. Allanach, G. Bélanger, F. Boudjema and A. Pukhov, JHEP 0412 (2004) 020.

[289] For recent analyses in non–univesal mSGRA models, see: J.R. Ellis, T. Falk, K.A. Olive and Y. Santoso, Nucl. Phys. B652 (2003) 259 and hep-ph/0405110; J.R. Ellis, K.A. Olive, Y. Santoso and V.C. Spanos, Phys. Lett. B573 (2003) 162; *ibid.* Phys. Rev. D70 (2004) 055005; D. Auto, H. Baer, A. Belyaev and T. Krupovnickas, JHEP 0410 (2004) 066; H. Baer, A. Belyaev, T. Krupovnickas and A. Mustafayev, JHEP 0406 (2004) 044; G. Bélanger, F. Boudjema, A. Cottrant, A. Pukhov and A. Semenov, Nucl. Phys. B706 (2005) 411.

[290] V. Bertin, E. Nezri and J. Orloff, JHEP 0302 (2003) 046.

[291] For a review, see eg. M. Quiros, Nucl. Phys. Proc. Suppl. 101 (2001) 401.

[292] K. Griest and D. Seckel, Phys. Rev. D43 (1991) 3191.

[293] M. Drees and M.M. Nojiri, Phys. Rev. D47 (1993) 376.

[294] T. Nihei, L. Roszkowski and R. Ruiz de Austri, JHEP 0105 (2001) 063.

[295] J.L. Lopez, D.V. Nanopoulos and K. Yuan, Phys. Rev. D48 (1993) 2766; P. Nath and R. Arnowitt, Phys. Rev. Lett. 70 (1993) 3696; M. Drees and A. Yamada, Phys. Rev. D53 (1996) 1586; L. Roszkowski, R. Ruiz de Austri and T. Nihei, JHEP 0108 (2001) 59; A.B. Lahanas and V.C. Spanos, Eur. Phys. J. C23 (2002) 185.

[296] S. Mizuta and M. Yamaguchi, Phys. Lett. B298 (1993) 120; J. Edsjö and P. Gondolo, Phys. Rev. D56 (1997) 1879.

[297] J.R. Ellis, T. Falk and K.A. Olive, Phys. Lett. B444 (1998) 367; M.E. Gomez, G. Lazarides and C. Pallis, Phys. Rev. D61 (2000) 123512; J.R. Ellis, T. Falk, K.A. Olive and M. Srednicki, Astropart. Phys. 13 (2000) 181 and (E) *ibid.* 15 (2001) 413.

[298] C. Boehm, A. Djouadi and M. Drees, Phys. Rev. D62 (2000) 035012.

[299] R. Arnowitt, B. Dutta and Y. Santoso, Nucl. Phys. B606 (2001) 59; J.R. Ellis, K.A. Olive and Y. Santoso, Astropart. Phys. 18 (2003) 395.

[300] A. Djouadi and M. Drees, Phys. Lett. B484 (2000) 183.

[301] M. Drees, G. Jungman, M. Kamionkowski and M. Nojiri, Phys. Rev. D49 (1994) 636.

[302] G. Gounaris, J. Layssac, P.I. Porfyriadis and F.M. Renard, Phys. Rev. D69 (2004) 075007.

[303] G. Bélanger *et al.*, Comp. Phys. Commun. 149 (2002) 103.

[304] J.A. Bagger, J.L. Feng and N. Polonsky, Nucl. Phys. B563 (1999) 3; J.A. Bagger, J.L. Feng, N. Polonsky and R.J. Zhang, Phys. Lett. B473 (2000) 264; J.L. Feng, K.T. Matchev and T. Moroi, Phys. Rev. D61 (2000) 075005.

[305] J. Silk, K. Olive and M. Srednicki, Phys. Rev. Lett. 55 (1985) 257.

[306] M.W. Goodman and E. Witten, Phys. Rev. D31 (1985) 3059.

[307] G.F. Giudice and E. Roulet, Nucl. Phys. B316 (1989) 429; M. Kamionkowski, Phys. Rev. D44 (1991) 3021.

[308] K. Griest, Phys. Rev. Lett. 61 (1988) 666; *ibid* Phys. Rev. D38 (1988) 2357; M. Srednicki and R. Watkins, Phys. Lett. B225 (1989) 140.

[309] M. Drees and M.M. Nojiri, Phys. Rev. D48 (1993) 3483.

[310] M.A. Shifman, A.I. Vainshtein and V.I. Zakharov, Phys. Lett. 78B (1978) 443.

[311] G. Jungman and M. Kamionkowski, Phys. Rev. D51 (1995) 3121; L. Bergstrom and P. Ullio, Nucl. Phys. B504 (1997) 27; Z. Bern, P. Gondolo and M. Perelstein, Phys. Lett. B411 (1997) 86; J. Hisano, S. Matsumoto and M. Nojiri, Phys. Rev. D67 (2003) 075014.

[312] P. Ullio and L. Bergstrom, Phys. Rev. D57 (1998) 1962.

[313] J.F. Gunion, H. Haber, F. Paige, W.K. Tung and S. Willenbrock, Nucl. Phys. B294 (1987) 621.

[314] H. Baer, M. Bisset, C. Kao and X. Tata, Phys. Rev. D46 (1992) 1067.

[315] J. Gunion and L. Orr, Phys. Rev. D46 (1992) 2052.

[316] S.L. Glashow, D. Nanopoulos and A. Yildiz, Phys. Rev. D18 (1978) 1724; J. Finjord, G. Girardi and P. Sorba, Phys. Lett. B89 (1979) 99.

[317] R.N. Cahn and S. Dawson, Phys. Lett. 136B (1984) 196 and (E) *ibid.* B138 (1984) 464; D. Dicus and S. Willenbrock, Phys. Rev. D32 (1985) 1642; G. Altarelli, B. Mele and F. Pitolli, Nucl. Phys. B287 (1987) 205.

[318] R. Raitio and W.W. Wada, Phys. Rev. D19 (1979) 941; J. Ng and P. Zakarauskas, Phys. Rev. D29 (1984) 876; Z. Kunszt, Nucl. Phys. B247 (1984) 339; A.S. Bagdasaryan *et al.*, Sov. J. Nucl. Phys. 46 (1987) 315.

[319] The NLO Fortran codes for $HV, Hqq, gg \rightarrow H$ and Higgs pair production and the LO Fortran code for $Q\bar{Q}H$ production, have been written by M. Spira and can be found at `http://people.web.psi.ch/spira/`. See also M. Spira, hep-ph/9510347 for the users manual of the program `HIGLU`. Illustrations for cross sections are given in Refs. [320–322].

[320] M. Spira, Fortschr. Phys. 46 (1998) 203.

[321] M. Spira, hep-ph/9711394 and hep-ph/9810289.

[322] A. Djouadi, Pramana 60 (2003) 215 [hep-ph/0205248], Pramana 62 (2004) 191 [hep-ph/0303097] and plenary talk given at the conference "Physics at the LHC", hep-ph/0412238.

[323] The code for charged Higgs production at hadron colliders has been written by J.L. Kneur; based on Ref. [324].

[324] F. Borzumati, J.L. Kneur and N. Polonsky, Phys. Rev. D60 (1999) 115011.

[325] M. Carena J. Conway, H. Haber and J. Hobbs (conv.) *et al.*, Report of the Higgs Working Group for "RUN II at the Tevatron", hep-ph/0010338.

[326] ATLAS Collaboration, *Technical Proposal*, CERN/LHCC/94-43.

[327] ATLAS Collaboration, *Detector and Physics Performance Technical Design Report*, Vols. 1 and 2, CERN–LHCC–99–14 and CERN–LHCC–99–15.

[328] CMS Collaboration, *Technical Proposal*, CERN–LHCC–94–38.

[329] CMS Collaboration, *ECAL Project Technical Design Report*, CERN/LHCC/97-33 and *The compact muon solenoid: the muon Technical Design Report*, CERN/LHCC/97-32.

[330] E. Richter–Was *et al.*, Int. J. Mod. Phys. A13 (1998) 1371 and ATLAS Note PHYS–No–074.

[331] D. Denegri *et al.*, *Summary of the CMS discovery potential for the MSSM SUSY Higgses*, hep-ph/0112045;

[332] S. Abdullin *et al.*, *Summary of the CMS potential for the Higgs boson discovery*, CMS–Note 2003/033.

[333] G. Branson *et al.* (CMS and ATLAS Collaborations), Eur. Phys. J. direct C4 (2002) N1.

[334] For a recent discussion of the physics capabilities of the ATLAS and CMS experiments, see the review talks given by P. Sphicas, at the conference "Physics at LHC" in Vienna, 13–17 July 2004, and by D. Froidevaux, at the final meeting of the European Network "Physics at Colliders", Montpellier, 26–27 September 2004.

[335] After completing this work, we received the paper, *Higgs bosons searches at hadron colliders* by V. Büsher and K. Jakobs (to appear in Mod. Phys. Lett. A), where the recent experimental analyses of the various channels for Higgs detection at the Tevatron and the LHC have been reviewed and where complementary material can be found. We thank Karl Jakobs for pointing this review to us.

[336] A. Djouadi, R. Kinnunen, E. Richter-Was, H.U. Martyn (conv.) *et al.*, Report of the Higgs Working Group, Proceedings of the Les Houches Workshop on "Physics at TeV Colliders", 1999, hep-ph/0002258.

[337] D. Cavalli, A. Djouadi, K. Jakobs, A. Nikitenko, M. Spira, C.E.M. Wagner, W.-M. Yao (conv.) *et al.*, Report of the Higgs Working Group, Proceedings of the Les Houches Workshop on "Physics at TeV Colliders", 2001, hep-ph/0203056.

[338] K.A. Assamagan, M. Narain, A. Nikitenko, M. Spira, D. Zeppenfeld (conv.) *et al.*, Report of the Higgs Working Group, Proceedings of the Les Houches Workshop on "Physics at TeV Colliders", 2003, hep-ph/0406152.

[339] M.L. Ciccolini, S. Dittmaier and M. Krämer, Phys. Rev. D68 (2003) 073003; O. Brein *et al.*, hep-ph/0402003 and in Ref. [338].

[340] T. Han and S. Willenbrock, Phys. Lett. B273 (1990) 167.

[341] T. Han, G. Valencia and S. Willenbrock, Phys. Rev. Lett. 69 (1992) 3274; T. Figy, C. Oleari and D. Zeppenfeld, Phys. Rev. D68 (2003) 073005; E. L. Berger and J. Campbell, Phys. Rev. D70 (2004) 073011.

[342] O. Brein, A. Djouadi and R. Harlander, Phys. Lett. B579 (2004) 149.

[343] A. Djouadi and M. Spira, Phys. Rev. D62 (2000) 014004.

[344] H.L. Lai, J. Huston, S. Kuhlmann, F. Olness, J. Owens, D. Soper, W.K. Tung and H. Weerts (CTEQ Collaboration), Phys. Rev. D55 (1997) 1280.

[345] C. Kao, Phys. Rev. D46 (1992) 4907; C. Kao, G. Lovelace and L.H. Orr, Phys. Lett. B567 (2003) 259.

[346] J. Yin, W.G. Ma, R.Y. Zhang and H.S. Hou, Phys. Rev. D66 (2002) 095008 and hep-ph/0209279.

[347] Q. Li, C.S. Li, J.J. Liu, L.G. Jin and C.P. Yuan, hep-ph/0501070.

[348] C. Kao and S. Sachithanandam, hep-ph/0411331.

[349] A.D. Martin, R.G. Roberts, W.J. Stirling and R.S. Thorne (MRST Collaboration), Eur. Phys. J. C28 (2003) 455,

[350] M. Spira, A. Djouadi, D. Graudenz and P.M. Zerwas, Phys. Lett. B318 (1993) 347.

[351] A. Djouadi, M. Spira and P.M. Zerwas, Phys. Lett. B264 (1991) 440; S. Dawson, Nucl. Phys. B359 (1991) 283.

[352] S. Dawson and R.P. Kauffman, Phys. Rev. D49 (1994) 2298.

[353] R. Harlander and W. Kilgore, Phys. Rev. Lett. 88 (2002) 201801; C. Anastasiou and K. Melnikov, Nucl. Phys. B646 (2002) 220; V. Ravindran, J. Smith and W. L. van Neerven, Nucl. Phys. B665 (2003) 325; S. Catani, D. de Florian, M. Grazzini and P. Nason, JHEP 0307 (2003) 028.

[354] R.V. Harlander and W.B. Kilgore, JHEP 0210 (2002) 017.

[355] C. Anastasiou and K. Melnikov, Phys. Rev. D67 (2003) 037501.

[356] R.K. Ellis, I. Hinchliffe, M. Soldate and J.J. van der Bij, Nucl. Phys. B297 (1988) 221; I. Hinchliffe and S.F. Novaes, Phys. Rev. D38 (1988) 3475; U. Baur and E. W. Glover, Nucl. Phys. B339 (1990) 38; S. Abdullin, M. Dubinin, V. Ilyin, D. Kovalenko, V. Savrin and N. Stepanov, Phys. Lett. B431 (1998) 410.

[357] O. Brein and W. Hollik, Phys. Rev. D68 (2003) 095006.

[358] B. Field, J. Smith, M.E. Tejeda-Yeomans and W.L. van Neerven, Phys. Lett. B551 (2003) 137; B. Field, S. Dawson and J. Smith, Phys. Rev. D69 (2004) 074013; B. Field, Phys. Rev. D70 (2004) 054008.

[359] G.J. Gounaris, J. Layssac and F.M. Renard, Phys. Rev. D58 (1998) 075006.

[360] D.A. Dicus and S. Willenbrock, Phys. Rev. D39 (1989) 751.

[361] L. Reina and S. Dawson, Phys. Rev. Lett. 87 (2001) 201804; W. Beenakker, S. Dittmaier, M. Krämer, B. Plümper, M. Spira and P.M. Zerwas, Phys. Rev. Lett. 87 (2001) 201805; *ibid.* Nucl. Phys. B653 (2003) 151; S. Dawson, L.H. Orr, L. Reina and D. Wackeroth, Phys. Rev. D67 (2003) 071503; S. Dawson, C. Jackson, L.H. Orr, L. Reina and D. Wackeroth, Phys. Rev. D68 (2003) 034022.

[362] S. Dittmaier, M. Krämer and M. Spira, Phys. Rev. D70 (2004) 074010; S. Dawson, C. Jackson, L. Reina and D. Wackeroth, Phys. Rev. D69 (2004) 074027.

[363] R.M. Barnett, H.E. Haber and D.E. Soper, Nucl. Phys. B306 (1988) 697; F.I. Olness and W.-K. Tung, Nucl. Phys. B308 (1988) 813.

[364] D. Dicus, T. Stelzer, Z. Sullivan and S. Willenbrock, Phys. Rev. D59 (1999) 094016; C. Balazs, H.–J. He and C.P. Yuan, Phys. Rev. D60 (1999) 114001; E. Boos and T. Plehn, Phys. Rev. D69 (2004) 094005.

[365] T. Plehn, Phys. Rev. D67 (2003) 014018.

[366] R. Harlander and W. Kilgore, Phys. Rev. D68 (2003) 013001.

[367] J. Campbell, S. Dawson, S. Dittmaier, C. Jackson, M. Krämer, F. Maltoni, L. Reina, M. Spira, D. Wackeroth and S. Willenbrock, in Ref. [338].

[368] J. Campbell, R. K. Ellis, F. Maltoni and S. Willenbrock, Phys. Rev. D67 (2003) 095002; F. Maltoni, Z. Sullivan and S. Willenbrock, Phys. Rev. D67 (2003) 093005; J.J. Cao, G.P. Gao, R.J. Oakes and J.M. Yang, Phys. Rev. D68 (2003) 075012.

[369] E.N. Glover and J. van der Bij, Nucl. Phys. B309 (1988) 282; D.A. Dicus, C. Kao and S. Willenbrock, Phys. Lett. B203 (1988) 457; G. Jikia, Nucl. Phys. B412 (1994) 57.

[370] T. Plehn, M. Spira and P. Zerwas, Nucl. Phys. B479 (1996) 46.

[371] A. Belyaev, M. Drees, O.J.P. Eboli, J.K. Mizukoshi and S.F. Novaes, Phys. Rev. D60 (1999) 075008; A. Belyaev, M. Drees and J. Mizukoshi, Eur. Phys. J. C17 (2000) 337.

[372] G. Cynolter, E. Lendvai and G. Pocsik, Acta Phys. Polon. B31 (2000) 1749; A.A. Barrientos-Bendezu and B. Kniehl, Phys. Rev. D64 (2001) 035006; M. Moretti, M. Moretti, F. Piccinini, R. Pitau and A. Polosa, hep-ph/0410334; U. Baur, T. Plehn and D. L. Rainwater, Phys. Rev. D69 (2004) 053004.

[373] W. Y. Keung, Mod. Phys. Lett. A2 (1987) 765; O. Eboli, G. Marques, S. Novaes and A. Natale, Phys. Lett. B197 (1987) 269; D. Dicus, K. Kallianpur and S. Willenbrock, Phys. Lett. B200 (1988) 187; K. Kallianpur, Phys. Lett. B215 (1988) 392; A. Abbasabadi, W. Repko, D. Dicus and R. Vega, Phys. Rev. D38 (1988) 2770; V. Barger, T. Han and R. Phillips, Phys. Rev. D38 (1988) 2766; V. Barger and T. Han, Mod. Phys. Lett. A5 (1990) 667; A. Dobrovolskaya and V. Novikov, Z. Phys. C52 (1991) 427.

[374] A. Djouadi, W. Kilian, M. Muhlleitner and P.M. Zerwas, Eur. Phys. J. C10 (1999) 45.

[375] S. Dawson, S. Dittmaier and M. Spira, Phys. Rev. D58 (1998) 115012.

[376] L.G Jin, C.S. Li, Q. Li, J.J. Liu and R.J. Oakes, hep-ph/0501279.

[377] S. Moretti et al., in preparation.

[378] E. Boos et al., in preparation.

[379] R. Lafaye in Ref. [338].

[380] A. Bialas and P.V. Landshoff, Phys. Lett. B256 (1991) 540; M. Boonekamp, R. Peschanksi and C. Royon, Phys. Rev. Lett. 87 (2001) 251806; *ibid.* Nucl. Phys. B669 (2003) 277; B.E. Cox, J.R. Forshaw and B. Heinemann, Phys. Lett. B540 (2002) 263; R. Enberg, G. Ingelman, A. Kissavos and N. Timneanu, Phys. Rev. Lett. 89 (2002) 081801; J.-R. Cudell and O.F. Hernandez, Nucl. Phys. B471 (1996) 471; E.M. Levin, hep-ph/9912402.

[381] V.A. Khoze, A.D. Martin and M.G. Ryskin, Eur. Phys. J. C23 (2002) 311; *ibid.* Eur. Phys. J. C26 (2002) 229; A. De Roeck *et al.*, Eur. Phys. J. C25 (2002) 391; A.B. Kaidalov, V.A. Khoze, A.D. Martin and M.G. Ryskin, Eur. Phys. J. C31 (2003) 387; *ibid.* Eur. Phys. J. C33 (2004) 261.

[382] V.A. Khoze, A.D. Martin and M.G. Ryskin, Eur. Phys. J C23 (2002) 311; *ibid.* Eur. Phys. J. C34 (2004) 327; B.E. Cow *et al.*, Phys. Rev. D68 (2003) 075004.

[383] V.A. Khoze, A.D. Martin and M.G. Ryskin, Eur. Phys. J. C34 (2004) 327.

[384] M. Boonekamp, R. Peschanksi and C. Royon, Phys. Lett. B599 (2004) 236.

[385] J.R. Ellis, J.S. Lee and A. Pilaftsis, hep-ph/0502251.

[386] A. Djouadi, W. Kilian and T. Plehn, in preparation.

[387] J. L. Diaz-Cruz and O. A. Sampayo, Phys. Lett. B276 (1992) 211; W. J. Stirling and D. J. Summers, Phys. Lett. B283 (1992) 411; A. Ballestrero and E. Maina, Phys. Lett. B299 (1993) 312; G. Bordes and B. van Eijk, Phys. Lett. B299 (1993) 315.

[388] F. Maltoni, K. Paul, T. Stelzer and S. Willenbrock, Phys. Rev. D64 (2001) 094023.

[389] S.L. Glashow and E.E. Jenkins, Phys. Lett. B196 (1987) 233; V. Barger and R.J.N. Phillips, Phys. Lett. B201 (1988) 553; *ibid.* Phys. Rev. D40 (1989) 2875; *ibid.* Phys. Rev. D41 (1990) 884.

[390] For a review of the top quark properties see, for instance, M. Beneke, I. Efthymiopoulos, M.L. Mangano and J. Womersley (conv.) *et al.*, *Top Quark Physics* in the Report of the "1999 CERN Workshop on SM Physics at the LHC", Report CERN-TH/2000-100, hep-ph/0003033.

[391] S. Dawson, P. Nason and R.K. Ellis, Nucl. Phys. B303 (1988) 607; *ibid.* Nucl. Phys. B327 (1989) 49; W. Beennakker, H. Kuijf, W. van Neerven and J. Smith, Phys. Rev. D40 (1989) 54. For later developments, see the review of S. Frixione, M. Mangano, P. Nason and G. Ridolfi, hep-ph/9702287.

[392] M. Guchait and S. Moretti, JHEP 0201 (2002) 001; J. Alwall, C. Biscarat, S. Moretti, J. Rathsman and A. Sopczak, Eur. Phys. J. direct C1 (2004) 005.

[393] J.L. Diaz-Cruz and O.A. Sampayo, Phys. Rev. D50 (1994) 6820.

[394] A.C. Bawa, C.S. Kim and A.D. Martin, Z. Phys. C47 (1990) 75; M. Drees and D.P. Roy in Ref. [206]; B.K. Bullock, K. Hagiwara and A.D. Martin, Phys. Rev. Lett. 67 (1991) 3055; D.P. Roy, Phys. Lett. B283 (1992) 403; V. Barger, R. Phillips and D.P. Roy, Phys. Lett. B324 (1994) 236; S. Moretti and K. Odagiri, Phys. Rev. D55 (1997) 5627; J. Gunion, Phys. Lett. B322 (1994) 125; S. Raychaudhuri and D.P. Roy, Phys. Rev. D52 (1995) 1556; *ibid.* Phys. Rev. D53 (1996) 4902; D.P. Roy, Phys. Lett. B459 (1999) 607; S. Moretti and D.P. Roy, Phys. Lett. B470 (1999) 209; A. Belyaev, D. Garcia, J. Guasch and J. Sola, JHEP 0206 (2002) 059; *ibid.* Phys. Rev. D65 (2002) 031701.

[395] D. Miller, S. Moretti, D.P. Roy and W. Stirling, Phys. Rev. D61 (2000) 055011.

[396] J.H. He and C.P. Yuan, Phys. Rev. lett. 83 (1999) 28; T. Tait and C.P. Yuan, Phys. Rev. D63 (2001) 014018; J.L. Diaz–Cruz, J.H. He and C.P. Yuan, Phys. Lett. B530 (2002) 179.

[397] M.V. Foursa, D.A. Murashov and R. Slabospitsky, Phys. Atom. Nucl. 67 (2004) 350.

[398] S. Slabospitsky, CMS NOTE–2002/10 and hep-ph/020394.

[399] E. Eichten, I. Hinchliffe, K. Lane and C. Quigg, Rev. Mod. Phys. 56 (1984) 579.

[400] Q.H. Cao, S. Kanemura and C.P. Yuan, Phys. Rev. D69 (2004) 075008.

[401] S.S.D. Willenbrock, Phys. Rev. D35 (1987) 173.

[402] Y. Jiang, W.-G. Ma, L. Han, M. Han and Z.-H. Yu, J. Phys. G23 (1997) 385; *ibid.* J. Phys. G24 (1998) 83; A. Krause, T. Plehn, M. Spira and P.M. Zerwas, Nucl. Phys. B519 (1998) 85; O. Brein and W. Hollik, Eur. Phys. J. C13 (2000) 175; Y.S. Yang *et al.*, Phys. Rev. D62 (2000) 095012; F. Zhou, Phys. Rev. D62 (2001) 015002.

[403] A.A. Barrientos Bendezú and B.A. Kniehl, Nucl. Phys. B568 (2000) 305; H.S. Hou, W.G. Ma, R.Y. Zhang, Y. Jiang, L. Han and L.R. Xing, hep-ph/0502214.

[404] S. Moretti, J. Phys. G28 (2002) 2567.

[405] D.A. Dicus, J.L. Hewett, C. Kao and T.G. Rizzo, Phys. Rev. D40 (1989) 787; S. Moretti and K. Odagiri, Phys. Rev. D59 (1999) 055008; A.A. Barrientos Bendezú and B.A. Kniehl, Phys. Rev. D61 (2000) 097701 and D63 (2001) 015009; O. Brein, W. Hollik and S. Kanemura, Phys. Rev. D63 (2001) 095001.

[406] A.A. Barrientos Bendezú and B.A. Kniehl, Phys. Rev. D59 (1999) 015009.

[407] J. Alwall and J. Rathsman, JHEP 0412 (2004) 050; J. Alwall, hep-ph/0503124.

[408] S. Zhou, Phys. Rev. D67 (2003) 075006; E. Berger, T. Han, J. Jiang and T. Plehn, hep-ph/0312286; N. Kidonakis in Ref. [338].

[409] W. Hollik and S. Zhu, Phys. Rev. D65 (2002) 075015.

[410] For a review, see S. Moretti, Pramana 60 (2003) 369 and hep-ph/0205104.

[411] J. Gunion, P. Kalyniak, M. Soldate and P. Galison, Phys. Rev. D34 (1986) 101.

[412] A. Stange, W.J. Marciano and S. Willenbrock, Phys. Rev. D49 (1994) 1354; *ibid.* Phys. Rev. D50 (1994) 4491; J. Gunion and T. Han, Phys. Rev. D51 (1995) 1051; S. Mrenna and G. L. Kane, hep-ph/9406337.

[413] R. Kinnunen, S. Lehti, A. Nikitenko and P. Salmi, J. Phys. G. 31 (2005) 71.

[414] R. Kleiss, Z. Kunszt and W.J. Stirling, Phys. Lett. B253 (1991) 269; W.J. Marciano and F.E. Paige, Phys. Rev. Lett. 66 (1991) 2433; J.F. Gunion, Phys. Lett. B261 (1991) 510.

[415] J. Dai, J.F. Gunion and R. Vega, Phys. Rev. Lett. 71 (1993) 2699.

[416] D. Froidevaux and E. Richter-Was, Z. Phys. C67 (1995) 213.

[417] D. Rainwater and D. Zeppenfeld, JHEP 9712 (1997) 005.

[418] D. Rainwater, D. Zeppenfeld and K. Hagiwara, Phys. Rev. D59 (1999) 014037; T. Plehn, D. Rainwater and D. Zeppenfeld, Phys. Rev. D61 (2000) 093005; *ibid.* Phy. Lett. B454 (1999) 297.

[419] J. Dai, J. F. Gunion and R. Vega, Phys. Lett. B315 (1993) 355; *ibid.* Phys. Lett. B345 (1995) 29; *ibid.* Phys. Lett. B387 (1996) 801; J. Gunion, L. Poggioli, R. V. Kooten, C. Kao, and P. Rowson, hep-ph/9703330; J.L. Diaz-Cruz, H. He, T. Tait and C.P. Yuan, Phys. Rev. Lett. 80 (1998) 4641; D. Choudhury, A. Datta and S. Raychaudhuri, hep-ph/9809552.

[420] H.S. Hou *et al.*, JHEP 0309 (2003) 074; *ibid.* Phys. Rev. D68 (2003) 035016; J.J. Cao, G. Gao, R. Oakes and J.M. Yang, Phys. Rev. D68 (2003) 075012; G. Gao, R. Oakes and J.M. Yang, hep-ph/0412356.

[421] M. Rocco, A. Belyaev and J. Valls in Ref. [325].

[422] E. Richter–Was and D. Froidevaux, Z. Phys. C76 (1997) 665.

[423] R. Kinnunen, J. Tuominiemi, and D. Denegri, CMS-TN/93-98 (1993) and CMS-TN/93-103; C. Seez, CMS-TN/93-84; D. Cavalli *et al.*, ATLAS Note PHYS-NO-025 (1993); R. Kinnunen and A. Nikitenko, CMS NOTE 1997/106; D. Cavalli and S. Resconi, ATL-PHYS-2000-005; S. Lehti, Dissertation, University of Helsinki, Report Series in Physics, HU-P-D93 (2001) and CMS NOTE 2002/035; D. Cavalli and G. Negri, ATL–PHYS–2003–009; S. Thomas, ATL–PHYS–2003–003; R. Kinnunen and A. Nikiteno, CMS NOTE–2003/006. A. Nikiteno *et al.*, CMS NOTE–2004/027.

[424] C. Kao and N. Stepanov, Phys. Rev. D52 (1995) 5025.

[425] L. Bellucci, Dissertation, Universita degli studi di Firenze (2001); S. Gonzales, E. Ros and M. Vos, ATL–PHYS–2002–024; S. Gentile, M. Paniccia and P. Violini, ATL–PHYS–2003–013.

[426] D. Chakraborty in Ref. [325].

[427] D. Cavalli *et al.*, ATLAS internal note PHYS-NO-053 (1994); R. Kinnunen, D. Denegri and J. Tuominiemi, CMS-TN/94-233 (1994); S. Banerjee and M. Maity, CMS Note–2000/039.

[428] C. Biscara and M. Dosil, ATL–PHYS–2003–038.

[429] R. Kinnunen, CMS NOTE 2000/045; K. A. Assamagan, Y. Coadou and A. Deandrea, Eur. Phys. J. direct C 4 (2002) 9; K. A. Assamagan and Y. Coadou, Acta. Phys. Polon. B33 (2002) 1347.

[430] R. Decker, S. Jadach, M. Jezabek, J.H. Kühn and Z. Was, Comp. Phys. Comm. 76 (1993) 361; *ibid.* Comp. Phys. Comm. 70 (1992) 69; *ibid.* Comp. Phys. Comm. 64 (1991) 275.

[431] P. Salmi, R. Kinunnen and N. Stepanov, CMS–NOTE–2000/045; K.A. Assamagan and M. Gollub, Note SN–ATLAS–2004-042 and hep-ph/0406013; K.A. Assamagan *et al.* in Ref. [338]; S. Penaranda, talk given at the conference "Physics at the LHC", Vienna, July 2004.

[432] S. Lowette, J. Heinninck and P. Vanlaer, CMS NOTE–2004/017; S. Lowette, poster given at the conference "Physics at the LHC", Vienna, July 2004.

[433] R. Lafaye, D.J. Miller, M. Muhlleitner and S. Moretti, hep-ph/0002238 and in Ref. [337].

[434] E. Richter-Was, D. Froidevaux and L. Poggioli, `ATLFAST2.0`: a fast simulation package for ATLAS, ATLAS Note ATL-PHYS-98-131.

[435] J. Gunion, H Haber and C. Kao, Phys. Rev. D46 (1992) 2907; H. Baer, C. Kao and X. Tata, Phys. Lett. B303 (1993) 284; S. Abdullin, H. Baer, C. Kao, N. Stepanov and X. Tata, Phys. Rev. D54 (1996) 6728; D. Kominis, Nucl. Phys. B427 (1994) 575.

[436] K. Gaemers and F. Hoogeveen, Phys. Lett. 146B (1984) 347; D. Dicus, A. Stange and S. Willenbrock, Phys. Lett. B333 (1994) 126.

[437] K.A. Assamagan, Acta Phys. Polon. B31 (2000) 881.

[438] C. Kao and N. Stepanov, Phys. Rev. D52 (1995) 5025; V. Barger and C. Kao, Phys. Lett. B424 (1998) 69; T. Han and B. McElrath, Phys. Lett. B528 (2002) 81; S. Dawson, D. Dicus and C. Kao, Phys. Lett. B545 (2002) 132.

[439] A. Pukhov *et al.*, `CompHEP`, hep-ph/9908288.

[440] D. Zeppenfeld, R. Kinnunen, A. Nikitenko and E. Richter-Was, Phys. Rev. D62 (2000) 013009 and in Ref. [336].

[441] M. Dührssen, S. Heinemeyer, H. Logan, D. Rainwater, G. Weiglein and D. Zeppenfeld in Ref. [338]; M. Dührssen, ATLAS Note PHYS-2003-030.

[442] R. Kinnunen, S. Lehti, F. Moortgat, A. Nikitenko and M. Spira in Ref. [338].

[443] See e.g., F. Gianotti and M. Pepe–Altarelli, Nucl. Phys. Proc. Suppl. 89 (2000) 177.

[444] See e.g., A. Djouadi and S. Ferrag, Phys. Lett. B586 (2004) 345.

[445] A. Djouadi, J.L. Kneur and G. Moultaka, Phys. Rev. Lett. 80 (1998) 1830.

[446] A. Djouadi, J.L. Kneur and G. Moultaka, Nucl. Phys. B569 (2000) 53.

[447] G. Bélanger, F. Boudjema and K. Sirdhar, Nucl. Phys. B568 (2000) 3; G. Bélanger *et al.*, in Ref. [336].

[448] A. Dedes and S. Moretti, Phys. Rev. D60 (1999) 015007; *ibid.* Eur. Phys. J. C10 (1999) 515.

[449] For a summary of higher order stop decays, see for instance: C. Boehm, A. Djouadi and Y. Mambrini, Phys. Rev. D61 (2000) 095006; A. Djouadi and Y. Mambrini, Phys. Rev. D63 (2001) 115005; M. Muhlleitner, A. Djouadi and Y. Mambrini, hep-ph/0311167.

[450] S. G. Frederiksen, N. Johnson, G. Kane and J. Reid, Phys. Rev. D50 (1994) 4244; S.P. Martin and J. D. Wells, Phys. Rev. D60 (1999) 035006.

[451] D. Choudhury and D.P. Roy, Phys. Lett. B322 (1994) 368; R.M. Godbole, M. Guchait, K. Mazumdar, S. Moretti and D.P. Roy, Phys. Lett. B571 (2003) 184; G. Bélanger et al. in [337].

[452] H. Davoudiasl, T. Han and H. Logan, hep-ph/0412269.

[453] J. Gunion, Phys. Rev. Lett. 72 (1994) 199.

[454] B. Di Girolamo, L. Neukermans, K. Mazumdar, A. Nikitenko and D. Zeppenfeld in Ref. [337].

[455] O. Eboli and D. Zeppenfeld, Phys. Lett. B495 (2000) 147.

[456] J.F. Gunion et al., Int. J. Mod. Phys. A2 (1987) 1035; H. Baer et al., Phys. Rev. D36 (1987) 1363; H. Baer, M. Bisset, D. Dicus, C. Kao and X. Tata, Phys. Rev. D47 (1993) 1062; H. Baer, M. Bisset, C. Kao and X. Tata, Phys. Rev. D50 (1994) 316; M. Bisset, M. Guchait and S. Moretti, Eur. Phys. J. C19 (2001) 143.

[457] F. Moortgat, hep-ph/0105081; F. Moortgat, S. Abdullin, D. Denegri, hep-ph/0112046.

[458] M. Bisset, F. Moortgat and S. Moretti, Eur. Phys. J. C30 (2003) 419; S. Moretti, Pramana 60 (2003) 369; M. Bisset, N. Kersting, J. Li, S. Moretti and F. Moortgat in Ref. [338].

[459] A. Bartl, W. Majerotto and W. Porod, Z. Phys. C64 (1994) 499; ibid. Phys. Lett. B465 (1999) 187; H. Baer, C.H. Chen, M. Drees, F. Paige and X. Tata, Phys. Rev. D59 (1999) 055014; ibid. Phys. Rev. Lett. 79 (1997) 986.

[460] J.F. Gunion et al., Int. J. Mod. Phys. A2 (1987) 1145; H. Baer, M. Bisset, X. Tata and J. Woodside, Phys. Rev. D46 (1992) 303.

[461] D. Denegri, W. Majerotto and L. Rurua, CMS-NOTE-1997-094, hep-ph/9711357; S. Abdullin et al. (CMS Collaboration), J. Phys. G28 (2002) 469; I. Hinchliffe et al. (ATLAS Collaboration), Phys. Rev. D55 (1997) 5520.

[462] A.K. Datta, A. Djouadi, M. Guchait and F. Moortgat, Nucl. Phys. B681 (2004) 31.

[463] H. Baer, ISAJET, F.E. Paige, S.D. Protopopescu and X. Tata, hep-ph/0001086.

[464] S. Abdullin, A. Khanov and N. Stepanov, CMS Note-1994/180; for the he CMS Simulation Package, see http://cmsdoc.cern.ch/cmsim/cmsim.html

[465] N. Marinelli, talk at "Physics at LHC", Vienna, 2004.

[466] For earlier reviews on MSSM Higgs physics in e^+e^- collisions, see for instance: S. Dawson and M. Oreglia, hep-ph/0403015; J. Gunion, H. Haber and R. Van Kooten, hep-ph/0301023; P. Derwent *et al.*, hep-ex/0107044; J. Bagger *et al.*, hep-ex/0007022; E. Accomando, Phys. Rept. 299 (1998) 1; P.M. Zerwas, Acta Phys. Polon. B30 (1999) 1871; H. Murayama and M. Peskin, Ann. Rev. Nucl. Part. Sci. 46 (1996) 533; P.M. Zerwas *et al.*, hep-ph/9605437; A. Djouadi, Int. J. Mod. Phys. A10 (1995) 1.

[467] P.M. Zerwas *et al.*, Proceddings of the ECFA–DESY Workshops *e^+e^- collisions at TeV energies: The physics Potential*, DESY-92-123A-B (1991), DESY-92-123C (1993) and DESY-96-123D (1996).

[468] T. Abe *et al.*, *Linear Collider Physics Resource Book for Snowmass 2001*, hep-ex/0106055-58.

[469] K. Abe *et al.*, *Particle Physics Experiments at JLC*, hep-ph/0109166.

[470] J.A. Aguilar-Saavedra *et al.*, TESLA Technical Design Report, Part III, *Physics at an e^+e^- Linear Collider*, Eds. R.D. Heuer, D. Miller, F. Richard and P. Zerwas, hep-ph/0106315.

[471] The LC notes on the ECFA–DESY Workshops used for the TESLA report and after can be found at: `http://www.desy.de/lcnotes`.

[472] M. Battaglia, A. de Roeck, J. Ellis and D. Schulte (eds), *Physics at the CLIC multi–TeV Linear Collider*, CERN Report CERN–2004–005 (june 2004), hep-ph/0412251.

[473] K. Desch *et al.*, Report of the Higgs Working Group for the *Extended ECFA–DESY Study*, Amsterdam 2003, hep-ph/0311092.

[474] S. Dawson and J.L. Rosner, Phys. Lett. B148 (1984) 497; K. Hikasa, Phys. Lett. 164B (1985) 385 and (E) *ibid.* 195B (1987) 623; W. Kilian, M. Kramer and P.M. Zerwas, Phys. Lett. B373 (1996) 135.

[475] J.F. Gunion, L. Roszkowski, A. Turski, H.E. Haber, G. Gamberini, B. Kayser, S.F. Novaes, F.I. Olness and J. Wudka, Phys. Rev. D38 (1988) 3444.

[476] A. Brignole, J. Ellis, J. F. Gunion, M. Guzzo, F. Olness, G. Ridolfi, L. Roszkowski and F. Zwirner, in Proceedings of the Workshop "e^+e^- Collisions at 500 GeV: The Physics Potential", Ref. [467].

[477] A. Djouadi, GDR-Note S12, unpublished. The program can be found at the web page: `http://www.cern.ch/djouadi/programs.html`.

[478] J. Fleischer and F. Jegerlehner, Nucl. Phys. B216 (1983) 469; B. A. Kniehl, Z. Phys. C55 (92) 605; A. Denner, J. Küblbeck, R. Mertig and M. Böhm, Z. Phys. C56 (92) 261.

[479] P.H. Chankowski, S. Pokorski and J. Rosiek, Nucl. Phys. B423 (1994) 497; V. Driesen and W. Hollik, Z. Phys. C68 (1995) 485.

[480] V. Driesen, W. Hollik and J. Rosiek, Z. Phys. C71 (1996) 259.

[481] S. Heinemeyer, W. Hollik, J. Rosiek and G. Weiglein, Eur. Phys. J. C19 (2001) 535.

[482] A. Denner, S. Dittmaier, M. Roth and M. M. Weber, Nucl. Phys. B660 (2003) 289; G. Bélanger, F. Boudjema, J. Fujimoto, T. Ishikawa, T. Kaneko, K. Kato and Y. Shimizu, Phys. Lett. B559 (2003) 252; F. Jegerlehner and O. Tarasov, Nucl. Phys. Proc. Suppl. 116 (2003) 83; F. Boudjema, J. Fujimoto, T. Ishikawa, T. Kaneko, K. Kato, Y. Kurihara, Y. Shimizu and Y. Yasui, Phys. Lett. B600 (2004) 65.

[483] T. Hahn, S. Heinemeyer and G. Weiglein, Nucl. Phys. B652 (2003) 229.

[484] H. Eberl, W. Majerotto and V. Spanos, Phys. Lett. B538 (2002) 353; *ibid.* Nucl. Phys. B657 (2003) 378.

[485] A. Arhrib, Phys. Rev. D67 (2003) 015003.

[486] T. Farris, J. Gunion, H. Logan and S. Su, Phys. Rev. D68 (2003) 075006.

[487] A. Arhrib, M. Capdequi–Peyranère and G. Moultaka, Phys. Lett. B341 (1995) 313.

[488] A. Arhrib and G. Moultaka, Nucl. Phys. B558 (1999) 3.

[489] J. Guasch, W. Hollik and A. Kraft, Nucl. Phys. B596 (2001) 66.

[490] M. Beccaria, F.M. Renard, S. Trimarchi and C. Verzegnassi, Phys. Rev. D68 (2003) 035014.

[491] M. Beccaria, H. Eberl, F.M. Renard and C. Verzegnassi, Phys. Rev. D69 (2004) 091301; *ibid.* Phys. Rev. D70 (2004) 071301.

[492] A. Djouadi, J. Kalinowski and P. M. Zerwas, Mod. Phys. Lett. A7 (1992) 1765; *ibid.* Z. Phys. C54 (1992) 255.

[493] S. Bar–Shalom, D. Atwood, G. Eilam, A. Soni and R. Mendez, Phys. Rev. D53 (1996) 1162; B. Grzadkowski, J.F. Gunion and X. He, Phys. Rev. Lett. 77 (1996) 5172; J.F. Gunion and X. He, hep-ph/9703330; H. Baer, S. Dawson and L. Reina, Phys. Rev. D61 (2000) 013002; B. Grzadkowski, J.F. Gunion and J. Kalinowski, Phys. Lett. B480 (2000) 287; U. Cotti, A. Guttierrez-Rodriguez, A. Rosado and O. Sampayo, Phys. Rev. D59 (1999) 095011; M. Berggren, R. Keranen and A. Sopczak, Eur. Phys. J. direct C2 (2000) 8; J.F. Gunion, T. Han, J. Jiang, S. Mrenna and A. Sopczak, hep-ph/0112334.

[494] J. Gunion, T. Han, J. Jiang and A. Sopczak, Phys. Lett. B565 (2003) 42.

[495] A. Djouadi, H.E. Haber and P.M. Zerwas, Phys. Lett. B375 (1996) 203; P. Osland, P.N. Pandita, Phys. Rev. D59 (1999) 055013; F. Boudjema and E. Chopin, Z. Phys. C73 (1996) 85; S. Kanemura *et al.*, Phys. Lett. B558 (2003) 157; Y. Yasui *et al.*, hep-ph/0211047; I. Ginzburg and M. Krawczyk, hep-ph/040811; S. Kanemura, Y. Okada and E. Senaha, hep-ph/0410048; S. Kanemura, Y. Okada, E. Senaha and C.P. Yuan, hep-ph/0408364.

[496] T. Farris, J.F. Gunion and H.E. Logan, hep-ph/0202087.

[497] A. Djouadi, V. Driesen and C. Junger, Phys. Rev. D54 (1996) 759.

[498] A. Abbasabadi, D. Bowser-Chao, D.A. Dicus and W. Repko, Phys. Rev. D52 (1995) 3919.

[499] A.G. Ackeroyd, A. Arhrib and M. Capdequi–Peyranère, Mod. Phys. Lett. A14 (1999) 2093; *ibid.* Phys. Rev. D64 (2001) 075007; B. Field, hep-ph/0502195.

[500] S. Kanemura, S. Moretti and K. Odagiri, JHEP 02 (2001) 011.

[501] B.A. Kniehl, F. Madricardo and M. Steinhauser, Phys. Rev. D66 (2002) 054016; A. Gutierrez-Rodriguez and O.A. Sampayo, Phys. Rev. D62 (2000) 055004; H.J. He and C.P. Yuan, Phys. Rev. Lett. 83 (1999) 28; H.J. He, S. Kanemura and C.P. Yuan, Phys. Rev. Lett. 89 (2002) 101803.

[502] S. Moretti, Eur. Phys. J. C34 (2004) 157.

[503] S. Moretti, Eur. Phys. J. direct C4 (2002) 15.

[504] S.H. Zhu, hep-ph/9901221; S. Kanemura, Eur. Phys. J. C17 (2000) 473; A. Arhrib, M. Capdequi-Peyranère, W. Hollik and G. Moultaka, Nucl. Phys. B581 (2000) 34; H.E. Logan and S. Su, Phys. Rev. D66 (2002) 035001; *ibid.* Phys. Rev. D67 (2003) 017703.

[505] O. Brein, hep-ph/0209124.

[506] O. Brein, T. Hahn, S. Heinemeyer and G. Weiglein, hep-ph/0402053.

[507] A.K. Datta, A. Djouadi and J.L. Kneur, Phys. Lett. B509 (2001) 299.

[508] G. Ferrera and B. Mele, hep-ph/0406256.

[509] G. Belanger, F. Boudjema, T. Kon and V. Lafage, Eur. Phys. J. C9 (1999) 511; *ibid.* Eur. Phys. J. C12 (2000) 323.

[510] A.K. Datta *et al.*, in preparation. We thank Aseshkrishna Datta for his efforts in producing the data for this figure and for very useful additional remarks.

[511] J.F. Gunion and H.E. Haber, Phys. Rev. D48 (1993) 5109; D. L. Borden, D. A. Bauer and D. O. Caldwell, Phys. Rev. D48 (1993) 4018; S. Brodsky and P.M. Zerwas, Nucl Instrum. Meth. A355 (1995) 19; M. Baillargeon, G. Bélanger and F. Boudjema, Phys. Rev. D51 (1995) 4712; J. Illana, hep-ph/9912467; S. Soldner-Rembold and G. Jikia, Nucl Instrum. Meth. A472 (2001) 133.

[512] D. Asner *et al.*, hep-ph/0308103.

[513] B. Badelek *et al.*, *The Photon Collider at TESLA*, hep-ph/0108012; A. de Roeck, hep-ph/0311138; E. Boos *et al.*, Nucl. Instrum. Meth. A472 (2001) 100.

[514] M.M. Velasco *et al.*, *Photon–Photon and Electron-Photon Colliders with energies below a TeV*, Snowmass 2001 Study, hep-ex/0111055; D. Asner, J. Gronberg and J.F. Gunion, Phys. Rev. D67 (2003) 035009.

[515] V. Barger, M. S. Berger, J. F. Gunion and T. Han, Phys. Rept. 286 (1997) 1; *ibid.* in *Proc. of the APS/DPF/DPB 2001 Snowmass Study*, hep-ph/0110340; J. Gunion, hep-ph/9707379 and hep-ph/9802258; C. Blöchinger *et al.*, *Physics Opportunities at $\mu^+\mu^-$ Higgs Factories,* hep-ph/0202199.

[516] B. Autin, A. Blondel and J. Ellis (conv.) *et al.*, *Prospective Study of Muon Storage Rings at CERN*, CERN Report 99–02 (1999).

[517] G. Weiglein *et al.* (LHC–LC Study Group), hep-ph/0410364.

[518] P. Garcia-Abia and W. Lohmann, Eur. Phys. J. direct C2 (2000) 2; P. Garcia-Abia, W. Lohmann and A. Resperaza, LC-PHSM-2000-62 in Ref. [471].

[519] K. Desch and N. Meyer, LC Note PHSM-2000; R. van Kooten, talk given at LCWS, Baltimore, March 2001.

[520] K. Desch, T. Klimkovich, T. Kuhl and A. Raspereza, hep-ph/0406229.

[521] A. Andreazza and C. Troncon, Report DESY–123–E in Ref. [466], p. 417.

[522] E. Boos, V. Bunichev, A. Djouadi and H.J. Schreiber, hep-ph/0412194.

[523] M. Muhlleitner, PhD Thesis, hep-ph/0008127.

[524] J. Jersak, E. Laermann and P.M. Zerwas Phys. Rev. D25 (1982) 1218 and (E) *ibid.* D36 (1987) 310; A. Djouadi, J. Kühn and P.M. Zerwas, Z. Phys. C46 (1990) 411; R. Harlander, M. Steinhauser, Eur. Phys. J. C2 (1998) 151; W. Beenakker, S.C. van der Marck and W. Hollik, Nucl. Phys. B365 (1991) 24; V. Driesen, W. Hollik and A. Kraft, hep-ph/9603398; J. Kühn, T. Hahn and R. Harlander, hep-ph/9912262.

[525] W. Beenakker, A. Denner and A. Kraft, Nucl. Phys. B410 (1993) 219; A. Djouadi, M. Drees and H. Konig, Phys. Rev. D48 (1993) 3081; W. Hollik and C. Schappacher, Nucl. Phys. B545 (1999) 98.

[526] P. Eerola and J. Sirkka, Report DESY–123–B in Ref. [466], p. 133; A. Sopczak, Z. Phys. C65 (1995) 449.

[527] A. Kiiskinen, M. Battaglia and P. Pöyhönen, Note LC–PHSM–2001–041; M. Battaglia, A. Ferrari, A. Kiiskinen and T. Maki, hep-ex/0112015.

[528] M. Schumacher, LC-PHSM-2003-096.

[529] R. van Kooten, talk given at the Chicago LC Workshop, Jan. 2002.

[530] P. Chen, G. Horton-Smith, T. Ohgaki, A.W. Weidemann and K. Yokoya, Nucl. Instrum. Meth. A355 (1995) 107.

[531] S.Y. Choi, J. Kalinowski, J.S. Lee, M.M. Mühlleitner, M. Spira and P.M. Zerwas, Phys. Lett. B606 (2005) 164.

[532] M. Mühlleitner, M. Krämer, M. Spira and P. Zerwas, Phys. Lett. B508 (2001) 311.

[533] P. Janot in Ref. [516].

[534] M.S. Berger, Phys. Rev. Lett. 87 (2001) 131801.

[535] H. Fraas, F. von der Pahlen and C. Sachse, Eur. Phys. J. C37 (2005) 495.

[536] E. Asakawa, A. Sugamoto and I. Watanabe, Eur. Phys. J. C17 (2000) 279; E. Asakawa, S. Y. Choi and J. S. Lee, Phys. Rev. D63 (2001) 015012.

[537] H. Fraas, F. Franke, G. Moortgat-Pick, F. von der Pahlen and A. Wagner, Eur. Phys. J. C29 (2003) 587.

[538] S.Y. Choi and M. Drees, Phys. Rev. Lett. 81 (1998) 5509.

[539] S.Y. Choi, M. Drees, B. Gaissmaier and Jae Sik Lee, Phys. Rev. D64 (2001) 095009.

[540] K. Desch and M. Battaglia, LC-PHSM-2001-053.

[541] K. Desch, E. Gross, S. Heinemeyer, G. Weiglein and L. Živković, in Ref. [517].